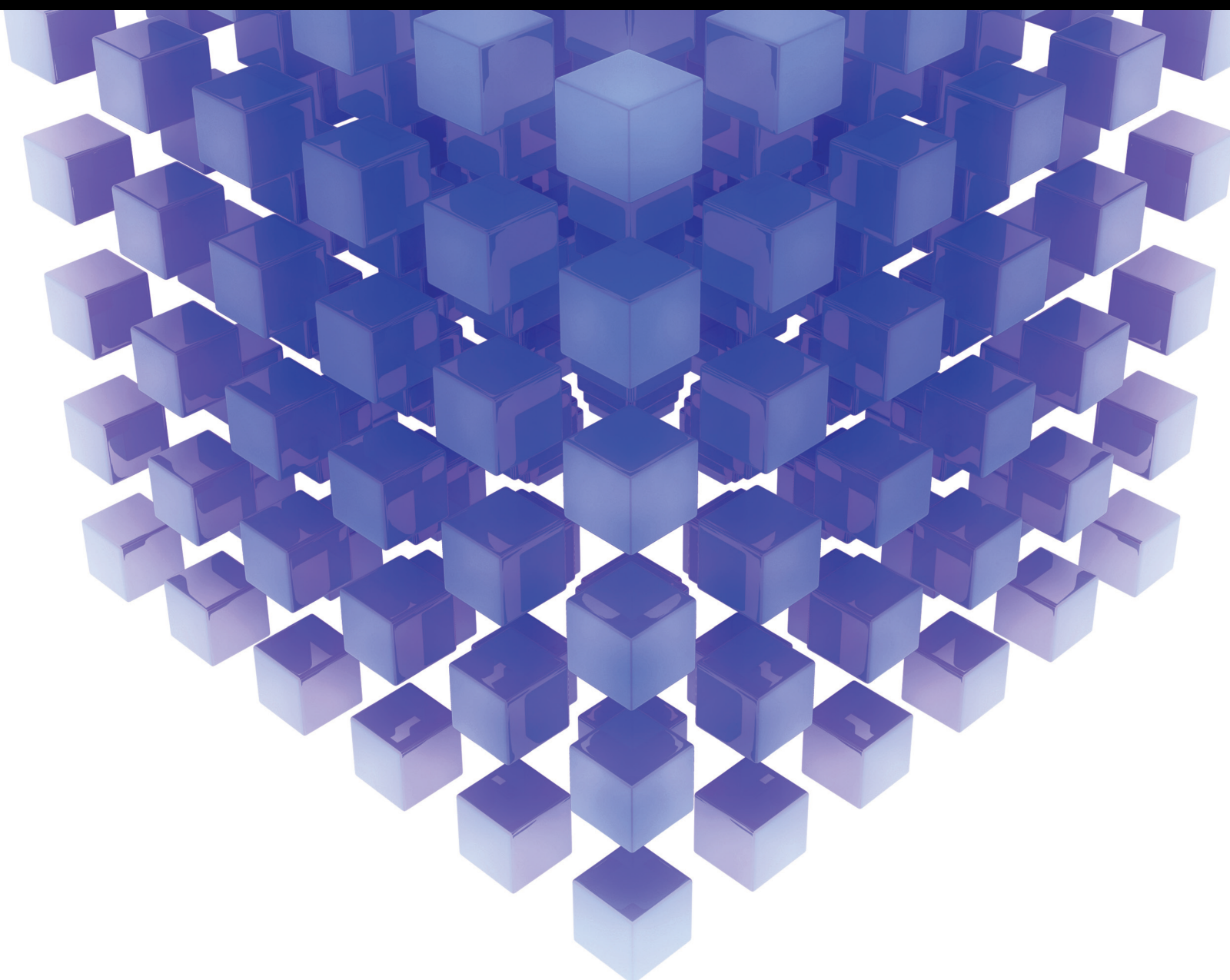# Applied Mathematics and Statistical Mechanics and their Applications

Lead Guest Editor: El-Sayed Abo-Dahab
Guest Editors: A. M. Abd-Alla, Fateh Mebarek-Oudina, and E.M. Khalil

Applied Mathematics and Statistical Mechanics and their Applications

Applied Mathematics and Statistical Mechanics and their Applications

Lead Guest Editor: El-Sayed Abo-Dahab
Guest Editors: A. M. Abd-Alla, Fateh Mebarek-Oudina, and E.M. Khalil

José António Fonseca De Oliveira Correia , Portugal
Jose Renato De Sousa , Brazil
Michael Defoort, France
Alessandro Della Corte, Italy
Laurent Dewasme , Belgium
Sanku Dey , India
Gianpaolo Di Bona , Italy
Roberta Di Pace , Italy
Francesca Di Puccio , Italy
Ramón I. Diego , Spain
Yannis Dimakopoulos , Greece
Hasan Dinçer , Turkey
José M. Domínguez , Spain
Georgios Dounias, Greece
Bo Du , China
Emil Dumic, Croatia
Madalina Dumitriu , United Kingdom
Premraj Durairaj , India
Saeed Eftekhar Azam, USA
Said El Kafhali , Morocco
Antonio Elipe , Spain
R. Emre Erkmen, Canada
John Escobar , Colombia
Leandro F. F. Miguel , Brazil
FRANCESCO FOTI , Italy
Andrea L. Facci , Italy
Shahla Faisal , Pakistan
Giovanni Falsone , Italy
Hua Fan, China
Jianguang Fang, Australia
Nicholas Fantuzzi , Italy
Muhammad Shahid Farid , Pakistan
Hamed Faroqi, Iran
Yann Favennec, France
Fiorenzo A. Fazzolari , United Kingdom
Giuseppe Fedele , Italy
Roberto Fedele , Italy
Baowei Feng , China
Mohammad Ferdows , Bangladesh
Arturo J. Fernández , Spain
Jesus M. Fernandez Oro, Spain
Francesco Ferrise, Italy
Eric Feulvarch , France
Thierry Floquet, France

Eric Florentin , France
Gerardo Flores, Mexico
Antonio Forcina , Italy
Alessandro Formisano, Italy
Francesco Franco , Italy
Elisa Francomano , Italy
Juan Frausto-Solis, Mexico
Shujun Fu , China
Juan C. G. Prada , Spain
HECTOR GOMEZ , Chile
Matteo Gaeta , Italy
Mauro Gaggero , Italy
Zoran Gajic , USA
Jaime Gallardo-Alvarado , Mexico
Mosè Gallo , Italy
Akemi Gálvez , Spain
Maria L. Gandarias , Spain
Hao Gao , Hong Kong
Xingbao Gao , China
Yan Gao , China
Zhiwei Gao , United Kingdom
Giovanni Garcea , Italy
José García , Chile
Harish Garg , India
Alessandro Gasparetto , Italy
Stylianos Georgantzinos, Greece
Fotios Georgiades , India
Parviz Ghadimi , Iran
Ştefan Cristian Gherghina , Romania
Georgios I. Giannopoulos , Greece
Agathoklis Giaralis , United Kingdom
Anna M. Gil-Lafuente , Spain
Ivan Giorgio , Italy
Gaetano Giunta , Luxembourg
Jefferson L.M.A. Gomes , United Kingdom
Emilio Gómez-Déniz , Spain
Antonio M. Gonçalves de Lima , Brazil
Qunxi Gong , China
Chris Goodrich, USA
Rama S. R. Gorla, USA
Veena Goswami , India
Xunjie Gou , Spain
Jakub Grabski , Poland

Francisco J. Martos, Spain
Elio Masciari, Italy
Paolo Massioni, France
Alessandro Mauro, Italy
Jonathan Mayo-Maldonado, Mexico
Pier Luigi Mazzeo, Italy
Laura Mazzola, Italy
Driss Mehdi, France
Zahid Mehmood, Pakistan
Roderick Melnik, Canada
Xiangyu Meng, USA
Jose Merodio, Spain
Alessio Merola, Italy
Mahmoud Mesbah, Iran
Luciano Mescia, Italy
Laurent Mevel, France
Constantine Michailides, Cyprus
Mariusz Michta, Poland
Prankul Middha, Norway
Aki Mikkola, Finland
Giovanni Minafò, Italy
Edmondo Minisci, United Kingdom
Hiroyuki Mino, Japan
Dimitrios Mitsotakis, New Zealand
Ardashir Mohammadzadeh, Iran
Francisco J. Montáns, Spain
Francesco Montefusco, Italy
Gisele Mophou, France
Rafael Morales, Spain
Marco Morandini, Italy
Javier Moreno-Valenzuela, Mexico
Simone Morganti, Italy
Caroline Mota, Brazil
Aziz Moukrim, France
Shen Mouquan, China
Dimitris Mourtzis, Greece
Emiliano Mucchi, Italy
Taseer Muhammad, Saudi Arabia
Ghulam Muhiuddin, Saudi Arabia
Amitava Mukherjee, India
Josefa Mula, Spain
Jose J. Muñoz, Spain
Giuseppe Muscolino, Italy
Marco Mussetta, Italy

Hariharan Muthusamy, India
Alessandro Naddeo, Italy
Raj Nandkeolyar, India
Keivan Navaie, United Kingdom
Soumya Nayak, India
Adrian Neagu, USA
Erivelton Geraldo Nepomuceno, Brazil
AMA Neves, Portugal
Ha Quang Thinh Ngo, Vietnam
Nhon Nguyen-Thanh, Singapore
Papakostas Nikolaos, Ireland
Jelena Nikolic, Serbia
Tatsushi Nishi, Japan
Shanzhou Niu, China
Ben T. Nohara, Japan
Mohammed Nouari, France
Mustapha Nourelfath, Canada
Kazem Nouri, Iran
Ciro Núñez-Gutiérrez, Mexico
Wlodzimierz Ogryczak, Poland
Roger Ohayon, France
Krzysztof Okarma, Poland
Mitsuhiro Okayasu, Japan
Murat Olgun, Turkey
Diego Oliva, Mexico
Alberto Olivares, Spain
Enrique Onieva, Spain
Calogero Orlando, Italy
Susana Ortega-Cisneros, Mexico
Sergio Ortobelli, Italy
Naohisa Otsuka, Japan
Sid Ahmed Ould Ahmed Mahmoud,
Saudi Arabia
Taoreed Owolabi, Nigeria
EUGENIA PETROPOULOU, Greece
Arturo Pagano, Italy
Madhumangal Pal, India
Pasquale Palumbo, Italy
Dragan Pamučar, Serbia
Weifeng Pan, China
Chandan Pandey, India
Rui Pang, United Kingdom
Jürgen Pannek, Germany
Elena Panteley, France
Achille Paolone, Italy

Zaoli Yang (iD), China
Jun Ye (iD), China
Min Ye (iD), China
Luis J. Yebra (iD), Spain
Peng-Yeng Yin (iD), Taiwan
Muhammad Haroon Yousaf (iD), Pakistan
Yuan Yuan, United Kingdom
Qin Yuming, China
Elena Zaitseva (iD), Slovakia
Arkadiusz Zak (iD), Poland
Mohammad Zakwan (iD), India
Ernesto Zambrano-Serrano (iD), Mexico
Francesco Zammori (iD), Italy
Jessica Zangari (iD), Italy
Rafal Zdunek (iD), Poland
Ibrahim Zeid, USA
Nianyin Zeng (iD), China
Junyong Zhai (iD), China
Hao Zhang (iD), China
Haopeng Zhang (iD), USA
Jian Zhang (iD), China
Kai Zhang, China
Lingfan Zhang (iD), China
Mingjie Zhang (iD), Norway
Qian Zhang (iD), China
Tianwei Zhang (iD), China
Tongqian Zhang (iD), China
Wenyu Zhang (iD), China
Xianming Zhang (iD), Australia
Xuping Zhang (iD), Denmark
Yinyan Zhang, China
Yifan Zhao (iD), United Kingdom
Debao Zhou, USA
Heng Zhou (iD), China
Jian G. Zhou (iD), United Kingdom
Junyong Zhou (iD), China
Xueqian Zhou (iD), United Kingdom
Zhe Zhou (iD), China
Wu-Le Zhu, China
Gaetano Zizzo (iD), Italy
Mingcheng Zuo, China

Contents

Research Article

Computing Simplicial Depth by Using Importance Sampling Algorithm and Its Application

Fanyu Meng,[1] **Wei Shao** (ID),[2,3] **and Yuxia Su**[3]

[1]*School of Mathematics, Shandong University, Jinan 250100, China*
[2]*School of Management, Qufu Normal University, Rizhao 276826, China*
[3]*School of Statistics, Qufu Normal University, Qufu 273165, China*

Correspondence should be addressed to Wei Shao; wshao1031@gmail.com

Simplicial depth (SD) plays an important role in discriminant analysis, hypothesis testing, machine learning, and engineering computations. However, the computation of simplicial depth is hugely challenging because the exact algorithm is an NP problem with dimension d and sample size n as input arguments. The approximate algorithm for simplicial depth computation has extremely low efficiency, especially in high-dimensional cases. In this study, we design an importance sampling algorithm for the computation of simplicial depth. As an advanced Monte Carlo method, the proposed algorithm outperforms other approximate and exact algorithms in accuracy and efficiency, as shown by simulated and real data experiments. Furthermore, we illustrate the robustness of simplicial depth in regression analysis through a concrete physical data experiment.

1. Introduction

With the development of computer technology and multivariate statistical analysis, scientists deal with a large amount of multidimensional data in many fields, such as biogenetics and industrial engineering. The demand for multivariate data analysis tools has become increasingly urgent. As a powerful multivariate nonparametric and robust statistical tool, the statistical depth function extends the concept of one-dimensional data order statistics and provides the central-outward sorting of multivariate data [1–4]. In recent years, the interest of researchers in statistical depth has increased due to the extensive application of the statistical depth function in multivariate statistical analysis, robust estimation, discriminant analysis, hypothesis testing, machine learning, economics, and hydrological data analysis [5, 6].

The first statistical depth function concept, which was proposed by Tukey in 1975, is known as the halfspace depth (also known as the Tukey depth) [7–9]. The other concepts of the statistical depth function include projection depth [3, 10], simplicial depth (SD) [11, 12], and regression depth

[13, 14]. Zuo and Serfling defined a general structural property of the statistical depth function [1]. Among the many concepts of this statistical depth function, SD is a relatively attractive one not only because of its simple form and ability to achieve the maximum depth value in the center and satisfy monotonicity but also because of its important applications in sign test and centralization test [1, 12].

However, the computation of SD is complicated. The exact calculation of SD is an NP problem, which is only feasible when the dimension is no higher than three. Serfling and Wang emphasized that the computation of SD for higher-dimensional data still requires further study [12]. The computation and application of the statistical depth function are active research topics.

Similarly, Monte Carlo (MC) methods have become important statistical, computational tools that are widely used in finance, engineering computation, genetic biology, computational chemistry, and other related fields [15–18]. As a critical MC strategy, the importance sampling (IS) method concentrates most of the test samples in the important area of the objective function by introducing the transfer probability density function [15, 19]. This method

dramatically improves the computational efficiency and is an important MC acceleration algorithm. In this study, we apply an efficient IS algorithm to the approximate computation of SD and demonstrate the advantages of such an algorithm over other MC methods and exact algorithms through simulated and real data examples. Furthermore, we extend the SD to regression analysis and obtain a robust estimation of regression analysis. The results of a real physical data experiment show that the estimation based on the SD method is more robust than that based on the traditional least squares (LS) method.

The remainder of this paper is organized as follows. In Section 2, we review the preliminary concept and existing algorithms for SD. Section 3 describes the IS algorithm used for the computation of SD. The advantages of the IS algorithm are illustrated through simulated data examples in Section 4. The extension of SD to regression analysis and a real data experiment are presented in Section 5. Lastly, the conclusions are provided in Section 6.

2. Preliminary of SD and the State of the Art

In this section, we present the preliminary of SD and the existing algorithms for its computation.

Consider a sample set $\mathbf{X}^n = \{\mathbf{X}_1, \mathbf{X}_2, \ldots, \mathbf{X}_n\}$ in $\mathbb{R}^d$, $(d \geq 2)$, where $\mathbf{X}^n$ is one sample of size n in $\mathbb{R}^d$ and $\mathbf{x}$ is a given point in $\mathbb{R}^d$. The sample version [11] of SD of $\mathbf{x}$ with respect to the sample set $\mathbf{X}^n$ is expressed as

$$\text{SD}\left(\mathbf{x}, \mathbf{X}^n\right) = \frac{1}{C_n^{d+1}} \sum_{1 \leq i_1 < \cdots < i_{d+1} \leq n} \mathbf{1}_{\left\{\mathbf{x} \in S\left[\mathbf{X}_{i_1}, \ldots, \mathbf{X}_{i_{d+1}}\right]\right\}}, \quad (1)$$

where $\mathbf{1}_{\{A\}}$ denotes the indicator function of event A, and $S[\mathbf{X}_{i_1}, \ldots, \mathbf{X}_{i_{d+1}}]$ denotes the simplex determined by the $d + 1$ sample points $\{\mathbf{X}_{i_1}, \ldots, \mathbf{X}_{i_{d+1}}\}$.

Serfling and Wang stated that no algorithms are faster than simply generating all simplices and counting the ones enclosing the given point (using $O(n^{d+1})$ complex time) when dimension $d \geq 5$ [12]. Therefore, designing an efficient approximate algorithm for the computation of SD is necessary.

A direct MC method for the computation of SD contains two steps: (1) randomly selecting $d + 1$ points from $\mathbf{X}^n$ and then (2) taking the average of the points that enclose the given point $\mathbf{x}$ (i.e., using $\widehat{\text{SD}}(\mathbf{x}, \mathbf{X}^n)$ to estimate the true SD value $\text{SD}(\mathbf{x}, \mathbf{X}^n)$).

$$\widehat{\text{SD}}\left(\mathbf{x}, \mathbf{X}^n\right) = \frac{1}{M} \sum_{i=1}^{M} \mathbf{1}_{\left\{\mathbf{x} \in S\left[\mathbf{X}_{i_1}, \ldots, \mathbf{X}_{i_{d+1}}\right]\right\}}, \quad (2)$$

where $\{\mathbf{X}_{i_1}, \ldots, \mathbf{X}_{i_{d+1}}\}$ is randomly chosen from $\mathbf{X}^n$ and M is the trying number for the estimation.

Another approach for the computation of SD is the use of the IS algorithm, which is the proposed method in this study. The computation of SD is an expectation computation. Therefore, SD can be estimated by the IS algorithm. The simple MC method uses the randomly selected $d + 1$ points to estimate the SD, whereas the IS approach selects $d + 1$ points with a high probability that they contain the given point $\mathbf{x}$. Theoretically, the results of the latter will have a

smaller variance than those of the former. The simulated data examples in Section 4 illustrate the advantage of the IS algorithm over the MC method.

3. New Algorithm for SD in R^d

3.1. Overview of the IS Algorithm.
Many engineering problems can be expressed as computations of a multidimensional integral. Using the MC method to compute the integral involves drawing samples from a uniform distribution on a regular area and using the sample mean to approximate the true integral. In higher-dimensional cases, the efficiency of the MC method is extremely low if the region where the target function is not equal to zero is extraordinarily sparse. On the contrary, the IS algorithm draws most samples in the important area. This strategy improves the efficiency of the integral computation. The IS algorithm plays an important role in the field of statistical physics, molecular simulation, and Bayesian statistics.

For example, we want to compute the integral of $h(\mathbf{x})$ on region A; that is,

$$\mu = \int_A h(\mathbf{x}) \mathrm{d}x, \quad (3)$$

and the integral computation (3) can be treated as an expectation calculation:

$$\mu = E_\pi\left(\frac{h(\mathbf{X})}{\pi(\mathbf{X})}\right), \quad (4)$$

where $\mathbf{X}$ is a random variable (r.v.) with its own probability density function (p.d.f.) $\pi(\mathbf{x})$; that is, $\mathbf{X} \sim \pi(\mathbf{x})$. If $\mathbf{X}_1, \ldots, \mathbf{X}_n$ denote samples with size n from $\mathbf{X}$, the MC method draws $\mathbf{X}$ from a uniform distribution on region A. From the Law of Large Numbers [20], the sample mean can be used to estimate the expectation in (4) as

$$\widehat{\mu} = \frac{1}{n} \sum_{i=1}^{n} h\left(\mathbf{X}_i\right) \cdot S(A), \quad (5)$$

where $S(A)$ is the area of A and $\mathbf{X}$ is the r.v. from the uniform distribution on A $(\mathbf{X} \sim U(\mathbf{x}))$.

However, the efficiency of the MC method (5) will be extremely low if region A is extremely wide or sparse (especially in high-dimensional cases). By contrast, the IS method uses a special p.d.f. $g(\mathbf{x})$ instead of $\pi(\mathbf{x})$ in (4) to compute mean μ and utilizes the corresponding sample mean to estimate the expectation in (4):

$$\widetilde{\mu} = \frac{1}{n} \sum_{i=1}^{n} \frac{h\left(\mathbf{X}_i\right)}{g\left(\mathbf{X}_i\right)}, \quad (6)$$

and the variance $\text{Var}(\widetilde{\mu}) = 1/n\text{Var}(h(\mathbf{X}_i)/g(\mathbf{X}_i))$, which means that we can choose appropriate $g(\mathbf{x})$ close to $h(\mathbf{x})$ to reduce the variance of $\widetilde{\mu}$. In extreme situations, if we select $g(\mathbf{x}) \propto h(\mathbf{x})$, that is, $g(\mathbf{x}) = c \cdot h(\mathbf{x})$ (where $c = 1/\int_A h(\mathbf{x})\mathrm{d}\mathbf{x}$), the variance of $\widetilde{\mu}$ will drop to zero, and $\widetilde{\mu}$ is equal to the exact value $\int_A h(\mathbf{x})\mathrm{d}\mathbf{x}$. However, we cannot directly use the IS method defined in (6) during such an extreme situation because we do not know the exact value of $\int_A h(\mathbf{x})\mathrm{d}\mathbf{x}$ in advance.

Nevertheless, it gives us a significant hint that the closer $g(\mathbf{x})$ and $h(\mathbf{x})$ are, the more accurate the IS method's result is. The steps of the IS method for the computation of integral (3) are listed as follows:

(1) Draw the samples ∞ from $g(\mathbf{x})$.

(2) Compute the importance weights $\omega_i = h(\mathbf{x}_i)/g(\mathbf{x}_i)$.

(3) Use the mean of the computed weights to estimate the integral in (3):

$$\widetilde{\mu} = \frac{1}{n} \sum_{i=1}^{n} \omega_i. \tag{7}$$

The following theorem shows that the IS estimator in (7) is unbiased.

Theorem 1. *The IS estimator $\widetilde{\mu}$ in (7) is an unbiased estimator of μ.*

Proof. To prove that the IS estimator is unbiased, we only need to show that the expectation of $\widetilde{\mu}$ is equal to μ:

$$
\begin{aligned}
E(\widetilde{\mu}) &= E\left(\frac{1}{n} \sum_{i=1}^{n} \omega_i\right) \\
&= \frac{1}{n} \sum_{i=1}^{n} E(\omega_i) \\
&= E(\omega_i).
\end{aligned} \tag{8}
$$

Because ω_i is a r.v. and $\omega_i = h(\mathbf{X}_i)/g(\mathbf{X}_i)$,

$$
\begin{aligned}
E(\omega_i) &= E\left(\frac{h(\mathbf{X}_i)}{g(\mathbf{X}_i)}\right) \\
&= \int_A \frac{h(\mathbf{x})}{g(\mathbf{x})} \cdot g(\mathbf{x}) d\mathbf{x} \\
&= \int_A (\mathbf{x}) d\mathbf{x} \\
&= \mu.
\end{aligned} \tag{9}
$$

We obtain the expression $E(\widetilde{\mu}) = \mu$, which verifies that the IS estimator $\widetilde{\mu}$ in (7) is unbiased. So we complete the proof of this theorem.

Aside from being an unbiased estimator of the integral presented in (3), the IS estimator exhibits a more efficient and powerful integral computation than the MC estimator defined in (5), especially in higher-dimensional cases. □

3.2. IS Algorithm for SD Computation. We use the previously described IS method to compute the SD. Using the definition of SD in (1) is not appropriate in computing the SD value of a data point with respect to a dataset. The MC method in (6) becomes extremely inefficient when dimension p or sample size n is excessively large because the number of simplices containing the original data point decreases with the increase in p or n.

The IS algorithm can transform the original p.d.f. into a highly efficient one that can construct the simplex containing the original data point. In the computation of SD, the MC method randomly selects p data points to construct the simplex, whereas the IS method chooses the data points that are likely to let the original data point inside the simplex. Figure 1 is a 2D example that is composed of 20 sample data points. The data point x_0 is used to compute the SD value. After sampling the two data points (x_1 and x_2), only two more (x_3 or x_4) are needed to construct the simplex that contains the original data point x_0. In this illustrated example, we do not need to count all the simplices after getting x_1 and x_2; only x_3 or x_4 is considered as the final vertex of the simplices containing x_0.

We list the details of the IS algorithm for the computation of SD in high-dimensional cases. Suppose that $\mathbf{X}^n$ is a sample with size n in $\mathbb{R}^d$ (i.e., $\mathbf{X}^n = \{\mathbf{X}_1, \mathbf{X}_2, \ldots, \mathbf{X}_n\}$) and x is a given point in $\mathbb{R}^d$, ($d \geq 2$). The data points are in general position (i.e., any d data points can define a unique $d-1$-dimensional hyperplane in $\mathbb{R}^d$). The procedure of using the IS algorithm to compute SD (i.e., the computation of $\mathrm{SD}(\mathbf{x}, \mathbf{X}^n)$) is summarized as follows:

(1) Set the IS parameters, including the number of samples tries N.

(2) Let $t = 1, 2, \ldots, N$. Compute the importance weight ω_t for the t-th sample try.

  (i) Randomly choose d sample points from $\{\mathbf{X}_1, \mathbf{X}_2, \ldots, \mathbf{X}_n\}$, and denote them as $\{\mathbf{X}_1^t, \mathbf{X}_2^t, \ldots, \mathbf{X}_d^t\}$.

  (ii) Let $k = 1, \ldots, d$, and compute the simplex data point set $\mathcal{U}_k^t$ (i.e., the datasets consist of the possible data points that can construct a simplex containing the original data point $\mathbf{x}$).

    Replace the k-th data point $\mathbf{X}_k^t$ with the original data point x to obtain a dataset P_k^t with size d (i.e., $P_k^t = \{X_1^t, \ldots, X_{k-1}^t, x, X_{k+1}^t, \ldots, X_d^t\}$).
Compute the unique director $\mathbf{d}_k^t$ which is perpendicular to the hyperplane determined by P_k^t.
Project all data points $\{\mathbf{X}_1, \mathbf{X}_2, \ldots, \mathbf{X}_n\}$ and $\mathbf{x}$ along $\mathbf{d}_k^t$, and compute the projected value $\{x_{t,k}^l\}$, where $t = 1, \ldots, N; k = 1, \ldots, d$; and $l = 0, 1, \ldots, n$, and $x_{t,k}^0$ is the projected value of $\mathbf{x}$ along $\mathbf{d}_k^t$.
Compute the simplex data point set $\mathcal{U}_k^t = \{\mathbf{X}_l \mid (x_{t,k}^l - x_{t,k}^0) \times (x_{t,} \quad k^k - x_{t,k}^0) < 0, l = 1, \ldots, n\}$.

  (iii) Let $\mathcal{U}^t = \cap_{k=1}^d \mathcal{U}_k^t$, and set $\omega_t = \#\{\mathcal{U}^t\}/(n-d)$, where $t = 1, \ldots, N$.

(3) The sample mean of ω_t ($t = 1, \ldots, N$) can be treated as the IS estimator of $\mathrm{SD}(x, X_n)$; that is,
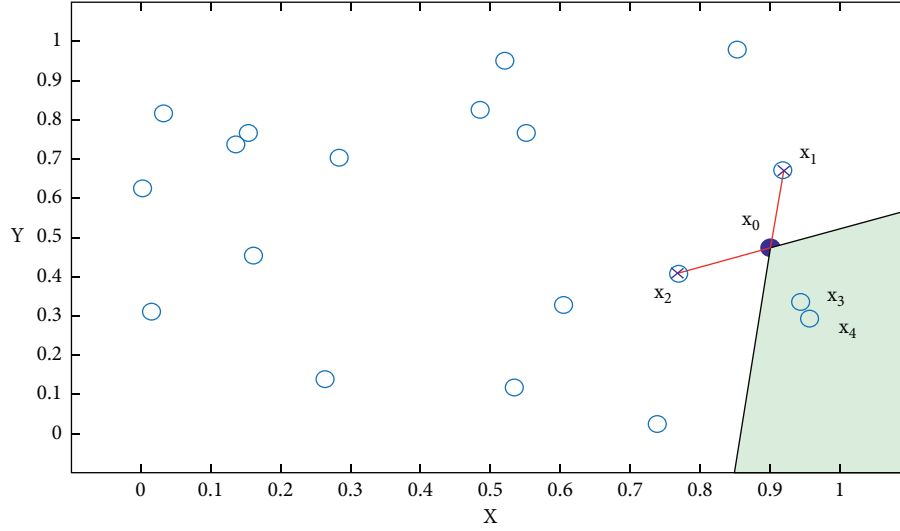
FIGURE 1: A 2D simulated example (sample size = 20) which indicates that only two possible trilaterals (or simplices) can contain the original data point x_0 (the vertexes of the trilaterals are $\{x_1, x_2, x_3\}$ and $\{x_1, x_2, x_4\}$).

$$\widetilde{SD}(\mathbf{x}, \mathbf{X}_n) = \frac{1}{N} \sum_{t=1}^{N} \omega_t. \qquad (10)$$

Theorem 2. *The computational complexity of using the IS algorithm to calculate SD is*

$$O(Nd^5 n), \qquad (11)$$

where N is the number of samples tries of the IS algorithm, d is the dimension of the sample data, and n is the sample size.

Proof. According to the steps for computing SD using the IS algorithm, we need to compute every ω_i for $i = 1, \ldots, N$. For every ω_i, every selected sample data point $\mathbf{X}_k^t$ for $k = 1, \ldots, d$ must be replaced. The computational complexity of finding the unique director perpendicular to the hyperplane is $O(d^3)$, whereas that of projecting all data points to the unique director is $O(dn)$. The total computational complexity is $O(Nd^5 n)$. Then we complete the proof of this theorem.

Theorem 2 shows that the computational complexity of the IS algorithm for the computation of SD is a polynomial with dimension d and sample size n as its input arguments. While all other exact algorithms for the computation of SD are NP problems, especially when the dimension $d \geq 5$, there is no algorithm that can run faster than simply generating all simplices and computing the exact SD value (i.e., using $O(n^{d+1})$ time) [12]. According to the definition of the IS algorithm in (7) and Theorem 1, the IS estimator defined in (10) is an unbiased estimator of $SD(\mathbf{x}, \mathbf{X}_n)$. $\square$

4. Performance Comparison

This section presents simulated and real data examples of SD computation. All results are obtained using R (version X64 3.6.2) and MATLAB (R2017a) on a Lenovo K42-80 laptop computer (Intel(R) Core(TM) i7-6500U CPU@2.5 GHz, RAM 16.00 GB, Windows 10). The R and MATLAB codes for the results in this section are available upon request from the corresponding author.

4.1. 2D Simulated Data Example. In the simulated data experiment, we compare the computed SD results of the IS, exact, and approximate algorithms, including the MC method. The simulated dataset is sampled from a 2D multivariate normal distribution (i.e., $N(\overrightarrow{\mathbf{0}}_2, \mathbf{E}_2)$, where $\overrightarrow{\mathbf{0}}_2$ is 2D zeros vector and $\mathbf{E}_2$ is a 2D unit matrix), and the sample size is 100.

We used the exact algorithm [21], the MC method, and the IS algorithm to compute the SD. The selected points $\mathbf{x}$ are $(0, 0)$, $(0.5, 0.5)$, $(1, 1)$, and $(2, 2)$. We used the exact and approximate algorithms to compute the SD of $\mathbf{x}$ with respect to the dataset. The number of random simplices was set to 100 for the MC and IS algorithms. All computations were repeated 50 times. The computed results (mean, standard deviation (sd), and total CPU time (s)) are summarized in Table 1 and Figure 2.

Since there is an exact algorithm for the SD computation in the 2D case, we can evaluate the accuracy of the IS and MC methods through their mean values and sd values. Moreover, the total CPU time consumed by every algorithm can reflect its efficiency. So, in this experiment, we use these three indicators (mean, sd, and total CPU time) to compare the performances of these algorithms (exact, MC, and IS methods) for the computation of SD.

The results reveal that (1) the exact algorithm consumes less CPU time (approximately 0.1 s), (2) the approximate algorithms (MC and IS) can achieve accurate results because their means are extremely close to the exact value, (3) IS performs better than MC as indicated by the smaller sd of the results of the former compared with those of the latter under the same CPU time, (4) all computed SD results from exact and approximate algorithms are zeros at point $(2, 2)$, which means that $(2, 2)$ is outside the data cloud, and (5), with the

TABLE 1: Computed results (mean, sd, and total CPU time in s) from different algorithms (exact, MC, and IS) in 2D experiments.

		Exact	MC	IS
$(0, 0)$	Mean	0.2407	0.2380	0.2437
	sd	0	0.0420	0.0150
	Time	0.099	1.545	1.229
$(0.5, 0.5)$	Mean	0.1607	0.1528	0.1608
	sd	0	0.0326	0.0177
	Time	0.149	1.51	1.364
$(1, 1)$	Mean	0.054 5	0.059 4	0.055 9
	sd	0	0.024 5	0.012 7
	Time	0.125	1.587	1.332
$(2, 2)$	Mean	0	0	0
	sd	0	0	0
	Time	0.223	1.594	1.492
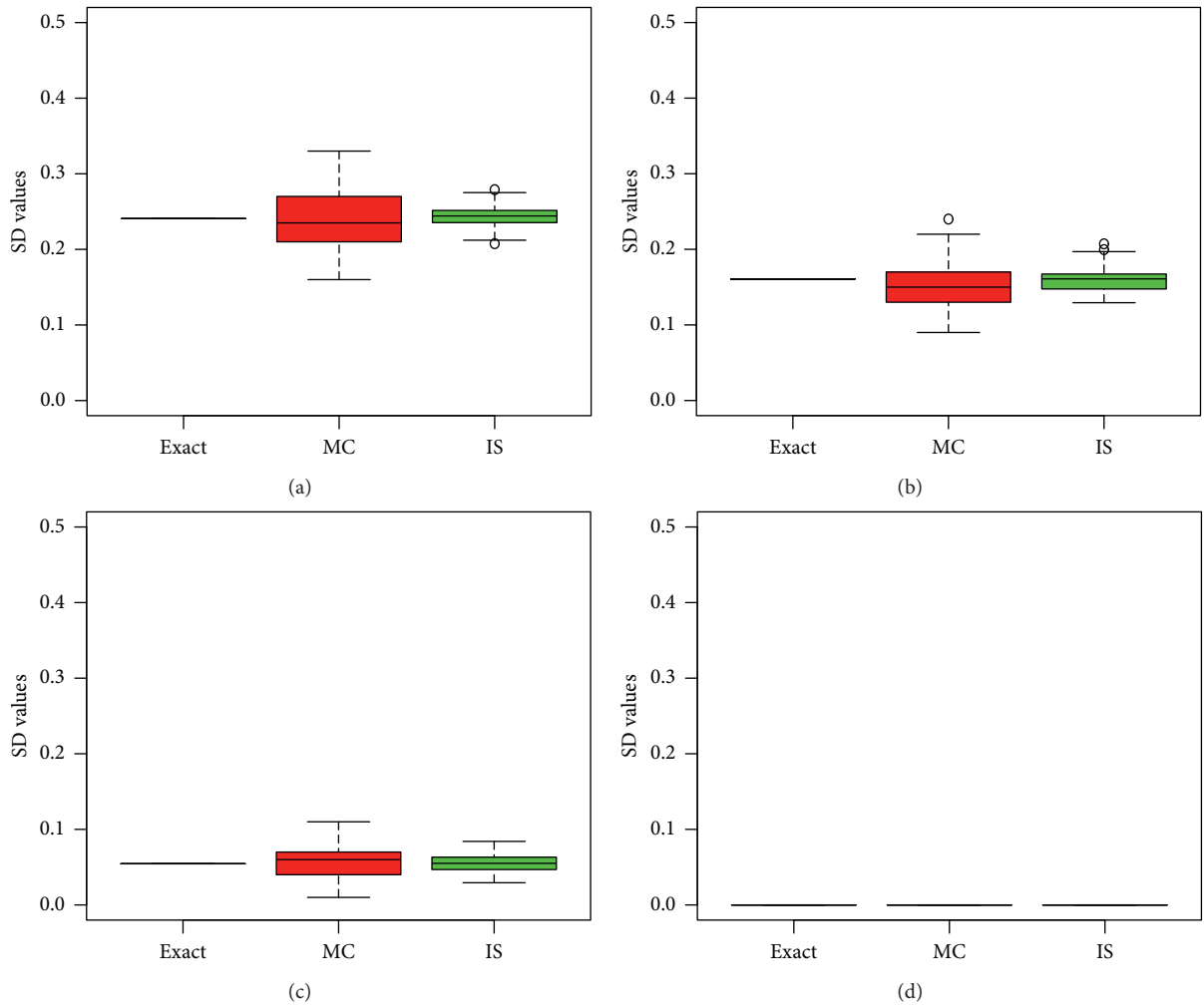
FIGURE 2: Boxplots of the results from different algorithms (exact, MC, and IS) in 2D experiments. (a–d) The results from the computed SD of $(0, 0)$, $(0.5, 0.5)$, $(1, 1)$, and $(2, 2)$, respectively.

exact algorithm, the simulated example also indicates that the IS algorithm can obtain highly accurate results.

4.2. Higher-Dimensional Simulated Data Example.
In this subsection, we compute the SD of different data points by using the MC and IS algorithms in 3D and five-dimensional simulated dataset. We did not use the exact algorithm [21] because it cannot obtain any result within three hours.

In the 3D case, the dataset was sampled from $N(\vec{\mathbf{0}}_3, \mathbf{E}_3)$, and the sample size was 1000. We used MC and IS methods to compute the SD of points $(0, 0, 0)$, $(0.5, 0.5, 0.5)$, and

TABLE 2: Results (mean, sd, and total CPU time in s) were obtained by MC and IS methods with respect to different data points in 3D experiments.

	$(0, 0, 0)$	$(0.5, 0.5, 0.5)$	$(1, 1, 1)$	Total CPU time
MC	$0.1254\,(0.0330)$	$0.0460\,(0.0242)$	$0.0054\,(0.0073)$	5.13
IS	$0.1280\,(0.0121)$	$0.0449\,(0.0078)$	$0.0050\,(0.0033)$	5.23

The sd values are listed in the parentheses behind the mean values.
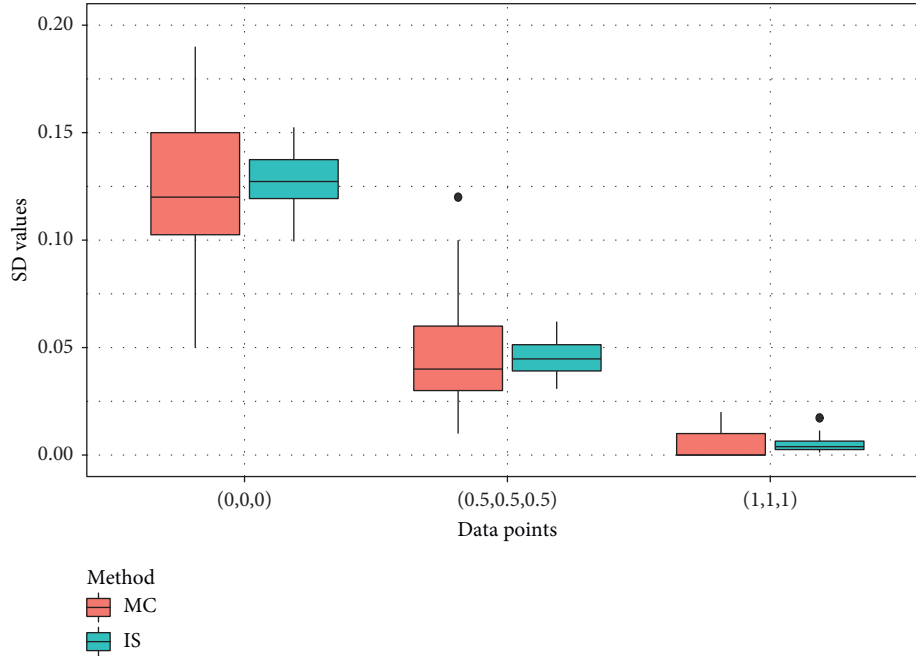
FIGURE 3: Boxplots of the results obtained by MC and IS methods in 3D experiments.

$(1, 1, 1)$. We set the number of random simplices to 100 and repeated the computation 50 times. The computed results are summarized in Table 2 and Figure 3.

Because the exact algorithm cannot get any computed SD results within three hours when dimension $d \geq 3$, we can only use MC and IS methods for the computation of SD in this subsection. Three indicators (mean, sd, and total CPU time) are summarized for the evaluation of the approximate methods. The mean values can be seen as the final computed SD results and the sd reflects the accuracy of the method (the smaller, the more accurate). The total CPU time reflects the efficiency of the method because it is more efficient if the method consumes less CPU time in the same computation of SD.

Table 2 and Figure 3 indicate that (1) the computed SD results decrease when the data points are changed from $(0, 0, 0)$ to $(1, 1, 1)$; the data point $(0, 0, 0)$ is deeper than the data point $(1, 1, 1)$ with respect to the dataset; (2) the two methods have similar computational efficiencies because they consume almost the same total CPU time; (3) the sd obtained by the IS method is smaller than that calculated by the MC method, which means that the former is more accurate than the latter in this case.

In the five-dimensional case, the dataset was sampled from $N(\overrightarrow{\mathbf{0}}_5, \mathbf{E}_5)$, and the sample size was 1000. We used

MC and IS methods to compute the SD of points $(0, 0, 0, 0, 0)$, $(0.5, 0.5, 0.5, 0.5, 0.5)$, and $(1, 1, 1, 1, 1)$. The number of random simplices was 100, and the computations were repeated 50 times. The computed results (mean, sd, and total CPU time in s) are presented in Table 3 and Figure 4.

Table 3 and Figure 4 show that (1) the computed SD values decrease when the data points are changed from $(0, 0, 0, 0, 0)$ to $(1, 1, 1, 1, 1)$, thereby suggesting that the former is deeper than the latter; (2) the SD values in the five-dimensional examples are slightly smaller than those in 3D examples because the sparsity of the data points increases when the dimension is increased from three to five; (3) the IS algorithm performs better than the MC approach as indicated by the smaller sd of the results of the former compared with those of the latter; (4) the two approximate algorithms consume almost the same CPU time; (5) even after using 100 random simplices, the MC algorithm cannot find any simplex containing point, whereas the IS algorithm can identify many simplices. In conclusion, the IS method outperforms the MC method in terms of accuracy in these simulated examples.

We also evaluated the MC and IS methods with other numbers of random samples tries in different datasets. The findings show that the result's accuracy increases with the

TABLE 3: Results (mean, sd, and total CPU time in s) were obtained by MC and IS methods in five-dimensional experiments.

	$(0, 0, 0, 0, 0)$	$(0.5, 0.5, 0.5, 0.5, 0.5)$	$(1, 1, 1, 1, 1)$	Total CPU time
MC	0.0360 (0.0160)	0.0036 (0.0066)	0 (0)	7.67
IS	0.0315 (0.0076)	0.0028 (0.0023)	2.8×10^{-6} (7.3×10^{-6})	8.42

The sd values are listed in the parentheses behind the mean values.
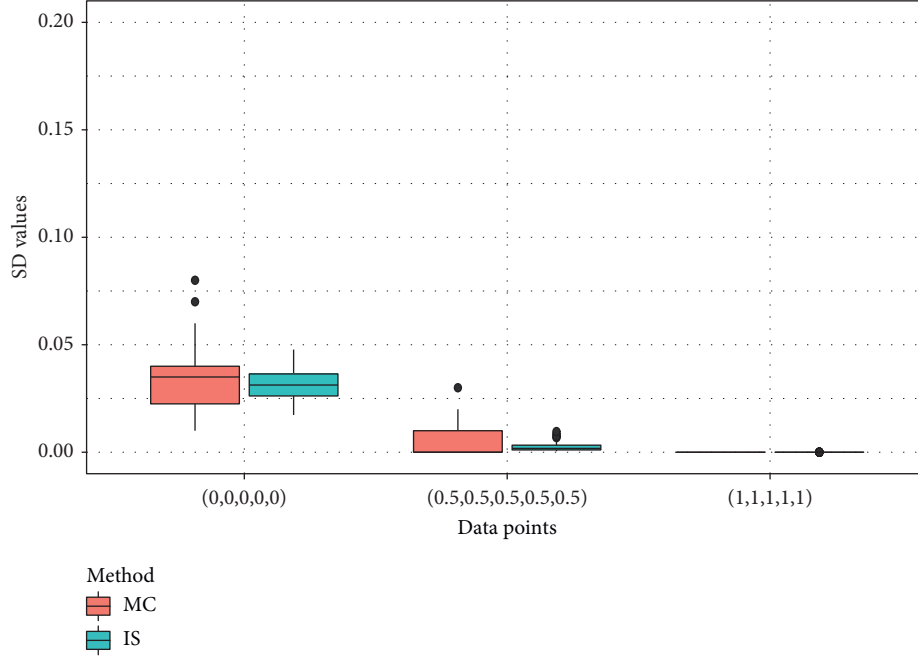
FIGURE 4: Boxplots of the results obtained by MC and IS methods in five-dimensional experiments.

increase in the number of random samples tries. In addition, the number of random samples tries can be used by IS method in lots of datasets. It is found in our experiments that, if we set the number of random samples tries $N = 1000$, the IS method can obtain the computed SD results within one second when dimension $d \leq 10$ and sample size $n \leq 10000$.

5. Application to Regression and Real Data Example

One of the most important extensions of SD is the robust estimation of regression based on SD. To demonstrate the relevant concept, we consider the linear regression model as follows:

$$Y = \alpha + \beta X + \varepsilon, \quad (12)$$

where random variables X and Y are in R^1, $\varepsilon \sim N(0, \sigma^2)$, and α, β, and σ^2 are unknown parameters.

Considering that $SD(\mathbf{x}, \mathbf{X}^n)$ can measure the depth of $\mathbf{x}$ with respect to $\mathbf{X}^n$, we extend the definition of SD to regression (12) and determine the simplicial regression depth:

$$SD(\theta, \mathbf{W}^n) = \binom{n}{3}^{-1} \sum_{i<j<k} A\left(r_i(\theta), r_j(\theta), r_k(\theta)\right), \quad (13)$$

where $\theta = (\alpha, \beta)$ are the parameters, $\mathbf{W}^n = (Y^n, X^n)$ are the samples of the model defined in (12), and $r_i(\theta) = Y_i - \alpha - \beta X_i$ is the residual based on the i-th sample and

$$A\left(r_i(\theta), r_j(\theta), r_k(\theta)\right)$$
$$= \begin{cases} 1, & r_i(\theta), r_j(\theta), r_k(\theta) \text{ have alternating signs,} \\ 0, & \text{otherwise.} \end{cases} \quad (14)$$

The SD based estimator of (12) can be defined as the maximum of $SD(\theta, \mathbf{W}^n)$; that is,

$$\widehat{\theta}_{SD} = \arg\max_\theta SD(\theta, \mathbf{W}^n). \quad (15)$$

We consider the physical experiment data concerning the relationship between the atmospheric pressure and boiling point of water, which was discussed by a Scottish physicist named James D. Forbes [22]. In the mid-nineteenth century, this experiment can illustrate whether the simple measurement of the boiling point of water can substitute for the direct reading of the barometric pressure. The dataset was collected in the Alps in Scotland (Table 4 and Figure 5).

The linear regression model in (12) was used to fit the Forbes dataset. We used LS and SD methods to estimate the parameters of the model in (12). The function "lm" in R Stats package ("stat") can be used to determine the LS estimator of

TABLE 4: Forbes data collected in Alps and Scotland. The temperature is measured using the boiling point (°F) and the pressure is obtained using barometric pressure (mmHg).

No.	Temperature	Pressure
1	194.5	20.79
2	194.3	20.79
3	197.9	22.40
4	198.4	22.67
5	199.4	23.15
6	199.9	23.35
7	200.9	23.89
8	201.1	23.99
9	201.4	24.02
10	201.3	24.01
11	203.6	25.14
12	204.6	26.57
13	209.5	28.49
14	208.6	27.76
15	210.7	29.04
16	211.9	29.88
17	212.2	30.06

the model in (12). For the SD based method, we combined quasi-Newton [23] and IS methods to find the maximum point of (15). Moreover, we performed three statistical tests (i.e., the R square value, normality test, and the test of goodness of fit [24]) for every fitted regression model to get a more insightful analysis. The R square (or adjusted R square) value from the significance test gives the percentage that the dependent variable (Y) can be explained by the fitted model ($\alpha + \beta X$) (see (12)). The normality test is used to test whether the residuals of the fitted model obey normal distribution which is the basis of other statistical tests. For example, under the assumption of normality, the F statistic value in the test of goodness of fit can be used to determine whether the fitted regression model makes sense.

We first used the LS method and SD approaches to compute the linear regression model with the original Forbes dataset (Table 4, denoted as original data in this section). The computed regression results are summarized in Table 5 and Figure 5(a); their corresponding statistical tests are summarized in Table 6 and Figure 6.

Table 5 and Figure 5(a) show that the LS and SD estimators obtained the very similar intercept parameter and slope parameter. This finding suggests that the SD method can capture the same accurate regression results compared with LS method.

The statistical test results have also confirmed the finding since the results from LS and SD methods were also very similar. They have very high R square values which indicate more than variance of the dependent variable that can be explained by the fitted model. Under significance level 0.01, we accept the assumption of normality and they pass the goodness of fit test (i.e., the p value of F statistic is almost zero). In addition, if one needs a higher level of significance (such as 0.05) in this example, then some statistical techniques (e.g., Box-Cox transformation or strong influence points detection) can be used to improve the regression model (see more details in [22]). However, this is another
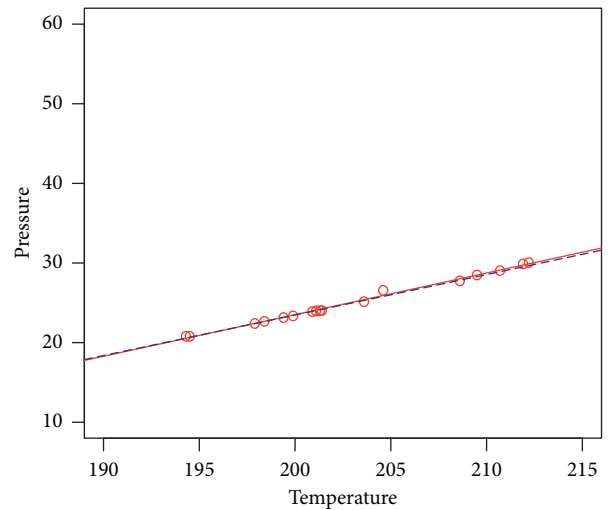
(a)
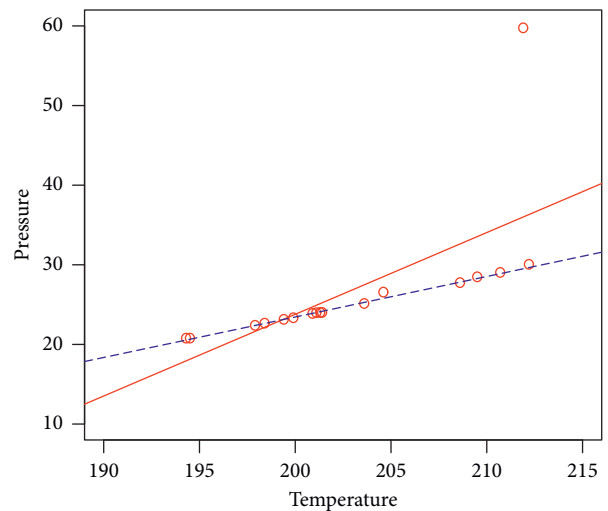
(b)

FIGURE 5: Regression analysis results from original (a) and contaminated (b) datasets.

research topic and there is a lack of sample points in this example; we only focus on the robustness of the regression model computed from different methods, especially when the dataset is contaminated, and that is what we do in the next experiment.

In the following experiment, we worked with a contaminated dataset from Forbes data. We intentionally changed the pressure of the 16th data point from 29.88 to 59.76. The new dataset was denoted as the contaminated data (Figure 5(b)). We compared the SD and LS methods' performances in the linear regression model with the contaminated dataset. The regression results are presented in Table 5 and Figure 5(b). Their corresponding statistical tests are summarized in Table 6 and Figure 7.

TABLE 5: Computed regression analysis results (original and contaminated) from Forbes data.

	Original data		Contaminated data	
	α	β	α	β
LS estimator	−81.0637	0.5229	−181.527	1.0266
SD estimator	−78.2631	0.5086	−78.2623	0.5085

TABLE 6: The statistical tests for regression analysis with original data and contaminated data using LS and SD methods.

	Original data			Contaminated data		
	R^2 (AdjustedR^2)	$F(p-\text{value})$	$S-W(p-\text{value})$	R^2 (AdjustedR^2)	$F(p-\text{value})$	$S-W(p-\text{value})$
LS	0.9944 (0.9941)	2677 (0)	0.8723 (0.024)	0.7650 (0.7493)	48.82 (4.37×10^{-6})	0.6473 (3.10×10^{-5})
SD	0.9922 (0.9918)	1928 (0)	0.8574 (0.0140)	0.9917 (0.9912)	1812 (0)	0.2861 (3.13×10^{-8})

Note: (Adjusted) is the adjusted R square value, F and $p$value are the F statistic value and its corresponding p value, and S–W and p value are the Shapiro–Wilk test statistic value and its corresponding p value.

(a)

(b)
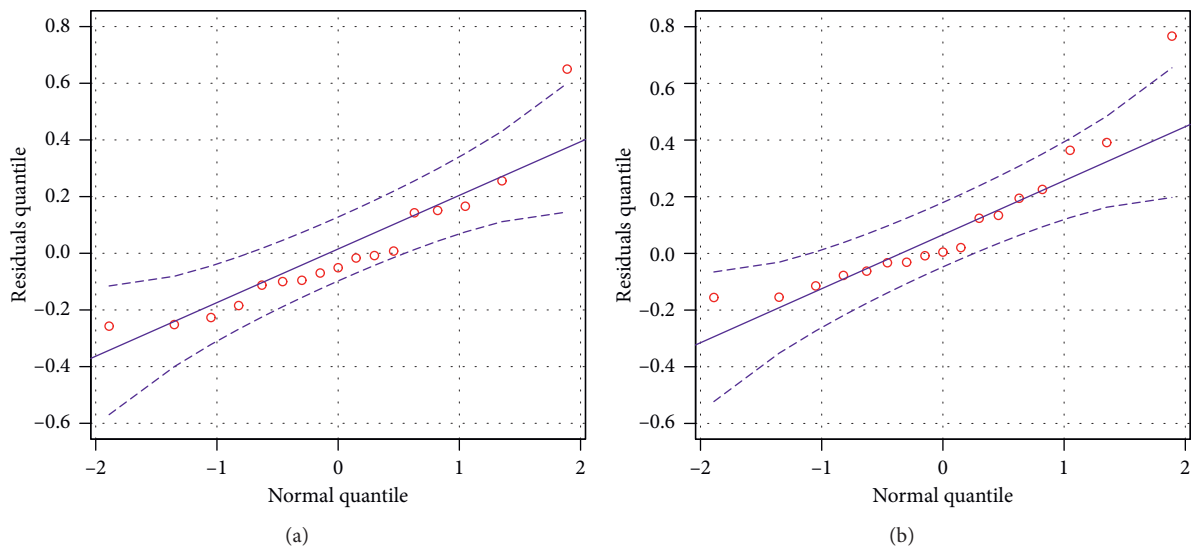
FIGURE 6: Quantile-quantile (QQ) plots of the residuals from LS and SD methods with the original data. (a) The QQ plot from the LS method. (b) The QQ plot from the SD method.

(a)

(b)
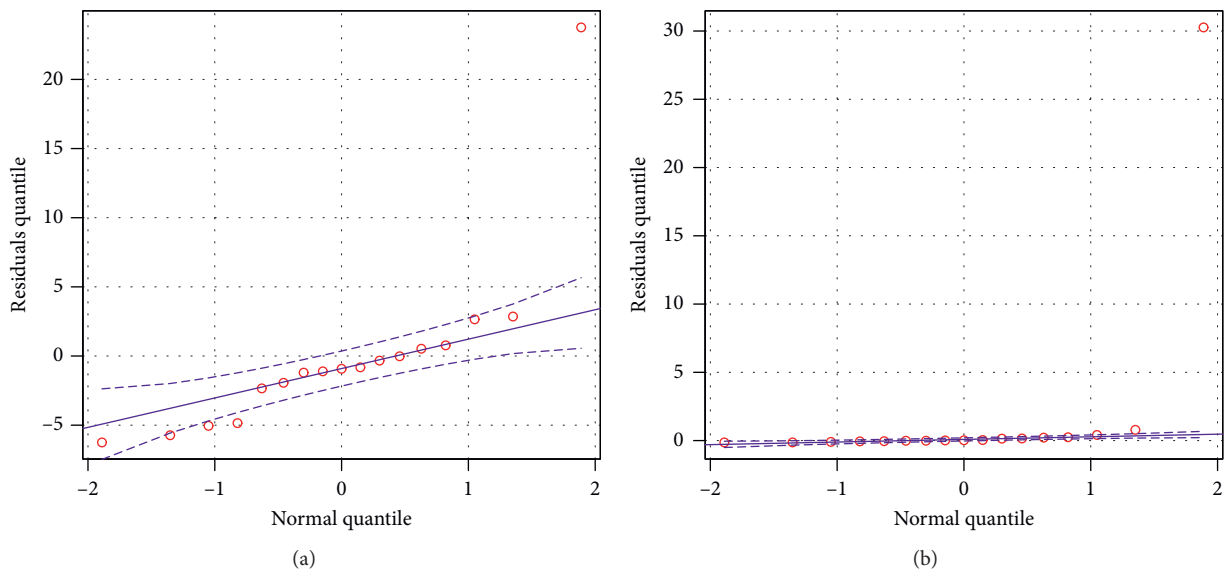
FIGURE 7: Quantile-quantile (QQ) plots of the residuals from LS and SD methods with the contaminated data. (a) The QQ plot from the LS method. (b) The QQ plot from the SD method.

The results show that the LS estimator is greatly influenced by the contaminated data point, whereas the SD estimator can maintain satisfactory performance. The slope parameter estimated by the LS estimator changes from 0.522 9 to 1.026 6, which cannot reflect the actual variation trend of the pressure-temperature curve. By contrast, the SD estimator is not affected by the contaminated data point and can still provide the actual variation trend. The estimated slope parameters obtained using SD method for two different datasets are 0.508 6 and 0.508 5, respectively. The statistical test results show that, under the influence of the contaminated data point, the residuals of the fitted models from the two methods do not pass the normality test. However, the R square (or Adjusted R square) value from the SD method (0.991 7) is much large than that of the LS method (0.765 0) which means that the regression line from the SD method can explain more percentage of the variance of dependence variable compared with that of the LS method. These results imply that the SD estimator outperforms the LS estimator in the contaminated dataset experiment in terms of robustness.

6. Conclusions

The concept of statistical depth plays an important role in mathematical sciences, engineering, regression analysis, and life sciences. In this study, we computed the SD using the IS method and found that this new approach performs better than other exact and MC methods in terms of accuracy and efficiency. The simulated and real data examples illustrated the advantage of this new method. Finally, we tested the SD method based regression analysis through a concrete physical data example. The result indicated the excellent robustness of the proposed method compared with the LS estimation.

Given the many favorable properties of the proposed method, further research can be conducted on different angles. First, the IS parameter (i.e., number of sample tries N) plays an important role in the computation of SD, so the determination of N before the performance of IS algorithm is yet to be thoroughly investigated. Second, the IS method for the SD computation can be improved by sampling the data points via other more important simplices (not the last data point in the possible simplices). Third, with the development of modern computer science, multicore high-performance computer is gaining popularity. Therefore, the IS method can be extended to a parallel computation based version. Lastly, the approximate algorithms (advanced MC methods) for other statistical depths (e.g., halfspace depth, projection depth, and regression depth) can be further explored.

Data Availability

The experimental data used to support the findings of this study are included within the article.

Conflicts of Interest

The authors declare that they have no conflicts of interest.

Acknowledgments

References

[1] Y. Zuo and R. Serfling, "General notions of statistical depth function," *Annals of Statistics*, vol. 28, pp. 461–482, 2000.

[2] Y. Zuo and R. Serfling, "Structural properties and convergence results for contours of sample statistical depth functions," *Annals of Statistics*, vol. 28, pp. 483–499, 2000.

[3] Y. Zuo, "Projection-based depth functions and associated medians," *Annals of Statistics*, vol. 31, no. 5, pp. 1460–1490, 2003.

[4] Y. Zuo, H. Cui, and X. He, "On the stahel-donoho estimators and depth-weighted means for multivariate data," *Annals of Statistics*, vol. 32, no. 1, pp. 167–188, 2004.

[5] Y. Zuo, "On general notions of depth in regression," 2018, https://arxiv.org/abs/1805.02046.

[6] W. Shao and Y. Zuo, "Computing the halfspace depth with multiple try algorithm and simulated annealing algorithm," *Computational Statistics*, vol. 35, no. 1, pp. 203–226, 2020.

[7] J. W. Tukey, "Mathematrics and the picturing of data," in *Proceedings of the International Congress of Mathemmaticians*, vol. 2, pp. 523–531, Vancouver, Canada, August 1974.

[8] X. Liu, Y. Zuo, and Q. Wang, "Finite sample breakdown point of Tukey's halfspace median," *Science China Mathematics*, vol. 60, no. 5, pp. 861–874, 2017.

[9] X. H. Liu, S. H. Luo, and Y. J. Zuo, "The limit of finite sample breakdown point of tukey's halfspace median for general data," *Acta Mathematica Sinica, English Series*, vol. 34, no. 9, pp. 1403–1416, 2018.

[10] W. Shao and Y. Zuo, "Simulated annealing for higher dimensional projection depth," *Computational Statistics & Data Analysis*, vol. 56, no. 12, pp. 4026–4036, 2012.

[11] R. Y. Liu, "On a notion of data depth based on random simplices," *Annals of Statistics*, vol. 18, no. 1, pp. 405–414, 1990.

[12] R. Serfling and Y. Wang, "On liu's simplicial depth and randles' interdirections," *Computational Statistics & Data Analysis*, vol. 99, pp. 235–247, 2016.

[13] P. J. Rousseeuw and M. Hubert, "Regression depth," *Journal of the American Statistical Association*, vol. 94, no. 446, pp. 388–402, 1999.

[14] X. Liu and Y. Zuo, "Computing halfspace depth and regression depth," *Communications in Statistics - Simulation and Computation*, vol. 43, no. 5, pp. 969–985, 2014.

[15] J. S. Liu, *Monte Carlo Strategies in Scientific Computing*, Springer, New York, USA, 2001.

[16] S. C. Kou, Q. Zhou, and W. H. Wong, "Eqri-energy sampler with allpications in statistical inference and statistical mechanics," *Annals of Statistics*, vol. 34, pp. 1581–1619, 2006.

[17] F. Liang, C. Liu, and R. J. Carroll, *Advanced Markov Chain Monte Carlo Methods: Learning from Past Samples*, John Wiley & Sons, NJ, USA, 2011.

[18] W. Shao, G. Guo, G. Zhao, and F. Meng, "Simulated annealing for the bounds of Kendall's τ and Spearman's ρ," *Journal of Statistical Computation and Simulation*, vol. 84, no. 12, pp. 2688–2699, 2014.

[19] W. Shao, G. Guo, F. Meng, and S. Jia, "An efficient proposal distribution for Metropolis-Hastings using a B-splines technique," *Computational Statistics & Data Analysis*, vol. 57, no. 1, pp. 465–478, 2013.

[20] J. Shao, *Mathematical Statistics*, Springer, Berlin, 2003.

[21] O. Pokotylo, P. Mozharovskyi, and R. Dyckerhoff, "Depth and depth-based classification with r-package ddalpha," 2016, https://arxiv.org/abs/1608.04109.

[22] S. Weisberg, *Applied Linear Regression*, John Wiley & Sons, New Jersey NY USA, 1980.

[23] R. H. Byrd, P. Lu, J. Nocedal, and C. Zhu, "A limited memory algorithm for bound constrained optimization," *SIAM Journal on Scientific Computing*, vol. 16, no. 5, pp. 1190–1208, 1995.

[24] R. R. Development Core Team, *A Language and Environment for Statistical Computing*, R Foundation for Statistical Computing, Vienna, Austria, 2020.

Research Article

Heat Transport Improvement and Three-Dimensional Rotating Cone Flow of Hybrid-Based Nanofluid

Azad Hussain,[1] **Qusain Haider** [iD],[1] **Aysha Rehman** [iD],[1] **M. Y. Malik** [iD],[2] **Sohail Nadeem** [iD],[3] **and Shafiq Hussain**[4]

[1]*Department of Mathematics, University of Gujrat, Gujrat 50700, Pakistan*
[2]*Department of Mathematics, College of Sciences, King Khalid University, Abha 61413, Saudi Arabia*
[3]*Department of Mathematics, Quaid-I-Azam University, Islamabad 44000, Pakistan*
[4]*Department of Computer Science, University of Sahiwal, Sahiwal, Pakistan*

Correspondence should be addressed to Qusain Haider; qusain.haider336@gmail.com

The current research aims to study the mixed convection of a hybrid-based nanofluid consisting of ethylene glycol-water, copper (II) oxide (CuO) and titanium dioxide (TiO$_2$) in a vertical cone. A hybrid base blend model is used to examine the nanofluid's hydrostatic and thermal behaviors over a diverse range of Reynolds numbers. The application of mixed nano-particles rather than simple nanoparticles is one of the most imperative things in increasing the heat flow of the fluids. To test such a flow sector, for the very first time, a hybrid-based mixture model was introduced. Also, the mixture framework is a single-phase model formulation, which was used extensively for heat transfer with nanofluids. Comparison of computed values with the experimental values is presented between two models (i.e., the model of a mixture with the model of a single-phase). The natural convection within the liquid phase of phase change material is considered through the liquid fraction dependence of the thermal conductivity. The predicted results of the current model are also compared with the literature; for numerical results, the bvp4c algorithm is used to quantify the effects of nanoparticle volume fraction diffusion on the continuity, momentum, and energy equations using the viscous model for convective heat transfer in nanofluids. Expressions for velocity and temperature fields are presented. Also, the expressions for skin frictions, shear strain, and Nusselt number are obtained. The effects of involved physical parameters (e.g., Prandtl number, angular velocity ratio, buoyancy ratio, and unsteady parameter) are examined through graphs and tables.

1. Introduction

Nanofluid is the mixture of hard nanoparticles with the base fluid. The study of nanofluid is of huge interest for the evaluation of increasing thermal conductivity, In the engineering, cooling is important, such as the cooling of nano-electromechanical systems and semiconductors. The convection of nanofluids flow in nanowires such as microchannels and microtubes is mandatory to use nanofluids for these low-scale cooling techniques. Nanofluids are served in related works with single-phase heterogeneous fluids (whereas the nanoparticles are consistently distributed in base fluids). Free convection is critical in thermal engineering in nanofluid within enclosures because rising heat flow is a significant problem for energy efficiency. The first attempts to improve heat transport using nanofluid. They simulated the heat transfer features of nanofluids in a two-dimensional insertion and originate that the heat transfer rate dramatically increases with postponed nanoparticles at every Grashof value. Elaziz and Marin [1] investigated one significant feature of theory, and it does not account for thermal energy dissipation. We discover a method for dealing with elastic interactions that do not take into account energy dissipation caused by heat sources and body forces. Remote as literature analysis is revised,

[2–12] scholars are doing notable nanofluid work. The analysis of heat transmission and nanofluid flow is an important unsolidified rheology issue. Experimenting on Cu-water nanofluid rheology, in which we noticed the conduct of a shear-thinning fluid obtained by Chang et al., [13] Santra et al. [14] introduced the forced conduction of Cu-water in Newtonian and non-Newtonian fluids in a channel. Das et al. [15] extended Aziz's attempt by looking at the Buongiorno fluid method for nanofluid flow. Xuan and Li [16] explored Cu-water nanofluid flow characteristics. Infrared photons are visible; sunlight or infrared and illumination are shown by the material nature produced from those radiations. Based on the way solar energy is collected and transmitted or transformed into solar power, energy sources and their technologies are mostly known as either active solar or inactive solar. Blackbody radioactivity is the radiation of electromagnetic waves from a superficial that exceeds absolute zero. In several practical applications, heat transport occurs via a porous medium flow. These inspections cover a wide range of fields of science and engineering, mainly grain storage, chemical hydrogen reactors, dampness movement by air-filled rubber protection, and much more. The efficiency of common base fluid thermal systems is relatively low. Suspending metallic nanoparticles in the sordid fluid is a recent way to improve the efficiency of those systems. Sheikholeslami et al. [17] investigated the free convection warmth transfer in a concentration halo between warm four-sided and heated curve cylinders in the non-attendance of the magnetic field. Kandelousi [18] investigated the consequence on ferrofluid flow of especially variable magnetic fields by considering the constant heat flux endpoint state. Sheikholeslami et al. [19–21] examined nanofluid flow alongside convective heat transfer through a different geometry. The fluid flows including chemical reaction has wide range in the processes of extrusion, refrigeration, and polymer industries. Under GN electromagnetic theory, Abd-Elaziz et al. [1] demonstrated the effect of Thomson and initial stress in a thermo-porous elastic solid. Vlase et al. [22] looked into the motion equation for a versatile one-dimensional element used in a multibody system's dynamical analysis. Malik et al. [23] proposed the idea of an incompressible fluid past MHD natural reaction over a heat-producing porous layer. The electrically transmitting non-Newtonian fluids can be used as a refrigeration liquid because their flow can be controlled by the outdoor magnetic field, which to some degree controls the heat transfer. Its usage of magnetic fields that impact heat preoccupation/generation system has several engineering applications, like crystallization and bottling of copper wires by dragging continuous polymers through inactive fluid [24–29].

Shirejini et al. [30] used a nanofluid and a gyratory scheme to restore the heat transfer rate after a decrease. Turkyilmazoglu [31–33] investigated the thermal broadcast of an electrically conductive fluid over a rotating infinite disk. Digital devices for stowage, rotating equipment, thermal energy generation systems, electrode material, geothermic industry, gas turbines, biological courses, and different types of medical equipment are examples of applications of such problems. Turkyilmazoglu investigated fluid stream and heat allocation on a rotating disk that was traveling vertically. A spinning cone induces warmth transfer and enables flow in a quiescent liquid. Kumar et al. [34] used a finite element method to research the randomness production of a nanofluid containing copper and aluminum oxide nanoparticles in the spaces between two coaxial spinning disks.

The above studies indicate that no attempt has been complete to analyze the 3D hybrid nanofluid flow model around the cone as poignant or immobile under fluid control. The effect of copper oxide (CuO) and titanium dioxide (TiO_2) nanoparticles on the thermal performance properties of ethylene glycol-water is investigated in this study, which has an extensive scientific and technological value. The second significance is to build on the principle of Refs. [35–37] which also contain the most important studies about the current model. In the case of counter-rotating, create a mathematical model for rotating cones that are called moving or stationary. The flow reckonings are reduced to an ordinary scheme, and then bvp4c is used to solve them. Figures illustrate the effects of corporeal relevant variable quantity on velocity and temperature. Superficial grind force and temperature incline numerical outputs are tabulated contrary to stimulating physical objects. The uniqueness of the latest work is emphasized.

(1) The current study considers three-dimensional $CuO + TiO_2/C_2H_6O_2$ hybrid nanofluid flow, while previous research [38, 39] has concentrated on viscous fluids and nanofluids.

(2) The MATLAB bvp4c algorithm has been used for the explanation of the non-linear problem.

(3) In comparison to other fluids, hybrid nanofluids have been found to increase the thermal efficiency of base fluids quickly.

2. Mathematical Formulations

To find another way to simplify the process of convection in fluids, the basis for this paper is a three-dimensional (3D) natural heat transfer of Newtonian two-phase nanofluid flow composed of TiO_2/CuO hybrid particles/ethylene glycol-water (50 percent-50 percent) combination of base fluid due to a pivoting cone. All conclusions and conditions considered for the geometry of this paper are clearly shown in Figure 1. Differential equations that model the problem according to the assumptions mentioned above and the physical terms that affect the problem are

$$x\frac{\partial u}{\partial z} + u + x\frac{\partial w}{\partial z} = 0, \tag{1}$$

$$\frac{\partial u}{\partial t} + u\frac{\partial u}{\partial x} - \frac{v^2}{x} + w\frac{\partial u}{\partial z} = -\frac{v_e^2}{x} + \frac{\nu_{hnf}\partial^2 u}{\partial z^2} + g\zeta \cos \alpha^* (T - T_\infty), \tag{2}$$
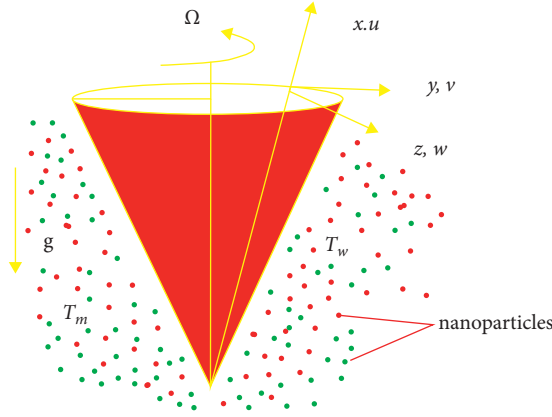
FIGURE 1: Corporeal geometry of the problem.

$$\frac{\partial v}{\partial t} + u\frac{\partial v}{\partial x} + u\frac{v}{x} + w\frac{\partial v}{\partial z} = \frac{\partial v_e}{\partial t} + v_{hnf}\frac{\partial^2 v}{\partial z^2}, \quad (3)$$

$$u\frac{\partial T}{\partial x} + w\frac{\partial T}{\partial z} + \frac{\partial T}{\partial t} = \alpha_{hnf}\frac{\partial^2 T}{\partial z^2}. \quad (4)$$

The velocity gears in the paths of x, y, and z-axis, separately, are in the above equations (u, v, and w). Also, ρ_{hnf} is the concentration of nanofluid, μ_{hnf} is the fluid viscosity of nanofluid, v_e is the free flow velocity, $(\rho\beta)_{hnf}$ is the coefficient of growth and contraction because of the temperature difference, T is the dynamic temperature, ζ is the electrical conductivity of the fluid, v_{hnf} is kinematic viscosity, $(\rho C_P)_{hnf}$ is nanofluid's heat capacity, k_{hnf} is nanofluid's heat conductivity, A is the Deborah number, and α_{hnf} is the thermal diffusivity.

The boundary conditions are

$$u(0, x, z) = v = w = u_i, v_i w_i,$$

$$T = T_i,$$

$$u(t, 0, z) = w = 0, \quad (5)$$

$$v = \frac{\Omega_1 x \sin \alpha^*}{1 - st^*},$$

$$T = T_W.$$

The momentum, temperature, and boundary conditions for this problem are [38, 39].

The most recent method would be the utilization of hybrid nanoparticles rather than single nanoparticles to advance the process of convection in fluids. Nanofluid formed by hybrid nanoparticles has higher conduction than nanofluid generated by one single nanoparticle. Furthermore, the impact of using nanoparticles of different shapes on conductivity and reducing the amount of convection cannot be simply overlooked.

Thermophysical Properties. The following are the different thermal properties of hybrid nanofluid and water [39]:

$$\rho_{hnf} = \left[(1 - \phi_2)(1 - \phi_1)\rho_f + \phi_1\rho_{cuo}\right] + \phi_2\rho_{Tio_2},$$

$$(\rho C_p)_{hnf} = \left[(1 - \phi_2)(1 - \phi_1)(\rho c_p)_f + \phi_1(\rho c_p)_{cuo}\right]$$
$$+ \phi_2(\rho c_p)_{Tio_2}, \quad (6)$$

$$\frac{k_{hnf}}{k_{nf}} = \frac{k_{cuo} + 2k_{nf} - 2\phi_1(k_{nf} - k_{cuo})}{k_{cuo} + 2k_{nf} + \phi_1(k_{nf} - k_{cuo})},$$

$$\frac{k_{nf}}{k_f} = \frac{k_{Tio_2} + 2k_{nf} - 2\phi_2(k_{nf} - k_{Tio_2})}{k_{Tio_2} + 2k_{nf} + \phi_2(k_{nf} - k_{Tio_2})}.$$

Define the following transformation:

$$\eta = \frac{(x\Omega \sin \alpha^*)^{0.5} z}{v(1 - st^*)^{0.5}},$$

$$v_e = \frac{x\Omega_2 \sin \alpha^*}{1 - st^*},$$

$$\alpha = \frac{\Omega_1}{\Omega},$$

$$t^* = \Omega \sin \alpha^* t,$$

$$w = \frac{(\sin \alpha^*)^{(1/2)} (v\Omega)^{(1/2)} f(\eta)}{(1 - st^*)^{(1/2)}},$$

$$T - T_\infty = (T_W - T_\infty)\theta(\eta),$$

$$u(t, x, z) = -\frac{2^{-1} \sin \alpha^* f' \Omega x}{1 - st^*}, \quad (7)$$

$$v = \Omega x \sin \alpha^* (1 - st^*)^{(1/2)} g(\eta),$$

$$T_W - T_\infty = \frac{(T_0 - T_\infty) x L^{-1}}{(1 - st^*)^2},$$

$$Gr_1 = \frac{\cos \alpha^* (T_0 - T_\infty) g\beta L^3}{v^2},$$

$$\gamma_1 = \frac{Gr_1}{Re_L^2},$$

$$Re_L = \sin \alpha^* \Omega L^2 v^{-1},$$

$$Pr = \frac{v}{\alpha}.$$

The functions required for the conversion of the partial differential equations (PDEs) ((2), (3), and (4)) to the ordinary differential equations (ODEs) are as follows.

In which the hybrid angular velocity is $\omega = \omega_1 + \omega_2$, the angular velocities of a cone are ω_1, the free torrent liquid is ω_2, and the unstable parameter is S. Also, θ and ζ are the variable and temperature without dimensions, respectively.

After substituting equation (7) into equations (2)–(4) and modifying and converting, the usual differential equations

relating the flow and temperature, together with the boundary conditions, are as follows:

$$\left(\frac{f'''}{(1-\phi)^{2.5}(1-\phi_2)^{2.5}\left[(1-\phi_2)\{(1-\phi_1)-\phi_1(\rho_{cuo}/\rho_f)\}+\phi_2(\rho_{Tio_2}/\rho_f)\right]}-\left(f+\frac{1}{2}s\eta\right)f'+\left(\frac{1}{2}f'-s\right)f'-2\left(g-(1-\alpha_1)^2\right)-2\gamma_1\theta\right), \quad (8)$$

$$\left(\frac{g''}{(1-\phi)^{2.5}(1-\phi_2)^{2.5}\left[(1-\phi_2)\{(1-\phi_1)-\phi_1(\rho_{cuo}/\rho_f)\}+\phi_2(\rho_{Tio_2}/\rho_f)\right]}-(-f'g+fg')+s\left(1-\alpha_1-g-\frac{1}{2}\eta g'\right)\right), \quad (9)$$

$$\left(\frac{1}{\mathrm{Pr}}\left(\frac{\kappa_{hnf}}{\kappa_f}\right)\theta''-\left(f\theta'-\frac{f'\theta}{2}\right)-2s\theta+\frac{1}{2}s\eta\theta'\right). \quad (10)$$

Now, the boundary conditions are

$$f(0) = 0,$$

$$g(\infty) = -1 + \alpha_1,$$

$$g(0) = \alpha_1,$$

$$\theta(0) = -1, \quad (11)$$

$$f'(\infty) = 0,$$

$$f'(0) = 0,$$

$$\theta(\infty) = 0.$$

The important natural quantities impacting the flow and the transfer of heat are the coefficient of skin friction C_{fx}, C_{fy} and the local Nusselt number Nu_x, respectively, which are clear as follows:

$$C_{fx} = -\mathrm{Re}_x^{-(1/2)}\left(\frac{2\mu}{\partial z}\frac{\partial u}{\partial z}\right)_{z=0}, \quad (12)$$

$$C_{fy} = \left(\frac{2\mu}{\partial z}\frac{\partial v}{\partial z}\right)_{z=0}\left(-\mathrm{Re}_x^{-(1/2)}\right). \quad (13)$$

Their dimensionless form is as follows:

$$C_{fx}\mathrm{Re}_x^{(1/2)} = \left(\frac{1}{(1-\phi_1)^{2.5}(1-\phi_2)^{2.5}}\right)(-f'')_{\eta=0}, \quad (14)$$

$$C_{fy}\mathrm{Re}_x^{(1/2)} = \left(\frac{1}{(1-\phi_1)(1-\phi_2)}\right)(-g')_{\eta=0}. \quad (15)$$

The factor of heat allocation in dimensionless form is given as

$$Nu_x\mathrm{Re}_x^{(1/2)} = -\left(\frac{k_{hnf}}{k_f}\right)\theta'(0). \quad (16)$$

3. Numerical Solution

The coupled ordinary, non-linear differential equations (8)–(10) and the limit conditions set out in equation (11) are numerically solved using the bvp4c MATLAB algorithm.

$$F = y_1,$$

$$\rho_f = b,$$

$$F' = y_2,$$

$$g = y_4,$$

$$F'' = y_3,$$

$$\rho_s = a,$$

$$g' = y_5,$$

$$g'' = y_5',$$

$$F'' = y_3', \quad (17)$$

$$\theta(0) = y_6,$$

$$\theta' = y_7,$$

$$\theta'' = y_7',$$

$$k_s = m,$$

$$k_f = n,$$

$$(\rho c_p)_s = c,$$

$$(\rho c_p)_f = d.$$

Now, the new equations are

$$y_3' = \left[\left[(1-\phi)^{2.5}(1-\phi_2)^{2.5}(1-\phi_2)(1-\phi_1) - \phi_1\left(\frac{a}{b}\right) + \phi_2\left(\frac{c}{b}\right)\right]\right.$$
$$\left. \cdot \left[\left(y(1)y(3) + \frac{1}{2}xsy(3)\right) - \frac{1}{2}y^2(2) + sy(2)\right) + 2y^2(4) - (1-\alpha_1)^2 + 2\gamma_1 y(6)\right], \tag{18}$$

$$y_5' = \left[(1-\phi)^{2.5}(1-\phi_2)^{2.5}(1-\phi_2)(1-\phi_1) - \phi_1\left(\frac{a}{b}\right) + \phi_2\left(\frac{c}{b}\right)\right]$$
$$\cdot \left[y(1)y(5) - y(4)y(2) - s + s\alpha_1 + sy(4) + \frac{1}{2}sxy(5)\right], \tag{19}$$

$$y_7' = \left[\frac{(m+2)(n+2)\phi(n-m)}{(m+2)(n-2)\phi(n-m)}\right]\left[\Pr y(7)y(1) - \frac{y(6)y(2)}{2}\left(2sy(6) - \frac{\Pr1}{2}sxy(7)\right)\right], \tag{20}$$

along with limitation

$$\begin{aligned} y(1) &= 0, \\ y_\infty(2) &= 0, \\ y(2) &= 0, \\ y(4) &= \alpha_1, \\ y(6) &= -1, \\ y_\infty(6) &= 0. \end{aligned} \tag{21}$$

4. Graphical Observations and Discussion

Non-linear standard differential equations (8)–(10) concerning boundary condition equation (11) are solved by the bvp4c method of numerical technique for evaluating the various physical parameters. Results indicate the effect on velocity $-f'(\eta)$, $g(\eta)$ and temperature $\theta(\eta)$ profiles of non-dimensional governing parameters laterally with the skin friction constant and limited Nusselt number for recommended fence temperature (PWT) cases. We considered entirely dimensional parameter values for numerical algorithms as $s = 2.0$, $\alpha_1 = 0.6$, $\phi = 0.8$, $\gamma_1 = 1.5$, and $Pr = 7.0$. These parameter values are samein the entire article except for the disparities in the corresponding figures and tables. We learned that the heat transfer rate has been further increased due to hybrid nanofluid ($TiO_2 - Cuo$/ethylene glycol-water). The rate of the heat transfer decreases when we increase the rotation parameter and the capacity fraction of nanoparticles. Figures 2–5 display the block diagram of the speed and temperature profiles for different models of the volume fractions of Tio_2 and Cuo nanoparticles. The rise in the medium fraction of nanotubes augments the tangential velocity $-f'(\eta)$ field and fluctuates the azimuthal velocity $g(\eta)$ field as well as the temperature profiles in the PWT case. As assumed, the improvement of the medium fraction of nanoparticles would enhance the colloidal interruption here amid solid particles, and due to this, the velocity fields are reduced. By contrast, the field of Tio_2 nanoparticle velocity is faster by enhancing the values of the nanoparticle volume fraction. For this motive, we saw an enrichment in the field of tangential velocity. Figures 2(a) and 2(b) describe the effect of the α_1 on prescribed wall temperature (PWT) case velocity $-f'$

profiles. The velocity curve decreases when increasing the values of α_1 in $Cuo - TiO_2$ cases. In Figures 4(a) and 4(b), α_1 indicates mixed solutions for both cases in fields of azimuthal velocity g. In both cases, velocity decreases if the value of this parameter increases. But with increasing values of α_1 the tangential boundary layer of velocity $-f'$ enables. Physically, the parameter of α_1 helps to increase the velocity of the flow because for this reason the velocity fields are initially enhanced. At Figures 3(a) and 3(b) under the impact of the parameter γ_1 almost similar behavior is observed, but here the thickness of the boundary layer increases rapidly with the growth. Velocity behavior for s the maximum value of s sluggish down the tangential speed of the fluid as well as velocity $-f'$ goes to zero far absent from the cone superficial for high values of s velocity profile goes down rdThe effects of the Pr on θ in both cases are shown in Figures 5(a) and 5(b). The depth of the thermal boundary layer and $\theta(\eta)$ increases by enhancing the values of Prandtl number Pr. The effect of the Reynolds number on tangential velocity is seen in Figures 5(a) and 5(b). It is represented in figures with an increase in Re because inertial forces have a direct relationship with Re; The curve in Figure 6(a) increases and in 6(b) decreases with the increasing values of tangential velocities near the cone wall. Figures 7(a) and 7(b) are devoted to the manifestation of the effect of γ_1 (buoyancy parameter) on the tangential skin friction coefficient. From these figures, it is clear that C_{fx} grows as γ_1 increases, while it decreases as α_1 increases. Figures 8(a) and 8(b) indicate the impact on the skin friction coefficients C_{fy} at the cone boundary of the rotation parameter (α_1) and Reynolds number. Skin friction coefficients are shown in figure 8(b) by increasing values of function of rotation parameters and 8(a) is decreasing by function of α_1 while showing declining behavior for the number of Reynolds. The effect of Pr is shown in Figure 9(a) on the Nusselt number by an improvement in the value of Pr the Nusselt number decrease. From Figure 9(b), it is noted that the Nusselt number is decreased when enhancing the value of Pr. Tables 1 and 2 demonstrate the impact of several parameters on skin friction and Nusselt number for Reynolds model. Amount of α_1 and γ_1 expand the skin and Nusselt number decline for α_1 and grow for α_1. Table 1 demonstrated the hybrid surface fluid and nanoparticles have fluid dynamics-physical properties

FIGURE 2: (a) Impact of α_1 on the velocity field distribution $-f'(\eta)$ for Cuo nanoparticles. (b) Impact of α_1 on the velocity distribution $-f'(\eta)$ for TiO_2 nanoparticles.
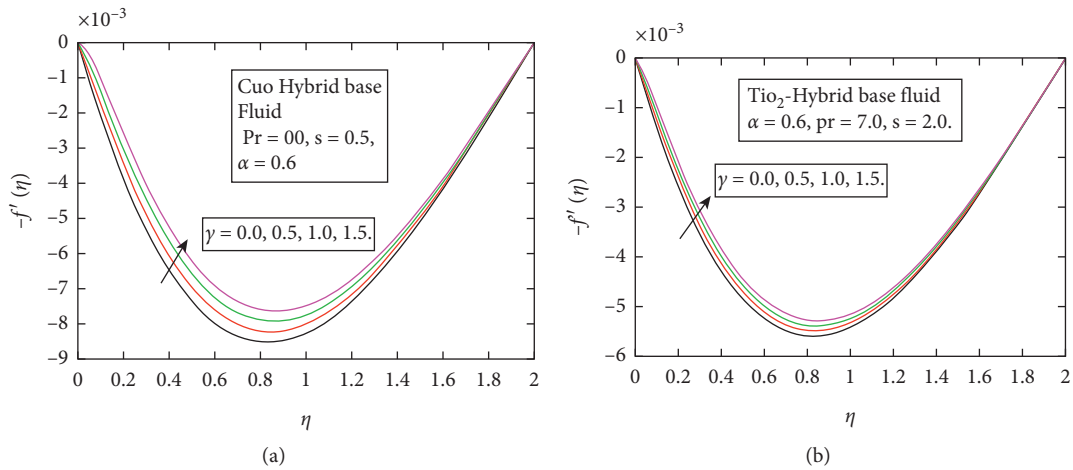
FIGURE 3: (a) Impact of γ_1 on velocity distribution $-f'$ for Cuo nanoparticles. (b) Impact of γ_1 on velocity distribution $-f'$ for TiO_2 nanoparticles.
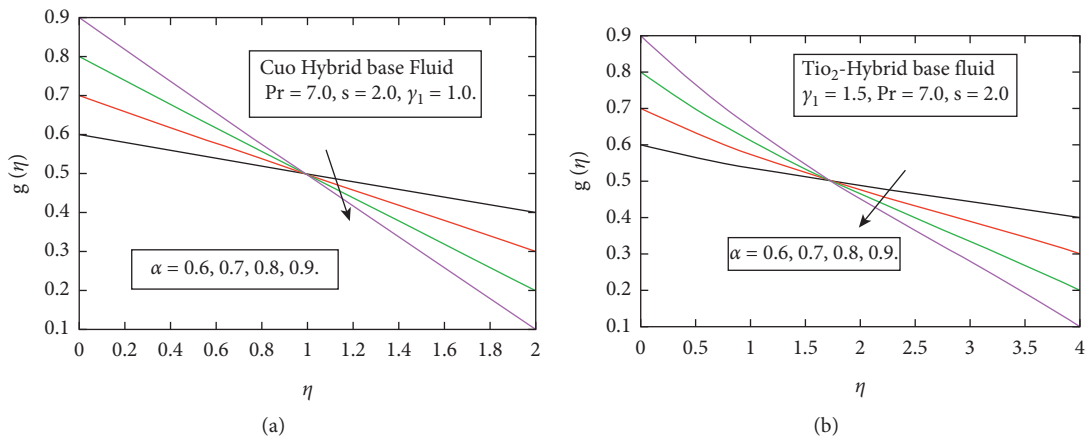
FIGURE 4: (a) Impact of α_1 on velocity profile $g(\eta)$ for CuO nanoparticles. (b) Impact of α_1 on velocity profile $g(\eta)$ for Tio_2 nanoparticles.
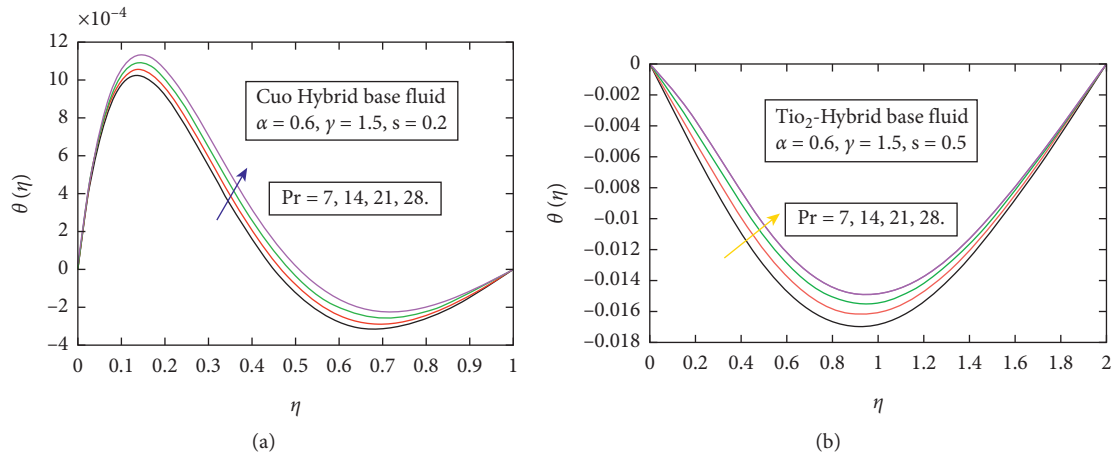
FIGURE 5: (a) Deviation of Pr on temperature profile $\theta(\eta)$ for CuO nanoparticles. (b) Deviation of Pr on temperature profile $\theta(\eta)$ for TiO_2 nanoparticles.
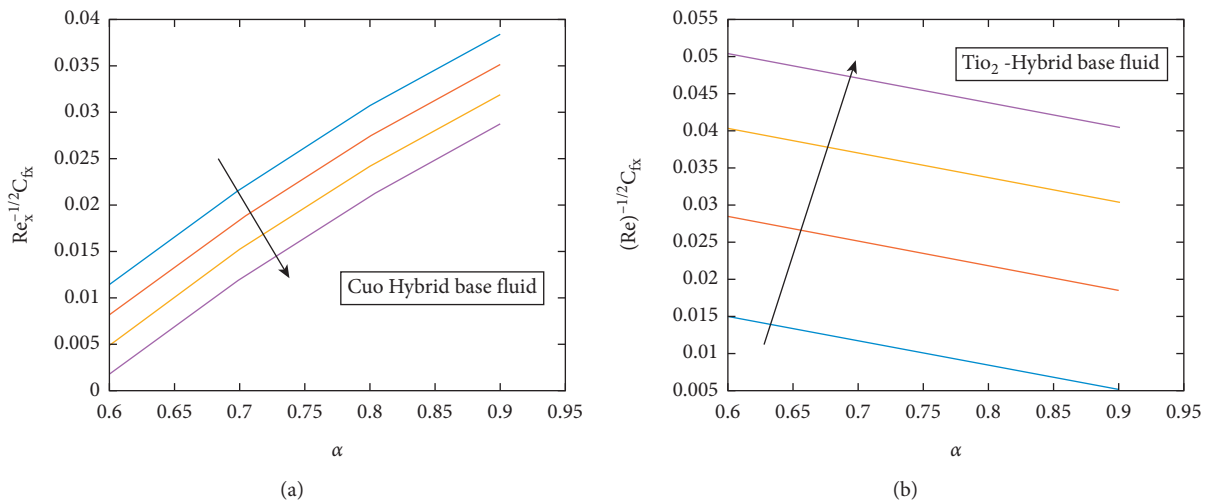
FIGURE 6: (a) Impact on skin friction C_{fx} along x-direction with α_1, for CuO nanoparticles. (b) Impact on skin friction C_{fx} along x-direction with α_1, for TiO_2 nanoparticles.
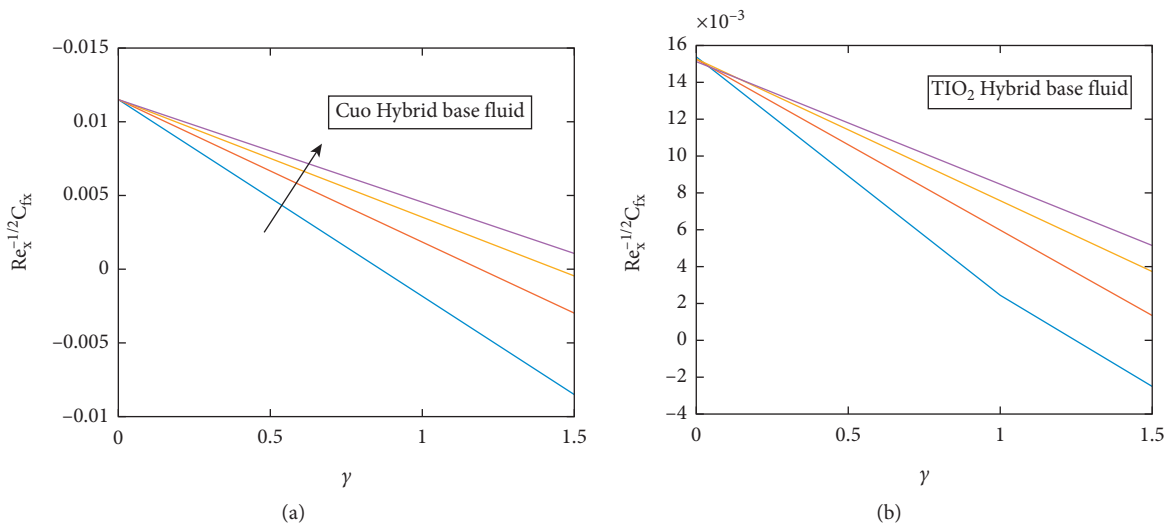
FIGURE 7: (a) Impact on skin friction of γ_1 along x-direction for $CuO - C_2H_6O_2$. (b) Impact on skin friction of γ_1 along x-direction for $TiO_2 - C_2H_6O_2$ + water.

(a)

(b)
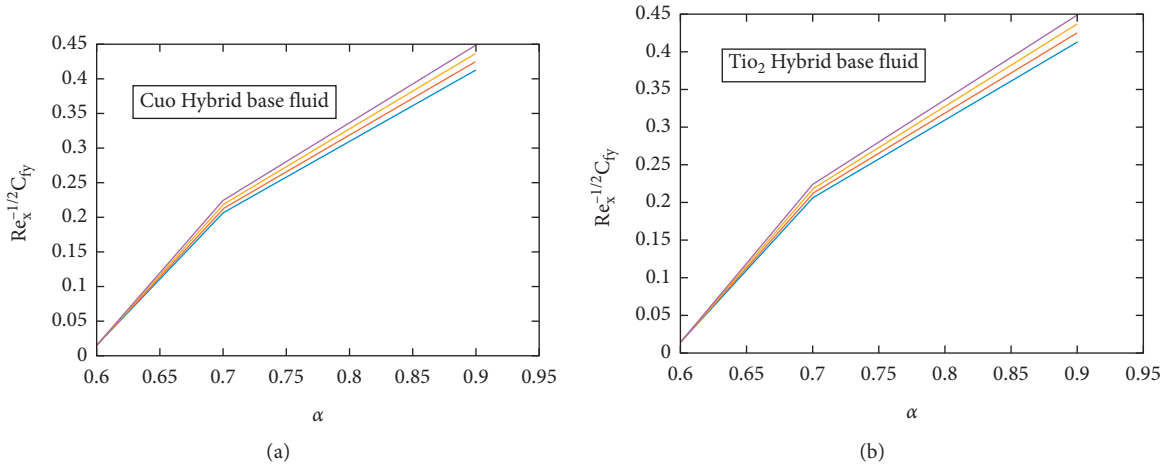
FIGURE 8: (a) Influence on skin friction C_{fy} along x-direction of α_1 for $CuO/C_2H_6O_2 + water$. (b) Influence on skin friction C_{fy} along y-direction of α_1 for $TiO_2 - C_2H_6O_2$.

(a)

(b)
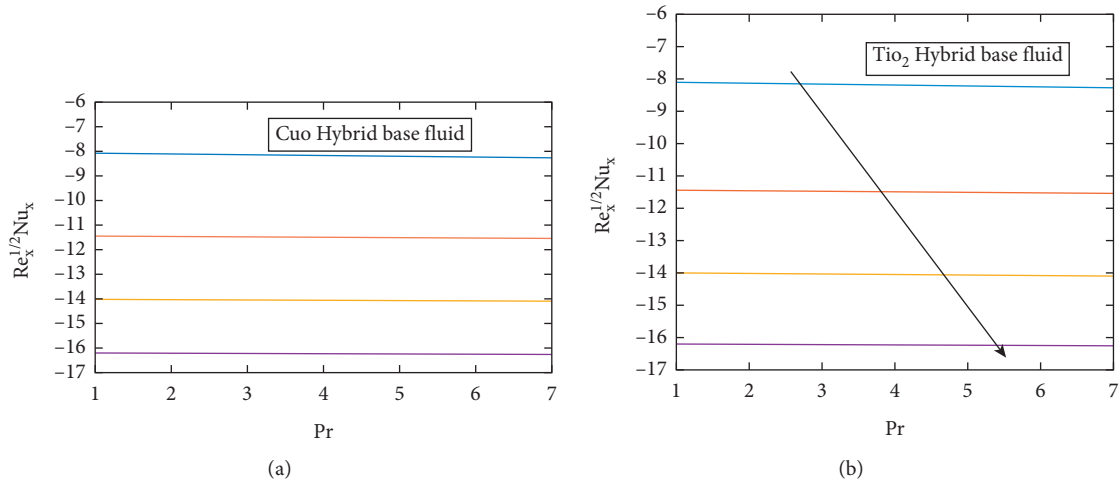
FIGURE 9: (a) Influence on Nusselt number of Pr for $CuO - C_2H_6O_2$. (b) Influence on Nusselt number of Pr for $TiO_2 - C_2H_6O_2$.

TABLE 1: Impact of different parameters and dimensions of nanomaterials on velocity and temperature profiles in CuO-hybrid base fluid.

α_1	γ_1	S	Pr	C_{fx}	C_{fy}	Nu_x
0.6	0.5	1.0	7.0	0.01573	0.01530	−5.01480
0.7				0.02965	0.00882	−4.83310
0.8				0.04081	0.00202	−4.45480
0.9				0.05035	0.00710	−4.01480
0.7	0.0	2.0	5.0	0.01171	0.02283	−7.24294
	0.5			0.02535	0.01107	−7.20510
	1.0			0.03678	0.08875	−7.16484
0.8	1.5	0.5	3.0	0.04706	0.00132	−7.12153
		1.0		0.00848	0.01523	−8.89947
		1.5		0.02186	0.01552	−8.88430
		2.0		0.03367	0.00754	−8.86861
0.9	0.5	0.5	1.0	0.04379	0.00375	−8.85267
			3.0	0.00517	0.01573	−10.2863
			5.0	0.01849	0.01171	−10.2791
			7.0	0.03054	0.00898	−10.2119

TABLE 2: Results of skin friction and Nusselt coefficient for **TIO$_2$**.

α_1	γ_1	S	Pr	C_{fx}	C_{fy}	Nu_x
0.6	0.5	1.0	7.0	0.01150	0.0114280	−8.09597
0.7				0.00487	0.0216298	−8.15971
0.8				−0.00617	0.0306057	−8.22153
0.9				−0.04201	0.0383555	−8.22153
0.7	0.0	2.0	5.0	0.01440	0.0049780	−11.4494
	0.5			0.00666	0.0151825	−11.4824
	1.0			0.00190	0.0241606	−11.5149
0.8	1.5	0.5	3.0	−0.00204	0.0319124	−11.5471
		1.0		0.01146	0.0082032	−14.0226
		1.5		0.00759	0.0184064	−14.0448
		2.0		0.00352	0.0273834	−14.0448
0.9	0.5	0.5	1.0	−0.00042	0.0351342	−14.0669
			3.0	0.01109	0.0017524	−16.1919
			5.0	0.00799	0.0119582	−16.2087
			7.0	0.00454	0.0209374	−16.2253

TABLE 3: The hybrid surface fluid and nanoparticles having fluid dynamic-physical properties.

Physical Properties	**CuO**	**TiO$_2$**	**C$_2$H$_6$O$_2$ − H$_2$O**
ρ (kg/m^3)	6500	4250	1063.8
c_p (J/kgk)	540	686.2	3630
K (w/mk)	18	8.9538	0.387

for *Cuo* and in Table 2 also shows the properties of TiO$_2$. The thermophysical properties of the nanofluid are discussed in Table 3.

5. Concluding Remarks

In the present paper, the influence of rotation and buoyancy force parameters on velocity and temperature is discussed in hybrid base nanofluid over a gyrating cone in the occurrence of gravity and film condensation and heat dissipation effect. By using the bvp4c algorithm, we solve PDEs with minimum errors and correct results. The results indicate that by increasing the value of α_1, the tangential and azimuthal velocity reduces near the boundary of the cone for *CuO* and TiO2 cases. Also, with the increase of γ_1, azimuthal velocity increases. The inclination of the Prandtl number results in an increase in the temperature profile. The skin friction factor is increasingby rotation and unstable parameters while it is decreasing with Reynolds number. The Nusselt number increases for larger *Pr* near the wall of the cone. The major outcomes of this study are given as follows:

(1) *TiO$_2$* nanofluid has a higher coefficient of friction factor as opposed to *Cuo* nanofluid. However, the heat transfer rate of *Tio$_2$* nanofluid is lower than that of *Cuo* nanofluid. *Cuo* nanofluid, therefore, improves the thermal transfer more than the *Tio$_2$* nanofluid.

(2) The parameter of viscous variation improves both temperature and the rate of heat transfer. Thus, we can say that viscosity dependent on temperature is helpful for processes of heat transfer modification.

(3) Hybridity reduces the velocity distribution while increasing the temperature distribution.

(4) As compared to nanofluid, hybrid nanofluid can have better heat transfer efficiency.

(5) The optimal heat transfer rate in hybrid nanofluid can be achieved by choosing distinct and sufficient nanoparticle increases.

(6) The heat source decreases the temperature field and enhances the heat transfer rate.

Abbreviations

Pr:	Prandtl number
t, t^*:	Dimensional and dimensionless times, respectively
T:	Temperature
(x, y, z):	The distance measured along the meridian of a circular segment parallel to the cone's superficial
C_{fx}:	Local skin friction in x-direction
α:	Semi-upright angle of the cone
C_{fy}:	Skin friction in y-direction
η:	Similarity variable
f, g:	Dimensionless stream function and velocity component in $x-$ and $y-$direction, respectively
θ:	Dimensionless temperature
K, L:	Thermal conductivity and characteristic length, respectively
$Km^{-1}K^{-1}$ γ_1:	Buoyancy parameter due to temperature
μ:	Dynamic viscosity (Nms^{-2})
v:	Kinematic viscosity (m^2s^{-1})
Nu_x:	Local Nusselt number
ρ:	Density (kgm^{-3})
Re_x:	Reynold number based on x

Re_L: Reynold number based on L
$(\rho C_p)_{hnf}$:   Heat capacity of hybrid nanofluid (jk^{-1})
ρ_{hnf}:   Nanofluid density (kgm^{-3})
μ_f: The viscosity of fluid (Nms^{-2})
(u, v, w):   Velocity components (ms^{-1})
μ_{hnf}:   Hybrid nanofluid viscosity (Nms^{-2})
α_{hnf}:   Hybrid nanofluid thermal diffusivity
                 $(m^2 s^{-1})$.

Data Availability

The data used to support the findings of this study are available from the corresponding author upon request.

Conflicts of Interest

The authors declare that they have no conflicts of interest.

Acknowledgments

References

[1] E. Abd-Elaziz, M. Marin, and M. Othman, "On the effect of Thomson and initial stress in a thermo-porous elastic solid under G-N electromagnetic theory," *Symmetry Plus*, vol. 11, no. 3, p. 413, 2019.

[2] M. Y. Malik, A. Hussain, and S. Nadeem, "Flow of a non-Newtonian nanofluid between coaxial cylinders with variable viscosity," *Zeitschrift für Naturforschung A*, vol. 67, no. 5, pp. 255–261, 2012.

[3] R. Ellahi, M. Hassan, and A. Zeeshan, "Aggregation effects on water base Al2O3-nanofluid over permeable wedge in mixed convection," *Asia-Pacific Journal of Chemical Engineering*, vol. 11, no. 2, pp. 179–186, 2016.

[4] T. Salahuddin, M. Y. Malik, A. Hussain, M. Awais, I. Khan, and M. Khan, "Analysis of tangent hyperbolic nanofluid impinging on a stretching cylinder near the stagnation point," *Results in Physics*, vol. 7, pp. 426–434, 2017.

[5] R. Ellahi, M. Hassan, and A. Zeeshan, "A study of heat transfer in power law nanofluid," *Thermal Science*, vol. 20, no. 6, pp. 2015–2026, 2016.

[6] M. Khan, A. Shahid, M. Y. Malik, and T. Salahuddin, "Thermal and concentration diffusion in Jeffery nanofluid flow over an inclined stretching sheet: a generalized Fourier's and Fick's perspective," *Journal of Molecular Liquids*, vol. 251, pp. 7–14, 2018.

[7] A. Zeeshan, M. Hassan, R. Ellahi, and M. Nawaz, "Shape effect of nanosize particles in unsteady mixed convection flow of nanofluid over disk with entropy generation," *Proceedings of the Institution of Mechanical Engineers - Part E: Journal of Process Mechanical Engineering*, vol. 231, no. 4, pp. 871–879, 2017.

[8] R. Ellahi, M. Hassan, and A. Zeeshan, "Study of natural convection MHD nanofluid by means of single and multi-walled carbon nanotubes suspended in a salt-water solution," *IEEE Transactions on Nanotechnology*, vol. 14, no. 4, pp. 726–734, 2015.

[9] F. Ur Rehman, S. Nadeem, H. Ur Rehman, and R. Ul Haq, "Thermophysical analysis for three-dimensional MHD stagnation-point flow of nano-material influenced by an exponential stretching surface," *Results in physics*, vol. 8, pp. 316–323, 2018.

[10] D. Belatrache, N. Saifi, A. Harrouz, and S. Bentouba, "Modelling and Numerical Investigation of the thermal properties effect on the soil temperature in Adrar region," *Algerian Journal of Renewable Energy and Sustainable Development*, vol. 2, no. 02, pp. 165–174, 2020.

[11] R. Ali, A. Shahzad, M. Khan, and M. Ayub, "Analytic and numerical solutions for axisymmetric flow with partial slip," *Engineering with Computers*, vol. 32, no. 1, pp. 149–154, 2016.

[12] A. Shahzad, R. Ali, M. Hussain, and M. Kamran, "Unsteady axisymmetric flow and heat transfer over time-dependent radially stretching sheet," *Alexandria Engineering Journal*, vol. 56, no. 1, pp. 35–41, 2017.

[13] H. Chang, C. S. Jwo, C. H. Lo, T. T. Tsung, M. J. Kao, and H. M. Lin, "Rheology of CuO nanoparticle suspension prepared by ASNSS," *Reviews on Advanced Materials Science*, vol. 10, no. 2, pp. 128–132, 2005.

[14] A. K. Santra, S. Sen, and N. Chakraborty, "Study of heat transfer due to laminar flow of copper-water nanofluid through two isothermally heated parallel plates," *International Journal of Thermal Sciences*, vol. 48, no. 2, pp. 391–400, 2009.

[15] K. Das, P. R. Duari, and P. K. Kundu, "Nanofluid flow over an unsteady stretching surface in presence of thermal radiation," *Alexandria engineering journal*, vol. 53, no. 3, pp. 737–745, 2014.

[16] Y. Xuan and Q. Li, "Investigation on convective heat transfer and flow features of nanofluids," *Journal of Heat Transfer*, vol. 125, no. 1, pp. 151–155, 2003.

[17] M. Sheikholeslami, D. Domiri Ganji, M. Younus Javed, and R. Ellahi, "Effect of thermal radiation on magnetohydrodynamics nanofluid flow and heat transfer by means of two phase model," *Journal of Magnetism and Magnetic Materials*, vol. 374, pp. 36–43, 2015.

[18] M. Sheikholeslami Kandelousi, "KKL correlation for simulation of nanofluid flow and heat transfer in a permeable channel," *Physics Letters A*, vol. 378, no. 45, pp. 3331–3339, 2014.

[19] M. Sheikholeslami and A. J. Chamkha, "Flow and convective heat transfer of a ferro-nanofluid in a double-sided lid-driven cavity with a wavy wall in the presence of a variable magnetic field," *Numerical Heat Transfer, Part A: Applications*, vol. 69, no. 10, pp. 1186–1200, 2016.

[20] M. Sheikholeslami and A. J. Chamkha, "Electrohydrodynamic free convection heat transfer of a nanofluid in a semi-annulus enclosure with a sinusoidal wall," *Numerical Heat Transfer, Part A: Applications*, vol. 69, no. 7, pp. 781–793, 2016.

[21] M. Sheikholeslami and A. J. Chamkha, "Influence of Lorentz forces on nanofluid forced convection considering Marangoni convection," *Journal of Molecular Liquids*, vol. 225, pp. 750–757, 2017.

[22] S. Vlase, M. Marin, A. Öchsner, and M. L. Scutaru, "Motion equation for a flexible one-dimensional element used in the dynamical analysis of a multibody system," *Continuum Mechanics and Thermodynamics*, vol. 31, no. 3, pp. 715–724, 2019.

[23] M. Y. Malik, "Effects of second order chemical reaction on MHD free convection dissipative fluid flow past an inclined porous surface by way of heat generation: a Lie group analysis," *Information Sciences Letters*, vol. 5, no. 2, p. 1, 2016.

[24] R. Sivaraj and B. Rushi Kumar, "Viscoelastic fluid flow over a moving vertical cone and flat plate with variable electric

conductivity," *International Journal of Heat and Mass Transfer*, vol. 61, pp. 119–128, 2013.

[25] A. Hussain, A. Rehman, S. Nadeem et al., "A combined convection carreau–yasuda nanofluid model over a convective heated surface near a stagnation point: a numerical study," *Mathematical Problems in Engineering*, vol. 2021, Article ID 6665743, 14 pages, 2021.

[26] W. A. Aissa and A. A. Mohammadein, "Joule heating effects on a micropolar fluid past a stretching sheet with variable electric conductivity," *Journal of Computational and Applied Mechanics*, vol. 6, no. 1, pp. 3–13, 2005.

[27] M. M. Rahman, M. J. Uddin, and A. Aziz, "Effects of variable electric conductivity and non-uniform heat source (or sink)on convective micropolar fluid flow along an inclined flat plate with surfaceheat flux," *International Journal of Thermal Sciences*, vol. 48, no. 12, pp. 2331–2340, 2009.

[28] M. M. Rahman, A. Aziz, and M. A. Al-Lawatia, "Heat transfer in micropolar fluid along an inclined permeable plate with variable fluid properties," *International Journal of Thermal Sciences*, vol. 49, no. 6, pp. 993–1002, 2010.

[29] C. J. Chrisman, P. Albuquerque, A. J. Guimaraes, E. Nieves, and A. Casadevall, "Phospholipids trigger Cryptococcus neoformans capsular enlargement during interactions with amoebae and macrophages," *PLoS Pathogens*, vol. 7, no. 5, Article ID e1002047, 2011.

[30] S. Z. Shirejini, S. Rashidi, and J. A. Esfahani, "Recovery of drop in heat transfer rate for a rotating system by nanofluids," *Journal of Molecular Liquids*, vol. 220, pp. 961–969, 2016.

[31] M. Turkyilmazoglu, "Effects of uniform radial electric field on the MHD heat and fluid flow due to a rotating disk," *International Journal of Engineering Science*, vol. 51, pp. 233–240, 2012.

[32] M. Turkyilmazoglu, "Fluid flow and heat transfer over a rotating and vertically moving disk," *Physics of Fluids*, vol. 30, no. 6, Article ID 063605, 2018.

[33] M. Turkyilmazoglu, "A note on the induced flow and heat transfer due to a deforming cone rotating in a quiescent fluid," *Journal of Heat Transfer*, vol. 140, no. 12, 2018.

[34] R. Kumar, G. S. Seth, and A. Bhattacharyya, "Entropy generation of von Karman's radiative flow with Al 2 O 3 and Cu nanoparticles between two coaxial rotating disks: a finite-element analysis," *The European Physical Journal Plus*, vol. 134, no. 12, pp. 1–20, 2019.

[35] M. Turkyilmazoglu, "On the fluid flow and heat transfer between a cone and a disk both stationary or rotating," *Mathematics and Computers in Simulation*, vol. 177, pp. 329–340, 2020.

[36] T. Gul, R. S. Gul, W. Noman et al., "CNTs-Nanofluid flow in a Rotating system between the gap of a disk and cone," *Physica Scripta*, vol. 95, no. 12, Article ID 125202, 2020.

[37] L. A. Lund, Z. Omar, J. Raza, and I. Khan, "Magnetohydrodynamic flow of Cu-Fe3O4/H2O hybrid nanofluid with effect of viscous dissipation: dual similarity solutions," *Journal of Thermal Analysis and Calorimetry*, vol. 143, no. 2, pp. 915–927, 2021.

[38] P. K. Kameswaran, P. Sibanda, C. RamReddy, and P. V. Murthy, "Dual solutions of stagnation-point flow of a nanofluid over a stretching surface," *Boundary Value Problems*, vol. 10, no. 1, pp. 1–12, 2013.

[39] S. U. Devi and S. A. Devi, "Heat transfer enhancement of Cu–Al2O3/water hybrid nanofluid flow over a stretching sheet," *Journal of the Nigerian Mathematical Society*, vol. 36, no. 2, pp. 419–433, 2017.

Research Article

A New Heat Dissipation Model and Convective Two-Phase Nanofluid in Brittle Medium Flow over a Cone

Azad Hussain,[1] **Qusain Haider** [ID][,1] **Aysha Rehman** [ID][,1] **Aishah Abdussattar,**[1] **and M. Y Malik** [ID][2]

[1]*Department of Mathematics, University of Gujrat, Gujrat 50700, Pakistan*
[2]*Department of Mathematics, College of Sciences, King Khalid University, Abha 61413, Saudi Arabia*

Correspondence should be addressed to Qusain Haider; qusain.haider336@gmail.com

A time-dependent convectional flow of a two-phase nanofluid over a rotating cone with the impact of heat and mass rates is elaborated in this article. The instability in the flow field is induced by the cone angular velocity that depends on the time. The Navier–Stokes self-similar solution and the energy equations are obtained numerically. Here, the achieved solution is not only for Navier–Stokes equations but also for the equations of the boundary layers. In this work, the concentration, Brownian motion, and thermal buoyancy effects have important significance. We have assumed viscous dissipation with heat-absorbing fluid. Similarity answers for spinning cones with divider temperature boundary conditions give an arrangement of nonlinear differential conditions that have been handled numerically. The MATLAB methodology BVP4C is used to resolve the reduced structure of nonlinear differential equations numerically. Observation for skin friction and Nusselt number is also taken into account. Velocity and temperature impact is depicted graphically, while the outward shear stress values and heat allocation rate are included in tables.

1. Introduction

The design of reliable equipment in manufacturing industries relies heavily on convective flow ended a cone through radiative heat and form transfer. Due to its relevance in modern technology and applications in geothermal engineering, as well as other hydrological and astrophysical biofluid studies, researchers have shown a strong interest in heat and mass transfer in Newtonian flows in recent years. The analysis of fluid flow in a cone encompasses a wide variety of subjects. It is used in plastic processing, elastic sheet cooling, polymer technology, polymer chemistry, and engineering, to name a few. So, because of its enormous applications, the researchers are holding a purpose in this area. Dependence of viscosity on temperature plays a vital role in the realm of fluids flow. The viscosity of water decreases as the temperature increases, while the viscosity of gases rises as the temperature rises. The increase in temperature in lubricating fluids causes internal friction that affects the fluid's viscosity and will no longer remain

constant. Because of this inadequacy, many researchers are interested to understand the effects of using different variable viscosity models.

Nanofluids remain a class of heat allocation fluids which caused suspended nanoparticles are distributed in the fluid (1–100 nm). In base fluids, locomotive oil, polymer solutions, bio-fluids, other critical fluids, water, and organic fluids (e.g., ethylene and diethylene) are commonly used. Nanoparticles are generally made of carbon in diverse edifices (e.g., carbon nanotubes, black lead, and diamond), metals (e.g., copper, hoary, and gold), and metal oxides (e.g., titanium and zirconia), besides functionalized nanoparticles. A wide-range of possible applications has been initiated for the use of nanofluids. Choi remained the first to research updraft conductivity development in nanofluids [1–12]. Nanofluids, bio and pharmacological nanofluids, remedial nanofluids, environmental nanofluids, and other heat transfer fluids are categorized according to their applications. Many researchers have looked into how extent, concentration, form, and other

assets affect the warmth transfer rate of a fluid. For the Prandtl number of airs, Hering and Grosh [13] investigated a steady mixed convection boundary layer flow from a vertical cone in an ambient fluid. For a broad range of Prandtl numbers, Himasekhar et al. [14] solved the similarity solution of the mixed convection boundary layer flow over a vertical rotating cone in an ambient fluid. Body solutions of unstable mixed convection flow from a rotating cone in a rotating fluid were obtained by Anil Kumar and Roy [15] a few years ago. Chamkha and Mudhaf [16] examined heat generation, consumption, and unstable heat and mass transfer from a revolving vertical cone with a magnetic field. Ravindran et al. [17] suggested a new approach for investigating the effects of fluid flow (suction/injection) on a vertical porous cone's steady natural convection boundary layer flow. The impact of heat-dependent viscosity with viscous heat generation on third-grade fluid flow in a standard pipe was examined by Nadeem and Hussain [18]. Exploitation the finite simple difference method, numerical solutions were obtained. Different fluids like water, ethylene glycol, and oil, due to their poor thermal conductivity, have low heat transfer properties. It is now realized that by retaining nano-sized metal flakes such as Al, titanium, silver, gold, Cu, or their oxides, the thermophysical characteristics of such fluids could be enhanced, ending in what is commonly known as nanofluid [19]. Several researchers have spent the last few years studying the edge layer movement of nanofluid fluids in various geometries and under various conditions. Kameswaran et al. [20] investigated the flow of hydromagnetic nanofluids due to a shrinking surface. Over a stretching field, Kameswaran et al. [21] discovered solutions for the deflation-point flow equations. Fauzi et al. [22] explored the time-independent nanofluid boundary film flowing along a perpendicular cone in a brittle medium. Boutra et al. [23] investigated unrestricted convection induction in a nanofluid-filled framework through round heaters, and Ambethkar and Kumar [24] investigated 2D noncompressible flow solutions with the transfer of heat in a powered square cavity singing stream function-vorticity model. Cheng [25] addressed natural convection flowing through a formatted cone in a brittle medium in the boundary layer. Chamkha et al. [26] examined the issue of mixed convection boundary layer flow in a continuous, turbulent flow over a rigid cone enclosed in a brittle thermal radiation medium. Nadeem and Saleem [27] examined turbulent nanofluid flow in a turning cone subjected to an induced magnetic field. In this paper, we look at a two-phase nanofluid flow along a vertically stretching cone.

The work of Heiring and Grosh [28] on natural convection over a multi-isothermal cone is one of the most recent cone-shaped surface boundary layer studies. A theoretical study of forced convection flow in relation to a rotating cone was suggested by Tien and Tsuji [29]. Koh and Price [30] have evaluated the transfer of heat past a pivoting cone. Ellahi et al. [31] have studied the analysis of simplified third-grade slide Couette fluid flow. There are some related studies about this phenomenon provided in References [32–43]. Extrusion processes, plastic product processing, polymers, and silicone slips, wire and copper-coating, glass and fiber optic production, hot spinning manufacture, metal rolling, food preparation, and a variety of other topics are frequently mentioned.

The combination of fluids has a broad range of applications, including cooling systems, heating processes, as well as biomedical and automotive science and technologies that control heat and mass transfer rates. The persistence of this article is to inspect the flow of liquid-based two-phase nanofluids (copper oxide and silver added to water) over a rotating cone. Two-phase flows include the flows that transition from pure liquid to vapor as a result of external heating, separated flows, and scattered two-phase flows in which phase is observed in a continuous carrier phase in the form of particles, droplets, or leaks. We have solved governing differential equations with the assistance of the BVP4V scheme under MATLAB. It also describes the possessions of relevant bodily parameters that affect the velocities, surface strain tensors, temperature, and convection rate with the help of graphs and tables.

2. Mathematical Formulations

We deliberate the flow of a compressible viscous nanofluid along an erect turning cone enclosed in a brittle medium as a two-dimensional time-dependent boundary layer. Figure 1 displays the scheme of coordinates and the corporal model. We have used a rectangular coordinate system in which the x−axis is determined along a meridian, the y−axis is determined along a round section, and the z−axis is determined on the cone's surface. Let u, v, and w be velocity gears, with x (tangential), y (azimuthal), and z (horizontal) orders (normal). The equations can be written as follows:

$$u + \frac{x}{\partial z}\frac{\partial u}{\partial z} + x\frac{\partial w}{\partial z} = 0, \tag{1}$$

$$\frac{\partial u}{\partial t} + u\frac{\partial u}{\partial x} + \frac{w\partial u}{\partial z} - \frac{v^2}{x} = \frac{v_{nf}}{\partial z^2}\frac{\partial^2 u}{\partial z^2} - \frac{v_e^2}{x} + g\zeta \cos \alpha^* (T - T_\infty), \tag{2}$$
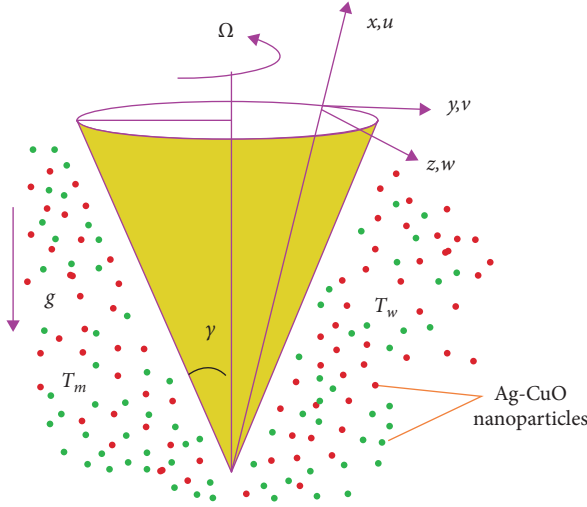
FIGURE 1: Bodily geometry of the problem.

$$\frac{\partial v}{\partial t} + \frac{u\partial v}{\partial x} + w\frac{\partial v}{\partial z} + u\frac{v}{x} = \frac{\partial v_e}{\partial t} + v_{nf}\frac{\partial^2 v}{\partial z^2}, \quad (3)$$

$$u\frac{\partial T}{\partial x} + \frac{\partial T}{\partial t} + w\frac{\partial T}{\partial z} = \alpha_{nf}\frac{\partial^2 T}{\partial z^2}. \quad (4)$$

The boundaries conditions are set, subject to initial terms and conditions as follows:

$$u(0, x, z) = v = w = u_i,$$

$$v_i w_i,$$

$$T = T_i,$$

$$u(t, 0, z) = w = 0, \quad (5)$$

$$v = \frac{\Omega_1 x \sin \alpha^*}{1 - st^*},$$

$$T = T_W.$$

Reference [15] provides the momentum, temperature, initial conditions, and boundary conditions for this issue.

The following transformation is defined where A is the Deborah number and γ_1 and γ_2 are the buoyancy parameters. The things of physical importance use in the two-phase model are as follows: α_{nf} is the thermal diffusivity, v_{nf} is the kinematic viscosity, μ_{nf} is the effective dynamic viscosity, ρ_{nf} is the density, (ρC_P)nf is the heat capacity, κ_{nf} is the nanofluid thermal conductivity, and $(\rho\beta)_{nf}$ is the nanofluid thermal expansion coefficient:

$$\eta = \frac{(x\Omega \sin \alpha^*)^{0.5} z}{v(1 - st^*)^{0.5}},$$

$$v_e = \frac{x\Omega_2 \sin \alpha^*}{1 - st^*},$$

$$\alpha = \frac{\Omega_1}{\Omega},$$

$$t^* = \Omega \sin \alpha^* t,$$

$$w = \frac{(\sin \alpha^*)^{1/2} (v\Omega)^{1/2} f(\eta)}{(1 - st^*)^{1/2}},$$

$$T - T_\infty = (T_W - T_\infty)\theta(\eta),$$

$$u(t, x, z) = -\frac{2^{-1} \sin \alpha^* f' \Omega x}{1 - st^*}, \quad (6)$$

$$v = \Omega x \sin \alpha^* {}^{1/2}_{(1-st^*)} g(\eta),$$

$$T_W - T_\infty = \frac{(T_0 - T_\infty)xL^{-1}}{(1 - st^*)^2},$$

$$Gr_1 = \frac{\cos \alpha^* (T_0 - T_\infty)g\beta L^3}{v^2},$$

$$\gamma_1 = \frac{Gr_1}{Re_L^2},$$

$$Re_L = \sin \alpha^* \Omega L^2 v^{-1},$$

$$Pr = \frac{v}{\alpha}.$$

$$v_{nf} = \frac{\mu_{nf}}{\rho_{nf}},$$

$$\alpha_{nf} = \frac{k_{nf}}{(\rho c_p)_{nf}},$$

$$\mu = \mu_f (1 - \phi)^{-2.5},$$

$$\rho_{nf} = (1 - \phi) * \rho_f + \phi\rho_s,$$

$$(\rho c_p)_{nf},$$

$$\rho_f = (1 - \phi) * (c_p\rho)_f + \phi(\rho c_p)_f, \quad (7)$$

$$\frac{k_{nf}}{k_f} = \frac{((k_s + 2k_f) - 2\phi(k_f - k_s))}{(k_s + 2k_f + \phi(k_f - k_s))},$$

$$(\rho\beta)_{nf} = (1 - \phi)(\rho\beta)_f + \phi(\rho\beta)_s.$$

The transformation's equations (7) and (6) are replaced into (1)–(3). After that equation (1) will be fulfilled automatically, and equations (2)–(4) diminish to the form as follows:

$$\left(\frac{f'''}{(1-\phi)^{2.5}\left(1-\phi+\phi(\rho_s/\rho_f)\right)} - \left(f+\frac{1}{2}s\eta\right)f' + \left(\frac{1}{2}f'-s\right)f' - 2\left(g-(1-\alpha_1)^2\right) - 2\gamma_1\theta \right),$$

$$\left(\frac{g''}{(1-\phi)^{2.5}\left(1-\phi+\phi(\rho_s/\rho_f)\right)} - (-f'g+fg') + s\left(1-\alpha_1-g-\frac{1}{2}\eta g'\right) \right), \tag{8}$$

$$\left(\frac{1}{Pr}\left(\frac{\kappa_{nf}}{\kappa_f}\right)\theta'' - \left(f\theta'-\frac{f'\theta}{2}\right) - 2s\theta + \frac{1}{2}s\eta\theta' \right).$$

Now, the boundary conditions are

$$
\begin{aligned}
f(0) &= 0, \\
g(\infty) &= -1 + \alpha_1, \\
g(0) &= \alpha_1, \\
\theta(0) &= -1, \\
f\prime(\infty) &= 0, \\
f\prime(0) &= 0, \\
\theta(\infty) &= 0.
\end{aligned}
\tag{9}
$$

The skin friction C_{fx} across the x-axis, C_{fy} along y-axis, and Nusselt sum Nu_x are physical quantities of our distinct interest where

$$C_{fx} = -Re_x^{-(1/2)}\left(\frac{2\mu}{\partial z}\frac{\partial u}{\partial z}\right)_{z=0},$$

$$C_{fy} = \left(\frac{2\mu}{\partial z}\frac{\partial v}{\partial z}\right)_{z=0}\left(-Re_x^{-(1/2)}\right), \tag{10}$$

or in the form of dimensionless

$$
\begin{aligned}
C_{fx}Re_x^{1/2} &= (-f'')_{\eta=0}, \\
C_{fy}Re_x^{1/2} &= (-g\prime)_{\eta=0}.
\end{aligned}
\tag{11}
$$

In dimensionless form, the heat transfer coefficient is given as

$$Nu_x Re_x^{1/2} = -\theta\prime(0). \tag{12}$$

Now, the Reynolds number is

$$Re_x \; \blacksquare \; \frac{x^2 \, \text{🖐}\sin \text{☺} \, \text{🎧} \, \mathscr{s}t \, \text{💚}^{\text{d}}}{m_{\!/\!\!/}}. \tag{13}$$

3. Numerical Solution

The numerical technique performs the solutions of the joined linear sinusoidal differential equations. The following initial estimates and nonlinear operators are f_0, g_0, and θ_0, respectively, for velocity components and temperature fields.

New variables are defined simplifying differential equations of high order in the form of first-order equation, i.e.,

$$
\begin{aligned}
F &= y_1, \\
\rho_f &= b, \\
f' &= y_2, \\
g &= y_4, \\
F'' &= y_3, \\
\rho_s &= a, \\
g' &= y_5, \\
g'' &= y_5', \\
F''' &= y_3', \\
\theta(0) &= y_6, \\
\theta' &= y_7, \\
\theta'' &= y_7', \\
k_s &= m, \\
k_f &= n, \\
(\rho c_p)_s &= c, \\
(\rho c_p)_f &= d.
\end{aligned}
\tag{14}
$$

Now, the new equations are

$$y_3' = \left[\left[(1-\phi)^{2.5}\left(1-\phi+\frac{\phi a}{b}\right) \right]\left[\left(y(1)y(3)+\frac{1}{2}xsy(3)\right) - \frac{1}{2}y^2(2) + sy(2) \right) + 2y^2(4) - (1-\alpha_1)^2 + 2\gamma_1 y(6) \right],$$

$$y_5' = \left[(1-\phi)^{2.5}\left(1-\phi+\frac{\phi a}{b}\right) \right]\left[y(1)y(5) - y(4)y(2)\left(-s+s\alpha_1+sy(4)+\frac{1}{2}sxy(5)\right) \right], \tag{15}$$

$$y_7' = \left[\frac{(m+2)(n+2)\phi(n-m)}{(m+2)(n-2)\phi(n-m)} \right]\left[Pr\,y(7)y(1) - \frac{y(6)y(2)}{2}\left(2sy(6)-\frac{Pr1}{2}sxy(7)\right) \right].$$
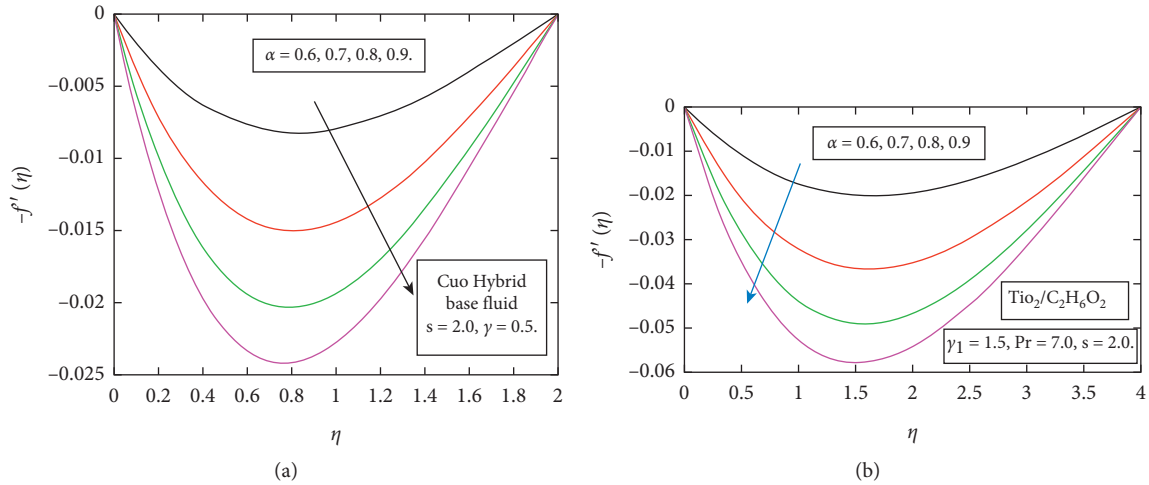
Along with limitation,
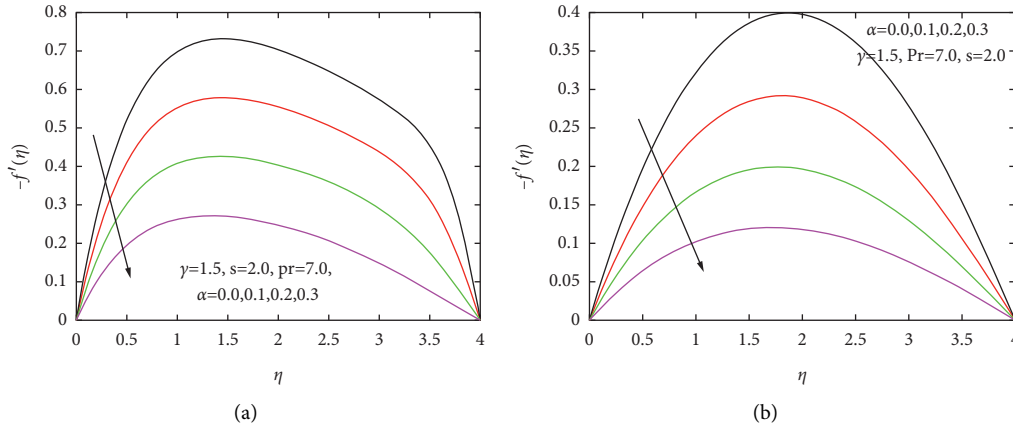
FIGURE 2: (a) Impact of α_1 on the velocity distribution $-f\prime(n)$ for Cuo nanoparticles. (b) Impact of α_1 on the velocity distribution $-f\prime(n)$ for Ag nanoparticles.

$$y(1) = 0,$$
$$y(6) = -1,$$
$$y_\infty(2) = 0,$$
$$y(2) = 0, \qquad (16)$$
$$y(4) = \alpha_1,$$
$$y_\infty(6) = 0.$$

4. Graphical Observations and Discussion

This section of the learning includes the graphical and mathematical outcomes of multiple major parameters on velocities, temperature, coefficients of surface stress, and coefficient of heat transfer. Such variations are noted in figures. Figures 2(a) and 2(b) and Figures 3(a) and 3(b) are sketched to demonstrate primary velocity activity for parameter mixed convection. The positive parameter of buoyancy functions as a desirable gradient of pressure is mended to improve the property of the fluid. It is foretold from Figures 2(a) and 2(b) and Figures 3(a) and 3(b) that the thickness of the upper and lower layers will decrease with increase in α_1 and γ_1 values; further, the primary velocity will have a higher magnitude for γ_1. The effect of mixed convection on buoyancy parameter γ_1 is to decrease the secondary velocity g (see Figures 4(a) and 4(b), respectively). The secondary velocity g is also seen to have the greater magnitude for α_1. A vertically spinning or expanding cone was analyzed on the unstable frontier layer flow of both water-based nanofluids. The flow was contrary to viscous debauchery, the cohort of excess heat, and a natural process. The numerical technique is used to resolve the equations. We studied the belongings on the nanofluid velocity ($f \& g$) and temperature (θ) profiles and even the skin friction ($C_{fx} \& C_{fy}$) coefficient, energy, and mass exchange coefficients of the nanoparticle volume segment, buoyancy parameter γ_1, heat production, and chemical reaction. We considered nanoparticles of copper oxide (Cuo) and silver

(Ag) with water as the basis fluid. In Figures 2(a) and 2(b) and Figures 3(a) and 3(b), see the variation of the angular velocity ratio α_1, and the buoyancy coefficient γ_1 on tangential velocity $-f\prime$ is plotted. Tangential velocities are observed to decrease for α_1 and γ_1 parameters. Figures 4(a) and 4(b) display the variance of the angular velocity ratio α_1 on azimuthal velocity g. At g, the action of α_1 is contrary to that of tangential velocity $-f\prime$. Here, Figures 5(a) and 5(b) are shown in the temperature sector θ for specific Pr values. The width of the thermoelectric boundary layer is indicated to reduce for rising Pr values. This is because the higher Prandtl number fluid has more heat conductivity resulting in a softer heat boundary layer. Now, see in Cuo case Figure 5(a) temperature decrease with increases the value of Pr but contrary in Ag case Figure 5(b). Figures 6(a) and 6(b) address the variance in the ratio of the γ_1 buoyancy parameter on the secondary velocity skin friction coefficient. Skin values decrease in Cuo case but enhance in Tio_2 case. Figures 7(a) and 7(b) show changes in the coefficient of C_{fy} skin friction by rising α_1. Figure 7(a) shows that C_{fy} values increase in Cuo but Figure 7(b) shows decline values of C_{fy}. Physically, we can conclude that the surface temperature is higher than the fluid temperature close to the cone boundaries; therefore, larger γ_1 gives the greater values of skin friction. It is examined that the coefficient of tangential skin friction ($C_{fx} \& C_{fy}$) decreases as α_1 increases (see Figures 7(a) and 7(b)). Figures 8(a) and 8(b) and Figures 9(a) and 9(b) show that the primary skin friction coefficients increase or decrease with the rise in α_1, also the same behavior for γ_1. In Figures 8(a) and 9(a), C_{fy} values decline for Cuo, and we see that in Figures 8(b) and 9(b), the values of C_{fx} are enhanced when the values of α_1 and γ_1 are increased. Since the impact of Pr in the primary $-f'$ and secondary g directions on the velocity profiles is relatively small, therefore, the profiles are ignored. In Figures 10(a) and 10(b), the heat exchange rate has decreased, with increase in Pr. In Figures 10(a) and 10(b), see that the Nusselt number decreases when the values of Pr increase. Finally, figures also display the positive impact of heat dissipation on the local
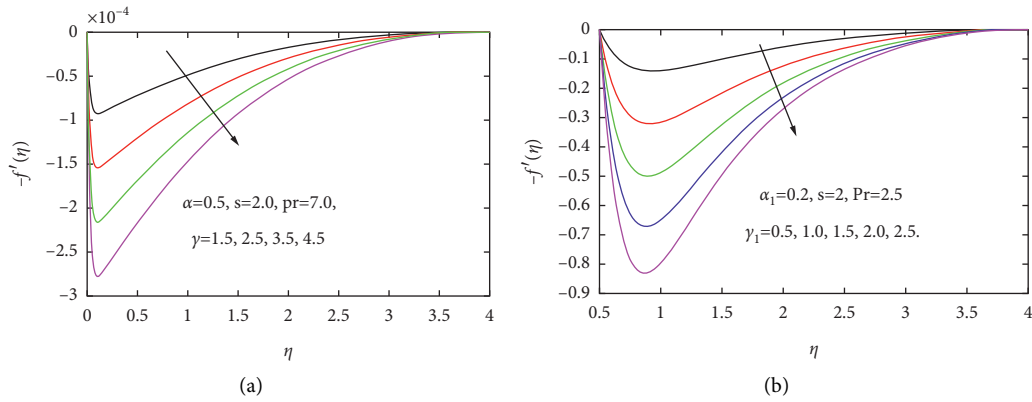
Figure 3: (a) Impact of γ_1 on velocity distribution $-f\prime$ for Cuo nanoparticles. (b) Impact of γ_1 on velocity distribution $-f\prime$ for Ag nanoparticles.
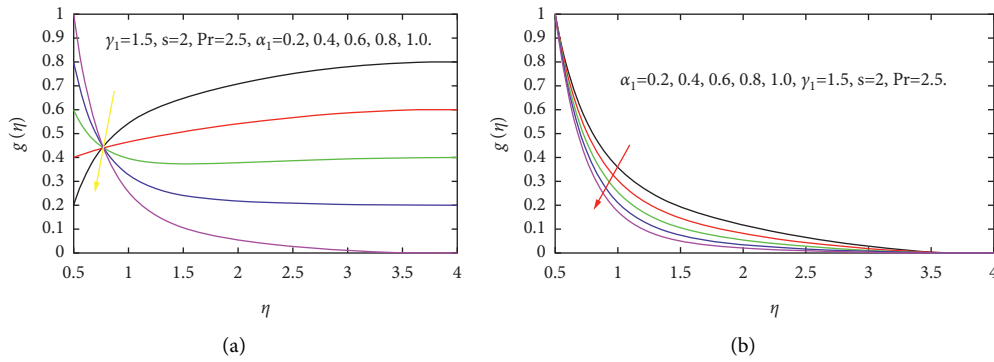
Figure 4: (a) Impact of α_1 on velocity profile $g(\eta)$ for Cuo nanoparticles. (b) Impact of α_1 on velocity profile $g(\eta)$ for Ag nanoparticles.
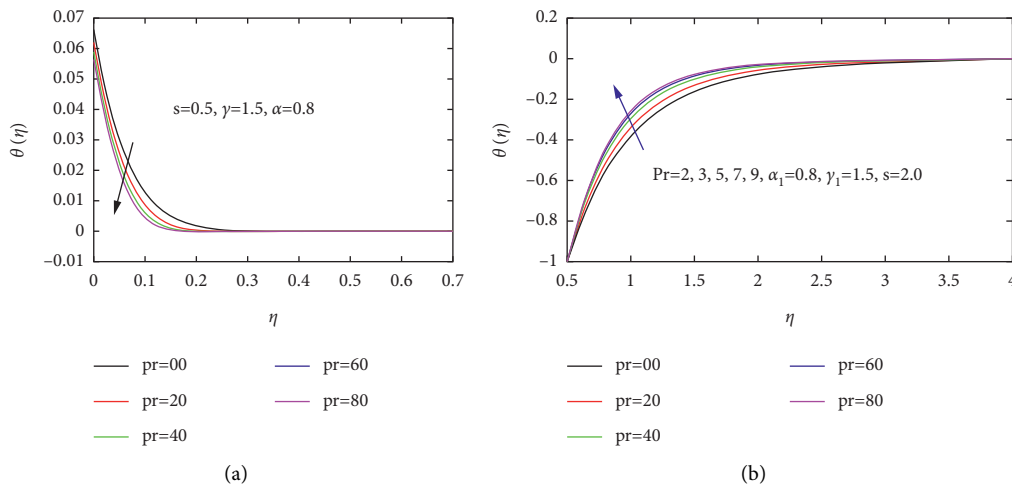
Figure 5: (a) Deviation of Pr on temperature profile $\theta(\eta)$ for Cuo nanoparticles. (b) Deviation of Pr on temperature profile $\theta(\eta)$ for Ag nanoparticles.
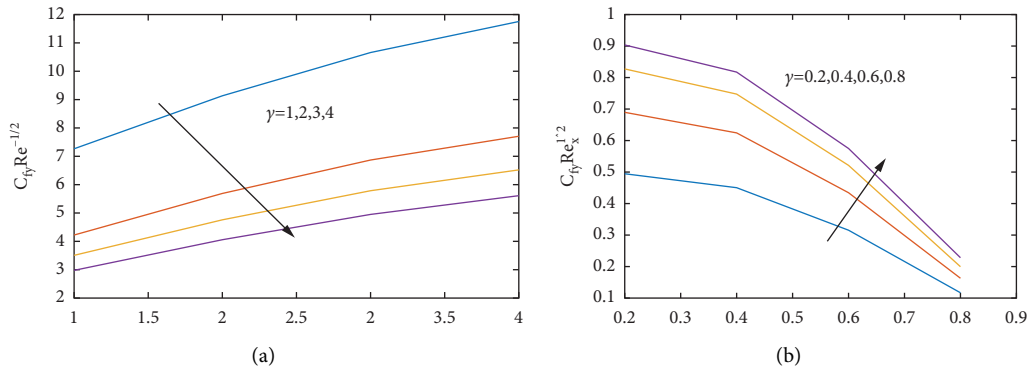
FIGURE 6: (a) Impact on skin friction C_{fy} along y-direction of γ_1 for Cuo nanoparticles. (b) Impact on skin friction C_{fy} along y-direction of γ_1 for Ag nanoparticles.
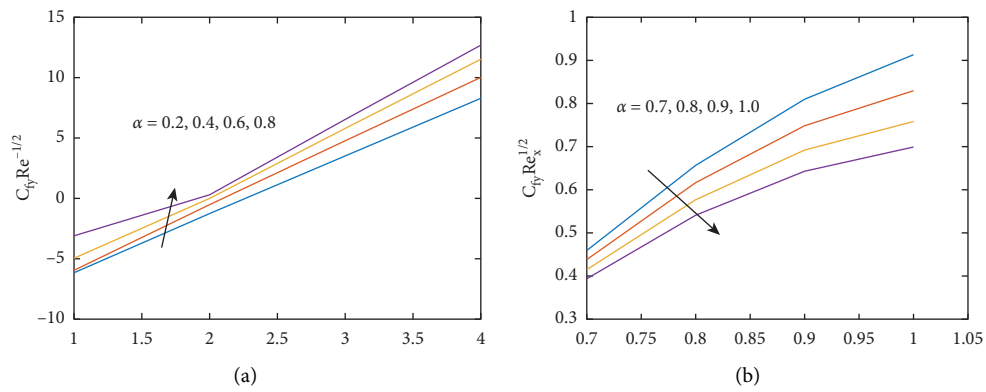
FIGURE 7: (a) Impact on skin friction of α_1 besides y-direction for $Cuo - water$. (b) Impact on skin friction of α_1 besides y-direction for $Ag - water$.
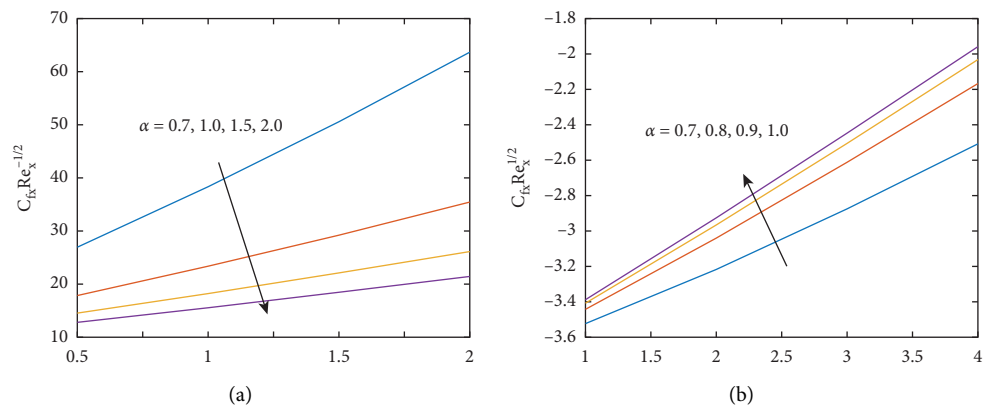
FIGURE 8: (a) Influence on skin friction C_{fx} along x-direction of α_1 for $Cuo - water$. (b) Influence on skin friction C_{fx} along x-direction of α_1 for $Ag - water$

(a)   (b)
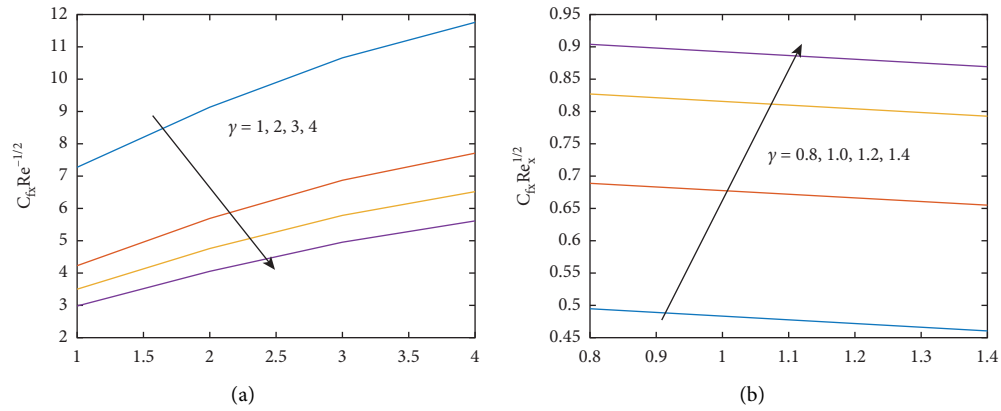
FIGURE 9: (a) Influence on skin friction of γ_1 along y-direction for Cuo $-$ water. (b) Influence on skin friction of γ_1 along y-direction for Ag $-$ water.

(a)   (b)
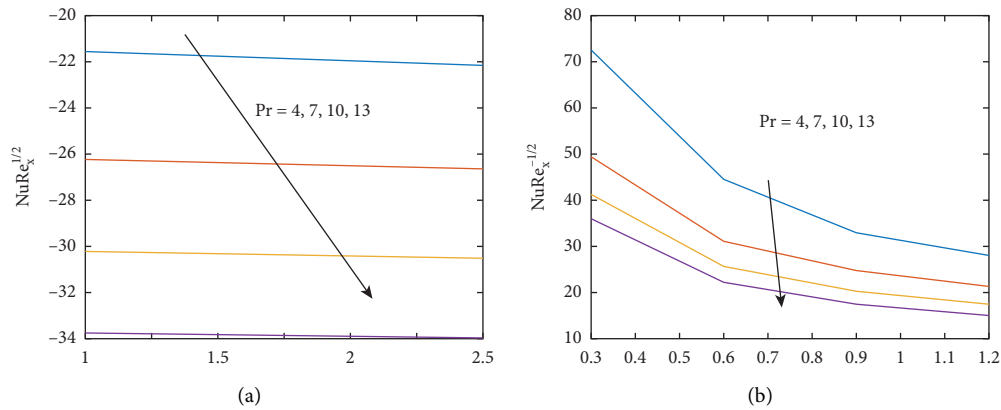
FIGURE 10: (a) Impact on the Nusselt number of Pr for Cuo $-$ water of nanoparticles. (b) Impact on the Nusselt number of Pr for water Ag of nanoparticles.

TABLE 1: Variations of α, γ, s, and $\mathbf{Pr}$ on the coefficient of skin friction $\mathbf{C_{fx}}$ and $\mathbf{C_{fy}}$ and local Nusselt number $(\mathbf{Nu_x})$ for $\mathbf{Cuo - water}$.

α_1	γ_1	s	Pr	C_{fx}	C_{fy}	Nu_x
0.5	1.5	2.0	1.0	0.56971	0.64524	−33.7303
	2.5			0.55597	0.61825	−33.8036
	3.5			0.54147	0.59124	−33.8762
	4.5			0.52733	0.56420	−33.9481
0.8				0.75065	0.35930	−65.5158
1.0	2.5	0.8	2.5	0.73655	0.55678	−65.6143
1.2				0.72245	0.81300	−65.7122
1.4				0.70835	0.86329	−65.8094
		0.6		0.55559	0.54225	−71.2271
		0.8		0.54147	0.52817	−71.1483
		1.0		0.52735	0.51408	−71.1877
1.2	2.5	1.2	3.5	0.51323	0.50000	−71.1087
			1.0	−21.5615	−26.2363	−30.2121
			1.5	−21.7700	−26.3719	−30.3089
1.2	3.5	1.0	2.0	−21.9711	−26.5047	−30.4045
			2.5	−22.1854	−26.1654	−30.4988

Nusselt number. It must be noted that the shape effects in all figures are positive and growing factor in the ratio of heat flow. Table 1 and Table 2 represent the variations of α_1, γ_1, s, and Pr on the coefficient of skin friction $(C_{fx} \& C_{fy})$ and local Nusselt number (Nu_x). Table 3 shows the physical properties of copper oxide and silver.

TABLE 2: Effects of the parameter on skin friction and Nusselt number for **Ag – water**.

α_1	γ_1	s	Pr	C_{fx}	C_{fy}	Nu_x
0.5	1.5	2.0	1.0	0.160744	0.161692	−33.7303
	2.5			0.159905	0.164064	−33.8036
	3.5			0.161692	0.166214	−33.8762
	4.5			0.161762	0.161692	−33.9481
0.8				0.161825	0.161568	−65.5158
1.0	2.5	0.8	2.5	0.161692	0.161442	−65.6143
1.2				0.160717	0.161692	−65.7122
1.4				1.159742	0.162193	−65.8094
		0.6		0.161692	0.863293	−71.2271
		0.8		0.227089	0.542258	−71.1483
		1.0		0.292715	0.528174	−71.1877
1.2	2.5	1.2	3.5	0.161692	0.514088	−71.1087
			1.0	0.093331	0.500001	−30.2121
			1.5	0.032939	−26.2363	−30.3089
1.2	3.5	1.0	2.0	0.161692	−26.3719	−30.4045
			2.5	0.039527	−26.5047	−30.4988

TABLE 3: Base fluid and nanoparticles have thermophysical characteristics.

Physical properties	C_P	ρ	κ
H_2o	4179	997.1	0.613
Cuo	531.80	6320	76.50
Ag	235	10500	429

List of Symbols

Pr:	Prandtl number
T:	Temperature
C_{fx}:	In the x-direction, there is local skin friction
C_{fy}:	Skin friction in y-direction
f, g:	The velocity of a dimensionless stream function component in $x-$ and $y-$direction, respectively
K, L:	Thermal conductivity and area of the indentation, respectively, $\text{Km}^{-1}\text{K}^{-1}$
μ:	Dynamic viscosity Nms^{-2}
Nu_x:	Local Nusselt number
Re_x:	Reynold number based on x
Re_L:	Reynold number based on L
$(\rho C_p)_{nf}$:	Heat capacity of nanofluid jk^{-1}
(u, v, w):	Velocity components ms^{-1}
t, t^*:	Dimensional and dimensionless times, respectively
(x, y, z):	The distance measured along the meridian of a circular segment parallel to the cone's superficial
α:	Semiupright angle of the cone
η:	Similarity variable
θ:	Dimensionless temperature
γ_1:	Buoyancy parameter due to temperature
v:	Kinematic viscosity m^2s^{-1}
ρ:	Density kgm^{-3}
ρ_{nf}:	Nanofluid density kgm^{-3}
μ_f:	The viscosity of fluid Nms^{-2}
μ_{nf}:	Nanofluid viscosity Nms^{-2}
α_{nf}:	Nanofluid thermal diffusivity m^2s^{-1}.

5. Concluding Remarks

\In this numerical study, we have considered an unstable two-phase nanofluid flow and heat transfer attitudes over a cone littered with two diverse metal types specifically Ag and Cuo. Unsteady mixed convection flow has been investigated in a moving viscous fluid on a turning cone. Numerical solution of ordinary differential equations BVP4C has been implemented successfully. The afresh determined outcomes are recognized to be accessible in the literature in traditional agreement with the findings previously reported. Viscous dissipation was found to have the consequence of swelling the nanofluid temperature within the gravity effects area when the heat transfer rate from the layer decreases with an increase in a viscous heat generation. The analysis summary is as follows:

(1) For increasing γ_1 and α_1, the tangential velocity field $-f'$ declines. However, s near to the boundary often causes $-f\prime$ to decrease and increases it far away from the boundary for increasing γ_1 and α_1.

(2) On elevating α_1, the azimuthal velocity field g decreases and decreases with increase in s.

(3) For higher values of Pr, the temperature profile $\theta(\eta)$ increases for Ag but decreases for Cuo.

(4) Growing the importance of shape effects has raised the temperature profile and also the local Nusselt number.

(5) The two-phase nanoparticle model has always a bigger impact than nanoparticles on the temperature profile.

Data Availability

The data used to support the findings of the study are available from the corresponding author upon request.

Conflicts of Interest

The authors declare that they have no conflicts of interest.

Acknowledgments

References

[1] S. U. S. Choi, "Enhancing thermal conductivity of a fluids with nanoparticles," *ASME Int*, vol. 66, pp. 99–105, 1995.

[2] S. Chen, M. K. Hassanzadeh-Aghdam, and R. Ansari, "An analytical model for elastic modulus calculation of SiC whisker-reinforced hybrid metal matrix nanocomposite containing SiC nanoparticles," *Journal of Alloys and Compounds*, vol. 767, pp. 632–641, 2018.

[3] X. Wang, J. Wang, X. Sun et al., "Hierarchical coral-like NiMoS nanohybrids as highly efficient bifunctional electrocatalysts for overall urea electrolysis," *Nano Research*, vol. 11, no. 2, pp. 988–996, 2018.

[4] M. R. Eid and A. F. Al-Hossainy, "Combined experimental thin film, DFT-TDDFT computational study, flow and heat transfer in [PG-MoS2/ZrO2]C hybrid nanofluid," *Waves in Random and Complex Media*, pp. 1–26, 2021.

[5] P. Wang, X. Zhang, W. Duan, W. Teng, Y. Liu, and Q. Xie, "Superhydrophobic flexible supercapacitors formed by integrating hydrogel with functional carbon nanomaterials," *Chinese Journal of Chemistry*.

[6] M. Wang, M. Hu, B. Hu et al., "Bimetallic cerium and ferric oxides nanoparticles embedded within mesoporous carbon matrix: electrochemical immunosensor for sensitive detection of carbohydrate antigen 19-9," *Biosensors and Bioelectronics*, vol. 135, pp. 22–29, 2019.

[7] Y. Liu, Q. Zhang, M. Xu et al., "Novel and efficient synthesis of Ag-ZnO nanoparticles for the sunlight-induced photocatalytic degradation," *Applied Surface Science*, vol. 476, pp. 632–640, 2019.

[8] H. Alotaibi, S. Althubiti, M. R. Eid, and K. L. Mahny, "Numerical treatment of mhd flow of casson nanofluid via convectively heated non-linear extending surface with viscous dissipation and suction/injection effects," *Computers, Materials & Continua*, vol. 66, no. 1, pp. 229–245, 2020.

[9] W.-C. Tzeng, P.-Y. Su, N.-S. Tzeng, C.-B. Yeh, T.-H. Chen, and C.-H. Chen, "A moral life after a suicide death in Taiwan," *Qualitative Health Research*, vol. 20, no. 7, pp. 999–1007, 2010.

[10] M. Ferdows, M. D. Shamshuddin, S. O. Salawu, and K. Zaimi, "Numerical simulation for the steady nanofluid boundary layer flow over a moving plate with suction and heat generation," *SN Applied Sciences*, vol. 3, no. 2, pp. 1–11, 2021.

[11] A. A. Alaidrous and M. R. Eid, "3-D electromagnetic radiative non-Newtonian nanofluid flow with Joule heating and higher-order reactions in porous materials," *Scientific Reports*, vol. 10, no. 1, pp. 14513–14519, 2020.

[12] A. F. Al-Hossainy and M. R. Eid, "Structure, DFT calculations and heat transfer enhancement in [ZnO/PG + H2O]C hybrid nanofluid flow as a potential solar cell coolant application in a double-tube," *Journal of Materials Science: Materials in Electronics*, vol. 31, no. 18, pp. 15243–15257, 2020.

[13] R. G. Hering and R. J. Grosh, "Laminar free convection from a non-isothermal cone," *International Journal of Heat and Mass Transfer*, vol. 5, no. 11, pp. 1059–1068, 1962.

[14] K. Himasekhar, P. K. Sarma, and K. Janardhan, "Laminar mixed convection from a vertical rotating cone," *International Communications in Heat and Mass Transfer*, vol. 16, no. 1, pp. 99–106, 1989.

[15] D. Anilkumar and S. Roy, "Unsteady mixed convection flow on a rotating cone in a rotating fluid," *Applied Mathematics and Computation*, vol. 155, no. 2, pp. 545–561, 2004.

[16] A. J. Chamkha and A. Al-Mudhaf, "Unsteady heat and mass transfer from a rotating vertical cone with a magnetic field and heat generation or absorption effects," *International Journal of Thermal Sciences*, vol. 44, no. 3, pp. 267–276, 2005.

[17] R. Ravindran, S. Roy, and E. Momoniat, "Effects of injection (suction) on a steady mixed convection boundary layer flow over a vertical cone," *International Journal of Numerical Methods for Heat and Fluid Flow*, vol. 19, no. 3/4, pp. 432–444, 2009.

[18] S. Nadeem, A. Hussain, and M. K, "Stagnation flow of a Jeffrey fluid over a shrinking sheet," *Zeitschrift für Naturforschung A*, vol. 65, no. 6-7, pp. 540–548, 2010.

[19] S. U. S. Choi and J. A. Eastman, "Enhancing thermal conductivity of fluids with nanoparticles, San Francisco," *ASME International Mechanical Engineering Congress and Exposition*, vol. 231, pp. 99–103, 1995.

[20] P. K. Kameswaran, M. Narayana, P. Sibanda, and P. V. S. N. Murthy, "Hydromagnetic nanofluid flow due to a stretching or shrinking sheet with viscous dissipation and chemical reaction effects," *International Journal of Heat and Mass Transfer*, vol. 55, no. 25-26, pp. 7587–7595, 2012.

[21] P. K. Kameswaran, P. Sibanda, C. Ramreddy, and P. V. Murthy, "Dual solutions of stagnation-point flow of a nanofluid over a stretching surface," *Boundary Value Problems*, vol. 2013, no. 1, pp. 1–12, 2013.

[22] E. L. A. Fauzi, S. Ahmad, and I. Pop, "Mixed convection boundary layer flow from a vertical cone in a porous medium filled with a nanofluid," *Engineering and Technology*, vol. 6, pp. 15–18, 2012.

[23] A. Boutra, K. Ragui, N. Labsi, and Y. Benkahla, "Free convection enhancement within a nanofluid' filled enclosure with square heaters," *International Journal of Heat and Technology*, vol. 35, no. 3, pp. 447–458, 2017.

[24] V. Ambethkar and M. Kumar, "Numerical solutions of 2-D unsteady incompressible flow with heat transfer in a driven square cavity using streamfunction-vorticity formulation," *International Journal of Heat and Technology*, vol. 35, no. 3, pp. 459–473, 2017.

[25] C.-Y. Cheng, "Natural convection boundary layer flow over a truncated cone in a porous medium saturated by a nanofluid," *International Communications in Heat and Mass Transfer*, vol. 39, no. 2, pp. 231–235, 2012.

[26] A. J. Chamkha, S. Abbasbandy, A. M. Rashad, and K. Vajravelu, "Radiation effects on mixed convection about a cone embedded in a porous medium filled with a nanofluid," *Meccanica*, vol. 48, no. 2, pp. 275–285, 2013.

[27] S. Nadeem and S. Saleem, "Unsteady mixed convection flow of nanofluid on a rotating cone with magnetic field," *Applied Nanoscience*, vol. 4, no. 4, pp. 405–414, 2014.

[28] R. G. Hering and R. J. Grosh, "Laminar combined convection from a rotating cone," *Journal of Heat Transfer*, vol. 85, no. 1, pp. 29–34, 1963.

[29] C. L. Tien and I. J. Tsuji, "A theoretical analysis of laminar forced flow and heat transfer about a rotating cone," *Journal of Heat Transfer*, vol. 87, no. 2, pp. 184–190, 1965.

[30] J. C. Y. Koh and J. F. Price, "Nonsimilar boundary-layer heat transfer of a rotating cone in forced flow," *Journal of Heat Transfer*, vol. 89, no. 2, pp. 139–145, 1967.

[31] R. Ellahi, T. Hayat, and F. M. Mahomed, "Generalized Couette flow of a third-grade fluid with slip: the exact solutions," *Zeitschrift für Naturforschung A*, vol. 65, no. 12, pp. 1071–1076, 2010.

[32] R. Ellahi, T. Hayat, F. M. Mahomed, and S. Asghar, "Effects of slip on the non-linear flows of a third grade fluid," *Nonlinear Analysis: Real World Applications*, vol. 11, no. 1, pp. 139–146, 2010.

[33] O. D. Makinde, "Computational modelling of MHD unsteady flow and heat transfer toward a flat plate with Navier slip and Newtonian heating," *Brazilian Journal of Chemical Engineering*, vol. 29, no. 1, pp. 159–166, 2012.

[34] M. R. Hajmohammadi and S. S. Nourazar, "On the insertion of a thin gas layer in micro cylindrical Couette flows involving power-law liquids," *International Journal of Heat and Mass Transfer*, vol. 75, pp. 97–108, 2014.

[35] M. R. Hajmohammadi, S. Salman Nourazar, and A. Campo, "Analytical solution for two-phase flow between two rotating cylinders filled with power law liquid and a micro layer of gas," *Journal of Mechanical Science and Technology*, vol. 28, no. 5, pp. 1849–1854, 2014.

[36] W. A. Khan, Z. H. Khan, and M. Rahi, "Fluid flow and heat transfer of carbon nanotubes along a flat plate with Navier slip boundary," *Applied Nanoscience*, vol. 4, no. 5, pp. 633–641, 2014.

[37] M. Qasim, Z. H. Khan, W. A. Khan, and I. Ali Shah, "MHD boundary layer slip flow and heat transfer of ferrofluid along a stretching cylinder with prescribed heat flux," *PLoS One*, vol. 9, no. 1, Article ID e83930, 2014.

[38] A. Hussain, A. Rehman, S. Nadeem et al., "A Combined Convection Carreau–Yasuda Nanofluid Model over a Convective Heated Surface Near a Stagnation Point: A Numerical Study," *Mathematical Problems in Engineering*, vol. 2021, Article ID 6665743, 14 pages, 2021.

[39] M. Y. Malik, A. Hussain, and S. Nadeem, "Analytical treatment of an oldroyd 8-constant fluid between coaxial cylinders with variable viscosity," *Communications in Theoretical Physics*, vol. 56, no. 5, pp. 933–938, 2011.

[40] M. Y. Malik, I. Khan, A. Hussain, and T. Salahuddin, "Mixed convection flow of MHD Eyring-Powell nanofluid over a stretching sheet: a numerical study," *AIP Advances*, vol. 5, no. 11, p. 117118, 2015.

[41] D. Anilkumar and S. Roy, "Unsteady mixed convection flow on a rotating cone in a rotating fluid," *Applied Mathematics and Computation*, vol. 155, no. 2, pp. 545–561, 2004.

[42] A. Rehman, A. Hussain, and S. Nadeem, "Assisting and opposing stagnation point pseudoplastic nano liquid flow towards a flexible riga sheet: a computational approach," *Mathematical Problems in Engineering*, vol. 2021, Article ID 6610332, 14 pages, 2021.

[43] A. Rehman, A. Hussain, and S. Nadeem, "Physical aspects of convective and radiative molecular theory of liquid originated nanofluid flow in the existence of variable properties," *Physica Scripta*, vol. 96, no. 3, 2020.

Research Article

A Computational Model for the Radiated Kinetic Molecular Postulate of Fluid-Originated Nanomaterial Liquid Flow in the Induced Magnetic Flux Regime

Azad Hussain,[1] Aysha Rehman [ID],[1] Sohail Nadeem,[2] M. Riaz Khan,[3] and Alibek Issakhov[4,5]

[1]*Department of Mathematics, University of Gujrat, Gujrat 50700, Pakistan*
[2]*Department of Mathematics, Quaid-I-Azam University, Islamabad 44000, Pakistan*
[3]*LSEC and ICMSEC, Academy of Mathematics and Systems Science, Chinese Academy of Sciences,*
  School of Mathematical Science, University of Chinese Academy of Sciences, Beijing 100190, China
[4]*Department of Mathematical and Computer Modeling, Al-Farabi Kazakh National University, Almaty, Kazakhstan*
[5]*Department of Mathematical and Computer Modeling, Kazakh British-Technical University, Almaty, Kazakhstan*

Correspondence should be addressed to Aysha Rehman; aysharehman1986@gmail.com

The performance of mass transfer rate, friction drag, and heat transfer rate is illustrated in the boundary layer flow region via induced magnetic flux. In this recent analysis, the Buongiorno model is introduced to inspect the induced magnetic flux and radiative and convective kinetic molecular theory of liquid-initiated nanoliquid flow near the stagnant point. The energy equation is modified by radiation efficacy using the application of the Rosseland approximation. Through similarity variables, the available formulated partial differential equations are promoted into the nondimensional structure. The variation of the induced magnetic field near the wall goes up, and very far away, it decays when the size of the radiation characteristic ascends. The velocity amplitude expands by enlargement in the amount of the magnetic parameter, mixed convection, thermophoresis parameter, and fluid characteristic. The nanoparticle concentration reduces if the reciprocal of the magnetic Prandtl number expands. The temperature spectrum declines by enhancing the amount of the magnetic parameter. Drag friction decreases by the increment in the values of radiation and thermophoresis parameters. Heat transport rate increases when there is an increase in the values of Brownian and magnetic parameters. Mass transfer rate increases when there is incline in the values of the magnetic Prandtl and fluid parameter.

1. Introduction

Improving the thermal efficiency of fluid flows under different conditions and applications has always been a famous research area. Besides, the significance of this issue because of the very wide range of applications in industries has made this area attractive to scientists and companies working in this field. To improve effectiveness, any solution proposed for this in any application can have different technical aspects that should be considered and investigated adequately [1]. For example, Ellahi et al. [2] explored the slip effect in the Newtonian fluid two-phase flow. Particles of the nanosized Hafnium are utilized in the base fluid. Two cases are discussed for fluid under

consideration, namely, (i) phase of particles and (ii) fluid phase. Three forms of geometries are investigated in both cases. Relevant studies of nanofluids are discussed in recent articles [3–19].

There are many engineering applications of the mixed convective boundary layer flow such as food processing, solidification system, and nuclear reactors. Convection also plays an important role in managing the production cycle such as medications and cosmetics. The transverse magnetic field that merged with the boundary layer-mixed convection flow towards an inclined plate with a wave is examined. The retardation inflow far from the magnetic field and leading-edge yield acceleration in the leading-edge close flow of the wavy sheet is observed by Wang and Chi-Chang [20]. Many

researchers analyzed the regime of mixed convection flows in their articles [21–26].

There are several uses of free convection in the presence of Lorentz forces, such as fire engineering and geophysics. Newly proposed nanotechnology is a new passive way to enhance heat transfer [27]. The induced magnetic field's influence on temperature curves is represented by Ghosh et al. [28]. Vanita and Kumar [29] have examined transient flow towards a cone with the inclined magnetic field. Akbar et al. [30] investigated nanoparticle interaction for peristaltic flow in an asymmetric channel towards the magnetic field induced. Nadeem and Ijaz [31] explored the impulse of nanoparticles as a drug carrier to investigate theoretically stenosis arteries in the existence of the induced magnetic effect. Hayat et al. [32] observed second-grade nanoliquid flow with the induced magnetic field towards a stretched convectively heated surface. Rashid et al. [33] inspected the induced magnetic field effects of the Williamson peristaltic fluid flow in a curved channel.

The radiation may be sunlight, infrared, or visible and the nature of the material emitted by such radiation depends on its exposure. Depending on how solar heat is collected and distributed or converted into solar electricity, a heat source and its systems are also categorized as either passive solar or active solar. Thermal radiations are defined as electromagnetic emissions from a sheet with a temperature greater than zero [34]. Viskant and Grosh [35] noted that when considering the power plants, hypersonic flights, cooling systems, and combustion chambers, radiations became an important part. Using Rosseland's approximations, they addressed thermal radiation impacts for the flow of Falkner-Skan. Hayat et al. [36] portrayed the Ag-CuO/H_2O rotating hybrid nanofluid flow in the existence of partial slip radiation impacts. Hussain et al. [37] noted the non-Newtonian fluid flow with radiation efficacy and time-dependent viscosity. Li et al. [38] examined the radiation impacts in the heat storage system by adding nanoparticles. Zeeshan et al. [39] investigated, due to entropy generation, the impacts of electro-magnetohydrodynamics radiative diminishing internal energy of the pressure-driven dioxide-water titanium nanofluid flow.

The non-Newtonian fluid is more naturalistic to consider because of the rheological characteristics of physiological and industrial fluids. There is no extensive model that can describe the moving structure of all fluids due to the complex behavior of non-Newtonian fluids. Thus, to study non-Newtonian fluid flow characteristics, numerous models have been developed. The Eyring–Powell model was obtained from a liquid molecular hypothesis. And the inclusion of additional analytical constants was further improved. It accurately reflects the essence of Newtonian for low and high shear values. For example, rubber melts, condensed liquids, toiletries, cosmetics, and vegetable products are included in these fluids [40]. Appropriate studies of Eyring–Powell fluid may be mentioned in these articles [41–45].

This report is to narrate the specifications of radiative mass and heat transfer enhancement and flow analysis of

the molecular kinetic theory of liquid-initiated boundary layer stagnation point nanofluid towards a vertical stretched surface. The non-Newtonian nanofluid model is manifested with the induced magnetic field, radiation efficacy, combined convection, Brownian, and thermophoresis diffusion. The flow field describes that, in the form of partial differential equations, the laws of conservation of momentum are considered. By reducing the number of independent variables by using the technique of similarity transformation, these coupled equations are then purified into the system of ordinary differential equations. The results are interpreted by the MATLAB bvp4c technique. Induced magnetic pattern near the wall decreases, and far away, it increases with an increase in the values of the reciprocal of the magnetic Prandtl number. The concentration curve enhances when the number of magnetic, stretching, and Prandtl characteristics incline. This study of nanofluid is mainly applied in heat transfer devices such as electrical cooling systems, radiators, and heat exchangers.

2. Mathematical Formulations

Consider the incompressible, steady, two-dimensional (2D) stagnant point flow under the assumption of the induced magnetic field in the molecular kinetic theory of liquid-initiated nanofluid and heat transport enhancement in the existence of combined convection and radiation towards a vertical stretched sheet as shown in Figure 1. The surface stretching with velocity $u_w(x) = dx$ and ambient velocity is $u_\infty(x) = bx$ while the origin is fixed at O; see Figure 1.

Taken the Cartesian coordinate structure, the velocity of liquid flow will change through x- and y-axes in a way that $x-$axis is assumed vertically and $y-$axis is supposed horizontally. The fundamental form of the kinetic molecular postulate of liquid-originated nanofluid is [45]

$$\tau = \left[\mu + \frac{1}{\delta\dot{\gamma}}\sinh^{-1}\left(\frac{1}{c_1}\dot{\gamma}\right)\right]A_1, \qquad (1)$$

where

$$\dot{\gamma} = \sqrt{\operatorname{tr}\left(A_1^2\right)\frac{1}{2}}, \qquad (2)$$

where δ, c_1, μ, A_1, and tr are fluid parameters, dynamic viscosity, first Rivlin-Ericksen tensor, and trace, respectively. Here, τ is the extra stress tensor and $A_1 = [(\operatorname{grad}v)^t + \operatorname{grad}v]$. We consider the second-order approximation for $\sinh^{-1}$ function as

$$\sinh^{-1}\left(\frac{1}{c_1}\dot{\gamma}\right) \cong \frac{\dot{\gamma}}{c_1} - \frac{\dot{\gamma}^3}{6c_1^3}, \quad \text{where} \left|\frac{1}{c_1}\dot{\gamma}\right| \ll 1. \qquad (3)$$

Then, equation (1) becomes

$$\tau = \left[\mu + \frac{1}{\delta c_1} - \frac{\dot{\gamma}^2}{6\delta c_1^3}\right]A_1. \qquad (4)$$

Under these premises, the governing equations of this particular investigation are as follows:
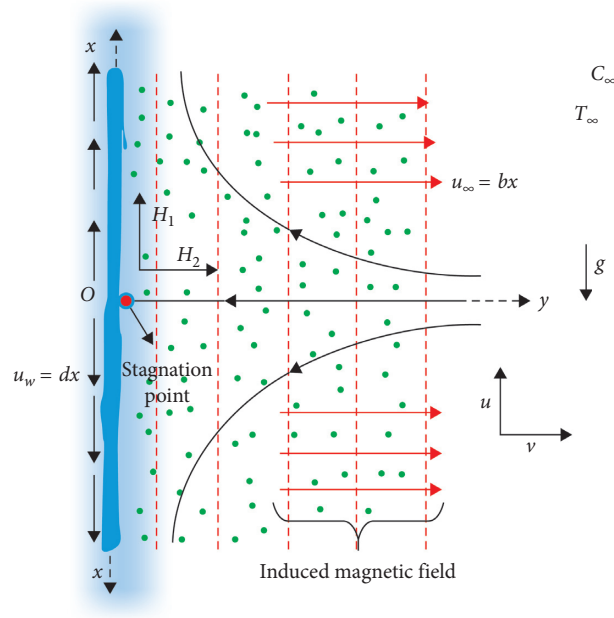
FIGURE 1: Geometry of the problem.

$$\frac{\partial u}{\partial x} + \frac{\partial v}{\partial y} = 0, \tag{5}$$

$$\frac{\partial H_1}{\partial x} + \frac{\partial H_2}{\partial y} = 0, \tag{6}$$

$$u\frac{\partial u}{\partial x} + v\frac{\partial u}{\partial y} - \frac{\mu_\infty}{4\pi\rho_f}\left(H_1\frac{\partial H_1}{\partial x} + H_2\frac{\partial H_1}{\partial y}\right) = \left(u_\infty\frac{du_\infty}{dx} - \frac{\mu_\infty H_\infty}{4\pi\rho_f}\frac{dH_\infty}{dx}\right) + \left[\nu + \frac{1}{\delta c_1\rho_f}\right]\frac{\partial^2 u}{\partial y^2}$$

$$-\left[\frac{1}{2\delta c_1^3\rho_f}\left(\frac{\partial u}{\partial y}\right)^2\frac{\partial^2 u}{\partial y^2}\right] + g\frac{(1-C)\beta\rho_{\mathrm{fm}}}{\rho_f}(T - T_\infty) \tag{7}$$

$$-g\left(\frac{\rho_p - \rho_{\mathrm{fm}}}{\rho_f}\right)(C - C_\infty),$$

$$u\frac{\partial H_1}{\partial x} + v\frac{\partial H_1}{\partial y} - H_1\frac{\partial u}{\partial x} - H_2\frac{\partial u}{\partial y} = \alpha_1^*\frac{\partial^2 H_1}{\partial y^2}, \tag{8}$$

$$u\frac{\partial T}{\partial x} + v\frac{\partial T}{\partial y} = \alpha\frac{\partial^2 T}{\partial y^2} + \frac{(\rho c_p)_p}{(\rho c_p)_f}\left[D_B\frac{\partial C}{\partial y}\frac{\partial T}{\partial y} + \left(\frac{D_T}{T_\infty}\right)\left(\frac{\partial T}{\partial y}\right)^2\right] - \frac{1}{(\rho c_p)_f}\left(\frac{\partial q_r}{\partial y}\right), \tag{9}$$

$$u\frac{\partial C}{\partial x} + v\frac{\partial C}{\partial y} = D_B\frac{\partial^2 C}{\partial y^2} + \left(\frac{D_T}{T_\infty}\right)\frac{\partial^2 T}{\partial y^2}. \tag{10}$$

The above equations narrate the viscosity coefficient ν, where (u, v) and (H_1, H_2) describe the velocity and magnetic field components along the x and y directions, respectively, whereas $u_w(x) = dx$ and $H_\infty(x) = xH_0$ are the

x velocity and y magnetic field at the edge of the boundary layer and H_0 is the uniform value of the vertical magnetic field at infinity.

The radiation heat flux is given by using Rosseland approximation:

$$q_r = -\frac{4\sigma^*}{3k^*}\left(\frac{\partial T^4}{\partial y}\right), \tag{11}$$

where σ^*, k^* are the Stefan–Boltzmann and the mean absorption coefficient, respectively, whereas via extending T^4 about T_∞ in Taylor's series and ignoring the larger terms,

$$T^4 \cong 4T_\infty^3 T - 3T_\infty^4. \tag{12}$$

Substituting equations (11) and (12) into (9), the heat equation takes the form

$$u\frac{\partial T}{\partial x} + v\frac{\partial T}{\partial y} = \frac{k}{(\rho c_p)_f}\frac{\partial^2 T}{\partial y^2}$$

$$+ \frac{(\rho c_p)_p}{(\rho c_p)_f}\left[D_B\frac{\partial C}{\partial y}\frac{\partial T}{\partial y} + \left(\frac{D_T}{T_\infty}\right)\left(\frac{\partial T}{\partial y}\right)^2 + \frac{16\sigma^* T_\infty^3}{3\rho c_p k^*}\left(\frac{\partial^2 T}{\partial y^2}\right)\right]. \tag{13}$$

The relevant boundary conditions are

$$u = u_w(x) = dx,$$

$$v = 0, \ \frac{\partial H_1}{\partial y} = 0, \tag{14}$$

$$H_2 = 0, \quad T \longrightarrow T_w, \text{ at } y \longrightarrow 0,$$

$$u = u_\infty(x) = bx,$$
$$H_1 = H_\infty, \tag{15}$$
$$T \longrightarrow T_\infty, \quad C \longrightarrow C_w, \text{ at } y \longrightarrow \infty.$$

Invoking similarity transformations are defined by

$$\psi = \sqrt{d\nu}xF(\gamma),$$

$$\gamma = \sqrt{\frac{d}{\nu}}y,$$

$$u = \frac{\partial \psi}{\partial y} = dxF(\gamma),$$

$$v = -\frac{\partial \psi}{\partial x} = -\sqrt{d\nu}F(\gamma),$$

$$H_1 = \left(\frac{H_0 x}{L}\right)h'(\gamma),$$

$$H_2 = -\sqrt{\left(\frac{\nu}{d}\right)}\left(\frac{H_0}{L}\right)h(\gamma), \tag{16}$$

$$u = u_w(x) = dx,$$

$$H_\infty = H_0\frac{x}{L},$$

$$\theta(\gamma) = \frac{T - T_\infty}{T_w - T_\infty},$$

$$\varphi(\gamma) = \frac{C - C_\infty}{C_w - C_\infty}.$$

The magnetized pressure is described as

$$p = p + \frac{\mu|H|^2}{8\pi}. \tag{17}$$

Equations (5) and (6) are satisfied identically. Equations (7), (8), (10), and (13)–(15) reduce to

$$[1 + \varepsilon - \varepsilon m_1]F''' + FF'' - (F')^2 + \eta^2 + \beta\left[(h')^2 - hh'' - 1\right] + \lambda_1\theta - N_r\varphi = 0, \tag{18}$$

$$\alpha_1 h''' + Fh'' - hF'' = 0, \tag{19}$$

$$\frac{1}{\text{Pr}}\left(1 + \frac{4}{3}R_d\right)\theta'' + \theta'F + \text{Nb}\varphi'\theta' + \text{Nt}(\theta')^2 = 0, \tag{20}$$

$$\varphi'' + \text{Le}\,\text{Pr}F\varphi' + \frac{N_t}{N_b}\theta'' = 0, \tag{21}$$

with boundary conditions

$$F = 0,$$
$$F' = 1,$$
$$\theta = 1,$$
$$\varphi = 0,$$
$$h = 0,$$
$$h'' = 0, \quad \text{at } \gamma \longrightarrow 0,$$

(22)

$$F' = \eta,$$
$$\theta = 0,$$
$$\varphi = 1,$$
$$h' = 1, \quad \text{at } \gamma \longrightarrow \infty.$$

(23)

Here, prime denotes derivative for γ and other dimensionless parameters are described as

$$\lambda_1 = \frac{(1 - C)\beta\rho_{\text{fm}}(T_w - T_\infty)g}{d^2 x \rho_f},$$

$$N_r = \frac{(\rho_p - \rho_{\text{fm}})(C_w - C_\infty)g}{d^2 x \rho_f},$$

$$\eta = \frac{b}{d}, R_d = \frac{4T_\infty^3 \sigma^*}{k^* k_f}, N_t = \frac{(\rho c_p)_p D_T (T_w - T_\infty)}{(\rho c_p)_f \nu T_\infty}, \text{Pr} = \frac{\nu}{\alpha},$$

$$N_b = \frac{(\rho c_p)_p D_B (C_w - C_\infty)}{(\rho c_p)_f \nu}, \quad \text{Le} = \frac{\alpha}{D_B}, \quad \alpha = \frac{K}{(\rho c_p)_f},$$

$$\varepsilon = \frac{1}{\delta c_1 \mu}, \quad m_1 = \frac{d^3 x^2}{2c_1^2 \nu}, \quad \nu = \frac{\mu}{\rho_f}, \quad \alpha_1 = \frac{\alpha_1^*}{\nu}, \quad \text{Re}_x^{(1/2)} = \sqrt{\frac{u_w x}{\nu}},$$

$$\beta = \frac{H_0^2 \mu_\infty}{4d^2 \pi \rho_f}.$$

(24)

Physical quantities are very valuable from an engineering point of view. These quantities reported the flow behavior which is defined by local Nusselt number Nu_x, skin friction C_f, and local Sherwood number Sh_x definitions as follows:

$$C_f = \frac{\tau_w}{\rho u_w^2},$$

$$\text{Nu}_x = \frac{x q_w}{k(T_w - T_\infty)},$$

(25)

$$\text{Sh}_x = \frac{x q_m}{D_B (C_w - C_\infty)},$$

where τ_w represents the surface shear stress, q_w denotes the surface heat flux, and q_m presents the surface mass flux for fluid:

$$\tau_w = \left[\left(\mu + \frac{1}{\delta c_1} - \frac{1}{6\delta c_1^3} \left(\frac{\partial u}{\partial y} \right)^2 \right) \frac{\partial u}{\partial y} \right]_{y=0},$$

$$q_w = \left[-k \frac{\partial T}{\partial y} - \frac{16\sigma^* T_\infty^3}{3k^*} \left(\frac{\partial T}{\partial y} \right) \right]_{y=0},$$

(26)

$$q_m = -D_B \left[\frac{\partial C}{\partial y} \right]_{y=0}.$$

Using invoking transformation equation (16), the dimensionless local Nusselt number, skin friction, and the local Sherwood number become

$$C_f \text{Re}_x^{(1/2)} = \left[(1 + \varepsilon) f''(0) - \frac{\varepsilon m_1}{3} (f''(0))^3 \right],$$

$$\text{Nu}_x \text{Re}_x^{-(1/2)} = -\left[1 + \frac{4}{3} R_d \right] \theta'(0),$$

(27)

$$\text{Sh}_x \text{Re}_x^{-(1/2)} = -\varphi'(0).$$

3. Results and Discussion

Coupled nonlinear differential equations (18)–(21) and their boundary conditions (22) and (23) are numerically worked out by employing the MATLAB scheme. This portion illustrates the impact of nondimensional sundry characteristics on induced magnetic, temperature, velocity, and concentration flow characteristics numerically and graphically. Figure 2 portrays the impact of η versus $h'(\gamma)$. It is noticeable that the induced magnetic spectrum falls when increasing in η. Figure 3 designates the effects of α_1 on the induced magnetic pattern. Dual behavior has been seen for α_1, near the wall, it is getting down, and far away, it moves upward. The field of $h'(\gamma)$ rises by enhancing the amount of β in Figure 4. With larger values of mixed convection characteristic, the flow of induced magnetic expands as shown in Figure 5. Figures 6 and 7 demonstrate the effect of Brownian and thermophoresis diffusion on the induced magnetic field, respectively. When there is increase in the amount of Brownian diffusion, the induced magnetic field decreases, and the induced magnetic field increases by growing quantity of thermophoresis. Figure 8 shows the consequence of the Prandtl number on the induced magnetic curve, and profile falls by a bigger amount of Prandtl. The impacts of thermal radiation flux on the magnetic field are described in Figure 9. The variation of $h'(\gamma)$ near the wall moves upward and very far away it moves downward by increasing the amount of thermal radiation. Figure 10 exhibits the outcome of the fluid parameter on $h'(\gamma)$ expands in the values of ε which cause rise in $h'(\gamma)$. Figure 11 exhibits the deviation of β on velocity curve. When there is expansion in the amount of β, then there is increase in
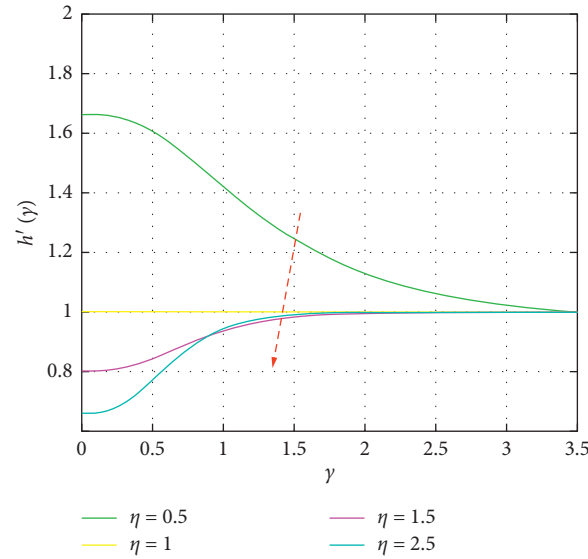
FIGURE 2: Outcomes of η on $h'(\gamma)$.
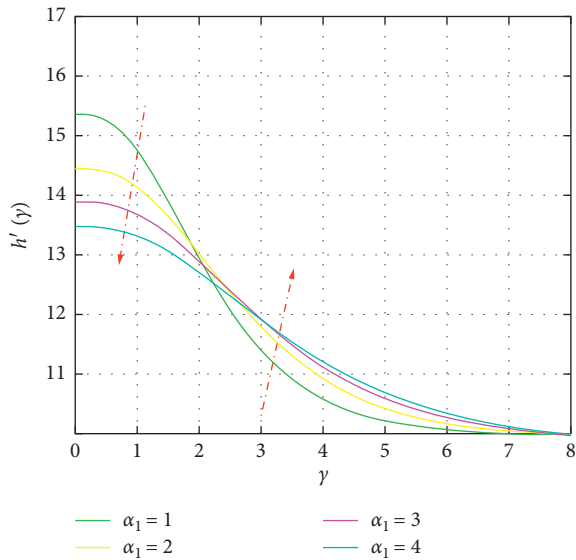
FIGURE 3: Impacts of α_1 on $h'(\gamma)$.

velocity flow. Figure 12 portrays the effect of λ_1 on the flow of velocity. The diagram shows that the fluctuation shoots up by increment in the mixed convection parameter. Nanofluid behaviour is shown by Brownian and thermophoretic characteristics in in Figures 13 and 14. It is depicted that the contrary attitude showed variation in velocity decline for Nb and incline for Nt by enhancing the quantity of these parameters. Figure 15 investigates that the velocity graph expands if the fluid parameter ε rises. Figure 16 demonstrates that the field of velocity shrinks by rising the amount of the reciprocal of the magnetic Prandtl number. Figure 17 shows that when increasing stretching parameter, the field of $F'(\gamma)$ enhances. Figures 18 and 19 show opposite behavior against the parameters of α_1 and β, respectively. The temperature profile increases and decreases against the characteristics of α_1 and β. Figure 20 explores the impact of Lewis number on temperature distribution, $\theta(\gamma)$ rises

near the wall, and far away, it declines compared to Le. The temperature reduction against the Brownian motion diffusion is shown in Figure 21. Figure 22 describes that temperature sketch grows by inclining the quantity of thermophoresis diffusion. It is easily noticed that enlarging the amount of Prandtl number causes the figure of temperature decline in Figure 23. Figure 24 depicts the influence of η on the temperature field. The amplitude of temperature diminishes when the size of the stretching parameter boosts up. Figure 25 explores the influence of radiation characteristics on temperature portraits; field enhances by rising the amount of radiation parameter. Figure 26 shows the influence of buoyancy ratio parameter on temperature distribution field increases by increasing the amount of buoyancy ratio parameter. The nanoparticle concentration field decreases if the reciprocal of the magnetic Prandtl number rises in Figure 27. Figure 28 exhibits the outcome of β on the concentration field. The figure of concentration inclines when the number of β grows. Figure 29 portrays the result of buoyancy ratio characteristics on nanoparticle concentration. It is easily observed that the field of concentration reduces if the number of N_r increases. Figures 30 and 31 define the matching outcomes on the concentration profile. When the size of Pr and η expands, the nanoparticle concentration grows. Streamlines graphs against the distinct amount of α_1 and ε are shown in Figures 32–35. Table 1 shows the impact of different characteristics on drag friction $C_f \mathrm{Re}_x^{(1/2)}$. The Nusselt number for noticeable amounts of R_d, Nt, Nb, ε, λ_1, m_1, β, and α_1 is analyzed and characterized in Table 2. Table 3 portrays the deviation of different amounts of parameters on the local Sherwood number.

4. Concluding Remarks

We studied the molecular theory of liquid-originated non-Newtonian nanofluids which are commonly used in heat transfer devices such as heat exchangers, engine oils, electrical cooling systems (such as flat plates), nuclear
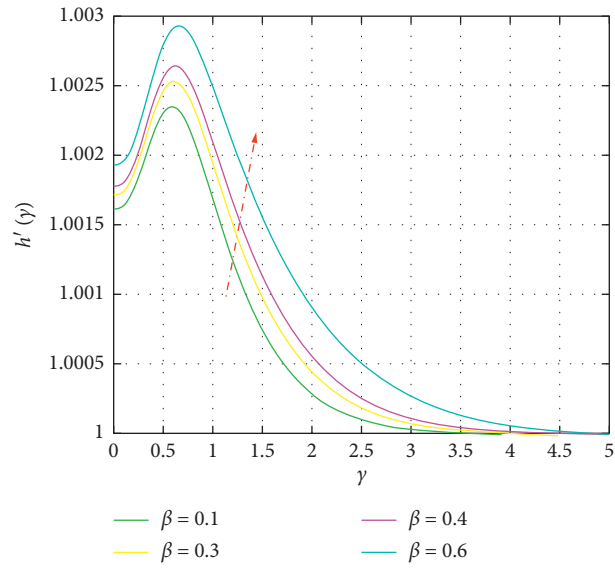
FIGURE 4: Upshot of β on $h'(\gamma)$.
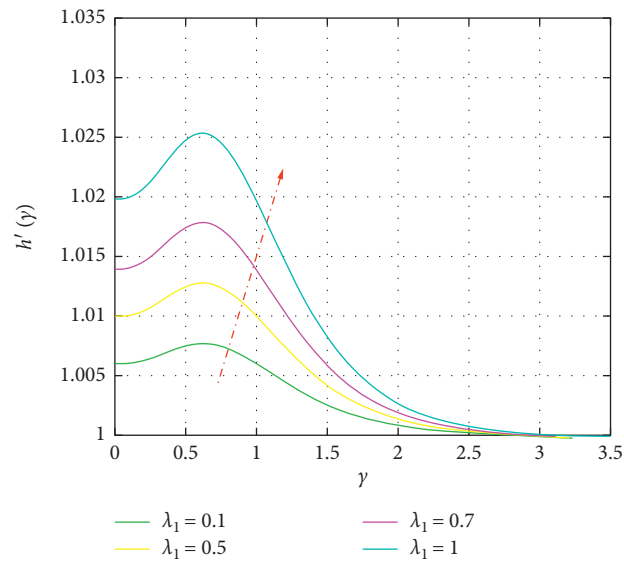
FIGURE 5: Results of λ_1 on $h'(\gamma)$.
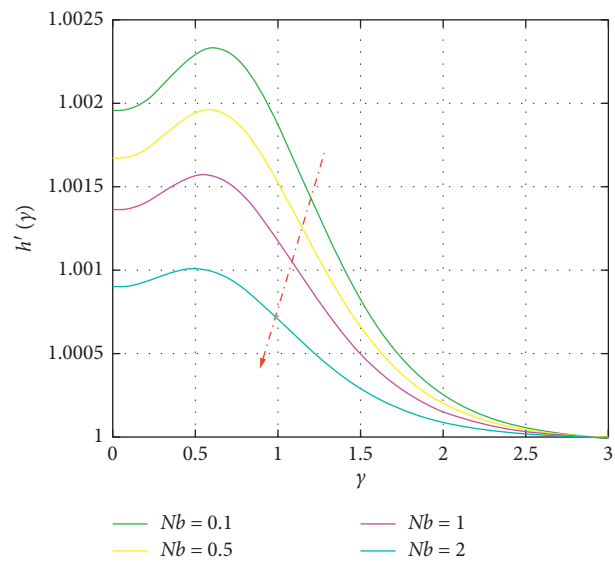
FIGURE 6: Effects of Nb on $h'(\gamma)$.
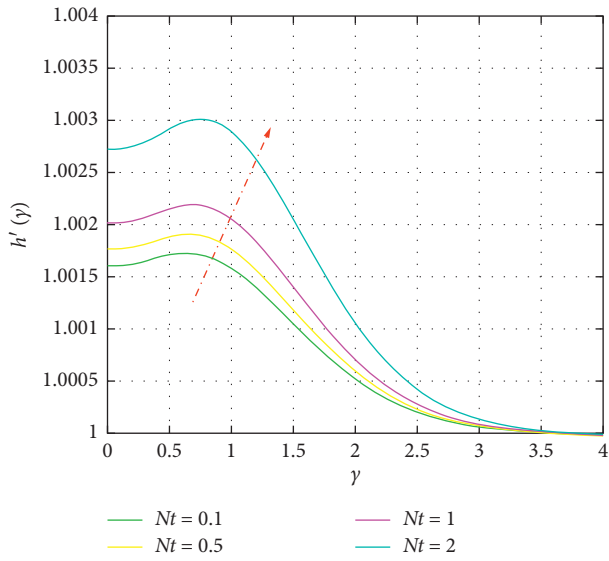
FIGURE 7: Consequences of Nt on $h'(\gamma)$.
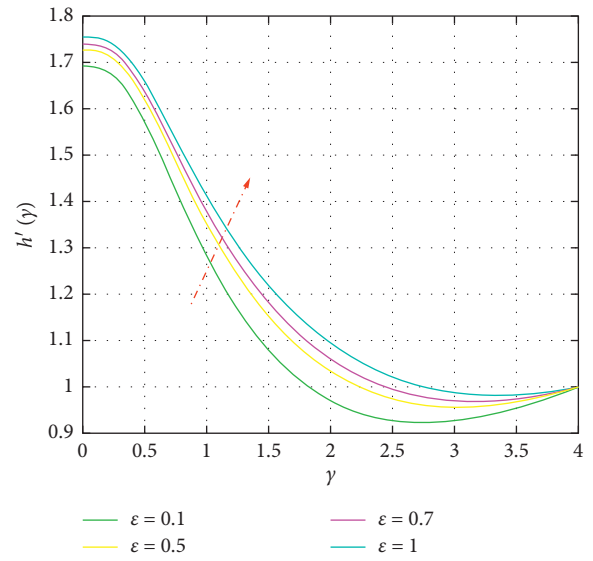
FIGURE 10: Upshot of ε on $h'(\gamma)$.
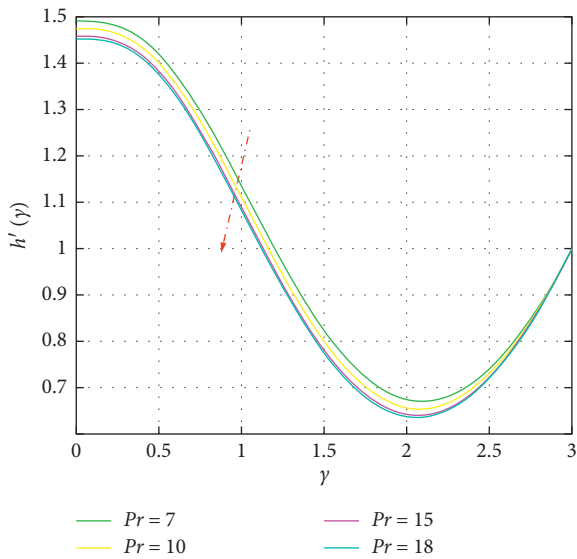
FIGURE 8: Upshot of Pr on $h'(\gamma)$.
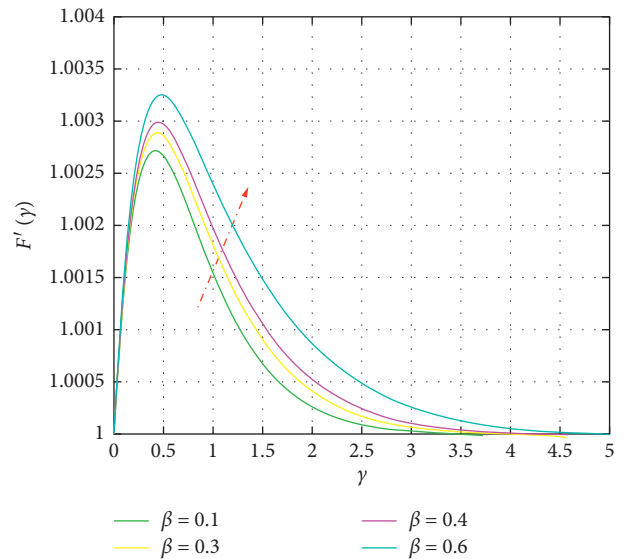
FIGURE 11: Result of β on $F'(\gamma)$.
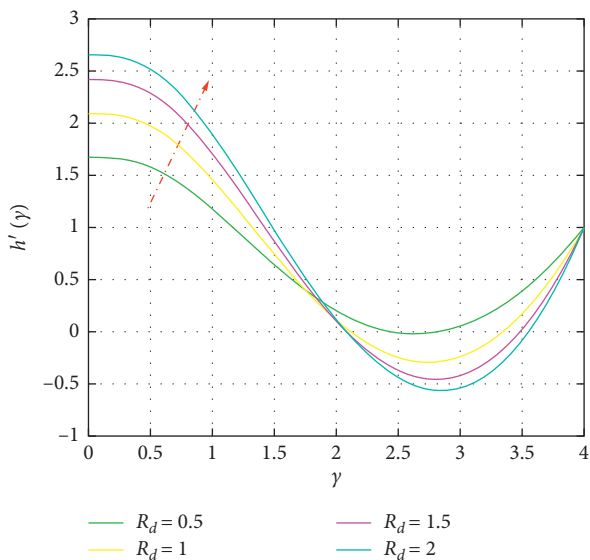
FIGURE 9: Consequence of R_d on $h'(\gamma)$.
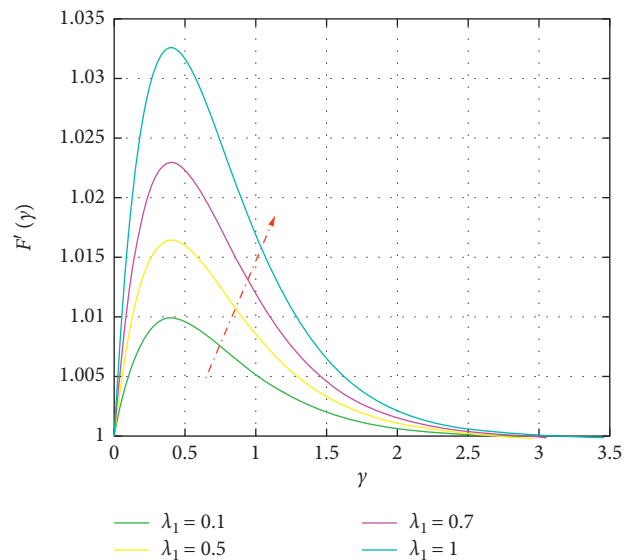
FIGURE 12: Outcome of λ_1 on $F'(\gamma)$.
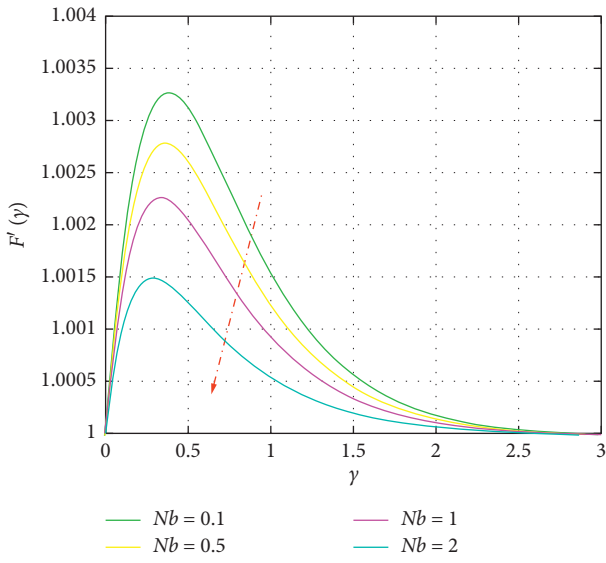
FIGURE 13: Result of Nb on $F'(\gamma)$.
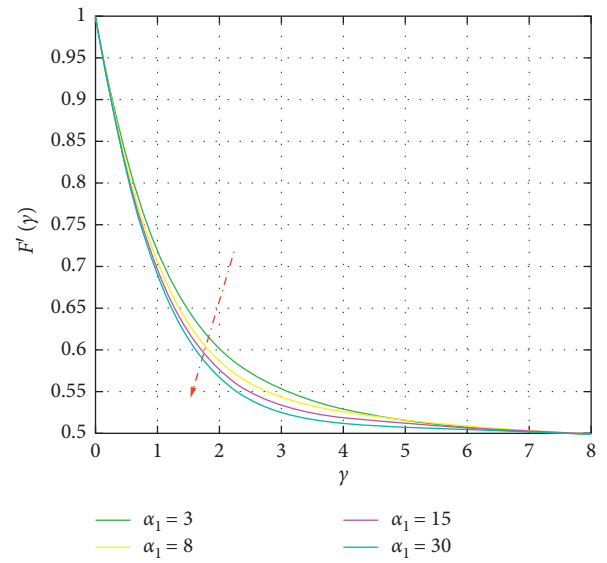
FIGURE 16: Influence of α_1 on $F'(\gamma)$.
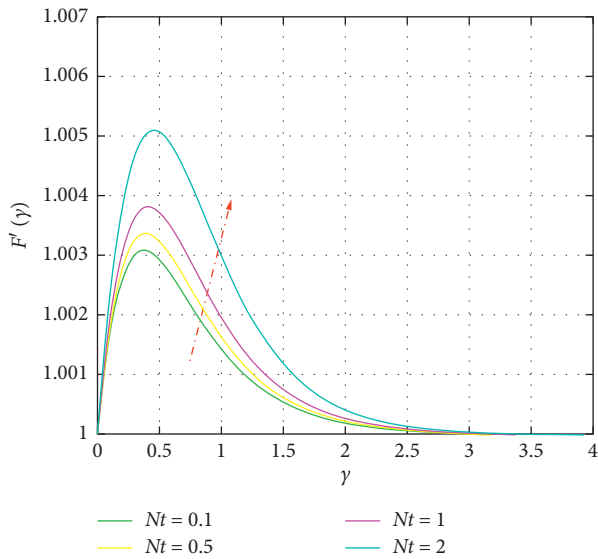
FIGURE 14: Impact of Nt on $F'(\gamma)$.
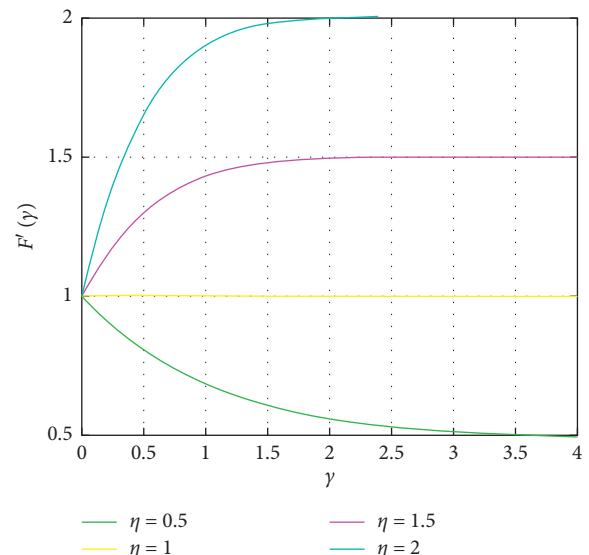
FIGURE 17: Outcome of η on $F'(\gamma)$.
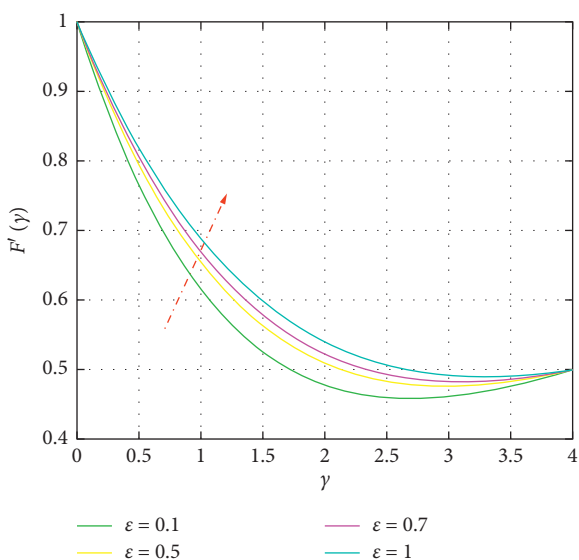
FIGURE 15: Upshot of ε on $F'(\gamma)$.
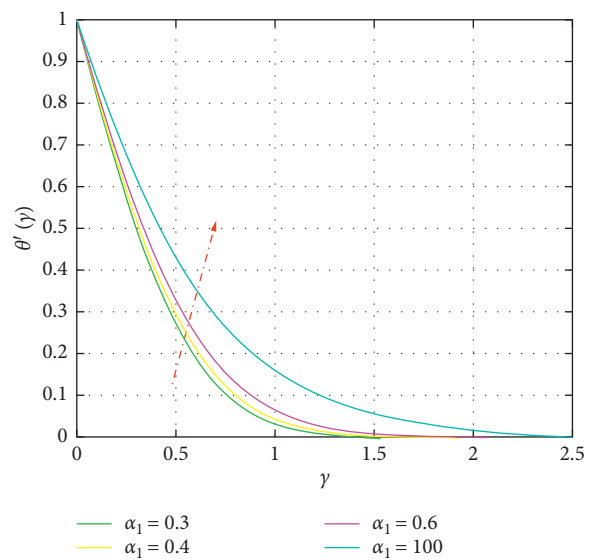
FIGURE 18: Upshot of α_1 on $\theta(\gamma)$.
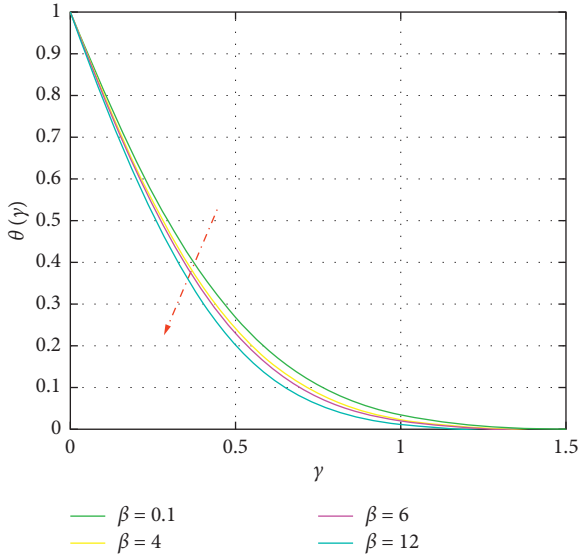
FIGURE 19: Result of β on $\theta\,(\gamma)$.
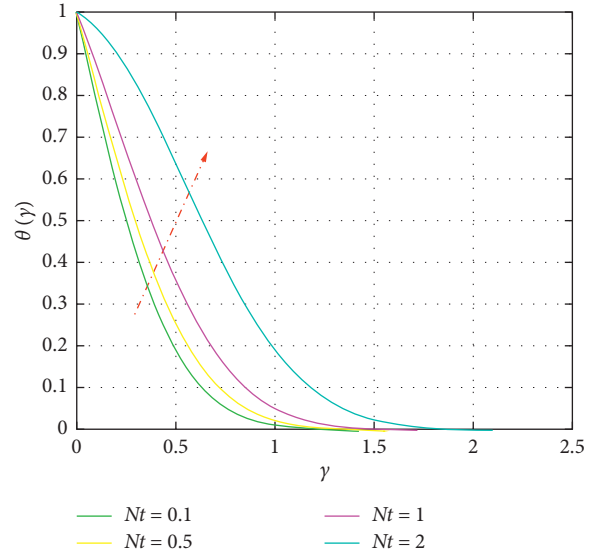
FIGURE 22: Deviation of Nt on $\theta\,(\gamma)$.
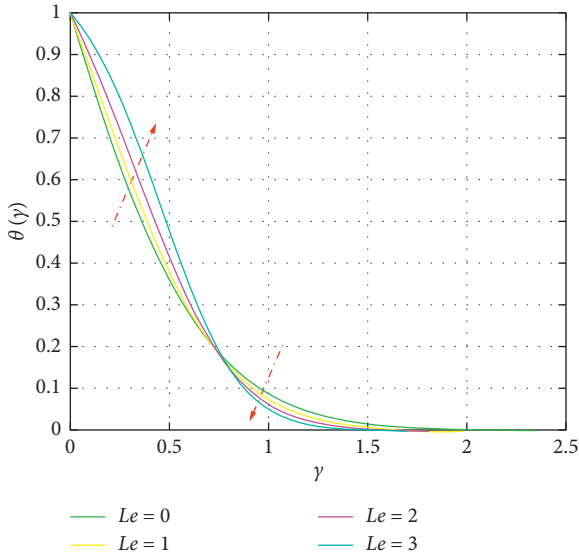
FIGURE 20: Outcome of Le on $\theta\,(\gamma)$.
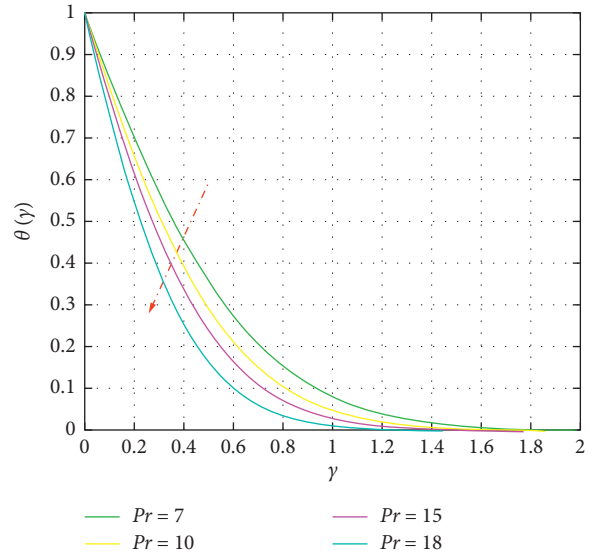
FIGURE 23: Consequence of Pr on $\theta\,(\gamma)$.
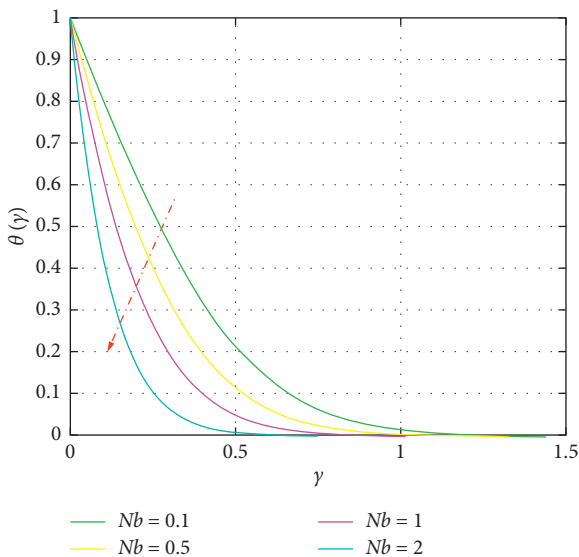
FIGURE 21: Influence of Nb on $\theta\,(\gamma)$.
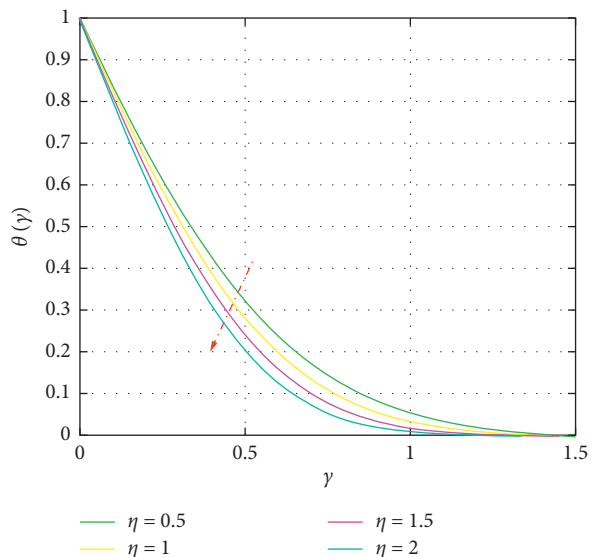
FIGURE 24: Influence of η on $\theta\,(\gamma)$.
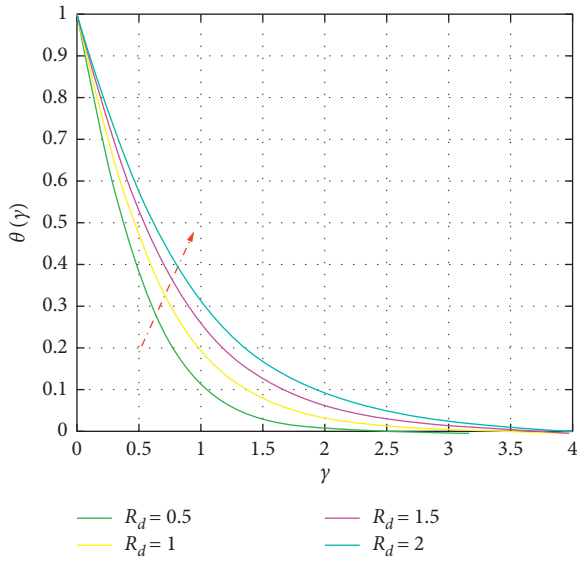
FIGURE 25: Conclusion of R_d on $\theta(\gamma)$.
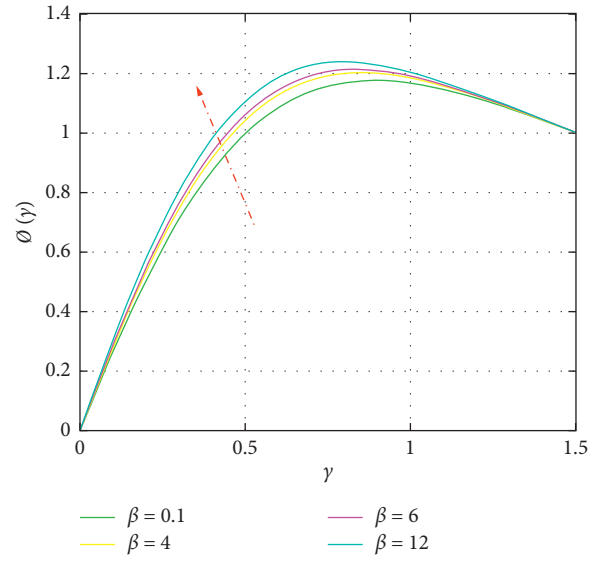
FIGURE 28: Upshot of β on $\theta(\gamma)$.
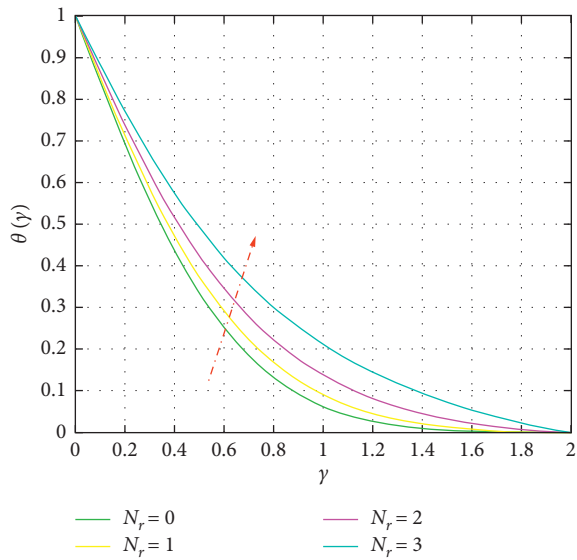
FIGURE 26: Result of N_r on $\theta(\gamma)$.
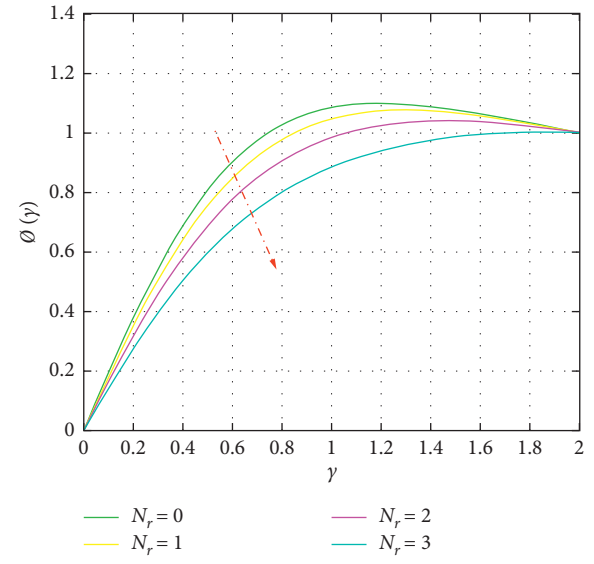
FIGURE 29: Effect of N_r on $\phi(\gamma)$.
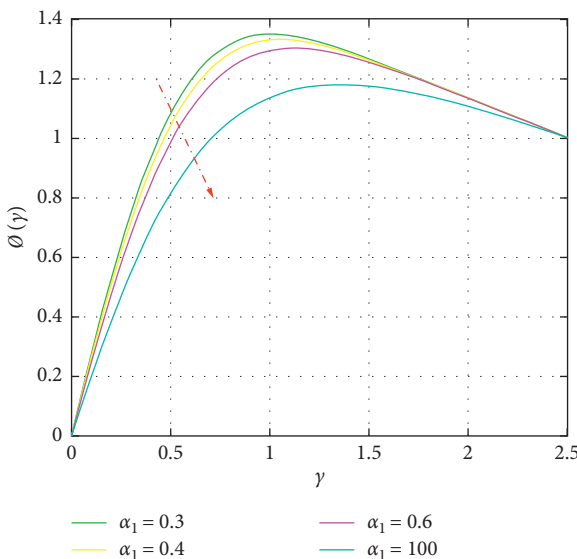
FIGURE 27: Outcome of α_1 on $\theta(\gamma)$.
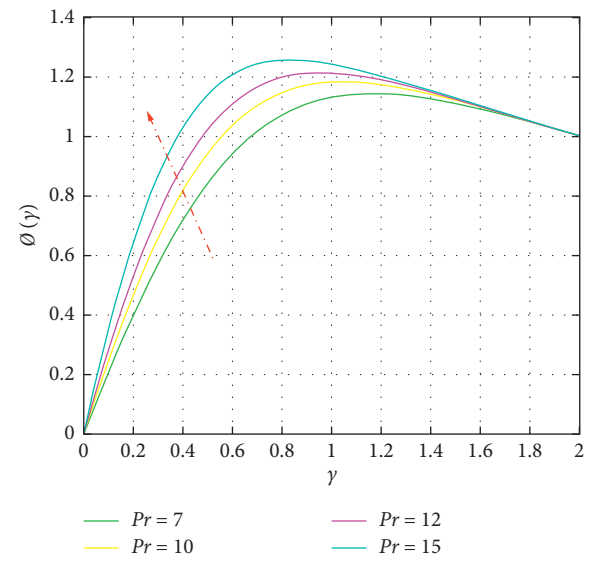
FIGURE 30: Impact of Pr on $\phi(\gamma)$.
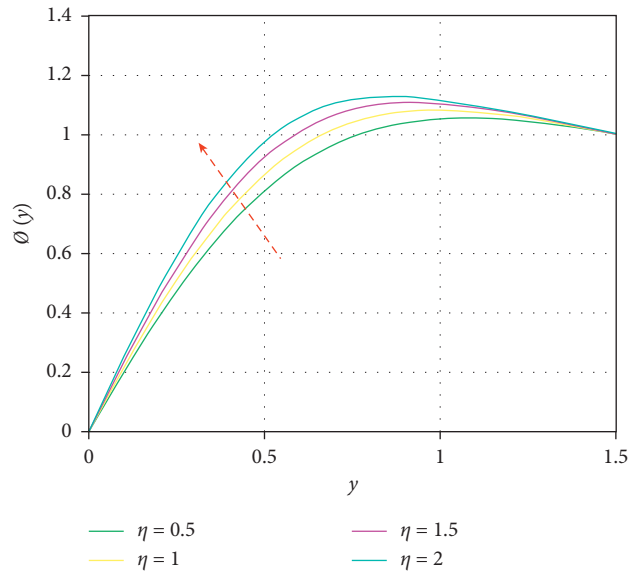
Figure 31: Result of Pr on $\phi(\gamma)$.
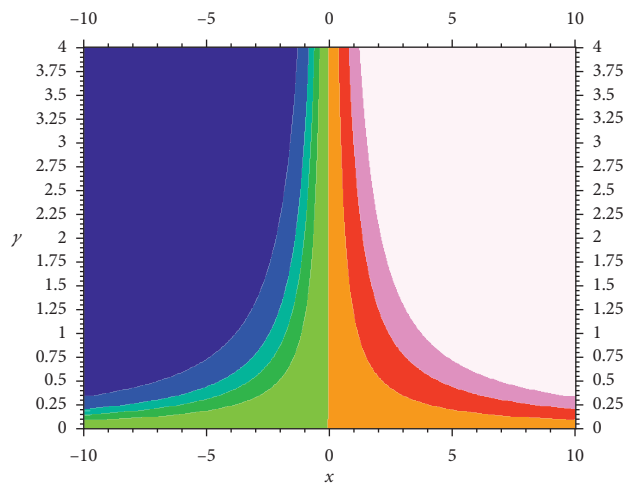
Figure 32: Flowlines for $\alpha_1 = 0.5$.
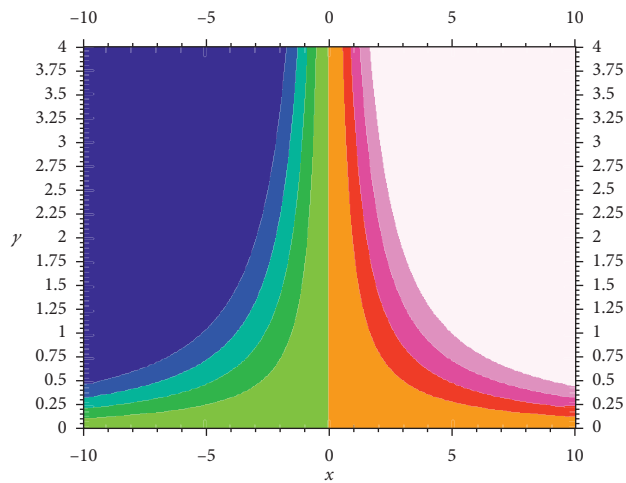
Figure 33: Flowlines for $\alpha_1 = 1.5$.

FIGURE 34: Flowlines for $\varepsilon = 0.1$.

FIGURE 35: Flowlines for $\varepsilon = 1$.

TABLE 1: Variation of $C_f (\mathrm{Re}_x)^{(1/2)}$ for distinct amounts of nondimensional parameters.

R_d	Nt	Nb	ε	Pr	λ_1	m_1	η	N_r	Le	β	α_1	$C_f (\mathrm{Re}_x)^{(1/2)}$
0.1	0.1	0.1	1	7	0.1	0.1	0.5	0.1	0.1	0.1	0.5	−0.85974
0.3												−0.87093
0.5												−0.88148
	0.2	0.1	1	7	0.1	0.1	0.5	0.1	0.1	0.1	0.5	−0.93303
0.1	0.3											−1.00570
	0.5											−1.14835
	0.1	0.2	1	7	0.1	0.1	0.5	0.1	0.1	0.1	0.5	−0.82344
0.1		0.3										−0.81182
		0.4										−0.80635
	0.1	0.1	1.2	7	0.1	0.1	0.5	0.1	0.1	0.1	0.5	−1.43201
0.1			1.3									−1.40042
			1.4									−1.37091
	0.1	0.1	1	7	0.2	0.1	0.5	0.1	0.1	0.1	0.5	−0.83200
0.1					0.3							−0.80432
					0.4							−0.77670

---

reactors, biomedicine lubricants, and radiators. The key points of observation in the recent analysis are as follows:

(i) Induced magnetic pattern near the wall declines, and far away, it inclines when (α_1) intensifies. The variation of $h'(\gamma)$ field near the wall goes up and very far away it decays when the size (R_d) ascends.

(ii) $h'(\gamma)$ (nondimensional induced magnetic function) falls, whereas (η), Brownian diffusion (Nb), and Prandtl number (Pr) rise. The field $h'(\gamma)$ expands by enhancing the amount of magnetic parameter (β), mixed convection (λ_1), thermophoresis parameter (Nt), and fluid parameter (ε). The variation of $h'(\gamma)$ profile near the wall moves upward and very far away it moves down when the size (R_d) ascends.

(iii) The velocity amplitude expands by enlargement in the amount of magnetic parameter (β), mixed convection (λ_1), thermophoresis parameter (Nt), fluid characteristic (ε), and stretching parameter (η). $F'(\gamma)$ collapses by Brownian motion (Nb) and (α_1).

(iv) The temperature spectrum increases when the values of (α_1), radiation parameter (R_d), and buoyancy ratio (N_r) increases and decreases by Prandtl number, magnetic parameter (β), Brownian motion diffusion (Nb), and stretching parameter (η). $\theta(\gamma)$ (nondimensional temperature function) rises near the wall, and far away, it diminishes when there is increase in the values of Le.

(v) The nanoparticle concentration portrait reduces if the reciprocal of the magnetic Prandtl number (α_1) and (N_r) rises. Concentration enlarges when the number of (β), (Pr), and (η) grows.

(vi) Drag friction decays by the inclination in the values of (R_d), (Nt), (m_1), and (α_1). When inclining the amount of (Nb), (ε), (λ_1), and (β), drag force expands.

(vii) Heat transfer rates are increased when there is an increase in the values of (Nb), (Pr), and (β) and decrease when there is an increase in the values of (R_d), (Nt), (m_1), and (α_1).

(viii) Mass transfer rates diminish, for (R_d), (Nt), (Pr), and (β), but increases by (Nb), (m_1), and (α_1).

Abbreviations

α_1:   Reciprocal of the magnetic Prandtl number $(-)$
μ: Dynamic viscosity (Nsm^{-2})
k^*:   Mean absorption coefficient $(-)$
b: Body forces (Nm^{-3})
C: Nanoparticles concentration $(\mathrm{kg\,m}^{-3})$
F: Dimensionless velocity function $(-)$
T: Temperature $(-)$
Nb: Brownian motion parameter $(-)$
Nu_x: Local Nusselt number $(-)$
C_∞:   Ambient fluid concentration $(\mathrm{kg\,m}^{-3})$
T_w: Hot fluid temperature (K)

(u, v):   Velocity components (ms^{-1})
m_1:   Fluid characteristic $(-)$
τ: Extra stress tensor $(-)$
ε: Fluid characteristics $(-)$
Sh_x: Local Sherwood number $(-)$
R_d: Radiation parameter $(-)$
λ_1:   Mixed convection parameter $(-)$
ρ_f: Density of the base fluid $(\mathrm{kg\,m}^{-3})$
q_w: Surface heat flux $(-)$
np: Nanoparticle $(-)$
α: Thermal diffusivity $(\mathrm{m}^2\mathrm{s}^{-1})$
α_1^*:   Magnetic diffusivity $(-)$
θ: Dimensionless heat transfer function $(-)$
γ: Similarity variable $(-)$
ρ: Density $(\mathrm{kg\,m}^{-3})$
β: Magnetic parameter $(-)$
tr: Trace $(-)$
C_w: Hot fluid concentration $(\mathrm{kg\,m}^{-3})$
A_1:   Rivlin–Ericksen tensor $(-)$
C_f: Skin friction coefficient $(-)$
D_B: Brownian diffusion coefficient $(\mathrm{m}^2\mathrm{s}^{-1})$
D_T: Thermophoresis diffusion coefficient $(\mathrm{m}^2\mathrm{s}^{-1})$
g: Gravity acceleration (ms^{-2})
Le: Lewis number $(-)$
Nt: Thermophoresis parameter $(-)$
Re_x: Local Reynolds number $(-)$
σ^*:   Stefan–Boltzmann constant $(\mathrm{Wm}^{-2}\mathrm{K}^{-4})$
T_∞:   Ambient temperature (K)
u_w: Stretching sheet velocity (ms^{-1})
u_∞:   External flow velocity (ms^{-1})
(x, y):   Cartesian coordinate components (m)
δ: Fluid characteristics $(-)$
c_1:   Fluid parameter $(-)$
Pr: Prandtl number $(-)$
N_r: Buoyancy ratio characteristics $(-)$
τ_w: Surface shear stress $(-)$
q_m: Surface mass flux $(-)$
f: Base fluid $(-)$
η: Stretching parameter $(-)$
h: Dimensionless magnetic function $(-)$
φ: Dimensionless concentration function $(-)$
ρ_p: The density of the nanoparticles $(\mathrm{kg\,m}^{-3})$.

Data Availability

The data that support the findings of this study are available from the corresponding author upon request.

Conflicts of Interest

The authors declare that they have no conflicts of interest.

References

[1] M. Sheikholeslami, A. Arabkoohsar, and K. A. R. Ismail, "Entropy analysis for a nanofluid within a porous media with magnetic force impact using non-Darcy model," *International*

Communications in Heat and Mass Transfer, vol. 112, Article ID 104488, 2020.

[2] R. Ellahi, F. Hussain, S. A. Abbas et al., "Study of two-phase Newtonian nanofluid flow hybrid with hafnium particles under the effects of slip," *Inventions*, vol. 5, no. 1, p. 6, 2020.

[3] N. Abbas, M. Y. Malik, and S. Nadeem, "Transportation of magnetized micropolar hybrid nanomaterial fluid flow over a Riga curface surface," *Computer Methods and Programs in Biomedicine*, vol. 185, p. 105136, 2020.

[4] S. Nadeem, N. Abbas, Y. Elmasry, and M. Y. Malik, "Numerical analysis of water based CNTs flow of micropolar fluid through rotating frame," *Computer Methods and Programs in Biomedicine*, vol. 186, p. 105194, 2020.

[5] N. Abbas, S. Nadeem, and M. Y. Malik, "Theoretical study of micropolar hybrid nanofluid over Riga channel with slip conditions," *Physica A: Statistical Mechanics and its Applications*, vol. 551, p. 124083, 2020.

[6] M. Khan, T. Salahuddin, M. Y. Malik et al., "3-D axisymmetric Carreau nanofluid flow near the Homann stagnation region along with chemical reaction: application Fourier's and Fick's laws," *Mathematics and Computers in Simulation*, vol. 170, pp. 221–235, 2020.

[7] S. Chen, M. K. Hassanzadeh-Aghdam, and R. Ansari, "An analytical model for elastic modulus calculation of SiC Whisker-reinforced hybrid metal matrix nanocomposite containing SiC nanoparticles," *Journal of Alloys and Compounds*, vol. 767, pp. 632–641, 2018.

[8] X. Wang, J. Wang, X. Sun et al., "Hierarchical coral-like NiMoS nanohybrids as highly efficient bifunctional electrocatalysts for overall urea electrolysis," *Nano Research*, vol. 11, no. 2, pp. 988–996, 2018.

[9] M. Wang, M. Hu, B. Hu et al., "Bimetallic cerium and ferric oxides nanoparticles embedded within mesoporous carbon matrix: electrochemical immunosensor for sensitive detection of carbohydrate antigen 19-9," *Biosensors and Bioelectronics*, vol. 135, pp. 22–29, 2019.

[10] Y. Liu, Q. Zhang, M. Xu et al., "Novel and efficient synthesis of Ag-ZnO nanoparticles for the sunlight-induced photocatalytic degradation," *Applied Surface Science*, vol. 476, pp. 632–640, 2019.

[11] M. R. Eid and F. Mabood, "Thermal analysis of higher-order chemical reactive viscoelastic nanofluids flow in porous media via stretching surface," *Proceedings of the Institution of Mechanical Engineers, Part C: Journal of Mechanical Engineering Science*, Article ID 09544062211008481, 2021.

[12] M. R. Eid and A. F. Al-Hossainy, "High-performance nanofluid synthesis and DFT-TDDFT study of graphene nanosheets along bent surface for enhanced oil-recovery implementations," *Case Studies in Thermal Engineering*, vol. 25, p. 100983, 2021.

[13] U. Khan, I. Waini, A. Ishak, and I. Pop, "Unsteady hybrid nanofluid flow over a radially permeable shrinking/stretching surface," *Journal of Molecular Liquids*, vol. 331, p. 115752, 2021.

[14] A. Wakif, I. L. Animasaun, U. Khan, and A. M. Alshehri, "Insights into the generalized Fourier's and Fick's laws for simulating mixed bioconvective flows of radiative-reactive Walters-B fluids conveying tiny particles subject to Lorentz force," *Preprint*, 2021.

[15] G. Rasool, A. Shafiq, M. S. Alqarni, A. Wakif, I. Khan, and M. S. Bhutta, "Numerical scrutinization of Darcy-Forchheimer relation in convective magnetohydrodynamic nanofluid flow bounded by nonlinear stretching surface in the perspective of heat and mass transfer," *Micromachines*, vol. 12, no. 4, p. 374, 2021.

[16] A. Rehman, A. Hussain, and S. Nadeem, "Assisting and opposing stagnation point pseudoplastic nano liquid flow towards a flexible Riga sheet: a computational approach," *Mathematical Problems in Engineering*, vol. 2021, Article ID 6610332, 14 pages, 2021.

[17] Y. X. Li, M. H. Alshbool, Y. P. Lv, I. Khan, M. R. Khan, and A. Issakhov, "Heat and mass transfer in MHD Williamson nanofluid flow over an exponentially porous stretching surface," *Case Studies in Thermal Engineering*, vol. 26, p. 100975, 2021.

[18] U. Khan, S. Bilal, A. Zaib, O. D. Makinde, and A. Wakif, "Numerical simulation of a nonlinear coupled differential system describing a convective flow of Casson gold–blood nanofluid through a stretched rotating rigid disk in the presence of Lorentz forces and nonlinear thermal radiation," *Numerical Methods for Partial Differential Equations*, 2020.

[19] G. Rasool and A. Shafiq, "Numerical exploration of the features of thermally enhanced chemically reactive radiative Powell–Eyring nanofluid flow via Darcy medium over nonlinearly stretching surface affected by a transverse magnetic field and convective boundary conditions," *Applied Nanoscience*, pp. 1–18, 2020.

[20] C.-C. Wang and C. O.-K. Chen, "Mixed convection boundary layer flow on inclined wavy plates including the magnetic field effect," *International Journal of Thermal Sciences*, vol. 44, no. 6, pp. 577–586, 2005.

[21] A. Zeeshan, M. Hassan, R. Ellahi, and M. Nawaz, "Shape effect of nanosize particles in unsteady mixed convection flow of nanofluid over disk with entropy generation," *Proceedings of the Institution of Mechanical Engineers, Part E: Journal of Process Mechanical Engineering*, vol. 231, no. 4, pp. 871–879, 2017.

[22] R. Ellahi, M. Hassan, and A. Zeeshan, "Aggregation effects on water base Al_2O_3-nanofluid over permeable wedge in mixed convection," *Asia-Pacific Journal of Chemical Engineering*, vol. 11, no. 2, pp. 179–186, 2016.

[23] A. Zeeshan, A. Majeed, R. Ellahi, and Q. M. Z. Zia, "Mixed convection flow and heat transfer in ferromagnetic fluid over a stretching sheet with partial slip effects," *Thermal Science*, vol. 22, no. 6 Part A, pp. 2515–2526, 2018.

[24] M. Mamourian, K. Milani Shirvan, R. Ellahi, and A. B. Rahimi, "Optimization of mixed convection heat transfer with entropy generation in a wavy surface square lid-driven cavity by means of Taguchi approach," *International Journal of Heat and Mass Transfer*, vol. 102, pp. 544–554, 2016.

[25] A. Zaib, R. U. Haq, M. Sheikholeslami, A. J. Chamkha, and M. M. Rashidi, "Impact of non-Darcy medium on mixed convective flow towards a plate containing micropolar water-based TiO_2 nanomaterial with entropy generation," *Journal of Porous Media*, vol. 23, no. 1, 2020.

[26] U. Farooq, D. Lu, S. Ahmed, M. Ramzan, J. D. Chung, and F. Ali Chandio, "Computational analysis for mixed convective flows of viscous fluids with nanoparticles," *Journal of Thermal Science and Engineering Applications*, vol. 11, no. 2, 2019.

[27] M. Sheikholeslami and H. B. Rokni, "Nanofluid two phase model analysis in existence of induced magnetic field," *International Journal of Heat and Mass Transfer*, vol. 107, pp. 288–299, 2017.

[28] S. K. Ghosh, O. Anwar Bég, and J. Zueco, "Hydromagnetic free convection flow with induced magnetic field effects," *Meccanica*, vol. 45, no. 2, pp. 175–185, 2010.

[29] A. Kumar, "Numerical study of effect of induced magnetic field on transient natural convection over a vertical cone," *Alexandria Engineering Journal*, vol. 55, no. 2, pp. 1211–1223, 2016.

[30] N. S. Akbar, M. Raza, and R. Ellahi, "Interaction of nanoparticles for the peristaltic flow in an asymmetric channel with the induced magnetic field," *The European Physical Journal Plus*, vol. 129, no. 7, p. 155, 2014.

[31] S. Nadeem and S. Ijaz, "Impulsion of nanoparticles as a drug carrier for the theoretical investigation of stenosed arteries with induced magnetic effects," *Journal of Magnetism and Magnetic Materials*, vol. 410, pp. 230–241, 2016.

[32] T. Hayat, W. A. Khan, S. Z. Abbas, S. Nadeem, and S. Ahmad, "Impact of induced magnetic field on second-grade nanofluid flow past a convectively heated stretching sheet," *Applied Nanoscience*, vol. 10, pp. 3001–3009, 2020.

[33] M. Rashid, K. Ansar, and S. Nadeem, "Effects of induced magnetic field for peristaltic flow of Williamson fluid in a curved channel," *Physica A: Statistical Mechanics and its Applications*, vol. 553, p. 123979, 2020.

[34] S. T. Hussain, R. U. Haq, N. F. Noor, and S. Nadeem, "Nonlinear radiation effects in mixed convection stagnation point flow along a vertically stretching surface," *International Journal of Chemical Reactor Engineering*, vol. 15, no. 1, 2017.

[35] R. Viskanta and R. J. Grosh, "Boundary layer in thermal radiation absorbing and emitting media," *International Journal of Heat and Mass Transfer*, vol. 5, no. 9, pp. 795–806, 1962.

[36] T. Hayat, S. Nadeem, and A. U. Khan, "Rotating flow of Ag-CuO/H$_2$O hybrid nanofluid with radiation and partial slip boundary effects," *The European Physical Journal E*, vol. 41, no. 6, p. 75, 2018.

[37] A. Hussain, S. Akbar, L. Sarwar, S. Nadeem, and Z. Iqbal, "Effect of time dependent viscosity and radiation efficacy on a non-Newtonian fluid flow," *Heliyon*, vol. 5, no. 2, Article ID e01203, 2019.

[38] Z. Li, M. Sheikholeslami, A. Shafee et al., "Influence of adding nanoparticles on solidification in a heat storage system considering radiation effect," *Journal of Molecular Liquids*, vol. 273, pp. 589–605, 2019.

[39] A. Zeeshan, N. Shehzad, T. Abbas, and R. Ellahi, "Effects of radiative electro-magnetohydrodynamics diminishing internal energy of pressure-driven flow of titanium dioxide-water nanofluid due to entropy generation," *Entropy*, vol. 21, no. 3, p. 236, 2019.

[40] Q. Hussain, N. Alvi, T. Latif, and S. Asghar, "Radiative heat transfer in Powell--Eyring nanofluid with peristalsis," *International Journal of Thermophysics*, vol. 40, no. 5, pp. 1–20, 2019.

[41] T. Muhammad, H. Waqas, S. A. Khan, R. Ellahi, and S. M. Sait, "Significance of nonlinear thermal radiation in 3D Eyring-Powell nanofluid flow with Arrhenius activation energy," *Journal of Thermal Analysis and Calorimetry*, vol. 143, pp. pp929–944, 2021.

[42] A. Majeed, A. Zeeshan, H. Xu, M. Kashif, and U. Masud, "Heat transfer analysis of magneto-Eyring-Powell fluid over a nonlinear stretching surface with multiple slip effects: application of Roseland's heat flux," *Canadian Journal of Physics*, vol. 97, no. 12, pp. 1253–1261, 2019.

[43] N. Sher Akbar, A. Ebaid, and Z. H. Khan, "Numerical analysis of magnetic field effects on Eyring-Powell fluid flow towards a stretching sheet," *Journal of Magnetism and Magnetic Materials*, vol. 382, pp. 355–358, 2015.

[44] S. Nadeem and S. Saleem, "Mixed convection flow of Eyring-Powell fluid along a rotating cone," *Results in Physics*, vol. 4, pp. 54–62, 2014.

[45] A. Rehman, A. Hussain, and S. Nadeem, "Physical aspects of convective and radiative molecular theory of liquid originated nanofluid flow in the existence of variable properties," *Physica Scripta*, vol. 96, no. 3, 2020.

Research Article

The Mixture of the Marshall–Olkin Extended Weibull Distribution under Type-II Censoring and Different Loss Functions

Refah Alotaibi,[1] Mervat Khalifa,[2,3] Lamya A. Baharith,[2] Sanku Dey,[4] and H. Rezk [ID][3]

[1]*Mathematical Sciences Department, College of Science, Princess Nourah Bint Abdulrahman University, P.O. Box 84428, Riyadh 11671, Saudi Arabia*
[2]*Department of Statistics, King Abdulaziz University, P.O. Box 80203, Jeddah 21589, Saudi Arabia*
[3]*Department of Statistics, Al-Azhar University, Cairo, Egypt*
[4]*Department of Statistics, St. Anthony's College, Shillong, Meghalaya, P.O. Box 793001, India*

Correspondence should be addressed to H. Rezk; hodaragab2009@yahoo.com

To study the heterogeneous nature of lifetimes of certain mechanical or engineering processes, a mixture model of some suitable lifetime distributions may be more appropriate and appealing as compared to simple models. This paper considers a mixture of the Marshall–Olkin extended Weibull distribution for efficient modeling of failure, survival, and COVID-19 data under classical and Bayesian perspectives based on type-II censored data. We derive several properties of the new distribution such as moments, incomplete moments, mean deviation, average lifetime, mean residual lifetime, Rényi entropy, Shannon entropy, and order statistics of the proposed distribution. Maximum likelihood and Bayes procedure are used to derive both point and interval estimates of the parameters involved in the model. Bayes estimators of the unknown parameters of the model are obtained under symmetric (squared error) and asymmetric (linear exponential (LINEX)) loss functions using gamma priors for both the shape and the scale parameters. Furthermore, approximate confidence intervals and Bayes credible intervals (CIs) are also obtained. Monte Carlo simulation study is carried out to assess the performance of the maximum likelihood estimators and Bayes estimators with respect to their estimated risk. The flexibility and importance of the proposed distribution are illustrated by means of four real datasets.

1. Introduction

In the history of statistics, the use of finite mixture models is very old. They were particularly used to model population heterogeneity, generalize distributional assumptions, clustering and classification, etc. The concept of the finite mixture distribution was pioneered by Newcomb [1] for modeling outliers. Eight years later, Pearson [2] considered a mixture of two univariate Gaussian distributions to estimate the parameters of the model using the method of moments (MOM) to analyze a dataset containing ratios of the forehead to body lengths for 1,000 crabs. Since then, several authors have studied finite mixture models under different scenarios. Mendenhall and Hader [3] considered exponentially distributed failure time distributions based on censored lifetime data to estimate the model parameters using the maximum likelihood method. In their study, they divided the failure population into two subpopulations, each representing a different cause or type of failure. Radhakrishna et al. [4] considered both moment and maximum likelihood estimators of the unknown parameters of a two-component mixture of generalized gamma distribution. Ahmed et al. [5] obtained approximate Bayes estimators for parameters of the mixture of two Weibull distributions under type-II censoring. Al-Hussaini et al. [6] applied both maximum likelihood and Bayes estimation methods on a two-component mixture of the Gompertz distribution based on type-I and type-II censoring. Jaheen [7] adopted both maximum

likelihood and Bayesian approach to discuss the problem of estimating the parameters using the finite mixture of two exponential distributions based on record statistics. Shawky and Bakoban [8] adopted both maximum likelihood and Bayesian approach to estimate the parameters of the model, reliability, and failure rate functions of two-component finite mixtures of exponentiated gamma distribution. Abu-Zinadah [9] used maximum likelihood and Bayes estimation methods to estimate the parameters, reliability, and hazard functions of a mixture of exponentiated Pareto and exponential distribution under complete and type-II censoring schemes. Prakash [10] adopted the Bayes method to estimate the parameters from the mixture of two Weibull distributions based on informative and noninformative priors. Zhang et al. [11] proposed a mixture Weibull proportional hazard model to predict the failure of a mechanical system with multiple failure modes. They estimated the mixed model parameters by combining historical lifetime and monitoring data of all failure modes. ALgfary [12] introduced the finite mixture of two exponentiated Kumaraswamy (MEKum) distributions and obtained the maximum likelihood estimates for the vector of the parameters of the MEKum distribution. Adham and ALgfary [13] adopted the Bayesian approach to estimate the vector of parameters of the finite mixture of two-component exponentiated Kumaraswamy distribution. They also obtained Bayesian predictive density functions of future observations from the MEKum distribution. Ateya and Al Khald [14] studied the finite mixture of truncated generalized Cauchy distribution based on type-I, type-II, and progressively type-II censored samples. Aslam et al. [15] studied the three-component mixture of exponential, Rayleigh, Pareto, and Burr type-XII distributions in relation to reliability analysis. Tahir et al. [16] studied the properties of the three-component mixture of Rayleigh distributions based on doubly censored lifetime data. Kalantan and Alrewely [17] studied the two-component Laplace mixture model and obtained the estimates of the parameters using maximum likelihood and method of moments. Recently, Tahir et al. [18] also studied the three-component mixture of exponential distributions from the Bayesian perspective based on type-II doubly censoring sampling scheme. Kharazmi et al. [19] studied the 2-component mixture of Topp–Leone distribution and obtained classical and Bayes estimators based on the complete sample and the references cited therein.

Wide applicability of mixture modeling motivates us to develop a two-component mixture of Marshall–Olkin extended Weibull distribution for efficient modeling of breaking stress of carbon fibers, survival times in days of 72 guinea pigs infected datasets, survival times in weeks of 33 patients suffering from acute myelogenous leukemia, and COVID-19 data belonging to Canada of 36 days. In this article, the primary objective of the paper is twofold. First, we obtain maximum likelihood estimators and corresponding approximate confidence intervals (CIs) of the unknown parameters of the 2-component mixture of the Marshall–Olkin extended Weibull (MOEW) distribution for type-II censored data. Next, we consider the Bayes estimation method. The Bayes estimators have been derived and

evaluated under the assumption of two loss functions using independent gamma priors. Symmetric $100(1 - \tau)\%$ two-sided Bayes credible intervals are also obtained, and they are compared with classical CIs. To the best of our knowledge, the 2-component mixture of the MOEW distribution is not discussed before using the aforementioned methods of estimation. Through this paper, we purport to provide some guidelines on selecting the best estimator that may be of significant interest to applied statisticians/practitioners/engineers.

The organization of this paper is as follows. The description of the model along with basic properties is reported in Section 2. We use the maximum likelihood estimation method based on type-II censoring as a part of frequentist methodology for parameter estimation in Section 3. We have also taken into account approximate CIs in the same section. In Section 4, we have derived the Bayes estimators of the unknown parameters of the model under squared error loss (SEL) and linear exponential (LINEX) loss functions using gamma priors for both scale and shape parameters. We have also obtained two-sided Bayes probability intervals in the same section. The simulation study is carried out in Section 5. For illustrative purposes, four real datasets are analyzed in Section 6. Finally, concluding remarks are presented in Section 7.

2. Model Description

The probability density function (pdf) of the Marshall–Olkin extended Weibull distribution (MOEW) for a random variable X is defined by (see Ghitany et al. [20] and Zhang and Xie [21])

$$f(x) = \frac{\alpha \lambda \theta x^{\theta - 1} e^{-\lambda x^{\theta}}}{\left(1 - \overline{a} e^{-\lambda x^{\theta}}\right)^{2}}, \quad x \geq 0, \alpha, \lambda, \theta > 0, \quad (1)$$

where $\overline{a} = 1 - a$, and the cumulative distribution function (cdf) of the distribution is

$$F(x) = \frac{1 - e^{-\lambda x^{\theta}}}{1 - \overline{\alpha} e^{-\lambda x^{\theta}}}, \quad x \geq 0. \quad (2)$$

The hazard rate function of MOEW takes the form

$$h(x) = \frac{\lambda \theta x^{\theta - 1}}{1 - \overline{\alpha} e^{-\lambda x^{\theta}}}, \quad x \geq 0. \quad (3)$$

A density function for the mixture of two components' densities with mixing proportions $(p_j, j = 1, 2)$ is

$$g(x) = \sum_{j=1}^{2} p_j f_j(x), \quad \text{where } f_j(x)$$
$$= \alpha_j \theta_j \lambda_j x^{\theta_j - 1} e^{-\lambda_j x^{\theta_j}} \left(1 - \overline{\alpha}_j e^{\lambda_j x^{\theta_j}}\right)^{-2}, \quad (4)$$

where p_j are the mixing proportions, satisfying the conditions $\sum_{j=1}^{2} p_j = 1$ and $p_j \geq 0$; all of them are unknowns, and the pdf is plotted in Figure 1. The cdf for the mixture model is

$$G(x) = \sum_{j=1}^{2} p_j F_j(x), \tag{5}$$

where

$$F_j(x) = \frac{\left(1 - e^{-\lambda_j x^{\theta_j}}\right)}{\left(1 - \overline{\alpha} e^{\lambda_j x^{\theta_j}}\right)}. \tag{6}$$

The reliability function for the mixture model is

$$S(x) = \sum_{j=1}^{2} p_j R_j(x), \tag{7}$$

where

$$R_j(x) = 1 - \frac{\left(1 - e^{-\lambda_j x^{\theta_j}}\right)}{\left(1 - \overline{\alpha} e^{\lambda_j x^{\theta_j}}\right)}. \tag{8}$$

Due to exponentiation of each component by a positive integer, the model is so flexible that shows different shapes of hazard rate function (hrf) of the mixture which is given by

$$H(x) = \sum_{j=1}^{2} p_j h_j(x),$$

$$h_j(x) = \frac{\alpha_j \theta_j \lambda_j x^{\theta_j - 1} e^{-\lambda_j x^{\theta_j}} \left(1 - \overline{\alpha}_j e^{\lambda_j x^{\theta_j}}\right)}{\left(1 - \overline{\alpha} e^{\lambda_j x^{\theta_j}}\right) - \left(1 - \overline{\alpha} e^{\lambda_j x^{\theta_j}}\right)\left(1 - e^{-\lambda_j x^{\theta_j}}\right)}. \tag{9}$$

3. General Properties of the MOEW Distribution

3.1. Moments. The rth moment of a finite mixture of the 2-component MOEW distribution is given by

$$\mu_r' = \sum_{j=1}^{2} p_j \mu_r = \int_0^{\infty} p_1 \alpha_1 \theta_1 \lambda_1 x^{\theta_1 + r - 1} e^{-\lambda_1} \left(1 - \overline{\alpha}_1 e^{\lambda_1 x^{\theta_1}}\right)^{-2}$$

$$+ \int_0^{\infty} (1 - p_1) \alpha_2 \theta_2 \lambda_2 x^{\theta_2 + r - 1} e^{-\lambda_2} \left(1 - \overline{\alpha}_2 e^{\lambda_2 x^{\theta_2}}\right)^{-2}$$

$$= \frac{p_1}{\alpha_1} \left[\lambda_1 (-\lambda_1)^{(-r/\theta_1)} \Gamma\left(\frac{r + \theta_1}{\theta_1}\right)\right]$$

$$+ \frac{(1 - p_1)}{\alpha_2} \left[\lambda_2 (-\lambda_2)^{(-r/\theta_2)} \Gamma\left(\frac{r + \theta_2}{\theta_2}\right)\right], \tag{10}$$

where $p_2 = (1 - p_1)$.
When $r = 1$, the mean is given by

$$\mu_1' = \frac{p_1}{\alpha_1} \left[\lambda_1 (-\lambda_1)^{(-1/\theta_1)} \Gamma\left(\frac{1 + \theta_1}{\theta_1}\right)\right]$$

$$+ \frac{(1 - p_1)}{\alpha_2} \left[\lambda_2 (-\lambda_2)^{(-1/\theta_2)} \Gamma\left(\frac{1 + \theta_2}{\theta_2}\right)\right]. \tag{11}$$

The moment-generating function of the mixture MOEW distribution is given by

$$\mu_x(t) = \int_0^{\infty} e^{tx} f_j(x) dx$$

$$= \frac{\left(p_1 \theta_1 \lambda_1 x^{\theta_1} e^{-\lambda_1 x^{\theta_1}} / \alpha_1\right) + \left((1 - p_1) \theta_2 \lambda_2 x^{\theta_2} e^{-\lambda_1 x^{\theta_2}} / \alpha_2\right)}{x^2}. \tag{12}$$

3.2. Incomplete Moments. The rth incomplete moment of a finite mixture of the 2-component mixture distribution is given by

$$T_r(z) = E(x^r) = \int_0^z x^r f(x) dx = \sum_{j=1}^{2} p_j \int_0^z x^r f_j(x) dx$$

$$= \sum_{j=1}^{2} p_j \mu_{jr}, \tag{13}$$

where $T_{jr} = \int_0^z x^r f_j(x) dx$ is the rth incomplete moment of the jth component so that the rth incomplete moment of a finite mixture of the 2-component MOEW distribution is given by

$$T_r(z) = \sum_{j=1}^{2} p_j = \int_0^z p_1 \alpha_1 \theta_1 \lambda_1 x^{\theta_1 + r - 1} e^{-\lambda_1} \left(1 - \overline{\alpha}_1 e^{\lambda_1 x^{\theta_1}}\right)^{-2}$$

$$+ \int_0^z (1 - p_1) \alpha_2 \theta_2 \lambda_2 x^{\theta_2 + r - 1} e^{-\lambda_2} \left(1 - \overline{\alpha}_2 e^{\lambda_2 x^{\theta_2}}\right)^{-2} dx. \tag{14}$$

The first incomplete moment of a finite mixture of the 2-component MOEW distribution is given by

$$T_1(z) = \sum_{j=1}^{2} p_j \mu_{j1} = \int_0^z p_1 \alpha_1 \theta_1 \lambda_1 x^{\theta_1} e^{-\lambda_1} \left(1 - \overline{\alpha}_1 e^{\lambda_1 x^{\theta_1}}\right)^{-2}$$

$$\cdot \int_0^z (1 - p_1) \alpha_2 \theta_2 \lambda_2 x^{\theta_2} e^{-\lambda_2} \left(1 - \overline{\alpha}_2 e^{\lambda_2 x^{\theta_2}}\right)^{-2} dx. \tag{15}$$

3.3. Mean Deviations. The mean deviations of the random variable X about the mean, μ, and the median, M, are given, respectively, by
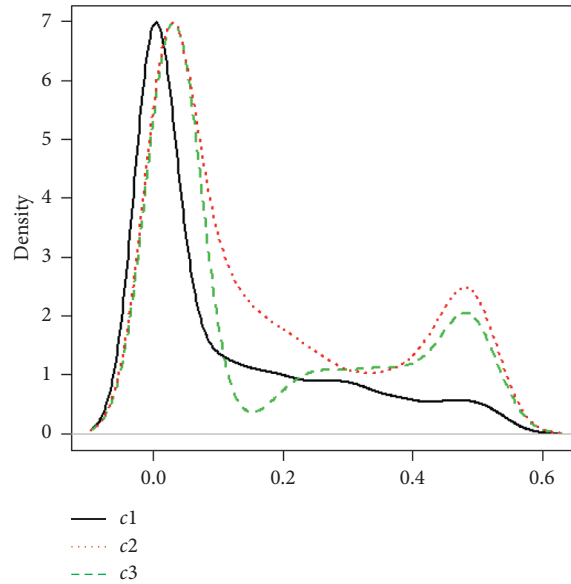
FIGURE 1: pdf of the two-component mixture of the Marshall–Olkin extended Weibull distribution for different values of the parameters, where $c1 = (\alpha 1 = 2, \theta 1 = 3, \lambda 1 = 1, \alpha 2 = 2, \theta 2 = 3, \lambda 2 = 1, p_1 = 0.4)$, $c2 = (\alpha 1 = 1, \theta 1 = 5, \lambda 1 = 2, \alpha 2 = 2, \theta 2 = 3, \lambda 2 = 5, p_1 = 0.3)$, and $c3 = (\alpha 1 = 1, \theta 1 = 5, \lambda 1 = 2, \alpha 2 = 4, \theta 2 = 3, \lambda 2 = 5, p_1 = 0.2)$.

$$\delta 1 = \int_x^{\cdot} |x - \mu| f(x, \alpha, \lambda, \theta) dx,$$

$$\delta 2 = \int_x^{\cdot} |x - M| f(x, \alpha, \lambda, \theta) dx, \tag{16}$$

where $\delta 1 = p_1 \delta 1_j + (1 - p_1) \delta 1_j$ and $\delta 2 = p_1 \delta 2_j + (1 - p_1) \delta 2_j$ since $\delta 1_j = \int_0^{\infty} |x - \mu| f_j(x, \alpha_j, \lambda_j, \theta_j) dx$ and $\delta 2_j = \int_0^{\infty} |x - M| f_j(x, \alpha_j, \lambda_j, \theta_j) dx$.

$$\delta 1 = \int_0^{\infty} |x - \mu| f(x, \alpha, \lambda, \theta) dx,$$

$$\delta 1 = \int_0^{\infty} |x - \mu| \left(p_1 \left\{ \frac{\alpha_1 \lambda_1 \theta_1 (x)^{\theta_1 - 1} e^{-\lambda_1 (x)^{\theta_1}}}{\left(1 - \overline{\alpha_1} e^{-\lambda_1 (x)^{\theta_1}}\right)^2} \right\} + (1 - p_1) \left\{ \frac{\alpha_2 \lambda_2 \theta_2 (x)^{\theta_2 - 1} e^{-\lambda_2 (x)^{\theta_2}}}{\left(1 - \overline{\alpha_2} e^{-\lambda_2 (x)^{\theta_2}}\right)^2} \right\} \right) dx$$

$$= p_1 \left\{ \frac{\alpha_1 \lambda_1 \theta_1 (x)^{\theta_1 - 1} e^{-\lambda_1 (x)^{\theta_1}}}{\left(1 - \overline{\alpha_1} e^{-\lambda_1 (x)^{\theta_1}}\right)^2} \right\} + (1 - p_1) \left\{ \frac{\alpha_2 \lambda_2 \theta_2 (x)^{\theta_2 - 1} e^{-\lambda_2 (x)^{\theta_2}}}{\left(1 - \overline{\alpha_2} e^{-\lambda_2 (x)^{\theta_2}}\right)^2} \right\}, \tag{17}$$

$$\delta 2 = \int_0^{\infty} |x - M| \left(p_1 \left\{ \frac{\alpha_1 \lambda_1 \theta_1 (x)^{\theta_1 - 1} e^{-\lambda_1 (x)^{\theta_1}}}{\left(1 - \overline{\alpha_1} e^{-\lambda_1 (x)^{\theta_1}}\right)^2} \right\} + (1 - p_1) \left\{ \frac{\alpha_2 \lambda_2 \theta_2 (x)^{\theta_2 - 1} e^{-\lambda_2 (x)^{\theta_2}}}{\left(1 - \overline{\alpha_2} e^{-\lambda_2 (x)^{\theta_2}}\right)^2} \right\} \right) dx.$$

The median follows from the nonlinear equation $F(x, \alpha, \lambda, \theta) = 1/2$. So, these quantities reduce to

$$\delta 1 F(x, \alpha, \lambda, \theta) 2\mu F(x, \alpha, \lambda, \theta) - 2T1(\mu),$$

$$\delta 2 = \mu - 2T1(M), \tag{18}$$

where $T1(z)$ is the first incomplete moment of X obtained from (15),

$$\delta 1_j = 2\mu_j F_j(x, \alpha_j, \lambda_j, \theta_j) - 2T1(\mu_j),$$

$$\delta 2_j = \mu_j - 2T1(M_j), \tag{19}$$

where

$$\delta 1 = 2\mu \left(p_1 \left[\frac{1 - e^{-\lambda_1 x_0^{\theta_1}}}{1 - \overline{\alpha_1} e^{-\lambda_1 x_0^{\theta_1}}} \right] \right.$$

$$\left. + \left((1 - p_1) \left[\frac{1 - e^{-\lambda_2 x_0^{\theta_2}}}{1 - \overline{\alpha_2} e^{-\lambda_2 x_0^{\theta_2}}} \right] \right) \right) - 2T1(\mu), \quad (20)$$

$$\delta 1 = \mu - 2T1(M).$$

3.4. Average Lifetime and Mean Residual Lifetime Functions.
The average lifetime is given by

$$t_m = \int_0^\infty [1 - F(x, \alpha, \lambda, \theta)] dx,$$

$$t_m = \int_0^\infty \left[1 - \left\{ p_1 \left[\frac{1 - e^{-\lambda_1 x^{\theta_1}}}{1 - \overline{\alpha_1} e^{-\lambda_1 x^{\theta_1}}} \right] \right. \right.$$

$$\left. \left. + (1 - p_1) \left[\frac{1 - e^{-\lambda_2 x^{\theta_2}}}{1 - \overline{\alpha_2} e^{-\lambda_2 x^{\theta_2}}} \right] \right\} \right] dx. \quad (21)$$

The application of mean residual lifetime can be seen in the paper of Guess and Proschan [22]. The mean residual lifetime is given by

$$m(x_0, \alpha, \lambda, \theta) = E(X - x_0 | X \geq x_0, \alpha, \lambda, \theta)$$

$$= \int_{(X: X - x_0)}^\infty \frac{(X - x_0) f(x, \alpha, (k+1)\lambda, \theta)}{\Pr[X \geq x_0]} dx = [\Pr[X \geq x_0]]^{-1} \int_0^\infty y f(x_0 + y, \alpha, \lambda, \theta) dy$$

$$= \left[1 - \left\{ p_1 \left[\frac{1 - e^{-\lambda_1 x_0^{\theta_1}}}{1 - \overline{\alpha_1} e^{-\lambda_1 x_0^{\theta_1}}} \right] + (1 - p_1) \left[\frac{1 - e^{-\lambda_2 x_0^{\theta_2}}}{1 - \overline{\alpha_2} e^{-\lambda_2 x_0^{\theta_2}}} \right] \right\} \right]^{-1} \quad (22)$$

$$= \int_0^\infty y \left(p_1 \left\{ \frac{\alpha_1 \lambda_1 \theta_1 (x_0 + y)^{\theta_1 - 1} e^{-\lambda_1 (x_0 + y)^{\theta_1}}}{\left(1 - \overline{\alpha_1} e^{-\lambda_1 (x_0 + y)^{\theta_1}} \right)^2} \right\} + (1 - p_1) \left\{ \frac{\alpha_2 \lambda_2 \theta_2 (x_0 + y)^{\theta_2 - 1} e^{-\lambda_2 (x_0 + y)^{\theta_2}}}{\left(1 - \overline{\alpha_2} e^{-\lambda_2 (x_0 + y)^{\theta_2}} \right)^2} \right\} \right) dy.$$

Then, $m(x_0, \alpha, \lambda, \theta) \longrightarrow E(X)$ as $x_0 \longrightarrow 0$.

3.5. Rényi Entropy.
The Rényi entropy of X with pdf (4) is given by

$$H_R^S(x) = \frac{1}{1 - S} \log \left(\int_x^. f(x, \alpha, \lambda, \theta)^S dx \right), \quad (23)$$

where $S \in (0, 1) \cup (1, \infty)$.

$$H_R^S(x) = \frac{1}{1 - S} \log \left(\int_0^\infty \left(p_1 \left\{ \frac{\alpha_1 \lambda_1 \theta_1 (x)^{\theta_1 - 1} e^{-\lambda_1 (x)^{\theta_1}}}{\left(1 - \overline{\alpha_1} e^{-\lambda_1 (x)^{\theta_1}} \right)^2} \right\} + (1 - p_1) \left\{ \frac{\alpha_2 \lambda_2 \theta_2 (x)^{\theta_2 - 1} e^{-\lambda_2 (x)^{\theta_2}}}{\left(1 - \overline{\alpha_2} e^{-\lambda_2 (x)^{\theta_2}} \right)^2} \right\} \right)^S dx \right). \quad (24)$$

It is difficult to obtain $H_R^S(x)$ in the closed form for a finite mixture of the 2-component MOEW distribution.

3.6. Shannon Entropy.
The Shannon entropy of X is given by

$$H_s(x) = E_x \{ -\log(f(x, \alpha, \lambda, \theta)) \}. \quad (25)$$

Thus, from (4), we can get the log-likelihood function as

$$\log[f_j(x, \alpha_j, \lambda_j, \theta_j)] = \log(\alpha_j \lambda_j) + \log[\theta_j x^{\theta_j - 1}] - \lambda_j x^{\theta_j}$$

$$- 2 \log \{ 1 - \overline{\alpha_j} \cdot \exp[-\lambda_j x^{\theta_j}] \}. \quad (26)$$

Thus, the above equation can be rewritten as

$$H_s(x) = -\log \{ P[(\alpha_1 \lambda_1) + 2E[\log\{1 - \overline{\alpha_1} \exp[-\lambda_1 x^{\theta_1}]\}]$$

$$- E_x \{ \log(\theta_1 x^{\theta_1 - 1}) \} + \lambda_1 E(x^{\theta_1})] + q[(\alpha_2 \lambda_2)$$

$$+ 2E[\log\{1 - \overline{\alpha_2} \cdot \exp[-\lambda_2 x^{\theta_2}]\}]$$

$$- E_x \{ \log(\theta_2 x^{\theta_2 - 1}) \} + \lambda_2 E(x^{\theta_2})] \}. \quad (27)$$

3.7. Distribution of Order Statistics.
The pdf of the rth order statistic for a random sample $x_1, x_2, x_3, \ldots, x_n$ from the MOEW distribution with pdf and cdf given in equations (1) and (2), respectively, is given by

$$f_{r,n}(x) = \frac{n!}{(n-r)!(r-1)!} f(X)[F(X)]^{r-1}[1-F(X)]^{n-r},$$

$$(28)$$

where

$$[1-F(X)]^{n-r} = \sum_{i=0}^{n-r} (-1)^i \binom{n-r}{i}[F(X)]^i. \qquad (29)$$

The rth order statistics for a finite mixture of the 2-component MOEW distribution can be obtained by substituting equations (4) and (6) into (28); thus, we have

$$f_{r,n}(x) = \frac{n!}{(n-r)!(r-1)!}$$

$$\sum_{i=0}^{n-r} (-1)^i \binom{n-r}{i} \left\{ \left[p_1 \left\{ \frac{\alpha_1 \lambda_1 \theta_1 x^{\theta_1-1} e^{-\lambda_1 x^{\theta_1}} \left(1 - e^{-\lambda_1 x^{\theta_1}}\right)^{r+i-1}}{\left(1 - \overline{\alpha_1} e^{-\lambda_1 x^{\theta_1}}\right)^{r+i+1}} \right\} \right] \right.$$

$$\left. + \left[(1 - p_1) \left\{ \frac{\alpha_2 \lambda_2 \theta_2 x^{\theta_2-1} e^{-\lambda_2 x^{\theta_2}} \left(1 - e^{-\lambda_2 x^{\theta_2}}\right)^{r+i-1}}{\left(1 - \overline{\alpha_2} e^{-\lambda_2 x^{\theta_2}}\right)^{r+i+1}} \right\} \right] \right\}. \qquad (30)$$

3.8. *Maximum Likelihood Estimation Based on Type-II Censoring.* Here, we discuss the maximum likelihood estimates of the unknown parameters of the 2-component mixture of the MOEW distributions. In a life testing experiment, n items from the above mixture model are employed to test and get terminated when a preassigned number of items, say r ($<n$), have failed. The samples obtained from such an experiment are called failure-censored

samples or type-II censored samples. In the failure-censored case, data comprise the lifetime of the r items that have failed (say $x_1 < x_2 < \cdots < x_r$), and the remaining $(n-r)$ items have survived beyond x_r with the assumption that the lifetime distribution of the items is independent and identically distributed MOEW distribution; the likelihood function for the type-II censoring scheme can be written as

$$L(\theta_1, \theta_2, \lambda_1, \lambda_2, \alpha_1, \alpha_2, p_1 | \underline{x}) \propto \prod_{i=1}^{r} f_j(x_i) R_j(x_r)^{(n-r)}$$

$$= p_1^r \theta_1^r \lambda_1^r \alpha_1^r \prod_{i=1}^{r} x_i^{\theta_1-1} e^{-\lambda_1 x_i^{\theta_1}} \left(1 - (1-\alpha_1)e^{-\lambda_1 x_i^{\theta_1}}\right)^{-2} \left[1 - \frac{\left(1 - e^{-\lambda_1 x_r^{\theta_1}}\right).}{\left(1 - (1-\alpha_1)e^{-\lambda_1 x_r^{\theta_1}}\right)}\right]^{(n-r)}$$

$$+ (1 - p_1)^r \theta_2^r \lambda_2^r \alpha_2^r \prod_{i=1}^{r} x_i^{\theta_2-1} e^{-\lambda_2 x_i^{\theta_2}} \left(1 - (1-\alpha_2)e^{-\lambda_2 x_i^{\theta_2}}\right)^{-2} \left[1 - \frac{\left(1 - e^{-\lambda_2 x_r^{\theta_2}}\right)}{\left(1 - (1-\alpha_2)e^{-\lambda_2 x_r^{\theta_2}}\right)}\right]^{(n-r)}. \qquad (31)$$

The corresponding log-likelihood function can be written as

$$\ell = \log L = r \log p_1 + r \log \theta_1 + r \log \lambda_1 + r \log \alpha_1$$

$$+ (\theta_1 - 1) \sum_{i=1}^{r} \log x_i - \lambda_1 \sum_{i=1}^{r} x_i^{\theta_1} - 2 \sum_{i=1}^{r} \log\left(1 - (1 - \alpha_1)e^{-\lambda_1 x_i^{\theta_1}}\right)$$

$$+ (n-r)\log\left[1 - \frac{\left(1 - e^{-\lambda_1 x_r^{\theta_1}}\right)}{\left(1 - (1-\alpha_1)e^{-\lambda_1 x_r^{\theta_1}}\right)}\right] + r \log(1 - p_1) + r \log \theta_2$$

$$+ r \log \lambda_2 + r \log \alpha_2 + (\theta_2 - 1) \sum_{i=1}^{r} \log x_i$$

$$- \lambda_2 \sum_{i=1}^{r} x_i^{\theta_2} - 2 \sum_{i=1}^{r} \log\left(1 - (1 - \alpha_2)e^{-\lambda_2 x_i^{\theta_2}}\right) + (n-r)\log\left[1 - \frac{\left(1 - e^{-\lambda_2 x_r^{\theta_2}}\right)}{\left(1 - (1-\alpha_2)e^{-\lambda_2 x_r^{\theta_2}}\right)}\right].$$

(32)

The resulting normal equations are

$$\frac{\partial \ell}{\partial \alpha_1} = \frac{r}{\alpha_1} - 2 \sum_{i=1}^{r} \frac{e^{-\lambda_1 x_i^{\theta_1}}}{\left(1 - (1-\alpha_1)e^{-\lambda_1 x_i^{\theta_1}}\right)} + \frac{(n-r)e^{-\lambda_1 x_r^{\theta_1}}\left(1 - (1-\alpha_1)e^{-\lambda_1 x_r^{\theta_1}}\right)^{-2}}{\left[1 - \left(\left(1 - e^{-\lambda_1 x_r^{\theta_1}}\right) / \left(1 - (1-\alpha_1)e^{-\lambda_1 x_r^{\theta_1}}\right)\right)\right]},$$

(33)

$$\frac{\partial \ell}{\partial \alpha_2} = \frac{r}{\alpha_2} - 2 \sum_{i=1}^{r} \frac{e^{-\lambda_2 x_i^{\theta_2}}}{\left(1 - (1-\alpha_2)e^{-\lambda_2 x_i^{\theta_2}}\right)} + \frac{(n-r)e^{-\lambda_2 x_r^{\theta_2}}\left(1 - (1-\alpha_2)e^{-\lambda_2 x_r^{\theta_2}}\right)^{-2}}{\left[1 - \left(\left(1 - e^{-\lambda_2 x_r^{\theta_2}}\right) / \left(1 - (1-\alpha_2)e^{-\lambda_2 x_r^{\theta_2}}\right)\right)\right]},$$

(34)

$$\frac{\partial \ell}{\partial \theta_1} = \frac{r}{\theta_1} + \sum_{i=1}^{r} \log x_i - \lambda_1 \sum_{i=1}^{r} x_i^{\theta_1} \log x_i$$

$$+ 2 \sum_{i=1}^{r} \frac{(1-\alpha_1)\lambda_1 \log x_i x_i^{\theta_1} e^{-\lambda_1 x_i^{\theta_1}}}{\left(1 - (1-\alpha_1)e^{-\lambda_1 x_i^{\theta_1}}\right)} - (n-r)\frac{\left(\alpha_1 \lambda_1 \log x_r x_r^{\theta_1} e^{-\lambda_1 x_i^{\theta_1}}\left(1 - (1-\alpha_1)e^{-\lambda_1 x_r^{\theta_1}}\right) / \left(1 - (1-\alpha_1)e^{-\lambda_1 x_r^{\theta_1}}\right)^2\right)}{\left[1 - \left(\left(1 - e^{-\lambda_1 x_r^{\theta_1}}\right) / \left(1 - (1-\alpha_1)e^{-\lambda_1 x_r^{\theta_1}}\right)\right)\right]},$$

(35)

$$\frac{\partial \ell}{\partial \theta_2} = \frac{r}{\theta_2} + \sum_{i=1}^{r} \log x_i - \lambda_2 \sum_{i=1}^{r} x_i^{\theta_2} \log x_i$$

$$+ 2 \sum_{i=1}^{r} \frac{(1-\alpha_2)\lambda_2 \log x_i x_i^{\theta_2} e^{-\lambda_2 x_i^{\theta_2}}}{\left(1 - (1-\alpha_2)e^{-\lambda_2 x_i^{\theta_2}}\right)} - (n-r)\frac{\left(\alpha_2 \lambda_2 \log x_r x_r^{\theta_2} e^{-\lambda_2 x_i^{\theta_2}}\left(1 - (1-\alpha_2)e^{-\lambda_2 x_r^{\theta_2}}\right) / \left(1 - (1-\alpha_1)e^{-\lambda_1 x_r^{\theta_1}}\right)^2\right)}{\left[1 - \left(\left(1 - e^{-\lambda_2 x_r^{\theta_2}}\right) / \left(1 - (1-\alpha_2)e^{-\lambda_2 x_r^{\theta_2}}\right)\right)\right]},$$

(36)

$$\frac{\partial \ell}{\partial \lambda_1} = \frac{r}{\lambda_1} - \sum_{i=1}^{r} x_i^{\theta_1} - 2 \sum_{i=1}^{r} \frac{(1-\alpha_1) x_i^{\theta_1} e^{-2\lambda_1 x_i^{\theta_1}}}{\left(1 - (1-\alpha_1) e^{-\lambda_1 x_i^{\theta_1}}\right)}$$
$$+ \frac{(n-r)\left(x_r^{\theta_1} e^{-\lambda_1 x_r^{\theta_1}} \left[\left(1 - (1-\alpha_1) e^{-\lambda_1 x_r^{\theta_1}}\right) + (1-\alpha_1)\left(1 - e^{-\lambda_1 x_r^{\theta_1}}\right)\right] / \left(1 - (1-\alpha_1) e^{-\lambda_1 x_r^{\theta_1}}\right)^2\right)}{\left[1 - \left(\left(1 - e^{-\lambda_1 x_r^{\theta_1}}\right) / \left(1 - (1-\alpha_1) e^{-\lambda_1 x_r^{\theta_1}}\right)\right)\right]}, \tag{37}$$

$$\frac{\partial \ell}{\partial \lambda_2} = \frac{r}{\lambda_2} - \sum_{i=1}^{r} x_i^{\theta_2} - 2 \sum_{i=1}^{r} \frac{(1-\alpha_2) x_i^{\theta_2} e^{-2\lambda_2 x_i^2}}{\left(1 - (1-\alpha_2) e^{-\lambda_2 x_i^{\theta_2}}\right)}$$
$$+ \frac{(n-r)\left(x_r^{\theta_2} e^{-\lambda_2 x_r^{\theta_2}} \left[\left(1 - (1-\alpha_2) e^{-\lambda_2 x_r^{\theta_2}}\right) + (1-\alpha_2)\left(1 - e^{-\lambda_2 x_r^{\theta_2}}\right)\right] / \left(1 - (1-\alpha_2) e^{-\lambda_2 x_r^{\theta_2}}\right)^2\right)}{\left[1 - \left(\left(1 - e^{-\lambda_2 x_r^{\theta_2}}\right) / \left(1 - (1-\alpha_2) e^{-\lambda_2 x_r^{\theta_2}}\right)\right)\right]}, \tag{38}$$

$$\frac{\partial \ell}{\partial p_1} = \frac{r}{p_1} - \frac{r}{1 - p_1}. \tag{39}$$

The MLEs of $\Phi = (\alpha_1, \alpha_2, \theta_1, \theta_2, \lambda_1, \lambda_2)$ and p_1 can be obtained by solving equations (32)–(39) simultaneously. Since explicit solutions cannot be obtained from the above equations, thus, we propose to use a suitable numerical technique to solve these seven nonlinear equations; however, one may use Newton–Raphson to solve these equations. This can be routinely done using R packages.

3.9. Approximate Confidence Intervals. In this section, under the normality property of MLEs of the parameters $\Phi = (\alpha_1, \alpha_2, \theta_1, \theta_2, \lambda_1, \lambda_2, p_1)$, we obtain the asymptotic confidence interval. The asymptotic distribution of the MLE $\hat{\Phi}$ is $(\hat{\Phi} - \Phi) \longrightarrow N(0, I^{-1}(\Phi))$, see Lawless [23], where $I^{-1}(\Phi)$, the inverse of the observed information matrix of the unknown parameters $\Phi = (\alpha_1, \alpha_2, \theta_1, \theta_2, \lambda_1, \lambda_2, p_1)$, is $I^{-1}(\Phi) = [(\partial^2 \ell / \partial \Phi^2)]^{-1}_{(\alpha_1, \alpha_2, \theta_1, \theta_2, \lambda_1, \lambda_2, p_1) = (\hat{\alpha}_1, \hat{\alpha}_2, \hat{\theta}_1, \hat{\theta}_2, \hat{\lambda}_1, \hat{\lambda}_2, \hat{p}_1)}$.

The above approach is used to derive approximate $100(1 - \tau)\%$ confidence intervals of the parameters Φ of the forms $\hat{\Phi} \mp z_{(\tau/2)} \sqrt{\text{var}(\hat{\Phi})}$, where $z_{(\tau/2)}$ is the upper $(\tau/2)^{\text{th}}$ percentile of the standard normal distribution.

4. Bayesian Estimation Using the Gamma Prior Distribution

In this section, the Bayes estimates of the model parameters are obtained under the assumption that the random variables Φ have independent gamma prior distributions (see Dey et al. [24–26]) with hyperparameters a_k and b_k, $k = 1, 2, 3, 4, 5, 6, 7$, and are given by

$$f(\Phi; a, b) = \frac{b_k^{a_k}}{\Gamma a_k} \Phi^{a_k - 1} e^{-b_k \Phi}, \quad \Phi > 0, \tag{40}$$

where $\Phi = (\alpha_j, \theta_j, \lambda_j, p_j)$. By multiplying (31) with (40), the joint posterior density for the vector of parameters Φ given the data becomes

$$\pi(\Phi | \underline{x}) \propto L(x | \Phi) f(\Phi; a_k, b_k). \tag{41}$$

Thus,

$$\pi(\Phi | \underline{x}) \propto (n-r) \cdot p_1^r \theta_1^r \lambda_1^r \alpha_1^r \prod_{i=1}^{r} x_i^{\theta_1 - 1} e^{-\lambda_1 x_i^{\theta_1}} \left(1 - (1-\alpha_1) e^{-\lambda_1 x_i^{\theta_1}}\right)^{-2} \left[1 - \frac{\left(1 - e^{-\lambda_1 x_r^{\theta_1}}\right)}{\left(1 - (1-\alpha_1) e^{-\lambda_1 x_r^{\theta_1}}\right)}\right]$$
$$+ (n-r)(1 - p_1)^r \theta_2^r \lambda_2^r \alpha_2^r \prod_{i=1}^{r} x_i^{\theta_2 - 1} e^{-\lambda_2 x_i^{\theta_2}} \left(1 - (1-\alpha_2) e^{-\lambda_2 x_i^{\theta_2}}\right)^{-2} \left[1 - \frac{\left(1 - e^{-\lambda_2 x_r^{\theta_2}}\right)}{\left(1 - (1-\alpha_2) e^{-\lambda_2 x_r^{\theta_2}}\right)}\right] \frac{b_k^{a_k}}{\Gamma a_k} \Phi^{a_k - 1} e^{-b_k \Phi}. \tag{42}$$

Marginal distributions of Φ can be obtained by integrating with respect to the nuisance parameters. Next, we consider the loss function that will be used to derive the estimators from the marginal posterior distributions.

4.1. Bayes Estimators of the Vector of Parameters Φ. In this section, we derive the Bayes estimators of the model parameters under symmetric as well asymmetric loss functions. A much known symmetric loss function is the squared error loss (SEL) function which is defined as

$$L(\hat{\Phi} - \Phi) = (\Phi - \hat{\Phi})^2. \tag{43}$$

The popularity of this loss function is due to its relationship to least squares theory; it also makes the calculations simpler. Under the SELF in (43), the Bayes estimates of any function $\Phi = (\alpha_j, \theta_j, \lambda_j, p_j)$ can be derived as

$$\hat{\Phi}_{SEL} = E(\Phi|\underline{t}) = A = \pi r^2 \int_{\Phi} (\Phi - \hat{\Phi})^2 \pi(\Phi|\underline{x}) d\Phi. \tag{44}$$

All the above integrals have no closed form; so, we employ the numerical method to estimate the parameters. A useful asymmetric loss function, known as LINEX loss function, was introduced by Varian [27] and widely used by several authors (see Zellner [28] and Pandey and Rai [29]). We noticed that the LINEX loss function does not perform well for the estimation of the scale parameter in the whole parametric space, but performs well for a certain specified value of Φ. Basu and Ebrahimi [30] also suggested that the LINEX loss function is proper for the location parameter, and it appears not to be suitable for the estimation of the scale parameter. The linear exponential (LINEX) is an asymmetric loss function defined as

$$L(\hat{\Phi} - \Phi) = e^{\nu(\Phi - \hat{\Phi})} - \nu(\Phi - \hat{\Phi}) - 1. \tag{45}$$

Under the LINEX loss function, the Bayes estimators of any function $\Phi = (\alpha_j, \theta_j, \lambda_j, p)$ can be written as

$$\hat{\Phi}_{LINEX} = E(\Phi|\underline{t}) = \int_{\Phi} \left(e^{\nu(\Phi - \hat{\Phi})} - \nu(\Phi - \hat{\Phi}) - 1 \right) \pi(\Phi|\underline{x}) d\Phi. \tag{46}$$

All the above integrals have no closed form. So, they are solved by the analytical method.

4.2. Credible Intervals. In this section, a symmetric $100(1 - \tau)\%$ two-sided Bayes probability interval estimate of Φ, denoted by $[L_{\Phi}, U_{\Phi}]$, is obtained by satisfying the following expression:

$$p[L(\underline{t}) < \Phi < U(\underline{t})] = \int_{L(\underline{t})}^{U(\underline{t})} \pi(\theta, \beta, \lambda|\underline{t}) d\Phi = 1 - \tau. \tag{47}$$

Since it is difficult to find the interval L_{Φ} and U_{Φ} analytically, thus, we apply suitable numerical techniques to solve this nonlinear equation.

5. Simulation Study and Comparisons

Here, we have carried out Monte Carlo simulation study to assess the performance of the maximum likelihood estimators and Bayes estimators with respect to their estimated risk. Here, for the simulation study, we have considered the parameter values as $a_1 = (1.9, 5), a_2 = (2, 4), \theta_1 = (1.3, 4), \theta_2 = (1.6, 3), \lambda_1 = (1, 2.5), \lambda_2 = (1.3, 3.5)$, and $p_1 = (0.5,$

0.6) and different values of the mixing proportion. We set sample sizes $n = 20, 40$, and 80.

Probabilistic mixing is used here to generate the mixture data. For each observation, a random number u is generated from the uniform $(0, 1)$ distribution. If $u < p_1$, the observation is taken randomly from F_1 (the MOEW distribution with parameters a_1, θ_1, and λ_1); otherwise, from F_2 (the MOEW distribution with parameters a_2, θ_2, and λ_2). The choice of the censoring failure is made in such a way that the censoring rate of the resultant sample is approximately 10%. To implement censored samplings, the observations $x_{11}, \ldots, x_{1r}$ and $x_{21}, \ldots, x_{2r}$, of failed items come from first and second subpopulations, respectively. The rest of the observations, which are greater than x_{1r} and x_{2r}, have been assumed to be censored from each component.

The simulated datasets have been obtained using the following steps:

> Step 1: generate a uniform random number u corresponding to each observation
>
> Step 2: if $u < p_1$, take the observation $x_{11}, \ldots, x_{1n1}$ from the first subpopulation; otherwise, from the second subpopulation $x_{21}, \ldots, x_{2n2}$
>
> Step 3: determine the test termination points on the right, that is, x_r
>
> Step 4: the observations which are greater than x_r have been considered to be censored from each component (type-II censoring)

To avoid an extreme sample, we simulate 5000 datasets each of size n. The abbreviations used in the tables are estimate, estimated risk, and length of CIs based on the maximum likelihood method, Bayes estimates based on the squared loss function, and Bayes estimates based on the LINEX loss function. The Bayes estimates, estimated risk, and length of the confidence interval are computed using R package. These results are reported in Table 1. We assume that the prior distributions follow gamma distribution with hyperparameters a_k and b_k, $k = 1, 2, 3, 4, 5, 6, 7$, $(a_1, b_1) = (1.3, 1.8), (a_2, b_2) = (2.1, 1.7), (a_3, b_3) = (2.3, 2.5), (a_4, b_4) = (1.6, 2.2), (a_5, b_5) = (0.7, 2.3), (a_6, b_6) = (2.7, 0.8), (a_7, b_7) = (1.9, 2.4)$.

From Table 1, we observe that, as sample size increases, estimated values of the parameters converge to the true values, and Bayes posterior risk tends to decrease. We also observe that, as sample size increases, the length of the classical confidence interval and Bayes credible interval decreases. It is to be noted that the Bayes estimates perform better than maximum likelihood estimates. In comparison of loss functions, the squared loss function provides better results than the LINEX loss function.

6. Real Data Analysis

In this section, we use four real-life datasets to illustrate the importance and flexibility of the MMOEW distribution. We compare the fits of the new MMOEW distribution with some other competitive models, such as Weibull (W), exponentiated Weibull (EW), exponentiated exponential

TABLE 1: The estimate, estimated risk, and length of the interval, Bayes method based on the squared loss function, and Bayes method based on the LINEX function when the prior distribution is gamma at different sample sizes.

n	20			40			80		
	MLEs								
Parameter	Estimate	Estimated risk	Length	Estimate	Estimated risk	Length	Estimate	Estimated risk	Length
α_1	2.2266962	0.45522293	1.7844411	1.9255029	0.26150688	1.0250881	1.7196975	0.17338100	0.679611
	5.4480750	0.74643451	2.9259695	4.8738022	0.4519073	1.7714444	4.6622334	0.29481590	1.1556571
α_2	2.6050691	0.4696128	1.8408485	2.3622973	0.32997054	1.2934608	2.1965263	0.2134274	0.8366198
	4.9593311	0.74254833	2.9107360	4.6106123	0.4359577	1.7089228	4.4158906	0.28053577	1.0996800
θ_1	2.1842048	0.78639415	3.2410730	1.8386415	0.3436788	1.3471963	1.7059249	0.18937750	0.7423461
	4.8291733	1.51823446	5.9513697	4.1635412	0.7380715	2.8931873	3.8762212	0.40641529	1.5931187
θ_2	2.2241709	0.8904526	3.5851222	1.9410834	0.4002303	1.5688740	1.8120731	0.23350051	0.9153052
	4.5922180	1.32300762	5.1860946	4.1184271	0.7396291	2.8992929	3.8127630	0.39210727	1.5370323
λ_1	1.78123132	0.51279547	2.0599757	1.7370224	0.327979	1.2856868	1.7424558	0.22229935	0.8713974
	4.1672100	1.27710513	5.0061601	3.7528999	0.7512598	2.9448842	3.3100211	0.44260320	1.7349727
λ_2	1.6369791	0.56717175	2.2361035	1.4859141	0.3043238	1.1929277	1.3966339	0.18769952	0.7357686
	5.0407180	1.56241461	6.1245527	4.3449870	0.8754458	3.4316845	3.8052724	0.51894037	2.0342089
p_1	0.4997187	0.07901453	0.309731	0.4993052	0.0558837	0.2190601	0.994209	0.03951937	0.1549131
	0.4797218	0.07900847	0.3097075	0.5003156	0.0558811	0.2190499	0.5000605	0.03952083	0.1549188
	Bayes estimates based on the squared loss function								
α_1	2.1729181	0.004552293	0.9784551	1.08645905	0.00227611	0.48922755	0.543229525	0.001138055	0.244613775
	4.980901	0.05829461	1.9342585	2.4904505	0.0291473	0.9671291	1.245225	0.014574	0.483565
α_2	2.056629	0.4696128	1.1297355	1.0283145	0.2348064	0.56486775	0.514157	0.117403	0.282434
	4.5283112	0.07326548	2.4938260	2.2641556	0.03663274	1.246913	1.132078	0.018316	0.623457
θ_1	1.7043984	0.092688415	2.3864156	0.8521992	0.0463442075	1.1932078	0.4261	0.023172	0.596604
	4.1261944	0.0692846326	2.5368135	2.0630972	0.03464231	1.2684065	1.031549	0.017321	0.634203
θ_2	2.1368209	0.0845269	2.1851222	1.06841045	0.0422636	1.0925611	0.534205	0.021132	0.546281
	4.3123180	0.032300762	1.9860946	2.1561599	0.01615036	0.9930473	1.07808	0.008075	0.496524
λ_1	1.2926875	0.051279547	2.0599757	0.64634375	0.02563897	1.02998785	0.323172	0.012819	0.514994
	3.9683190	0.49710513	3.0061601	0.9841595	1.9841595	1.50308005	0.99208	0.099208	0.75154
λ_2	1.4398321	0.06717175	2.2361035	0.71991605	0.71991605	1.1180515	0.359958	0.359958	0.559026
	4.28437120	1.56241461	0.9245527	2.1421856	0.014021856	0.46227635	1.071093	0.007011	0.231138
p_1	0.4991957857	0.07901453	0.6309731	0.24959785	0.03495978	0.31548655	0.124799	0.0124799	0.157743
	0.6389978	0.07900847	0.0309792	0.3194989	0.02194989	0.0154896	0.159749	0.019749	0.007745
	Bayes estimates based on the LINEX function								
α_1	2.272918	0.104552	1.078455	1.186459	0.102276	0.589228	0.64323	0.101138	0.344614
	5.080901	0.158295	2.034259	2.590451	0.129147	1.067129	1.345225	0.114574	0.583565
α_2	2.156629	0.569613	1.229736	1.128315	0.334806	0.664868	0.614157	0.217403	0.382434
	4.628311	0.173265	2.593826	2.364156	0.136633	1.346913	1.232078	0.118316	0.723457
θ_1	1.804398	0.192688	2.486416	0.952199	0.146344	1.293208	0.5261	0.123172	0.696604
	4.226194	0.169285	2.636814	2.163097	0.134642	1.368407	1.131549	0.117321	0.734203
θ_2	2.236821	0.184527	2.285122	1.16841	0.142264	1.192561	0.634205	0.121132	0.646281
	4.412318	0.132301	2.086095	2.25616	0.11615	1.093047	1.17808	0.108075	0.596524
λ_1	1.392688	0.15128	2.159976	0.746344	0.125639	1.129988	0.423172	0.112819	0.614994
	4.068319	0.597105	3.10616	1.08416	2.08416	1.60308	1.09208	0.199208	0.85154
λ_2	1.539832	0.167172	2.336104	0.819916	0.819916	1.218052	0.459958	0.459958	0.659026
	4.384371	1.662415	1.024553	2.242186	0.114022	0.562276	1.171093	0.107011	0.331138
p_1	0.599196	0.179015	0.730973	0.349598	0.13496	0.415487	0.224799	0.11248	0.257743
	0.738998	0.179008	0.130979	0.419499	0.12195	0.11549	0.259749	0.119749	0.107745

(EE), Marshall–Olkin Weibull (MOW), and Marshall–Olkin extended Weibull (MOEW) distributions. The comparisons are done based on some measures of goodness of fit, namely, the maximized log-likelihood under the model ($-\hat{\ell}$), Akaike information criterion (AIC), Bayesian information criterion (BIC), Hannan–Quinn information criterion (HQIC), consistent Akaike information criterion (CAIC), and Kolmogorov–Smirnov (KS) statistic with its p value (PV). We observe that all the distributions in Tables 2–5 show a reasonably good fit for the given four datasets. The plots of

empirical and fitted cdfs (Figures 2–5) also support the results in Tables 2–5. However, according to the cited statistics, the MMOEW model fits dataset II better than the other models.

Dataset I: the first dataset consists of 100 observations of breaking stress of carbon fibers. This dataset is obtained from Nichols and Padgett [31]. These data are stated as follows: 0.98, 5.56, 5.08, 0.39, 1.57, 3.19, 4.90, 2.93, 2.85, 2.77, 2.76, 1.73, 2.48, 3.68, 1.08, 3.22, 3.75, 3.22, 3.70, 2.74, 2.73, 2.50, 3.60, 3.11, 3.27, 2.87, 1.47, 3.11, 4.42, 2.40, 3.15, 2.67, 3.31,

TABLE 2: Comparison among MMOEW, EW, MOEW, Weibull, EE, and MOW based on MLEs, the measures AIC, BIC, HQIC, CAIC, and KS, and p value for real data I.

Distribution	Par.	Estimates	$-\hat{\ell}$	AIC	BIC	HQIC	CAIC	KS	p value
MMOEW	$\hat{\theta}_1$	2.93	80.13	174.26	192.49	181.64	183.38	0.09	0.3730
	$\hat{\alpha}_1$	0.62							
	$\hat{\lambda}_1$	0.06							
	$\hat{\theta}_2$	0.39							
	$\hat{\alpha}_2$	0.88							
	$\hat{\lambda}_2$	0.71							
	$\hat{\rho}$	0.93							
EW	$\hat{\theta}$	2.40	141.69	289.39	297.20	292.55	293.29	0.06	0.84
	$\hat{\alpha}$	1.49							
	$\hat{\lambda}$	0.38							
MOEW	$\hat{\theta}$	2.60	142.12	290.24	298.06	293.41	294.15	0.12	0.1282
	$\hat{\alpha}$	1.81							
	$\hat{\lambda}$	0.08							
MOW	$\hat{\theta}$	2.81	142.08	290.15	297.97	293.32	294.06	0.05	0.9684
	$\hat{\alpha}$	1.33							
	$\hat{\lambda}$	0.36							
Weibull	$\hat{\theta}$	3.00	142.03	288.05	293.26	290.16	290.66	0.05	0.9604
	$\hat{\lambda}$	0.34							
EE	$\hat{\alpha}$	12.81	150.48	304.96	310.17	307.07	307.57	0.08	0.5089
	$\hat{\lambda}$	1.16							

TABLE 3: Comparison among MMOEW, EW, MOEW, Weibull, EE, and MOW based on MLEs, the measures AIC, BIC, HQIC, CAIC, and KS, and p value for real data II.

Distribution	Par.	Estimates	$-\hat{\ell}$	AIC	BIC	HQIC	CAIC	KS	p value
MMOEW	$\hat{\theta}_1$	3.07	90.91	195.82	211.75	202.16	203.78	0.07	0.8695
	$\hat{\alpha}_1$	0.51							
	$\hat{\lambda}_1$	0.15							
	$\hat{\theta}_2$	1.02							
	$\hat{\alpha}_2$	2.54							
	$\hat{\lambda}_2$	0.33							
	$\hat{\rho}$	0.78							
EW	$\hat{\theta}$	1.55	104.70	215.40	222.23	218.12	218.81	0.09	0.6466
	$\hat{\alpha}$	1.79							
	$\hat{\lambda}$	0.69							
MOEW	$\hat{\theta}$	1.86	111.13	228.27	235.10	230.98	231.68	0.09	0.5932
	$\hat{\alpha}$	1.72							
	$\hat{\lambda}$	0.40							
MOW	$\hat{\theta}$	2.40	107.47	220.94	227.77	223.66	224.36	0.09	0.5301
	$\hat{\alpha}$	0.46							
	$\hat{\lambda}$	0.42							
Weibull	$\hat{\theta}$	2.11	111.12	226.24	230.79	228.05	228.52	0.08	0.6951
	$\hat{\lambda}$	0.52							
EE	$\hat{\alpha}$	5.04	102.46	208.92	213.47	210.73	211.19	0.07	0.8247
	$\hat{\lambda}$	1.33							

TABLE 4: Comparison among MMOEW, EW, MOEW, Weibull, EE, and MOW based on MLEs, the measures AIC, BIC, HQIC, CAIC, and KS, and p value for real data III.

Distribution	Par.	Estimates	$-\hat{\ell}$	AIC	BIC	HQIC	CAIC	KS	p value
MMOEW	$\hat{\theta}_1$	3.34	108.74	231.48	241.95	237.82	236.72	0.15	0.4473
	$\hat{\alpha}_1$	1.04							
	$\hat{\lambda}_1$	0.26							
	$\hat{\theta}_2$	0.53							
	$\hat{\alpha}_2$	3.22							
	$\hat{\lambda}_2$	0.28							
	$\hat{\rho}$	0.02							

<div align="center">TABLE 4: Continued.</div>

Distribution	Par.	Estimates	$-\hat{\ell}$	AIC	BIC	HQIC	CAIC	KS	p value
EW	$\hat{\theta}$	0.58	154.20	314.41	318.90	315.92	316.6524	0.089	0.9546
	$\hat{\alpha}$	1.27							
	$\hat{\lambda}$	0.04							
MOEW	$\hat{\theta}$	0.71	154.09	314.17	318.66	315.68	316.42	0.20	0.1588
	$\hat{\alpha}$	0.73							
	$\hat{\lambda}$	0.07							
MOW	$\hat{\theta}$	0.63	154.20	314.39	318.88	315.90	316.64	0.10	0.8945
	$\hat{\alpha}$	1.41							
	$\hat{\lambda}$	0.04							
Weibull	$\hat{\theta}$	0.67	154.10	312.20	315.19	313.21	313.69	0.09	0.9474
	$\hat{\lambda}$	0.03							
EE	$\hat{\alpha}$	0.58	153.93	311.85	314.85	312.86	313.35	0.15	0.4131
	$\hat{\lambda}$	0.02							

TABLE 5: Comparison among MMOEW, EW, MOEW, Weibull, EE, and MOW based on MLEs, the measures AIC, BIC, HQIC, CAIC, and KS, and p value for real data IV.

Distribution	Par.	Estimates	$-\hat{\ell}$	AIC	BIC	HQIC	CAIC	KS	p value
MMOEW	$\hat{\theta}_1$	4.92	-61.62	137.24	148.32	141.11	142.78	0.09	0.9144
	$\hat{\alpha}_1$	1.26							
	$\hat{\lambda}_1$	0.002							
	$\hat{\theta}_2$	2.68							
	$\hat{\alpha}_2$	2.88							
	$\hat{\lambda}_2$	1.59							
	$\hat{\rho}$	0.93							
EW	$\hat{\theta}$	5.19	-72.34	150.68	155.43	152.34	153.06	0.09	0.8747
	$\hat{\alpha}$	0.88							
	$\hat{\lambda}$	0.29							
MOEW	$\hat{\theta}$	5.57	-68.33	142.66	147.41	144.31	145.03	0.11	0.8012
	$\hat{\alpha}$	0.49							
	$\hat{\lambda}$	0.0006							
MOW	$\hat{\theta}$	6.53	-75.96	157.92	162.67	159.57	160.29	0.08	0.9614
	$\hat{\alpha}$	0.27							
	$\hat{\lambda}$	0.25							
Weibull	$\hat{\theta}$	4.86	-68.32	140.64	142.22	141.74	142.22	0.09	0.8893
	$\hat{\lambda}$	0.29							
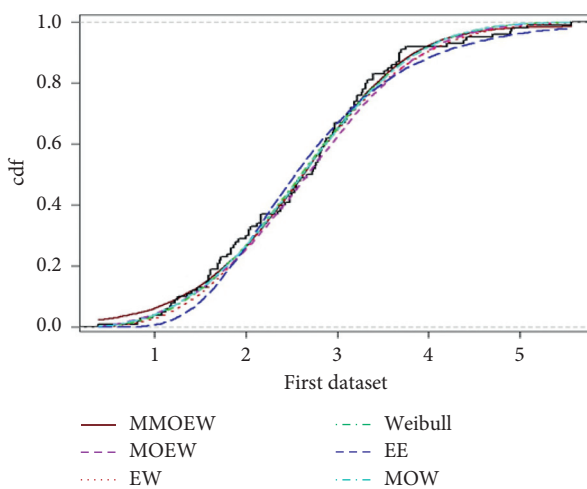
FIGURE 2: Empirical and fitted cdfs for the breaking stress data for MMOEW, MOEW, EW, Weibull, EE, and MOW distributions.
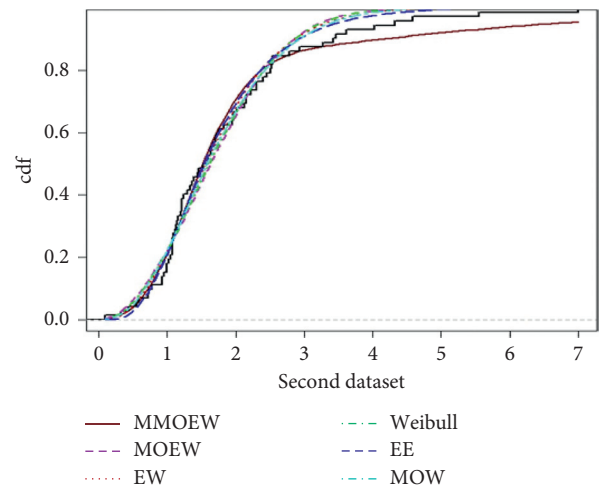
FIGURE 3: Empirical and fitted cdfs for survival times in days of 72 guinea pigs infected with virulent tubercle bacilli for MMOEW, MOEW, EW, Weibull, EE, and MOW distributions.
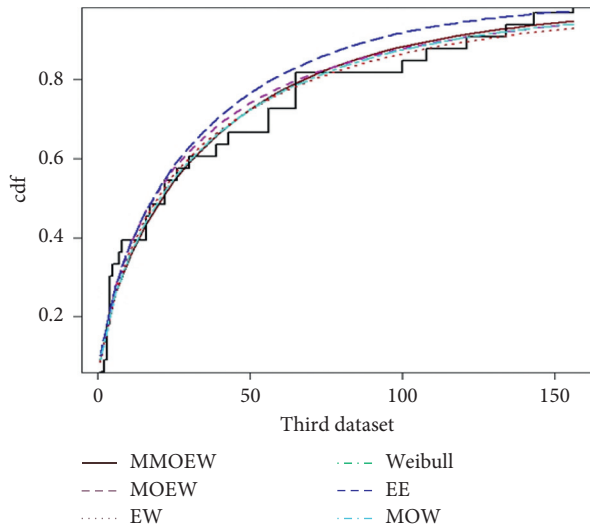
FIGURE 4: Empirical and fitted cdfs for survival times of 33 patients suffering from acute myelogenous leukemia for MMOEW, MOEW, EW, Weibull, EE, and MOW distributions.
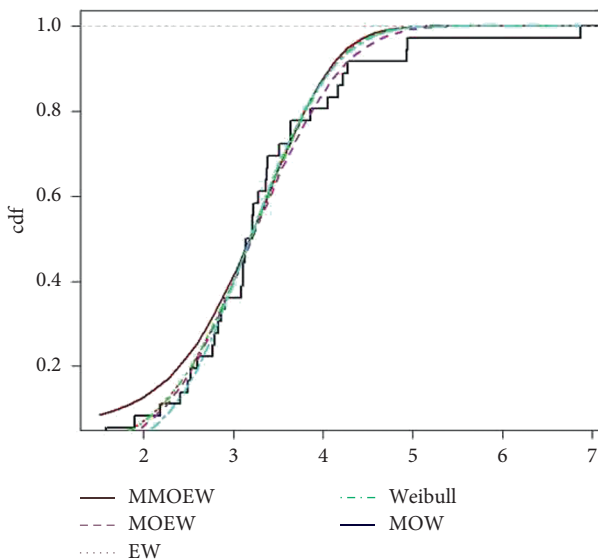
FIGURE 5: Empirical and fitted cdfs for the COVID-19 data belonging to Canada of 36 days for MMOEW, MOEW, EW, Weibull, EE, and MOW distributions.

2.81, 2.56, 2.17, 4.91, 1.59, 1.18, 2.48, 2.03, 1.69, 2.43, 3.39, 3.56, 2.83, 3.68, 2.00, 3.51, 0.85, 1.61, 3.28, 2.95, 2.81, 3.15, 1.92, 1.84, 1.22, 2.17, 1.61, 2.12, 3.09, 2.97, 4.20, 2.35, 1.41, 1.59, 1.12, 1.69, 2.79, 1.89, 1.87, 3.39, 3.33, 2.55, 3.68, 3.19, 1.71, 1.25, 4.70, 2.88, 2.96, 2.55, 2.59, 2.97, 1.57, 2.17, 4.38, 2.03, 2.82, 2.53, 3.31, 2.38, 1.36, 0.81, 1.17, 1.84, 1.80, 2.05, and 3.65.

Dataset II: the second dataset consists of survival times in days of 72 guinea pigs infected with virulent tubercle bacilli. This dataset is taken from Bjerkedal [32]. These data are illustrated as follows: 0.1, 0.33, 0.44, 0.56, 0.59, 0.72, 0.74,

0.77, 0.92, 0.93, 0.96, 1, 1, 1.02, 1.05, 1.07, 07, 1.08, 1.08, 1.08, 1.09, 1.12, 1.13, 1.15, 1.16, 1.2, 1.21, 1.22, 1.22, 1.24, 1.3, 1.34, 1.36, 1.39, 1.44, 1.46, 1.53, 1.59, 1.6, 1.63, 1.63, 1.68, 1.71, 1.72, 1.76, 1.83, 1.95, 1.96, 1.97, 2.02, 2.13, 2.15, 2.16, 2.22, 2.3, 2.31, 2.4, 2.45, 2.51, 2.53, 2.54, 2.54, 2.78, 2.93, 3.27, 3.42, 3.47, 3.61, 4.02, 4.32, 4.58, and 5.55.

Dataset III: the third dataset consists of the survival times in weeks of 33 patients suffering from acute myelogenous leukemia. This dataset is taken from Mahmoudi [33]. These data are illustrated as follows: 65, 156, 100, 134, 16, 108, 121, 4, 39, 143, 56, 26, 22, 1, 1, 5, 65, 56, 65, 17, 7, 16, 22, 3, 4, 2, 3, 8, 4, 3, 30, 4, and 43.

Dataset IV: the fourth dataset consists of drought mortality rate. The data represent COVID-19 data belonging to Canada of 36 days from 10 April to 15 May, 2020 (see the link https://covid19.who.int/). The data are as follows: 3.1091, 3.3825, 3.1444, 3.2135, 2.4946, 3.5146, 4.9274, 3.3769, 6.8686, 3.0914, 4.9378, 3.1091, 3.2823, 3.8594, 4.0480, 4.1685, 3.6426, 3.2110, 2.8636, 3.2218, 2.9078, 3.6346, 2.7957, 4.2781, 4.2202, 1.5157, 2.6029, 3.3592, 2.8349, 3.1348, 2.5261, 1.5806, 2.7704, 2.1901, 2.4141, and 1.9048.

7. Concluding Remarks

In this paper, we have introduced a two-component mixture model based on Marshall–Olkin extended Weibull distributions. Maximum likelihood and Bayes methods of estimation have been used to estimate the parameters of the mixture model. The numerical evidence shows that Bayes estimates perform better than the maximum likelihood estimates. Our simulated results follow the consistency property. The length of Bayes credible intervals is shorter than classical ones. From the simulation study, we may conclude that the Bayesian estimation has an advantage because of its small posterior risks as compared to the MLE method. If we compare the estimates with respect to loss functions, SELF performs better as compared to the LINEX loss function. Finally, for precise estimation of the unknown parameters of the Marshall–Olkin extended Weibull mixture model, Bayes method of estimation is preferable over maximum likelihood estimation, especially when the suitable prior information of the unknown parameters is available. The contents of the study may be useful in different fields where lifetime models are used for analysis of more than one causal factor of failure and where the data are type-II censored. The scope of this study may also be extended to other censoring schemes as well as for more than two-component mixture models.

Data Availability

The data used to support the findings of this study are included within the article.

Conflicts of Interest

The authors declare that there are no conflicts of interest regarding the publication of this paper.

Acknowledgments

References

[1] S. Newcomb, "A generalized theory of the combination of observations so as to obtain the best result," *American Journal of Mathematics*, vol. 8, no. 4, pp. 343–366, 1886.

[2] K. Pearson, "Contributions to the Mathematical theory of Evolution," *Philosophical Transactions, A*, vol. 185, pp. 71–110, 1894.

[3] W. Mendenhall and R. J. Hader, "Estimation of parameters of mixed exponentially distributed failure time distributions from censored life test data," *Biometrika*, vol. 45, no. 3-4, pp. 504–520, 1958.

[4] C. Radhakrishna, A. V. Dattatreya Rao, and G. V. S. R. Anjaneyulu, "Estimation of parameters in a two-component mixture generalized gamma distribution," *Communications in Statistics-Theory and Methods*, vol. 21, no. 6, pp. 1799–1805, 1992.

[5] K. E. Ahmed, H. M. Moustafa, and A. M. Abd-Elrahman, "Approximate Bayes estimation for mixture of two Weibull distributions under type-2 censoring," *Journal of Statistical Computation and Simulation*, vol. 58, pp. 269–285, 1997.

[6] E. K. AL-Hussaini, G. H. AL-Dayian, and S. A. Adham, "On finite mixture of two-component Gompertz lifetime model," *Journal of Statistical Computation and Simulation*, vol. 67, pp. 1–20, 2000.

[7] Z. F. Jaheen, "On record statistics from a mixture of two exponential distributions," *Journal of Statistical Computation and Simulation*, vol. 75, pp. 1–11, 2005.

[8] A. I. Shawky and R. A. Bakoban, "On infinite mixture of two-component exponentiated gamma distribution," *Journal of Applied Sciences Research*, vol. 5, no. 10, pp. 1351–1369, 2009.

[9] H. H. Abu-Zinadah, "A study on mixture of exponentiated Pareto and exponential distributions," *Journal of Applied Sciences Research*, vol. 6, pp. 358–376, 2012.

[10] G. Prakash, "Bayes estimation for a mixture of the Weibull distributions," *International Journal of Mathematics and Scientific Computing*, vol. 2, no. 1, pp. 2231–5330, 2012.

[11] Q. Zhang, C. Hua, and G. Xu, "A mixture Weibull proportional hazard model for mechanical system failure prediction utilizing lifetime and monitoring data," *Mechanical Systems and Signal Processing*, vol. 43, no. 1-2, pp. 103–112, 2014.

[12] A. A. ALgfary, "On finite mixture of exponentiated kumaraswamy distributions," Masters thesis, King Abdulaziz University, Jeddah, Saudi Arabia, 2015.

[13] S. A. Adham and A. A. ALgfary, "Bayesian estimation and prediction for a mixture of exponentiated Kumaraswamy distributions," *International Journal of Contemporary Mathematical Sciences*, vol. 11, pp. 497–508, 2016.

[14] S. F. Ateya and H. A. Al Khald, "Bayes estimation under a finite mixture of truncated generalized Cauchy distributions based on censored data with application," *Biostatistics and Biometrics Open Access Journal*, vol. 5, no. 1, pp. 1–7, 2018.

[15] M. Aslam, M. Tahir, and Z. Hussain, "Reliability analysis of three-component mixture of distributions," *ScientiaIranica,*

Transactions E: Industrial Engineering, vol. 25, pp. 1768–1781, 2018.

[16] M. Tahir, M. Aslam, H. Hussain, M. Abid, and S. H. Bhatti, "Bayesian analysis of heterogeneous doubly censored lifetime data using the 3-component mixture of Rayleigh distributions: a Monte Carlo simulation study," *ScientiaIranica*, vol. 26, no. 3, pp. 1789–1808, 2019.

[17] Z. I. Kalantan and F. Alrewely, "A 2-component Laplace mixture model: properties and parametric estimations," *Mathematics and Statistics*, vol. 7, no. 4A, pp. 9–16, 2019.

[18] M. Tahir, M. Aslam, M. Abid, S. Ali, and M. Ahsanullah, "A 3-component mixture of exponential distribution assuming doubly censored data: properties and Bayesian estimation," *Journal of Statistical Theory and Applications*, vol. 19, no. 2, pp. 197–211, 2020.

[19] O. Kharazmi, S. Dey, and D. Kumar, "Statistical inference on 2-component mixture of Topp-Leone distribution, Bayesian and non-Bayesian estimation," *Journal of Mathematical Extension*, In press, 2020.

[20] M. E. Ghitany, E. K. Al-Hussaini, and R. A. Al-Jarallah, "Marshall-Olkin extended Weibull distribution and its application to censored data," *Journal of Applied Statistics*, vol. 32, no. 10, pp. 1025–1034, 2005.

[21] T. Zhang and M. Xie, "Failure data analysis with extended Weibull distribution," *Communications in Statistics-Simulation and Computation*, vol. 36, no. 3, pp. 579–592, 2007.

[22] F. Guess and F. Proschan, "Mean residual life: theory and applications," *Handbook in Statistics*, vol. 7, pp. 512–224, 1988.

[23] J. F. Lawless, *Statistical Models and Methods for Lifetime Data*, John Wiley & Sons, New York, NY, USA, 1982.

[24] S. Dey, S. Ali, and C. Park, "Weighted exponential distribution: properties and different methods of estimation," *Journal of Statistical Computation and Simulation*, vol. 85, no. 18, pp. 3641–3661, 2015.

[25] S. Dey, T. Dey, S. Ali, and M. S. Mulekar, "Two-parameter Maxwell distribution: properties and different methods of estimation," *Journal of Statistical Theory and Practice*, vol. 10, no. 2, pp. 291–310, 2016.

[26] S. Dey, D. Kumar, and P. L. Ramos, "Exponentiated chen distribution: properties and estimation," *Communications in Statistics—Simulation and Computation*, vol. 46, no. 10, pp. 8118–8139, 2017.

[27] H. Varian, "A Bayesian approach to real estate Assessment," in *Studies in Bayesian Econometrics and Statistics*, S. E. Fienberg and A. Zellner, Eds., Scientific Research, Amsterdam, Netherlands, 1975.

[28] A. Zellner, "Bayesian and non-Bayesian estimation using Balanced loss functions," in *Statistical Decision Theory and Related Topics V*, S. S. Gupta and J. O. Burger, Eds., Springer, Berlin, Germany, 1986.

[29] B. N. Pandey and O. Rai, "Bayesian estimation of mean and square of mean of normal distribution using LINEX loss function," *Communication in Statistics Theory and Methods*, vol. 21, pp. 3369–3391, 1992.

[30] A. P. Basu and N. Ebrahimi, "Bayesian approach to life testing and reliability estimation using asymmetric loss function," *Journal of Statistical Planning and Inference*, vol. 29, pp. 21–31, 1991.

[31] M. D. Nichols and W. J. Padgett, "A bootstrap control chart for Weibull percentiles," *Quality and Reliability Engineering International*, vol. 22, pp. 141–151, 2006.

[32] T. Bjerkedal, "Acquisition of resistance in Guinea pigs infected with different doses of virulent tubercle bacilli," *American Journal of Public Hygiene*, vol. 72, pp. 130–148, 1960.

[33] E. Mahmoudi, "The beta generalized Pareto distribution with application to lifetime data," *Mathematics and Computers in Simulation*, vol. 81, no. 11, pp. 2414–2430, 2011.

Research Article

Stationary Wavelet with Double Generalised Rayleigh Distribution

Hassan M. Aljohani 📵

Department of Mathematics & Statistics, College of Science, Taif University, P.O. Box 11099, Taif 21944, Saudi Arabia

Correspondence should be addressed to Hassan M. Aljohani; h.m.sarhan@gmail.com

Statistics are mathematical tools applying scientific investigations, such as engineering and medical and biological analyses. However, statistical methods are often improved. Nowadays, statisticians try to find an accurate way to solve a problem. One of these problems is estimation parameters, which can be expressed as an inverse problem when independent variables are highly correlated. This paper's significant goal is to interpret the parameter estimates of double generalized Rayleigh distribution in a regression model using a wavelet basis. It is difficult to use the standard version of the regression methods in practical terms, which is obtained using the likelihood. Since a noise level usually makes the result of estimation unstable, multicollinearity leads to various estimates. This kind of problem estimates that features of the truth are complicated. So it is reasonable to use a mixed method that combines a fully Bayesian approach and a wavelet basis. The usual rule for wavelet approaches is to choose a wavelet basis, where it helps to compute the wavelet coefficients, and then, these coefficients are used to remove Gaussian noise. Recovering data is typically calculated by inverting the wavelet coefficients. Some wavelet bases have been considered, which provide a shift-invariant wavelet transform, simultaneously providing improvements in smoothness, in recovering, and in squared-error performance. The proposed method uses combining a penalized maximum likelihood approach, a penalty term, and wavelet tools. In this paper, real data are involved and modeled using double generalized Rayleigh distributions, as they are used to estimate the wavelet coefficients of the sample using numerical tools. In practical applications, wavelet approaches are recommended. They reduce noise levels. This process may be useful since the noise level is often corrupted in real data, as a significant cause of most numerical estimation problems. A simulation investigation is studied using the MCMC tool to estimate the underlying features as an essential task statistics.

1. Introduction

Parameters' estimation, to provide an interpreted model, is often the biggest challenge in statistics since data might contain noise, blur, or both. These kinds of problems were found in science, geophysics, engineering, and medicine. This kind of situation received much attention from researchers over the past decade. In practical applications, the biggest challenge in estimating the unknown parameters is that real data usually contain white noise. Hence, using a pretreatment may reduce noise, where it might provide a suitable fit. More precisely, it is used in the statistical approaches of data corrupted with white noise arising from the collocation of equipment. There are two types of statistical tools that are usually involved in processing the data. The first one is data pretreatment, which is applied to reduce the independent variable's correlation or noise level. The second is model calibration, which can be related to using Bayesian and wavelet methods. Hence, the key issues can be presented as working with many unknown features compared to the number of observations and then an ill-posed or ill-conditioned order in the model; that is, the maximum likelihood estimation is unsuitable for estimating underlying parameters. The widespread problem is to study real data collected by magnetometer or voltage reading, which are usually highly correlated. This process is needed since the sample's measured spectral characteristics may have noise levels and blur. Statistically, several established methods can be applied, such as classical thresholding approaches. Early work for studying this procedure can be found in [1, 2] who

introduced a new tool for removing noise (see [3, 4] for explicit motivation). Bayesian approaches were studied using different probability distributions in many fields over the last century. A common practice would be to perform exponential [5], and others were applied to various density distributions. For example, the authors in [6] studied the exponential distribution and estimated their parameters, whereas those in [7] employed the Weibull distribution to estimate the parameters using censored data. Also, the authors in [8] studied the Rayleigh distribution using consorted data. Hence, the idea of this article is to combine Bayesian and wavelet methods for estimating underlying parameters. Wavelets can be powerful mathematical tools applied to reduce the impact of multicollinearity problems. Wavelet basis can be explained as a special complicated level of the Fourier transform. However, the main reason for using wavelet approaches is that it is easy to choose between different wavelet bases. Many summaries were written about this topic by several authors. For example, Mallat [9] states that a probability density function of wavelet coefficients is notably peaked and centered around at zero. Also, the algorithm of discrete wavelet transform can be found in [10]. In wavelet, the stationary basis is recommended for the reconstruction (see [11] for more details). Then, the wavelets have received many comments from scientists, while several authors analyzed some real-statistical applications (see [12] for a direct result). Different approaches to the use of the wavelet can be found in [13]. Considerable details about wavelets can found in [14]. The central concept of the Bayesian approach is using the construction of theory. However, when the rules are built carefully, the model provides a good fit afterward as the estimation process. There are several papers on Bayesian methods (see [15] who studied Bayesian approaches in the wavelet domain). Wavelet via Bayesian approaches can be studied in many articles, such as in [16]. More details about the combination of Bayesian and wavelet can be studied in [17]. Besides, using the MCMC algorithm is extracting a sample at each run of simulation from the rule. The posterior rule is more complicated for an analytic solution. The easy type of MCMC is in [18], which can be implemented to extract notation. More details about the MCMC tool can be studied in [19–21]. Moreover, the estimation of the unknown parameters of the double generalized Rayleigh DGRay $(\gamma_j, \kappa_j, \lambda_j)$ distributions is proposed to provide a new tool, where $\mathscr{J} = 0, 1, \ldots, j-1$ for some indexes $\mathscr{J}$. In practical terms, this type of investigation is sometimes called the "level-dependent" models since the distribution parameters are estimated for each level j, especially when the measurable characteristics are assumed under two or more different conditions. For example, some wavelet coefficients have defects that are close to be around zero, whereas wavelet coefficients without defects may take a form far from zero. Consider the linear inverse problem defined by

$$\mathbf{x} = \theta + \varepsilon, \tag{1}$$

with observed measurement $\mathbf{x}_{n \times 1} = \{X_i : i = 1, \ldots, n\}$, the vector of the unknown parameters $\theta_{n \times 1} = \{\theta_i : i = 1, \ldots, n\}$,

and errors $\varepsilon_{n \times 1}$. Furthermore, $\varepsilon \sim N_n(0, \sigma^2 I_n)$, the noise level is usually assumed to be independent and identically distributed normally random, and $n = 2^{\mathscr{J}}$. Consider the unknown parameters Θ defined by

$$\Theta^{\mathscr{C}, D} = K\Theta, \tag{2}$$

where K is an orthonormal matrix containing the wavelet basis. Hence, the unknown parameters Θ can be defined by their discrete wavelet transform $\Theta^{\mathscr{C}, D} = \left\{ \theta_{0,0}^{\mathscr{C}}, \theta_{j,l}^{\mathscr{D}} : j = 0, 1, \ldots, \mathscr{J} - 1, l = 0, 1, \ldots, n-1 \right\}$, and the stationary transform is used in this article. So the number of wavelet coefficients and observations is equal. Also, the wavelet coefficients of the observed data $\mathbf{x}$ are defined by

$$\mathbf{x}^{\mathscr{C}, D} = \Theta^{\mathscr{C}, D} + \varrho, \tag{3}$$

where $\mathbf{x}^{\mathscr{C}, D}$ is the set of the wavelet coefficients of $\mathbf{x}$ and $\Theta^{\mathscr{C}, D} \subset \mathbf{R}$ is also the set of Θ, where $\varrho \sim N_n(0, \sigma^2 I_n)$. Level-dependent models play a significant role in wavelet applications—this procedure allows us to investigate the value of unknown parameters at each resolution j of wavelet coefficients. There are numerous methods for specifying values of unknown parameters of the double generalized Rayleigh distributions. Moreover, the MCMC algorithms are implemented to investigate the unknown parameters from complicated or nonstandard posterior distributions [22]. In statistics, there are many tools that can be applied to estimate parameters, such as EM and MCMC algorithms. In this article, two types of methods are supposed; the first one is the posterior mean (PM), and the second is maximum a posteriori (MAP).

Figure 1 illustrates the shape of the double Rayleigh distribution for different values of γ. It can be seen that as $\gamma \longrightarrow 0$, the density double Rayleigh approaches infinity, and this type of distribution can be used to fit the density of the empirical wavelet coefficients. More precisely, the wavelet coefficients are nearby the zero, which is found using the double generalized Rayleigh distribution with $\gamma = 0$ and $0 < \kappa \leq 0.5$. In the other words, the density double Rayleigh approaches infinity as x approaches zero when $\kappa \in (0, 0.5]$ and $\gamma = 0$, which is equivalent to the summary of Mallat. This article is structured as follows: introduction to the double generalized Rayleigh distribution is explained in Section 2. All technical arguments are referred to in Sections 3 and 4. Numerical work confirming their features and simulation study to investigate estimation properties is provided in Sections 5 and 6. Section 7 gives the result of the proposed rule to real data. The final summary and conclusions are presented in Section 8.

2. Double Generalized Rayleigh Distribution

The generalized Rayleigh DGRay $(\gamma_j, \kappa_j, \lambda_j)$ distribution was proposed by Aykroyd et al. as a generalized distribution. They showed the properties of the model, such as cumulative and survivor functions. Also, Aykroyd et al. [23] showed that the generalized Rayleigh distribution works well to fit data. They also used the Bayesian approaches to estimate

unknown parameters of the generalized Rayleigh distribution. In this paper, a double generalized Rayleigh distribution will be used to model the wavelet coefficients,

equivalent to the density of the wavelet coefficients. Let single wavelet coefficient $\theta_{j,l}^D$ at the level j be the probability density function (pdf) given by

$$
f\left(\theta_{j,l}^D | \lambda_j, \kappa_j, \gamma_j\right) = \begin{cases} \dfrac{\lambda_j \kappa_j}{2} \left|\theta_{j,l}^D\right| \left(\theta_{j,l}^{D2} - \gamma_j\right)^{\kappa_j - 1} \exp\left\{-\dfrac{\lambda_j \left(\theta_{j,l}^{D2} - \gamma_j\right)^{\kappa_j}}{2}\right\}, & -\sqrt{\gamma_j} < \theta_{j,l}^D < \sqrt{\gamma_j}, \\[4mm] 0, & O.W, \end{cases} \tag{4}
$$

where $|.|$ is the absolute value. The cumulative distribution function (cdf) is defined by

$$
F\left(\theta_{j,l}^D | \lambda_j, \kappa_j, \gamma_j\right) = \begin{cases} 1 - \exp\left\{-\dfrac{\lambda_j \left(\theta_{j,l}^{D2} - \gamma_j\right)^{\kappa_j}}{2}\right\}, & \theta_{j,l}^D > \sqrt{\gamma_j}, \\[4mm] \exp\left\{-\dfrac{\lambda_j \left(\theta_{j,l}^{D2} - \gamma_j\right)^{\kappa_j}}{2}\right\}, & \theta_{j,l}^D < -\sqrt{\gamma_j}, \\[4mm] 0, & O.W. \end{cases} \tag{5}
$$

The survivor function (sf) is given by

$$
S\left(\theta_{j,l}^D | \lambda_j, \kappa_j, \gamma_j\right) = \begin{cases} \exp\left\{-\dfrac{\lambda_j \left(\theta_{j,l}^{D2} - \gamma_j\right)^{\kappa_j}}{2}\right\}, & \theta_{j,l}^D > \sqrt{\gamma_j}, \\[4mm] 1 - \exp\left\{-\dfrac{\lambda_j \left(\theta_{j,l}^{D2} - \gamma_j\right)^{\kappa_j}}{2}\right\}, & \theta_{j,l}^D < -\sqrt{\gamma_j}, \\[4mm] 0, & O.W, \end{cases} \tag{6}
$$

and the failure function (hrf) is given by

$$
h\left(\theta_{j,l}^D | \lambda_j, \kappa_j, \gamma_j\right) = \begin{cases} \lambda_j \kappa_j \theta_{j,l}^D \left(\theta_{j,l}^{D2} - \gamma_j\right)^{\kappa_j - 1}, & \theta_{j,l}^D > \sqrt{\gamma_j}, \\[4mm] \dfrac{\left(\lambda_j \kappa_j / 2\right) \left|\theta_{j,l}^D\right| \left(\theta_{j,l}^{D2} - \gamma_j\right)^{\kappa_j - 1} \exp\left\{-\left(\lambda_j \left(t^2 - \gamma_j\right)^{\kappa_j} / 2\right)\right\}}{1 - \exp\left\{-\left(\lambda_j \left(\theta_{j,l}^{D2} - \gamma_j\right)^{\kappa_j} / 2\right)\right\}}, & \theta_{j,l}^D < \sqrt{\gamma_j}, \\[4mm] 0, & O.W, \end{cases} \tag{7}
$$

where $\gamma_j > 0, \kappa_j > 0$ and $\lambda_j > 0$. In some indexes, $\mathcal{J} = \log_2(n)$. The parameters λ_j and κ_j are shape

parameters, and γ_j is a location parameter. Setting $\gamma_j = 0$ and $\kappa_j = 1$ in (4)–(6), the results of the standard of the double Rayleigh distribution with parameter λ_j are obtained.

3. Bayesian Approach

In statistics, Bayesian tools play important roles, where the approach has two keys. The first one is the likelihood, concocted between observation and unknown parameters, say $p(\mathbf{x}|\zeta)$, where ζ and $\mathbf{x}$ are sets of underlying parameters and observations, respectively. The second key is the prior distribution, say $p(\zeta)$, and then the combining posterior distribution. Assuming the link between the model of $\mathbf{x}$ and the unknown of wavelet coefficients $(K^T \Theta^D)$,

$$
p(\mathbf{x}|\Theta^D, \sigma^2) = \prod_{i=1}^{n} \left(\frac{1}{\sqrt{2\pi\sigma^2}} \right)^n
$$
$$
\exp\left\{ -\frac{1}{2\sigma^2} \sum_{i=1}^{n} \left(x_i - \left(K^T \Theta^D \right)_i \right)^2 \right\}, \qquad (8)
$$
$$
\mathbf{x}, \Theta^D \subset \mathbf{R}^n; \sigma > 0,
$$

where σ^2 is the variance of data and can be assumed by

$$
p(\sigma^2|\tau) = \tau \exp\{-\tau\sigma^2\}, \quad \tau > 0, \qquad (9)
$$

using equation (2) and the marginal likelihood given by

$$
p(x|\theta, \tau) = \int_0^{\infty} p(x|\theta, \sigma^2) p(\sigma^2|\tau) \mathrm{d}\sigma^2
$$
$$
= \frac{\sqrt{2\tau}}{2} \exp\{-\sqrt{2\tau}\,|x - \theta|\}. \qquad (10)
$$

The result of the previous integration can be found in [24]. The equivalent likelihood is defined by

$$
p(\mathbf{x}|\Theta^D, \tau) = \prod_{i=1}^{n} \left(\frac{\sqrt{2\tau}}{2} \right)^n
$$
$$
\exp\left\{ -\sqrt{2\tau} \sum_{i=1}^{n} \left| x_i - \left(K^T \Theta^D \right)_i \right| \right\}, \quad \mathbf{x}, \Theta^D \subset \mathbf{R}^n; \sigma > 0. \qquad (11)
$$

In addition, the posterior distribution for Θ^D given $\mathbf{x}$ is

$$
p\left(\Theta^D | \mathbf{x}, \lambda_{\mathcal{J}-1}, \ldots, \lambda_0, \kappa_{\mathcal{J}-1}, \ldots, \kappa_0\right)
$$
$$
= p\left(\mathbf{x}|K^T\Theta^D\right) p\left(\theta_{\mathcal{J}-1}^D | \lambda_{\mathcal{J}-1}, \kappa_{\mathcal{J}-1}\right), \ldots, p\left(\theta_0^D | \lambda_0, \kappa_0\right)
$$
$$
\propto \prod_{i=1}^{n} \exp\left\{ -\sqrt{2\tau} \sum_{i=1}^{n} \left| x_i - \left(K^T\Theta^D \right)_i \right| \right\} \times \frac{(2\tau)^{n/2} \lambda_{\mathcal{J}-1}^{n_{\mathcal{J}-1}} \kappa_{\mathcal{J}-1}^{n_{\mathcal{J}-1}}}{2^n} \prod_{l=0}^{n_{\mathcal{J}-1}} \left| \theta_{\mathcal{J}-1,l}^D \right| \left(\theta_{\mathcal{J}-1,l}^{D2} \right)^{\kappa_{\mathcal{J}-1}-1}
$$
$$
\times \exp\left\{ -\frac{\lambda_{\mathcal{J}-1}\left(\theta_{\mathcal{J}-1,l}^{D2} \right)^{\kappa_{\mathcal{J}-1}}}{2} \right\} \cdots \times \lambda_0^{n_0} \kappa_0^{n_0} \left| \theta_{0,0}^D \right| \times \left(\theta_{0,0}^{D2} \right)^{\kappa_0-1} \exp\left\{ -\frac{\lambda_0\left(\theta_{0,0}^{D2} \right)^{\kappa_0}}{2} \right\}, \quad x_i, \theta_{j,l}^D \in \mathbf{R}; \left(\lambda_{\mathcal{J}-1}, \ldots, \lambda_0, \kappa_{\mathcal{J}-1}, \ldots, \kappa_0 \right) > 0, \ \sigma > 0,
$$

$$(12)$$

where $n_{\mathcal{J}-1}, \ldots, n_0$ are the size of the coefficients at each level $\mathcal{J} - 1, \ldots, 0$. Hence, the value of κ_j is suggested as $0 < \kappa_j \leq 0.5$. The main reason for choosing the double generalized Rayleigh is that as the value of $\gamma_j \longrightarrow 0$ and $|\theta_{j,l}^D| \longrightarrow 0$, the proposed distribution approaches infinity, which is followed by the saying of Mallat about the interpretation of the wavelet coefficients distribution. Clearly, equation (12) can be used to estimate the unknown parameters Θ^D given $\mathbf{x}, \lambda_{\mathcal{J}-1}, \ldots, \lambda_0, \kappa_{\mathcal{J}-1}, \ldots, \kappa_0$, and then these unknown parameters can be employed to describe the reconstruction. Hence, the unknown parameters are made up of one set, say with $\zeta = \{\theta_{0,0}^{\mathscr{C}}, \theta_{1,0}^{\mathscr{C}}, \theta_{1,1}^{\mathscr{C}}, \ldots, \theta_{\mathcal{J}-1,n-1}^{\mathscr{C}}, \lambda_{\mathcal{J}-1}, \ldots, \lambda_0, \kappa_{\mathcal{J}-1}, \ldots, \kappa_0, \tau\}$, and then, the previous form (12) becomes

$$
p(\zeta|\mathbf{x}) \propto p(\mathbf{x}|\zeta) p(\zeta) = p\left(\mathbf{x}|K^T\Theta^D, \omega\right) p\left(\Theta^D\right) p(\omega) p(\tau), \qquad (13)
$$

where $\Theta^{\mathscr{C},D} = \left\{ \theta_{0,0}^{\mathscr{C}}, \theta_{j,l}^{\mathscr{D}} \colon j = 0, 1, \ldots, \mathcal{J} - 1, l = 0, 1, \ldots, n - 1 \right\}$ and suppose that $\omega = \{\tau, \lambda, \kappa\}$ at the level j. Aykroyd et al. considered gamma prior density for λ and κ with hyperprior parameters (α_1, β_1) and (α_2, β_2). Also, gamma distribution is proposed for τ with hyperparameters (α_3, β_3), with density function

$$
p(\omega_i|\alpha_i, \beta_i) = \frac{1}{\Gamma(\alpha_i)} \beta_i^{\alpha} \omega^{\alpha_i-1} \exp\{-\beta_i\omega\}, \quad (\alpha, \beta) > 0, i = 1, 2, 3. \qquad (14)
$$

Then, the posterior density of the single value of $\theta_{j,l}^D$ with parameters τ, λ_j, and κ_j at the level j, given the data x, is given by

$$p\left(\theta_{j,l}^{\mathscr{D}}, \tau, \lambda_j, \kappa_j | x_i\right) = \frac{p\left(x_i | \left(K^T \Theta^D\right)_i, \tau\right) p(\tau) p(\lambda_j) p(\kappa_j)}{\int_{\theta_{j,l}^D} \int_{\lambda_j} \int_{\kappa_j} \int_{\tau} p\left(x_i | \left(K^T \Theta^D\right)_i, \tau\right) p(\tau) p(\lambda_j) p(\kappa_j) \mathrm{d}\kappa_j \mathrm{d}\lambda_j \mathrm{d}\theta_{j,l}^D},$$

$$p\left(\Theta^D, \tau, \lambda_{\mathscr{J}-1}, \ldots, \lambda_0, \kappa_{\mathscr{J}-1}, \ldots, \kappa_0 | \mathbf{x}\right) \propto p\left(\mathbf{x} | K^T \Theta^D, \tau\right) p(\tau) p\left(\boldsymbol{\theta}_{\mathscr{J}-1}^D\right) \cdots$$

$$\times p\left(\theta_0^D\right) p\left(\lambda_{\mathscr{J}-1}\right) \cdots p\left(\lambda_0\right) p\left(\kappa_{\mathscr{J}-1}\right) \cdots p\left(\kappa_0\right),$$

(15)

and the joint posterior density given data, x, can be written as

$$p\left(\Theta^D, \tau, \lambda_{\mathscr{J}-1}, \ldots, \lambda_0, \kappa_{\mathscr{J}-1}, \ldots, \kappa_0 | \mathbf{x}\right)$$

$$\propto \frac{(2\tau)^{n/2} \tau^{n+\alpha_1-1} \lambda_{\mathscr{J}-1}^{n_{\mathscr{J}-1}+\alpha_{2,\mathscr{J}-1}-1} \cdots \lambda_0^{n_0+\alpha_{2,0}-1} \kappa_{\mathscr{J}-1}^{n_{\mathscr{J}-1}+\alpha_{3,\mathscr{J}-1}-1} \cdots \kappa_0^{n_0+\alpha_{3,0}-1}}{2^n \Gamma(\alpha_{1,n}) \beta_{1,n}^{\alpha_{1,n}} \Gamma(\alpha_{2,\mathscr{J}-1}) \beta_{2,\mathscr{J}-1}^{\alpha_{2,\mathscr{J}-1}} \cdots \Gamma(\alpha_{2,0}) \beta_{2,0}^{\alpha_{2,0}} \Gamma(\alpha_{3,\mathscr{J}-1}) \beta_{3,\mathscr{J}-1}^{\alpha_{3,\mathscr{J}-1}} \cdots \Gamma(\alpha_{3,0}) \beta_{3,0}^{\alpha_{3,0}}}$$

$$\exp\left\{-\left(\frac{\tau}{\beta_{1,n}} + \frac{\lambda_{\mathscr{J}-1}}{\beta_{2,\mathscr{J}-1}} + \cdots + \frac{\lambda_0}{\beta_{2,0}} + \frac{\kappa_{\mathscr{J}-1}}{\beta_{3,\mathscr{J}-1}} + \cdots + \frac{\kappa_0}{\beta_{3,0}}\right)\right\} \prod_{l=0}^{n_{\mathscr{J}-1}} \left|\theta_{\mathscr{J}-1,l}^D\right| \left(\theta_{\mathscr{J}-1,l}^D\right)^{2\kappa_{\mathscr{J}-1}-1} \exp\left\{\frac{\lambda_{\mathscr{J}-1}\left(\theta_{\mathscr{J}-1,l}^D\right)^{2\kappa_{\mathscr{J}-1}}}{2}\right\}$$

$$\times \cdots \left|\theta_0^D\right| \left(\theta_0^D\right)^{2\kappa_0-1} \exp\left\{-\frac{\lambda_0\left(\theta_0^D\right)^{2\kappa_0}}{2}\right\} \prod_{i=1}^{n} \exp\left\{-\sqrt{2\tau} \sum_{i=1}^{n} \left|x_i - \left(K^T \Theta^D\right)_i\right|\right\}, \quad x_i, \theta_{j,l}^D \in \mathbf{R}; \left(\lambda_{\mathscr{J}-1}, \ldots, \lambda_0, \kappa_{\mathscr{J}-1}, \ldots, \kappa_0\right) > 0, \ \sigma > 0.$$

(16)

The hyperprior parameters τ, $\kappa = \{\kappa_{1,\mathscr{J}-1}, \ldots, \kappa_{1,0}, \kappa_{2,\mathscr{J}-1}, \ldots, \kappa_{2,0}\}$, and $\beta = \{\beta_{1,\mathscr{J}-1}, \ldots, \beta_{1,0}, \beta_{2,\mathscr{J}-1}, \ldots, \beta_{2,0}\}$ can be fixed, as follows: let the expectation and variance of ω_j at resolution j, say $t_{i,j}$ and $r_{i,j}$, where $i = 1, 2, 3$. By solving the following equations

$$E(\omega_j) = \alpha_{i,j} \beta_{i,j},$$
$$\text{Var}(\omega_j) = \alpha_{i,j} \beta_{i,j}^2, \quad i = 1, 2, 3,$$

(17)

the corresponding hyperprior parameters can be defined as $\alpha_{i,j} = t_{i,j}^2 / r_{i,j}$ and $\beta_{i,j} = r_{i,j} / t_{i,j}$.

4. Stationary Approaches

The vital task in the wavelet approaches is to choose a basis. For more details, the interpretation of the wavelet basis is to start with two functions. The first one is scaling or father function ϕ, where the main task of this function is to compute the scaling coefficients. The other is a wavelet or mother function ψ, where it can be used to calculate the wavelet coefficients. Several wavelet bases are now available with different degrees of smoothness. However, the Haar basis is a simple version of the wavelet transform. Moreover, there are several established wavelet families demonstrated (see [25–29] for details). Stationary wavelet transforms (SWTs) attracted much attention for many applications over the last few years. In particular, the classical stationary wavelet transform was introduced in [30], while the authors in [31, 32] applied at that time as the maximal overlap for discrete wavelet.

In 1995, Nason extended the discrete wavelet and recalled it as the "stationary." In the same year, Ronald and David [33] proposed a new tool: stationary wavelet coefficients and is sometimes referred to as "cycle spinning." In general, the SWT can be described as "fills in the gaps" between the decimated wavelet coefficients; that is, there is no missing computation between two different values of wavelet coefficients. Nason stated that this leads to an overdetermined redundancy of the original data (see the below example for more explanation). The producer gives a shift-invariant removing noisy tool, which simultaneously shows improvements in reconstruction quality (see Ronald and

David). For example, of the SWT, the Haar wavelet is applied to the data $\mathbf{x} = \{x_1, x_2, x_3, x_4\}$. The first and second sets of the scaling and detail coefficients can be computed:

$$\theta_{1,l}^C = \begin{bmatrix} \dfrac{\sqrt{2}}{2} & \dfrac{\sqrt{2}}{2} & 0 & 0 \\[2mm] 0 & \dfrac{\sqrt{2}}{2} & \dfrac{\sqrt{2}}{2} & 0 \\[2mm] 0 & 0 & \dfrac{\sqrt{2}}{2} & \dfrac{\sqrt{2}}{2} \\[2mm] \dfrac{\sqrt{2}}{2} & 0 & 0 & \dfrac{\sqrt{2}}{2} \end{bmatrix} \times \begin{bmatrix} x_1 \\ x_2 \\ x_3 \\ x_4 \end{bmatrix},$$

$$\theta_{0,l}^C = \begin{bmatrix} \dfrac{\sqrt{2}}{2} & 0 & \dfrac{\sqrt{2}}{2} & 0 \\[2mm] 0 & \dfrac{\sqrt{2}}{2} & 0 & \dfrac{\sqrt{2}}{2} \\[2mm] \dfrac{\sqrt{2}}{2} & 0 & \dfrac{\sqrt{2}}{2} & 0 \\[2mm] 0 & \dfrac{\sqrt{2}}{2} & 0 & \dfrac{\sqrt{2}}{2} \end{bmatrix} \times \begin{bmatrix} \theta_{1,0}^C \\ \theta_{1,1}^C \\ \theta_{1,2}^C \\ \theta_{1,3}^C \end{bmatrix},$$

$$\theta_{0,l}^C = \begin{bmatrix} \dfrac{\sqrt{2}}{2} & 0 & \dfrac{\sqrt{2}}{2} & 0 \\[2mm] 0 & \dfrac{\sqrt{2}}{2} & 0 & \dfrac{\sqrt{2}}{2} \\[2mm] \dfrac{\sqrt{2}}{2} & 0 & \dfrac{\sqrt{2}}{2} & 0 \\[2mm] 0 & \dfrac{\sqrt{2}}{2} & 0 & \dfrac{\sqrt{2}}{2} \end{bmatrix} \times \begin{bmatrix} \theta_{1,0}^C \\ \theta_{1,1}^C \\ \theta_{1,2}^C \\ \theta_{1,3}^C \end{bmatrix},$$

$$\theta_{1,l}^D = \begin{bmatrix} \dfrac{\sqrt{2}}{2} & \dfrac{-\sqrt{2}}{2} & 0 & 0 \\[2mm] 0 & \dfrac{\sqrt{2}}{2} & \dfrac{-\sqrt{2}}{2} & 0 \\[2mm] 0 & 0 & \dfrac{\sqrt{2}}{2} & \dfrac{-\sqrt{2}}{2} \\[2mm] \dfrac{-\sqrt{2}}{2} & 0 & 0 & \dfrac{\sqrt{2}}{2} \end{bmatrix} \times \begin{bmatrix} x_1 \\ x_2 \\ x_3 \\ x_4 \end{bmatrix}, \quad (18)$$

where $\theta_{1,l}^C$, $\theta_{0,l}^C$, $\theta_{1,l}^D$, and $\theta_{0,l}^D$ are the matrices of transform at level $j = \{0, 1\}$, respectively. Hence, the number N of vanishing moments decreases. This implicates that the smoothness of the corresponding shape decreases. In this paper, Daubechies father function ϕ and mother ψ with $N =$

8 vanishing moments are used to provide a smooth reconstruction.

The plotting procedure for the stationary wavelet transform is shown in Figure 2. It can be seen that each level j has the same number of wavelet coefficients. Figure 3 shows the scaling and wavelet functions for Daubechies with $N = 8$ vanishing moments. Table 1 shows the wavelet coefficients for Daubechies compact, phase $N = 8$. Here, we present the idea of Daubechies, omitting some technical details.

5. Numerical Methods

The goal of the Bayesian computation is to extract a posterior sample for some unknown parameters ζ. However, computational statistics can be explained as inverse problems. Some tools can be used to make the estimation more efficient. They include the standard version of the MCMC algorithms, Metropolis-Hastings tools, to extract a random sample from the posterior rule $p(\zeta|\mathbf{x})$ in (16). The procedure of the technique for parameter estimation, through the MCMC approach, can be found in [34]; for more information, see [35,36] and more recent works such as [37].

Figure 4 shows the diagram of the procedure of the proposed methods, where the procedure starts with data, which is corrupted by noise. The data are transformed to wavelet coefficients, which are used to estimate the unknown wavelet coefficients using the suggested method, and then, the underlying signal is calculated by inverting the estimation of wavelet coefficients. The main idea of the MCMC algorithms is that the parameter can take at any valued point in the parameter space Ω, say ζ_i is the value point. Then, at each step, MCMC creates values, say $\zeta_i^1, \zeta_i^2, \dots, \zeta_i^r$. Each single parameter updates separately in the order that the MCMC algorithms depend on a random walk. More precisely, the general framework of the tool is defined as follows:

(i) Starting with an initial value for $\Theta^{C,D} = 0$ and for each level $j = 0, 1, \dots, 2^{\mathcal{J}-1}$, that is, for parameters, let $\omega^0 = \left\{\kappa_0^0, \kappa_1^0, \dots \kappa_{2^{\mathcal{J}-1}}^0, \beta_0^0, \beta_1^0, \dots \beta_{2^{\mathcal{J}-1}}^0\right\}$.

(ii) For times $k = 1, \dots, K$.

(1) Generate a new value $\omega_j^* = \omega_j^{k-1} + \varepsilon$, where $\varepsilon \sim N(0, \varsigma_{\omega,j}^{2k-1})$. Hence, the current value of the prior parameters is proposed with a variance parameter for each resolution j, which is chosen to obtain an acceptable convergence rate.

(2) Compute the posterior distribution in (16).

For $s = 1, 2, \dots, n$, that is, for each wavelet coefficient $\theta_{j,l}^D$.

(a) Generate a new wavelet coefficient $\theta_{j,l}^{D*} = \theta_{j,l}^{Ds-1} + \varepsilon$, where $\varepsilon \sim N(0, \varsigma_{\theta,j}^{2s-1})$.

(b) Again, compute the posterior distribution in (16).

(c) Generate $u \sim U(0, 1)$.

(d) When $\alpha(\zeta^* | \zeta^{sk}) = \min\left\{1, \left(p\left(\theta_{0,0}^{\mathscr{D}}, \theta_{1,0}^{\mathscr{D}}, \dots, \theta_{j,l}^{\mathscr{D}*}, \dots, \theta_{\mathscr{J}-1,n-1}^{\mathscr{D}}, \lambda_{\mathscr{J}-1}, \dots, \lambda_j^*, \dots, \lambda_0, \kappa_{\mathscr{J}-1}, \dots, \kappa_j^*, \dots, \kappa_0\right)/p\left(\theta_{0,0}^{\mathscr{D}}, \theta_{1,0}^{\mathscr{D}}, \dots, \theta_{j,l}^{\mathscr{D}s-}\right.\right.$ $1, \dots, \theta_{\mathscr{J}-1,n-1}^{\mathscr{D}}, \lambda_{\mathscr{J}-1}, \dots, \lambda_j^{k-}$
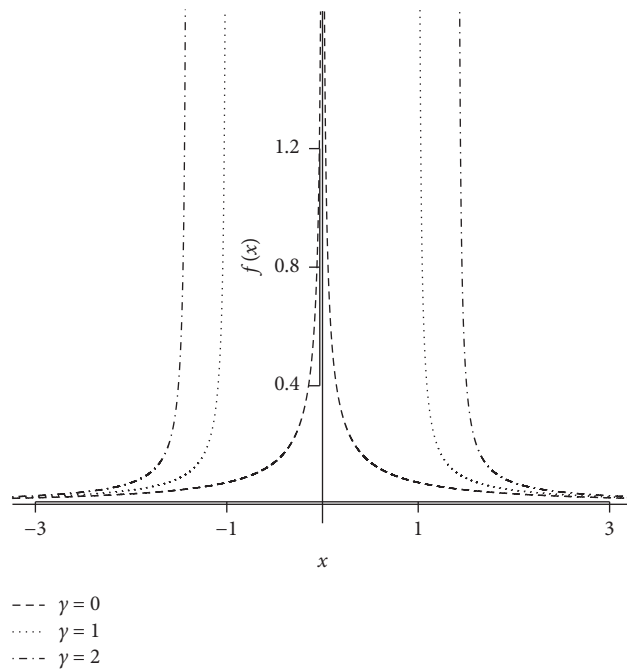
Figure 1: Typical data (points) derived from the generalized Rayleigh distribution (dashed line) along with different values of γ, while $\kappa = 0.5$ and $\lambda = 10$.
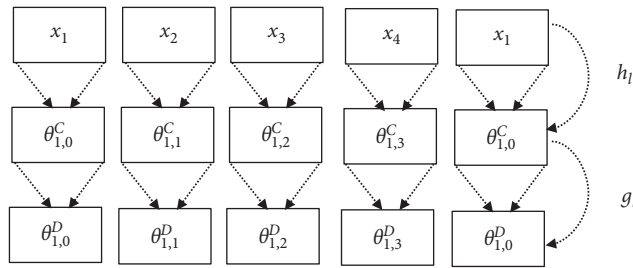
Figure 2: Graphical depiction of the stationary wavelet transform. The first row depicts the data, the second row indicates the wavelet coefficients, and the third shows the correspondence to the detailed wavelets. h_l and g_l are high- and low-pass quadrature mirror filters.

(a)

(b)
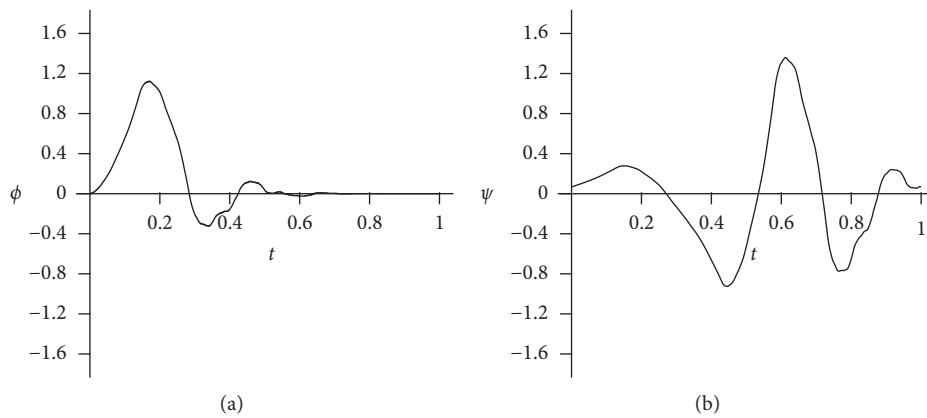
Figure 3: Plots of the father ϕ and mother ψ wavelets with $N = 8$ vanishing moments.

$1, \ldots, \lambda_0, \kappa_{\mathcal{J}-1}, \ldots, \kappa_j^{k-1}, \ldots, \kappa_0))\} > u$, accept the proposal and set $\theta_{j,l}^{Ds} = \theta_{j,l}^{D*}$ and $\omega_j^k = \omega_j^*$; else, $\theta_{j,l}^{Ds} = \theta_{j,l}^{Ds-1}$ and $\omega_j^k = \omega_j^{k-1}$.

Hence, all parameters are generated from the Gaussian distribution, while the current amount of the parameter is the expectation of the normal distribution with updating

TABLE 1: Orthogonal Daubechies coefficients for filter number 8.

l	0	1	2	3	4
h_l	0.0544158422	0.3128715909	0.6756307363	0.5853546837	−0.0158291053
l	5	6	7	8	9
h_l	−0.2840155430	0.0004724846	0.1287474266	−0.0173693010	−0.0440882539
l	10	11	12	13	14
h_l	0.0139810279	0.0087460940	−0.0048703530	−0.0003917404	0.0006754494
l	15	16	17	18	19
h_l	−0.0001174768	0	0	0	0
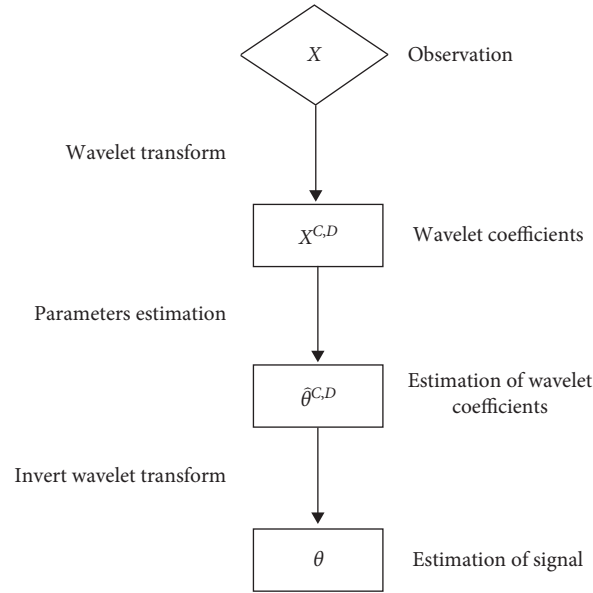
FIGURE 4: Diagram showing the structure of the suggested methods.

variance, which is based on the acceptance rate. It is essential to realize to pick up a random value around the current value, that is, both low and high, with variances $\varsigma_{\zeta,j}^2$ chosen to depend on an acceptance rate. More precisely, choosing any valued point ω in the parameter space is accepted. The authors in [38] stated determining value is between 20% and 30% for an acceptance rate. Hence, we considered the following gamma prior density for the variance of noise σ^2, where the starting point is computed from the finest level of the wavelet coefficients, $\Theta_{\mathcal{J}-1,}^D$ (see Nason).

Once the sample is collected from the posterior rule, the posterior mean for ζ can be calculated by

$$\widehat{\zeta} = \overline{\zeta} = \frac{1}{K - M} \sum_{k=M+1}^{K} \zeta^k, \tag{19}$$

and also, the posterior variance can be calculated by

$$\widehat{\sigma}^2 = \frac{1}{K - M} \sum_{k=M+1}^{K} \left(\zeta^k - \overline{\zeta} \right)^2, \tag{20}$$

where K and M are the number of run and burn-in, respectively. Hence, there is an enormous method to compute the estimate point and interval. For the MAP rule, the previous procedure is changed into a simulated annealing process of Geman and Geman; this process can answer more quickly than the posterior mean. More accurately, the MAP estimate is chosen as the final iteration $\widehat{\theta}_{\mathrm{MAP}} = \widehat{\theta}^K$. In other words, sample mean and variance can not be computed. The maximum a posteriori estimator (MAP) is defined as

$$\widehat{\zeta}_{\mathrm{MAP}} = \arg\max_{\zeta} p(\zeta|\mathbf{x})^K, \tag{21}$$

where K indicates the final iteration of the run of the MCMC algorithms.

6. Simulation

The investigation of the proposed rule is considered. Then, the results are compared to some established wavelet-based methods. The authors in [39] introduced four test signals: bumps, Doppler, heavisine, and blocks. Moreover, these functions were corrupted by the independent Gaussian noise $N_n(0, I_n \varsigma_\theta^2)$. Different sizes are studied to investigate the proposed method's performance, which is $n = 64$ and 128, where the four test functions were simulated. Also, various wavelet bases were used: Daubechies with $N = 8$ applied for the test functions heavisine, Doppler, and bumps, while Haar basis was used for blocks. The starting level was $j_0 = 3$, as recommended in [40]. The average mean squared-error

TABLE 2: The results of the simulation based on different methods.

Signal	σ	BAYES.THR	ABWS	BAMS	SWTMAP	SWTPM
		64				
Block	0.1	7.8638	0.0168	0.0144	0.0183	0.0124
	0.4	8.8873	0.1615	0.0756	0.0470	0.0446
	0.8	9.9290	0.6249	0.3282	0.0498	0.0512
Doppler	0.1	4.0397	0.0142	0.0467	0.0202	0.0144
	0.4	4.0528	0.1600	0.2326	0.0612	0.0581
	0.8	4.4217	0.6146	0.6219	0.0834	0.0707
Heavisine	0.1	0.1215	0.0192	0.0197	0.0146	0.0115
	0.4	0.2981	0.1541	0.3688	0.0344	0.0375
	0.8	0.5775	0.6227	0.6369	0.0642	0.0718
Bumps	0.1	10.6644	0.0135	0.0110	0.0018	0.0026
	0.4	10.8529	0.3605	0.0865	0.0210	0.0281
	0.8	11.5967	0.6120	0.3033	0.0684	0.0674
		128				
Block	0.1	7.874	0.0151	0.0134	0.0092	0.0120
	0.4	8.8243	0.1585	0.1615	0.0427	0.0482
	0.8	9.9474	0.6196	0.5358	0.0447	0.0594
Doppler	0.1	1.2554	0.0105	0.0218	0.0198	0.0113
	0.4	1.3098	0.1575	0.1440	0.0420	0.0431
	0.8	1.7197	0.6317	0.4826	0.0861	0.0682
Heavisine	0.1	0.0541	0.0097	0.0191	0.0128	0.0146
	0.4	0.1404	0.1572	0.3324	0.0317	0.0370
	0.8	0.3421	0.6324	0.6257	0.0506	0.0500
Bumps	0.1	16.9746	0.0102	0.0159	0.0014	0.0084
	0.4	17.2119	0.1592	0.0989	0.0207	0.0276
	0.8	17.6878	0.6350	0.3713	0.0674	0.0650

(AMSE) evaluated the results of the estimation, which is defined as

$$\text{AMSE} = \frac{1}{KN} \sum_{j=1}^{K} \sum_{i=1}^{N} \left(\widehat{\theta}_{j,i} - \theta_i \right)^2, \tag{22}$$

where N and K are the numbers of the data and the runs of the MCMC algorithms. Moreover, the results from the proposed method are denoted by $\widehat{\theta}_{k,i}, i = 1, \ldots, N$ at k-th run of MCMC algorithms.

The proposed estimators were compared to various methods, such as the Bayesian wavelet thresholding (BAYES.THR) method of Abramovich and Silverman, the ABWS rule of Chipman, Kolaczyk, and McCulloch, and the BAMS rule of Vidakovic and Ruggeri. Table 2 shows the results of the simulation when decimated and the nonstationary wavelet were used. It shows the result of AMSE; for our simulation, two bases are used. The first one is the basis with zero vanishing moments, and the other is the Daubechies' wavelets with $N = 8$ vanishing moments. The proposed technique always gives the best reconstructions. The main interest is to improve the result of the reconstruction. This can be seen when the size of the sample is large because extensive observations contain massive information about the feature of the signal. In general, the MAP method provides a fair resolution in the test functions. However, the worst of the results is better than the other of the competed wavelet rules. The biggest problem in the MAP estimate is that the confidence intervals

can not be computed because the latest sample of posterior is picked.

7. Application to Medical Data

The suggested method is studied and investigated to a real-world inductance plethysmography data to evaluate the excellent performance of the proposed rules, compared to the state-of-the-art methods. The Department of Anaesthesia at the Bristol Royal Infirmary collected these observations. The number of observations is 2048, equally spaced points. Readers can obtain these data within WaveThresh using data (BabyECG). Also, the structure of the sleep state can be downloaded using data (BabySS). Figure 5 shows the plots of BabyECG and sleep state. Hence, the aim of the investigation of the BabyECG was to specify the sleep state successfully from the observations. These data were studied and investigated by other authors (for example, [41]). The reconstruction of the unbalanced Haar approach (red line) is illustrated in Figure 6. It is not accessible to describe every moment using the unbalanced Haar method or to talk in general about the sleep state for the babies. Figures 7 and 8 show the reconstructions of the underlying feature with the MAP method using the Haar wavelet basis and Daubechies wavelet with $N = 8$ vanishing moments. In our reconstruction, the value of the shape κ_j is set within the interval $(0, 0.4)$. Table 3 shows the results of the simulations using the MAP and PM estimators. As the level j decreases, the value of κ increases. In contrast, the value of the parameter λ is slightly changed.
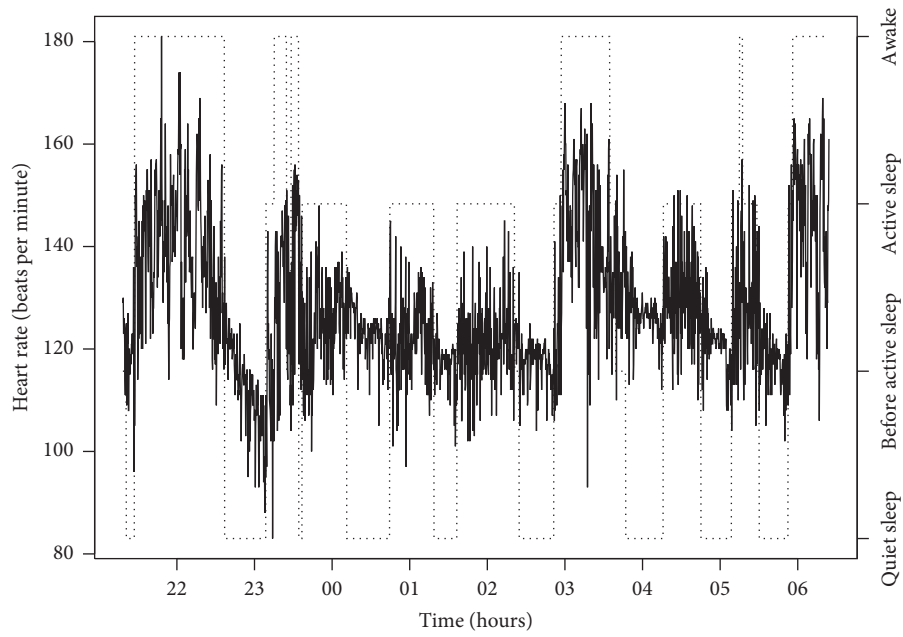
Figure 5: Plots of BabyECG data (solid line) and sleep state (dashed line).
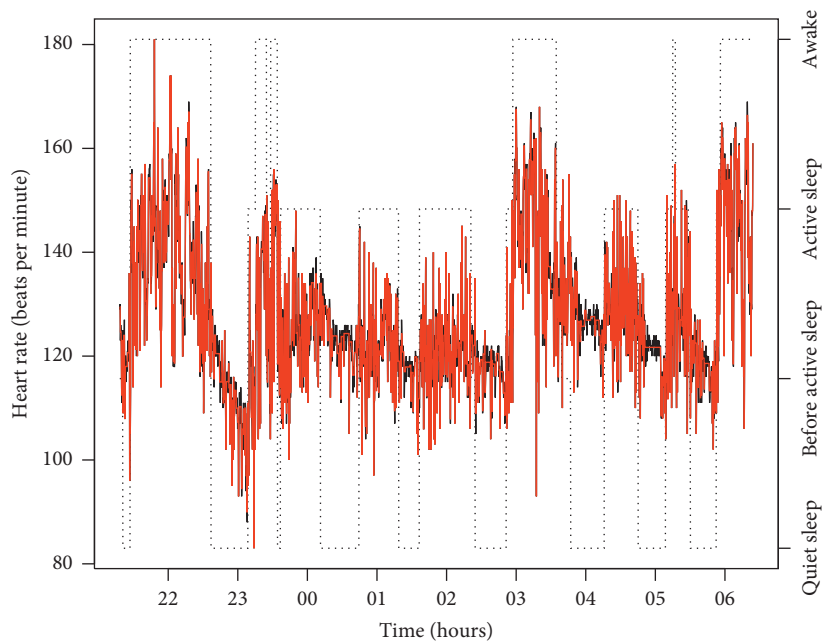
Figure 6: Plots of the reconstructions using the unbalanced Haar estimator (red line) and BabyECG data (black line).
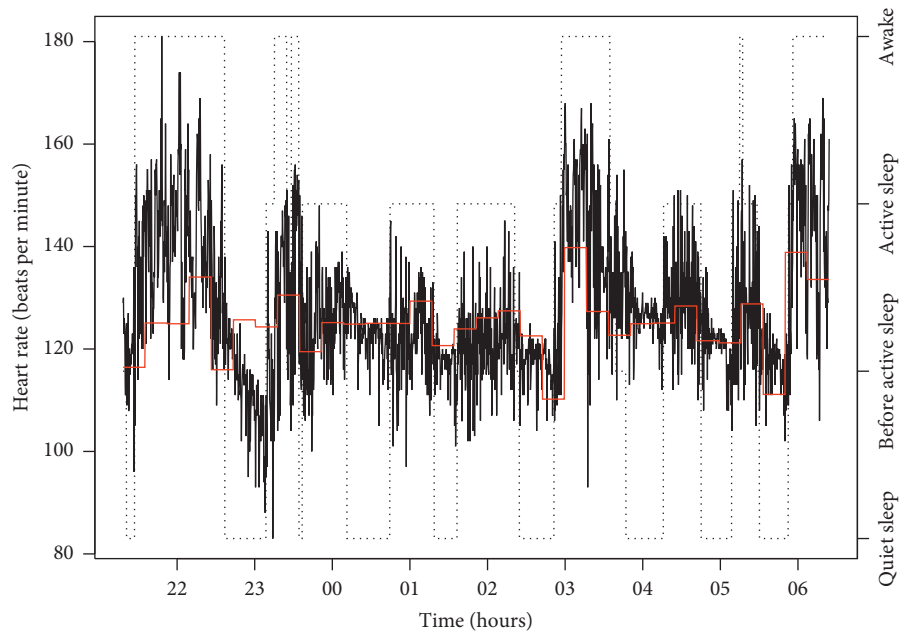
FIGURE 7: Plots of the reconstructions using the MAP estimator with a Haar basis.
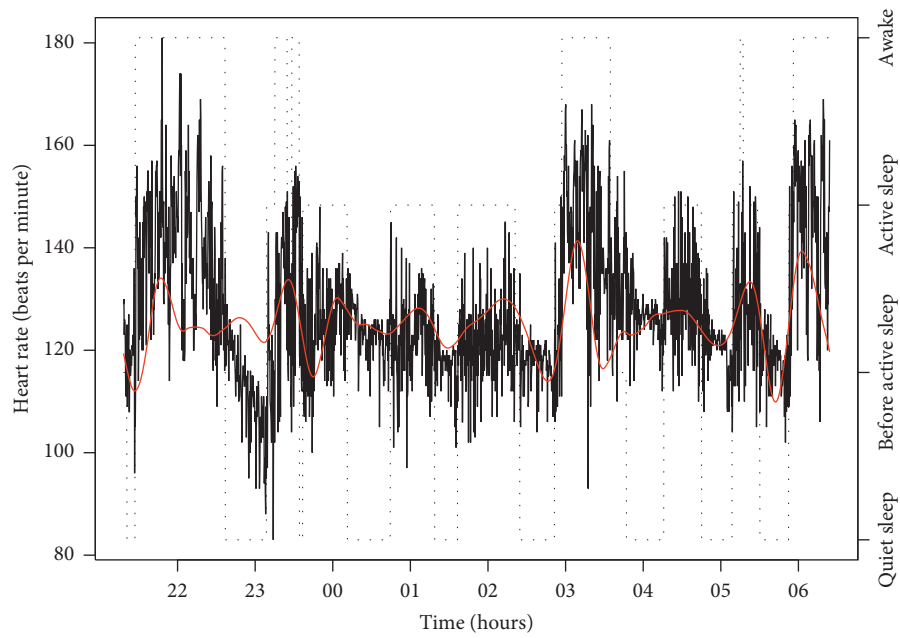
FIGURE 8: Plots of the reconstructions using the MAP estimator with $N = 8$ vanishing moments.

TABLE 3: The results of the simulation based on different methods.

Number of vanishing moments	κ_4	κ_5	κ_6	κ_7	κ_8	κ_9	κ_{10}	κ_{11}	λ_4	λ_5	λ_6	λ_7	λ_8	λ_9	λ_{10}	λ_{11}
						MAP estimator										
$N = 0$	0.3811	0.2259	0.2307	0.2249	0.2259	0.2287	0.0103	0.0121	0.0686	0.0411	0.1228	0.0943	0.1230	0.1798	0.1321	0.0614
$N = 8$	0.3478	0.2230	0.2188	0.2243	0.2172	0.2101	0.0003	0.0001	0.1053	0.0648	0.1016	0.0519	0.1430	0.0548	0.0229	0.0941
						PM estimator										
$N = 0$	0.3992	0.2220	0.2211	0.2243	0.2201	0.2322	0.0002	0.0013	0.0232	0.0966	0.0178	0.0646	0.0214	0.1528	0.1007	0.0232
$N = 8$	0.2718	0.2150	0.2347	0.2215	0.2131	0.2236	0.0003	0.0001	0.1600	0.1376	0.1534	0.0647	0.0257	0.1622	0.0351	0.0476

8. Conclusion

In this article, we show various ways in which the Bayesian rules and wavelet methods were used successfully in the practical problem. Also, a procedure for estimating the scale parameters, k and λ, of double generalized Rayleigh was estimated based on the BabyECG sample. This approach was adopted from the wavelet method for the independent level j and Bayesian approaches. Prior probability distributions for the parameters were assumed to be gamma distribution. Bayesian estimates for the points were proposed in the cases of artificial samples under the squared-error loss. The simulation studies are showing that the proposed rules worked well, and the proposed Bayesian estimate performed better than the existing state-of-the-art methods based on signal functions by reducing the AMSE. We discussed the proposed method estimates to estimate the underlying parameters. Numerical results were obtained to compare the theoretical performance results. Some points are observed from numerical results, which are summarized as follows:

(i) From the results in Table 2, the suggested method process provides better excellent results for artificial data.

(ii) Estimation results under the PM and MAP methods provide better estimation than the other established wavelet denoising methods according to the MSE.

(iii) The use of the suggested method allows to describe the main feature of the real data, especially when observations are large.

This paper has confirmed that the wavelet approach provides attractive alternatives to other established wavelet methods, especially when underlying signals are inhomogeneous.

Data Availability

The data used to support the findings of this study are included within the article.

Conflicts of Interest

The author declares that there are no conflicts of interest.

Acknowledgments

References

[1] H. A. Chipman, E. D. Kolaczyk, and R. E. McCulloch, "Adaptive Bayesian wavelet shrinkage," *Journal of the American Statistical Association*, vol. 92, no. 440, pp. 1413–1421, 1997.

[2] M. A. Clyde and E. I. George, "Empirical Bayes estimation in wavelet nonparametric regression," *Bayesian Inference in Wavelet-Based Models*, vol. 141, pp. 309–322, 1999.

[3] F. Abramovich, C. Trevor, and T. Sapatinas, "Wavelet analysis and its statistical applications," *Journal of the Royal Statistical Society, Series D (The Statistician)*, vol. 49, no. 1, 2000.

[4] F. Abramovich, P. Besbeas, and T. Sapatinas, "Empirical Bayes approach to block wavelet function estimation," *Computational Statistics & Data Analysis*, vol. 39, no. 4, pp. 435–451, 2002.

[5] J. F. Lewless, *Statistical Models and Methods for Lifetime Data*, John Wiley & Sons, Hoboken, NJ, USA, 2011.

[6] D. Kundu and B. Pradhan, "Estimating the parameters of the generalized exponential distribution in presence of hybrid censoring," *Communications in Statistics-Theory and Methods*, vol. 38, no. 12, pp. 2030–2041, 2009.

[7] N. Balakrishnan and M. Kateri, "On the maximum likelihood estimation of parameters of Weibull distribution based on complete and censored data," *Statistics & Probability Letters*, vol. 78, no. 17, pp. 2971–2975, 2008.

[8] J. Arturo, "Bayesian inference from type II doubly censored Rayleigh data," *Statistics & Probability Letters*, vol. 48, no. 4, pp. 393–399, 2000.

[9] S. G. Mallat, "A theory for multiresolution signal decomposition: the wavelet representation," *IEEE Transactions on Pattern Analysis and Machine Intelligence*, vol. 11, no. 7, pp. 674–693, 1989.

[10] G. P. Nason and B. W. Silverman, "The discrete wavelet transform in S," *Journal of Computational and Graphical Statistics*, vol. 3, no. 2, pp. 163–191, 1994.

[11] G. P. Nason and B. W. Silverman, "The stationary wavelet transform and some statistical applications," *Wavelets and Statistics, In: Antoniadis and Oppenheim*, vol. 103, pp. 281–299, 1995.

[12] J. Klapper and S. Barber, "Wavelet analysis of high performance liquid chromatography data," in *Proceedings of the 58th WSC of the ISI, 2011*, Dublin, Ireland, August 2011.

[13] F. Abramovich and B. W. Silverman, "Wavelet decomposition approaches to statistical inverse problems," *Biometrika*, vol. 85, no. 1, pp. 115–129, 1998.

[14] N. Guy, *Wavelet Methods in Statistics with R*, Springer, New York, NY, USA, 2010.

[15] F. Ruggeri and B. Vidakovic, "Bayesian modeling in the wavelet domain," *Handbook of Statistics Modeling and Computation*, vol. 25, pp. 315–338, 2005.

[16] B. Vidakovic, "Nonlinear wavelet shrinkage with Bayes rules and Bayes factors," *Journal of the American Statistical Association*, vol. 93, no. 441, pp. 173–179, 1998.

[17] B. Vidakovic and F. Ruggeri, "BAMS method: theory and simulations," *Sankhyā: The Indian Journal of Statistics, Series B*, vol. 63, no. 2, pp. 234–249, 2001.

[18] N. Metropolis, A. W. Rosenbluth, M. N. Rosenbluth, A. H. Teller, and E. Teller, "Equation of state calculations by fast computing machines," *The Journal of Chemical Physics*, vol. 21, no. 6, pp. 1087–1092, 1953.

[19] S. Geman and D. Geman, "Stochastic relaxation, Gibbs distributions, and the Bayesian restoration of images," *IEEE Transactions on Pattern Analysis and Machine Intelligence*, vol. 6, no. 6, pp. 721–741, 1984.

[20] A. Gelman and D. B. Rubin, "Inference from iterative simulation using multiple sequences," *Statistical Science*, vol. 457472 pages, 1992.

[21] R. G. Aykroyd, "Statistical image reconstruction," in *Industrial Tomography: Systems and Applications*, M. Wang, Ed., Woodhead Publishing, Cambridge, UK, 2015.

[22] S. Chib and E. Greenberg, "Understanding the metropolis-hastings algorithm," *The American Statistician*, vol. 49, no. 4, pp. 327–335, 1995.

[23] R. G. Aykroyd, M. A. W. Mahmoud, and H. M. Aljohani, "Bayesian analysis using MCMC methods of record values based on a new generalised Rayleigh distribution," *Stochastic Modeling and Applications*, vol. 21, no. 2, pp. 49–66, 2017.

[24] D. F. Andrews and C. Mallows, "Scale mixtures of normal distributions," *Journal of the Royal Statistical Society, Series B (Methodological)*, vol. 61, pp. 99–102, 1974.

[25] I. Daubechies, "Ten lectures on wavelets," 1992.

[26] R. Tibshirani, "Regression shrinkage and selection via the lasso," *Journal of the Royal Statistical Society: Series B (Methodological)*, vol. 58, no. 1, pp. 267–288, 1996.

[27] S. Barber and G. P. Nason, "Real nonparametric regression using complex wavelets," *Journal of the Royal Statistical Society: Series B (Statistical Methodology)*, vol. 66, no. 4, pp. 927–939, 2004.

[28] L. Cutillo, Y. Y. Jung, F. Ruggeri, and B. Vidakovic, "Larger posterior mode wavelet thresholding and applications," *Journal of Statistical Planning and Inference*, vol. 138, no. 12, pp. 3758–3773, 2008.

[29] N. Reményi and B. Vidakovic, "Wavelet shrinkage with double Weibull prior," *Communications in Statistics-Simulation and Computation*, vol. 44, no. 1, pp. 88–104, 2013.

[30] M. Holschneider, R. Kronland-Martinet, J. Morlet, and P. Tchamitchian, "A real-time algorithm for signal analysis with the help of the wavelet transform," in *Wavelets:Time-Frequency Methods and Phase Space*, J. M. Combers, A. Grossmann, and P. Tchamitchian, Eds., pp. 286–297, Springer, Heidelberg, German, 1989.

[31] D. P. Percival, "On estimation of the wavelet variance," *Biometrika*, vol. 82, no. 3, pp. 619–631, 1995.

[32] J.-C. Pesquet, K. Hamid, and H. Carfantan, "Time-invariant orthonormal wavelet representations," *Transactions on Signal Processing*, vol. 44, no. 8, pp. 1964–1970, 1996.

[33] R. R. Coifman and D. L. Donoho, "Translation-invariant de-noising," in *Wavelets and Statistics*, A. Antoniadis and G. Oppenheim, Eds., pp. 125–150, Springer, Heidelberg, German, 1995.

[34] C. Robert and C. George, "A short history of Markov chain Monte Carlo: subjective recollections from incomplete data," *Statistical Science*, vol. 26, no. 1, pp. 102–115, 2011.

[35] R. Walter, S. Richardson, and D. J. Spiegelhalter, "Introducing markov chain monte carlo," *Markov Chain Monte Carlo in Practice*, vol. 1, p. 19, 1996.

[36] J. S. Lui, *Chain Monte CarloStrategies in Scientific Computing*, Springer-Verlag, Berlin, Heidelberg, German, 2001.

[37] S. Brooks, A. Gelman, G. Jones, and X.-Li Meng, *Handbook of Markov Chain Monte Carlo*, Chapman and Hall/CRC press, London, UK, 2011.

[38] G. O. Roberts, A. Gelman, R. Walter et al., "Weak convergence and optimal scaling of random walk Metropolis algorithms," *The Annals of Applied Probability*, vol. 7, no. 1, pp. 110–120, 1997.

[39] D. L. Donoho and I. M. Johnstone, "Ideal spatial adaptation by wavelet shrinkage," *Biometrika*, vol. 81, no. 3, pp. 425–455, 1994.

[40] A. Antoniadis, J. Bigot, and T. Sapatinas, "Wavelet estimators in nonparametric regression: a comparative simulation study," *Journal of Statistical Software*, vol. 6, pp. 1–83, 2001.

[41] G. P. Nason, "Wavelet shrinkage using cross-validation," *Journal of the Royal Statistical Society. Series B (Methodological)*, vol. 1, pp. 463–479, 1996.

Research Article

Combined Effects of Heat and Mass Transfer on MHD Free Convective Flow of Maxwell Fluid with Variable Temperature and Concentration

Muhammad Bilal Riaz [ID],[1,2] **Maryam Asgir,**[3,4] **A. A. Zafar,**[3] **and Shaowen Yao** [ID][5]

[1]*Department of Mathematics, School of Science, University of Management and Technology, C-II Johar Town, Lahore 54770, Pakistan*
[2]*Institute for Groundwater Studies (IGS), University of the Free State Bloemfotain, South Africa*
[3]*Department of Mathematics, Government College University Lahore, Lahore,54000, Pakistan*
[4]*Department of Mathematics, Riphah International University, QIE Township, Lahore 54000, Pakistan*
[5]*School of Mathematics and Information Science, Henan Polytechnic University, Jiaozuo, China*

Correspondence should be addressed to Shaowen Yao; yaoshaowen@hpu.edu.cn

Heat and mass transfer combined effects on MHD natural convection for a viscoelastic fluid flow are investigated. The dynamics of the fluid are controlled by the motion of the plate with arbitrary velocity along with varying temperature and mass diffusion. The non-dimensional forms of the governing equations of the model are developed along with generalized boundary conditions and the resulting forms are solved by the classical integral (Laplace) transform technique/method and closed-form solutions are developed. Obtained generalized results are very important due to their vast applications in the field of engineering and applied sciences; few of them are highlighted here as limiting cases. Moreover, parametric analysis of system parameters $P_r, S, K_c, G_T, G_c, M, S_c, \lambda$ is done via graphical simulations.

1. Introduction

In science and in many engineering applications such as in condensation, evaporation, and chemical process, many transport processes are influenced by the combined action of the buoyancy forces from both heat and mass diffusion. Heat and mass transfer combined effects are studied extensively due to their significant role in chemical processing equipment, oceanic circulation, emergency cooling system of advanced nuclear reactors, cooling process of plastic sheets, formation and dissipation of the fog, processing and drying the food, temperature distribution and moisture of agriculture fields, and production of polymer. In recent years, a lot of practical applications attracted many scientists and engineers to pay a considerable amount of focus to learn the heat and mass effects either analytically or numerically [1–4].In

industrial and engineering processes, most fluids are non-Newtonian. Since the non-Newtonian fluids deal more complexities due to the rheological behavior than Newtonian fluids, distinct models were proposed. The influence of heat and mass transfer in the non-Newtonian fluid is an important subject from the theoretical as well as practical point of view due to its abundant applications in industry and engineering. Common examples include polymer extrusion, the emergency cooling system of nuclear reactors, food processing, thermal welding, to name a few. Convective flow is a self-sustained flow with the effect of the temperature gradient. In literature, different theories are made to see the occurrence of heat and mass transfer in convective flows of different fluids. Mebarek-Oudina et al. [5] investigated the natural convective heat transfer phenomenon of water-based hybrid nanofluid in a porous medium along with the magnetic field. Das et al. [6]

considered the natural convective flow of the electrically conducting fluid past on vertical plate embedded in a permeable medium and explored the impacts of heat and mass transfer. The heat transfer phenomenon of Casson nanofluid flow is taken into account by Abo-Dahab et al. [7]. They analyzed the problem with the convective boundary conditions and discussed the influence of chemical reaction and heat source. Sajad et al.[8] studied the heat transfer and magnetic effect on hybrid nanofluid. Nazish et al. [9] explored the influence of heat and concentration/mass transform with the existence of fields developed by magnetic in the Maxwell fluid model. Ahmad [10] explored the heat transfer for the Maxwell fluid on the stretching plate with the slip boundary on the velocity. They explored the numerical solutions and showed the heat flux effect using the Nusselt number and the Prandtl number. A computational analysis is performed to study the effects of the transverse magnetic field at the unsteady Poiseuille–Rayleigh–Benard flow by Marzougui et al. [11]. The thermal properties' effects on the soil temperature are modeled and investigated numerically by Belatrache [12]. To have more insight about heat and mass transfer mechanisms in fluid flow and their applications, readers are referred to review references [13–16].On the other hand, many researchers paid a significant amount of attention to the study of MHD free convective flows due to its numerous applications in solar and stellar structure, radio propagation, MHD pumps, MHD bearings, aerodynamics, polymer technology, petroleum industry, crude oil purification, glass fiber drawing, etc. In light of these applications, many researchers such as Rajput [17], Gupta [18], and El Amin [19] studied the MHD flow of different fluids. They found the exact solution for velocity, concentration, and temperature by the Laplace transform method. Heat and mass transfer simultaneous effects on MHD flow of Maxwell fluid have been investigated by Nadeem et al. [20]. Recently, the study of the unsteady boundary layer heat transfer of Maxwell viscoelastic fluid was carried out by Zhao et al. [21]. Ahmad [22] studied MHD viscous, with constant density, electro-conducting fluid in the existence of the radiation, thermal diffusion, free convection, and mass transfer flow. These results motivated Chaudhry et al. [23] and they used classical integral transform to obtain the exact solutions of natural MHD convective flow past on an accelerated surface submerged in a permeable medium. Das [24] developed the closed-form solution of the unsteady

MHD natural convection flow on a moving vertical plate accompanied by mass transfer and thermal radiation. Carrying on, Das et al. [25] investigated the time-dependent MHD natural convection flow past a moving vertical plate dipped in a porous medium and studied the different aspects of heat and mass transfer. They discussed the problem with the uniform, oscillating, and impulsive motions of the plate besides considering the constant heat and mass diffusion and implemented the Laplace integral transform to develop the analytic solutions.Motivated by these investigations, the objective of this manuscript is to study the combined effect of heat and mass transfer on MHD Maxwell fluid. Laplace integral transformation is used to obtain the unique solution of temperature, velocity, and concentration under the impact of generalized boundary conditions on temperature, velocity, and concentration. The importance of the problem is highlighted by showing its impact/applications in the field of engineering and applied sciences. The paper is organized into six sections. After the introductory section in Section 2, the dimensionless governing equations are developed. In Section 3, Laplace integral transform is implemented to find the exact solution of the temperature, velocity, and concentration field. In Section 4, some applications in different fields are discussed as limiting cases to justify our results. In Section 5, the effect of physical parameters is analyzed graphically. The concluding observation is listed at the end.

2. Problem Formulation

We studied here the motion of the viscoelastic, incompressible, electronically conducting Maxwell fluid due to plate motion with arbitrary velocity $u_0 f'(t')$. The plate is along $x-$axis and $y-$axis is considered normal on the plate. In the first instance, at $t = 0$ the plate and fluid are at temperature T_∞' and concentration C_∞'. With the time $t = 0^+$, the plate starts to move in its own axis. Then, the level of temperature and concentration takes up to $T_\infty \left\{\hat{\imath}\right\} + T_w \left\{\hat{\imath}\right\} h'(t')$ and $C_\infty \left\{\hat{\imath}\right\} + C_w \left\{\hat{\imath}\right\} g'(t')$ where $f'(t'), h'(t')$ and $g'(t')$ are piecewise continuous functions that vanish at $t = 0$. Details of different parameters are given in Table 1. Momentum, energy, and concentration equations are formed as follows:

TABLE 1: Nomenclature.

Symbol	Quantity
u	Velocity of fluid
B_0	Magnetic field parameter
q	Laplace transforms parameter
D	Mass diffusivity
B_T	Thermal expansion parameter
B_C	Concentration expansion coefficient
K	Thermal conductivity
ρ	Density of fluid
λ	Relaxation time
σ	Electric conductivity coefficient
μ	Dynamic viscosity
v	Kinematic viscosity
c_p	Specific heat
S	Heat source parameter
K_c	Chemical reaction coefficient
g	Gravitational acceleration
S_C	Schmidt number
M	Parameter due to magnetic field
P_r	Prandtl number
G_T	Grashof number due to thermal effect
G_C	Grashof number due to concentration

$$\left(1 + \lambda' \frac{\partial}{\partial t'}\right) \frac{\partial u'(\chi', t')}{\partial t'} = v \frac{\partial^2 u'(\chi', t')}{\partial \chi'^2}$$

$$+ g B_T \left(1 + \lambda' \frac{\partial}{\partial t'}\right)(\varphi' - \varphi_\infty') + g B_C$$

$$\left(1 + \lambda' \frac{\partial}{\partial t'}\right)(C' - C_\infty') - \frac{\sigma B_0^2}{\rho}\left(1 + \lambda' \frac{\partial}{\partial t'}\right) u'(\chi', t'),$$

$$\rho C_p \frac{\partial \varphi'(\chi', t')}{\partial t'} = K \frac{\partial^2 \varphi'(\chi', t')}{\partial \chi'^2} - S'(\varphi' - \varphi_\infty'),$$

$$\frac{\partial C'(\chi', t')}{\partial t'} = D \frac{\partial^2 C'(\chi', t')}{\partial \chi'^2} - K_c'(C' - C_\infty').$$

(1)

The imposed initial and boundary conditions are

$$t' \leq 0, \quad u'(\chi', t') = 0,$$

$$\varphi'(\chi', t') = \varphi_\infty',$$

$$C'(\chi', t') = C_\infty', \quad \chi' \geq 0,$$

$$t' \geq 0, \quad u'(0, t') = u_0 f'(t'),$$

$$\varphi'(0, t') = \varphi_\infty' + \varphi_w' h'(t'), \quad (2)$$

$$C'(0, t') = C_\infty' + C_w' g'(t'),$$

$$u'(\chi', t') \longrightarrow 0,$$

$$\varphi'(\chi', t') \longrightarrow \varphi_\infty',$$

$$C'(\chi', t') \longrightarrow C_\infty', \quad \chi' \longrightarrow \infty.$$

For dimensionless problem, we use the following relations:

$$t = \frac{u_0^2}{\nu}t',$$

$$y = \frac{u_0}{\nu}\chi',$$

$$S_c = \frac{\nu}{D},$$

$$K_c = \frac{\nu}{u_0^2}K_c',$$

$$\lambda = \frac{u_0^2}{\nu}\lambda',$$

$$u' = u_0 u,$$

$$C = \frac{C' - C_\infty'}{C_w'},$$

$$T = \frac{\varphi' - \varphi_\infty'}{\varphi_w'},$$

$$S = \frac{\nu}{\rho C_P u_0^2 S'},$$ (3)

$$P_r = \frac{\mu C_P}{K},$$

$$K_p' = \frac{u_0^2}{\nu^2}K_p G_c = \frac{g\left(B_C/\nu\right)}{u_0^3}C_w',$$

$$G_T = \frac{gB_T\nu}{u_0^3}\varphi_w',$$

$$M = \frac{\sigma B_0^2 \nu}{\rho u_0^2},$$

$$f = \frac{\nu}{u_o^2}f',$$

$$g = \frac{\nu}{u_o^2}g',$$

$$h = \frac{\nu}{u_o^2}h'.$$

After non-dimensionalizing, the governing equations become

$$\left(1 + \lambda\frac{\partial}{\partial t}\right)\frac{\partial u(y,t)}{\partial t} = \frac{\partial^2 u(y,t)}{\partial y^2} + G_T\left(1 + \lambda\frac{\partial}{\partial t}\right)T(y,t)$$

$$+ G_C\left(1 + \lambda\frac{\partial}{\partial t}\right)C(y,t)$$

$$- M\left(1 + \lambda\frac{\partial}{\partial t}\right)u(y,t),$$ (4)

$$\frac{\partial T(y,t)}{\partial t} = \frac{1}{P_r}\frac{\partial^2 T(y,t)}{\partial y^2} - ST(y,t),$$ (5)

$$\frac{\partial C(y,t)}{\partial t} = \frac{1}{S_c}\frac{\partial^2 C(y,t)}{\partial y^2} - K_c C(y,t).$$ (6)

along the following initial and boundary conditions:

$$u(y,0) = 0, \ T(y,0) = 0, \ C(y,0) = 0,$$ (7)

$$u(0,t) = f(t), \ T(0,t) = h(t), \ C(0,t) = g(t),$$ (8)

$$u(y,t) \longrightarrow 0, \ T(y,t) \longrightarrow 0, \ C(y,t) \longrightarrow 0, \quad \text{as } y \longrightarrow \infty.$$ (9)

3. Solution of the Problem

3.1. Concentration. Transforming equation (7) after applying the Laplace integral transform and utilizing the corresponding initial condition, we get

$$\frac{\partial^2 \overline{C}(y,q)}{\partial y^2} - S_c\left(K_c + q\right)\overline{C}(y,q) = 0,$$ (10)

The above differential equation solution is

$$\overline{C}(y,q) = C_1 e^{-y\sqrt{S_c\left(K_c+q\right)}} + C_2 e^{y\sqrt{S_c\left(K_c+q\right)}}.$$ (11)

The solution of equation (11) with the transformed form of boundary conditions becomes

$$\overline{C}(y,q) = G(q)e^{-y\sqrt{S_c\left(K_c+q\right)}}.$$ (12)

Applying the Laplace inverse on equation (12) and using the $L^{-1}\{G(q)\} = g'(t)$ with $g(0) = 0$, convolution theorem and equation (A.22), the generalized solution for concentration is

$$C(y,t) = \int_0^t g'(t-s)\Phi(y, \sqrt{S_c}, s; K_c)\,ds, \qquad (13)$$

and Φ is specified in equation (A.23).

3.2. Temperature Distribution.
Implementing the Laplace transform on equation (5) and using the concerned the initial condition, we get

$$\frac{\partial^2 \overline{T}(y,q)}{\partial y^2} - P_r(S+q)\overline{T}(y,q) = 0. \qquad (14)$$

The solution is

$$\overline{T}(y,q) = C_1 e^{-y\sqrt{P_r(S+q)}} + C_2 e^{y\sqrt{P_r(S+q)}}. \qquad (15)$$

After implementing the boundary conditions, equation (15) becomes

$$\overline{T}(y,q) = H(q)e^{-y\sqrt{P_r(S+q)}}. \qquad (16)$$

The Laplace inverse on equation (16) and using the $L^{-1}\{H(q)\} = h'(t)$ with $h(0) = 0$, convolution theorem and equation (A.24), the generalized solution for temperature obtained is

$$T(y,t) = \int_0^t h'(t-s)\Psi(y, \sqrt{P_r}, s; S)\,ds, \qquad (17)$$

where Ψ is defined in equation (A.25).

3.3. Velocity.
Employing the Laplace transform on equation (4) and using the corresponding initial condition on velocity form the following differential equation:

$$\frac{\partial^2 \overline{u}(y,q)}{\partial y^2} - ((1+\lambda q)(q+M))\overline{u}(y,q)$$
$$= -G_T(1+\lambda q)\overline{T}(y,q)) - G_c(1+\lambda q)\overline{C}(y,q). \qquad (18)$$

In order to solve equation (18), we use the value of $\overline{C}(y,q)$, $\overline{T}(y,q)$ from equation (12) and equation (16), respectively. With boundary conditions use on velocity, the following solution is obtained:

$$\overline{u}(y,q) = F(q)e^{-y\sqrt{(q+M)(1+\lambda q)}} + \frac{G_T H(q)(1+\lambda q)\left(e^{-y\sqrt{(q+M)(1+\lambda q)}} - e^{-y\sqrt{P_r(S+q)}}\right)}{(P_r(S+q) - (1+\lambda q)(q+M))}$$
$$+ \frac{G_c G(q)(1+\lambda q)\left(e^{-y\sqrt{(q+M)(1+\lambda q)}} - e^{-y\sqrt{S_c(K_c+q)}}\right)}{(S_c(K_c+q) - (1+\lambda q)(q+M))}. \qquad (19)$$

Further simplification reduces equation (19):

$$\overline{u}(y,q) = F(q)e^{-y\sqrt{\lambda\left((q+\alpha_1)^2 + \alpha_3^2\right)}}$$
$$- \frac{G_T H(q)(1+\lambda q)\left(e^{-y\sqrt{\lambda\left[(q+\alpha_1)^2 + \alpha_3^2\right]}} - e^{-y\sqrt{P_r(S+q)}}\right)}{\lambda\left((q+\alpha_4)^2 - \alpha_6^2\right)}$$
$$- \frac{G_c G(q)(1+\lambda q)\left(e^{-y\sqrt{\lambda\left[(q+\alpha_1)^2 + \alpha_3^2\right]}} - e^{-y\sqrt{S_c(K_c+q)}}\right)}{\lambda\left((q+\alpha_7)^2 - \alpha_9^2\right)}, \qquad (20)$$

where $2\alpha_1 = (\lambda M + 1/\lambda)$, $\alpha_2 = (M/\lambda)$, $\alpha_3^2 = \alpha_2 - \alpha_1^2$, $2\alpha_4 = (\lambda M + 1 - P_r/\lambda)$, $\alpha_5 = (M - P_r S/\lambda)$, $\alpha_6^2 = \alpha_4^2 - \alpha_5$, $2\alpha_7 = (\lambda M + 1 - S_c/\lambda)$, $\alpha_8 = (M - S_c K_c/\lambda)$, $\alpha_9^2 = \alpha_7^2 - \alpha_8$.

Generalized expression for velocity field is acquired by employing the inverse Laplace transform on equation (20):

$$u(y,t) = I_1 + \frac{G_T}{\lambda}I_2 - \frac{G_T}{\lambda}I_3 + \frac{G_c}{\lambda}I_4 - \frac{G_c}{\lambda}I_5, \qquad (21)$$

where

$$I_1 = L^{-1}\left(F(q)e^{-y\sqrt{\lambda\left((q+\alpha_1)^2 + \alpha_3^2\right)}}\right),$$
$$= L^{-1}(B_1(y,q)) * L^{-1}(B_2(q)),$$
$$= B_1(y,t) * B_2(t), \qquad (22)$$

where $B_1(y,q) = (e^{-\sqrt{\lambda}\, y\sqrt{((q+\alpha_1)^2 + \alpha_3^2)}}/\sqrt{((q+\alpha_1)^2 + \alpha_3^2)})$, $B_2(q) = F(q)\sqrt{((q+\alpha_1)^2 + \alpha_3^2)}$.

By using equation (A.20) and equation (A.21), expressions for the $B_1(y,t)$ and $B_2(t)$ are evaluated as follows:

$$B_1(y,t) = \begin{cases} 0, & 0 < t < y\sqrt{\lambda}, \\ e^{-\alpha_1 t} I_0\left(i\alpha_3 \sqrt{t^2 - \lambda y^2}\right), & t > y\sqrt{\lambda}, \end{cases}$$

(23)

$$B_2(t) = \left(e^{-\alpha_1 t}\left((i\alpha_3)I_1(i\alpha_3 t) + \delta(t)\right)\right)^* \left(f'(t) + \alpha_1 f(t)\right)$$
$$+ \left(\alpha_3^2 e^{-\alpha_1 t} I_0(i\alpha_3 t)\right)^* f(t),$$

(24)

$$I_2 = L^{-1}\left(\frac{H(q)(1+\lambda q)e^{-y\sqrt{P_r(S+q)}}}{\left((q+\alpha_4)^2 - \alpha_6^2\right)}\right),$$
$$= (h(t) + \lambda h'(t))^* \left(e^{-\alpha_4 t}\cosh(\alpha_6 t)\right.$$
$$+ \frac{(S-\alpha_4)}{\alpha_6} e^{-\alpha_4 t}\sinh(\alpha_6 t)\right)$$
$$^* \mathrm{erfc}\left(\frac{y\sqrt{P_r}}{2\sqrt{t}}\right)e^{-St}.$$

(25)

$$I_3 = L^{-1}\left(\frac{H(q)(1+\lambda q)e^{-y\sqrt{\lambda\left((q+\alpha_1)^2 + \alpha_3^2\right)}}}{\left((q+\alpha_4)^2 - \alpha_6^2\right)}\right),$$
$$= B_1(y,t)^* B_3(t),$$

(26)

where $B_1(y,t)$ is given in equation (23) and

$$B_3(t) = (h'(t) + \lambda H(t)^* h'(t))$$
$$^* \left(A^* + B^* e^{-(\alpha_4+\alpha_6)t} + C^* e^{-(\alpha_4-\alpha_6)t}\right)$$
$$^* e^{-\alpha_1 t} I_0(i\alpha_3 t),$$

(27)

where

$$A^* = \frac{\left(\alpha_1^2 + \alpha_3^2\right)}{\alpha_4^2 - \alpha_6^2},$$
$$B^* = \frac{2(\alpha_4 - \alpha_6)A^* - (2\alpha_1 - \alpha_4 - \alpha_6)}{2\alpha_6},$$

(28)

$$C^* = 1 - A^* - B^*.$$

$$I_4 = L^{-1}\left(\frac{G(q)(1+\lambda q)e^{-y\sqrt{S_c(K_c+q)}}}{\left((q+\alpha_7)^2 - \alpha_9^2\right)}\right),$$
$$= (g(t) + \lambda g'(t))^* \left(e^{-\alpha_7 t}\cosh(\alpha_9 t)\right.$$
$$+ \frac{(K_c - \alpha_7)}{\alpha_9} e^{-\alpha_7 t}\sinh(\alpha_9 t)\right),$$
$$^* \mathrm{erfc}\left(\frac{y\sqrt{S_c}}{2\sqrt{t}}\right)e^{-K_c t}.$$

(29)

Similarly,

$$I_5 = L^{-1}\left(\frac{G(q)(1+\lambda q)e^{-y\sqrt{\lambda\left((q+\alpha_1)^2 + \alpha_3^2\right)}}}{\left((q+\alpha_7)^2 - \alpha_9^2\right)}\right),$$

(30)

$$= B_1(y,t)^* B_4(t),$$

where $B_1(y,t)$ is given in equation (23) and

$$B_4(t) = (g'(t) + \lambda H(t)^* g'(t))$$
$$^* \left(C^* + D^* e^{-(\alpha_7+\alpha_9)t} + E^* e^{-(\alpha_7-\alpha_9)t}\right)$$
$$^* e^{-\alpha_1 t} I_0(i\alpha_3 t),$$

$$D^* = \frac{\left(\alpha_1^2 + \alpha_3^2\right)}{\alpha_7^2 - \alpha_9^2},$$

(31)

$$E^* = \frac{2(\alpha_7 - \alpha_9)A^* - (2\alpha_1 - \alpha_7 - \alpha_9)}{2\alpha_9},$$

$$F^* = 1 - D^* - E^*.$$

The above results are obtained for generalized time-dependent boundary conditions on velocity, concentration, and temperature. These results have many applications in engineering and applied science. Now, we will consider and discuss its few applications.

4. Applications

4.1. Application 1: $f(t) = H(t)$, $g(t) = H(t)$, $h(t) = H(t)$. This function value shows the motion of the fluid is because of the motion of an infinite plate in its plane with constant velocity. This function has importance in a lot of engineering problems such as signal waves, driving forces that act for a short time only, and impulsive forces acting for an instance such as a hammer blow.Substituting the value of $G(q) = (1/q)$ into equation (12) and applying the Laplace inverse, the expression for concentration is

$$C(y,t) = (\delta(t) + K_c t)^* \mathrm{erfc}\left(\frac{y\sqrt{S_c}}{2\sqrt{t}}\right)e^{-K_c t},$$

(32)

where $\delta(.)$ is known as Dirac delta function.

Embedding the value of $H(q) = (1/q)$ into equation (16) and taking Laplace inverse make the expression of temperature

$$T(y,t) = (\delta(t) + St)^* \mathrm{erfc}\left(\frac{y\sqrt{P_r}}{2\sqrt{t}}\right)e^{-St}.$$

(33)

The equation of velocity

$$u(y,t) = I_1^I + \frac{G_T}{\lambda}I_2^I - \frac{G_T}{\lambda}I_3^I + \frac{G_c}{\lambda}I_4^I - \frac{G_c}{\lambda}I_5^I, \qquad (34)$$

where

$$I_1^I = B_1(y,t)^*B_2^I(t), \qquad (35)$$

$B_2^I(t)$ is obtained as

$$B_2^I(t) = \left(e^{-\alpha_1 t}\left((i\alpha_3)I_1(i\alpha_3 t) + \delta(t)\right)\right)^*\left(\delta(t) + \alpha_1 H(t)\right) + \alpha_3^2 e^{-\alpha_1 t}I_0(i\alpha_3 t)^* H(t), \qquad (36)$$

and for $B_1(y,t)$ (see equation (A.1)).

After substituting the value of $H(q) = (1/q)$ into equation (25)

$$I_2^I = (H(t) + \lambda\delta(t))\left(e^{-\alpha_4 t}\cosh(\alpha_6 t) + \frac{(S-\alpha_4)}{\alpha_6}e^{-\alpha_4 t}\sinh(\alpha_6 t)\right) \qquad (37)$$

$$^*\mathrm{erfc}\left(\frac{y\sqrt{P_r}}{2\sqrt{t}}\right)e^{-St}.$$

Equation (26) takes the form after employing the value of $H(q) = (1/q)$

$$I_3^I = B_1(y,t)^*B_3^I(t), \qquad (38)$$

where

$$B_3^I(t) = \left(\delta(t) + \lambda H(t)^*\delta(t)\right) {}^*\left(A^* + B^* e^{-(\alpha_4+\alpha_6)t} + C^* e^{-(\alpha_4-\alpha_6)t}\right) \qquad (39)$$

$$^*e^{-\alpha_1 t}I_0(i\alpha_3 t),$$

and for $B_1(y,t)$ (see equation (A.1)).

After substituting the value of $G(q) = (1/q)$ into equation (29)

$$I_4^I = (H(t) + \lambda\delta(t))\left(e^{-\alpha_7 t}\cosh(\alpha_9 t) + \frac{(K_c-\alpha_7)}{\alpha_9}e^{-\alpha_7 t}\sinh(\alpha_9 t)\right)$$

$$^*\mathrm{erfc}\left(\frac{y\sqrt{S_c}}{2\sqrt{t}}\right)e^{-K_c t}. \qquad (40)$$

Similarly, equation (30) after substituting the value of $G(q) = (1/q)$

$$I_5^I = B_1(y,t)^*B_4^I(t), \qquad (41)$$

and

$$B_4^I(t) = \left(\delta(t) + \lambda H(t)^*\delta(t)\right) {}^*\left(D^* + E^* e^{-(\alpha_7+\alpha_9)t} + E^* e^{-(\alpha_7-\alpha_9)t}\right) \qquad (42)$$

$$^*e^{-\alpha_1 t}I_0(i\alpha_3 t),$$

and for $B_1(y,t)$ (see equation (A.1).

Similar result for concentration was obtained by Nehad Ali Shah [26] (equation (35)). Thus, our result supports the result already present in literature.

4.2. Application 2: $f(t) = t$, $g(t) = t$, $h(t) = t$. The important concepts of engineering are based around linear functions. They are often used in engineering to explain data and evaluate the lines that best fit the given data sets. It has a lot of applications in engineering and it can be represented in a variety of ways. One of the particular interests is direct variation, which forms many engineering applications such as Hooke's law and Ohm's law. To learn about slope, engineers use linear functions to interpret and understand graphs that describe displacement, velocity, and acceleration. They use these functions to analyze data to learn how to design their engineering products more efficiently, reliably, and safely. For the choice of $F(q)$, $G(q)$, $H(q)$ equal to $(1/q^2)$ in the appropriate equations and employing the Laplace inverse, the expression of $C(y,t)$, $T(y,t)$, $u(y,t)$, and then I_1^{II}, I_2^{II}, I_3^{II}, I_4^{II} and I_5^{II} changes into, respectively,

$$C(y,t) = (1 + K_c t)^*\mathrm{erfc}\left(\frac{y\sqrt{S_c}}{2\sqrt{t}}\right)e^{-K_c t},$$

$$T(y,t) = (1 + St)^*\mathrm{erfc}\left(\frac{y\sqrt{P_r}}{2\sqrt{t}}\right)e^{-St}, \qquad (43)$$

$$u(y,t) = I_1^{II} + \frac{G_T}{\lambda}I_2^{II} - \frac{G_T}{\lambda}I_3^{II} + \frac{G_c}{\lambda}I_4^{II} - \frac{G_c}{\lambda}I_5^{II},$$

where

$$I_1^{II} = B_1(y,t)^*B_2^{II}(t), \qquad (44)$$

where $B_1(y,t)$ (see equation (A.1)) and $B_2^{II}(t)$ (see equation (A.2)).

$$I_2^{II} = (t+\lambda)^*\left(e^{-\alpha_4 t}\cosh(\alpha_6 t) + \frac{(S-\alpha_4)}{\alpha_6}e^{-\alpha_4 t}\sinh(\alpha_6 t)\right)$$

$$^*\mathrm{erfc}\left(\frac{y\sqrt{P_r}}{2\sqrt{t}}\right)e^{-St},$$

$$I_3^{II} = B_1(y,t)^*B_3^{II}(t), \qquad (45)$$

where $B_1(y,t)$ (see equation (A.1)) and $B_3^{II}(t)$ (see equation (A.3)).

$$I_4^{II} = (t+\lambda)^*\left(e^{-\alpha_7 t}\cosh(\alpha_9 t) + \frac{(K_c-\alpha_7)}{\alpha_9}e^{-\alpha_7 t}\sinh(\alpha_9 t)\right)$$

$$^*\mathrm{erfc}\left(\frac{y\sqrt{S_c}}{2\sqrt{t}}\right)e^{-K_c t},$$

$$I_5^{II} = B_1(y,t)^*B_4^{II}(t), \qquad (46)$$

where $B_1(y, t)$ (see equation (A.1)) and $B_4^{II}(t)$ (see equation (A.4)).

4.3. Application 3: $f(t) = \sin t$, $g(t) = \sin t$, $h(t) = \sin t$.
The choice of this function shows the fluid motion due to the oscillation of the plate. It has a lot of applications in physics such as wave motion, other oscillatory motions, and engineering. It is used to model the behavior that repeats. Trigonometric functions are used to calculate angles in many engineering problems. In civil and mechanical engineering, trigonometry is used to calculate torque and forces on objects, which help build bridges and girders. In the construction of bridges, we need to consider the forces which keep the bridges at their balance and trigonometry helps us to calculate the static force which keeps the bridges static. In engineering, trigonometry is used to decompose the forces into horizontal and vertical components that can be analyzed. The expression for concentration after putting the value of $G(q) = (1/q^2 + 1)$ into equation (12) is

$$C(y, t) = \left(\cos t + K_c \sin t\right)^* \text{erfc}\left(\frac{y\sqrt{S_c}}{2\sqrt{t}}\right)e^{-K_c t}, \quad (47)$$

the expression for temperature become after putting the value of $H(q) = (1/q^2 + 1)$ into equation (16) is

$$T(y, t) = \left(\cos t + S \sin t\right)^* \text{erfc}\left(\frac{y\sqrt{P_r}}{2\sqrt{t}}\right)e^{-S t}, \quad (48)$$

and velocity change after substitute the value of $F(q) = (1/q^2 + 1)$ into equation (21) is

$$u(y, t) = I_1^{III} + \frac{G_T}{\lambda}I_2^{III} - \frac{G_T}{\lambda}I_3^{III} + \frac{G_c}{\lambda}I_4^{III} - \frac{G_c}{\lambda}I_5^{III}, \quad (49)$$

where

$$I_1^{III} = B_1(y, t)^* B_2^{III}(t), \quad (50)$$

where $B_1(y, t)$ (see equation (A.1)) and $B_2^{III}(t)$ (see equation (A.5)).

$$I_2^{III} = (\sin t + \lambda \cos t)^* \left(e^{-\alpha_4 t}\cosh(\alpha_6 t) + \frac{(S - \alpha_4)}{\alpha_6}e^{-\alpha_4 t}\sinh(\alpha_6 t)\right)$$

$$\qquad {}^* \text{erfc}\left(\frac{y\sqrt{P_r}}{2\sqrt{t}}\right)e^{-S t},$$

$$I_3^{III} = B_1(y, t)^* B_3^{III}(t),$$

(51)

where $B_1(y, t)$ (see equation (A.1)) and $B_3^{III}(t)$ (see equation (A.6)).

$$I_4^{III} = (\sin t + \lambda \cos t)^* \left(e^{-\alpha_7 t}\cosh(\alpha_9 t) + \frac{(K_c - \alpha_7)}{\alpha_9}e^{-\alpha_7 t}\sinh(\alpha_9 t)\right)$$

$$\qquad {}^* \text{erfc}\left(\frac{y\sqrt{S_c}}{2\sqrt{t}}\right)e^{-K_c t},$$

$$I_5^{III} = B_1(y, t)^* B_4^{III}(t),$$

(52)

where $B_1(y, t)$ (see equation (A.1)) and $B_4^{III}(t)$ (see equation (A.7)).

4.4. Application 4: $f(t) = e^t$, $g(t) = e^t$, $h(t) = e^t$.
The exponent functions are used for real-world application as for calculating area, volume, determining growth or decay, and impacts of force. In engineering, it helps them to design, build, and improve the machinery, structure, and equipment. For example, in sound engineering, it is used to calculate sound waves. In basic engineering, it is used to compute the tensile strength, which finds out the amount of stress that a structure can withstand. In aeronautical engineering, it is used to predict how airplanes, rockets, and jets will perform during flight. To determine the kinetic and potential energy, pressure, heat, and airflow of waves behavior, it is very helpful. Nuclear power sources are one of the important things developed by nuclear engineers. They used the exponents to work with extremely small numbers to make the big things happen. Substituting the value of $G(q) = (1/q - 1)$ into equation (12), the concentration equation after implementing the Laplace inverse becomes

$$C(y, t) = \left(e^t + K_c e^t\right)^* \text{erfc}\left(\frac{y\sqrt{S_c}}{2\sqrt{t}}\right)e^{-K_c t}, \quad (53)$$

and equation of temperature distribution after putting the value of $H(q) = (1/q - 1)$ into equation (16) and applying Laplace inverse

$$T(y, t) = \left(e^t + S e^t\right)^* \text{erfc}\left(\frac{y\sqrt{P_r}}{2\sqrt{t}}\right)e^{-S t}. \quad (54)$$

The expression for velocity is

$$u(y, t) = I_1^{IV} + \frac{G_T}{\lambda}I_2^{IV} - \frac{G_T}{\lambda}I_3^{IV} + \frac{G_c}{\lambda}I_4^{IV} - \frac{G_c}{\lambda}I_5^{IV}, \quad (55)$$

where

$$I_1^{IV} = B_1(y, t)^* B_2^{IV}(t), \quad (56)$$

and $B_1(y, t)$ (see equation (A.1)) and $B_2^{IV}(t)$ (see equation (A.8)).

$$I_2^{IV} = \left(e^t + \lambda e^t\right)^* \left(e^{-\alpha_4 t}\cosh\left(\alpha_6 t\right) + \frac{(S-\alpha_4)}{\alpha_6}e^{-\alpha_4 t}\sinh\left(\alpha_6 t\right)\right)$$

$$^* \operatorname{erfc}\left(\frac{y\sqrt{P_r}}{2\sqrt{t}}\right)e^{-St},$$

$$I_3^{IV} = B_1\left(y,t\right)^* B_3^{IV}\left(t\right),$$

(57)

and $B_1\left(y,t\right)$ (see equation (A.1)) and $B_3^{IV}\left(t\right)$ (see equation (A.9)).

$$I_4^{IV} = \left(e^t + \lambda e^t\right)^* \left(e^{-\alpha_7 t}\cosh\left(\alpha_9 t\right) + \frac{(K_c-\alpha_7)}{\alpha_9}e^{-\alpha_7 t}\sinh\left(\alpha_9 t\right)\right)$$

$$^* \operatorname{erfc}\left(\frac{y\sqrt{S_c}}{2\sqrt{t}}\right)e^{-K_c t}.$$

(58)

Similarly,

$$I_5^{IV} = B_1\left(y,t\right)^* B_4^{IV}\left(t\right),$$

(59)

and $B_1\left(y,t\right)$ (see equation (A.1)) and $B_4^{IV}\left(t\right)$ (see equation (A.10)).

4.5. Application 5: $f(t)=te^t$, $g(t)=te^t$, $h(t)=te^t$. Inserting the $G(q) = (1/(q-1)^2)$ into equation (12) and applying the Laplace inverse, we get

$$C(y,t) = \left(e^t + (K_c + 1)te^t\right)^* \operatorname{erfc}\left(\frac{y\sqrt{S_c}}{2\sqrt{t}}\right)e^{-K_c t},$$

(60)

and insert the $H(q) = (1/(q-1)^2)$ into equation (16) and take Laplace inverse:

$$T(y,t) = \left(e^t + (S+1)te^t\right)^* \operatorname{erfc}\left(\frac{y\sqrt{P_r}}{2\sqrt{t}}\right)e^{-St},$$

$$u(y,t) = I_1^V + \frac{G_T}{\lambda}I_2^V - \frac{G_T}{\lambda}I_3^V + \frac{G_c}{\lambda}I_4^V - \frac{G_c}{\lambda}I_5^V.$$

(61)

The I_1^V takes the form after embedding the $F(q) = (1/(q-1)^2)$

$$I_1^V = B_1\left(y,t\right)^* B_2^V\left(t\right),$$

(62)

where $B_1\left(y,t\right)$ (see equation (A.1)) and $B_2^V\left(t\right)$ (see equation (A.11)).

$$I_2^V = \left(te^t + \lambda e^t\left(t+1\right)\right)^* \left(e^{-\alpha_4 t}\cosh\left(\alpha_6 t\right) + \frac{(S-\alpha_4)}{\alpha_6}e^{-\alpha_4 t}\sinh\left(\alpha_6 t\right)\right)$$

$$^* \operatorname{erfc}\left(\frac{y\sqrt{P_r}}{2\sqrt{t}}\right)e^{-St},$$

$$I_3^V = B_1\left(y,t\right)^* B_3^V\left(t\right),$$

(63)

where $B_1\left(y,t\right)$ (see equation (A.1)) and $B_3^V\left(t\right)$ (see equation (A.12)).

$$I_4^V = \left(te^t + \lambda e^t\left(t+1\right)\right)^* \left(e^{-\alpha_7 t}\cosh\left(\alpha_9 t\right) + \frac{(K_c-\alpha_7)}{\alpha_9}e^{-\alpha_7 t}\sinh\left(\alpha_9 t\right)\right)$$

$$^* \operatorname{erfc}\left(\frac{y\sqrt{S_c}}{2\sqrt{t}}\right)e^{-K_c t},$$

$$I_5^V = B_1\left(y,t\right)^* B_4^V\left(t\right),$$

(64)

where $B_1\left(y,t\right)$ (see equation (A.1)) and $B_4^V\left(t\right)$ (see equation (A.13)).

4.6. Application 6: $f(t)=e^t \sin t$, $g(t)=e^t \sin t$, $h(t)=e^t \sin t$. The choice of the value of $G(q) = (1/(q-1)^2 + 1)$, $H(q) = (1/(q-1)^2 + 1)$, $F(q) = (1/(q-1)^2 + 1)$ makes the expression

$$C(y,t) = \left(e^t\left(\cos t + (1 + K_c)\sin t\right)\right)^* \operatorname{erfc}\left(\frac{y\sqrt{S_c}}{2\sqrt{t}}\right)e^{-K_c t},$$

$$T(y,t) = \left(e^t\left(\cos t + (1 + S)\sin t\right)\right)^* \operatorname{erfc}\left(\frac{y\sqrt{P_r}}{2\sqrt{t}}\right)e^{-St},$$

$$u(y,t) = I_1^{VI} + \frac{G_T}{\lambda}I_2^{VI} - \frac{G_T}{\lambda}I_3^{VI} + \frac{G_c}{\lambda}I_4^{VI} - \frac{G_c}{\lambda}I_5^{VI},$$

$$I_1^{VI} = B_1\left(y,t\right)^* B_2^{VI}\left(t\right),$$

(65)

where $B_1\left(y,t\right)$ (see equation (A.1)) and $B_2^{VI}\left(t\right)$ (see equation (A.14)).

$$I_2^{VI} = \left(e^t \sin t\left(1+\lambda\right) + e^t \cos t\right)$$

$$^* \left(e^{-\alpha_4 t}\cosh\left(\alpha_6 t\right) + \frac{(S-\alpha_4)}{\alpha_6}e^{-\alpha_4 t}\sinh\left(\alpha_6 t\right)\right)$$

$$^* \operatorname{erfc}\left(\frac{y\sqrt{P_r}}{2\sqrt{t}}\right)e^{-St},$$

(66)

$$I_3^{VI} = B_1\left(y,t\right)^* B_3^{VI}\left(t\right),$$

where $B_1\left(y,t\right)$ (see equation (A.1)) and $B_3^{VI}\left(t\right)$ (see equation (A.15)).

$$I_4^{VI} = \left(e^t \sin t\left(1+\lambda\right) + e^t \cos t\right)$$

$$^* \left(e^{-\alpha_7 t}\cosh\left(\alpha_9 t\right) + \frac{(K_c-\alpha_7)}{\alpha_9}e^{-\alpha_7 t}\sinh\left(\alpha_9 t\right)\right)$$

$$^* \operatorname{erfc}\left(\frac{y\sqrt{S_c}}{2\sqrt{t}}\right)e^{-K_c t}.$$

(67)

Similarly,

$$I_5^{VI} = B_1\left(y,t\right)^* B_4^{VI}\left(t\right),$$

(68)

where $B_1\left(y,t\right)$ (see (A.1)) and $B_4^{VI}\left(t\right)$ (see equation (A.16)).

4.7. Application 7: $f(t) = t \sin t$, $g(t) = t \sin t$, $h(t) = t \sin t$. By putting the value of $G(q) = (2q/(q^2+1)^2)$ into equation (12) and employing Laplace inverse,

$$C(y,t) = (t \cos t + (K_c t + 1)\sin t) * \text{erfc}\left(\frac{y\sqrt{S_c}}{2\sqrt{t}}\right) e^{-K_c t}. \tag{69}$$

By putting the value of $H(q) = (2q/(q^2+1)^2)$ into equation (16) and Laplace inverse gives the expression

$$T(y,t) = (t \cos t + (St+1)\sin t) * \text{erfc}\left(\frac{y\sqrt{P_r}}{2\sqrt{t}}\right) e^{-St},$$

$$u(y,t) = I_1^{VII} + \frac{G_T}{\lambda} I_2^{VII} - \frac{G_T}{\lambda} I_3^{VII} + \frac{G_c}{\lambda} I_4^{VII} - \frac{G_c}{\lambda} I_5^{VII}, \tag{70}$$

where

$$I_1^{VII} = B_1(y,t) * B_2^{VII}(t), \tag{71}$$

and $B_1(y,t)$ (see equation (A.1)) and $B_2^{VII}(t)$ (see equation (A.17)).

$$I_2^{VII} = ((t+\lambda)\sin t + \lambda \cos t)$$

$$* \left(e^{-\alpha_4 t}\cosh(\alpha_6 t) + \frac{(S-\alpha_4)}{\alpha_6}e^{-\alpha_4 t}\sinh(\alpha_6 t)\right)$$

$$* \text{erfc}\left(\frac{y\sqrt{P_r}}{2\sqrt{t}}\right) e^{-St}, \tag{72}$$

$$I_3^{VII} = B_1(y,t) * B_3^{VII}(t),$$

where $B_1(y,t)$ (see equation (A.1)) and $B_3^{VII}(t)$ (see equation (A.18)).

$$I_4^{VII} = ((t+\lambda)\sin t + \lambda \cos t)$$

$$* \left(e^{-\alpha_7 t}\cosh(\alpha_9 t) + \frac{(K_c-\alpha_7)}{\alpha_9}e^{-\alpha_7 t}\sinh(\alpha_9 t)\right)$$

$$* \text{erfc}\left(\frac{y\sqrt{S_c}}{2\sqrt{t}}\right) e^{-K_c t},$$

$$I_5^{VII} = B_1(y,t) * B_4^{VII}(t), \tag{73}$$

and for $B_1(y,t)$ (see equation (A.1)) and $B_4^{VII}(t)$ (see equation (A.19)).These are solutions for the choice of same function for $f(t)$, $g(t)$, and $h(t)$ from the list of functions $H(t), t, \sin t, e^t, te^t, t \sin t, \sin te^t$. We can consider the problem with the different choice of function for $f(t), g(t), h(t)$, e.g., $f(t) = t, g(t) = e^t, h(t) = H(t)$ and find its solution. For the validation of results, if we take $\lambda = 0, G_T = 1, S = 0, h(t) = 1 - ae^{bt}, g(t) = 1$ with choice of $f(t) = H(t)t^\alpha, (\alpha > 0)$ or $\sin t$, in our system of equations (4)–(8), the results obtained are the same as the result obtained by Nehad Ali shah [27] (choosing the $\epsilon = 0, N = G_C$ in equation (9)).

5. Results and Discussion

The heat and mass transfer study of Maxwell fluid is discussed here. The solutions for dimensionless velocity, concentration, and temperature are assessed by the Laplace transform method. The application of these solutions in different fields of engineering sciences is also discussed. It brings to attention that these results are helpful to solve the complicated problems of engineering and applied science. The behavior of these solutions for velocity, concentration, and temperature profile is depicted graphically. The impacts of different pertinent parameters $\lambda, M, S_c, K_c, P_r, G_T, G_C, S$ on fluid flow are also deliberated using plots and their physical aspects described. To avoid repetition, only the most significant graphical representations regarding the effects of the concerned parameter will be included here.

The variation in the behavior of velocity and concentration with varying values of Schmidt number S_c is illustrated inFigures 1–3, respectively. An increase in Schmidt number results in the decline in the thickness of the boundary layer of concentration. Since the Schmidt number is defined as the ratio between kinematic viscosity and mass diffusivity, it reduced the concentration as well as velocity profile. In reality, the increase occurring in momentum diffusivity causes a decline in the fluid velocity.

The deviation in temperature profile for varying values of Prandtl number Pr is demonstrated in Figures 4 and 5. It is depicted that the thermal boundary layer thickness decreases rapidly with the increase in the values of Pr. For a small value of Pr, heat diffuses very quickly in comparison to the velocity. The reason is, the thermal boundary layer thickness in liquid metals is higher than the momentum boundary layer. Finally, Pr can be practiced to expand the percentage of cooling.

Similar effects can be seen for the heat absorption coefficient S on temperature profile with different values of the function $g(t)$ at different time scales depicted in Figure 6 and 7. The thermal buoyancy forces decrease with the increase of S which decreases the fluid temperature.

Impacts of magnetic parameter M displayed in Figure 8 depict the velocity decline with the increase of magnetic parameter values. Physically, when magnetic force is applied to the velocity field, it generates the drag force known as the Lorentz force which opposes the motion of the fluid. Figure 9 shows the impact of Pr on velocity. The increase of P_r results in a decrease in velocity. The velocity boundary layer gets thicker due to the low rate of thermal diffusion. Basically, in heat transfer problems, P_r control the relative thickness momentum boundary layer.

In Figure 10, the study of the effects of G_T on velocity describes the increase in behavior with increment in the values of G_T. Physically, the result of more induced fluid flows is due to a rise in buoyancy effects which is the result of the increase in G_T. The depiction of G_C on velocity is portrayed in Figure 11. We can see the rise in velocity with the rise in the value of G_C. The natural convection and
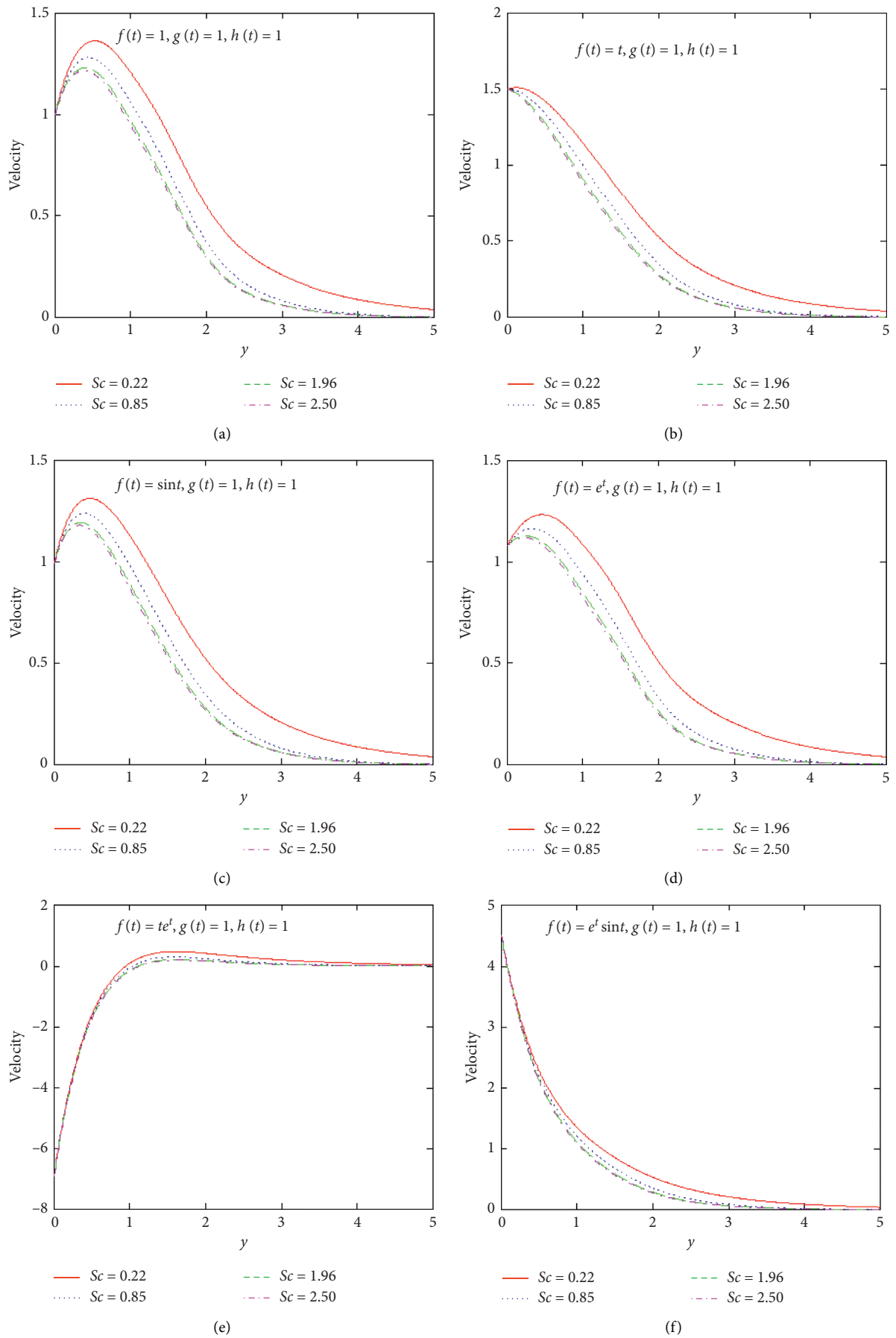
Figure 1: Continued.

(g)
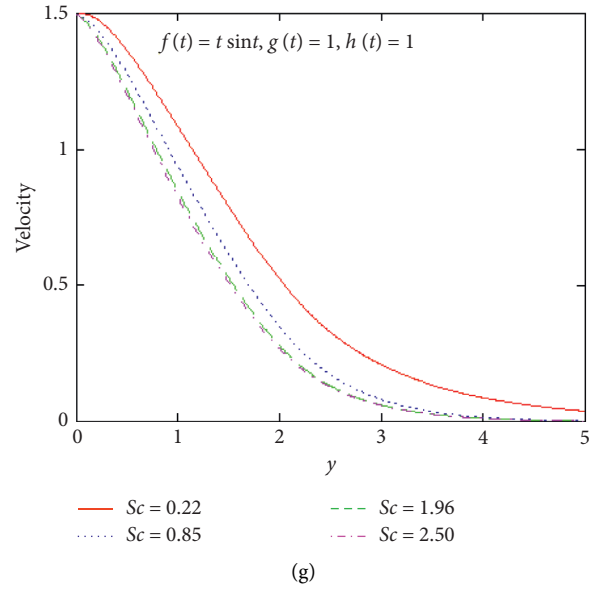
Figure 1: Profile of velocity for different values of S_c and $M = 2.0, \lambda = 0.6, S = 1.0.5, K_c = 0.5, G_T = 5.0, G_C = 2.0, P_r = 0.71$.

(a)

(b)

(c)

(d)
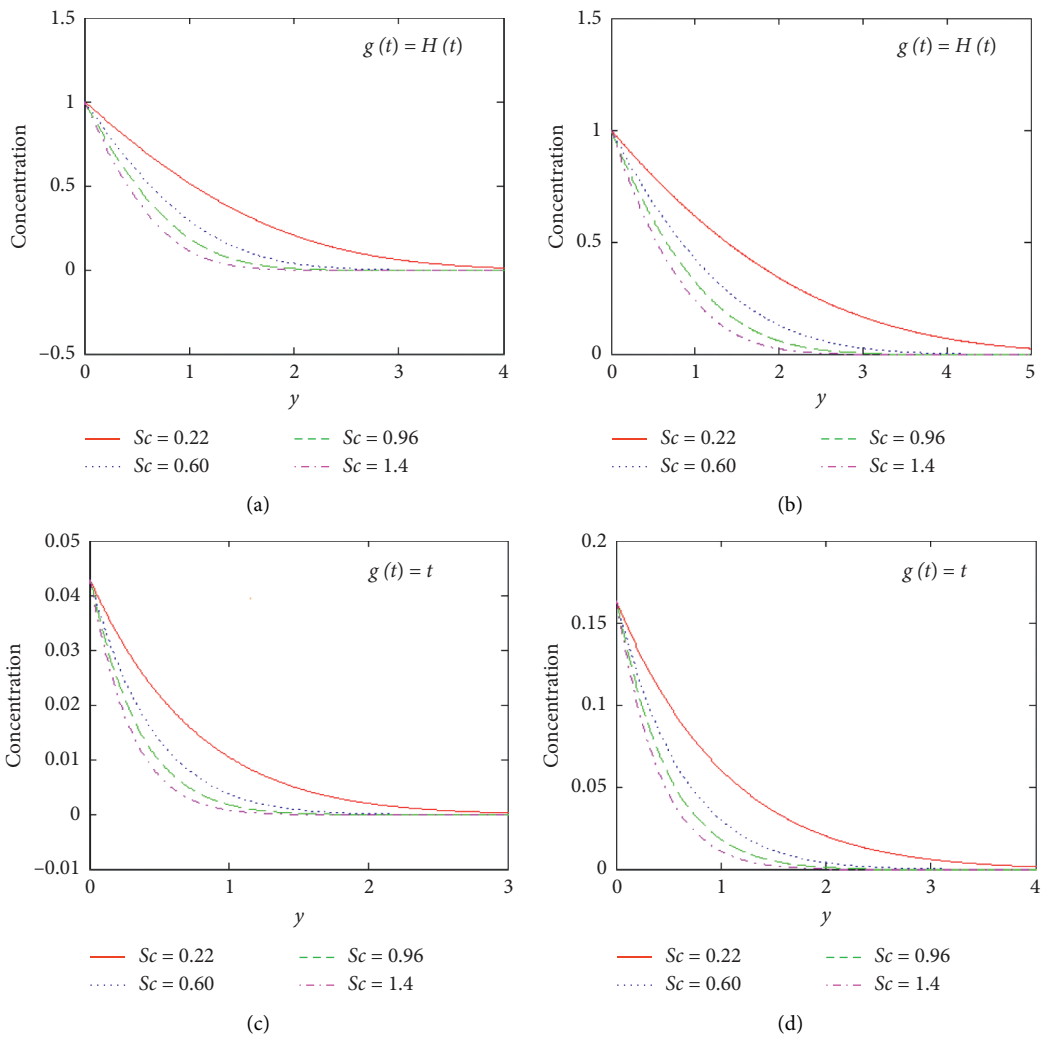
Figure 2: Continued.

(e)

(f)
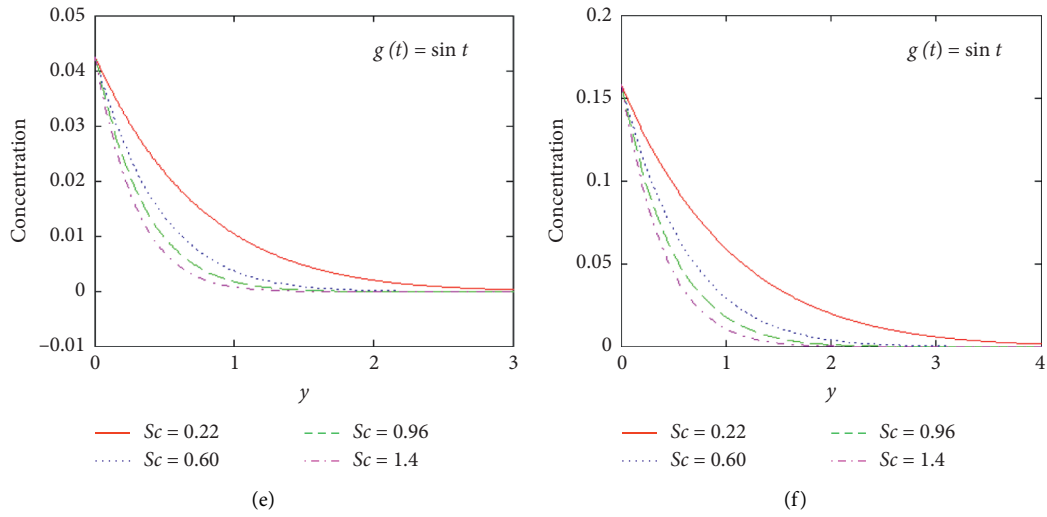
FIGURE 2: Profile of concentration for different values of S_c and variation of time.

(a)

(b)

(c)

(d)
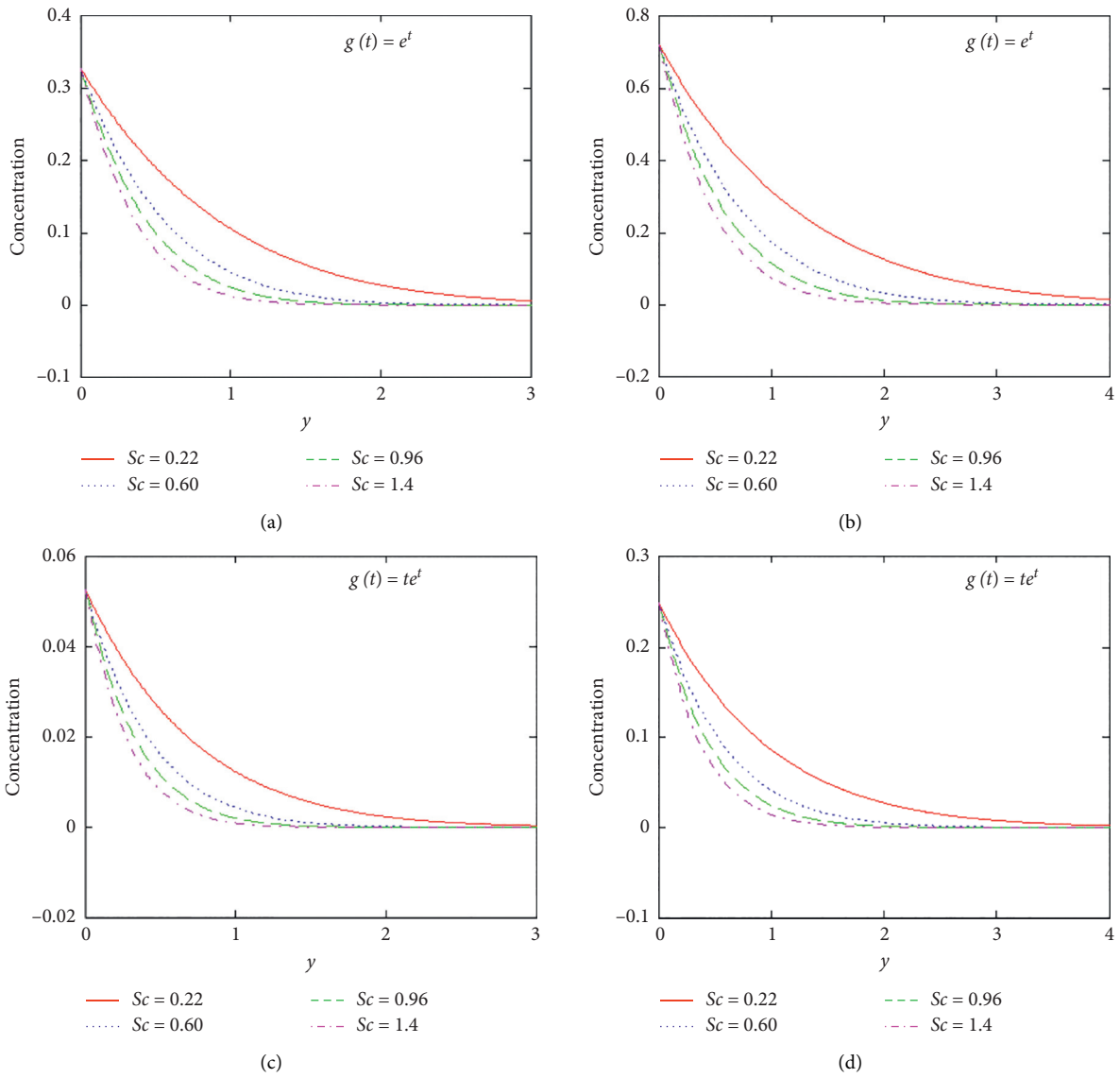
FIGURE 3: Continued.

(e)

(f)

(g)

(h)
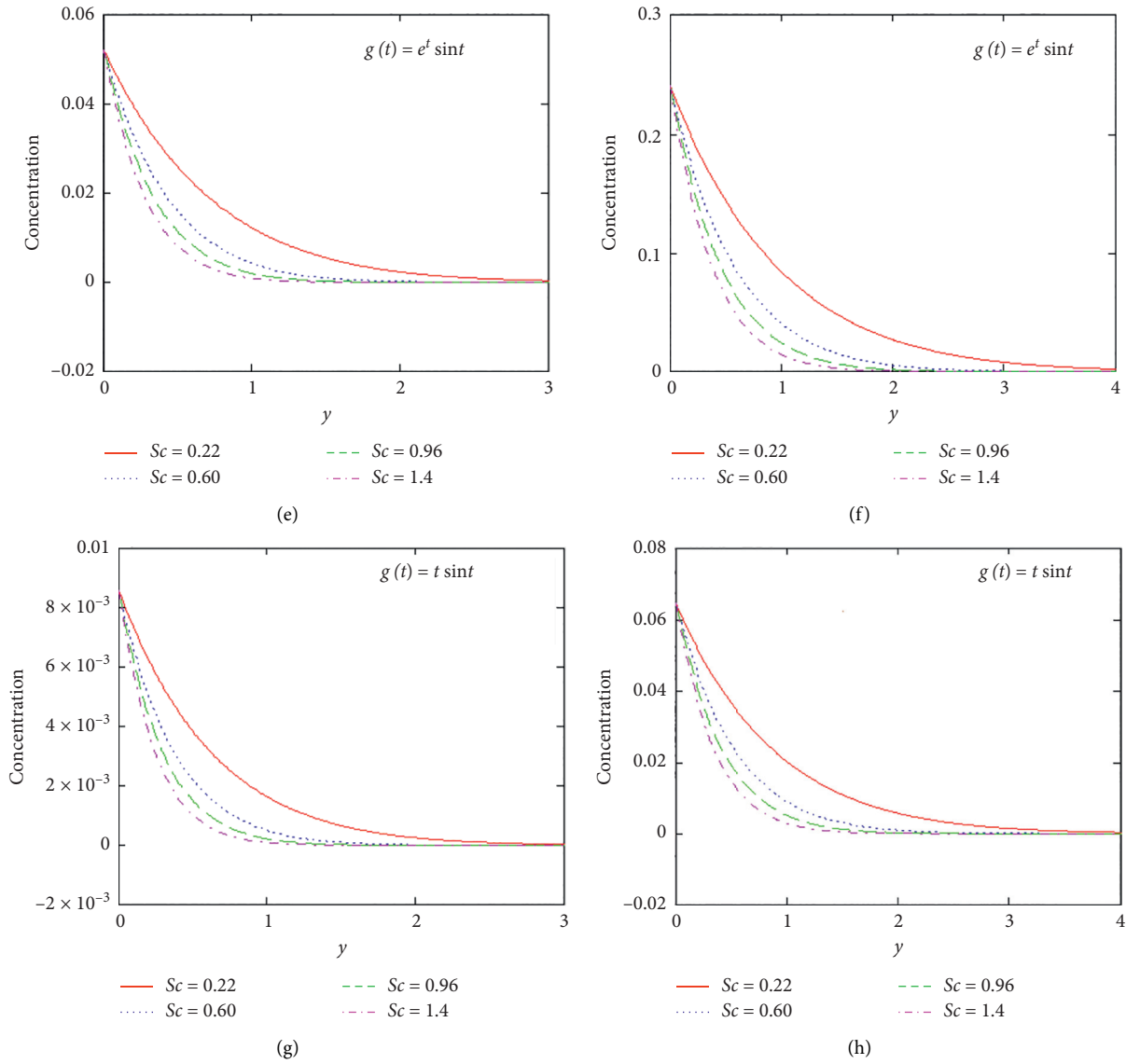
Figure 3: Profile of concentration for different values of S_c and variation of time.

(a)

(b)
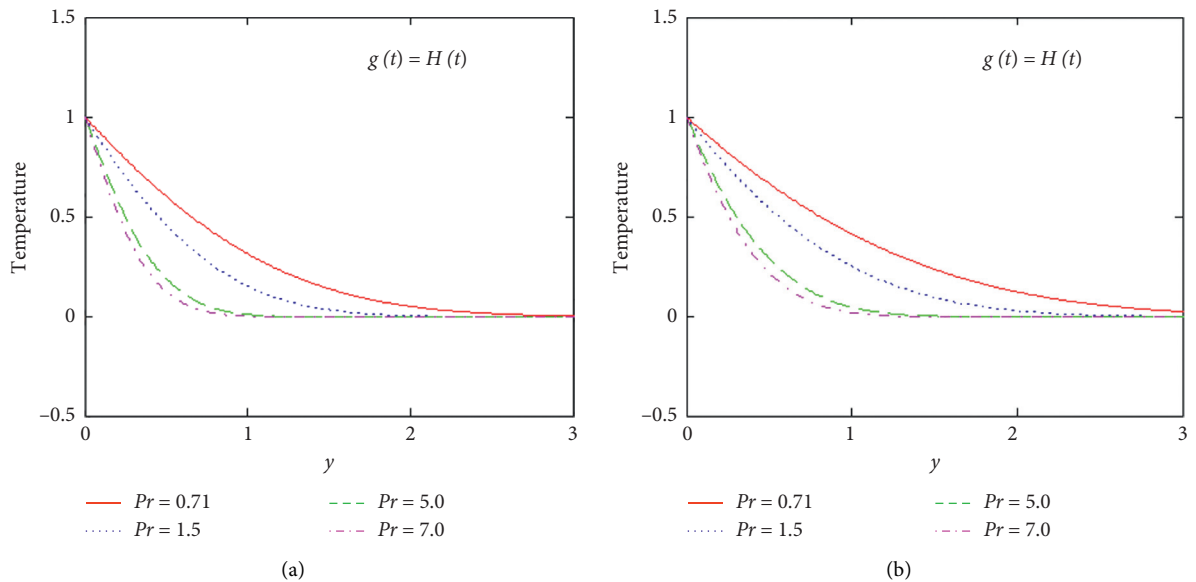
Figure 4: Continued.
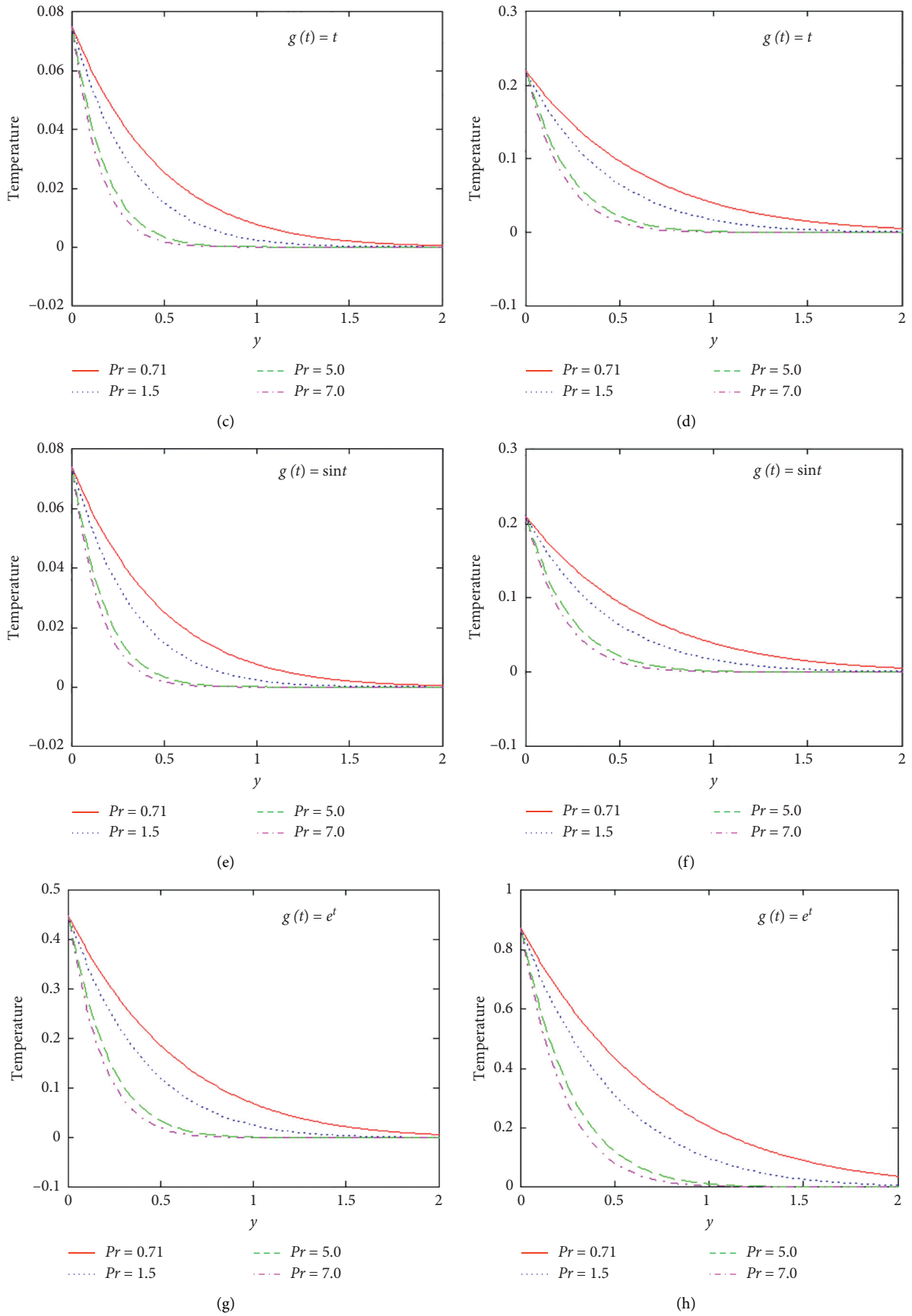
FIGURE 4: Profile of temperature for different values of P_r and variation of time.
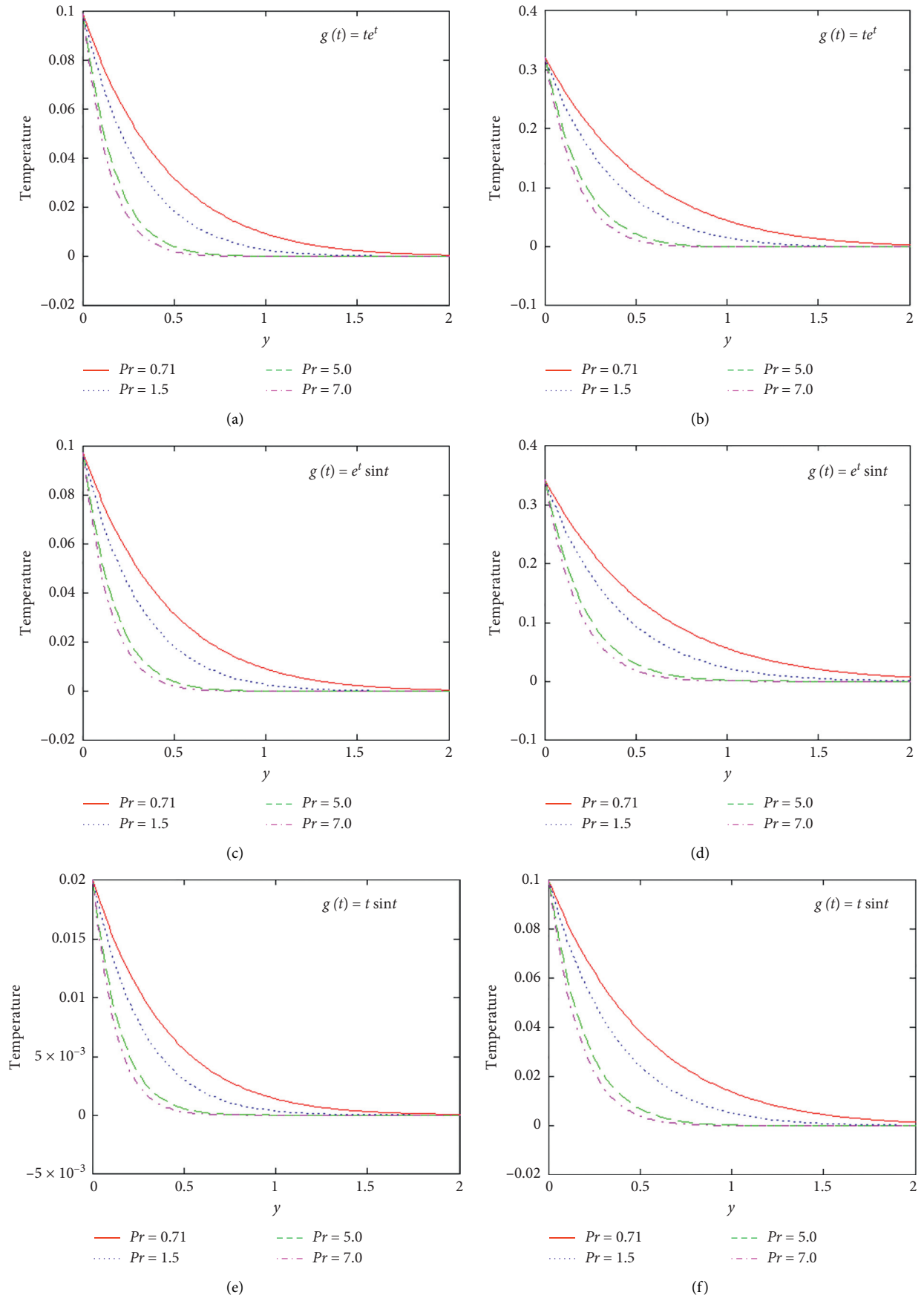
Figure 5: Profile of temperature for different values of P_r and variation of time.

(a)

(b)

(c)

(d)

(e)

(f)

Figure 6: Continued.

(g)

(h)
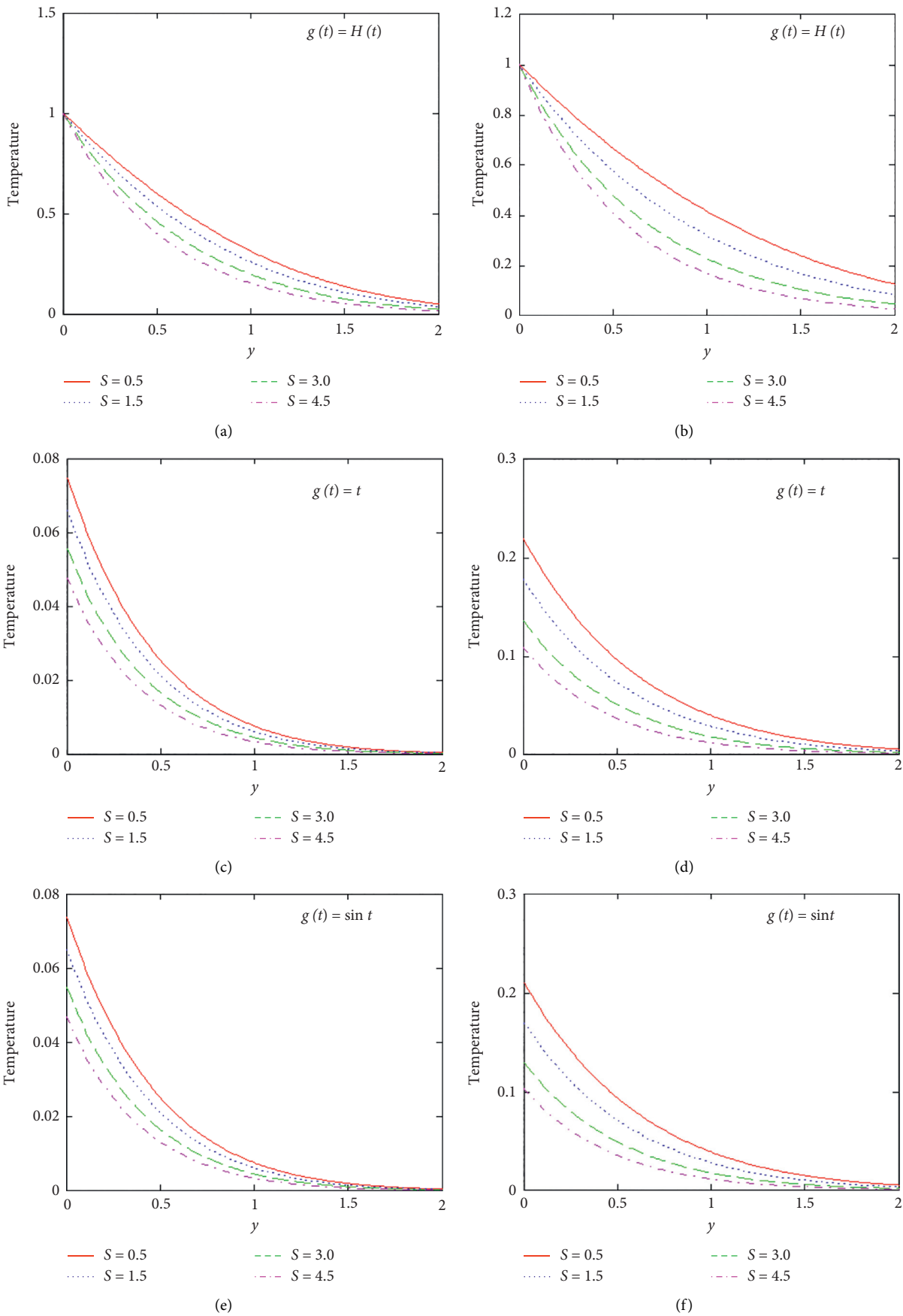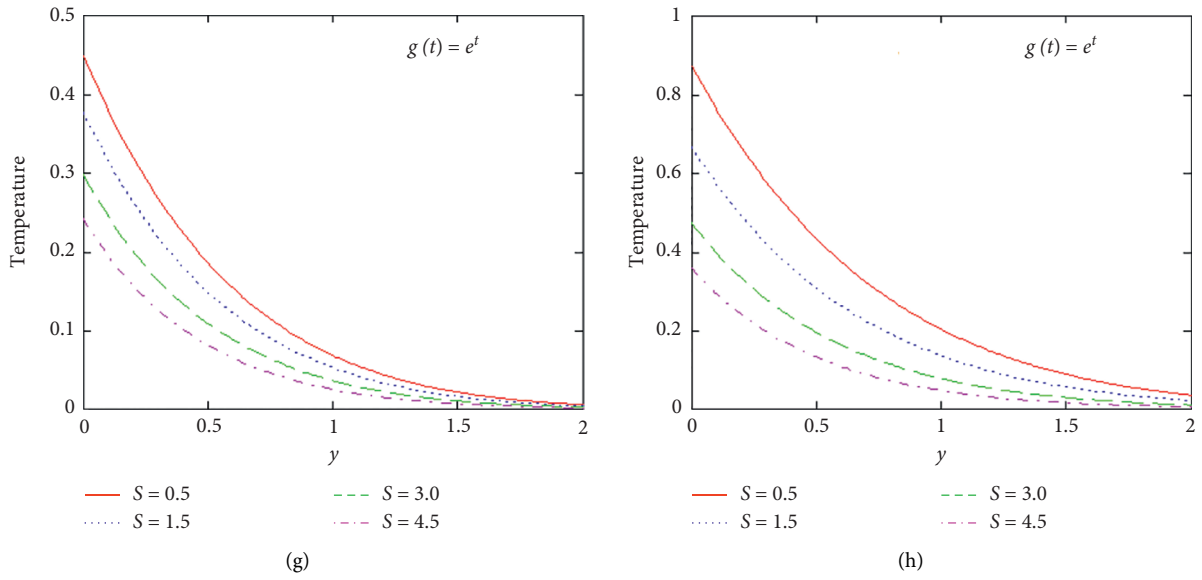
Figure 6: Profile of temperature for different values of S and variation of time.

(a)

(b)

(c)

(d)

Figure 7: Continued.

(e)

(f)
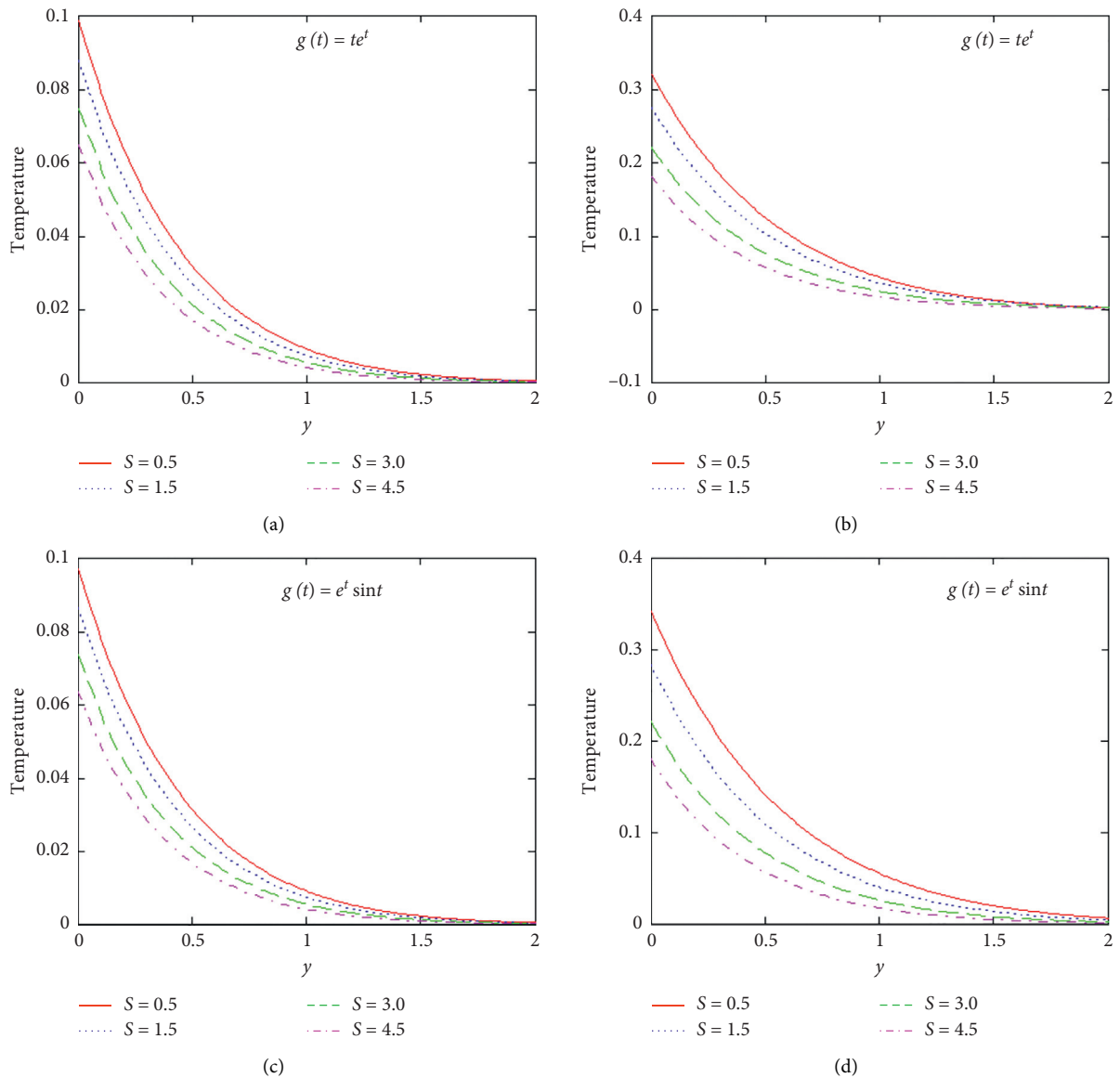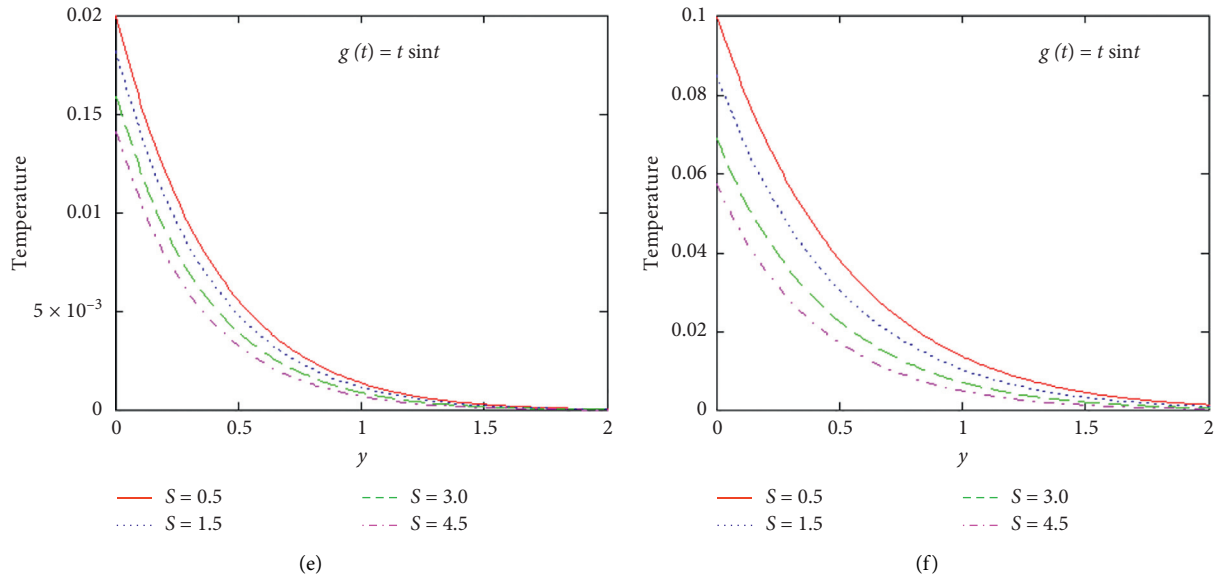
FIGURE 7: Profile of temperature for different values of S and variation of time.

(a)

(b)

(c)

(d)

FIGURE 8: Continued.

(e)

(f)

(g)
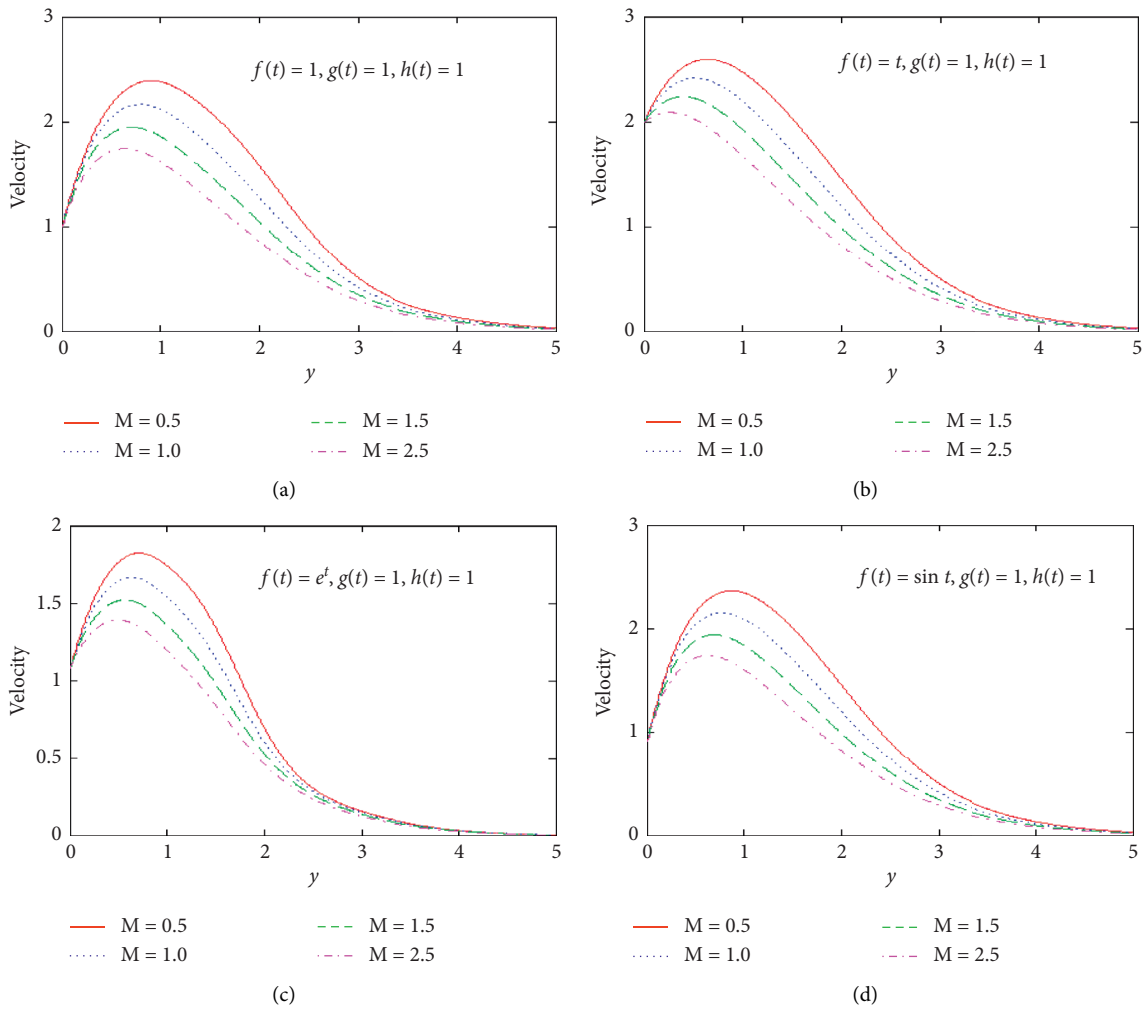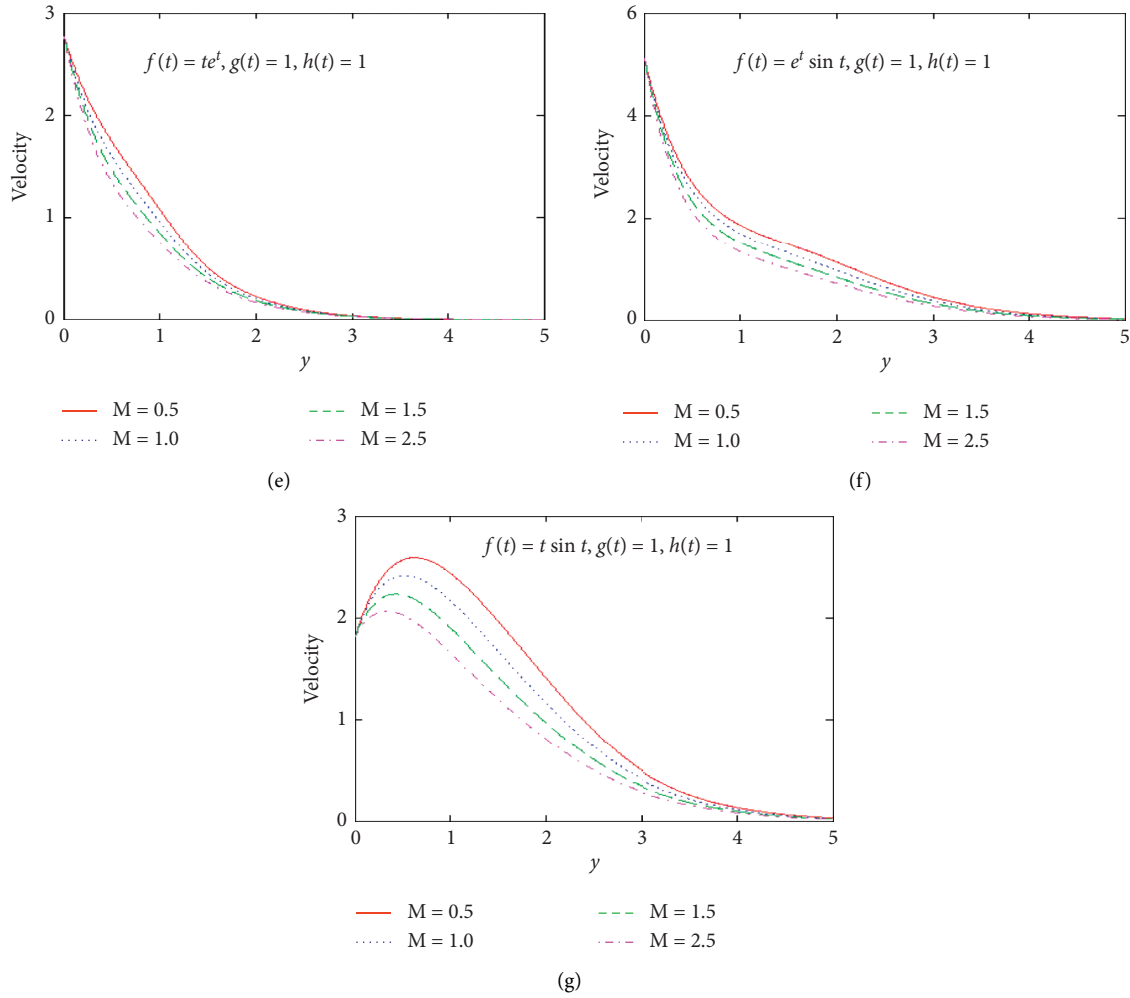
FIGURE 8: Profile of velocity for different values of M and $P_r = 0.71, \lambda = 0.6, S = 0.5, S_c = 0.60, K_c = 0.5, G_T = 5.0, G_C = 2.0$.

acceleration in fluid flow is due to the fact that buoyancy forces bcomes powerful than viscous forces.

Figures 12–14 show the chemical reaction K_c parameter effects on velocity and concentration description. The increase in K_c decreases the concentration and velocity profiles. Basically, chemical molecular diffusivity and species concentration drop with the higher values of K_c. The distribution in concentration falls at all the fluid flow field points with the rise in K_c. The curve for velocity for different values of the Maxwell fluid parameter λ is plotted in Figure 15. It is observed that an increase in λ produces a significant increase in the momentum boundary layer of the fluid which then increases the velocity. The rise in λ will therefore correspond to a fall in fluid viscosity, resulting in it accelerating the flow and hence velocity rising. Further, an increase in λ causes a rise in velocity near the plate surface. Although the trend is reversed away from the plate, the Newtonian fluid ($\lambda \longrightarrow 0$) has a higher velocity.

In Figure 16, velocity profiles are plotted against the heat absorption parameter S values. These curves show that the velocity is a decreasing function of parameter S. Furthermore, due to the absorption of heat, the fluid temperature diminishes and the thermal buoyancy force diminishes. These results have seen a fall in the velocity of a fluid with the increase in the values of S.

Figure 17 shows the behavior of velocity profile for different values of the parameters with a different choice of the function $f(t), g(t), h(t)$. For validation of our results, we consider some special cases of temperature profile already existing in literature and their graphical illustration is depicted in Figures 18–20. Figure 18 shows the temperature decrease with the increase in P_r for the variation of time with $g(t) = 1 - e^{-t}$. The effects of the heat absorption parameter can be observed in Figure (19) which depicts the decline in temperature. The impacts of $g(t) = 1 - ae^{-bt}$ for different choices of a and b are explained in Figure 20. We see the decline in temperature with the increasing values of a and b.

(a)

(b)

(c)

(d)

(e)

(f)
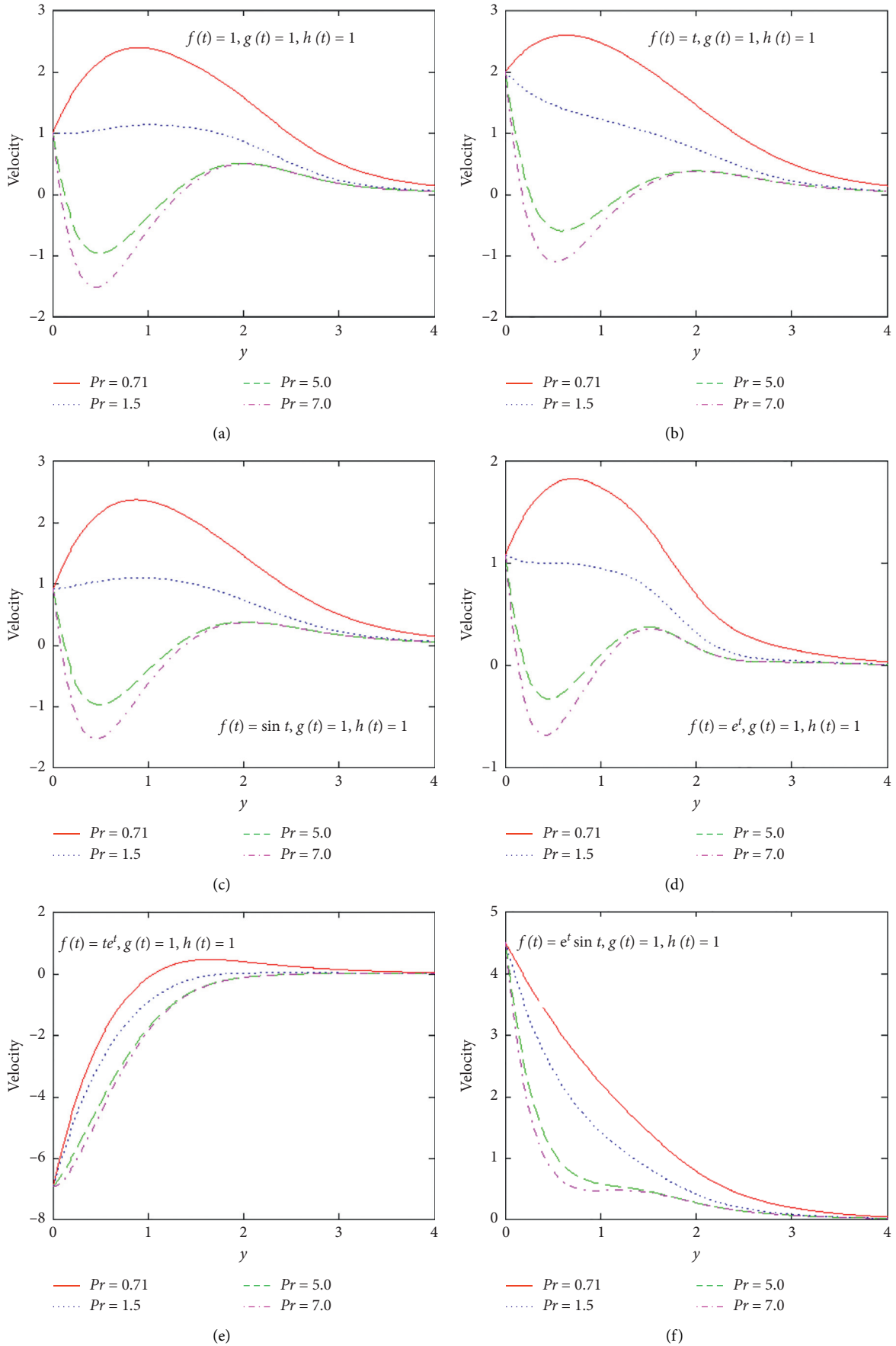
Figure 9: Continued.

(g)
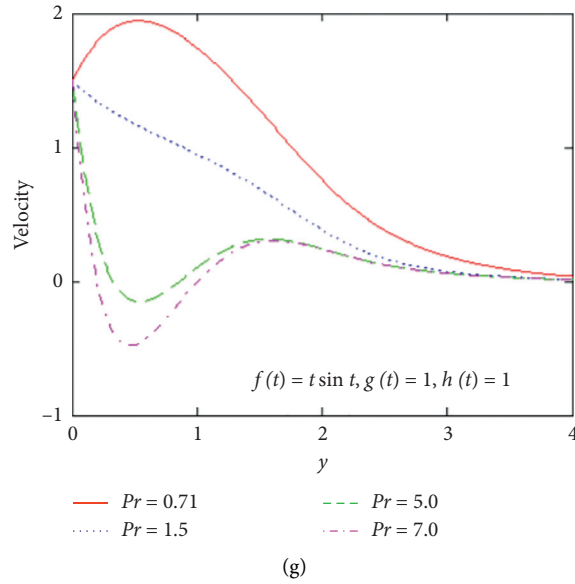
Figure 9: Profile of velocity for different values of P_r and $M = 0.5, \lambda = 0.6, S = 0.5, S_c = 0.60, K_c = 0.5, G_T = 5.0, G_C = 2.0$.

(a)

(b)

(c)

(d)

Figure 10: Continued.

(e)

(f)

$f(t) = te^t, g(t) = 1, h(t) = 1$

$f(t) = e^t \sin t, g(t) = 1, h(t) = 1$

| $G_T = 1.0$ | $G_T = 6.0$ |
| $G_T = 3.5$ | $G_T = 10$ |

$f(t) = t \sin t, g(t) = 1, h(t) = 1$

(g)

| $G_T = 1.0$ | $G_T = 6.0$ |
| $G_T = 3.5$ | $G_T = 10$ |
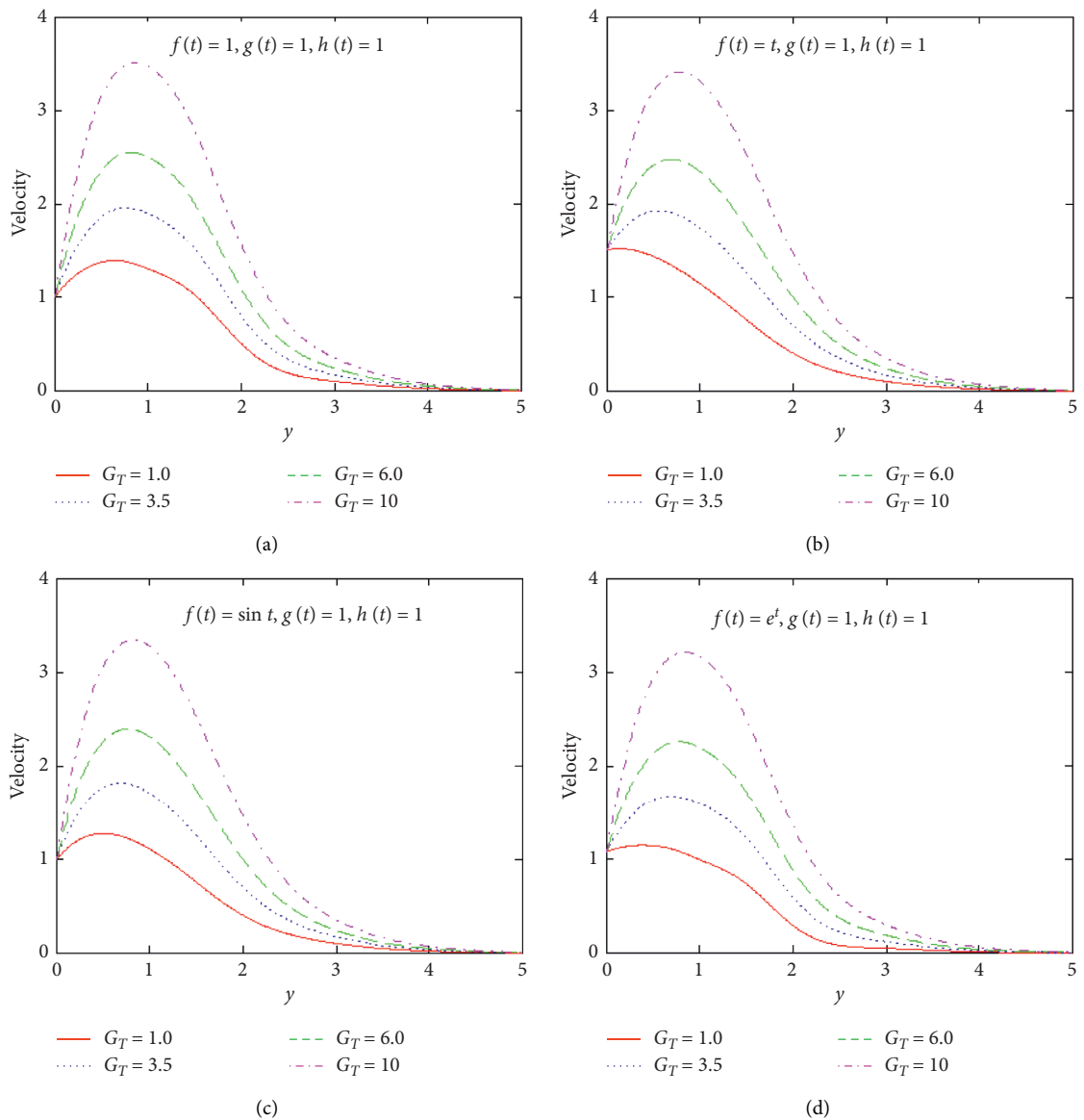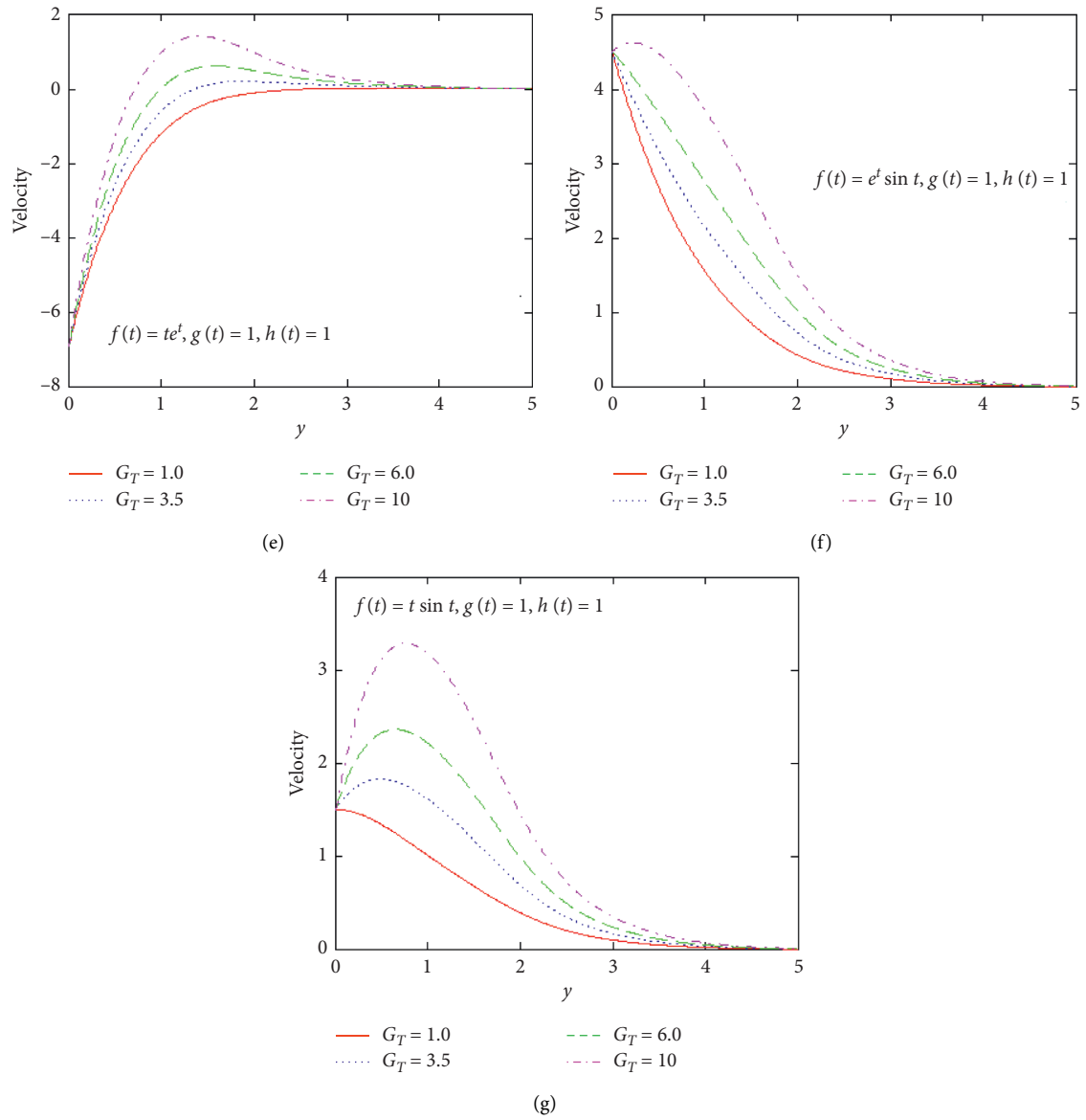
FIGURE 10: Profile of velocity for different values of G_T and $M = 0.2, \lambda = 0.6, S = 1.0.5, K_c = 0.5, S_c = 0.60, G_C = 2.0, P_r = 0.71$.

$f(t) = 1, g(t) = 1, h(t) = 1$

$f(t) = t, g(t) = 1, h(t) = 1$

| $G_C = 2.0$ | $G_C = 6.0$ |
| $G_C = 4.0$ | $G_C = 8.0$ |

| $G_C = 2.0$ | $G_C = 6.0$ |
| $G_C = 4.0$ | $G_C = 8.0$ |

(a)

(b)
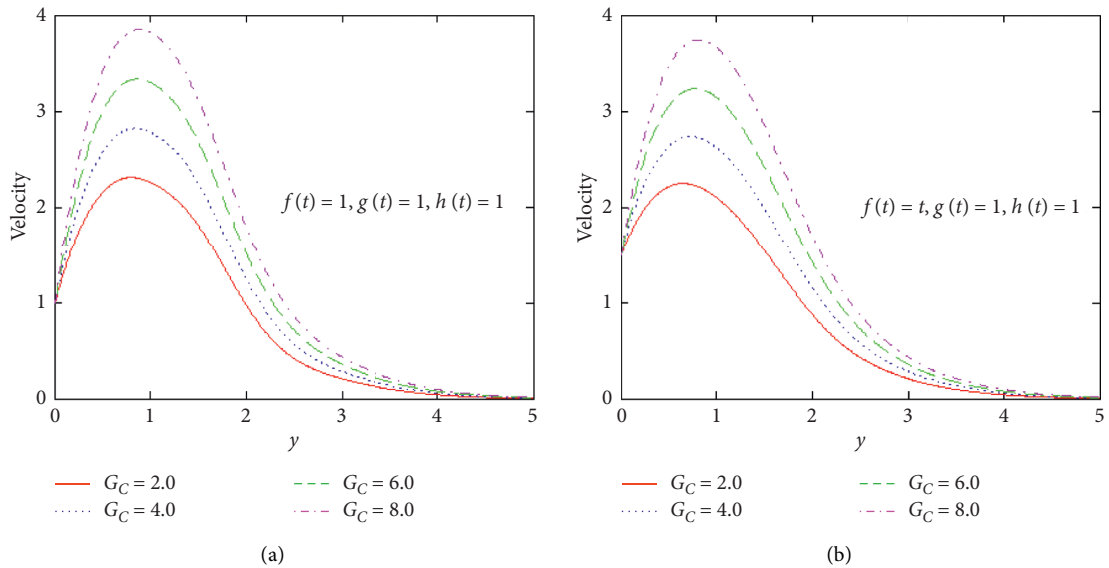
FIGURE 11: Continued.

(c)

(d)

(e)

(f)

(g)
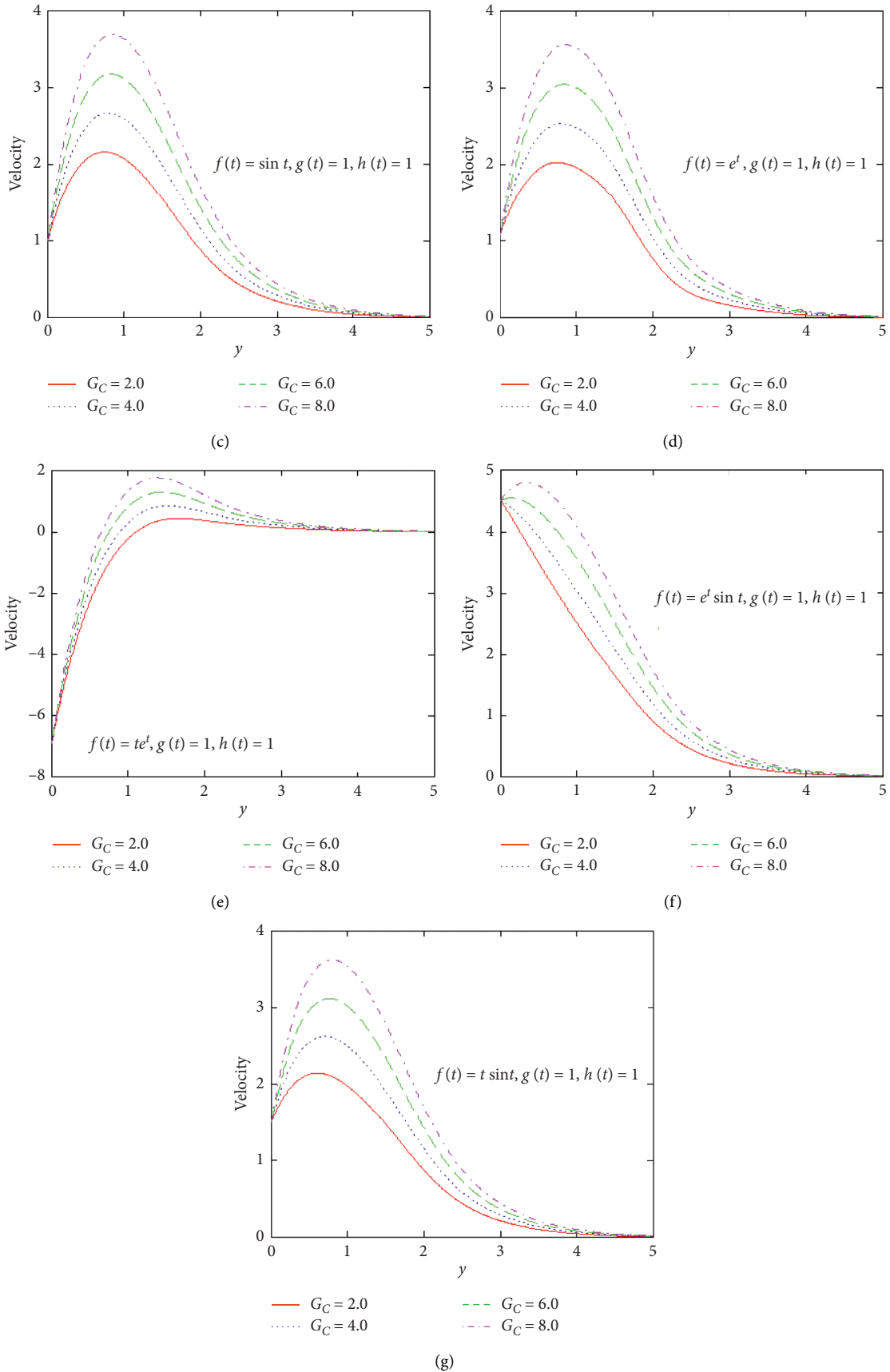
Figure 11: Profile of velocity for different values of G_C and $M = 0.2, \lambda = 0.6, S = 0.5, K_c = 0.5, S_c = 0.60, G_T = 5.0, P_r = 0.71$.

(a)

(b)

(c)

(d)

(e)

(f)
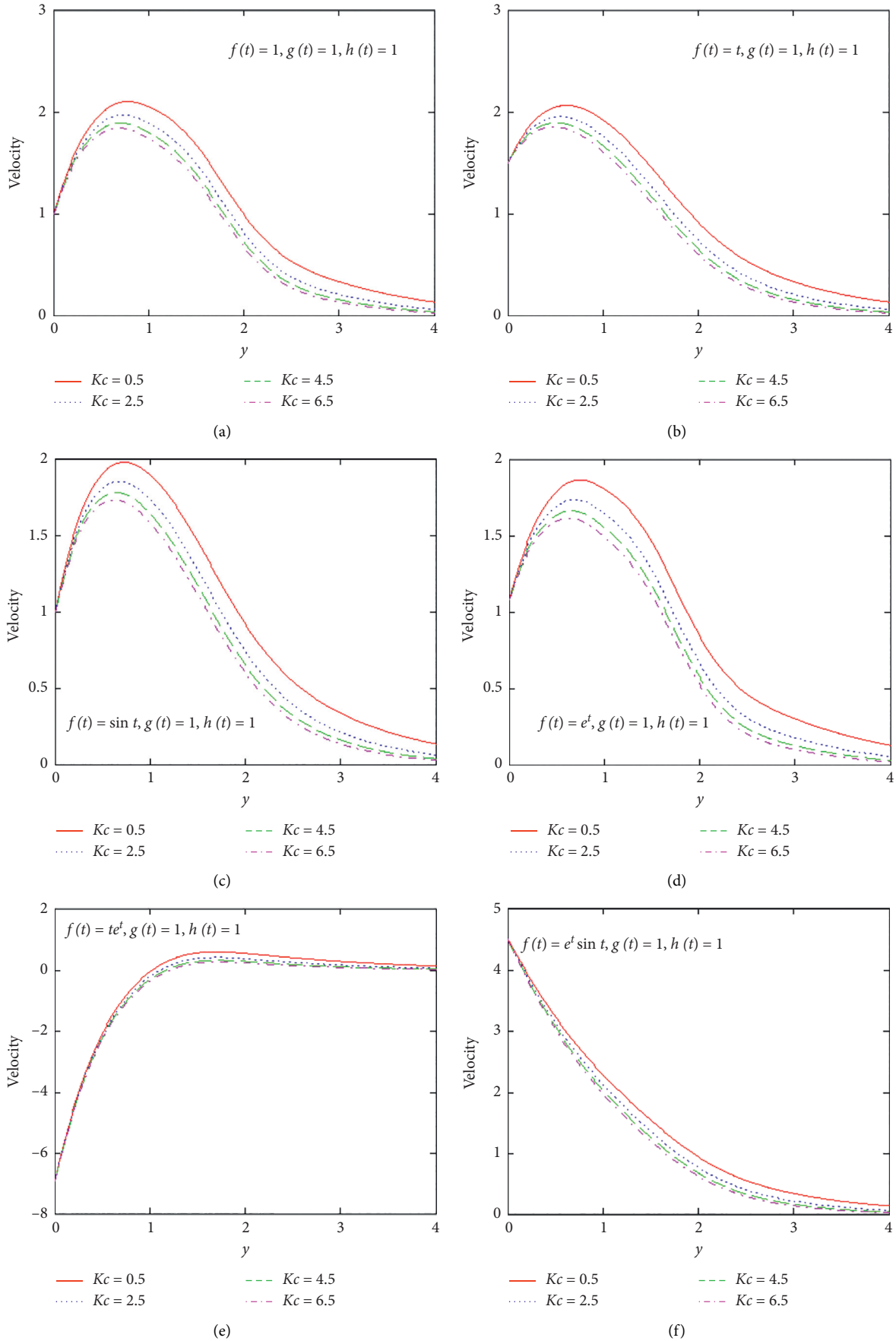
FIGURE 12: Continued.

(g)
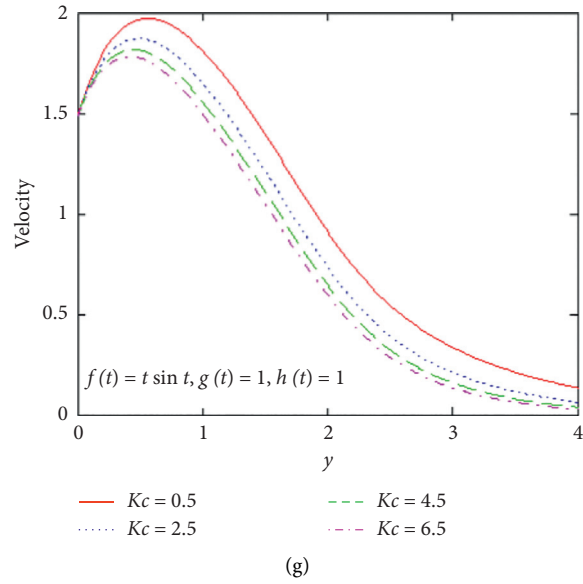
FIGURE 12: Profile of velocity for different values of K_c and $M = 0.5, \lambda = 0.6, S = 0.5, S_c = 0.60, G_T = 5.0, G_C = 2.0, P_r = 0.71$.

(a)

(b)

(c)

(d)
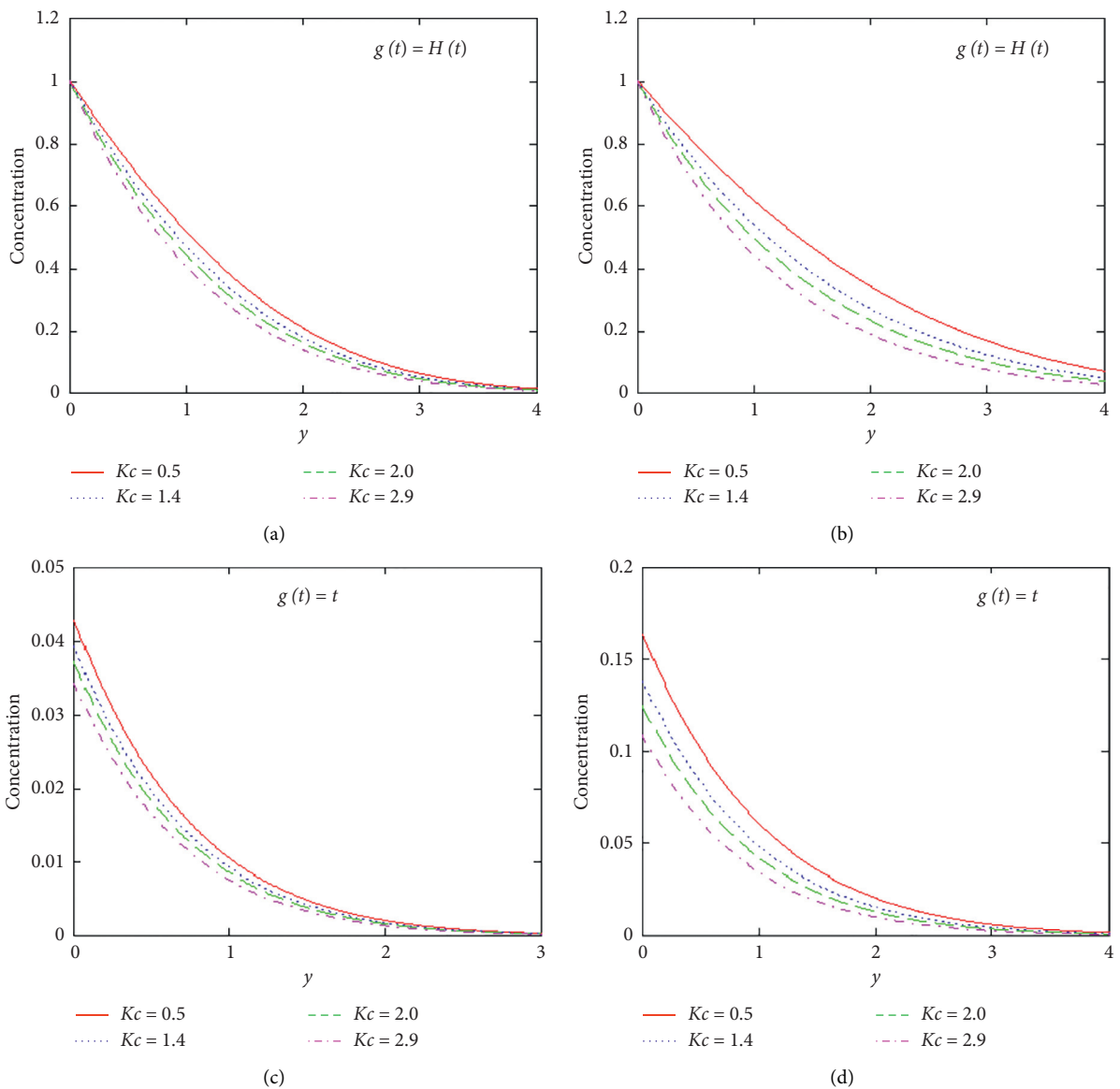
FIGURE 13: Continued.

(e)

(f)

(g)

(h)
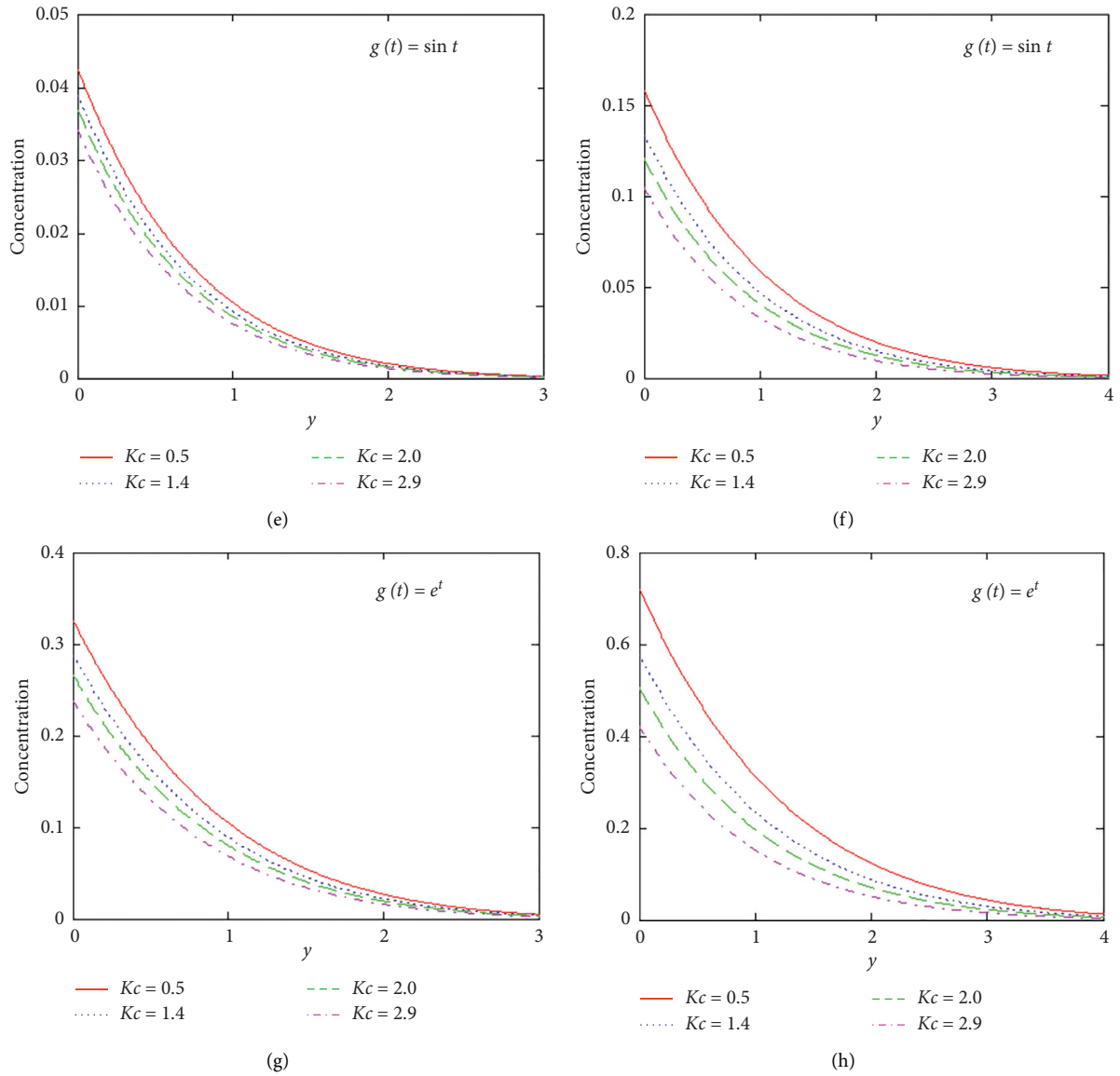
FIGURE 13: Profile of concentration for different values of K_c and variation of time.

(a)

(b)
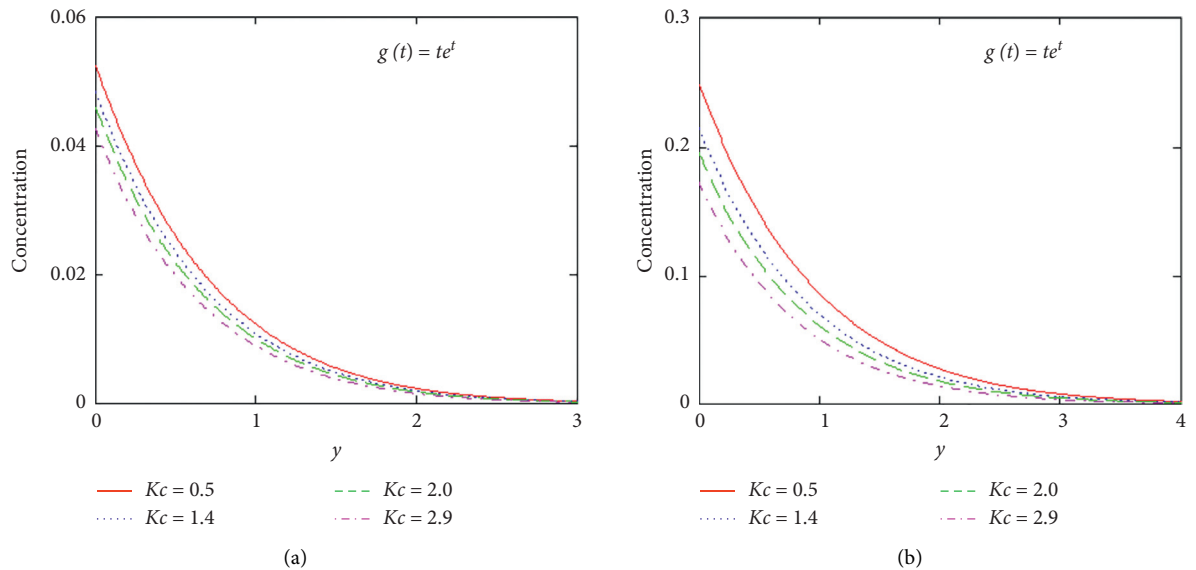
FIGURE 14: Continued.

(c)

(d)

(e)

(f)
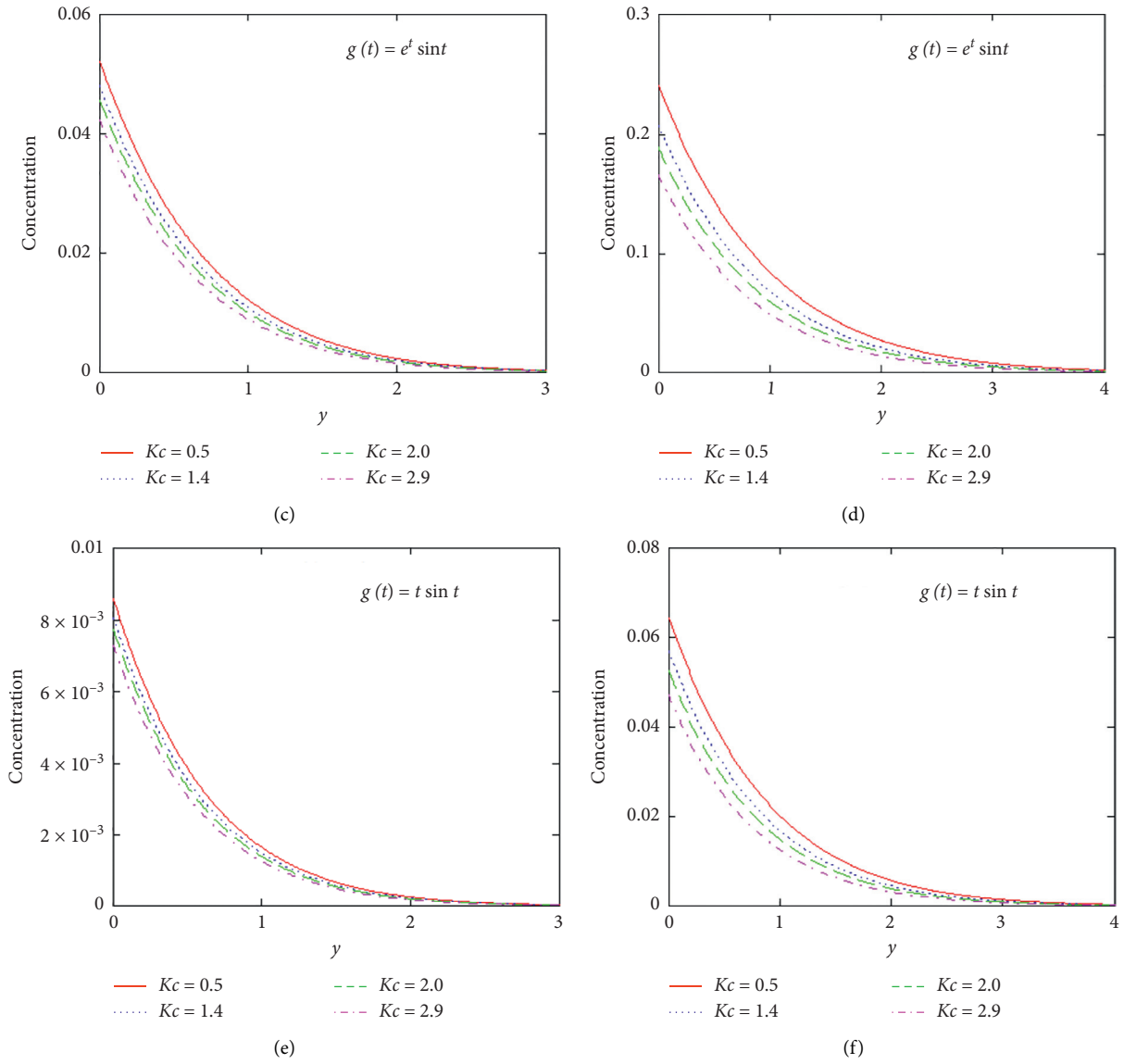
Figure 14: Profile of concentration for different values of K_c and variation of time.

(a)

(b)
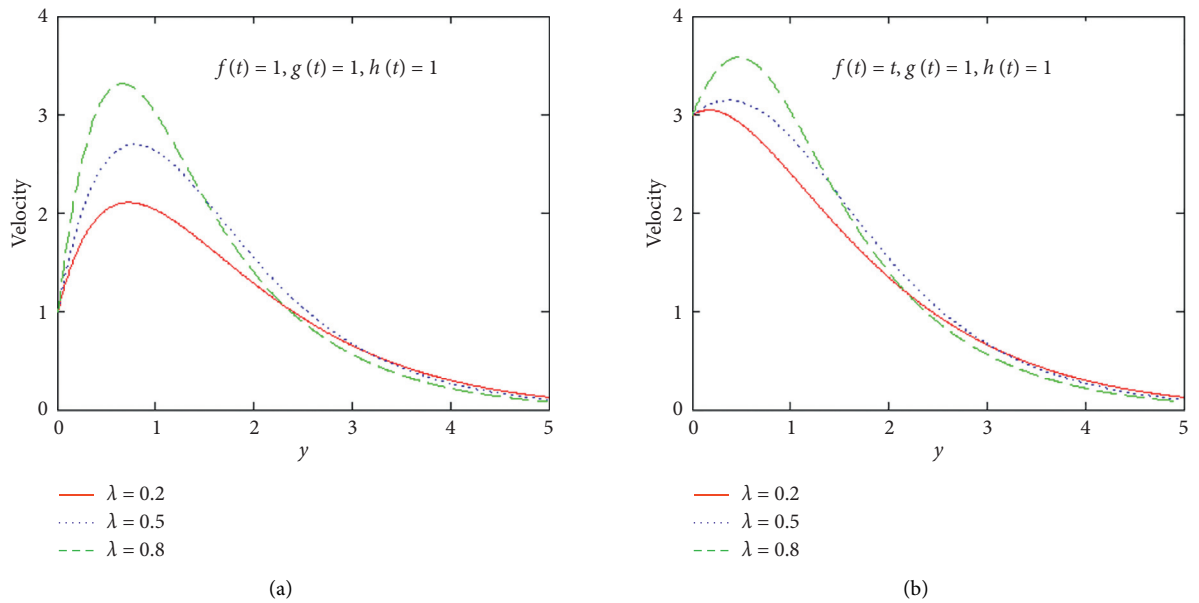
Figure 15: Continued.
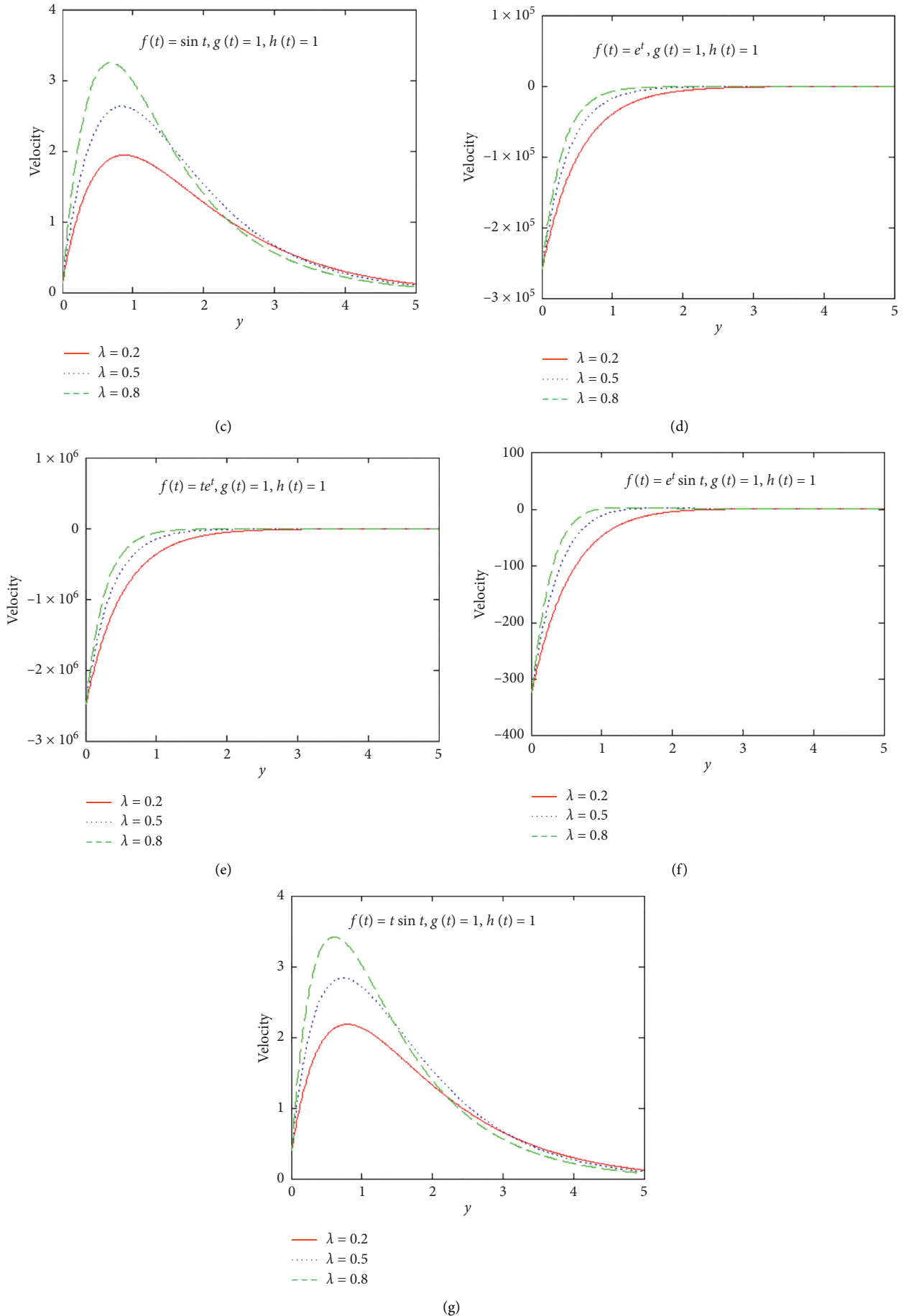
FIGURE 15: Profile of velocity for different values of λ and $M = 2.0, G_C = 2.0, S = 1.5, K_c = 0.5, S_c = 0.60, G_T = 10.0, P_r = 0.5$.

(a)

(b)

(c)

(d)

(e)

(f)
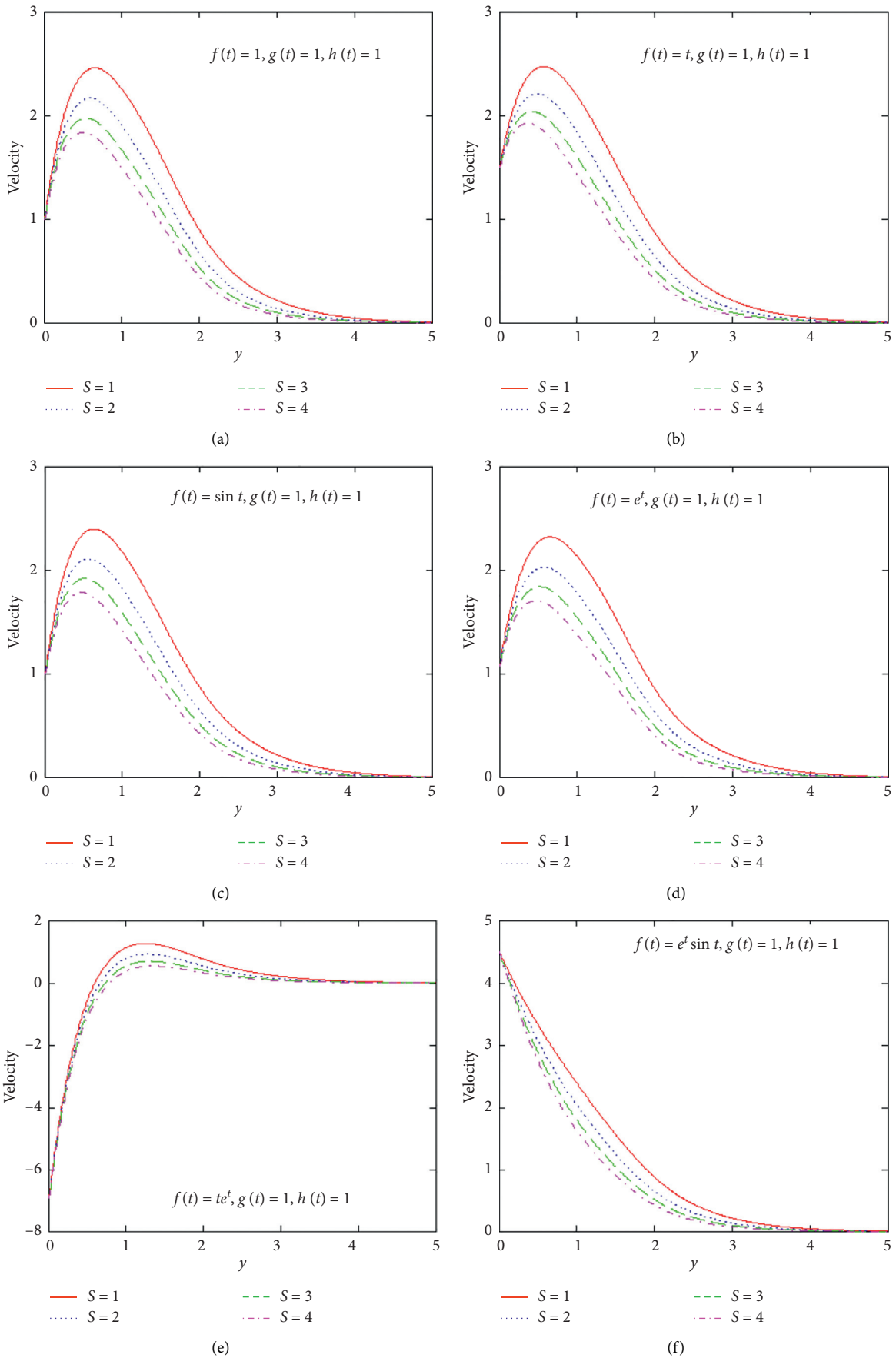
FIGURE 16: Continued.

(g)
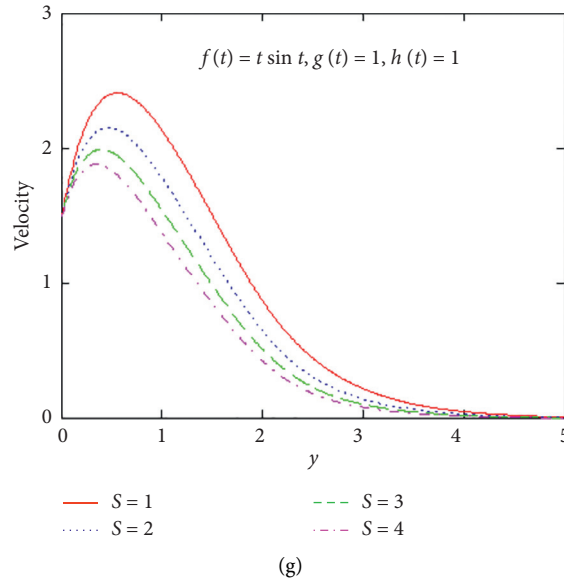
FIGURE 16: Profile of velocity for different values of S and $M = 2.0, G_C = 2.0, \lambda = 0.6, K_c = 0.5, S_c = 0.60, G_T = 10.0, P_r = 0.5$.

(a)

(b)

(c)

(d)
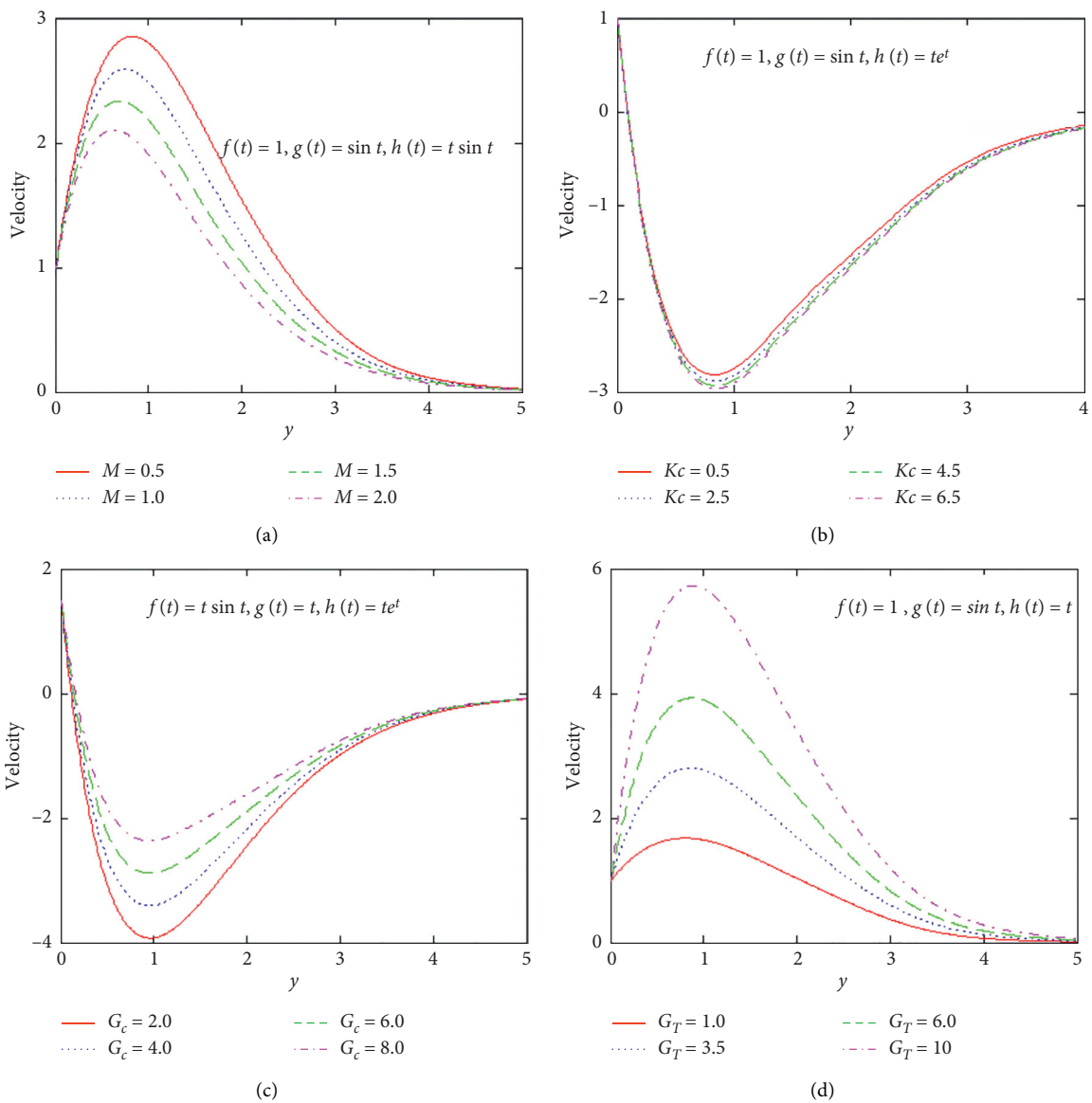
FIGURE 17: Continued.

(e)

(f)
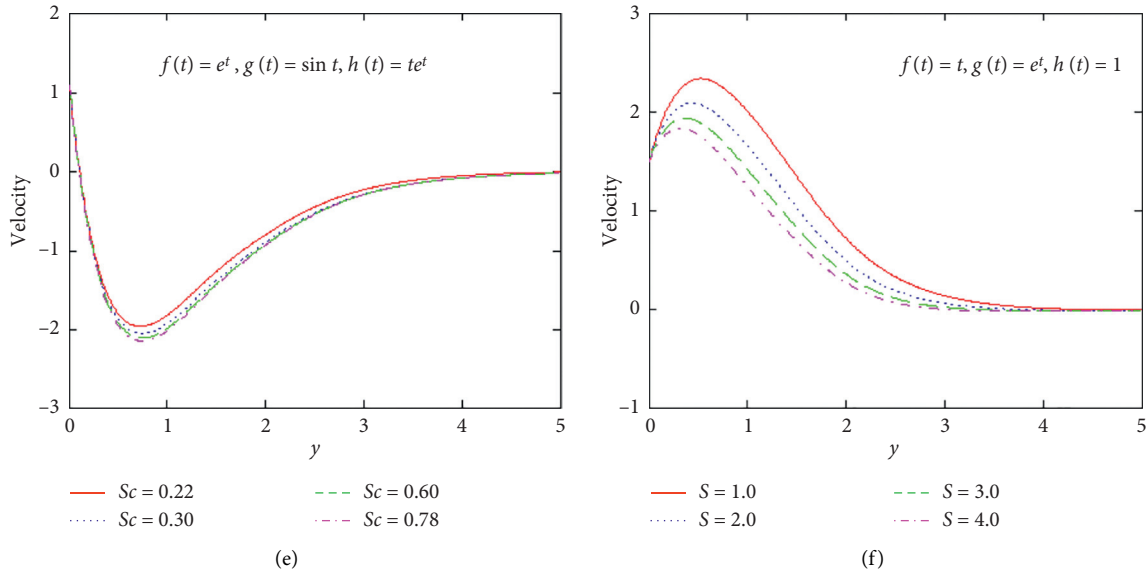
Figure 17: Profile of velocity for different values of M, S, S_c, K_c, G_T, G_C and different choice of function for $f(t), g(t), h(t)$.

(a)

(b)
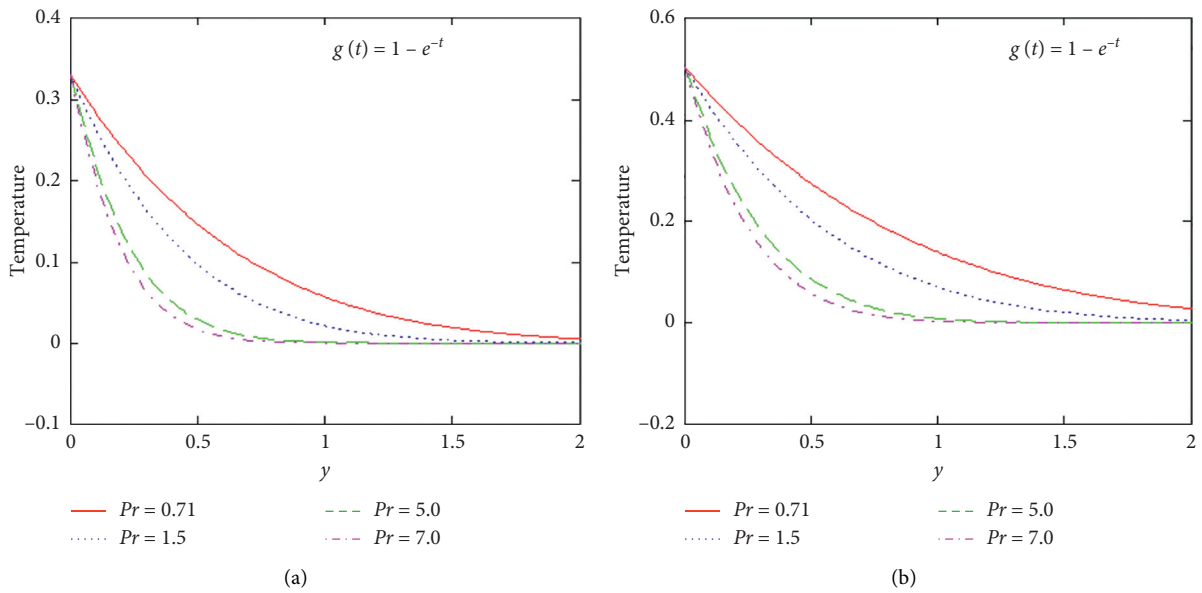
Figure 18: Temperature profile for different values of P_r with $S = 0.5$ and $g(t) = 1 - e^{-t}$.
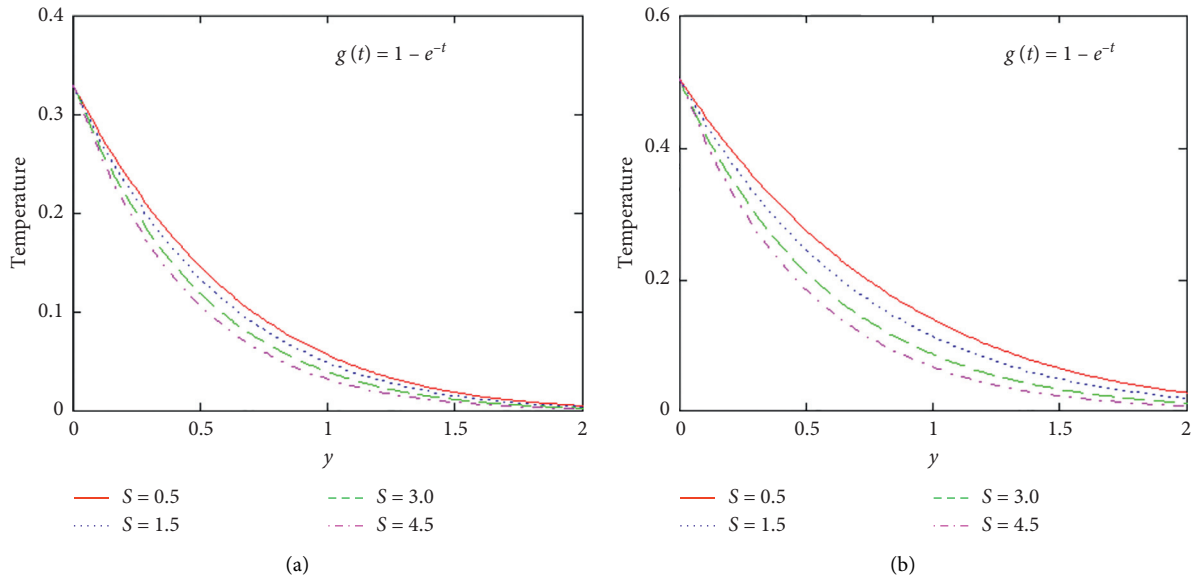
FIGURE 19: Temperature profile for different values of S with $P_r = 0.71$ and $g(t) = 1 - e^{-t}$.
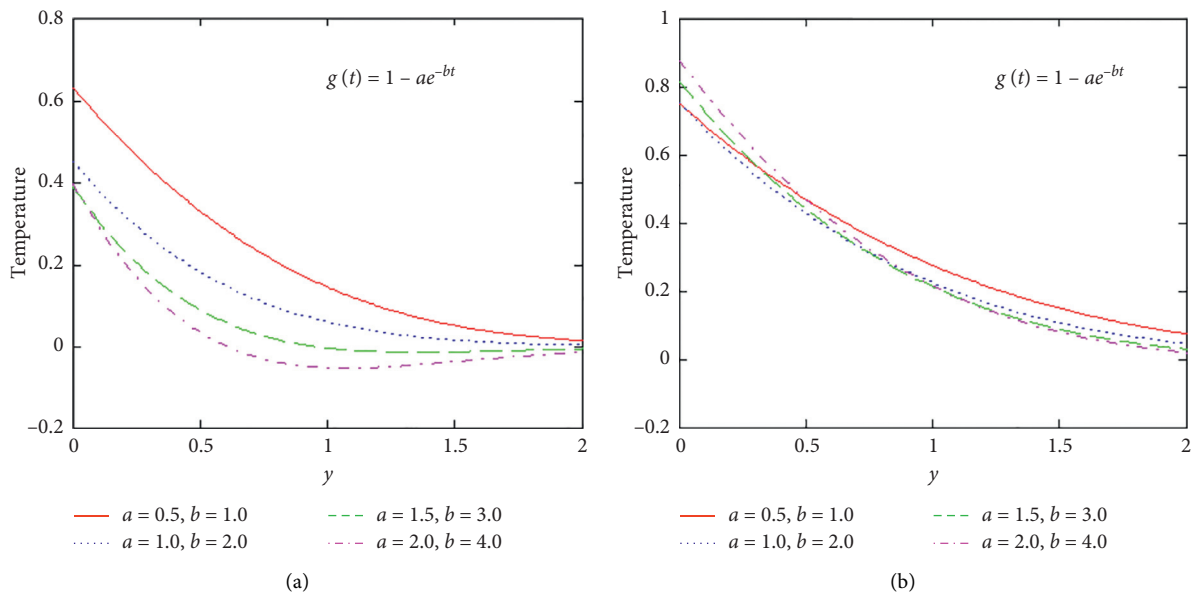
FIGURE 20: Temperature profile for different values of a, b with $P_r = 0.71$, $S = 0.5$ and $g(t) = 1 - ae^{-bt}$.

6. Conclusions

A thorough investigation of MHD Maxwell fluid motion has been studied here under the effects of different parameters. The exact solutions are obtained for concentration, temperature, and velocity which satisfied the described initial and boundary conditions. Laplace transform is employed to obtain the exact solution and the behavior of different parameters on the flow of fluid along with different boundary conditions is investigated. Effects of chemical reaction coefficient, Schmidt number, and different boundary conditions on concentration, effects of Prandtl number, heat

source, Newtonian heating, etc. on temperature, Magnetic parameter, Schmidt number, thermal Grashof number, relaxation parameter, mass Grashof number, Prandtl number, heat source, and chemical reaction impacts on the fluid motion are discussed. The results obtained are as follows:

(1) The boundary layer thickness of concentration decreases with the increase in the mass diffusivity S_c and chemical reaction parameter K_C.

(2) The thermal boundary layer decreases with the increase in momentum boundary layer due to P_r and heat absorption S.

(3) Lorentz force effects due to M, momentum boundary layer effects due to P_r, mass diffusivity effects due to S_c, chemical reaction K_c, and heat absorption decrease the velocity with the increase of these parameters.

(4) Increase in buoyancy forces due to G_T and G_C stimulates the speed of fluid flow.

(5) A rise in relaxation time λ reduces the fluid viscosity and results in acceleration of fluid flow.

Appendix

$$B_1(y,t) = \begin{cases} 0, & 0 < t < y\lambda, \\ e^{-\alpha_1 t} I_0\left(i\alpha_3\sqrt{t^2 - \lambda y^2}\right), & t > y\lambda, \end{cases} \tag{A.1}$$

$$B_2^{II}(t) = \left(e^{-\alpha_1 t}\left((i\alpha_3)I_1(i\alpha_3 t) + \delta(t)\right)\right)^* (1 + \alpha_1 t) + \left(\alpha_3^2 e^{-\alpha_1 t} I_0(i\alpha_3 t)\right)^* t, \tag{A.2}$$

$$B_3^{II}(t) = (1 + \lambda H(t))^* \left(A^* + B^* e^{-(\alpha_4 + \alpha_6)t} + C^* e^{-(\alpha_4 - \alpha_6)t}\right)^* e^{-\alpha_1 t} I_0(i\alpha_3 t), \tag{A.3}$$

$$B_4^{II}(t) = (1 + \lambda H(t)^* \left(D^* + E^* e^{-(\alpha_7 + \alpha_9)t} + F^* e^{-(\alpha_7 - \alpha_9)t}\right)^* e^{-\alpha_1 t} I_0(i\alpha_3 t), \tag{A.4}$$

$$B_2^{III}(t) = \left(e^{-\alpha_1 t}\left((i\alpha_3)I_1(i\alpha_3 t) + \delta(t)\right)\right)^* (\cos t + \alpha_1 \sin t) + \left(\alpha_3^2 e^{-\alpha_1 t} I_0(i\alpha_3 t)\right)^* \sin t, \tag{A.5}$$

$$B_3^{III}(t) = (\cos t + \lambda H(t)^* \cos t)^* \left(A^* + B^* e^{-(\alpha_4 + \alpha_6)t} + C^* e^{-(\alpha_4 - \alpha_6)t}\right)^* e^{-\alpha_1 t} I_0(i\alpha_3 t), \tag{A.6}$$

$$B_4^{III}(t) = (\cos t + \lambda H(t)^* \cos t)^* \left(D^* + E^* e^{-(\alpha_7 + \alpha_9)t} + F^* e^{-(\alpha_7 - \alpha_9)t}\right)^* e^{-\alpha_1 t} I_0(i\alpha_3 t), \tag{A.7}$$

$$B_2^{IV}(t) = \left(e^{-\alpha_1 t}\left((i\alpha_3)I_1(i\alpha_3 t) + \delta(t)\right)\right)^* \left((H(t) + \alpha_1)^* e^t\right) + \left(\alpha_3^2 e^{-\alpha_1 t} I_0(i\alpha_3 t)\right)^* e^t, \tag{A.8}$$

$$B_3^{IV}(t) = \left(e^t + \lambda H(t)^* e^t\right)^* \left(A^* + B^* e^{-(\alpha_4 + \alpha_6)t} + C^* e^{-(\alpha_4 - \alpha_6)t}\right)^* e^{-\alpha_1 t} I_0(i\alpha_3 t), \tag{A.9}$$

$$B_4^{IV}(t) = \left(e^t + \lambda H(t)^* e^t\right)^* \left(D^* + E^* e^{-(\alpha_7 + \alpha_9)t} + F^* e^{-(\alpha_7 - \alpha_9)t}\right)^* e^{-\alpha_1 t} I_0(i\alpha_3 t), \tag{A.10}$$

$$B_2^{V}(t) = \left(e^{-\alpha_1 t}\left((i\alpha_3)I_1(i\alpha_3 t) + \delta(t)\right)\right)^* \left(e^t + (1 + \alpha_1)t e^t\right) + \left(\alpha_3^2 e^{-\alpha_1 t} I_0(i\alpha_3 t)\right)^* t e^t, \tag{A.11}$$

$$B_3^{V}(t) = \left(e^t(1 + t) + \lambda H(t)^* e^t(1 + t)\right)^* \left(A^* + B^* e^{-(\alpha_4 + \alpha_6)t} + C^* e^{-(\alpha_4 - \alpha_6)t}\right) {}^* e^{-\alpha_1 t} I_0(i\alpha_3 t), \tag{A.12}$$

$$B_4^{V}(t) = \left(e^t(1 + t) + \lambda H(t)^* e^t(1 + t)\right)^* \left(D^* + E^* e^{-(\alpha_7 + \alpha_9)t} + F^* e^{-(\alpha_7 - \alpha_9)t}\right) {}^* e^{-\alpha_1 t} I_0(i\alpha_3 t). \tag{A.13}$$

$$B_2^{VI}(t) = \left(e^{-\alpha_1 t}\left((i\alpha_3)I_1(i\alpha_3 t) + \delta(t)\right)\right)^* \left(e^t \cos t + (1 + \alpha_1)e^t \sin t\right) + \left(\alpha_3^2 e^{-\alpha_1 t} I_0(i\alpha_3 t)\right) {}^* e^t \sin t. \tag{A.14}$$

$$B_3^{VI}(t) = \left(e^t \cos t + e^t \sin t + \lambda H(t)^* \left(e^t \cos t + e^t \sin t\right)\right)^* \left(A^* + B^* e^{-(\alpha_4 + \alpha_6)t} + C^* e^{-(\alpha_4 - \alpha_6)t}\right) {}^* e^{-\alpha_1 t} I_0(i\alpha_3 t). \tag{A.15}$$

$$B_4^{VI}(t) = \left(e^t \cos t + e^t \sin t + \lambda H(t)^* \left(e^t \cos t + e^t \sin t\right)\right)^* \left(D^* + E^* e^{-(\alpha_7 + \alpha_9)t} + F^* e^{-(\alpha_7 - \alpha_9)t}\right) \\ {}^* e^{-\alpha_1 t} I_0(i\alpha_3 t). \tag{A.16}$$

$$B_2^{VII}(t) = \left(e^{-\alpha_1 t}\left((i\alpha_3) I_1(i\alpha_3 t) + \delta(t)\right)\right)^* \left(H(t) + (1 + \alpha_1) t \sin t\right) + \left(\alpha_3^2 e^{-\alpha_1 t} I_0(i\alpha_3 t)\right) \\ {}^* t \sin t, \tag{A.17}$$

$$B_3^{VII}(t) = \left((t \sin t + t \cos t) + \lambda H(t)^* (\sin t + \lambda \cos t)\right)^* \left(A^* + B^* e^{-(\alpha_4 + \alpha_6)t} + C^* e^{-(\alpha_4 - \alpha_6)t}\right) \\ {}^* e^{-\alpha_1 t} I_0(i\alpha_3 t), \tag{A.18}$$

$$B_4^{VII}(t) = \left((t \sin t + t \cos t) + \lambda H(t)^* (\sin t + \lambda \cos t)\right)^* \left(D^* + E^* e^{-(\alpha_7 + \alpha_9)t} + F^* e^{-(\alpha_7 - \alpha_9)t}\right) \\ {}^* e^{-\alpha_1 t} I_0(i\alpha_3 t), \tag{A.19}$$

$$L^{-1}\left[\frac{e^{-b\sqrt{q^2 - a^2}}}{\sqrt{q^2 - a^2}}\right] = \begin{cases} 0, & 0 < t < b, b > 0, \\ I_0\left(a\sqrt{t^2 - b^2}\right), & t > b, \operatorname{Re}(q) > \operatorname{Re}(a), \end{cases} \tag{A.20}$$

$$L^{-1}[F(q + m)] = f(t) e^{-mt}, \tag{A.21}$$

$$L^{-1}\left[\frac{\exp(-y\sqrt{q + a})}{q - b}\right] = e^{bt} \Phi(y; t, a + b), \tag{A.22}$$

$$\Phi(y, t; a) = \frac{1}{2}\left\{e^{y\sqrt{a}} \operatorname{ercf}\left(\frac{y}{2\sqrt{t}} + \sqrt{at}\right) + e^{-y\sqrt{a}} \operatorname{ercf}\left(\frac{y}{2\sqrt{t}} - \sqrt{at}\right)\right\}, \tag{A.23}$$

$$L^{-1}\left[\frac{\exp(-y\sqrt{q + a})}{q - b}\right] = e^{bt} \Psi(y; t, a + b), \tag{A.24}$$

$$\Psi(y, t; a) = \frac{1}{2}\left\{e^{y\sqrt{a}} \operatorname{ercf}\left(\frac{y}{2\sqrt{t}} + \sqrt{at}\right) + e^{-y\sqrt{a}} \operatorname{ercf}\left(\frac{y}{2\sqrt{t}} - \sqrt{at}\right)\right\}. \tag{A.25}$$

Data Availability

The data used to support the findings of this study are included within the article.

Conflicts of Interest

The authors declare that they have no conflicts of interest.

Acknowledgments

References

[1] C.-Y. Cheng, "Natural convection heat and mass transfer from a sphere in micropolar fluids with constant wall temperature and concentration," *International Communications in Heat and Mass Transfer*, vol. 35, no. 6, pp. 750–755, 2008.

[2] K. R. Cramer and S. I. Pai, *Magneto Fluid Dynamics for Engineers and Applied Physicists*, pp. 204–237, McGraw-Hill Book Co New York, New York, NY, USA, 1973.

[3] N. F. M. Noor, S. Abbasbandy, and I. Hashim, "Heat and mass transfer of thermophoretic MHD flow over an inclined radiate isothermal permeable surface in the presence of heat source/sink," *International Journal of Heat and Mass Transfer*, vol. 55, no. 7-8, pp. 2122–2128, 2012.

[4] S. M. Mousazadeh, M. M. Shahmardan, T. Tavangar, K. Hosseinzadeh, and D. D. Ganji, "Numerical investigation on convective heat transfer over two heated wall-mounted cubes in tandem and staggered arrangement," *Theoretical and Applied Mechanics Letters*, vol. 8, no. 3, pp. 171–183, 2018.

[5] F. M. Oudina, F. Redouane, F. Redouane, and C. Rajashekhar, "Convection heat transfer of MgO-Ag/water magneto-hybrid nanoliquid flow into a special porous enclosure," *Algerian Journal of Renewable Energy and Sustainable Development*, vol. 2, no. 2, pp. 84–95, 2020.

[6] S. S. Das, A. Satapathy, J. K. Das, and J. P. Panda, "Mass transfer effects on MHD flow and heat transfer past a vertical porous plate through a porous medium under oscillatory suction and heat source," *International Journal of Heat and Mass Transfer*, vol. 52, no. 25-26, pp. 5962–5969, 2009.

[7] S. M. Abo-Dahab, M. A. Abdelhafez, F. Mebarek-Oudina, and S. M. Bilal, "MHD Casson nanofluid flow over nonlinearly heated porous medium in presence of extending surface effect with suction/injection," *Indian Journal of Physics*, vol. 23, 2021.

[8] S. Sajad, A. Nori, K. Hosseinzadeh, and D. D. Ganji, "Hydrothermal analysis of MHD squeezing mixture fluid suspended by hybrid nano particles between two parallel plates," *Case Studies in Thermal Engineering*, vol. 21, Article ID 100650, 2020.

[9] N. Iftikhar, S. M. Husnine, and M. B. Riaz, "Heat and mass transfer in MHD Maxwell fluid over an infinite vertical plate," *Journal of Prime Research in Mathematics*, vol. 15, pp. 63–80, 2019.

[10] M. Ahmed, "Megahed, Variable fluid properties and variable heat flux effects on the flow and heat transfer in a non-Newtonian Maxwell fluid over an unsteady stretching sheet with slip velocity," *Chinese Physics B*, vol. 922, Article ID 094701, 2013.

[11] S. Marzougui, M. Bouabid, F. Mebarek-Oudina, N. Abu-Hamdeh, M. Magherbi, and K. Ramesh, "A computational analysis of heat transport irreversibility phenomenon in a magnetized porous channel," *International Journal of Numerical Methods for Heat & Fluid Flow*, vol. 43, 2020.

[12] D. Belatrache, N. Saifi, A. Harrouz, and S. Bentouba, "Modelling and numerical investigation of the thermal properties effect on the soil temperature in Adrar region," *Algerian Journal of Renewable Energy and Sustainable Development*, vol. 2, no. 2, pp. 165–174, 2020.

[13] K. Hosseinzadeh, A. R. Mogharrebi, A. Asadi, M. Paikar, and D. D. Ganji, "Effect of fin and hybrid nano-particles on solid process in hexagonal triplex latent heat thermal energy storage system," *Journal of Molecular Liquids*, vol. 300, Article ID 112347, 2020.

[14] M. Gholinia, S. Gholinia, K. Hosseinzadeh, and D. D. Ganji, "Investigation on ethylene glycol nano fluid flow over a vertical permeable circular cylinder under effect of magnetic field," *Results in Physics*, vol. 9, pp. 1525–1533, 2018.

[15] J. Rahimi, D. D. Ganji, M. Khaki, and K. Hosseinzadeh, "Solution of the boundary layer flow of an Eyring-Powell non-Newtonian fluid over a linear stretching sheet by collocation method," *Alexandria Engineering Journal*, vol. 56, no. 4, pp. 621–627, 2017.

[16] K. Hosseinzadeh, M. A. E. Moghaddam, A. Asadi, A. R. Mogharrebi, and D. D. Ganji, "Effect of internal fins along with Hybrid Nano-Particles on solid process in star shape triplex Latent Heat Thermal Energy Storage System by numerical simulation," *Renewable Energy*, vol. 154, pp. 497–507, 2020.

[17] U. S. Rajput and S. Kumar, "Radiation effects on MHD flow past an impulsively started vertical plate with variable heat and mass transfer," *IJAMM, International Journal of Applied Mathematics and Mechanics*, vol. 8, pp. 66–85, 2012.

[18] A. S. Gupta, "Steady and transient free convection of an electrically conducting fluid from a vertical plate in the presence of magnetic field," *Archives of Applied Science Research*, vol. 8, pp. 319–333, 1961.

[19] M. F. El-Amin, "MHD free convection and mass transfer flow in micropolar fluid with constant suction," *Journal of Magnetism and Magnetic Materials*, vol. 243, no. 3, pp. 567–574, 2006.

[20] S. Nadeem, R. U. Haq, and Z. H. Khan, "Numerical study of MHD boundary layer flow of a Maxwell fluid past a stretching sheet in the presence of nanoparticles," *Journal of the Taiwan Institute of Chemical Engineers*, vol. 45, no. 1, pp. 121–126, 2014.

[21] J. Zhao, L. Zheng, X. Zhang, and F. Liu, "Unsteady natural convection boundary layer heat transfer of fractional Maxwell viscoelastic fluid over a vertical plate," *International Journal of Heat and Mass Transfer*, vol. 97, pp. 760–766, 2016.

[22] N. Ahmad, "Soret and radiation effects on transient MHD free convection from an impulsively started infinite verticl plate," *The Journal of Heat Transfer*, vol. 134, Article ID 062701, 2012.

[23] R. C. Chaudhary and A. Jain, "An exact solution of magnetohydrodynamic convection flow past an accelerated surface embedded in a porous medium," *International Journal of Heat and Mass Transfer*, vol. 53, no. 7-8, pp. 1609–1611, 2010.

[24] K. Das, "Exacat solution of MHD free convection flow and mass transfer near a moving vertical plate in presesnce of thermal radiation," *African Journal of Mathematical Physics*, vol. 8, pp. 29–41, 2010.

[25] K. Das and S. Jana, "Heat and mass transfer effects on unsteady MHD free convection flow near a moving plate in porous medium," *Bulletin of Society of Mathematicians*, vol. 17, pp. 15–32, 2010.

[26] C. Fetecau and N. A. Shah, "Dumitru vieru general solutions for hydromagnetic free convection flow over an infinite plate with Newtonian heating, mass diffusion and chemical reaction," *Communications in Theoretical Physics*, vol. 68, p. 6, 2017.

[27] N. A. Shah, "Heat and mass transfer in hydromagnetic flows of viscous fluids over a flat plate" Phd thesis, Government College University Lahore, Lahore, Pakistan, 2019.

Research Article

Generalized Type-I Hybrid Censoring Scheme in Estimation Competing Risks Chen Lifetime Populations

Neveen Sayed-Ahmed [iD],[1,2] **Taghreed M. Jawa,**[1] **Tahani A. Aloafi,**[1] **F. S. Bayones,**[1] **Azhari A. Elhag,**[1] **J. Bouslimi,**[3] **and G. A. Abd-Elmougod**[4]

[1]*Department of Mathematics and Statistics, College of Science, P.O. Box 11099, Taif University, Taif 21944, Saudi Arabia*
[2]*Statistics Department, Faculty of Commerce (Girl Branch), Al-Azhar University, Cairo, Egypt*
[3]*Department of Physics, College of Science, P.O. Box 11099, Taif University, Taif 21944, Saudi Arabia*
[4]*Mathematics Department, Faculty of Science, Damanhour University, Damanhour, Egypt*

Correspondence should be addressed to Neveen Sayed-Ahmed; nevensayd@yahoo.com

Different types of censoring scheme are investigated; however, statistical inference on censoring scheme which can save the ideal test time and the minimum number of failures is needed. The generalized type-I hybrid censoring scheme (GHCS) solves this problem. Competing the risk models under the GHCS when time to failure has Chen lifetime distribution (CD) is adopted in this research with consideration of only two cases of failure. Partially step-stress accelerated life tests (ALTs) are applied to obtain enough failure times in a small period to achieve a highly reliable product. The problem of parameter estimation under maximum likelihood (ML) and Bayes methods is discussed. The asymptotic confidence interval as well as the Bayes credible interval is constructed. The validity of theoretical results is assessed and compared through simulation study. Finally, brief comments are reported to describe the behaviour of the estimation results.

1. Introduction

Information about the lifetime products is presented in complete or censored data with respect to time or cost considerations. The complete failure time data is used when all the units under the test fail through the determined period of time. However, the censoring failure time data is used when some units under the test fail through a determined period of time. Various types of censoring are available and the common types are called type-I and type-II censoring schemes. The first scheme has a prefixed test time and a random number of failures but the second scheme has a prefixed number of failures and a random test time. In serval cases of censoring, the test is required to run joint case of type-I and type-II censoring schemes described by the hybrid censoring scheme (HCS). The HCS can be described statistically as follows: suppose (τ, T_m) denote the ideal test time and the time of m failure which is used for statistical inference, respectively, and the test is removed at

the only one time of them. Then, HCS is defined under type-I and type-II censoring schemes and is called type-I HCS and type-II HCS. The test is removed at min (τ, T_m) in the type-I HCS, but at max (τ, T_m) in the type-II HCS, there is more information about the type of censoring presented by [1–3]. Furthermore, type-I censoring scheme or type-I HCS may satisfy the properties that the test has the smallest number of failures or maybe zero. However, type-II censoring scheme or type-II HCS satisfies the properties that the test has the largest number of failures; see [4]. The problem that appeared in these censoring schemes can be overcome in the generalized form of HSC; see [5] as type-I GHCS and type-II GHCS.

(1) In type-I GHCS, suppose n independent units are put under test and the prior integers r and m satisfy that $1 \leq r < m \leq n$ and prior time τ. If the smallest number r is satisfied before τ $(T_r < \tau)$, then the test is terminated at min (T_m, τ) and the observed test times data are given by

$$\underline{t} = \left(t_{1;n} < t_{1;n} < \cdots < t_{r;n} < \cdots < t_{s;n} \right), \quad r \leq s \leq m. \tag{1}$$

However, if the smallest number r does not satisfy before τ ($\tau < T_r$), then the test is terminated at T_r and the observed test times data are given by

$$\underline{t} = \left(t_{1;n} < t_{1;n} < \cdots < t_{r;n} \right). \tag{2}$$

Finally, if the largest number m is satisfied before τ ($T_m < \tau$),, then the test is terminated at T_m and the observed test times are given by

$$\underline{t} = \left(t_{1;n} < t_{1;n} < \cdots < t_{m;n} \right). \tag{3}$$

Therefore, the type-I GHCS saves the minimum number which is necessary for statistical inferences.

(2) In type-II GHCS, let n independent units be put under test and the two prior times τ_1 and τ_2 such that $\tau_1 < \tau_2$ and integer m satisfies $1 \leq m \leq n$. If the required number of failures is observed before τ_1 ($T_m < \tau_1$), then the test is terminated at τ_1 and the observed test times data are given by

$$\underline{t} = \left(t_{1;n} < t_{1;n} < \cdots < t_{m;n} < \cdots < t_{s;n} \right), \quad m \leq s \leq n. \tag{4}$$

On the other hand, if the required number of failures observed satisfies $\tau_1 < T_m < \tau_2$, then the test is terminated at T_m and the observed test times data are given by

$$\underline{t} = \left(t_{1;n} < t_{1;n} < \cdots < t_{m;n} \right). \tag{5}$$

Finally, if the required number of failures is observed to satisfy $\tau_1 < \tau_2 < T_m$, then the test is terminated at τ_2 and the observed test times are given by

$$\underline{t} = \left(t_{1;n} < t_{1;n} < \cdots < t_{s;n} \right), \quad 1 \leq s \leq m. \tag{6}$$

In life testing experiments, the common problem is that units fail due to several fetal risks which are known as competing risks problem.

The effect of any risk factor in the presence of other risk factors need to be assessed. This problem has been discussed early in [6–10] and recently in [11]. Under the consideration of two causes of failure, the competing risks model in the presence of type-I GHCS is presented as follows.

For a randomly selected n independent unit, a life testing experiment with priors integers r and m, $1 \leq r < m \leq n$, is considered. At each step of the experiment, time $T_{i;n}$ and the cause of failure ρ_i are recorded for $i = 1, 2, \ldots, d$, where d satisfies $r < d < m$ and $\rho_i \in \{1, 2\}$. Then, the joint likelihood function of type-I GHCS where $t = \{(t_{1;n}, \rho_1), (t_{2;n}, \rho_2), \ldots, (t_{d;n}, \rho_d)\}$ under the competing risks model is reported as

$$L(\underline{t} \mid \Theta) = A [S_1(t_d) S_2(t_d)]^{(n-d)} \prod_{i=1}^{d} [h_1(t_i)]^{\delta(\rho_i=1)} [h_2(t_i)]^{\delta(\rho_i=2)}, \tag{7}$$

where $A = n!/(n-d)!$, $S(.) = 1 - F(.)$, $h(.) = f(.)/F(.)$, $\delta(\rho_i = j) = \begin{cases} 1, & \rho_i = j, \\ 0, & \rho_i \neq j, \end{cases}$ and for $t_i = t_{i;n}$, $0 < t_1 < t_2 < \cdots < t_m < \infty$.

To obtain more information about the lifetime of products industrial process, accelerated life tests (ALTs) present a suitable manner for reducing test time rather than using conditions. As we see in [12], ALTs are presented in different types; one of them is constant-stress ALTs, in which the test is kept with a constant level of stress; see [13–15]. The second type is called progressive-stress ALTs, in which the stress is kept with a continuously increasing level; see [16–18]. The third type is called step-stress ALTs, in which the stress level is changed through a prior time or the number of failures; see [19, 20]. Furthermore, the ALTs can be done under the accelerated condition which is known by partial ALTs; see [21–26].

This paper aims to build and analyze type-I GHC competing risks sample under the model of partially step-stress ALTs from Chen lifetime products. The results of statistical analysis are built under maximum likelihood and Bayes method for point and interval estimation. The performances of the developed results are assessed and compared with mean squared error (MSE), average interval length (AL), and probability coverage (PC) through the Monte Carlo study.

This paper is structured as follows: the model formulation and abbreviation are presented in Section 2. The MLEs of model parameters as well as the asymptotic confidence intervals are investigated in Section 3. Bayes estimation with credible intervals is discussed in Section 4. The quality points and interval estimators are assessed via the Monte Carlo study in Section 5. Finally, the discussion and conclusion are presented in Section 6 (Table 1).

2. Abbreviation and Model Formulation

2.1. Abbreviations

2.1.1. Model Formulation. Suppose n identical units are under life testing and two prior integer numbers r and m satisfy that $1 \leq r < m \leq n$ and prior fixed time τ. The failure times T_i and cause of failure ρ_i are recorded through the test steps. If the smallest number of failure units r is satisfied before time τ, then the test is terminated at $\min(T_m, \tau)$. However, if r is satisfied after the time τ, then the test is terminated at T_r. The test is running under conditions until a fixed time η; then, the test is ruining under accelerated conditions. Considering that, the failure time has an independent CD and two independent causes of failure to satisfy the following assumptions:

(1) The random variable T_{ji} is distributed with CD(α, β_j), $j = 1, 2$ with PDF given by

$$f_{j1}(t) = \alpha \beta_j t^{\alpha-1} e^{t^\alpha + \beta_j [1 - e^{t^\alpha}]}, \quad t > 0, \alpha, \beta_j > 0, \tag{8}$$

and CDF is given by

Table 1: List of abbreviations.

PDF	Probability density function
CDF	Cumulative probability function
t_i	The i-th unit failure time
t_{ji}	The i-th unit failure time under cause j, $j = 1, 2$
$f(.)$	The PDF of t_i
$F(.)$	The CDF of t_i
$S(.)$	Survival function of t_i
$h(.)$	Hazard failure rate of t_i
$f_j(.)$	The PDF of t_{ji}
$F_j(.)$	The CDF of t_{ji}
$S_j(.)$	Survival function of t_{ji}
$h_j(.)$	Hazard failure rate function of t_{ji}
ρ_i	The cause of failure form i-th unit failure time
$CD(\alpha, \beta)$	Chen distribution with PDF $\alpha\beta t^{\alpha-1} e^{\{t^\alpha + \beta[1 - e^{t^\alpha}]\}}$
MLE	Maximum likelihood estimators
AV	Average estimate
MSE	Mean squared error
AL	Average interval length
PC	Probability coverage

$$F_{j1}(t) = 1 - e^{\beta_j [1 - e^{t^\alpha}]}. \tag{9}$$

Also, $S_{j1}(t)$ and $h_{j1}(t)$ of $CD(\alpha, \beta_j)$ are, respectively, given by

$$S_{j1}(t) = e^{\beta_j [1 - e^{t^\alpha}]}, \tag{10}$$
$$h_{j1}(t) = \alpha\beta_j t^{\alpha-1} e^{t^\alpha}.$$

(2) The random failure times T_i, $i = 1, 2, \ldots, d$, with the failure times under cause j T_{ji}, satisfy $T_i = \min\{T_{1i}, T_{2i}\}$.

(3) The total lifetime under use and accelerated condition W under accelerated stress change η is defined by

$$W = \begin{cases} T, & T < \eta, \\ \eta + \dfrac{T - \eta}{\lambda}, & T > \eta, \end{cases} \tag{11}$$

where λ is the accelerated factor. The random variable W is distributed with Chen lifetime distribution with PDF and is given by

$$f_l(w) = \begin{cases} 0, & w < 0, \\ f_{j1}(w), & 0 < w < \eta, \\ f_{j2}(w), & w \geq \eta, \end{cases} \tag{12}$$

where

$$f_{j2}(w) = \alpha\lambda\beta_j (\eta + \lambda(w - \eta))^{\alpha-1} e^{(\eta + \lambda(w-\eta))^\alpha + \beta_j [1 - e^{(\eta+\lambda(w-\eta))^\alpha}]}, \tag{13}$$

and $f_{j1}(z)$ is given by (8). The CDF, $S_{j2}(z)$, and hazard rate function $h_{j2}(z)$ are given by

$$F_{j2}(w) = 1 - e^{\beta_j [1 - e^{(\eta + \lambda(w-\eta))^\alpha}]}, \tag{14}$$

$$S_{j2}(w) = e^{\beta_j [1 - e^{(\eta + \lambda(w-\eta))^\alpha}]}, \tag{15}$$

$$h_{j2}(w) = \alpha\lambda\beta_j (\eta + \lambda(w - \eta))^{\alpha-1} e^{(\eta + \lambda(w-\eta))^\alpha}. \tag{16}$$

(4) Under competing risks type-I GHC sample and partially step-stress ALTs model, the test is terminated at T_r at $\tau < T_r$ and $\min(\tau, T_m)$ at $\tau > T_r$. Then, the random sample of the total lifetime W is described by

$$\underline{W} = \{(W_1, \rho_1) < (W_2, \rho_2) < \cdots < (W_k, \rho_k) < \eta \\ < (W_{k+1}, \rho_{k+1}) < \cdots < (W_m, \rho_d)\}, \tag{17}$$

where d denotes the number of fail units, where $r < d < m$ and k and $m - k$ are the numbers of fail units under using and accelerated conditions, respectively. For this model, we can consider three different cases, $\tau < \eta$, $\tau = \eta$, or $\tau < \eta$. Hence, the joint likelihood function of the observed values $\underline{w} = \{(w_1, \rho_1) \ < (w_2, \rho_2) < \cdots < (w_k, \rho_k) \ < \eta < (w_{k+1}, \rho_{k+1}) < \cdots < (w_m, \rho_d)\}$ is obtained as follows:

$$L(\underline{t} \mid \underline{\Theta}) = A[S_{12}(w_d) S_{22}(w_d)]^{(n-d)} \prod_{i=1}^{k} [h_{11}(w_i)]^{\delta(\rho_i=1)}$$
$$[h_{21}(w_i)]^{\delta(\rho_i=2)} S_{11}(w_i) S_{21}(w_i) \times$$
$$\prod_{i=k+1}^{d} [h_{12}(w_i)]^{\delta(\rho_i=1)} [h_{22}(w_i)]^{\delta(\rho_i=2)} S_{12}(w_i) S_{22}(w_i). \tag{18}$$

3. Maximum Likelihood Estimation

When only two independent causes of failure and the test are running under the model of partially step-stress ALTs with type-I GHCS, the test information sample is used to obtain the point and interval MLEs which is reported in this section as follows.

3.1. MLEs. The joint likelihood function (18) under CDF (9) and (14) for the observed type-I GHC sample $\underline{w} = \{(w_1, \rho_1) < (w_2, \rho_2) < \cdots < (w_k, \rho_k) < \eta < (w_{k+1}, \rho_{k+1}) < \cdots < (w_m, \rho_d)\}$ is given by

$$L\left(\alpha,\beta_1,\beta_2,\lambda \mid \underline{w}\right) \propto \alpha^d \beta_1^{m_1} \beta_2^{m_2} \lambda^{d-k} \prod_{i=1}^{k} w_i^{\alpha-1} \prod_{i=k+1}^{d} \left(\eta + \lambda\left(w-\eta\right)\right)^{\alpha-1}$$

$$e^{-\left(\beta_1+\beta_2\right)\left\{(n-d)\left[e^{\left(\eta+\lambda\left(w_d-\eta\right)\right)^{\alpha}}\right]+\sum_{i=1}^{k} e^{w_i^{\alpha}}+\sum_{i=k+1}^{d} e^{\left(\eta+\lambda\left(w_i-\eta\right)\right)^{\alpha}}-n\right\}}$$

$$e^{\sum_{i=1}^{k} w_i^{\alpha}+\sum_{i=k+1}^{d}\left(\eta+\lambda\left(w-\eta\right)\right)^{\alpha}},$$

(19)

where integers k and $(d-k)$ are denoted to failure units under using and stress conditions, respectively, and integers m_1 and m_2 denoted failure units under causes (ρ_1, ρ_2). Then, the log-form from (19) is reduced to

$$\ell\left(\alpha,\beta_1,\beta_2,\lambda|\underline{w}\right) = d \log \alpha + m_1\log \beta_1 + m_2\log \beta_2 + (d-k)\log \lambda - \left(\beta_1 + \beta_2\right)$$

$$\times \left\{(n-d)e^{\left(\eta+\lambda\left(w_d-\eta\right)\right)^{\alpha}} + \sum_{i=1}^{k} e^{w_i^{\alpha}} + \sum_{i=k+1}^{d} e^{\left(\eta+\lambda\left(w_i-\eta\right)\right)^{\alpha}} - n\right\}$$

$$+ (\alpha-1)\left\{\sum_{i=1}^{k} \log w_i + \sum_{i=k+1}^{d} \log[\eta + \lambda\left(w-\eta\right)]\right\} + \sum_{i=1}^{k} w_i^{\alpha}$$

$$+ \sum_{i=k+1}^{m} \left(\eta + \lambda\left(w-\eta\right)\right)^{\alpha}.$$

(20)

The partial derivatives of log-likelihood function (20) are reduced to the likelihood equations solved with some numerical methods to obtain the estimates as follows:

$$0 = \frac{\partial\left(\alpha,\beta_1,\beta_2,\lambda|\underline{w}\right)}{\partial\beta_l}, \quad l = 1,2,$$

(21)

is reduced to

$$\beta_1 = \frac{m_1}{(n-d)e^{\left(\eta+\lambda\left(w_d-\eta\right)\right)^{\alpha}} + \sum_{i=1}^{k} e^{w_i^{\alpha}} + \sum_{i=k+1}^{d} e^{\left(\eta+\lambda\left(w_i-\eta\right)\right)^{\alpha}} - n},$$

(22)

$$\beta_2 = \frac{m_2}{(n-d)e^{\left(\eta+\lambda\left(w_d-\eta\right)\right)^{\alpha}} + \sum_{i=1}^{k} e^{w_i^{\alpha}} + \sum_{i=k+1}^{d} e^{\left(\eta+\lambda\left(w_i-\eta\right)\right)^{\alpha}} - n}.$$

(23)

Also,

$$0 = \frac{\partial\left(\alpha,\beta_1,\beta_2,\lambda|\underline{w}\right)}{\partial\alpha},$$

(24)

is reduced to

$$\frac{d}{\alpha} - \left(\beta_1 + \beta_2\right)\left\{(n-d)\left(\eta + \lambda\left(w_d - \eta\right)\right)^{\alpha} e^{\left(\eta+\lambda\left(w_d-\eta\right)\right)^{\alpha}} \log\left(\eta + \lambda\left(w_d - \eta\right)\right)\right.$$

$$+ \sum_{i=1}^{k} w_i^{\alpha} e^{w_i^{\alpha}} \log w_i + \sum_{i=k+1}^{d} \left(\eta + \lambda\left(w_i - \eta\right)\right)^{\alpha} e^{\left(\eta+\lambda\left(w_i-\eta\right)\right)^{\alpha}} \log\left(\eta + \lambda\left(w_i - \eta\right)\right)\bigg\}$$

$$+ \sum_{i=1}^{k} \log w_i + \sum_{i=k+1}^{d} \log[\eta + \lambda\left(w-\eta\right)] + \sum_{i=1}^{k} w_i^{\alpha}\log w_i$$

$$+ \sum_{i=k+1}^{m} \left(\eta + \lambda\left(w-\eta\right)\right)^{\alpha}\log\left(\eta + \lambda\left(w-\eta\right)\right) = 0,$$

$$0 = \frac{\partial\left(\alpha,\beta_1,\beta_2,\lambda|\underline{w}\right)}{\partial\lambda},$$

(25)

which is reduced to

$$\frac{(d-k)}{\lambda} - (\beta_1 + \beta_2) \left\{ \alpha (n-d)(w_d - \eta)(\eta + \lambda (w_d - \eta))^{\alpha-1} e^{(\eta + \lambda (w_d - \eta))^{\alpha}} \right.$$

$$+ \alpha \sum_{i=k+1}^{d} (w_i - \eta)(\eta + \lambda (w_i - \eta))^{\alpha-1} e^{(\eta + \lambda (w_i - \eta))^{\alpha}} \right\}$$

$$+ (\alpha - 1) \sum_{i=k+1}^{d} \frac{(w - \eta)}{\eta + \lambda (w - \eta)} + \alpha \sum_{i=k+1}^{m} (w_i - \eta)(\eta + \lambda (w_i - \eta))^{\alpha-1} = 0. \tag{26}$$

The likelihood equations are reduced to two nonlinear equations which are solved numerically with any iteration method such as Newton Raphson to obtain $\hat{\alpha}$ and $\hat{\lambda}$ which are used in (22) and (23) to present $\hat{\beta}_1$ and $\hat{\beta}_2$.

3.2. Interval Estimation. For the parameters vectors $\Theta = (\alpha, \beta_1, \beta_2, \lambda)$, the second partial derivatives of (20) with respect to Θ_i, where $\Theta_1 = \alpha$, $\Theta_2 = \beta_1$, $\Theta_3 = \beta_2$, $\Theta_4 = \lambda$, are given by

$$\frac{\partial (\alpha, \beta_1, \beta_2, \lambda | \underline{w})}{\partial \Theta_i \partial \Theta_l}, \quad i, l = 1, 2, 3, 4, \tag{27}$$

and the Fisher information matrix Σ is given by

$$\Sigma = -E\left(\frac{\partial^2 (\alpha, \beta_1, \beta_2, \lambda | \underline{w})}{\partial \Theta_i \partial \Theta_l}\right), \tag{28}$$

which is computed as the negative expectation of second partial derivatives (27). The approximate information matrix is used as the approximate form of the Fisher information matrix Σ specially in a large sample. The approximate information matrix Σ_0 at the maximum likelihood estimates $\hat{\Theta} = (\hat{\alpha}, \hat{\beta}_1, \hat{\beta}_2, \hat{\lambda})$ is given by

$$\Sigma_0 = -\left(\frac{\partial^2 (\alpha, \beta_1, \beta_2, \lambda | \underline{w})}{\partial \Theta_i \partial \Theta_l}\right)_{\hat{\Theta} = \{\hat{\alpha}, \hat{\beta}_1, \hat{\beta}_2, \hat{\lambda}\}}. \tag{29}$$

The asymptotic normality distribution of estimating $\hat{\alpha}$, $\hat{\beta}_1$, $\hat{\beta}_2$, and $\hat{\lambda}$ with mean $(\alpha, \beta_1, \beta_2, \lambda)$ and a variance covariance matrix $\Sigma_0^{-1}(\hat{\alpha}, \hat{\beta}_1, \hat{\beta}_2, \hat{\lambda})$ is as follows:

$$(\hat{\alpha}, \hat{\beta}_1, \hat{\beta}_2, \hat{\lambda}) \text{ distributed as } N\left((\alpha, \beta_1, \beta_2, \lambda), \Sigma_0^{-1}(\hat{\alpha}, \hat{\beta}_1, \hat{\beta}_2, \hat{\lambda})\right). \tag{30}$$

Therefore, $100(1 - \xi)$ intervals estimation of parameters vector $\Theta = \{\alpha, \beta_1, \beta_2, \lambda\}$ are computed by

$$\hat{\Theta}_i \mp z_{\xi/2} \sqrt{\Sigma_{ii}}, \quad i = 1, 2, 3, 4, \tag{31}$$

where $\hat{\Theta}_i$ denotes the parameters estimate and value Σ_{ii} denotes the diagonal of variance covariance matrix Σ_0^{-1} with standard normal probability $\xi/2$.

4. Bayesian Approach with MCMC

Information about the model parameters and the information which is obtained from the life sample is used in this section to build the Bayes approach with the MCMC method. Besides, the estimators of parameters of CD and noninformative about accelerated factor are computed under squared error loss (SEL) function and independent prior distributions. Therefore, independent gamma prior is adapted as follows:

$$\pi_l^*(\Theta_l) \propto \Theta_l^{a_l-1} e^{-b_l \Theta_l}, \quad l = 1, 2, 3, \text{ and } \pi_4^*(\Theta_4) \propto \Theta_4^{-1}, \tag{32}$$

$$\pi^*(\underline{\Theta}) = \prod_{l=1}^{4} \pi_l^*(\Theta_l), \tag{33}$$

where $\Theta = (\alpha, \beta_1, \beta_2, \lambda)$. Then, the posterior distribution of Θ is defined by

$$\pi(\underline{\Theta} | \underline{w}) = \frac{\pi^*(\underline{\Theta}) L(\underline{\Theta} | \underline{w})}{\int_{\underline{\Theta}} \pi^*(\underline{\Theta}) L(\underline{\Theta} | \underline{w}) d\underline{\Theta}}. \tag{34}$$

Then, the Bayes estimate for any function $\phi(\underline{\Theta})$ under SEL function is given by

$$\hat{\phi}_B(\underline{\Theta}) = \frac{\int_{\underline{\Theta}} \phi(\underline{\Theta}) \pi^*(\underline{\Theta}) L(\underline{\Theta} | \underline{w}) d(\underline{\Theta})}{\int_{(\underline{\Theta})} \pi^*(\underline{\Theta}) L(\underline{\Theta} | \underline{w}) d(\underline{\Theta})}. \tag{35}$$

Generally, the ratio in (35) needs numerical approximation to compute, such as numerical integration and Lindley approximation. However, MCMC methods are the important tools that were applied recently with high accuracy and are obtained as follows.

4.1. Gibbs with MH Method. The posterior distribution in (34) with prior distribution (33) and likelihood function (19) is calculated as;

$$\pi\left(\alpha,\beta_1,\beta_2,\lambda|\underline{w}\right) \propto \alpha^{a_1+d-1}\beta_1^{a_2+m_1-1}\beta_2^{a_3+m_2-1}\lambda^{d-k-1}\prod_{i=1}^{k}w_i^{\alpha-1}\prod_{i=k+1}^{d}\left(\eta+\lambda\left(w-\eta\right)\right)^{\alpha-1}$$

$$\cdot\, e^{-\left(\beta_1+\beta_2\right)\left\{(n-d)\left[e^{\left(\eta+\lambda\left(w_d-\eta\right)\right)^{\alpha}}\right]+\sum_{i=1}^{k}e^{w_i^{\alpha}}+\sum_{i=k+1}^{d}e^{\left(\eta+\lambda\left(w_i-\eta\right)\right)^{\alpha}}-n\right\}} \tag{36}$$

$$\cdot\, e^{-b_1\alpha-b_2\beta_1-b_3\beta_2+\sum_{i=1}^{k}e^{w_i^{\alpha}}+\sum_{i=k+1}^{m}\left(\eta+\lambda\left(w-\eta\right)\right)^{\alpha}}.$$

Then, the conditional PDFs of the posterior distribution is given by

$$\pi_1\left(\alpha|\beta_1,\beta_2,\lambda|\underline{w}\right)=\alpha^{a_1+d-1}e^{-\left(\beta_1+\beta_2\right)\left\{(n-d)\left[e^{\left(\eta+\lambda\left(w_d-\eta\right)\right)^{\alpha}}\right]+\sum_{i=1}^{k}e^{w_i^{\alpha}}+\sum_{i=k+1}^{d}e^{\left(\eta+\lambda\left(w_i-\eta\right)\right)^{\alpha}}\right\}}$$

$$e^{-b_1\alpha+\sum_{i=1}^{k}w_i^{\alpha}+\sum_{i=k+1}^{m}\left(\eta+\lambda\left(w-\eta\right)\right)^{\alpha}}\prod_{i=1}^{k}w_i^{\alpha-1}\prod_{i=k+1}^{d}\left(\eta+\lambda\left(w-\eta\right)\right)^{\alpha-1}, \tag{37}$$

$$\pi_2\left(\beta_1|\alpha,\beta_2,\lambda|\underline{w}\right)\propto\beta_1^{a_2+m_1-1}e^{-\beta_1\left\{b_2+(n-d)\left[e^{\left(\eta+\lambda\left(w_d-\eta\right)\right)^{\alpha}}\right]+\sum_{i=1}^{k}e^{w_i^{\alpha}}+\sum_{i=k+1}^{d}e^{\left(\eta+\lambda\left(w_i-\eta\right)\right)^{\alpha}}-n\right\}}, \tag{38}$$

$$\pi_3\left(\beta_2|\alpha,\beta_1,\lambda|\underline{w}\right)\propto\beta_2^{a_3+m_2-1}e^{-\beta_2\left\{b_3+(n-d)\left[e^{\left(\eta+\lambda\left(w_d-\eta\right)\right)^{\alpha}}\right]+\sum_{i=1}^{k}e^{w_i^{\alpha}}+\sum_{i=k+1}^{d}e^{\left(\eta+\lambda\left(w_i-\eta\right)\right)^{\alpha}}-n\right\}}, \tag{39}$$

$$\pi_4\left(\lambda|\alpha,\beta_1,\beta_2,\underline{w}\right)\propto\lambda^{d-k-1}e^{-\left(\beta_1+\beta_2\right)\left[(n-d)\left[e^{\left(\eta+\lambda\left(w_d-\eta\right)\right)^{\alpha}}\right]+\sum_{i=k+1}^{k}e^{\left(\eta+\lambda\left(w_i-\eta\right)\right)^{\alpha}}\right]}$$

$$+\sum_{i=k+1}^{m}\left(\eta+\lambda\left(w-\eta\right)\right)^{\alpha} \tag{40}$$

$$\prod_{i=k+1}^{d}\left(\eta+\lambda\left(w-\eta\right)\right)^{\alpha-1}.$$

From equations (37) and (38), the conditional posterior PDFs are reduced to two conditional gamma density equations (38) and (39). Two functions are plotted similar to the normal distribution in (37) and (40). Then, the process of generation from posterior distribution under the conditional posterior distribution by using Gibbs with the MH algorithms with normal proposal distribution [27] is given as follows:

(1) Begin with initial vectors $\Theta^{(0)}=(\alpha^{(0)},\beta_1^{(0)},\beta_2^{(0)},\lambda^{(0)})$ and indicator $\kappa=1$.

(2) The two values $\beta_1^{(\kappa)}$ and $\beta_2^{(\kappa)}$ are generated from conditional gamma densities (38) and (39).

(3) The two values $\alpha^{(\kappa)}$ and $\lambda^{(\kappa)}$ are generated from conditional densities (37) and (40) by MH algorithms with normal proposal distributions. The symmetric normal distributions are applied with mean $\alpha^{(\kappa-1)}$ or $\lambda^{(\kappa-)}$ and variance obtained from the diagonal of the approximate information matrix, respectively. Also, the generated values are accepted

with acceptance probability $\min[1,(\pi_4(\alpha^{(\kappa)}|\lambda^{(\kappa-1)},\beta_1^{(\kappa)},\beta_2^{(\kappa)},\underline{w})/\pi_4(\alpha^{(\kappa-1)}|\lambda^{(\kappa-1)},\beta_1^{(\kappa)},\beta_2^{(\kappa)},\underline{w}))]$ or $\min[1,(\pi_4(\lambda^{(\kappa)}|\alpha^{(\kappa)},\beta_1^{(\kappa)},\beta_2^{(\kappa)},\underline{w})/\pi_4(\lambda^{(\kappa-1)}|\alpha^{(\kappa)},\beta_1^{(\kappa)},\beta_2^{(\kappa)},\underline{w}))]$, respectively, with respect to uniform $(0,1)$.

(4) The vector $\Theta^{(\kappa)}=(\alpha^{(\kappa)},\beta_1^{(\kappa)},\beta_2^{(\kappa)},\lambda^{(\kappa)})$ is a built vector with Gibbs manner.

(5) Put $\kappa=1+1$ and then repeat steps 2–4 N times.

(6) The Bayes estimates and the corresponding variance are given by $\widehat{\Theta}_B=(1/N-N)\sum_{i=N+1}^{N}\Theta^{(i)}$ and $\mathrm{Var}(\widehat{\Theta}_B)=(1/N-N)\sum_{i=N+1}^{N}(\widehat{\Theta}_B-\Theta^{(i)})^2$, where $\mathbf{N}$ is the number of iteration used to get stationary distribution.

(7) The Bayes credible intervals can be obtained after ordered values of $\Theta_l^{(\kappa)}$ in acceding order of $\Theta_l^{(N+1)}$, $\Theta_l^{(N+2)},\ldots,\Theta_l^{[N]}$ as $\Theta_l^{[1]},\Theta_l^{[2]},\ldots,\Theta_l^{[N-N]}$. Then, the $100(1-\zeta)\%$ symmetric credible intervals are obtained as $(\Theta_l^{(N-N)(\zeta/2)},\Theta_l^{(N-N)(1-(\zeta/2))})$, $l=1,2,3,4$.

TABLE 2: The AV and MSE of parameters estimates for Θ (2, 0.1, 0.2, 2.0).

(η, τ)	(r, m, n)	MLE				MCMC/Prior 0				MCMC/Prior 1			
		α	β_1	β_1	λ	α	β_1	β_1	λ	α	β_1	β_1	λ
(0.8, 1.0)	(15, 20, 30)	2.321	0.152	0.231	2.412	2.301	0.140	0.218	2.392	2.321	0.132	0.211	2.355
		0.514	0.042	0.062	0.641	0.505	0.041	0.059	0.613	0.428	0.032	0.042	0.517
	(15, 25, 30)	2.305	0.150	0.229	2.400	2.299	0.140	0.215	2.366	2.309	0.132	0.213	2.341
		0.485	0.033	0.057	0.632	0.481	0.035	0.056	0.629	0.376	0.028	0.029	0.488
	(20, 25, 30)	2.317	0.147	0.224	2.389	2.294	0.136	0.209	2.359	2.290	0.124	0.208	2.337
		0.479	0.029	0.049	0.628	0.478	0.029	0.050	0.624	0.371	0.024	0.024	0.480
	(20, 30, 50)	2.301	0.132	0.201	2.340	2.290	0.129	0.208	2.338	2.287	0.113	0.207	2.324
		0.401	0.025	0.022	0.589	0.422	0.019	0.019	0.582	0.342	0.014	0.017	0.402
	(20, 40, 50)	2.303	0.125	0.212	2.338	2.289	0.124	0.207	2.334	2.279	0.112	0.206	2.319
		0.398	0.019	0.021	0.560	0.410	0.018	0.018	0.563	0.332	0.012	0.013	0.388
	(30, 40, 50)	2.298	0.124	0.207	2.327	2.279	0.118	0.208	2.332	2.269	0.109	0.206	2.314
		0.379	0.017	0.018	0.549	0.390	0.016	0.018	0.544	0.314	0.011	0.013	0.371

TABLE 3: The AV and MSE of parameters estimates for Θ (2, 0.1, 0.2, 2.0).

(η, τ)	(r, m, n)	MLE				MCMC/Prior 0				MCMC/Prior 1			
		α	β_1	β_1	λ	α	β_1	β_1	λ	α	β_1	β_1	λ
(1.0, 1.0)	(15, 20, 30)	2.311	0.140	0.222	2.401	2.289	0.129	0.209	2.380	2.313	0.121	0.201	2.344
		0.490	0.032	0.051	0.620	0.490	0.031	0.048	0.594	0.412	0.022	0.031	0.500
	(15, 25, 30)	2.294	0.139	0.218	2.391	2.288	0.129	0.204	2.357	2.298	0.121	0.201	2.330
		0.461	0.023	0.045	0.612	0.464	0.025	0.047	0.608	0.355	0.018	0.019	0.469
	(20, 25, 30)	2.307	0.138	0.215	2.379	2.285	0.126	0.200	2.348	2.288	0.114	0.200	2.329
		0.460	0.018	0.038	0.609	0.456	0.018	0.041	0.601	0.352	0.014	0.013	0.461
	(20, 30, 50)	2.291	0.122	0.195	2.330	2.280	0.119	0.190	2.328	2.275	0.102	0.198	2.313
		0.385	0.014	0.011	0.574	0.403	0.008	0.009	0.564	0.325	0.005	0.008	0.385
	(20, 40, 50)	2.295	0.115	0.203	2.327	2.278	0.113	0.198	2.324	2.268	0.100	0.195	2.308
		0.378	0.010	0.011	0.542	0.401	0.009	0.009	0.544	0.315	0.004	0.007	0.368
	(30, 40, 50)	2.288	0.112	0.195	2.318	2.268	0.109	0.200	2.322	2.249	0.100	0.197	2.301
		0.358	0.007	0.008	0.530	0.371	0.009	0.007	0.521	0.290	0.004	0.004	0.356

TABLE 4: The AV and MSE of parameters estimates for Θ (2, 0.1, 0.2, 2.0).

(η, τ)	(r, m, n)	MLE				MCMC/Prior 0				MCMC/Prior 1			
		α	β_1	β_1	λ	α	β_1	β_1	λ	α	β_1	β_1	λ
(1.2, 1.0)	(15, 20, 30)	2.341	0.162	0.252	2.430	2.322	0.160	0.239	2.412	2.342	0.153	0.231	2.374
		0.545	0.073	0.095	0.671	0.535	0.074	0.090	0.645	0.460	0.061	0.071	0.550
	(15, 25, 30)	2.325	0.170	0.249	2.419	2.318	0.161	0.236	2.386	2.328	0.151	0.233	2.360
		0.515	0.073	0.088	0.672	0.507	0.065	0.086	0.661	0.399	0.059	0.061	0.510
	(20, 25, 30)	2.337	0.165	0.244	2.410	2.310	0.156	0.228	2.379	2.310	0.143	0.227	2.358
		0.509	0.060	0.081	0.660	0.508	0.058	0.081	0.658	0.399	0.055	0.056	0.503
	(20, 30, 50)	2.319	0.150	0.224	2.365	2.310	0.148	0.228	2.355	2.305	0.133	0.227	2.345
		0.431	0.055	0.052	0.610	0.452	0.050	0.049	0.605	0.372	0.044	0.048	0.437
	(20, 40, 50)	2.323	0.145	0.233	2.358	2.307	0.144	0.226	2.355	2.299	0.131	0.227	2.338
		0.428	0.050	0.052	0.594	0.440	0.038	0.039	0.594	0.365	0.041	0.042	0.411
	(30, 40, 50)	2.308	0.141	0.227	2.347	2.298	0.138	0.229	2.351	2.290	0.131	0.228	2.333
		0.408	0.047	0.048	0.578	0.421	0.047	0.048	0.574	0.345	0.042	0.045	0.399

5. Monte Carlo Simulations

Different theoretical results that were developed in this study are assessed and compared in this section through the Monte Carlo study. The numerical computation is formulated to measure the effect of changing the total size n and the sample size m as well as stress time η and censoring time τ and the effect of parameters change. Different three cases of two time ($\tau < \eta$, $\tau = \eta$, $\tau > \eta$) and two values of parameters vector $\Theta = (\alpha, \beta_1, \beta_2, \lambda) = \{(2.0, 0.1, 0.2, 2.0), (0.7, 1.5, 2.0, 2.5)\}$ are assumed. Point and interval estimation results are measured. Average (AV) and mean squared error (MSE) are used to

Table 5: The AL and CP of parameters estimates for Θ (2, 0.1, 0.2, 2.0).

(η, τ)	(r, m, n)	MLE				MCMC/Prior 0				MCMC/Prior 1			
		α	β_1	β_1	λ	α	β_1	β_1	λ	α	β_1	β_1	λ
(0.8, 1.0)	(15, 20, 30)	4.321	0.321	0.421	5.212	4.314	0.318	0.419	5.209	4.045	0.298	0.318	5.009
		0.89	0.90	0.90	0.88	0.90	0.91	0.91	0.90	0.90	0.92	0.90	0.91
	(15, 25, 30)	4.300	0.299	0.401	5.180	4.280	0.295	0.400	5.189	4.045	0.266	0.300	4.975
		0.90	0.91	0.91	0.90	0.91	0.91	0.92	0.91	0.93	0.94	0.91	0.92
	(20, 25, 30)	4.271	0.268	0.375	5.154	4.255	0.265	0.381	5.174	4.018	0.239	0.271	4.944
		0.91	0.91	0.92	0.91	0.91	0.93	0.92	0.93	0.93	0.94	0.96	0.93
	(20, 30, 50)	4.248	0.241	0.348	5.125	4.230	0.235	0.351	5.144	4.001	0.211	0.242	4.914
		0.92	0.92	0.92	0.90	0.93	0.93	0.93	0.93	0.93	0.95	0.95	0.92
	(20, 40, 50)	4.219	0.215	0.321	5.100	4.201	0.203	0.318	5.115	3.971	0.180	0.215	4.850
		0.91	0.93	0.93	0.91	0.93	0.94	0.93	0.93	0.94	0.97	0.95	0.93
	(30, 40, 50)	4.185	0.194	0.300	4.990	4.150	0.164	0.270	5.070	3.941	0.149	0.176	4.817
		0.92	0.93	0.93	0.92	0.93	0.94	0.93	0.93	0.94	0.93	0.95	0.94

Table 6: The AL and CP of parameters estimates for Θ (2, 0.1, 0.2, 2.0).

(η, τ)	(r, m, n)	MLE				MCMC/Prior 0				MCMC/Prior 1			
		α	β_1	β_1	λ	α	β_1	β_1	λ	α	β_1	β_1	λ
(1.0, 1.0)	(15, 20, 30)	4.285	0.291	0.387	5.088	4.300	0.290	0.400	5.187	4.019	0.270	0.294	4.980
		0.90	0.91	0.90	0.89	0.91	0.91	0.91	0.92	0.90	0.92	0.91	0.91
	(15, 25, 30)	4.272	0.271	0.375	5.152	4.253	0.269	0.374	5.158	4.014	0.249	0.274	4.948
		0.91	0.91	0.92	0.90	0.91	0.91	0.92	0.93	0.93	0.94	0.91	0.94
	(20, 25, 30)	4.242	0.235	0.342	5.118	4.255	0.239	0.351	5.149	3.980	0.208	0.241	4.915
		0.92	0.93	0.92	0.92	0.91	0.93	0.92	0.95	0.93	0.94	0.96	0.94
	(20, 30, 50)	4.219	0.212	0.318	5.100	4.204	0.208	0.328	5.113	3.971	0.185	0.214	4.875
		0.93	0.92	0.94	0.90	0.93	0.93	0.97	0.93	0.93	0.95	0.97	0.92
	(20, 40, 50)	4.181	0.185	0.284	5.079	4.172	0.169	0.280	5.081	3.940	0.151	0.179	4.821
		0.96	0.92	0.93	0.91	0.93	0.93	0.93	0.93	0.94	0.97	0.95	0.94
	(30, 40, 50)	4.158	0.166	0.274	4.965	4.118	0.135	0.241	5.040	3.915	0.118	0.148	4.782
		0.92	0.94	0.93	0.92	0.93	0.94	0.92	0.93	0.94	0.95	0.95	0.94

Table 7: The AL and CP of parameters estimates for Θ (2, 0.1, 0.2, 2.0).

(η, τ)	(r, m, n)	MLE				MCMC/Prior 0				MCMC/Prior 1			
		α	β_1	β_1	λ	α	β_1	β_1	λ	α	β_1	β_1	λ
(1.2, 1.0)	(15, 20, 30)	4.371	0.369	0.470	5.269	4.370	0.371	0.466	5.255	4.098	0.345	0.361	5.057
		0.88	0.89	0.90	0.88	0.91	0.90	0.91	0.91	0.91	0.92	0.90	0.91
	(15, 25, 30)	4.347	0.245	0.453	5.230	4.330	0.345	0.450	5.238	4.091	0.299	0.348	5001
		0.89	0.90	0.91	0.91	0.91	0.92	0.92	0.93	0.93	0.94	0.93	0.92
	(20, 25, 30)	4.318	0.310	0.415	5.198	4.294	0.310	0.428	5.221	4.071	0.288	0.321	4.989
		0.90	0.91	0.92	0.90	0.92	0.93	0.92	0.93	0.94	0.94	0.96	0.97
	(20, 30, 50)	4.291	0.287	0.389	5.176	4.280	0.279	0.398	5.188	4.056	0.261	0.289	4.961
		0.92	0.91	0.92	0.90	0.92	0.93	0.93	0.93	0.93	0.93	0.95	0.94
	(20, 40, 50)	4.270	0.265	0.372	5.164	4.245	0.253	0.359	5.164	4.008	0.220	0.266	4.894
		0.92	0.93	0.90	0.91	0.93	0.94	0.93	0.92	0.94	0.97	0.94	0.93
	(30, 40, 50)	4.221	0.243	0.351	5.011	4.194	0.210	0.320	5.123	3.990	0.187	0.516	4.866
		0.92	0.90	0.93	0.91	0.93	0.94	0.93	0.93	0.94	0.94	0.95	0.96

measure point estimate and average lengths (AL) and the probability coverage (CP) are used to measure interval estimate. For Bayes estimation with MCMC methods, prior parameters are selected to satisfy the expectation of gamma prior as $E(\Theta_l) = (a_l/b_l) \cong \Theta_l$, $l = 1, 2, 3$. Then, informative prior information (Prior 1) and noninformative prior are obtained when the posterior distribution is proportional with the likelihood function (Prior 0). Also, Chan is built for 11,000 iterations with the first 1000 as bur-in. Average Bayes estimates, mean squared errors (MSEs), coverage

Table 8: The AV and MSE of parameters estimates for Θ (1.0, 0.8, 1.0, 2.5).

(η, τ)	(r, m, n)	MLE				MCMC/Prior 0				MCMC/Prior 1			
		α	β_1	β_1	λ	α	β_1	β_1	λ	α	β_1	β_1	λ
(0.3, 0.5)	(15, 20, 30)	1.235	1.001	1.321	2.821	1.214	0.982	1.301	2.805	1.201	0.854	1.241	2.754
		0.254	0.221	0.243	0.647	0.241	0.213	0.232	0.641	0.185	0.167	0.200	0.425
	(15, 25, 30)	1.219	0.985	1.307	2.809	1.200	0.968	1.280	2.791	1.189	0.842	1.229	2.742
		0.237	0.205	0.218	0.622	0.221	0.190	0.214	0.628	0.165	0.155	0.193	0.417
	(20, 25, 30)	1.221	0.982	1.313	2.814	1.201	0.955	1.275	2.792	1.178	0.840	1.214	2.735
		0.227	0.201	0.212	0.619	0.218	0.183	0.208	0.614	0.145	0.147	0.190	0.409
	(20, 30, 50)	1.214	0.977	1.307	2.817	1.194	0.948	1.269	2.790	1.160	0.825	1.204	2.727
		0.209	0.192	0.200	0.604	0.201	0.164	0.201	0.601	0.139	0.132	0.179	0.401
	(20, 40, 50)	1.195	0.899	1.265	2.800	1.191	0.888	1.255	2.718	1.124	0.801	1.176	2.702
		0.182	0.176	0.166	0.550	0.183	0.161	0.164	0.547	0.101	0.108	0.151	0.382
	(30, 40, 50)	1.184	0.875	1.240	2.741	1.179	0.872	1.221	2.719	1.127	0.789	1.154	2.701
		0.174	0.160	0.142	0.514	0.156	0.140	0.133	0.519	0.099	0.089	0.132	0.314

Table 9: The AV and MSE of parameters estimates for Θ (1.0, 0.8, 1.0, 2.5).

(η, τ)	(r, m, n)	MLE				MCMC/Prior 0				MCMC/Prior 1			
		α	β_1	β_1	λ	α	β_1	β_1	λ	α	β_1	β_1	λ
(0.5, 0.5)	(15, 20, 30)	1.219	0945	1.300	2.800	1.184	0.973	1.290	2.780	1.212	0.866	1.254	2.767
		0.233	0.207	0.219	0.618	0.215	0.200	0.211	0.619	0.155	0.149	0.179	0.403
	(15, 25, 30)	1.201	0.971	1.219	2.800	1.203	0.954	1.275	2.787	1.180	0.845	1.217	2.732
		0.219	0.187	0.204	0.604	0.200	0.172	0.189	0.611	0.152	0.141	0.173	0.401
	(20, 25, 30)	1.211	0.975	1.300	2.801	1.192	0.947	1.269	2.790	1.179	0.842	1.207	2.725
		0.209	0.175	0.200	0.601	0.197	0.164	0.187	0.600	0.132	0.125	0.174	0.390
	(20, 30, 50)	1.204	0.961	1.310	2.807	1.182	0.941	1.260	2.784	1.163	0.817	1.191	2.708
		0.191	0.179	0.183	0.581	0.180	0.162	0.189	0.580	0.117	0.111	0.160	0.382
	(20, 40, 50)	1.190	0.880	1.260	2.803	1.190	0.878	1.247	2.725	1.132	0.715	1.160	2.650
		0.161	0.156	0.149	0.535	0.168	0.145	0.145	0.538	0.089	0.079	0.138	0.365
	(30, 40, 50)	1.176	0.871	1.233	2.742	1.165	0.869	1.217	2.731	1.130	0.776	1.151	2.690
		0.155	0.143	0.128	0.500	0.141	0.128	0.117	0.504	0.081	0.076	0.114	0.301

Table 10: The AV and MSE of parameters estimates for Θ (1.0, 0.8, 1.0, 2.5).

(η, τ)	(r, m, n)	MLE				MCMC/Prior 0				MCMC/Prior 1			
		α	β_1	β_1	λ	α	β_1	β_1	λ	α	β_1	β_1	λ
(0.3, 0.5)	(15, 20, 30)	1.235	1.001	1.321	2.821	1.214	0.982	1.301	2.805	1.201	0.854	1.241	2.754
		0.254	0.221	0.243	0.647	0.241	0.213	0.232	0.641	0.185	0.167	0.200	0.425
	(15, 25, 30)	1.219	0.985	1.307	2.809	1.200	0.968	1.280	2.791	1.189	0.842	1.229	2.742
		0.237	0.205	0.218	0.622	0.221	0.190	0.214	0.628	0.165	0.155	0.193	0.417
	(20, 25, 30)	1.221	0.982	1.313	2.814	1.201	0.955	1.275	2.792	1.178	0.840	1.214	2.735
		0.227	0.201	0.212	0.619	0.218	0.183	0.208	0.614	0.145	0.147	0.190	0.409
	(20, 30, 50)	1.214	0.977	1.307	2.817	1.194	0.948	1.269	2.790	1.160	0.825	1.204	2.727
		0.209	0.192	0.200	0.604	0.201	0.164	0.201	0.601	0.139	0.132	0.179	0.401
	(20, 40, 50)	1.195	0.899	1.265	2.800	1.191	0.888	1.255	2.718	1.124	0.801	1.176	2.702
		0.182	0.176	0.166	0.550	0.183	0.161	0.164	0.547	0.101	0.108	0.151	0.382
	(30, 40, 50)	1.184	0.875	1.240	2.741	1.179	0.872	1.221	2.719	1.127	0.789	1.154	2.701
		0.174	0.160	0.142	0.514	0.156	0.140	0.133	0.519	0.099	0.089	0.132	0.314

TABLE 11: The AL and CP of parameters estimates for Θ (1.0, 0.8, 1.0, 2.5).

(η, τ)	(r, m, n)	MLE				MCMC/Prior 0				MCMC/Prior 1			
		α	β_1	β_1	λ	α	β_1	β_1	λ	α	β_1	β_1	λ
(0.3, 0.5)	(15, 20, 30)	2.824	2.541	3.104	5.512	2.801	2.549	3.097	5.489	2.612	2.325	2.900	5.342
		0.89	0.88	0.89	0.87	0.89	0.90	0.90	0.88	0.90	0.90	0.90	0.90
	(15, 25, 30)	2.804	2.525	3.077	5.500	2.785	2.525	3.077	5.468	2.591	2.301	2.879	5.324
		0.90	0.90	0.90	0.90	0.91	0.91	0.91	0.91	0.91	0.92	0.91	0.92
	(20, 25, 30)	2.781	2.507	3.059	5.480	2.766	2.508	3.059	5.455	2.579	2.284	2.862	5.304
		0.91	0.91	0.92	0.92	0.91	0.93	0.92	0.92	0.93	0.94	0.98	0.93
	(20, 30, 50)	2.759	2.487	3.042	5.461	2.745	2.592	3.040	5.439	2.565	2.271	2.842	5.281
		0.91	0.92	0.91	0.90	0.93	0.93	0.91	0.93	0.93	0.92	0.92	0.92
	(20, 40, 50)	2.744	2.464	3.031	5.449	2.736	2.581	3.024	5.418	2.548	2.255	2.819	5.260
		0.912	0.93	0.92	0.90	0.93	0.94	0.93	0.93	0.93	0.92	0.94	0.93
	(30, 40, 50)	2.719	2.439	3.008	5.413	2.714	2.547	3.004	5.400	2.521	2.228	2.801	5.239
		0.92	0.92	0.93	0.92	0.92	0.94	0.93	0.94	0.94	0.93	0.95	0.95

TABLE 12: The AL and CP of parameters estimates for Θ (1.0, 0.8, 1.0, 2.5).

(η, τ)	(r, m, n)	MLE				MCMC/Prior 0				MCMC/Prior 1			
		α	β_1	β_1	λ	α	β_1	β_1	λ	α	β_1	β_1	λ
(0.5, 0.5)	(15, 20, 30)	2.801	2.514	3.076	5.500	2.783	2.515	3.072	5.471	2.593	2.304	2.879	5.319
		0.90	0.90	0.89	0.89	0.90	0.90	0.91	0.90	0.90	0.91	0.90	0.92
	(15, 25, 30)	2.782	2.507	3.058	5.483	2.769	2.507	3.061	5.454	2.576	2.279	2.864	5.308
		0.92	0.91	0.90	0.91	0.92	0.91	0.92	0.91	0.91	0.92	0.93	0.93
	(20, 25, 30)	2.756	2.486	3.035	5.464	2.748	2.492	3.041	5.441	2.568	2.269	2.847	5.292
		0.92	0.93	0.92	0.93	0.91	0.93	0.94	0.92	0.93	0.95	0.96	0.95
	(20, 30, 50)	2.743	2.461	3.020	5.443	2.738	2.582	3.025	5.428	2.547	2.256	2.821	5.255
		0.93	0.92	0.93	0.93	0.93	0.93	0.93	0.93	0.93	0.95	0.94	0.93
	(20, 40, 50)	2.725	2.451	3.014	5.432	2.718	2.563	3.011	5.408	2.531	2.241	2.808	5.245
		0.92	0.93	0.92	0.90	0.94	0.94	0.93	0.93	0.94	0.92	0.94	0.96
	(30, 40, 50)	2.719	2.439	3.008	5.413	2.714	2.547	3.004	5.400	2.521	2.228	2.801	5.239
		0.92	0.92	0.93	0.92	0.92	0.94	0.93	0.94	0.94	0.93	0.95	0.95

TABLE 13: The AL and CP of parameters estimates for Θ (1.0, 0.8, 1.0, 2.5).

(η, τ)	(r, m, n)	MLE				MCMC/Prior 0				MCMC/Prior 1			
		α	β_1	β_1	λ	α	β_1	β_1	λ	α	β_1	β_1	λ
(0.7, 0.5)	(15, 20, 30)	2.861	2.579	3.142	5.544	2.832	2.580	3.180	5.511	2.645	2.349	2.932	5.361
		0.89	0.88	0.89	0.88	0.91	0.90	0.91	0.89	0.90	0.90	0.90	0.91
	(15, 25, 30)	2.835	2.559	3.103	5.528	2.810	2.561	3.098	5.488	2.670	2.342	2.915	5.357
		0.90	0.91	0.90	0.91	0.91	0.91	0.91	0.92	0.91	0.92	0.91	0.92
	(20, 25, 30)	2.799	2.538	3.071	5.499	2.784	2.541	3.075	5.478	2.611	2.315	2.881	5.338
		0.90	0.91	0.93	0.92	0.91	0.93	0.92	0.92	0.94	0.94	0.98	0.92
	(20, 30, 50)	2.782	2.499	3.073	5.486	2.774	2.615	3.069	5.470	2.592	2.298	2.869	5.298
		0.92	0.90	0.91	0.91	0.93	0.93	0.91	0.94	0.93	0.92	0.93	0.92
	(20, 40, 50)	2.771	2.492	3.059	5.480	2.764	2.598	3.052	5.441	2.563	2.277	2.842	5.285
		0.90	0.93	0.92	0.92	0.93	0.94	0.94	0.93	0.93	0.92	0.94	0.95
	(30, 40, 50)	2.741	2.458	3.032	5.439	2.742	2.568	3.032	5.429	2.544	2.253	2.834	5.257
		0.92	0.91	0.93	0.92	0.92	0.94	0.93	0.92	0.94	0.93	0.93	0.93

percentages, and average confidence interval lengths based on 1000 replications are reported. The results are shown in Tables 2–13.

6. Conclusions

A suitable censoring scheme and a suitable accelerated type for competing risk populations are developed. The results are computed when the products have Chen lifetime distribution. The model parameters are estimated with MLEs and Bayes methods; then, the numerical results are reported in Tables 2–13. The following comments are observed for the numerical results.

(1) From all tables, the proposed methods serve well for all choices.

(2) The numerical results which are obtained from MLEs and Bayes with noninformative prior are approximately similar.

(3) The Bayes method under informative prior serves very well compared to the other cases.

(4) The censoring scheme of type-I GHCS has saved the minimum number of failures which present suitable numerical results of all choices

(5) For the effective (r, m) sample increases, the MSEs and the AL of different estimators are reduced.

(6) The best results are obtained for the cases of $\eta \cong \tau$.

Data Availability

No data were used to support the findings of this study.

Conflicts of Interest

The authors have no conflicts of interest regarding the publication of the paper.

Acknowledgments

References

[1] R. D. Gupta and D. Kundu, "Hybrid censoring schemes with exponential failure distribution," *Communications in Statistics-Theory and Methods*, vol. 27, no. 12, pp. 3065–3083, 1998.

[2] D. Kundu and B. Pradhan, "Estimating the parameters of the generalized exponential distribution in presence of hybrid censoring," *Communications in Statistics-Theory and Methods*, vol. 38, no. 12, pp. 2030–2041, 2009.

[3] A. Childs, B. Chandrasekar, N. Balakrishnan, and D. Kundu, "Exact likelihood inference based on Type-I and Type-II hybrid censored samples from the exponential distribution," *Annals of the Institute of Statistical Mathematics*, vol. 55, no. 2, pp. 319–330, 2003.

[4] M. G. M. Ghazal, "Prediction of exponentiated family distributions observables under type-II hybrid censored data," *Journal of Statistics Applications & Probability*, vol. 7, no. 2, pp. 307–319, 2018.

[5] B. Chandrasekar, A. Childs, and N. Balakrishnan, "Exact likelihood inference for the exponential distribution under generalized Type-I and Type-II hybrid censoring," *Naval Research Logistics*, vol. 51, no. 7, pp. 994–1004, 2004.

[6] D. R. Cox, "The analysis of exponentially distributed life-times with two types of failure," *Journal of the Royal Statistical Society: Series B (Methodological)*, vol. 21, no. 2, pp. 411–421, 1959.

[7] H. A. David and M. L. Moeschberger, *The Theory of Competing Risks*, Grin, London, UK, 1978.

[8] M. J. Crowder, *Classical Competing Risks*, Chapman & Hall, London. UK, 2001.

[9] N. Balakrishnan and D. Han, "Exact inference for a simple step-stress model with competing risks for failure from exponential distribution under Type-II censoring," *Journal of Statistical Planning and Inference*, vol. 138, no. 12, pp. 4172–4186, 2008.

[10] A. Ganguly and D. Kundu, "Analysis of simple step-stress model in presence of competing risks," *Journal of Statistical Computation and Simulation*, vol. 86, no. 10, pp. 1989–2006, 2016.

[11] H. H. Abu-Zinadah and N. Sayed-Ahmed, "Competing risks model with partially step-stress accelerate life tests in analyses lifetime chen data under type-II censoring scheme," *Open Physics*, vol. 17, no. 1, pp. 192–199, 2019.

[12] W. Nelson, *Accelerated Testing: Statistical Models, Test Plans and Data Analysis*, Wiley, NewYork, NY, USA, 1990.

[13] C. M. Kim and D. S. Bai, "Analyses of accelerated life test data under two failure modes," *International Journal of Reliability, Quality and Safety Engineering*, vol. 09, no. 02, pp. 111–125, 2002.

[14] V. Bagdonavicius and M. Nikulin, *Accelerated Life Models: Modeling and Statistical Analysis*, Chapman and Hall/CRC Press, Boca Raton, FL, USA, 2002.

[15] E. K. AL-Hussaini and A. H. Abdel-Hamid, "Bayesian estimation of the parameters, reliability and hazard rate functions of mixtures under accelerated life tests," *Communications in Statistics - Simulation and Computation*, vol. 33, no. 4, pp. 963–982, 2004.

[16] E. K. AL-Hussaini and A. H. Abdel-Hamid, "Accelerated life tests under finite mixture models," *Journal of Statistical Computation and Simulation*, vol. 76, no. 8, pp. 673–690, 2006.

[17] D. S. Bai, M. S. Kim, and S. H. Lee, "Optimum simple step-stress accelerated life tests with censoring," *IEEE Transactions on Reliability*, vol. 38, no. 5, pp. 528–532, 1989.

[18] R. Wang and H. Fei, "Statistical inference of Weibull distribution for tampered failure rate model in progressive stress accelerated life testing," *IEEE Transactions on Reliability*, vol. 17, pp. 237–243, 2004.

[19] A. H. Abdel-Hamid and E. K. Al-Hussaini, "Progressive stress accelerated life tests under finite mixture models," *Metrika*, vol. 66, no. 2, pp. 213–231, 2007.

[20] G. K. Bhattacharyya and Z. Soejoeti, "A tampered failure rate model for step-stress accelerated life test," *Communications in Statistics-Theory and Methods*, vol. 18, no. 5, pp. 1627–1643, 1989.

[21] H. Seunggeun and J. Lee, "Constant-stress partially accelerated life testing for log-logistic distribution with censored data," *IEEE Transactions on Reliability*, vol. 2, pp. 193–201, 2015.

[22] A. A. Tahani and A. A. Soliman, "Estimating the Pareto parameters under progressive censoring data for constant-partially accelerated life tests," *IEEE Transactions on Reliability*, vol. 85, pp. 917–934, 2015.

[23] G. A. Abd-Elmougod and E. E. Mahmoud, "Paramters estimation of compound Rayleigh distribution under an adaptive type-II progressively hybrid censored data for constant partially accelerated life tests," *Global Journal of Pure and Applied Mathematics*, vol. 13, pp. 8361–8372, 2016.

[24] A. A. Soliman, G. A. Abd-Elmougod, and M. M. Al- Sobhi, "Estimation in step-stress partially accelerated life tests for the Chen distribution using progressive Type-II censoring," *Applied Mathematics & Information Sciences*, vol. 11, no. 1, pp. 325–332, 2017.

[25] A. M. Almarashi, AlgarniA, G. A. Abd-Elmougod, and S. M. Sayed Abdel-Khalek, "MCMC in estimation for generalized exponential distribution with constant partially

accelerated life tests under type-II censoring scheme," *Transylvanian Review*, vol. 32, pp. 8369–8376, 2019.

[26] A. M. Almarashia, A. Ali, G. A. Abd-Elmougod, and S. Abdel-Khalek, "Statistical analysis of Rayleigh competing risks models based on partially step stress Type-II censoring samples," *Journal of Nonlinear Science and Applications*, vol. 12, pp. 230–238, 2019.

[27] Q. Guan and Y. Tang, "Optimal step-stress test under Type-I censoring for multivariate exponential distribution," *Journal of Statistical Planning and Inference*, vol. 142, no. 7, pp. 1908–1923, 2012.

Research Article

Kinematics Analysis of 6-DoF Articulated Robot with Spherical Wrist

Seemal Asif (ID) **and Philip Webb**

School of Aerospace, Transport and Manufacturing, Cranfield University, Bedford MK43 0AL, Cranfield, UK

Correspondence should be addressed to Seemal Asif; s.asif@cranfield.ac.uk

The aim of the paper is to study the kinematics of the manipulator. The articulated robot with a spherical wrist has been used for this purpose. The Comau NM45 Manipulator has been chosen for the kinematic model study. The manipulator contains six revolution joints. Pieper's approach has been employed to study the kinematics (inverse) of the robot manipulator. Using this approach, the inverse kinematic problem is divided into two small less complex problems. This reduces the time of analysing the manipulator kinematically. The forward and inverse kinematics has been performed, and mathematical solutions are detailed based on D-H (Denavit–Hartenberg) parameters. The kinematics solution has been verified by solving the manipulator's motion. It has been observed that the model is accurate as the motion trajectory was smoothly followed by the manipulator.

1. Introduction

Locomotion is the process of causing a rigid body to move. The body needs force to move. Dynamics is the study of the motion of the body in which forces are modelled which helps the body to move, whereas kinematics is the geometrical study of the motion of the body without considering the forces that can affect the motion of the body.

Kinematics is the motion description of the rigid body. [1] Links are the connectivity body/member between joints. The kinematic chain is a grouping of links connected by joints, as illustrated in Figure 1. In the kinematic chain, the number of DoF (degree of freedom) is equal to the number of joints.

Maintaining a strong connection between the two joints is called the kinematics function of a link. This connection can be described with the following factors:

(i) a: link length

(ii) α: link twist

Link length is measured along the line which is mutually perpendicular to both joints/axes. The perpendicularity in joints always exists except when both joints are parallel. Link

twist is the angle of projection from the previous joint $(i-1)$ to the next joint (i) onto the axis $i-1$ (previous joint); the projection line is parallel to the next joint (axis i). The relationship between link length and twist is described in Figure 2.

(i) A joint axis is formed at the connection of two links. This joint will have two parameters (one for each link) connected to it. These parameters are as follows:

(ii) d: distance between links

(iii) Θ: angle between links

The relative position or distance between the links is called link offset. Figure 3 describes these parameters, in which the joint angle is the angle between the links.

The four parameters demonstrated above are associated with each link. Axes can be aligned using these parameters. The parameters are also known as Denavit–Hartenberg link parameters. These are illustrated in Table 1 below:

The link numbering convention follows from the base of the arm till the last moving link. As mentioned in Figure 4, the first link is the connection between the base and first joint.
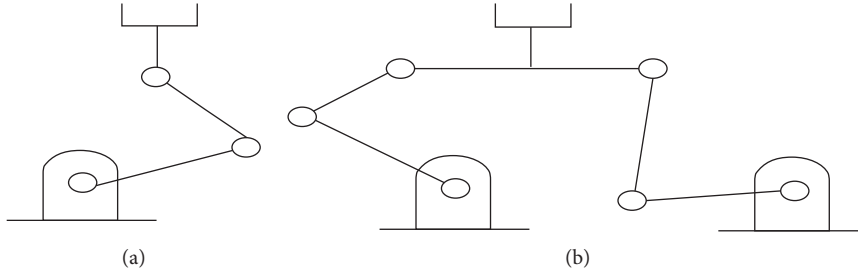
FIGURE 1: Kinematics of the manipulator: (a) open chain; (b) closed chain [2].
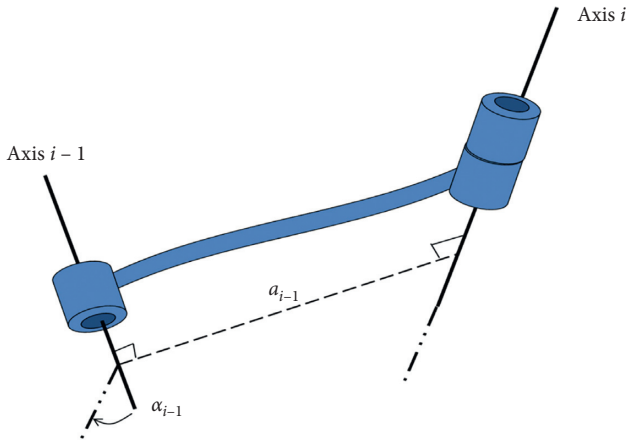
FIGURE 2: Kinematic function of link.
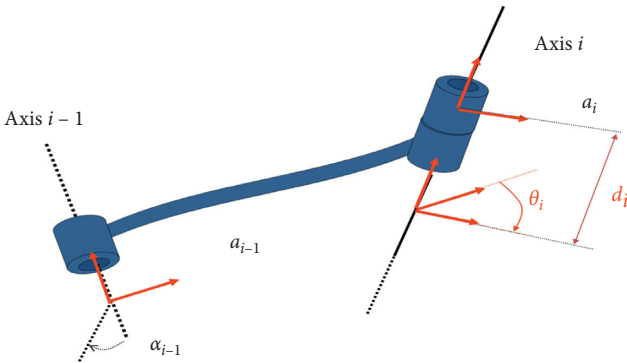
FIGURE 3: Link and joint parameters. Joint parameters are highlighted in red.

TABLE 1: Denavit–Hartenberg link parameters.

Link parameters	Joint parameters
a: link length	d: distance between links
α: link twist	Θ: angle between links

The parameters mentioned above in Table 1 are used for kinematic modelling of the robot. In kinematics, modelling the geometry of the robot is represented. Homogenous transformation (of the matrix) is commonly used as the definition of the kinematics model (particularly for chains mechanism). As described below,
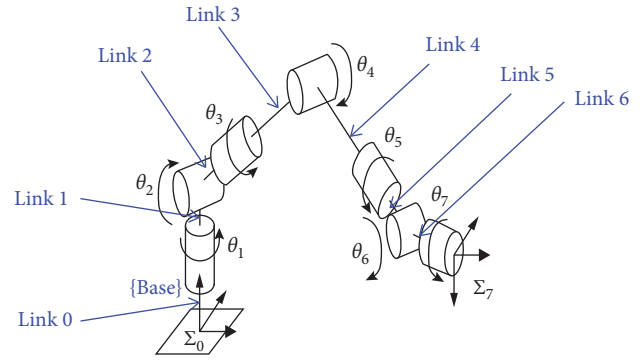
FIGURE 4: A 7-DoF manipulator arm [3].

$$\,^0_nT = T_1 T_2 T_3 \ldots T_i \ldots T_n, \qquad (1)$$

where n is the number of links, T_i is the link transformation from the ith joint, and $\,^0_nT$ is the final pose for end-effector relative to the base.

There are two main types of kinematic models: forward kinematics and inverse kinematics. In forward kinematics, the length of each link and angle of each joint is given, and through that, position of any point (x, y, z) can be found. In inverse kinematics, the length of each link and position of some points (x, y, z) is given, and the angle of each joint is needed to find to obtain that position.

Several models are developed for kinematic modelling, but the D-H (Denavit–Hartenberg) model [4] is the most popular model. Limitations of the D-H model are discussed, and CPC (completeness and parametric continuity) model and its mapping with the D-H model were proposed [5]. The parametric continuity of the CPC model was achieved by using singularity free line representation.

2. Forward Kinematics of Comau NM45

The Comau NM45 [6] is a medium-scale robot. It has 6 degree of freedom joints. It is an articulated arm with a spherical wrist. The wrist joint intersects at one point. Figure 5 shows the manipulator with its link length and working envelope.

Forward kinematics is the study of the manipulator to find out its tip or end-effector position and orientation by using joint values of the manipulator. The first step of performing the forward kinematics is to label link lengths.
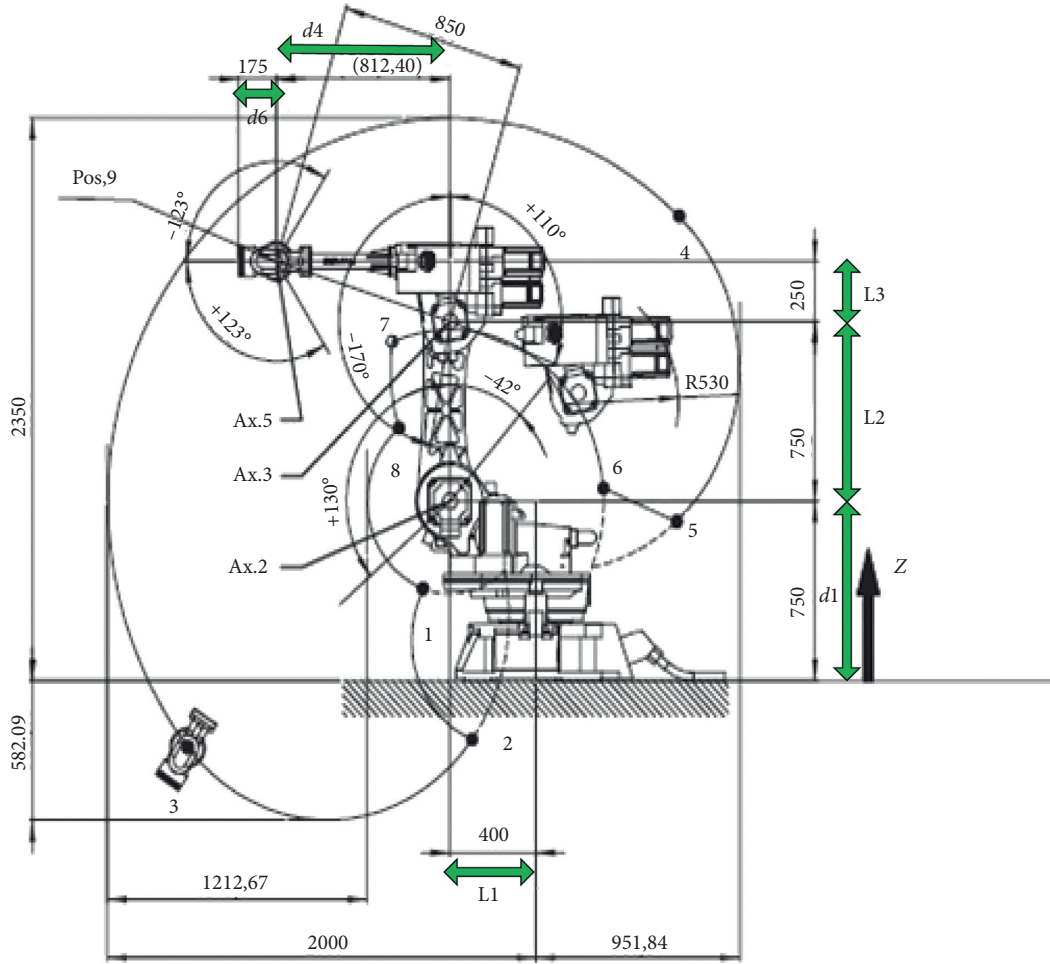
FIGURE 5: Comau NM45 (inline) operative area and link lengths.

This step has been performed in Figure 5. The second step to find the forward kinematics of the manipulator is to assign the frames. The frame assignment is done in Figure 6.

The D-H parameters can be found based on the frame assignment. The modified DH convention has been used for the frame assignment and DH parameters [7, 8]. These parameters are illustrated in Table 2.

The transformation matrix for a link **i** is described as follows:

$$A_i = \begin{bmatrix} \cos\theta i & -\sin\theta i \cos\alpha i & \sin\theta i \sin\alpha i & \alpha i \cos\theta i \\ \sin\theta i & \cos\theta i \cos\alpha i & -\cos\theta i \sin\alpha i & \alpha i \sin\theta i \\ 0 & \sin\alpha i & \cos\alpha i & di \\ 0 & 0 & 0 & 1 \end{bmatrix}. \quad (2)$$

A_1 is the transformation matrix T_1^0:

$$T_1^0 = \begin{bmatrix} \cos\theta1 & -\sin\theta1 \cos\alpha1 & \sin\theta1 \sin\alpha1 & \alpha1 \cos\theta1 \\ \sin\theta1 & \cos\theta1 \cos\alpha1 & -\cos\theta1 \sin\alpha1 & \alpha1 \sin\theta1 \\ 0 & \sin\alpha1 & \cos\alpha1 & d1 \\ 0 & 0 & 0 & 1 \end{bmatrix}, \quad (3)$$

and $\alpha = 90$, so T_1^0 will be as follows:

$$T_1^0 = \begin{bmatrix} \cos\theta1 & 0 & \sin\theta1 & \alpha1 \cos\theta1 \\ \sin\theta1 & 0 & -\cos\theta1 & \alpha1 \sin\theta1 \\ 0 & 1 & 0 & d1 \\ 0 & 0 & 0 & 1 \end{bmatrix}, \quad (4)$$

whereas $a1 = l1 = 0.4$ and $d1 = 0.75$; by placing these values above, the following equation which is the resultant for the transformation between the base and joint 1 is obtained:

$$T_1^0 = \begin{bmatrix} \cos\theta1 & 0 & \sin\theta1 & \alpha1 \cos\theta1 \\ \sin\theta1 & 0 & -\cos\theta1 & \alpha1 \sin\theta1 \\ 0 & 1 & 0 & 0.75 \\ 0 & 0 & 0 & 1 \end{bmatrix}. \quad (5)$$

For A2 = T_2^1,

$$T_2^1 = \begin{bmatrix} \cos\theta2 & -\sin\theta2 & 0 & \alpha2 \cos\theta2 \\ \sin\theta2 & \cos\theta2 & 0 & \alpha2 \sin\theta2 \\ 0 & 0 & 1 & d2 \\ 0 & 0 & 0 & 1 \end{bmatrix}, \quad (6)$$
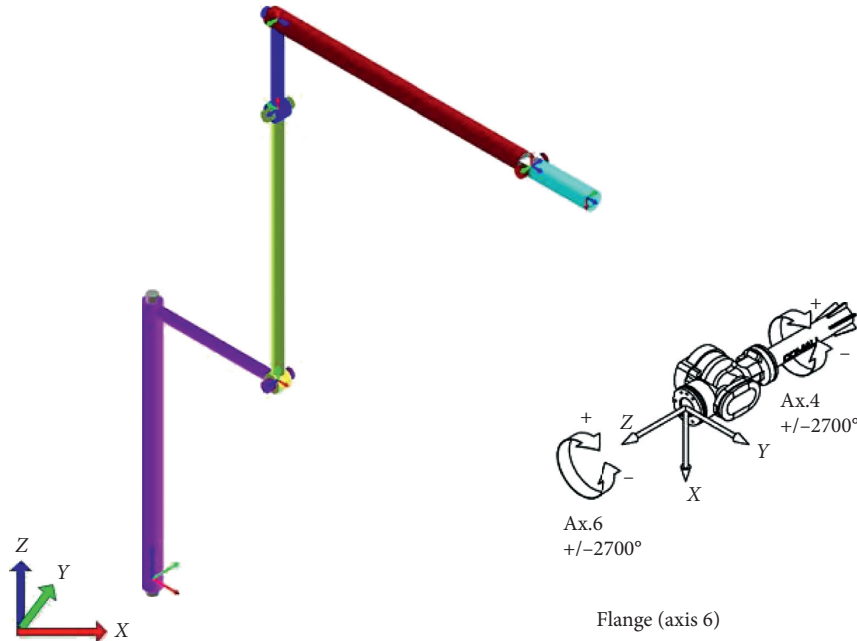
FIGURE 6: NM45 model with coordinates mapping.

TABLE 2: Comau NM45 DH parameters.

Link	Link length (αi), m	Twist angle (αi), deg	Joint offset	Joint angle (θi), deg
1	$L1 = 0.4$	90	$D1 = 0.75$	($\theta 1$)
2	$L2 = 0.75$	0	0	($\theta 2$)
3	$L3 = 0.25$	90	0	($\theta 3$)
4	0	−90	$D4 = 0.8124$	($\theta 4$)
5	0	90	0	($\theta 5$)
6	0	0	$D6 = 0.175$	($\theta 6$)

whereas $a2 = l2 = 0.75$ and $d2 = 0$; by placing these values above, the following equation which is the resultant for the transformation between joint 1 and joint 2 is obtained:

$$T_2^1 = \begin{bmatrix} \cos\theta2 & -\sin\theta2 & 0 & 0.75\cos\theta2 \\ \sin\theta2 & \cos\theta2 & 0 & 0.75\sin\theta2 \\ 0 & 0 & 1 & 0 \\ 0 & 0 & 0 & 1 \end{bmatrix}. \tag{7}$$

For A3 = T_3^2,

$$T_3^2 = \begin{bmatrix} \cos\theta3 & 0 & \sin\theta3 & \alpha3\cos\theta3 \\ \sin\theta3 & 0 & -\cos\theta3 & \alpha3\sin\theta3 \\ 0 & 1 & 0 & d3 \\ 0 & 0 & 0 & 1 \end{bmatrix}, \tag{8}$$

whereas $a3 = l3 = 0.25$ and $d3 = 0$; by placing these values above, the following equation which is the resultant for the transformation between joint 2 and joint 3 is obtained:

$$T_3^2 = \begin{bmatrix} \cos\theta3 & 0 & \sin\theta3 & 0.25\cos\theta3 \\ \sin\theta3 & 0 & -\cos\theta3 & 0.25\sin\theta3 \\ 0 & 1 & 0 & 0 \\ 0 & 0 & 0 & 1 \end{bmatrix}. \tag{9}$$

For A4 = T_4^3 and $\alpha = 90$,

$$T_4^3 = \begin{bmatrix} \cos\theta4 & 0 & -\sin\theta4 & \alpha4\cos\theta4 \\ \sin\theta4 & 0 & \cos\theta4 & \alpha4\sin\theta4 \\ 0 & -1 & 0 & d4 \\ 0 & 0 & 0 & 1 \end{bmatrix}, \tag{10}$$

whereas $a4 = 0$; by placing the value of $a4$ in the above equation, the following equation which is the resultant for the transformation between joint 3 and joint 4 is obtained:

$$T_4^3 = \begin{bmatrix} \cos\theta4 & 0 & -\sin\theta4 & 0 \\ \sin\theta4 & 0 & \cos\theta4 & 0 \\ 0 & -1 & 0 & d4 \\ 0 & 0 & 0 & 1 \end{bmatrix}. \tag{11}$$

For A4 = T_5^4,

$$T_5^4 = \begin{bmatrix} \cos\theta5 & 0 & \sin\theta5 & \alpha5\cos\theta5 \\ \sin\theta5 & 0 & -\cos\theta5 & \alpha5\sin\theta5 \\ 0 & 1 & 0 & d5 \\ 0 & 0 & 0 & 1 \end{bmatrix}, \tag{12}$$

whereas $a5 = 0$ and $d5 = 0$; by placing these values in the above equation, the following equation which is the resultant for the transformation between joint 4 and joint 5 is obtained:

$$T_5^4 = \begin{bmatrix} \cos\theta5 & 0 & \sin\theta5 & 0 \\ \sin\theta5 & 0 & -\cos\theta5 & 0 \\ 0 & 1 & 0 & 0 \\ 0 & 0 & 0 & 1 \end{bmatrix}. \tag{13}$$

For $A5 = T_6^5$ and $\alpha = 0$,

$$T_6^5 = \begin{bmatrix} \cos\theta6 & -\sin\theta6 & 0 & \alpha6\cos\theta6 \\ \sin\theta6 & \cos\theta6 & 0 & \alpha6\sin\theta6 \\ 0 & 0 & 1 & d6 \\ 0 & 0 & 0 & 1 \end{bmatrix}, \tag{14}$$

whereas $a6 = 0$; by placing the value of $a6$ in the above equation, the following equation which is the resultant for the transformation between joint 5 and joint 6 is obtained:

$$T_6^5 = \begin{bmatrix} \cos\theta6 & -\sin\theta6 & 0 & 0 \\ \sin\theta6 & \cos\theta6 & 0 & 0 \\ 0 & 0 & 1 & d6 \\ 0 & 0 & 0 & 1 \end{bmatrix}. \tag{15}$$

2.1. Transformation. For simplification, the following has been substituted:

$$\begin{aligned} \theta1 &= u, \\ \theta2 &= v, \\ \theta3 &= w, \\ \theta4 &= a, \\ \theta5 &= b, \\ \theta6 &= m. \end{aligned} \tag{16}$$

For $A12 = T_2^0 = T_1^0 \times T_2^1$, substitute values from equations (5) and (7):

$$T_2^0 = T_1^0 X T_2^1 = \begin{pmatrix} \cos(u) & 0 & \sin(u) & 0.4\cos(u) \\ \sin(u) & 0 & -\cos(u) & 0.4\sin(u) \\ 0 & 1 & 0 & 0.75 \\ 0 & 0 & 0 & 1 \end{pmatrix} \cdot \begin{pmatrix} \cos(v) & -\sin(v) & 0 & 0.75\cos(v) \\ \sin(v) & \cos(v) & 0 & 0.75\sin(v) \\ 0 & 0 & 1 & 0 \\ 0 & 0 & 0 & 1 \end{pmatrix}. \tag{17}$$

The resultant transformation between the base and joint 2 is illustrated as follows:

$$T_2^0 = \begin{bmatrix} \cos(u)\cos(v) & -\cos(u)\sin(v) & \sin(u) & \cos(u)(0.75\cos(v)+0.4) \\ \cos(v)\sin(u) & -\sin(u)\sin(v) & -\cos(u) & (0.75\cos(v)+0.4)\sin(u) \\ \sin(v) & \cos(v) & 0 & 0.75\sin(v)+0.75 \\ 0 & 0 & 0 & 1 \end{bmatrix}, \tag{18}$$

For $A123 = T_3^0 = T_1^0 \times T_2^1 \times T_3^2$, for simplicity,

$$\begin{aligned} m &= \cos(u)(0.75\cos(v)+0.4), \\ n &= (0.75\cos(v)+0.4)\sin(u), \\ u &= 0.75\sin(v)+0.75, \end{aligned}$$

$$T_3^0 = T_2^0 X T_3^2 = \begin{pmatrix} \cos(u)\cos(v) & -\cos(u)\sin(v) & \sin(u) & m \\ \cos(v)\sin(u) & -\sin(u)\sin(v) & -\cos(u) & n \\ \sin(v) & \cos(v) & 0 & o \\ 0 & 0 & 0 & 1 \end{pmatrix} \cdot \begin{pmatrix} \cos(w) & 0 & \sin(w) & 0.25\cos(w) \\ \sin(w) & 0 & -\cos(w) & 0.25\sin(w) \\ 0 & 1 & 0 & 0 \\ 0 & 0 & 0 & 1 \end{pmatrix}. \tag{19}$$

The resultant transformation between the base and joint 3 is illustrated as follows:

$$
T_3^0 = \begin{pmatrix} \cos(u)\cos(v+w) & \sin(u) & \cos(u)\sin(v+w) & m + 0.25\ \cos(u)\cos(v+w) \\ \cos(v+w)\sin(u) & -\cos(u) & \sin(u)\sin(v+w) & n + 0.25\ \cos(v+w)\sin(u) \\ \sin(v+w) & 0 & -\cos(v+w) & 0 + 0.25\ \sin(v+w) \\ 0 & 0 & 0 & 1 \end{pmatrix}.
$$

(20)

For A456 $= T_6^3 = T_4^3 \times T_5^4 \times T_6^5$,

$$
A45 = T_5^3 = T_4^3 \times T_5^4 = \begin{pmatrix} \cos(a) & 0 & -\sin(a) & 0 \\ \sin(a) & 0 & \cos(a) & 0 \\ 0 & -1 & 0 & 0.8124 \\ 0 & 0 & 0 & 1 \end{pmatrix} \cdot \begin{pmatrix} \cos(b) & 0 & \sin(b) & 0 \\ \sin(b) & 0 & -\cos(b) & 0 \\ 0 & 1 & 0 & 0 \\ 0 & 0 & 0 & 1 \end{pmatrix},
$$

$$
A45 = T_5^3 = \begin{pmatrix} \cos(a)\cos(b) & -\sin(a) & \cos(a)\sin(b) & 0 \\ \sin(a)\cos(b) & \cos(a) & \sin(a)\sin(b) & 0 \\ -\sin(b) & 0 & \cos(b) & 0.8124 \\ 0 & 0 & 0 & 1 \end{pmatrix},
$$

(21)

$$
T_6^3 = T_4^3 \times T_5^4 \times T_6^5 = T_5^3 \times T_6^5 = \begin{pmatrix} \cos(a)\cos(b) & -\sin(a) & \cos(a)\sin(b) & 0 \\ \sin(a)\cos(b) & \cos(a) & \sin(a)\sin(b) & 0 \\ -\sin(b) & 0 & \cos(b) & d^4 \\ 0 & 0 & 0 & 1 \end{pmatrix} \cdot \begin{pmatrix} \cos(m) & -\sin(m) & 0 & 0 \\ \sin(m) & \cos(m) & 0 & 0 \\ 0 & 0 & 1 & d^6 \\ 0 & 0 & 0 & 1 \end{pmatrix}.
$$

The resultant transformation between joint 3 and joint 6 is illustrated as follows:

$$
T_6^3 = \begin{pmatrix} \cos(a)\cos(b)\cos(m) - \sin(a)\sin(m) & -\cos(m)\sin(a) - \cos(a)\cos(b)\sin(m) & \cos(a)\sin(b) & d^6\cos(a)\sin(b) \\ \cos(b)\cos(m)\sin(a) + \cos(a)\sin(m) & \cos(a)\cos(m) - \cos(b)\sin(a)\sin(m) & \sin(a)\sin(b) & d^6\sin(a)\sin(b) \\ -\cos(m)\sin(b) & \sin(b)\sin(m) & \cos(b) & \cos(b)d^6 + d^4 \\ 0 & 0 & 0 & 1 \end{pmatrix}.
$$

(22)

Spherical wrist position can be extracted using the last column of T_6^0 transformation matrix, where

$$
T_6^0 = \begin{bmatrix} r_{11} & r_{12} & r_{13} & P_x \\ r_{21} & r_{22} & r_{23} & P_y \\ r_{31} & r_{32} & r_{33} & P_z \\ 0 & 0 & 0 & 1 \end{bmatrix},
$$

(23)

Which means the T_6^0 the transformation matrix can be represented in terms of R_6^0 and P_6^0 illustrated as follows:

$$
T_6^0 = \begin{bmatrix} R_6^0 & P_6^0 \\ 0 & 1 \end{bmatrix},
$$

(24)

and spherical wrist position is illustrated as

$$
P_6^0 = \begin{bmatrix} Px \\ Py \\ Pz \end{bmatrix}.
$$

(25)

Transformation matrix from base to end-effector is

$$T_6^0 = T_1^0 \times T_2^1 \times T_3^2 \times T_4^3 \times T_5^4 \times T_6^5,$$

$$T_6^0 = \begin{bmatrix} r11 & r12 & r13 & Px \\ r21 & r22 & r23 & Py \\ r31 & r32 & r33 & Pz \\ 0 & 0 & 0 & 1 \end{bmatrix}, \quad (26)$$

$$T_6^0 = \begin{bmatrix} R_6^0 & P_6^0 \\ 0 & 1 \end{bmatrix}.$$

3. Inverse Kinematics of Comau NM45

Inverse kinematics is finding the joint values $(\theta1, \theta2, \theta3, \theta4, \theta5, \theta6)$ of the robot arm for the given position (p) and orientation (o). For inverse kinematics, the inverse orientation R and inverse position P are needed.

The Comau NM45 is an articulated arm with a spherical wrist. For finding anthropomorphic/articulated arm position and joint values $\theta1, \theta2, \theta3$, the inverse position is needed.

Let O_c be intersecting the last 3 joints. The motion of joints 4, 5, and 6 will not change the position of O_c, as stated in Figure 7 [19] This is according to Pieper's approach [7], in which the manipulator is divided to analyse the inverse kinematics [10].

According to T_6^3 matrix from equation (22), the position P_6^3 is always as mentioned in the following equation:

$$P_6^3 = \begin{bmatrix} 0 \\ 0 \\ d_{\partial 6} \end{bmatrix}. \quad (27)$$

So, the position O will be as follows:

$$O = O_c^0 + d_6 R \begin{bmatrix} 0 \\ 0 \\ 1 \end{bmatrix}, \quad (28)$$

where O is the position P_6^0 and R is the orientation which is R. The above equation can be written in terms of O_c^0 as follows:

$$O_c^0 = O - d_6 R \begin{bmatrix} 0 \\ 0 \\ 1 \end{bmatrix}, \quad (29)$$

The first three joints can be found in the following steps. They will determine the position of the manipulator:

$$O = \begin{bmatrix} o_x \\ o_y \\ o_z \end{bmatrix},$$

$$O_c^0 = \begin{bmatrix} x_c \\ y_c \\ z_c \end{bmatrix}, \quad (30)$$

$$\begin{bmatrix} x_c \\ y_c \\ z_c \end{bmatrix} = \begin{bmatrix} o_x - d_6 r_{13} \\ o_x - d_6 r_{23} \\ o_x - d_6 r_{33} \end{bmatrix}.$$
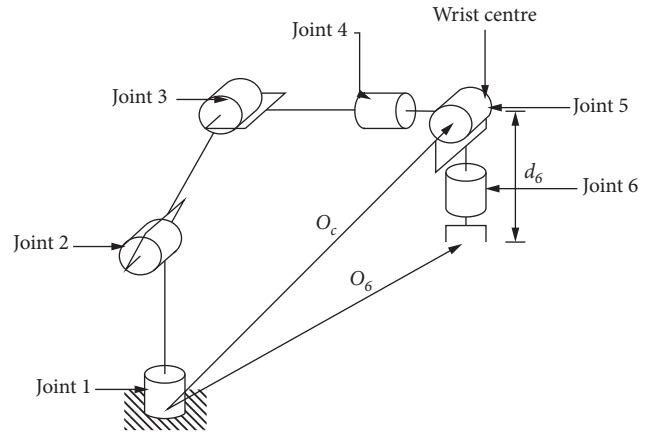
Figure 7: Kinematics decoupling (Spong, Hutchinson, and Vidyasagar, 2006).

For the orientation, the last three joints orientation is needed. The following equation shows the overall rotation of the manipulator in terms of R_3^0 and R_6^3:

$$R = R_3^0 R_6^3. \quad (31)$$

Rearrangement of equation (31) will yield R_6^3 below, through which the last three joint angles can be found:

$$R_6^3 = R_3^{0-1} R \longrightarrow \theta4, \theta5, \theta6. \quad (32)$$

For articulated manipulator, the first three joints tell the position, as illustrated in Figure 8.

Projection of wrist onto x_0, y_0 plane has been shown in Figure 9.

This projection yields the triangle through which the angle value for $\theta1$ can be found as follows:

$$\theta1 = A \tan 2 (x_c, y_c). \quad (33)$$

If the wrist is rotated, then it will result in the following equation:

$$\theta1 = A \tan 2 (x_c, y_c) + \pi. \quad (34)$$

Another projection, as mentioned in Figure 10, on the plane formed with link 2 and link 3 can help to find the value of joint angle 2 $(\theta_2, 2)$ and joint angle 3 $(\theta_3, 3)$.

Law of cosines can be applied to obtain the joint angle 3 $(\theta_3, 3)$, as follows:

$$\cos \theta_3 = \frac{r^2 + s^2 - a_2^2 - a_3^2}{2a_2 a_3}. \quad (35)$$

By substituting the values of r and s, these can be extracted by using Figure 8:

$$\cos \theta_3 = \frac{\left(x_c^2 + y_c^2 - d^2\right) + (z_c - d_1)^2 - a_2^2 - a_3^2}{2a_2 a_3}. \quad (36)$$

As NM45 2.0 is inline, no shoulder is offset and, hence, $d = 0$.
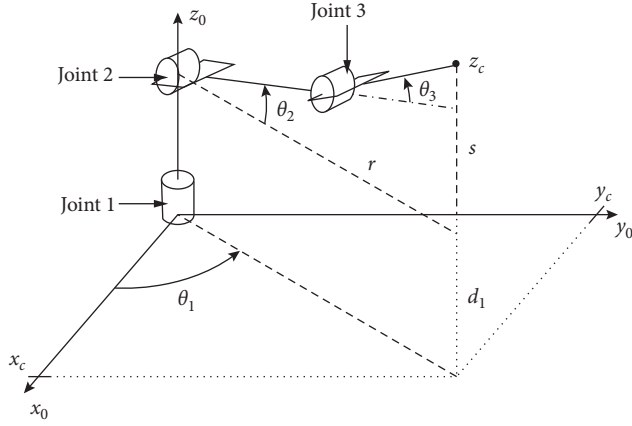
FIGURE 8: Comau NM45 (articulated arm) first three joints (Spong, Hutchinson, and Vidyasagar, 2006).
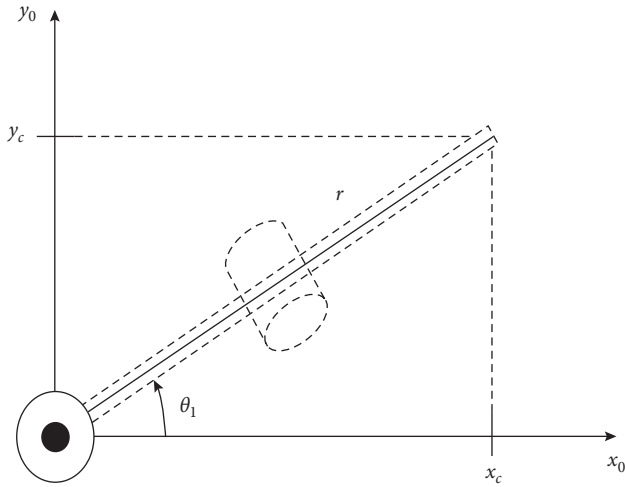
FIGURE 9: Projection of wrist centre onto x0, y0 plane (Spong, Hutchinson, and Vidyasagar, 2006).
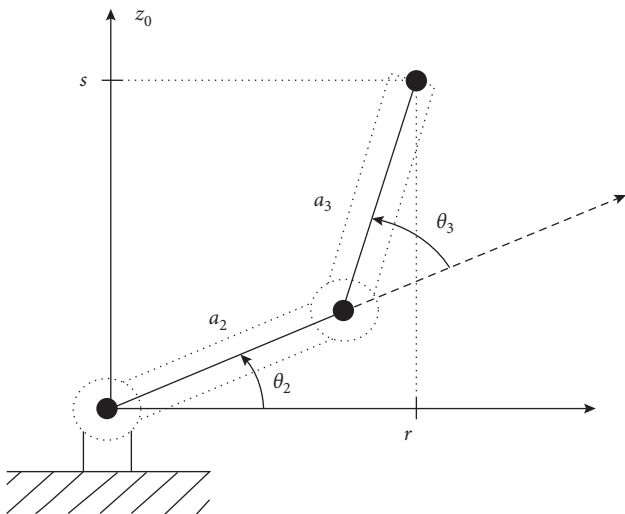
FIGURE 10: Projection on the plane (Link2 l2, Link3 l3) (Spong, Hutchinson, and Vidyasagar, 2006).

So,

$$\cos \theta_3 = \frac{x_c^2 + y_c^2 + (z_c - d_1)^2 - a_2^2 - a_3^2}{2a_2 a_3}, \tag{37}$$

where $a_2 = L_2$ according to DH labelled figure, and

$$\cos \theta_3 = \frac{x_c^2 + y_c^2 + (z_c - d_1)^2 - L_2^2 - a_3^2}{2L_2 a_3}, \tag{38}$$

$$\sin \theta_3 = \sqrt{1 - \cos \theta_3^2}.$$

Also,

$$\tan \theta_3 = \sqrt{\frac{1 - \cos \theta_3^2}{\cos \theta_3}} = \frac{\sqrt{1 - D^2}}{D}. \tag{39}$$

The value of θ_3 can be written in terms of atan2 and D as follows:

$$\theta_3 = a \tan 2 \left(D, \ \pm \sqrt{1 - D^2} \right), \tag{40}$$

where $+$ is for elbow up and $-$ is for elbow down.

The projection in Figure 11 has been drawn onto the link 2 and link 3 plane to find θ_2:

$$\theta_2 = h1 - h2,$$

$$h1 = a \tan 2 (r, s) = a \tan 2 \left(\sqrt{x_c^2 + y_c^2}, Z_c - d_1 \right), \tag{41}$$

$$h_2 = a \tan 2 (a_2 + a_3 \cos \theta_3, a_3 \sin \theta_3).$$

So, the value of θ_2 can be written as follows:

$$\begin{aligned} \theta_2 = &\ a \tan 2 \left(\sqrt{x_c^2 + y_c^2}, z_c - d_1 \right) \\ &- a \tan 2 (a_2 + a_3 \cos \theta 3, a3 \ \sin \theta_3). \end{aligned} \tag{42}$$

3.1. Finding Spherical Wrist Joint Values (Rotation) Using Euler Angles. The last three joint variables, $\theta 4$, $\theta 5$, $\theta 6$, are the Euler angles. So,

$$\begin{aligned} \theta 4 &= \varnothing, \\ \theta 5 &= \theta, \\ \theta 6 &= \varphi. \end{aligned} \tag{43}$$

These angles are concerning the coordinate frame $o3, x3, y3, z3$. Now we need to calculate the transformation from T_4^3 to T_6^5 which is T_6^3:

$$T_6^3 = A5XA5XA6 = T_4^3 \times T_5^4 X T_6^5, \tag{44}$$

where T_6^3 can be written in terms of R_6^3 and O_6^3 mentioned as follows:

$$T_6^3 = \begin{bmatrix} R_6^3 & O_6^3 \\ 0 & 1 \end{bmatrix}, \tag{45}$$

where O_6^3 is the position.
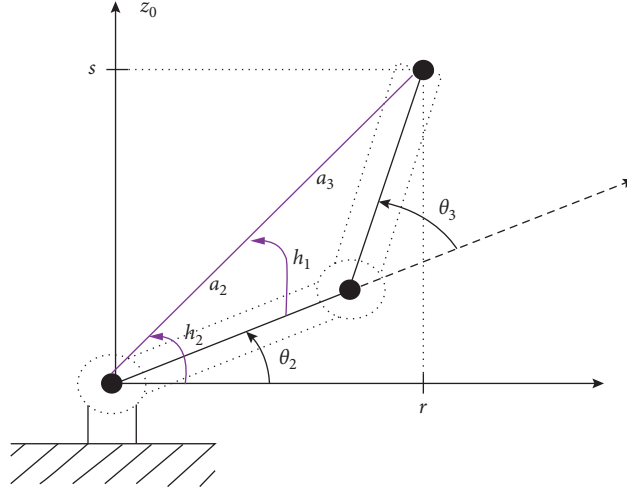
FIGURE 11: Projection onto l2 and l3 plane to find θ_2. θ_2 can be written in terms of angles $h1$ and $h2$.

For the spherical wrist, the ZYZ Euler transformation is needed. $\mathbf{R}_6^3$ is captured from equation (22), so $\mathbf{R}_6^3$ can be written as

$$R_{ZYZ} = R_6^3 = \begin{bmatrix} \cos(\varnothing)\cos(\theta)\cos(\varphi) - \sin(\varnothing)\sin(\varphi) & -\cos(\varphi)\sin(\varnothing) - \cos(\varnothing)\cos(\theta)\sin(\varphi) & \cos(\varnothing)\sin(\theta) \\ \cos(\theta)\cos(\varphi)\sin(\varnothing) + \cos(\varnothing)\sin(\varphi) & \cos(\varnothing)\cos(\varphi) - \cos(\theta)\sin(\varnothing)\sin(\varphi) & \sin(\varnothing)\sin(\theta) \\ -\cos(\varphi)\sin(\theta) & \sin(\theta)\sin(\varphi) & \cos(\theta) \end{bmatrix},$$

$$R_6^3 = \begin{bmatrix} r11 & r12 & r13 \\ r21 & r22 & r23 \\ r31 & r32 & r33 \end{bmatrix},$$

(46)

Whereas angles a, b, m are $\varnothing$, θ, φ, respectively.

The $\cos\theta$ can be extracted from $r33$ from the following equation:

$$\cos(b) = \cos\theta,$$
$$\sin(b) = \sin\theta\sqrt{1 - \cos^2\theta}.$$

(47)

The above $\cos\theta$ and $\sin\theta$ can be written in form of tan to find the value of θ:

$$\theta = \tan^{-1}\left(\frac{\sqrt{1 - \cos^2\theta}}{r33}\right),$$
$$\theta = \tan^{-1}\left(\frac{\sqrt{1 - r33^2}}{r33}\right).$$

(48)

For nonsingular case, if both $r13$ and $r23$ are not zero, then equation (49) will yield the value of θ:

$$\theta = a\tan 2\left(r33, \pm\sqrt{1 - r33^2}\right),$$

(49)

or

$$\tan\theta = \frac{\sqrt{r13^2 + r23^2}}{r33} = \frac{\sqrt{(\cos(\varnothing)\sin(\theta))^2 + (\sin(\varnothing)\sin(\theta))^2}}{\cos(\theta)},$$

$$\theta = \tan^{-1}\left(\frac{\sqrt{r13^2 + r23^2}}{r33}\right).$$

(50)

Equation (51) shows the value of θ in terms of $r13$, $r23$ and $r33$:

$$\theta = a\tan 2\left(r33, \pm\sqrt{r13^2 + r23^2}\right).$$

(51)

The last column of R_6^3 from equation (46) can help to yield the value of $\varnothing$:

$$\tan\varnothing = \frac{r23}{r13} = \frac{\sin(\varnothing)\sin(\theta)}{\cos(\varnothing)\sin(\theta)}.$$

(52)

$\varnothing$ can be represented in terms of $r13$ and $r23$, as follows:
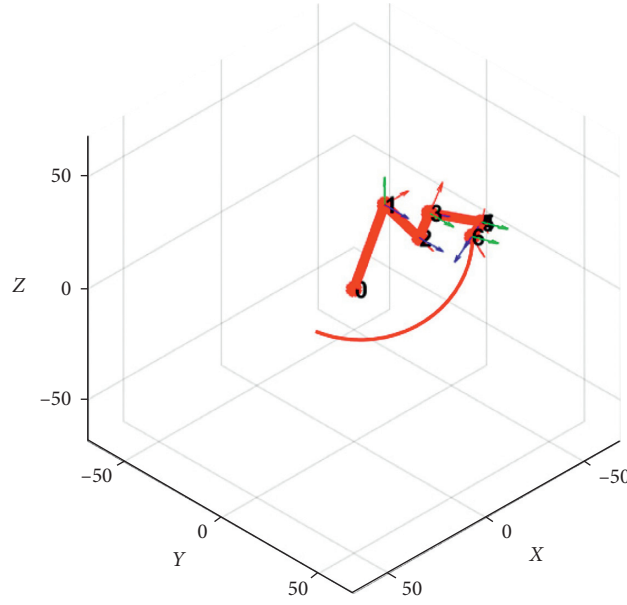
FIGURE 12: The trajectory of Comau NM45.
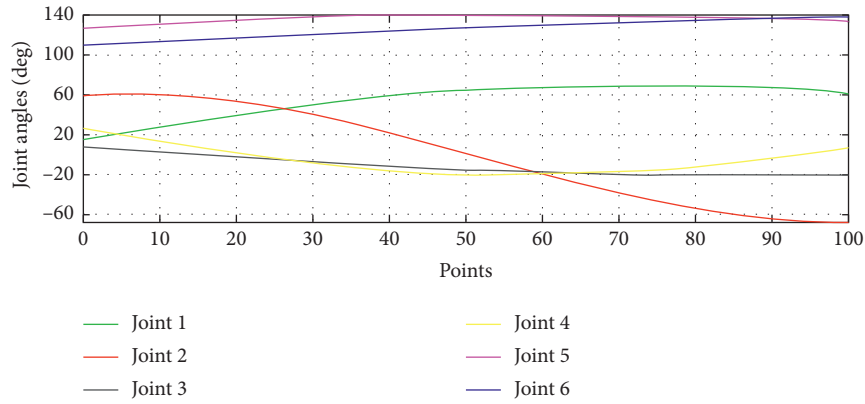
FIGURE 13: Joint trajectory of Comau NM45.

$$\varnothing = a \tan 2 \, (r13, r23). \tag{53}$$

For φ,

$$\tan \varphi = \frac{r32}{-r21} = \frac{\sin(\theta)\sin(\varphi)}{-(-\cos(\varphi)\sin(\theta))}. \tag{54}$$

The φ can be represented in terms of $r31$ and $r32$ mentioned as follows:

$$\varphi = a \tan 2 \, (-r31, r32). \tag{55}$$

For catering singularity, if $\sin(\theta) > 0$, whereas $0 < \theta < \pi$, then solution will be

$$\varnothing = a \tan 2 \, (-r13, -r23),$$
$$\theta = a \tan 2 \left(r33, \ \pm \ \sqrt{r13^2 + r23^2} \right), \tag{56}$$
$$\varphi = a \tan 2 \, (r31, -r32).$$

If $\sin(\theta) < 0$, whereas $-\pi < \theta < 0$, then the solution will be

$$\varnothing = a \tan 2 \, (-r13, -r23),$$
$$\theta = a \tan 2 \left(r33, \ \pm \ \sqrt{r13^2 + r23^2} \right), \tag{57}$$
$$\varphi = a \tan 2 \, (r31, -r32).$$

The last three joint values have been resolved by using the above equations of $\varnothing$, θ, and φ.

For the trajectory planning, the program was written in Matlab by using forward and inverse kinematics equations mentioned in the above sections. The planned trajectory required the smooth motion of the end-effector. The joint angles were calculated using the inverse kinematics equations. Figure 12 shows the trajectory planning and robot motion along with the trajectory for the Comau NM45. The robot was able to follow the trajectory smoothly.

Figure 13 shows the mapping of the values of joints to move on 100 points to follow the trajectory. It shows that the achievement was smooth as there are no sudden spikes in the joint values.

4. Conclusion

The modified DH convention has been used to perform the forward kinematics for the manipulator. The kinematics decoupling has been used to perform the inverse kinematics. The manipulator was divided into two parts to make the inverse kinematics problem simpler. The first 3 joints were resolved by using a geometrical approach, whereas the last three joints were resolved using the algebraic approach. The resultant kinematics solution was applied on the manipulator, and it was able to follow a test trajectory successfully. A similar approach can be used while solving the articulated robot with a spherical wrist. The techniques are applied for the 6-DoF robot.

Data Availability

All the data used are presented as part of paper.

Conflicts of Interest

The authors declare that they have no conflicts of interest.

References

[1] Z. Gan and Q. Tang, "Robot kinematic calibration," in *Visual Sensing and its Applications*, pp. 166–192, Springer Berlin Heidelberg, Berlin, Germany, 2011.

[2] M. Ceccarelli, *Fundamentals of Mechanics of Robotic Manipulationtle*, Kluwer Academic Publishers, Dordrecht, Netherlands, 2004, http://books.google.co.uk/books?id=49eIUfSfOygC&printsec=frontcover&source=gbs_ge_summary_r&cad=0#v=onepage&q&f=false, 27th edition.

[3] M. Shimizu, H. Kakuya, and W.-K. Yoon, "Analytical inverse kinematic computation for 7-DOF redundant manipulators with joint limits and its application to redundancy resolution," *IEEE Transactions on Robotics*, vol. 86, 2008.

[4] J. Denavit, "A kinematic notation for lower-pair mechanisms based on matrices," *Journal of Applied Mechanics*, pp. 215–221, 1955.

[5] J. B Zhuang, "Review of drug treatment for Down's syndrome persons 'a complete and parametrically continuous kinematic model for robot manipulators', robotics and automation," *American Journal of Mental Deficiency*, vol. 80, no. 4, pp. 388–393, 1976.

[6] C. Robots, *Coamu NM45 Specifications, Industrial-Robots*, Robots, Bedford, MA, USA, 2015, http://industrial-robotics.co.uk/comau/nm_spec.htm.

[7] J. J. Craig, *Introduction to Robotics: Mechanics and Control*, Pearson Education, Inc. Pearson Prentice Hall, London, UK, pp. 1–388, 2005.

[8] M. Summers, "Robot capability test and development of industrial robot positioning system for the aerospace industry," *SAE Technical Paper Series*, vol. 114, no. 1, pp. 1108–1118, 2005.

[9] M.W. Spong, S. Hutchinson, and M. Vidyasagar, "Robot Modeling and Control," *John Wiley & Sons*, Inc., Hoboken, NJ, USA, 2006.

[10] S. Megahed, "Inverse kinematics of spherical wrist robot arms: analysis and simulation," *Journal of Intelligent and Robotic Systems*, vol. 5, no. 3, pp. 211–227, 1992.

Research Article

A Dynamic Intersecting Arrangement Model Based on Isolated Draw Zones for Stope Structure Optimization during Sublevel Caving Mining

Guanghui Li [ID],[1] **Fengyu Ren** [ID],[1] **Hangxing Ding** [ID],[1] **Huan Liu** [ID],[1] **Mingzhi Sun** [ID],[1] **and Guang Li** [ID][2]

[1]*School of Resources and Civil Engineering, Northeastern University, Shenyang 110819, China*
[2]*Yanqianshan Branch of Ansteel Mining Co., Ltd., Anshan 621010, China*

Correspondence should be addressed to Hangxing Ding; dinghangxing@mail.neu.edu.cn

In this paper, stope structure optimization during sublevel caving mining is considered under the condition that the isolated draw zones (IDZs) are nonstandard ellipsoid, which is realized by dynamically adjusting the arrangement of IDZs and quantifying the degree of intersection of IDZs according to an ore profit and loss calculation model. A dynamic intersecting arrangement model based on IDZs was proposed, which can dynamically adjust the sublevel height and drift spacing according to the ore-rock bulk flow parameters, economic indicators, occurrence condition of the ore body, drilling machine, and so forth. Based on the model, the range of drift spacing, the lower volume of crestal residual ore, and the higher volume of mixing waste rock are calculated. By deducing the function of ore profit and loss, a calculation model for ore profit and loss is established to quantify the degree of intersection of IDZs and determine the best stope structure. Using the constructed dynamic intersecting arrangement model, a stope structure of −213 m to −303 m in the Yanqianshan Iron Mine was designed, with a sublevel height of 22.5 m and a drift spacing of 20.5 m. A physical drawing model was designed, and three physical simulation experiment schemes were conducted to compare and analyse the ore loss and dilution of the intersecting arrangement model and the traditional tangent arrangement model. The results showed that the loss rate decreased by 3.66% and the dilution rate increased by only 0.22%, thus verifying the effectiveness and applicability of the model to optimize the stope structure.

1. Introduction

The sublevel caving method is one of the oldest methods for underground mining. This method has many advantages with regard to safety and mechanization, so it is widely used in various kinds of metallic mines worldwide [1, 2]. With the extension of deep underground mining and the transformation of open-pit mines to underground mines, the application of this mining method is continuously growing, developing towards intelligent mining equipment and stope structure optimization [3]. The stope structure, including sublevel height, drift spacing, and caving spacing, is the main factor that causes ore loss and dilution. An optimal stope structure can adapt to the fluidity of ore-rock, thus reducing ore loss and dilution.

The sublevel caving method is used for mining between sublevels from top to bottom. When ore is extracted, overlying waste rock fills the void created by ore extraction, so the ore is always surrounded by the overlying waste rock. The caved ore is drawn from drifts under loose cover-layer-rock, so ore loss and dilution readily occur [4–6]. This is a significant disadvantage of this method. Obviously, the optimal stope structure from a scientific drawing model can accelerate the flow of ore and control the mixing of waste rock, thus mitigating the shortcomings of serious ore loss and dilution [5, 7]. Therefore, relevant studies that can help improve the recovery and utilization of mineral resources and increase the economic benefit of mines are very significant.

To optimize the stope structure to reduce ore loss and dilution in sublevel caving mines, scholars have proposed different basic theories; those theories with practical value include ellipsoid draw theory and stochastic medium draw theory [8, 9]. These theories study the movement trends of caved ore and overlying waste rock but adopt different research methods [10]. Ellipsoid draw theory experimentally proves that isolated draw zones (IDZs) (the geometrical locus defined by the initial location of the caved ore that is recovered from a drawpoint in underground mining) are approximately ellipsoids [11]. Then, the properties of IDZs are studied and used to explain the flow characteristics of the ore-rock bulk. Stochastic medium draw theory simplifies the ore-rock bulk into a continuous flowing random medium and then studies the movement process of the ore-rock bulk through probability theory [12, 13]. In the final analysis, these theories are ultimately used to optimize caving mining schemes and to determine reasonable stope structures. Based on ellipsoid draw theory, Kvapil [14] expanded from a single IDZ and used IDZ spatial arrangement theory to design stope structures. This design principle later evolved into two stope structures: wide drift spacing structure and high sublevel structure. In wide drift spacing structure, the upper and lower ellipsoids are directly tangent, while the left and right discharge ellipsoids are separated and tangent to the upper and lower ellipsoids (see Figure 1(a)). Similarly, in high sublevel structure, the left and right ellipsoids are directly tangent to each other, while the upper and lower discharge ellipsoids are separated and tangent to both the left and right ellipsoids (see Figure 1(b)). According to the design principle, the sublevel height of caving mines worldwide is 15 m to 30 m, and the drift spacing is generally slightly less than or equal to the sublevel height. However, under these stope structures, a certain proportion of ore is outside the IDZ (see Figure 1); therefore, this cannot be regarded as the optimal stope structure, and it has been proven that these stope structures do not yield a good recovery effect in practical mining applications. Some mines, such as the Xiadian Gold Mine in China and the Kamoto Copper Mine in Zambia, have recoveries of less than 80% [15]. Yuan et al. [16] analysed the coincident relationship between the caved ore, crestal residual ore, and IDZ and concluded that, within a certain temporal period and spatial area, increasing the distance between the drawpoints reduces the recovery rate of ore. Wang et al. [17] numerically simulated drift spacings of 12 m to 20 m, and the results showed that there were no obvious changes in the waste in-ore rate as the drift spacing increased, but the ore recovery rate decreased from 63% to 46% with increasing drift spacing. Tan et al. [18] discussed the wide drift spacing structure based on the ellipsoid drawing theory and pointed out the defects of the design scheme. The above studies are all based on qualitative descriptions of stope structure and analyse the influence of drift spacing on ore recovery. The specific stope structure is still determined according to mining experience and experiments. Moreover, for the whole mine, the stope structure is fixed and cannot be dynamically adjusted.
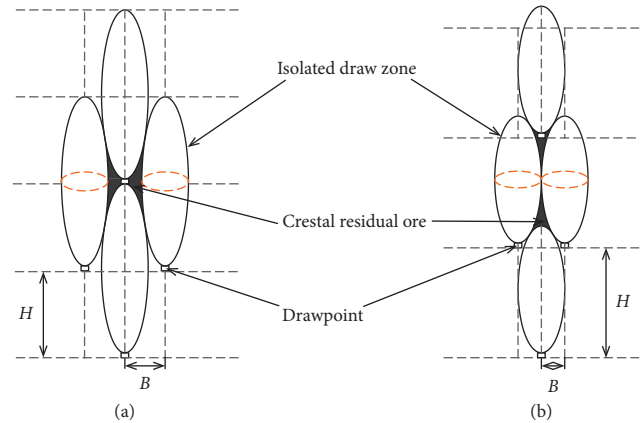
Figure 1: The conventional tangent arrangement model based on IDZs [14]. (a) Wide drift spacing structure. (b) High sublevel structure.

When mining by the sublevel caving method, the shape of the IDZ is affected by many factors, including not only the physical properties of particles, such as the ore-rock bulk geometry, lumpiness, concrete gradation, humidity, and loose factor, but also the mechanical properties of particles, such as the lateral pressure and friction [19]. Therefore, the shape of the IDZ is not a regular ellipsoid. Marano et al. [9, 20] believe that the IDZ is composed of different shapes, such as an ellipsoid in the upper part and a parabolic rotating body in the lower part. Janelid and Kvapil [3, 21, 22] proved that the ellipsoid is an approximate ellipsoid, but there are cases in which the upper part is thick and the lower half is thin and vice versa. The nonstandard ellipsoid shape of the IDZ means that the tangent arrangement model cannot be completely applied to the design of the stope structure.

In this study, stope structure optimization during sublevel caving mining is considered under the condition that the IDZs are nonstandard ellipsoids, which is realized by dynamically adjusting the arrangement of IDZs and quantifying the degree of intersection of IDZs according to an ore profit and loss calculation model. A dynamic intersecting arrangement model based on IDZs which can dynamically adjust the stope structure according to the ore-rock bulk flow parameters, economic indicators, occurrence conditions of ore bodies, drilling machines, and so forth is proposed. Then, taking the ore profit and loss as the research object, a calculation model is established to quantify the degree of intersection of the IDZs and determine the best sublevel height and drift spacing. Finally, with the dynamic intersecting arrangement model, the optimal stope structure of the Yanqianshan Iron Mine is designed; moreover, three experimental schemes using the Yanqianshan Iron Mine as the background were carried out to compare the tangent arrangement model based on IDZs and the intersecting arrangement model based on IDZs.

2. The Intersecting Arrangement Model Based on IDZs

The design and optimization of the stope structure generally follow the principle that the shape of the caved ore heap is

consistent with that of the IDZ [14], which means that the IDZ should contain as much caved ore and residual ore as possible. According to the conclusion of Yuan and Liu [16, 23], if the distance between drawpoints is reduced so that the IDZs intersect, the crestal residual ore will be reduced (see Figure 2), which has a significant impact on the ore recovery rate. Therefore, the intersecting arrangement model based on IDZs can better reflect the principle that the shape of the caved ore heap is consistent with that of the IDZ, especially when the IDZ is a nonstandard ellipsoid.

Stochastic medium draw theory of Ren [12] simplifies the ore-rock bulk into a continuous flowing random medium, which better reflects the shape of the IDZ. Based on stochastic medium draw theory, for the end ore drawing of the sublevel caving method, the shape of IDZ is given by

$$\frac{\left(x - kz^{(\alpha/2)}\right)^2}{\beta z^{\alpha}} + \frac{y^2}{\beta_1 z^{\alpha_1}} = \left(\frac{\alpha + \alpha_1}{2} + 1\right)\ln\frac{2H}{z} \quad [12], \quad (1)$$

where $\alpha, \beta, \alpha_1,$ and β_1 are the ore-rock bulk flow parameters (α and β represent the vertical direction of the drift, and α_1 and β_1 represent the horizontal direction of the drift); k is the impact coefficient of the ore body and depends on the damping degree of the ore-rock bulk by the ore body (in general, $k = 0.1 \sim 0.15$); and H is the sublevel height. Equation (1) is mainly used to determine the width of the IDZ in the vertical direction of the drift to design the drift spacing.

When mining by the sublevel caving method, the shape of the IDZ is not a regular ellipsoid, and the tangent arrangement model based on IDZs will reduce the density of the spatial arrangement, causing more ore to be outside the range of the IDZ. Under these conditions, it is more appropriate to adopt the intersecting arrangement model based on IDZs. The drift spacing is shortened so that IDZs R_2 and R_3 intersect with the upper and lower IDZs R_1 and R_3, respectively, and then the crestal residual ore will be reduced (see Figure 3). Of course, this shortening will promote the mixing of waste rock, but this problem can be addressed by calculating the comprehensive economic benefits of the ore. The best intersection degree of the IDZ corresponds to the maximum economic benefit.

3. Optimization of the Stope Structure

The sublevel height is determined by occurrence conditions of the ore body, drilling machine, demolition equipment, and so forth. Once the sublevel height is determined, it is difficult to change. The drift spacing is a quantitative representation of the intersecting arrangement model based on IDZs, and the degree of intersection determines the drift spacing. In this section, on the basis of establishing the intersecting arrangement model based on IDZs, the method for determining the optimal stope structure is given.

3.1. Range of the Drift Spacing. In this section, equations of the four adjacent IDZs are established at the same coordinate according to the shape of the IDZ (equation (1)). On this basis, we derived the calculation method of the width of the IDZ in the vertical direction of the drift and provided the
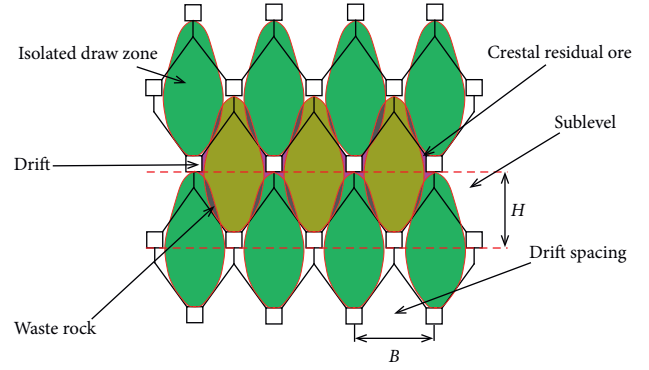
Figure 2: Stope structure of the intersecting arrangement model based on IDZs.
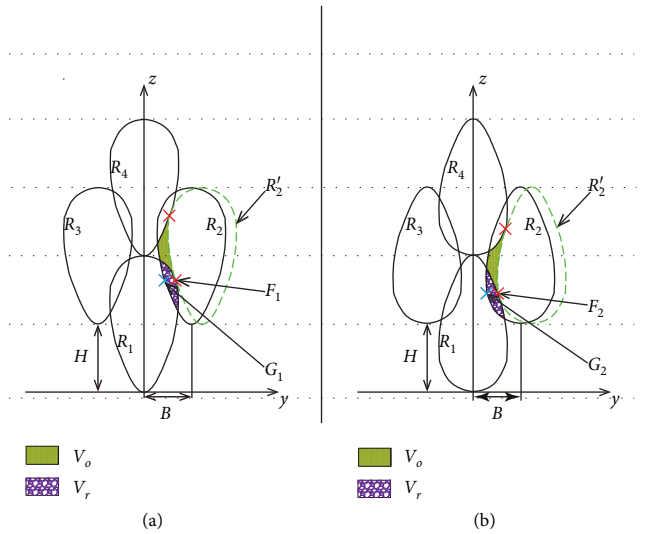
Figure 3: The intersecting arrangement model based on IDZs. (a) $\alpha < 1.44$. (b) $\alpha > 1.44$.

determination method for the drift spacing by using the arrangement of the IDZs.

From equation (1) and Figure 3, the equation of the IDZ R_1 is as follows:

$$R_1: \frac{\left(x - kz^{(\alpha/2)}\right)^2}{\beta z^{\alpha}} + \frac{y^2}{\beta_1 z^{\alpha_1}} = \left(\frac{\alpha + \alpha_1}{2} + 1\right)\ln\frac{2H}{z} \quad [12]. \quad (2)$$

By transforming the coordinates of the centre point of IDZ R_1, the equations of R_2, R_3, and R_4 are as follows:

$$R_2: \frac{\left(x - k(z - H)^{(\alpha/2)}\right)^2}{\beta(z - H)^{\alpha}} + \frac{(y - B)^2}{\beta_1(z - H)^{\alpha_1}} = \left(\frac{\alpha + \alpha_1}{2} + 1\right)\ln\frac{2H}{z - H}, \quad (3)$$

$$R_3: \frac{\left(x - k(z - 2H)^{(\alpha/2)}\right)^2}{\beta(z - 2H)^{\alpha}} + \frac{y^2}{\beta_1(z - 2H)^{\alpha_1}} = \left(\frac{\alpha + \alpha_1}{2} + 1\right)\ln\frac{2H}{z - 2H}, \quad (4)$$

$$R_4: \quad \frac{\left(x - k(z-H)^{(\alpha/2)}\right)^2}{\beta(z-H)^{\alpha}} + \frac{(y+B)^2}{\beta_1(z-H)^{\alpha_1}} = \left(\frac{\alpha + \alpha_1}{2} + 1\right)\ln\frac{2H}{z-H}, \tag{5}$$

where B is the drift spacing, which refers to the distance between two drawpoints; R_1 is the lower IDZ; R_2 is the right IDZ; R_3 is the upper IDZ; and R_4 is the left IDZ.

For R_1, along the direction of $x = kz^{\hat{}}(\alpha/2)$, which is the vertical direction of the drift, the profile equation of R_1 is as follows:

$$y^2 = \left(\frac{\alpha + \alpha_1}{2} + 1\right)\beta_1 z^{\alpha_1}\ln\frac{2H}{z}. \tag{6}$$

For R_2, along the direction of $x = k(z-H)^{\hat{}}(\alpha/2)$, which is the vertical direction of the drift, the profile equation of R_2 is as follows:

$$(y-B)^2 = \left(\frac{\alpha + \alpha_1}{2} + 1\right)\beta_1(z-H)^{\alpha_1}\ln\frac{2H}{(z-H)}. \tag{7}$$

The height of the widest part of R_1 is denoted by h, and the normal slope of R_1 at $z = h$ is zero; for equation (6), $dy/dz = 0$. Then,

$$z = h = 2He^{-(1/\alpha_1)}. \tag{8}$$

Next, the maximum and minimum values of the drift spacing are calculated for different IDZ shapes.

(1) $\alpha < 1.44$

The widest part of the IDZ is located at the lower part, and the IDZ is similar to an ellipsoid with a thin upper part and thick lower part (see Figure 3(a)).

For R_2, by equations (7) and (8), the widest part is located at z, where

$$z = 2He^{-(1/\alpha_1)} + H. \tag{9}$$

Point G_1 is defined as follows:

$$G_1\left(2He^{-(1/\alpha_1)} + H, \quad -\sqrt{\frac{((\alpha + \alpha_1/2) + 1)\beta_1(2H)^{\alpha_1}}{\alpha_1 e}} + B\right). \tag{10}$$

For R_1, by equations (6), (8), and (9), point F_1 is defined as follows:

$$F_1\left(2He^{-(1/\alpha_1)} + H, \quad \sqrt{\left(\frac{\alpha + \alpha_1}{2} + 1\right)\beta_1 H^{\alpha_1}\left(1 + 2e^{-(1/\alpha_1)}\right)^{\alpha_1}\ln\frac{2}{1 + 2e^{-(1/\alpha_1)}}}\right). \tag{11}$$

When R_2 is tangent to R_1 and R_3, the drift spacing is maximized, and points G_1 and F_1 coincide; therefore,

$$B\max = \sqrt{\left(\frac{\alpha + \alpha_1}{2} + 1\right)\beta_1 H^{\alpha_1}\left(1 + 2e^{-(1/\alpha_1)}\right)^{\alpha_1}\ln\frac{2}{1 + 2e^{-(1/\alpha_1)}}} + \sqrt{\frac{((\alpha + \alpha_1/2) + 1)\beta_1(2H)^{\alpha_1}}{\alpha_1 e}}. \tag{12}$$

When R_2 is tangent to the z-axis, the drift spacing is minimized; therefore,

$$B\min = \sqrt{\frac{((\alpha + \alpha_1/2) + 1)\beta_1(2H)^{\alpha_1}}{\alpha_1 e}}, \tag{13}$$

where $B_{\max}$ is the maximum drift spacing and $B_{\min}$ is the minimum drift spacing.

(2) $\alpha > 1.44$

The widest part of the IDZ is located in the upper part, and the IDZ is similar to an ellipsoid with a thick upper part and thin lower part (see Figure 3(b)).

For R_1, according to equations (6) and (8), the widest part is located at z, and point F_2 is defined as follows:

$$F_2\left(2He^{-(1/\alpha_1)}, \quad \sqrt{\frac{((\alpha + \alpha_1/2) + 1)\beta_1(2H)^{\alpha_1}}{\alpha_1 e}}\right). \tag{14}$$

For R_2, according to equations (7) and (8), point G_2 is defined as follows:

$$G_2\left(2He^{-(1/\alpha_1)}, \quad -\sqrt{\left(\frac{\alpha + \alpha_1}{2} + 1\right)\beta_1 H^{\alpha_1}\left(2e^{-(1/\alpha_1)} - 1\right)^{\alpha_1}\ln\frac{2}{2e^{-(1/\alpha_1)} - 1}} + B\right). \tag{15}$$

When R_2 is tangent to R_1 and R_3, the drift spacing is maximized, and points G_2 and F_2 coincide:

$$B\max = \sqrt{\left(\frac{\alpha+\alpha_1}{2}+1\right)\beta_1 H^{\alpha_1}\left(2e^{-(1/\alpha_1)}-1\right)^{\alpha_1}\ln\frac{2}{2e^{-(1/\alpha_1)}-1}} + \sqrt{\frac{((\alpha+\alpha_1/2)+1)\beta_1(2H)^{\alpha_1}}{\alpha_1 e}}. \tag{16}$$

When R_2 is tangent to the z-axis, the drift spacing is minimized:

$$B\min = \sqrt{\frac{((\alpha+\alpha_1/2)+1)\beta_1(2H)^{\alpha_1}}{\alpha_1 e}}. \tag{17}$$

In summary, when the IDZ is a nonstandard ellipsoid, the range of the drift spacing is as follows:

$$\left[\sqrt{\frac{((\alpha+\alpha_1/2)+1)\beta_1(2H)^{\alpha_1}}{\alpha_1 e}}\ \sqrt{\left(\frac{\alpha+\alpha_1}{2}+1\right)\beta_1 H^{\alpha_1}\left(1+2e^{-(1/\alpha_1)}\right)^{\alpha_1}\ln\frac{2}{1+2e^{-(1/\alpha_1)}}}\right.$$

$$\left.+\sqrt{\frac{((\alpha+\alpha_1/2)+1)\beta_1(2H)^{\alpha_1}}{\alpha_1 e}}\right]\quad \alpha<1.44, \tag{18}$$

$$\left[\sqrt{\frac{((\alpha+\alpha_1/2)+1)\beta_1(2H)^{\alpha_1}}{\alpha_1 e}}\ \sqrt{\left(\frac{\alpha+\alpha_1}{2}+1\right)\beta_1 H^{\alpha_1}\left(2e^{-(1/\alpha_1)}-1\right)^{\alpha_1}\ln\frac{2}{2e^{-(1/\alpha_1)}-1}}\right.$$

$$\left.+\sqrt{\frac{((\alpha+\alpha_1/2)+1)\beta_1(2H)^{\alpha_1}}{\alpha_1 e}}\right]\quad \alpha>1.44. \tag{19}$$

3.2. Volume Calculation.

When the sublevel height is determined, with decreasing drift spacing, the arrangement model based on IDZs changes from tangent to intersecting, the amount of crestal residual ore decreases, and the mixing amount of waste rock increases. V_o is the lower crestal residual ore volume, and V_r is the higher mixing waste rock volume. When V_o and V_r are calculated, the functional relations of V_o and B as well as those of V_r and B are fitted (see Figure 4).

The solution steps are as follows:

Step 1: determine the sublevel height, parameter value, and range of B. The sublevel height is determined by occurrence conditions of the ore body, drilling machine, demolition equipment, and so forth. Once the sublevel height is determined, it is difficult to change. The parameters include the ore-rock bulk flow parameters $(\alpha, \beta, \alpha_1\ and\ \beta_1)$, the impact coefficient of the ore body (k), and the sublevel height (H). The ore-rock bulk flow parameters can be obtained by laboratory or mining field drawing experiments, and the impact coefficient of the ore body is generally between 0.1 and 0.15. The range of B can be determined by equation (18) or (19).

Step 2: divide the areas of V_o and V_r. As shown in Figure 3, the areas of V_o and V_r can be calculated by $V_o = 1/2[R_2 - (R_2 \cap R_2') - (R_2 \cap R_1) - (R_2 \cap R_4)]$ and $V_r = R_1 \cap R_2$.

Step 3: find the Monte Carlo solution for V_o and V_r. With equations (2)–(5) and the parameters that are determined in step 1, the IDZ boundary is established. Using the Monte Carlo method with the IDZ boundary, the membership function, which is used to judge whether a point is within the boundary of the IDZ, is written. Statistical points in the V_o and V_r areas and V_o and V_r are determined [24, 25].

Step 4: determine the functional relationship between V_o and B as well as that between V_r and B. Data analysis is performed on V_o and B as well as V_r and B, and then the functional relationship between V_o and B and that between V_r and B are fitted.

$$\begin{aligned} Vo &= f_1(B), \\ Vr &= f_2(B). \end{aligned} \tag{20}$$

3.3. Economic Evaluation.

The direct purpose of mining enterprises is to exploit ore, and the final profit product is the ore concentrate. To determine the optimal intersecting arrangement model based on IDZs, the economic benefit of the concentrate is taken as the final evaluation target. First, the calculation formula for ore profit and the calculation formula for ore loss are established. Then, combined with

| Sublevel height (H) |
| Ore-rock bulk flow parameters (α, β, α_1 and β_1) |
| Impact coefficient of the ore body (k, $k = 0.1 \sim 0.15$) |
| Range of B ($[B_{\min}, B_{\max}]$) |
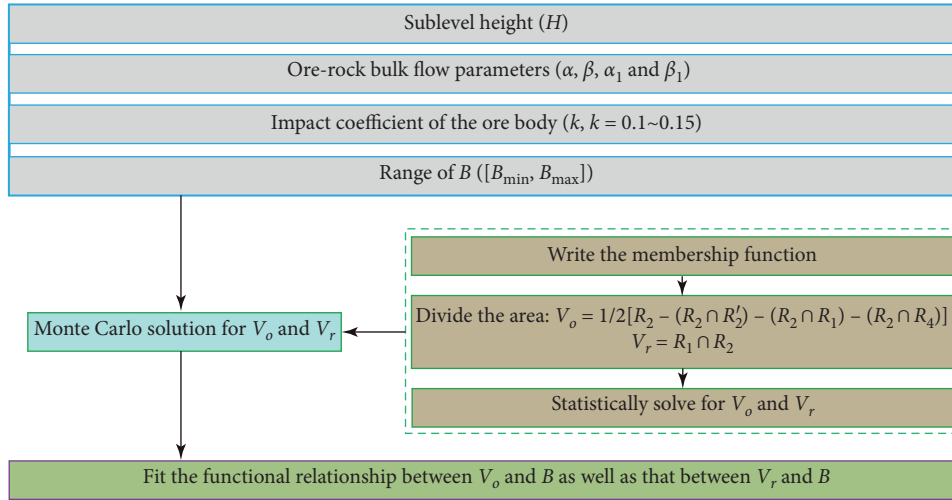
FIGURE 4: Technical route of the volume calculation.

equation (20), the ore profit and loss are calculated. Finally, the ore profit and loss are analysed comprehensively, and the optimal solution is determined to obtain the best stope structure.

3.3.1. Ore Profit and Loss. (1) *Ore Profit.* The crestal residual ore from drawing to dressing eventually becomes concentrate; in this process, the profit mainly considers the concentrate profit and cost loss [26].

The concentrate profit refers to the value of the concentrate produced after the ore is processed by the beneficiation plant [27].

The ore is processed by the beneficiation plant and finally becomes concentrate and tailings. According to the conservation of quality, one ton of ore is processed into concentrate and tailings, so $1 = Q_c + Q_t$. The conservation of the metal content is

$$1 \times c_o = Q_c \times c_c + Q_t \times c_t \ [27],\tag{21}$$

$$Q_c = \frac{c_o - c_t}{c_c - c_t}.\tag{22}$$

The profit from converting a ton of ore into concentrate is

$$p_1 = Q_c = \frac{(c_o - c_t)}{(c_c - c_t)} \times P,\tag{23}$$

where Q_c is the quality of the concentrate, Q_t is the quality of tailings, C_o is the ore grade, C_c is the concentrate grade, C_t is the tailings grade, p_1 is the profit of converting a ton of ore into concentrate, and P is the concentrate price.

The cost loss refers to the costs incurred by ore from drawing to dressing due to upgrading, ore blending, transportation, and so forth. Mining enterprises can statistically determine the actual technical and economic indicators of the year to obtain the cost loss per ton of ore, which is represented by p_2 [28].

Based on the above analysis, the profit generated by recovering one ton of crestal residual ore is $p_1 - p_2$, and, with equation (23),

$$p = \frac{(c_o - c_t)}{(c_c - c_t)} \times P - p_2,\tag{24}$$

where p is the ore profit.

(2) *Ore Loss.* The mixing of waste rock results in ore dilution, and the loss caused by this dilution mainly considers the loss of metal from tailings and the cost of waste rock mining and processing [26].

The loss of metal from tailings refers to waste rock that is of no grade or is lower than tailings grade; when this rock is treated as tailings, it needs to be matched with some low-grade ore, causing metal loss [27].

For one ton of waste rock in tailings, the resulting metal loss is

$$Q_m = \frac{1}{1 - c_t} \times c_t \ [27],\tag{25}$$

where Q_m is the metal quality.

The amount of metal lost due to one ton of waste rock in tailings is expressed as the amount of concentrate:

$$Q_m = Q_c \times c_c.\tag{26}$$

The conservation of the metal content is

$$\frac{1}{1 - c_t} \times c_t = Q_c \times c_c.\tag{27}$$

The loss of metal from converting a ton of waste rock into tailings is converted into concentrate:

$$Q_c = \frac{c_t}{c_c \times (1 - c_t)}.\tag{28}$$

The loss of metal from tailings is

$$l_1 = \frac{c_w}{c_j \times (1 - c_w)} \times P,\tag{29}$$

where l_1 is the loss of metal from tailings.

The cost of waste rock mining and processing refers to the expenses associated with mining, processing, transportation and stacking, and so forth incurred by the mixture of waste rock. Mining enterprises can calculate the actual technical and economic indicators of the year to obtain the cost loss per ton of waste rock, which is represented by l_2.

Based on the above analysis, the loss generated by mixing one ton of waste rock is $l_1 + l_2$, and, with equation (29),

$$l = \frac{c_w}{c_j \times (1 - c_w)} \times P + l_2, \tag{30}$$

where l is the ore loss.

3.3.2. Optimal Path Spacing.
When the spatial arrangement model based on IDZs changes from a tangent arrangement to an intersecting arrangement, as the drift spacing decreases, the amount of crestal residual ore decreases but the amount of mixed waste rock increases. A smaller amount of crestal residual ore increases the profitability of the mine, and a larger amount of mixing waste rock increases the mine loss. With equations (24) and (30), the economy of the intersecting arrangement model based on IDZs can be calculated as

$$s = V_O \times \rho_O \times p - V_r \times \rho_r \times l, \tag{31}$$

where ρ_o is the ore density and ρ_r is the rock density.

By equations (20), (31) can be rewritten as follows:

$$s = f_1(B) \times \rho_o \times p - f_2(B) \times \rho_r \times l. \tag{32}$$

Differentiating equation (32) with respect to B yields the drift spacing with the highest benefit, that is, the optimal intersection degree of IDZs.

4. Application of the Model

4.1. Engineering Background.
The Yanqianshan Iron Mine is located in the Anshan mining area in Northeast China, the largest mining area currently in China. After the previous open-pit mining phase, there were approximately 357.27 million tons of geological reserves outside the open-pit boundary. In 2009, the mine officially entered the transition period from open pit to underground mining, which lasted for 5 years. After the transition period, the mine was fully converted to underground mining and the sublevel caving method was adopted (see Figure 5). The stope structure parameters are as follows: the sublevel height is 18 m and the drift spacing is 20 m. Under the conditions of the stope structure, the loss rate and dilution rate are approximately 15% and 18%, respectively, and there is still room for improvement [29, 30].

In 2019, the design of the mining scheme for elevations of −213 m to −303 m in the Yanqianshan Iron Mine began in preparation for production over the next five years. Under the premise that the mining equipment meets the production needs, the intent is to divide the ore body from elevations of −213 m to −303 m into four sublevels; then, the sublevel height is 22.5 m. This can reduce the cost of preliminary mining and the cutting of a sublevel (see Figure 6). However, the drift spacing has not been matched with the sublevel height, and the drift spacing has been included in the design and experimentation of the Yanqianshan Iron Mine.

According to the intersecting arrangement model based on IDZs, the optimal stope structure of elevations from −213 m to −303 m in the Yanqianshan Iron Mine is determined. Moreover, three experimental schemes are designed to compare and analyse the differences between the conventional tangent arrangement model based on IDZs and the intersecting arrangement model based on IDZs.

4.2. Stope Structure Determination.
According to the intersecting arrangement model based on IDZs and combined with the stope characteristics of the Yanqianshan Iron Mine, the sublevel height is 22.5 m. The next step is to calculate the optimal drift spacing of elevations from −213 m to −303 m.

The ore-rock bulk flow parameters are determined by ore drawing experiments, with reference to stochastic medium draw theory of Ren. To improve the consistency between the experiment and the mining site, the ore from the stope is used as the experimental material, and the similarity ratio is set to $1:100$. After three experiments, the experimental results are averaged, and the ore-rock bulk flow parameters of the −213 m to −303 m sublevels of the Yanqianshan Iron Mine are as follows: $\alpha = 1.21$, $\beta = 1.63$, $\alpha_1 = 1.32$, and $\beta_1 = 1.98$. Based on the mine design, the sublevel height H is 22.5 m, and $k = 0.1$.

Because $\alpha = 1.21$, the IDZ of the Yanqianshan Iron Mine is similar to an ellipsoid with a thin upper part and thick lower part; according to equation (18), the range of the drift spacing is [17.9106 m, 22.4647 m].

Using the calculation formula of V_o and V_r, the values of $\alpha, \beta, \alpha_1, \beta_1, k$ and H are input, and then V_o and V_r corresponding to different drift spacings are obtained. Data analysis is performed on V_o and B as well as V_r and B, and then the functional relationship between V_o and B as well as that between V_r and B are fit (see Figure 7).

$$V_o = -15.08 \times B^2 + 467.37 \times B - 1108.36, \tag{33}$$

$$V_r = 13.90 \times B^2 - 791.98 \times B + 9087.28. \tag{34}$$

The economic and technical indicators obtained from statistical analysis of the production and economic situation in 2019 by the Technical Department of the Yanqianshan Iron Mine are shown in Table 1.

According to equation (24), the profit generated by recovering one ton of crestal residual ore is 51.09 USD/t; $p = 51.09$ USD/t.

According to equation (30), the loss generated by mixing one ton of waste rock is 24.2 USD/t; $l = 24.2$ USD/t.
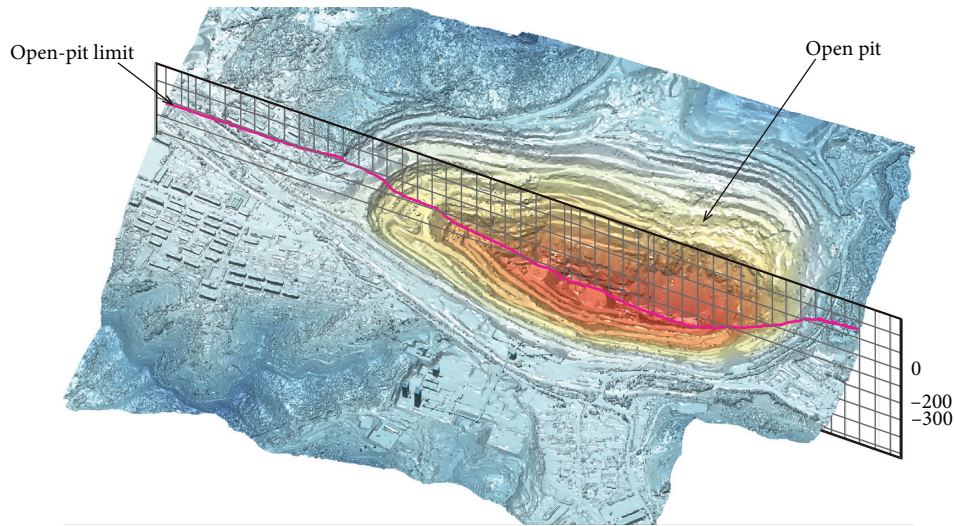
FIGURE 5: The mining status model of the Yanqianshan Iron Mine.
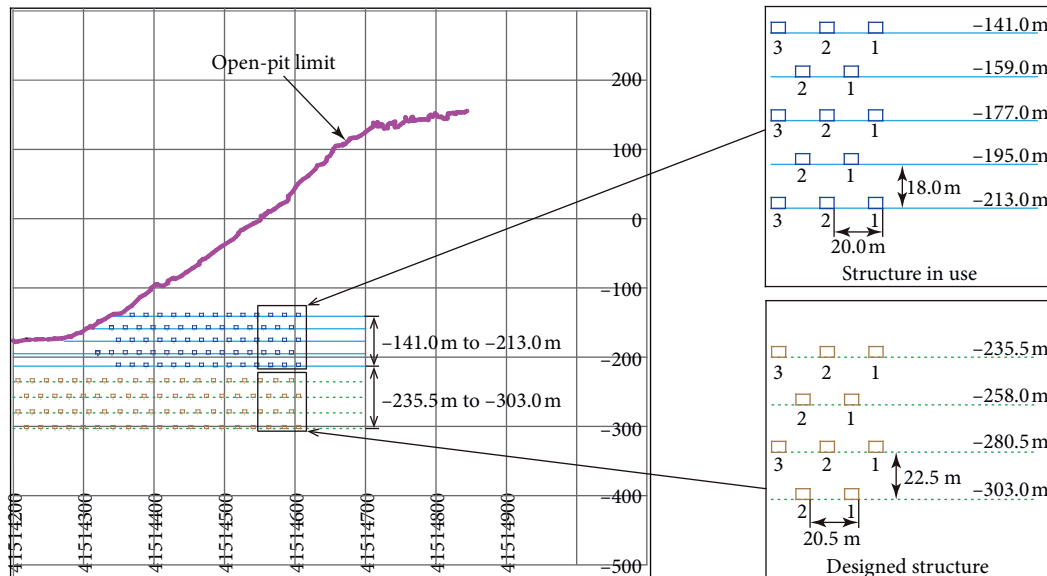
FIGURE 6: Underground mining structure of the Yanqianshan Iron Mine.

The amount of crestal residual ore recovered is $2V_o$, and the amount of waste rock is $4V_r$ (see Figure 3). The ore density is measured as 5.0 t/m^3, and the rock density is 3.5 t/m^3. According to equations (32)–(34),

$$s = -12413.47 \times B^2 + 507102.13 \times B - 3645031.58. \quad (35)$$

According to equation (35), the derivative with respect to B yields $B = 20.43$ m. Considering the construction and operation of the mine, the optimal approach spacing is set to 20.5 m.

4.3. Physical Simulation Experiments.

Based on the above analysis, the stope structure from −213 m to −303 m in the Yanqianshan Iron Mine is determined, the sublevel height is 22.5 m, and the drift spacing is 20.5 m. To verify the

rationality of the scheme, physical simulation experiments are carried out to compare and analyse the loss and dilution degree of ore under the three conditions of the stope structure: the intersecting model, tangent model, and original stope structure.

4.3.1. Materials and Device.

Magnetite and dolomite are used as the simulation materials in the experiments, in which magnetite is regarded as the caved ore and dolomite is regarded as the overlying waste rock. The lumpiness ratio of magnetite to stope caved ore is 1 : 100, which is obtained by screening at the crushing station, and the magnetite size is 1 mm to 3 mm. Dolomite has a slightly larger size than magnetite, ranging from 2 mm to 3 mm. Due to the fluidity of the ore-rock bulk, the size of overlying waste rock is larger
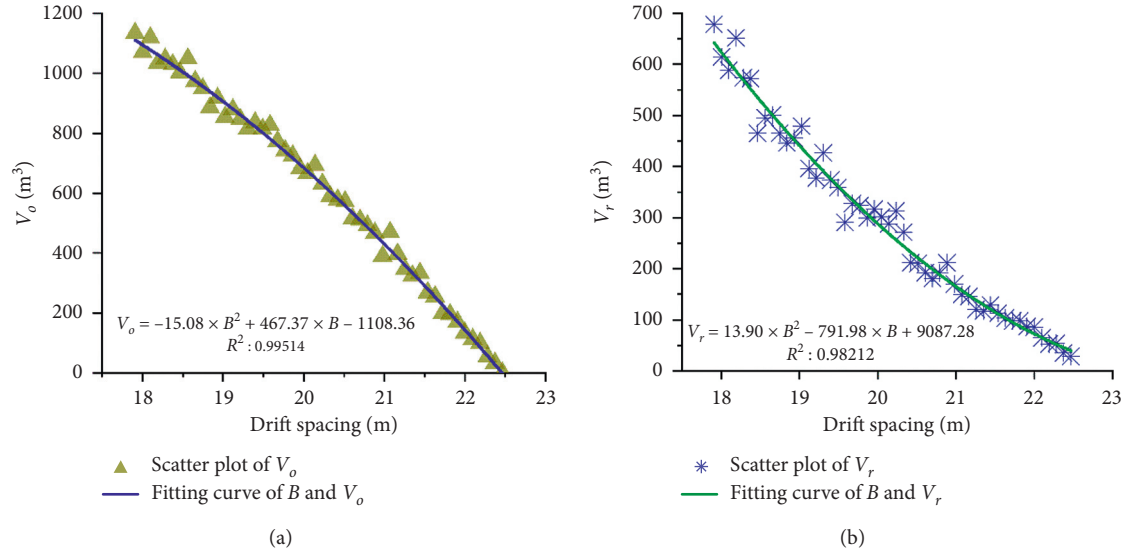
FIGURE 7: Fitting of the drift spacing and volume. (a) B and V_O. (b) B and V_r.

TABLE 1: Economic and technical indicators of the Yanqianshan Iron Mine in 2019.

Economic and technical indicators	Symbols & units	Value
Ore grade	Co %	34
Concentrate grade	Cc %	65.5
Tailings grade	Ct %	10
Concentrate price	P USD/t	125.7
Cost loss	p_2 USD/t	2.96
Cost of waste rock	$l2$ USD/t	2.96

than that of caved ore, which can reduce the mixing of waste rock and reduce ore dilution.

A self-designed physical stope model (see Figure 8) with a geometric scale of 1 : 100 is used to compare the loss and dilution degree of ore under the three stope structure conditions. A 10 mm thick transparent organic glass plate is used to simulate the stope work-plane. The work-plane has five sublevels, each sublevel has 4 or 5 drawpoints, and the drawpoints are in a staggered arrangement shaped like a rhombus. In this experiment, three organic glass plates are made to simulate three groups of different stope structures. An aluminum frame is used to hold the organic glass plates in place to form the stope model. The left, right, and back sides of the stope model are covered with a 10 mm thick transparent organic glass plate, which is convenient for loading experimental materials and observing the experimental process. There are slots on the left and right sides of the organic glass plate at a distance of 2 cm from the front stope work-plane to simulate caving space.

4.3.2. Schemes. As presented in Table 2, three physical simulation schemes are designed and 9 groups of experiments are conducted to compare and analyse the loss and dilution degree of the ore under the three stope structure conditions. The objective is to verify the rationality and

superiority of the intersecting arrangement model based on IDZs.

4.3.3. Process. The experiment is divided into three steps: filling, drawing, and weighing. During filling, a steel plate should be inserted into the slots of the organic glass plates on the left and right sides to form the caving space, magnetite should be used to fill the caving space, and dolomite should be used to fill the outside of the caving space. Magnetite and dolomite are added simultaneously up to sublevel 5; then, the steel plate is drawn out, and dolomite is continually added to a filling height greater than 2 times the height of a sublevel. The cut-off grade drawing method of the Yanqianshan Iron Mine is simulated for drawing, and the cut-off grade is 20%. To facilitate the experiment operation, the cut-off grade is converted into the waste rock mixing rate, which is calculated to be 26%. For each drawing, the magnetite and dolomite weights are determined, and when the weight of the dolomite divided by the weight of the magnetite and dolomite reaches 26%, drawing at this drawpoint is stopped. Drawing is carried out from top to bottom and from left to right in turn. In the process, the overlying dolomite should be added in a timely manner to maintain a steady drawing pressure. After drawing, the magnetite and dolomite are separated to prepare for the next experiment.

In the drawing process, with the drawing of the ore, the overlying waste rock flows downward, resulting in ore and rock mixtures. When the ore and waste rock are mixed to the cut-off grade, drawing at this drawpoint is stopped. Through the transparent organic glass plate, part of the crestal residual ore can be seen (see Figure 9(a)). When the overlying waste rock is exfoliated layer by layer, residual ore can be seen (see Figure 9(b)). As ore drawing continues, the residual ore moves down with the overlying waste rock and is concentrated in the lowest sublevel.
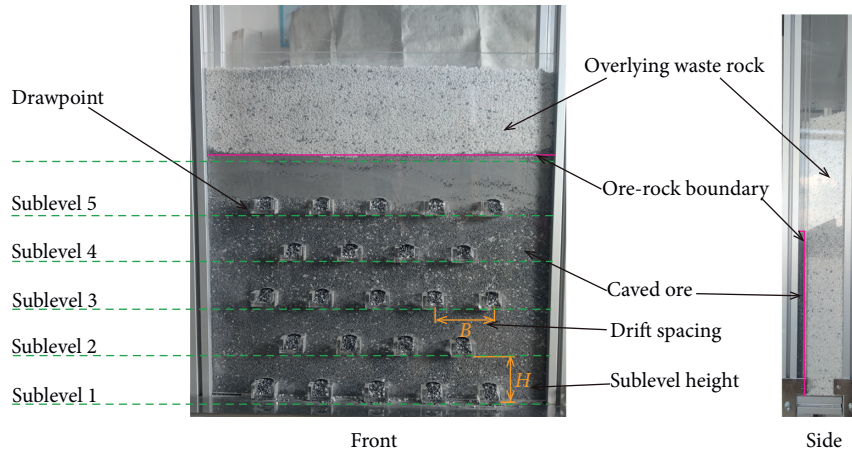
FIGURE 8: Physical stope model of ore drawing.

TABLE 2: Experimental schemes.

Number	Name	Sublevel height (m)	Drift spacing (m)
1	Original	18	20
2	Intersecting model	22.5	20.5
3	Tangent model	22.5	22.5

(a)

(b)
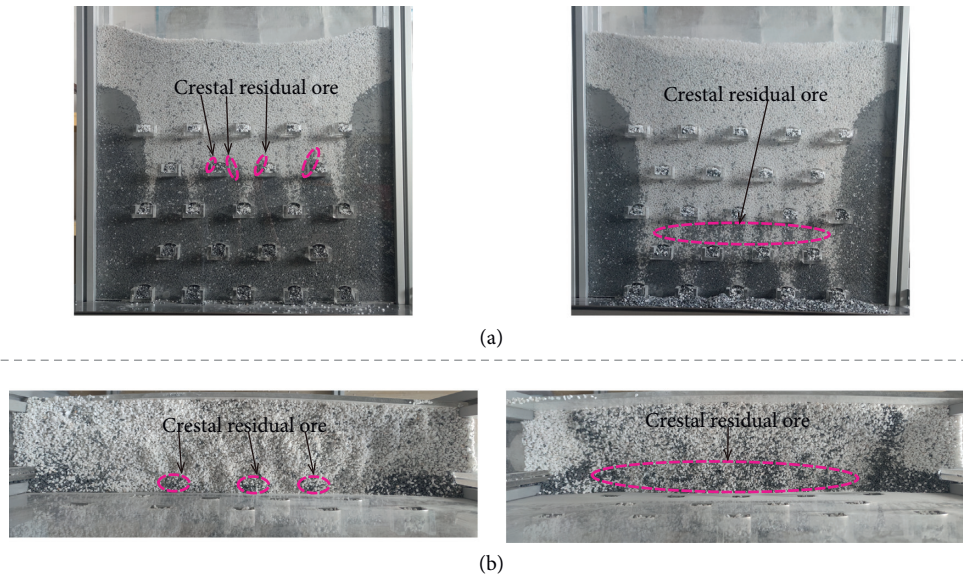
FIGURE 9: Drawing phenomenon and effect. (a) Front view. (b) Top view.

4.3.4. Experimental Results and Analysis. Through comparative experiments under different IDZ arrangement models, the ore loss rate and the ore dilution rate are obtained. A comparison of the drawing effects under different IDZ arrangement models is presented in Table 3 and Figure 10.

Table 3 shows that, compared to the original stope structure, a sublevel height of 22.5 m can effectively reduce the ore loss and dilution rate, which proves the feasibility of large stope structure. When the sublevel height is 22.5 m, the drift spacing is set as 22.5 m in the tangent model, and the

ore loss rate and ore dilution rate are 14.18% and 12.08%, respectively. However, when the drift spacing is set as 20.5 m in the intersecting model, the ore loss rate and ore dilution rate are 10.52% and 12.30%, respectively, and the loss rate is significantly reduced, but the dilution rate changes slightly. Therefore, the intersecting arrangement model based on IDZs can have a beneficial drawing effect. It is further verified that the intersecting arrangement model based on IDZs can reduce the crestal residual ore and improve the recovery of the ore. Although there is also mixing of waste rock, it has little effect on the ore dilution.

TABLE 3: Comparison of the drawing effects with different IDZ arrangement models.

Number	Stope height (m)	Drift spacing (m)	Loss rate (%)	Dilution rate (%)
1	18	20	17.96	20.45
2	22.5	20.5	10.52	12.30
3	22.5	22.5	14.18	12.08

(a)

(b)
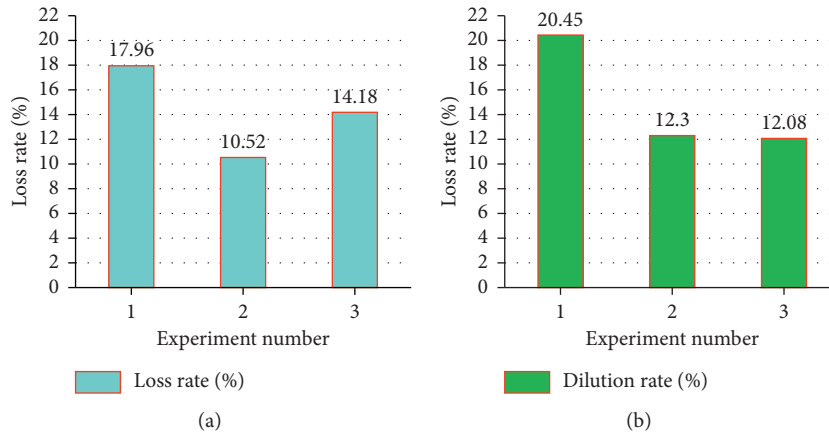
FIGURE 10: A comparison of the drawing effects with different IDZ arrangement models. (a) Loss rate. (b) Dilution rate.
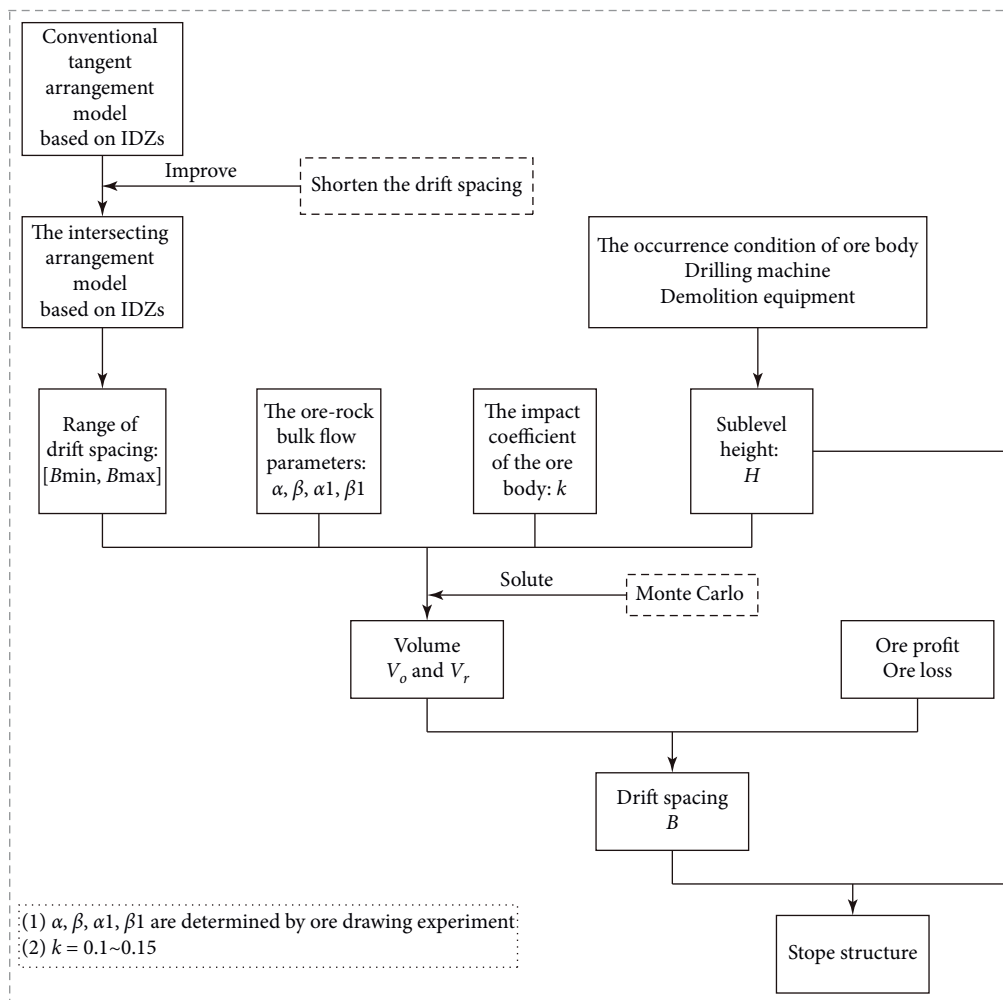
FIGURE 11: Schematic of the dynamic intersecting arrangement model based on IDZs for stope structure optimization.

5. Discussion and Conclusion

The concept of the intersecting arrangement of IDZs was first proposed by Kvapil [3]; later, Laubscher [31] developed and established interaction theory. However, these studies were based on the ellipsoid draw theory, and no reasonable evidence has been provided to quantify the intersecting arrangement of IDZs [32]. In this paper, based on stochastic medium draw theory, a dynamic intersecting arrangement model based on IDZs was established for the case in which the shape of the IDZ is a nonstandard ellipsoid. The dynamic intersecting arrangement model can dynamically adjust the stope structure according to the ore-rock bulk flow parameters, economic indicators, occurrence conditions of the ore body, drilling machine, and so forth. Then, taking the ore profit and loss as the research object, a calculation model was established to quantify the degree of intersection of the IDZs and to determine the best stope structure. The schematic of the study setup is as follows (see Figure 11).

From the analysis of this model (see Figure 11), the main results are as follows:

(1) A dynamic intersecting arrangement model based on IDZs is established

(2) The range of the drift spacing $[B_{min}, B_{max}]$ is determined

(3) With the Monte Carlo algorithm, the calculation method of the ore recovery volume (V_o) and rock mixed volume (V_r) when the IDZs intersect is provided

(4) A calculation model is established for the ore profit and loss

Ore profit: $p = ((c_o - c_t)/(c_c - c_t)) \times P - p_2$

Ore loss: $l = (c_w/c_j \times (1 - c_w)) \times P + l_2$

(5) A method for determining the drift spacing: $s = V_O \times \rho_O \times p - V_r \times \rho_r \times l = f_1(B) \times \rho_o \times p - f_2(B) \times \rho_r \times l$ is established, and the drift spacing is determined by finding the derivative with respect to B

According to the intersecting arrangement model based on IDZs, the stope structure of elevations from −213 m to −303 m in the Yanqianshan Iron Mine in China was determined; the optimal drift spacing is 20.5 m, and the sublevel height is 22.5 m. Nine physical experiments under three stope structure conditions, namely, the intersecting model, tangent model, and original stope structure, were carried out. The experimental results showed that the sublevel height of 22.5 m can effectively reduce the ore loss and dilution rate; at a drift spacing of 20.5 m, the ore loss rate decreased by 3.66%, but the dilution rate changed little, with an increment of 0.22%. This finding verifies the rationality and superiority of the intersecting arrangement model based on IDZs to optimize the stope structure.

An intersecting arrangement model based on Kvapil and Laubscher's interaction theory was proposed in this paper. This model is suitable for the case in which the shape of the IDZ is a nonstandard ellipsoid, and the model is more in line with actual mining conditions. The accurate shape of the IDZ is the basis for stope structure optimization, and future research should focus on the measurement of the shape of the IDZ. Moreover, the model does consider the mechanical properties of the movement of ore-rock bulk when dynamically adjusting the arrangement of IDZs. In future research, mechanical factors should be added to develop a stope structure optimization software program that dynamically adjusts the intersecting arrangement to better guide mine production.

Data Availability

The data used to support the findings of this study are included within the article.

Conflicts of Interest

The authors declare that they have no conflicts of interest.

Acknowledgments

References

[1] R. Castro and M. Pineda, "The role of gravity flow in the design and planning of large sublevel stopes," *Journal of the Southern African Institute of Mining and Metallurgy*, vol. 115, no. 2, pp. 113–118, 2015.

[2] Z.-X. Zhang and M. Wimmer, "A case study of dividing a single blast into two parts in sublevel caving," *International Journal of Rock Mechanics and Mining Sciences*, vol. 104, pp. 84–93, 2018.

[3] I. Janelid and R. Kvapil, "Sublevel caving," *International Journal of Rock Mechanics and Mining Sciences & Geomechanics Abstracts*, vol. 3, no. 2, pp. 129–132, 1966.

[4] G. Tao, M. Lu, X. Zhang, R. Zhang, and Z. Zhu, "A new diversion drawing technique for controlling ore loss and dilution during longitudinal sublevel caving," *International Journal of Rock Mechanics and Mining Sciences*, vol. 113, pp. 163–171, 2019.

[5] A. Jin, H. Sun, S. Wu, and Y. Gao, "Confirmation of the upside-down drop shape theory in gravity flow and development of a new empirical equation to calculate the shape," *International Journal of Rock Mechanics and Mining Sciences*, vol. 92, pp. 91–98, 2017.

[6] A. Gustafson, H. Schunnesson, J. Paraszczak, G. Shekhar, and P. Brnnman, "Operator influence on the loading process at LKAB's iron ore mines," *Journal of the Southern African Institute of Mining and Metallurgy*, vol. 120, no. 3, pp. 191–202, 2020.

[7] I. D. Brunton, S. J. Fraser, J. H. Hodgkinson, and P. C. Stewart, "Parameters influencing full scale sublevel caving material recovery at the Ridgeway gold mine," *International Journal of Rock Mechanics and Mining Sciences*, vol. 47, no. 4, pp. 647–656, 2010.

[8] X. Liu, *Theoretical Basis of Ore Drawing*, Metallurgical Industry Press, Beijing, China, 1995.

[9] G. Marano, "The interaction between adjacent draw points in free flowing materials and it application to mining," *Chamber of Mines Journal*, vol. 22, pp. 25–32, 1980.

[10] H. Ding, S. Chen, S. Chang, G. Li, and L. Zhou, "Prediction of surface subsidence extension due to underground caving: a case study of Hemushan iron mine in China," *Mathematical Problems in Engineering*, vol. 2020, Article ID 5086049, 10 pages, 2020.

[11] M. ГМ, *Drawing of Caving Ore Block*, Metallurgical Industry Press, Beijing, China, 1958.

[12] F. Ren, *The Stochastic Medium Draw Theory and its Application*, Qiyun Qing, Beijing, China, 1994.

[13] J. Litwiniszyn, "Application of the equation of stochastic processes to mechanics of loose bodies," *Archives of Mechanics*, vol. 8, no. 4, pp. 393–411, 1956.

[14] R. Kvapil, *Underground Mining Methods Handbook*, Society of Mining, Metallurgy and Explorations, Englewood, Colorado, USA, 1982.

[15] K. Yu, F. Ren, G. Chitombo, R. Puscasu, and L. Kang, "Optimum sublevel height and drift spacing in sublevel cave mining based on random medium theory," *Mining, Metallurgy & Exploration*, vol. 37, no. 2, pp. 681–690, 2020.

[16] P. Yuan, J. Zhao, Y. Ju, and S. Gong, "Study on large-space structural parameters of pillarless sublevel caving," *Metal Mine*, vol. 6, pp. 5–8, 2004.

[17] L. Wang, A. Shao, X. Liu, L. Yang, and H. Ding, "New computational framework for modeling the gravity flow behavior of sublevel caving material," *Computers and Geotechnics*, vol. 125, Article ID 103675, 2020.

[18] B. Tan, Z. Zhang, R. He, and Q. Zhu, "Discussion on the rationality and experimental research of the ore-drawing ellipsoid arrangement theory," *Journal of Northeastern University (Natural Science)*, vol. 40, no. 7, pp. 1014–1019, 2019.

[19] F. Melo, F. Vivanco, C. Fuentes, and V. Apablaza, "On drawbody shapes: from Bergmark-Roos to kinematic models," *International Journal of Rock Mechanics and Mining Sciences*, vol. 44, no. 1, pp. 77–86, 2007.

[20] R. J. McCormick, "How wide does a drawpoint draw?" *Engineering and Mining Journal*, pp. 106–166, 1968.

[21] R. Castro, R. Trueman, and A. Halim, "A study of isolated draw zones in block caving mines by means of a large 3D physical model," *International Journal of Rock Mechanics and Mining Sciences*, vol. 44, no. 6, pp. 860–870, 2007.

[22] Q. Chen, F. Zhao, Q. Chen, Y. Wang, Y. Zhong, and W. Niu, "Orthogonal simulation experiment for flow characteristics of ore in ore drawing and influencing factors in a single funnel under a flexible isolation layer," *JOM-Journal of the Minerals*, vol. 69, no. 12, pp. 2485–2491, 2017.

[23] X. Liu, G. Zhang, and X. Liu, "Analysis of ore loss and dilution in sublevel caving," *Metal Mine*, vol. 1, pp. 53–60, 2006.

[24] S. Liu, J. Zhang, and B. Zhu, "Volume computation using a direct Monte Carlo method," *Computing & Combinatorics*, vol. 4598, pp. 198–209, 2007.

[25] L. M. Popescu, "A geometry modeling system for ray tracing or particle transport Monte Carlo simulation," *Computer Physics Communications*, vol. 150, no. 1, pp. 21–30, 2003.

[26] E. J. Elbrond, "Economic effects of ore losses and rock dilution," *CIM Bulletin*, vol. 87, pp. 131–134, 1994.

[27] Z. Zhang, X. Liu, and G. Yu, *Sublevel Caving Method without Sill Pillars in the Base of Undiluted Ore Draw: Undiluted Ore Draw Theory and its Practice in Mine*, Northeastern University Press, Shenyang, China, 2007.

[28] J. Ming, L. Zhang, and J. Sun, "Analysis models of technical and economic data of mining enterprises based on big data analysis," in *Proceedings of the 2018 the 3rd IEEE International Conference on Cloud Computing and Big Data Analysis*, pp. 224–227, Chengdu, China, April 2018.

[29] A. L. Shao and H. L. Feng, "The prediction of northern slope deformation and failure caused by the transformation of open-pit to underground mining in the Yanqianshan iron mine," *Applied Mechanics and Materials*, vol. 580–583, pp. 364–370, 2014.

[30] Y. Hu, F. Ren, H. Ding, Y. Fu, and B. Tan, "Study on the process and mechanism of slope failure induced by mining under open pit slope: a case study from Yanqianshan iron mine, China," *Advances in Civil Engineering*, vol. 2019, Article ID 6862936, 26 pages, 2019.

[31] D. H. Laubscher, "Cave mining-the state of the art," *The Journal of the South African Institute of Mining and Metallurgy*, vol. 94, no. 10, pp. 279–293, 1994.

[32] A. A. E. Halim, *Study of the Influence of Interactive of Interactive Draw upon Drawpoint Spacing in Block and Sublevel Caving Mines*, University of Queensland, Brisbane, Australia, 2006.

Research Article

Managing a Dual-Channel Supply Chain with Fairness and Channel Preference

Xianjin Du [ID]**[1] and Weijie Zhao[1,2]**

[1]*School of Management, Hefei University of Technology, Hefei 230009, China*
[2]*Huishang Bank, Hefei 230009, China*

Correspondence should be addressed to Xianjin Du; xianjindu@hfut.edu.cn

This paper investigates a dual-channel supply chain in which a manufacturer sells the product via an offline retailer or online store. The manufacturer sets the wholesale and online price, and the retailer decides the retail price with the retailer's fairness preference and consumer's online channel preference. Through investigating the combined impacts of fairness preference and channel preference on the enterprises' operational strategies, this paper obtains some meaningful results. If a manufacturer thinks over the fairness preference, he decreases the wholesale price to mitigate a loss of retailer and benefit the supply chain design. The manufacturer intends to set up the online channel with a lower acceptance as the fairness preference grows. However, the gains from enhanced online channel acceptance cannot compensate for the manufacturer's loss by the fairness effect that benefits the retailer. Moreover, the manufacturer cannot neglect the retailer's fairness preference generating a "lose-lose" case for both members.

1. Introduction

With the increasing innovation of information technology and vigorous publicity by commercial organizations, consumers are getting used to online shopping. According to China Statistical Yearbook-2020, online sales in China reached 155.2 billion dollars in 2019, increasing 16.5% over the previous year (https://www.chinainternetwatch.com/30232/retail%202019/). To seize the Internet opportunity, many enterprises have set up the supply chain composed of online and offline channels such as Apple, Nike, Zara, and Huawei, and many scholars study dual-channel supply chain under different cases. A few papers focus on how the consumer's online channel preference impacts the dual-channel strategy (Chiang et al. [1], Xu et al. [2], and Zhang et al. [3]), while others try to find the operational strategy for the dual-channel supply chain (Guo et al. [4] and Zhu et al. [5]). There is also a lot of research (Chen et al. [6], Cui et al. [7], Guan et al. [8], Niu et al. [9], and Pan et al. [10]) studying

the impact of fairness preference in the supply chain, especially the supply chain design decisions and coordination. However, the combined effect of the retailer's fairness and consumer's online channel preference is ignored in the dual-channel design, which motivates our research. To fill this gap, our paper considers a dual-channel system in which the retailer has fairness preference, and the consumers are differentiated in online channel acceptance. The primary purposes of our research are to address the following issues:

(1) Varying with consumer's online channel preference and fairness concern, how do the manufacturer and retailer decide their operational strategy, including pricing and dual-channel design? Also, how do the related parameters affect the manufacturer's and retailer's strategy?

(2) With the increases in the consumer's online channel preference, can the manufacturer's profit be better when the retailer has a fairness preference?

(3) Can the manufacturer ignore the retailer's fairness preference? What strategy would be adopted by the retailer if the manufacturer ignores it?

To tackle these issues, the paper establishes a dual-channel decision model composed of a manufacturer (he) and a retailer (she). The model has three circumstances: the retailer without fairness preference, the manufacturer considering her fairness preference, and ignoring her fairness preference. The paper studies the synergistic impact of consumer online channel acceptance and retailer's fairness preference on members' pricing decisions and profits. It compares and analyzes optimal decisions under the above three circumstances. Different from other literatures that independently examine the influence of supply chain enterprises' decisions from the perspective of consumer's online channel preference or retailers' fairness, this paper obtains some meaningful conclusions as follows: (i) If a manufacturer thinks over the fairness preference, he decreases his wholesale price to mitigate a loss of retailer. The increase in consumer online channel acceptance would strengthen the trend. However, the manufacturer also intends to build an online channel with a lower consumer online channel acceptance to decrease his dependence on the retailer. (ii) Whether the manufacturer considers or ignores fairness preference, the increase of consumer online channel acceptance cannot compensate for the manufacturer's loss due to the retailer's fairness effect. The manufacturer's interest concessions via wholesale price reduction caused by the consideration of the retailer's fairness preference exceed the benefit from the increase of online shopping. (iii) If the manufacturer overlooks the retailer's fairness, they will fall into a "lose-lose" case. The retailer would price higher to make up for the online market's loss, which also injures her profit. This also brings harm to the sale resulting in the reduction of the manufacturer's profit.

The rest of the paper is arranged as follows. Section 2 is a review of relevant literature with two streams. Section 3 establishes a game model with one leading manufacturer and one following retailer. It examines the members' pricing decisions and profits when the retailer has no fairness preference as a benchmark case. Section 4 consists of two situations as comparative cases, where the manufacturer considers or ignores the retailer's fairness preference. The enterprises' decisions and profits in two different situations are obtained. Section 5 analyzes the manufacturer's decisions on setting up the online channel under different scenarios. Section 6 makes some comparisons between different situations. Section 7 concludes the paper.

2. Literature Review

This paper is related to two literature streams: the online channel preference and the retailer's fairness preference in the supply chain.

The first related stream of the literature focuses on the online channel preference that includes Zhang et al. [3], Guo et al. [4], Zhu et al. [5], Cai [11], Cao [12], Dumrongsiri et al. [13], Dan et al. [14], Gao et al. [15], Hua et al. [16], Huang

and Swaminathan [17], Li et al. [18], Lu and Liu [19], Ranjan and Jha [20], and Yoo and Lee [21]. For instance, Zhang et al. [3] find that the channel selections are determined by the consumer's online acceptance. Guo et al. [4] show that the dual channel may make traditional retailers feel threatened. Dumrongsiri et al. [13] show that the uncertain demand obviously affects the optimal pricing and the manufacturer's incentive to seek an online channel. Hua et al. [16] demonstrate that consumer acceptance of online purchases can positively affect the manufacturer's online pricing and lead to longer delivery lead times. Li et al. [18] find that, with the high consumer's online acceptance, the manufacturer provides customized products under the decentralized and centralized supply chain structures. Gao et al. [15] and Lu and Liu [19] investigate how the consumer's online acceptance affects the dual-channel excepted profits and obtain that the consumer's online acceptances positively affect the manufacturer's profit, while the retailer's gain is the opposite. Ranjan and Jha [20] think over the effect of retailers' risk attitude and demand uncertainty on the pricing mechanism among dual-channel members.

The second related stream of the literature concentrates on fairness preference in supply chain management including Chen et al. [6], Cui et al. [7], Guan et al. [8], Niu et al. [9], Caliskan-Demirag et al. [22], Du et al. [23], Ho et al. [24], Katok and Pavlov [25], Q. H. Li and B. Li [26], Nie and Du [27], and Du et al. [28]. Cui et al. [7] introduce members' fairness preference into the dyadic supply chain and conclude that the channel can be coordinated by using a wholesale price contract. Guan et al. [8] extend the analysis of the impact of peer-fairness or Nash bargaining fairness preference on the pricing of supply chain enterprises and the overall efficiency of the supply chain. Niu et al. [9] study the role of channel strength and fairness preference in online channel opening and find that supplier fairness concerns are not conducive to online channel development. Chen et al. [6] and Pan et al. [10] show that the enhancement of the retailer's rights will make her pay attention to the fairness of her own profits, which may improve the supply chain's performance. Caliskan-Demirag et al. [22] research channel coordination issues with different fairness concerns through a simple wholesale price and other nonlinear demands. Du et al. [23] analyze the impact of fairness preference behavior on enterprise decisions and channel efficiency and show that although channel efficiency will be reduced, fairness preference still coordinates the supply chain in specific cases. Q. H. Li and B. Li [26] study the channel issues with retailer's fairness preference and show the fairness concern's negative impacts on channel efficiency.

The above literature studies the influence of supply chain members' decision-making in the sense of consumer's online channel preference or retailers' fairness. Unlike the related research, our paper first studies the combining effect of both consumer's online channel preference differences and the retailer's fairness preference on supply chain decisions. Therefore, our paper theoretically enriches the supply chain design research, which is more practical. It helps decision-makers be aware of the critical role of fairness preference behavior and online consumer heterogeneity in

decision-making. Moreover, our research allows decision-makers to use these factors to reach supply chain efficiency improvement and provide guidance for the enterprises.

3. Benchmark Model

3.1. Model Description. This paper develops a dual-channel supply chain, including one manufacturer (he) and one retailer (she). There is a Stackelberg game between the manufacturer and the retailer, with the manufacturer dominating the supply chain and the retailer being the follower. The manufacturer wholesales the product at the wholesale price w to the retailer, with the cost c, while the retailer sells it to consumers at a retail price p_r. With the popularity of online shopping, the manufacturer opens up an online channel to increase market penetration with online price p_e and gain more profits. In turn, the manufacturer has a dual-channel structure, consisting of an offline channel and an online channel as shown in Figure 1.

The demand function refers to the analyses of Chiang et al. [1], Dan et al. [14], and Huang and Swaminathan [17]. The manufacturer's online channel demand function q_e and the retailer's offline channel demand function q_r are as follows:

$$q_e = \theta a - b p_e + \lambda p_r, \qquad (1)$$

$$q_r = (1 - \theta)a - b p_r + \lambda p_e, \qquad (2)$$

where a indicates the basic demand of the market. θ $(0 < \theta < 1)$ measures the consumer's online channel preference and $1 - \theta$ indicates the consumer's offline channel acceptance. b denotes the influence factor of the channel price on demand, while λ denotes the influence factor of the cross-price with $b > \lambda$.

The manufacturer's rationality means that the maximization of its profit is the decision-making process's decision-making goal. The fairness preference of a retailer indicates that the retailer is concerned with maximizing its utility when making decisions. The retailer's fairness preference model draws on the FS model [29], and its utility function is the following:

$$U_r = \prod_r - \alpha \max\left(\prod_m - \prod_r, 0\right) - \beta \max\left(\prod_r - \prod_m, 0\right). \qquad (3)$$

The coefficients of α and β are the disadvantage and advantage inequity aversion, respectively. Qin and Yang [30] show that, in the Stackelberg game of the two-tier supply chain, the member playing the leadership role can reap more than half of the overall profits. Thus, in this study, only the disadvantage inequity averseness of the retailer is considered. The retailer's utility function is as follows:

$$U_r = \prod_r - \alpha \max\left(\prod_m - \prod_r, 0\right). \qquad (4)$$

The relevant symbols are shown in Table 1.
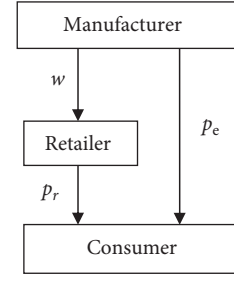
FIGURE 1: The dual-channel supply chain.

TABLE 1: Nomenclature.

Notation	Definition
Π_m	Manufacturer's profit
Π_r	Retailer's profit
U_m	Manufacturer's utility
U_r	Retailer's utility
w	Wholesale price
p_e	Online channel price
p_r	Offline channel price
c	Manufacturer's cost
θ	Consumer's online channel preference
a	Total market demand
b	Price elasticity
λ	Cross-price elasticity
α	Coefficient of retailer fairness preference

3.2. The Retailer without Fairness Preference. In this context, the profits functions of the manufacturer and the retailer are as follows:

$$\prod_m = (w - c)q_r + (p_e - c)q_e, \qquad (5)$$

$$\prod_r = (p_r - w)q_r, \qquad (6)$$

and, with backward induction to solve this problem, it can be easily verified that when the retailer has no fairness preference, the equilibrium pricing strategies and profits for the manufacturer and the retailer are

$$p_e = \frac{(\lambda + b\theta - \lambda\theta)a + \left(b^2 - \lambda^2\right)c}{2\left(b^2 - \lambda^2\right)}, \qquad (7)$$

$$w = \frac{(b + \lambda\theta - b\theta)a + \left(b^2 - \lambda^2\right)c}{2\left(b^2 - \lambda^2\right)}, \qquad (8)$$

$$p_r = \frac{\left[3b^2(1 - \theta) + \lambda\theta(2b + \lambda) - \lambda^2\right]a + c(b - \lambda)(b + \lambda)^2}{4b\left(b^2 - \lambda^2\right)}. \qquad (9)$$

According to the above optimal pricing decisions, the optimal profits for the retailer and the manufacturer without fairness preference are

$$\prod_r = \frac{[a(\theta - 1) + c(b - \lambda)]^2}{16b}, \tag{10}$$

$$\prod_m = \frac{a^2 A_1 - 2ac(b^2 - \lambda^2)A_2 + c^2(b - \lambda)^2 A_3}{8b(b^2 - \lambda^2)}, \tag{11}$$

where $A_1 = (3b^2 + \lambda^2)\theta^2 - 4b\lambda\theta(\theta - 1) + (1 - 2\theta)(b^2 + \lambda^2)$, $A_2 = \theta(b - \lambda) + (b + \lambda)$, and $A_3 = 3b^2 + \lambda^2 + 4b\lambda$.

4. The Model with the Retailer's Fairness Preference

There are two circumstances when the retailer has a fairness preference. One case is when the manufacturer considers the retailer's fairness preference and the other is when the manufacturer ignores it. The paper analyzes the different cases with Sections 4.1 and 4.2. The subscript * represents the manufacturer's optimal decisions considering the retailer's

fairness preference; the subscript ** means the optimal choices with the manufacturer ignoring the retailer's fairness preference.

4.1. The Manufacturer Considers the Retailer's Fairness Preference.
In this situation, the utility functions of the manufacturer and the retailer are

$$U_m = \prod_m, \tag{12}$$

$$U_r = \prod_r - \alpha\left(\prod_m - \prod_r\right) = (1 + \alpha)\prod_r - \alpha\prod_m. \tag{13}$$

Lemma 1. *When the manufacturer considers the retailer's fairness preference, the equilibrium pricing strategies and profits for the manufacturer and the retailer are*

$$p_e^* = \frac{(\lambda + b\theta - \lambda\theta)a + (b^2 - \lambda^2)c}{2(b^2 - \lambda^2)}, \tag{14}$$

$$w^* = \frac{(3\alpha c + c)b^3 - ((c\lambda + (\theta - 1)a)\alpha + (\theta - 1)a)b^2 + ((2a\lambda\theta - 3c\lambda^2)\alpha + a\lambda\theta - c\lambda^2)b - (-\lambda c + (\theta - 1)a)\lambda^2\alpha}{2b(b^2 - \lambda^2)(1 + 2\alpha)}, \tag{15}$$

$$p_r^* = \frac{[3b^2(1 - \theta) + \lambda\theta(2b + \lambda) - \lambda^2]a + c(b - \lambda)(b + \lambda)^2}{4b(b^2 - \lambda^2)}. \tag{16}$$

According to the above optimal pricing, it can be obtained that $\prod_r$ and $\prod_m$ in this case are

$$\prod_r^* = \frac{[a(\theta - 1) + c(b - \lambda)]^2(4\alpha + 1)}{16b(2\alpha + 1)}, \tag{17}$$

$$\prod_m^* = \frac{a^2 B_1 - 2ac(b^2 - \lambda^2)B_2 + c^2(b - \lambda)^2 B_3}{8b(b^2 - \lambda^2)(2\alpha + 1)}, \tag{18}$$

where $B_1 = [(5\alpha + 3)\theta^2 + (1 + \alpha)(1 - 2\theta)]b^2 + (3\alpha + 1)(\theta - 1)^2 + 4b\lambda(1 - \theta)(1 + 2\alpha)$, $B_2 = 3\alpha\theta(b - \lambda) + b(\alpha + \theta) + \lambda(3\alpha - \theta) + b + \lambda$, and $B_3 = (5\alpha + 3)b^2 + (3\alpha + 1)\lambda^2 + 4b\lambda(2\alpha + 1)$.

Proof of Lemma 1. Solving the Stackelberg game, the backward induction is used as follows.

Inserting (6) and (12) into (13) produces

$$U_r = (1 + \alpha)(p_r - w)((1 - \theta)a - bp_r + \lambda p_e) - \alpha(w - c)((1 - \theta)a - bp_r + \lambda p_e) - \alpha(p_e - c)(\theta a - bp_e + \lambda p_r). \tag{19}$$

As $(\partial U_r/\partial p_r) = 0$ and $(\partial^2 U_r/\partial p_r^2) = -2b(1 + \alpha) < 0$, the retailer has the only optimal retail price. The first-order partial derivative of U_r concerning p_r is expressed as follows:

$$p_r(w, p_e) = \frac{[a(1 - \theta) - c(b + \lambda) + 2bw]\alpha + a(1 - \theta) + bw - \lambda p_e}{2b(1 + \alpha)}. \tag{20}$$

To verify that $\prod_m$ is a joint concave function on wholesale price w and online price p_e, the second-order conditions can be obtained:

$$\begin{cases} \dfrac{\partial^2 \prod_m}{\partial w^2} = \dfrac{-b(1 + 2\alpha)}{1 + \alpha} < 0, \\[2ex] \dfrac{\partial^2 \prod_m}{\partial p_e^2} = \dfrac{\lambda^2}{(1 + \alpha)b} - 2b < 0, \\[2ex] \dfrac{\partial^2 \prod_m}{\partial w \, \partial p_e} = \dfrac{(1 + 2\alpha)\lambda}{1 + \alpha} > 0. \end{cases} \tag{21}$$

As the Hessian matrix of the $\prod_m$ above formulae is negative, it has a unique optimal solution. Then setting $(\delta\Pi_m/\delta w)$ and $(\delta\Pi_m/\delta p_e)$ to zero yields

$$
\begin{cases}
w = \dfrac{[a(1-\theta) + 3bc - 3c\lambda + 4\lambda p_e]\alpha + a(1-\theta) + bc - c\lambda + 2\lambda p_e}{2b(1+2\alpha)}, \\[4mm]
p_e = \dfrac{(2ab\theta - a\lambda\theta + 2b^2c - 3bc\lambda + 4bw\lambda + c\lambda^2 + a\lambda)\alpha + 2ab\theta - a\lambda\theta + 2b^2c - bc\lambda + 2bw\lambda - c\lambda^2 + a\lambda}{2(2b^2\alpha + 2b^2 - \lambda^2)}.
\end{cases}
\tag{22}
$$

Solving (20) and (22) can obtain the optimal pricing as (14)–(16). Then inserting (14)–(16) into (5) and (6) produces the equilibrium profits for the retailer and the manufacturer as (17) and (18). Lemma 1 is proved.

4.2. The Manufacturer Ignores the Retailer's Fairness Preference. In this subsection, the paper assumes that the retailer's fairness preference information is not taken into account by the manufacturer. Under this condition, the manufacturer still prices considering that the retailer has no fairness preference, which is represented by $w^{**} = w$ and $p_e^{**} = p_e$. However, the retailer has a fairness preference and uses the utility function of equation (13) to make optimal decisions.

Lemma 2. *When the manufacturer ignores the retailer's fairness preference, the offline price and the manufacturer's and retailer's profits are*

$$
p_r^{**} = \frac{(2ab\lambda\theta - 4ab^2\theta + 2a\lambda^2\theta + 2b^2c\lambda - 2c\lambda^3 + 4ab^2 - 2a\lambda^2)\alpha + [3b^2(1-\theta) + \lambda\theta(2b+\lambda) - \lambda^2]a + c(b-\lambda)(b+\lambda)^2}{4b(1+\alpha)(b^2-\lambda^2)}.
\tag{23}
$$

$\prod_r$ and $\prod_m$ can be calculated as

$$
\overset{**}{\prod_r} = \frac{[a(\theta-1) + c(b-\lambda)]^2(1+2\alpha)}{16b(1+\alpha)^2},
\tag{24}
$$

$$
\overset{**}{\prod_m} = \frac{a^2C_1 - 2ac(b^2-\lambda^2)C_2 + c^2(b-\lambda)^2C_3}{8b(b^2-\lambda^2)(1+\alpha)},
\tag{25}
$$

where $C_1 = (2\alpha+3)b^2\theta^2 - 4b\lambda\theta(\theta-1)(1+\alpha) + [2\alpha(\theta-1)^2 + \theta^2]\lambda^2 + (1-2\theta)(b^2+\lambda^2)$, $C_2 = \theta(b-\lambda)(2\alpha+1) + 2\alpha\lambda b + b + \lambda$, and $C_3 = [(b+\lambda)\alpha + 2b](b+\lambda)$.

Following the calculating process of the proof of Lemma 1 in Section 4.1, Lemma 2 can be easily proved. The detailed formulae are not provided here.

5. Supply Chain Design Analysis

This section analyzes the manufacturer's decisions on setting up the online channel under different scenarios. When the manufacturer ignores the fairness concern of the retailer, his strategy is the same as the retailer who has no fairness preference shown in Section 4.2. Therefore, the two possible situations are as follows.

5.1. The Retailer without Fairness Preference. As the manufacturer's online price is greater than the wholesale price ($p_e > w$), this results in $\theta > (1/2)$. If $0 < \theta < (1/2)$, then $p_e < w$. The retailer can purchase large quantities of goods from the online channel and then sell them offline to make more profits, contrary to the manufacturer's original intention to set up an online channel.

Moreover, the retailer's offline channel's price should be greater than the manufacturer's wholesale price, which means that $p_r > w$ and results in $\theta < ((a - c(b-\lambda))/a)$. If $((a - c(b-\lambda))/a) < \theta < 1$, then $p_r < w$. It will bring loss to the retailer and cause the retailer to abandon the offline channel. The dual-channel supply chain may need to be reconstructed if θ is out of $((1/2), ((a - c(b-\lambda))/a))$.

Following the same analytical process above, this paper could find that the range is as same as that when the manufacturer ignores the fairness concern of the retailer. The paper concludes the supply chain design strategy in Lemma 3 as follows.

Lemma 3. *If the retailer does not have fairness preference or the manufacturer ignores her preference, the manufacturer intends to build an online channel when $\theta > (1/2)$. When θ approaches $((a - c(b-\lambda))/a)$, the retailer may choose to quit the supply chain.*

Lemma 3 indicates that when the retailer has no fairness preference or the manufacturer ignores it, the manufacturer

chooses to develop an online channel when the consumers are more receptive to them. Furthermore, the retailer is unwilling to participate in the dual-channel operation if the online channel acceptance exceeds a threshold. For the manufacturer, if he continues to use the dual channel to protect market penetration, he may need to provide additional benefits for the retailer.

5.2. The Manufacturer Considers the Retailer's Fairness Preference. Now this paper discusses the supply chain design strategy when the retailer possesses the fairness preference. Following the analytic process in Section 5.1, it can get $\theta > ((\alpha c(b^2 - \lambda^2) + \alpha a(b - \lambda) + ab)/(a(3b\alpha - \alpha\lambda + 2b)))$ as $p_e^* > w^*$. With $p_r^* > w^*$, it gets $\theta < ((a - c(b - \lambda))/a)$. When the lower bound $((\alpha c(b^2 - \lambda^2) + \alpha a(b - \lambda) + ab)/(a(3b\alpha - \alpha\lambda + 2b)))$ is used to get the derivation of α, $((b(b + \lambda)[2c(b - \lambda) - a])/(a(3b\alpha - \alpha\lambda + 2b)^2)) < 0$ can be obtained. This shows that the manufacturer intends to develop a new road to market as he decreases the wholesale price for the retailer's fairness concerns. The upper bound of θ remains unchanged because the high consumer's online channel preference may lead to the suspension of the retailer's sales. So, the upper bound of θ is not affected by fairness preference.

Lemma 4 shows the manufacturer's supply chain design strategy when considering the retailer's fairness preference.

Lemma 4. *When the manufacturer takes the retailer's fairness into account, the dual-channel supply chain works if and only if $((\alpha c(b^2 - \lambda^2) + \alpha a(b - \lambda) + ab)/(a(3b\alpha - \alpha\lambda + 2b))) < \theta < ((a - c(b - \lambda))/a)$. With the increase of the fairness preference coefficient, the lower bound of θ will gradually decrease.*

Intuitively, if the retailer focuses on fairness, the manufacturer will transfer some profit to the retailer to eliminate its fairness. However, the manufacturer also wants to offset the offline supply chain's loss by adding an online channel. This brings a decrease in the starting point of opening an online channel. As the acceptance is low, the retailer does not think that the online channel is a threat, and the manufacturer can also get a little profit by adding an online channel. Lemma 4 shows that if a retailer pursues the fairness of her profit excessively, the manufacturer becomes urgent for setting up an online channel, even though consumers have a low preference for an online channel. However, this is not beneficial for the retailer, which means that she should maintain an appropriate level of fairness.

6. Comparative Analysis

Given the strategies under the three circumstances mentioned in Section 3 and 4, this paper compares operational strategies between the manufacturer and the retailer to analyze the effects of the retailer's fairness preference and consumer's online channel preference.

6.1. Pricing Comparison

Lemma 5. *For pricing strategies,*

(a) $p_e = p_e^* = p_e^{**}$, $w^* < w = w^{**}$, and $p_r = p_r^* < p_r^{**}$;

(b) $(\partial w^*/\partial\alpha) < 0$, $(\partial w^*/\partial\theta) < 0$, $(\partial p_r^{**}/\partial\alpha) > 0$, and $(\partial p_r^{**}/\partial\theta) < 0$.

Proof of Lemma 5. When the manufacturer considers the retailers' fairness preference, $w^* - w < 0$; $(\partial w^*/\partial\alpha) = ((a(\theta - 1) + c(b - \lambda))/(2b(1 + 2\alpha)^2))$ and $(\partial w^*/\partial\theta) = -((a[\alpha(b - \lambda) + b])/(2b(b + \lambda)(1 + 2\alpha))) < 0$ can be obtained when formula (15) is used to get the derivations of α and θ. $(\partial w^*/\partial\alpha) = ((a(\theta - 1) + c(b - \lambda))/(2b(1 + 2\alpha)^2)) < 0$ because $\theta < ((a - c(b - \lambda))/a)$ is demonstrated in Lemmas 3 and 4. When the manufacturer ignores the retailer's fairness preference, $p_r^{**} - p_r > 0$. $(\partial p_r^{**}/\partial\alpha) = ((a(1 - \theta) - c(b - \lambda))/(4b(1 + \alpha)^2)) > 0$ and $(\partial p^{**}/\partial\theta) = -((a[b(4\alpha + 3) + \lambda(2\alpha + 1)])/(4b(b + \lambda)(1 + \alpha))) < 0$ can be obtained when formula (23) is used to get the derivation of α.

It can be seen from Lemma 5 that when the manufacturer thinks over the retailer's fairness preference, the wholesale price reduces as the fairness preference coefficient increases. If the manufacturer ignores it, the retail price improves with the fairness preference coefficient increasing. Moreover, taking the rise in consumers' online channel preferences into account, the wholesale will decline faster, but the retail price growth slows down. To demonstrate the impact of the fairness preference coefficient on supply chain members' pricing decisions and profits in Lemma 5 more clearly, this paper numerically analyzes the above model and discusses the results. The numerical results are shown in Figures 2 and 3 with $a = 100, b = 1, \lambda = 0.4, c = 10$. The parameter values are also applicable to subsequent numerical legends. As shown in Figure 2, it can be seen directly that when θ is constant, with the increase of α, w^* continues to fall. In order to make the dual channels work, the value of θ should be greater than 1/2. Moreover, when α is constant, the wholesale price still deceases with the increase of θ. According to Figure 3, when θ is constant, with the increase of α, the retail price improves when the manufacturer ignores the retailer's fairness preference. If α is constant, the retail price decreases with the increase of θ.

When the manufacturer takes the retailer's fairness preference into account, he lowers the wholesale price to maintain the balance of channel profit distribution. When the increase in consumer's online channel preference weakens the retailer's market competitiveness, consumers are willing to choose shopping online. To compensate for the loss of the retailer, the manufacturer's wholesale price will fall more. Moreover, because the manufacturer ignores the retailer's fairness preference, with the fairness preference increase, the retailer's focus on fairness will force her to raise pricing for the sake of maintaining profits. However, with the increase of consumer's online preference, the retailer chooses to reduce the retail price attracting consumers to select the offline channel.
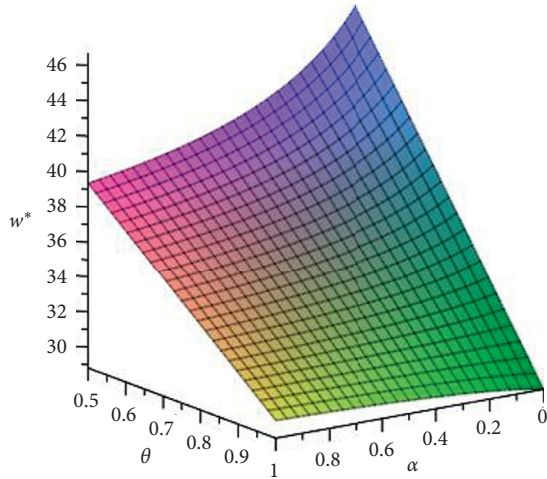
Figure 2: The influence of α and θ on w^*.
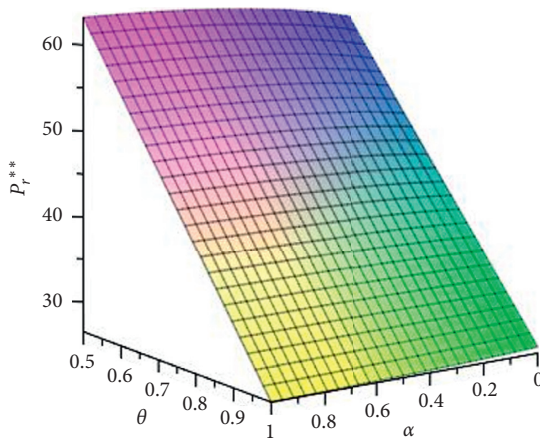
Figure 3: The influence of α and θ on p_r^{**}.

6.2. The Retailer's Profits Comparison

Lemma 6. For the retailer's profits under the above three circumstances,

(a) $\prod_r^* > \prod_r > \prod_r^{**}$

(b) $(\partial \prod_r^* /\partial\alpha) > 0$, $(\partial \prod_r^* /\partial\theta) < 0$, $(\partial \prod_r^{**} /\partial\alpha) < 0$, and $(\partial \prod_r^{**} /\partial\theta) < 0$

Proof of Lemma 6. It can be easily calculated from (10), (17), and (24) that $\prod_r^* - \prod_r > 0$ and $\prod_r - \prod_r^{**} > 0$. $(\partial \prod_r^* /\partial\alpha) = (([a(\theta-1) + c(b-\lambda)]^2)/(8b(2\alpha+1)^2)) > 0$ and $(\partial \prod_r^* /\partial\theta) = ((a(4\alpha+1)[a(\theta-1) + c(b-\lambda)])/(8b \ (1+2\alpha))) < 0$ can be obtained when (17) is used to get the derivation of α and θ. $(\partial \prod_r^{**} /\partial\alpha) = ((-\alpha[a(\theta-1) + c(b-\lambda)]^2)/(8b(1+\alpha)^3)) < 0$ and $(\partial \prod_r^{**} /\partial\theta) = ((a(2\alpha+1)[a(\theta-1) + c(b-\lambda)])/(8b(1+2\alpha)^2)) < 0$ can be obtained when (24) is used to get the derivation of α and θ.

Lemma 6 shows that the retailer can increase profitability when she focuses on fairness. The manufacturer considers the retailer's fairness preference, which enhances the retailer's bargaining power. He transfers profits to the retailer

in various ways, consistent with the recent literature, such as Caliskan-Demirag et al. [22] and Ho et al. [24]. However, it is obvious that the retailer's profit with the manufacturer considering the retailer's fairness preference improves when the consumer's online acceptance increases. If the manufacturer ignores her fairness preference, the retailer intends to increase profits by increasing her pricing demonstrated in Lemma 5. But this reduces the retailer's sales and results in a decrease in the retailer's profit. Moreover, the retailer's profit decreases faster as the consumer's online channel preference increases. It is easy to understand that the number of consumers choosing to shop offline reduces while the online channel acceptance increases. This decrease in retailer sales leads to a decline in profits if the manufacturer ignores the retailer's fairness preference and does not transfer the earning.

The numerical analysis also shows the above results more intuitively. From Figure 4, if θ is at a certain value, with the increase of α, the retailer's profit with the manufacturer considering her fairness preference improves. However, if α is at a certain value, the retailer's profit decreases with the increase of θ. Similarly, it is obvious from Figure 5 that when θ is at a certain value, with the increase of α, the retailer's profit with the manufacturer ignoring the retailer's fairness preference reduces. If α is at a certain value, the retailer's profit also decreases with the increase of θ.

6.3. The Manufacturer's Profits Comparison

Lemma 7. For the above three circumstances,

(a) $\prod_m > \prod_m^* > \prod_m^{**}$;

(b) $(\partial \prod_m^* /\partial\alpha) < 0$, $(\partial \prod_m^* /\partial\theta) > 0$, $(\partial \prod_m^{**} /\partial\alpha) < 0$, and $(\partial \prod_m^{**} /\partial\theta) > 0$.

Proof of Lemma 7. With formulae (11), (18), and (25), $\prod_m - \prod_m^* > 0$ and $\prod_m^* - \prod_m^{**} > 0$ are got. $(\partial \prod_m^* /\partial\alpha) = -(([a(\theta-1) + c(b-\lambda)]^2)/(8b(1+2\alpha)^2)) < 0$ and $(\partial \prod_m^* /\partial\theta) = ((a^2[\alpha\theta(5b-3\lambda) - \alpha(b-3\lambda) + \theta(3b-\lambda) - (b-\lambda)] - ac(3\alpha+1)(b-\lambda^2))/(4b(1+\alpha)(b+\lambda))) > 0$ can be obtained when (18) is used to get the derivation of α and θ. Calculating with (25), $(\partial \prod_m^{**} /\partial\alpha) = -(([a(\theta-1) + c(b-\lambda)]^2)/(8b(1+2\alpha)^2)) < 0$ and $(\partial \prod_m^{**} /\partial\theta) = ((a^2[\theta(3b-\lambda) + 2\alpha\lambda + (b-\lambda)(2\alpha\theta-1)] - ac(2\alpha+1)(b^2-\lambda^2))/(4b(1+\alpha)(b+\lambda))) > 0$.

Lemma 7 shows that whether the manufacturer considers the retailer's fairness preference or not, the manufacturer's profit will be lower than the case when the retailer has no fairness preference. When the manufacturer thinks over the retailer's fairness preference, he will reduce his profit to add the retailer's profit, thus ensuring the fairness of channel profit distribution. Moreover, the manufacturer's profit when he considers the retailer's fairness preference is higher than that when he ignores it. When the manufacturer ignores the retailer's fairness preference, this may enlarge the retailer's fairness concerns and lead to broader damage. This means that if the retailer has a fairness preference, the manufacturer should consider this behavior more favorable.
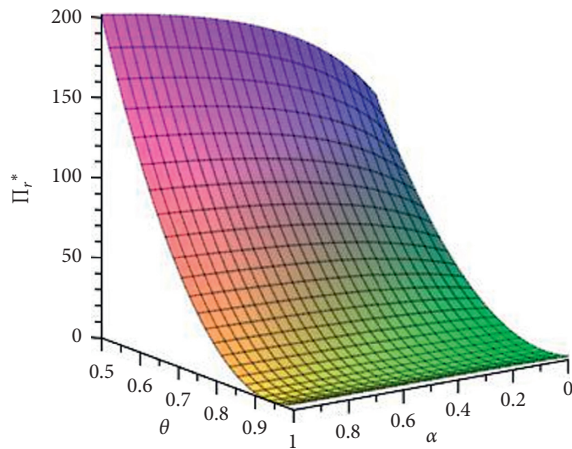
FIGURE 4: The influence of α and θ on $\prod_r^*$.
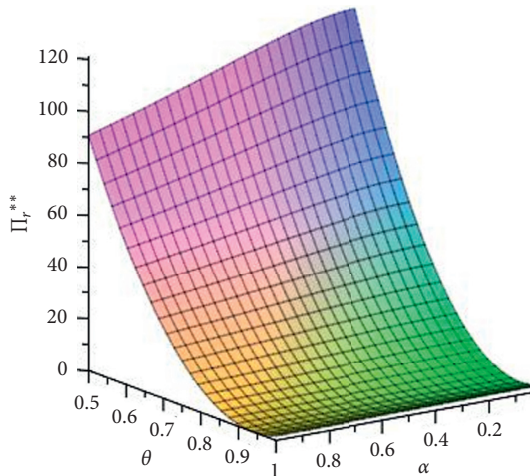
FIGURE 5: The influence of α and θ on $\prod_r^{**}$.
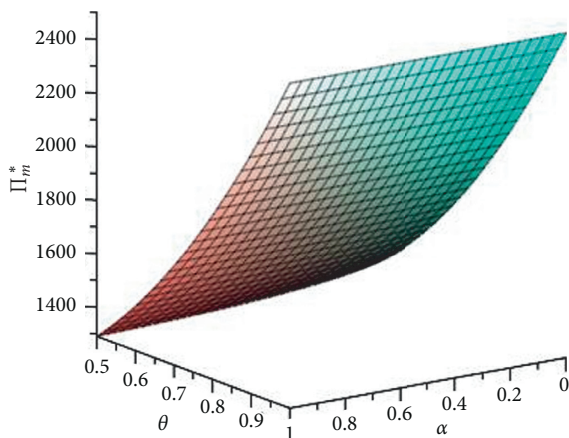

FIGURE 6: The influence of α and θ on $\prod_m^*$.
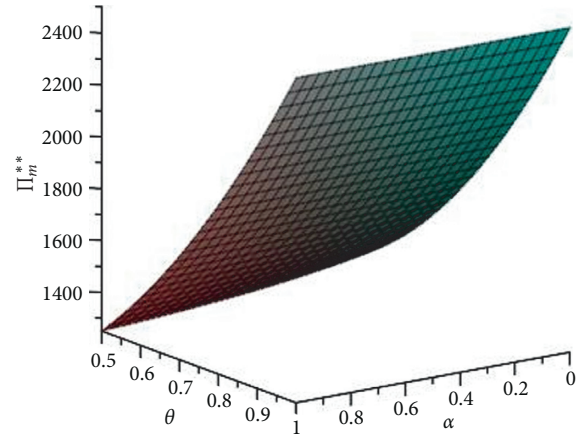
FIGURE 7: The influence of α and θ on $\prod_m^{**}$.

transfer for the retailer's fairness preference. When more consumers intend to shop online, this injures the retailer's profit and magnifies her fairness requirements. To ensure the channel operation, the manufacturer can only choose to give the retailer more incentives.

To visually show the analysis in Lemma 7, the paper applies a numerical example. As shown in Figures 6 and 7, it can be seen that whether the manufacturer considers the retailer's fairness concern or not, the manufacturer's profit will reduce with the increase of α but improve with the increase of θ. The main reason is that the enhancement of fairness preference makes the manufacturer have to give up profit; otherwise, it is difficult to carry out dual-channel cooperation. On the contrary, enhancing consumers' online acceptance enables the manufacturer to obtain more profit from an online channel, leading to an increased profit in the whole dual channels.

7. Conclusions

This paper first attempts to study the compound impact of the retailer's fairness preference and consumer's online channel preference on supply chain enterprises' operational strategy. A single manufacturer sells his products by online and offline channels with a retailer in the dual-channel supply chain. To observe supply chain enterprises' operational decisions, this paper uses three circumstances. The benchmark one is that the retailer has no fairness preference, while the manufacturer considers or ignores the retailer's fairness preference as comparative cases. The study shows that the manufacturer intends to build an online channel with lower consumer acceptance when the manufacturer takes the retailer's fairness preference into account. The wholesale price and manufacturer's profit are lower than those in the benchmark case, while the increase in consumer's online channel preference can narrow the gap. The retailer's profit is higher than that without fairness preference because of the manufacturer's interest concession. When the manufacturer ignores the retailer's fairness preference, the retailer will increase offline channel pricing, which hurts the manufacturer's and the retailer's profits,

Taking the increase of consumer's online channel preference into account would benefit the manufacturer's profit for both cases. However, the manufacturer's profit that increased by the online channel is smaller than the profit

although the increase of consumer's online channel acceptance benefits the manufacturer. These results demonstrate that the manufacturer needs to take fairness preference into account to avoid a "lose-lose" situation when the retailer possesses a fairness preference. If the acceptance degree of the online channel is high to a certain extent, the manufacturer needs to provide additional revenue for the retailer to ensure the operation of the dual-channel strategy. For the retailer, her fairness preference needs to be maintained at an appropriate level; otherwise, the manufacturer will start online channel construction earlier, which will affect his profit level.

This paper focuses on the retailer's fairness preference, but, in practical operation, all decision-makers may possess fairness preferences, and the fairness preference could be extended to a more elaborate setting. The market demand is determined to be a linear demand in the study. However, the market demand is random and uncertain or changes to dynamic, which also deserves further study.

Data Availability

The data used to support the findings of this study are available from the corresponding author upon request.

Conflicts of Interest

The authors declare that they have no conflicts of interest.

Acknowledgments

References

[1] W.-Y. K. Chiang, D. Chhajed, and J. D. Hess, "Direct marketing, indirect profits: a strategic analysis of dual-channel supply-chain design," *Management Science*, vol. 49, no. 1, pp. 1–20, 2003.

[2] H. Xu, Z. Z. Liu, and S. H. Zhang, "A strategic analysis of dual-channel supply chain design with price and delivery lead time considerations," *International Journal of Production Economics*, vol. 139, no. 2, pp. 654–663, 2012.

[3] P. Zhang, Y. He, and C. Shi, "Retailer's channel structure choice: online channel, offline channel, or dual channels?" *International Journal of Production Economics*, vol. 191, pp. 37–50, 2017.

[4] J. Guo, B. Cao, B. Xie, Y. Zhong, and Y.-W. Zhou, "Impacts of pre-sales service and delivery lead time on dual-channel supply chain design," *Computers & Industrial Engineering*, vol. 147, Article ID 106579, 2020.

[5] B. Zhu, B. Wen, S. Ji, and R. Qiu, "Coordinating a dual-channel supply chain with conditional value-at-risk under uncertainties of yield and demand," *Computers & Industrial Engineering*, vol. 139, Article ID 106181, 2020.

[6] J. Chen, Y.-W. Zhou, and Y. Zhong, "A pricing/ordering model for a dyadic supply chain with buyback guarantee financing and fairness concerns," *International Journal of Production Research*, vol. 55, no. 18, pp. 5287–5304, 2017.

[7] H. T. Cui, J. S. Raju, and Z. J. Zhang, "Fairness and channel coordination," *Management Science*, vol. 53, no. 8, pp. 1303–1314, 2007.

[8] Z. Guan, T. Ye, and R. Yin, "Channel coordination under Nash bargaining fairness concerns in differential games of goodwill accumulation," *European Journal of Operational Research*, vol. 285, no. 3, pp. 916–930, 2020.

[9] B. Niu, Q. Cui, and J. Zhang, "Impact of channel power and fairness concern on supplier's market entry decision," *Journal of the Operational Research Society*, vol. 68, no. 12, pp. 1570–1581, 2017.

[10] K. Pan, Z. Cui, A. Xing, and Q. Lu, "Impact of fairness concern on retailer-dominated supply chain," *Computers & Industrial Engineering*, vol. 139, Article ID 106209, 2020.

[11] G. Cai, "Channel selection and coordination in dual-channel supply chains," *Journal of Retailing*, vol. 86, no. 1, pp. 22–36, 2010.

[12] E. Cao, "Coordination of dual-channel supply chains under demand disruptions management decisions," *International Journal of Production Research*, vol. 52, no. 23, pp. 7114–7131, 2014.

[13] A. Dumrongsiri, M. Fan, A. Jain, and K. Moinzadeh, "A supply chain model with direct and retail channels," *European Journal of Operational Research*, vol. 187, no. 3, pp. 691–718, 2008.

[14] B. Dan, G. Xu, and C. Liu, "Pricing policies in a dual-channel supply chain with retail services," *International Journal of Production Economics*, vol. 139, no. 1, pp. 312–320, 2012.

[15] J. Gao, X. Wang, Q. Yang, and Q. Zhong, "Pricing decisions of a dual-channel closed-loop supply chain under uncertain demand of indirect channel," *Mathematical Problems in Engineering*, vol. 2016, Article ID 6053510, 13 pages, 2016.

[16] G. Hua, S. Wang, and T. C. E. Cheng, "Price and lead time decisions in dual-channel supply chains," *European Journal of Operational Research*, vol. 205, no. 1, pp. 113–126, 2010.

[17] W. Huang and J. M. Swaminathan, "Introduction of a second channel: implications for pricing and profits," *European Journal of Operational Research*, vol. 194, no. 1, pp. 258–279, 2009.

[18] G. Li, F. Huang, T. C. E. Cheng, and P. Ji, "Competition between manufacturer's online customization channel and conventional retailer," *IEEE Transactions on Engineering Management*, vol. 62, no. 2, pp. 150–157, 2015.

[19] Q. Lu and N. Liu, "Pricing games of mixed conventional and e-commerce distribution channels," *Computers & Industrial Engineering*, vol. 64, no. 1, pp. 122–132, 2013.

[20] A. Ranjan and J. K. Jha, "Pricing and coordination strategies of a dual-channel supply chain considering green quality and sales effort," *Journal of Cleaner Production*, vol. 218, pp. 409–424, 2019.

[21] W. S. Yoo and E. Lee, "Internet channel entry: a strategic analysis of mixed channel structures," *Marketing Science*, vol. 30, no. 1, pp. 29–41, 2011.

[22] O. Caliskan-Demirag, Y. Chen, and J. Li, "Channel coordination under fairness concerns and nonlinear demand," *European Journal of Operational Research*, vol. 207, no. 3, pp. 1321–1326, 2010.

[23] S. Du, T. Nie, C. Chu, and Y. Yu, "Newsvendor model for a dyadic supply chain with Nash bargaining fairness concerns," *International Journal of Production Research*, vol. 52, no. 17, pp. 5070–5085, 2014.

[24] T.-H. Ho, X. Su, and Y. Wu, "Distributional and peer-induced fairness in supply chain contract design," *Production and Operations Management*, vol. 23, no. 2, pp. 161–175, 2014.

[25] E. Katok and V. Pavlov, "Fairness in supply chain contracts: a laboratory study," *Journal of Operations Management*, vol. 31, no. 3, pp. 129–137, 2013.

[26] Q. H. Li and B. Li, "Dual-channel supply chain equilibrium problems regarding retail services and fairness concerns," *Applied Mathematical Modelling*, vol. 40, no. 15-16, pp. 7349–7367, 2016.

[27] T. Nie and S. Du, "Dual-fairness supply chain with quantity discount contracts," *European Journal of Operational Research*, vol. 258, no. 2, pp. 491–500, 2017.

[28] S. Du, L. Wei, Y. Zhu, and T. Nie, "Peer-regarding fairness in supply chain," *International Journal of Production Research*, vol. 56, no. 10, pp. 3384–3396, 2018.

[29] E. Fehr and K. M. Schmidt, "A theory of fairness, competition, and cooperation," *The Quarterly Journal of Economics*, vol. 114, no. 3, pp. 817–868, 1999.

[30] Z. Qin and J. Yang, "Analysis of a revenue-sharing contract in supply chain management," *International Journal of Logistics Research and Applications*, vol. 11, no. 1, pp. 17–29, 2008.

Research Article

Thermoelastic Characteristics of Functionally Graded Circular Disk Models under the Loading of Contact Forces

Jaegwi Go (ID)

Department of Mathematics, Changwon National University, 20 Changwondaehak-ro Uichang-gu, Changwon-si 51140, Gyeongsangnam-do, Republic of Korea

Correspondence should be addressed to Jaegwi Go; jggo@changwon.ac.kr

A rotating functionally graded circular disk undergoing a contact load is taken into account to investigate the thermoelastic characteristics. By considering contact force, a pair of partial differential equations is induced as the governing equations based on Hooke's law. The behavior of circular disk modes is described with the variations of contact force and homogeneous thickness. A finite volume model is introduced to obtain approximate solutions for the governing equations because of the complexity of the equations. Contact force is highly influential in the radial direction compared to the circumferential direction in the displacement distribution, while a large radial stress appears near the area of the contact point. In the strain distribution, the magnitude increases as the angle grows near part of the outer boundary in the circular domain. The radial distribution profiles are susceptible to the growth of contact force in nearby area of the outer boundary, whereas the influences on the circumferential direction profiles are trivial. The increase of homogeneous thickness dwindles the radial magnitude of displacement, stress, and strain distribution profiles over nearby area of the outer boundary of the circular domain. As a result, numerical approach demonstrates that contact force and homogeneous thickness are indispensable parameters and provide deep influence on the thermoelastic movements of a rotating circular disk. Thus, the results obtained may be useful to design an appropriate FGM circular disk model for the industrial area by controlling the above parameters.

1. Introduction

The analysis of thermoelastic characteristics of a rotating circular disk has been a challenging work due to complex processes generating during operations. Friction, wear, heat generation, and temperature deformation are representative processes developed during the load of a contact force. By the operation of a rotating circular disk, all parameters are connected mutually and complicated interactions progress. The thermoelastic characteristics of a circular disk are under complicated interaction influences and the variation of each parameter may not be ignorable to determine the thermo-elastic movements. Thus, the influences of temperature, contact pressure, and blushed wear on the rotating circular disk are interesting and valuable for research.

Ceramic is a typical material used at one surface to resist severe environmental effects such as high temperature, wear,

and friction. The other surface is composed of a metal to ensure higher toughness and thermal conductivity. The complementary functions of each material invoke the introduction of functionally graded materials (FGMs). FGMs are nonhomogeneous composites composed of two or more different material phases and the volume fractions continuously vary with space variables. Thus, FGMs are structures involving successively varying mechanical and thermal properties from one surface to another surface. FGMs were introduced to prosper thermal barrier coatings for propulsion system of space planes to endure high temperature and ensure high thermal conductivity at the beginning [1]. The graded material property provides improved bonding strength in various applications undergoing a high temperature gradient field.

On the pursuit superior properties such as strength, impact toughness, and fiber resistance, fiber metal laminates (FMLs) have drawn attention as promising hybrid

composite materials in last few decades. FMLs are composed of metallic and composite materials. The combination of fiber-reinforced composite layers and composite materials creates FMLs, which exhibit excellent durability. Thus, FMLs are applicable in various industries and are used in aircraft, wind turbine, and automobile. A laminated composite made with thin sheet/grass was investigated by BnvsGaneshGupta et al. [2] for the flexural properties. They evaluated flexural strength and failure analysis using stereo microscope. Zimmermann and Wang [3] analyzed failure modes and characteristics of adhesively and mechanically fastened joints in aircraft composite materials.

Meanwhile, the shape of circular disk is commonly employed for practical use in various industrial applications, and the physical behavior of circular disk models is a matter of interest to many engineering researchers. Obata and Noda [4] and Liew et al. [5] analyzed the thermal stresses of FGM circular cylinder and hollow sphere. Afsar et al. [6] investigated the brittle fracture characteristics of thick-walled FGM cylinders by considering incompatible eigenstrain, which is a cause of thermal residual stress. The characterization that oscillatory movements reduce cutting forces in operating process of a circular disk cutter was presented by Kovalyshen [7], and Huang and Li [8] studied the radial component effects on the bending of thin circular plates using Kirchhoff plate theory. The angular speed of a rotating circular disk varies during the start and stop process in machine operation. Dai et al. [9] investigated the displacement and stress fields of a FGM hollow circular disk subjecting an angular acceleration due to a changing temperature. Static behavior of functionally graded auxetic-porous structures was presented by Rad [10] considering torsional interaction and horizontal friction force. The static response of nonuniform bidirectional functionally graded auxetic-porous material circular plates is carried out based on poroelasticity theory. Friction induced a vibration in rotary contact system, and the vibration causes a misalignment problem. Tadokoro et al. [11] described the stabilizing effect arising from parallel misalignment in circular sliding contact. Infinitesimal theory of plane elasticity and Complementary Functions Method was employed to investigate hydrogen-induced stresses in functionally graded axisymmetric spheres, cylinders, and disks by Yildirim [12]. Sondhi et al. [13] used element-based gradation of material properties over the discretized domain to study linear elastic stress analysis of functionally graded rotating disks.

However, the comprehensive understanding and quantifying for the thermoelastic field of a rotating FGM circular disk may be useful in design FGM cutter or a grinding disk. In general, FGM cutter or a grinding disk experiences the thermal load and inertia force due to rotation of the disk. The previous study [14] demonstrated that proper control of some parameters such as temperature distribution, angular speed, and radial thickness improves thermoselastic characteristics in the design of a circular or grinding disk and reduces failure mechanism such as crack and brittle, but most of previous works progressed their studies without considering contact load even though contact load is a crucial parameter in determination of thermoelastic characteristics. The present study focuses on the analysis of thermoelastic characteristics of a rotating (Al_2O_3/Al) FGM disk subjected to a contact force. Young's modulus, CTE, and density of the FGM disk are assumed to vary exponentially only in the radial direction due to symmetry with respect to the axis of the disk, whereas Poisson's ratio is assumed to be constant because of insignificant effect on the thermoelastic characteristics of the disk. The research addresses the following: (i) the contact force and homogeneous thickness are crucial factors in the determination of the thermoelastic characteristics of FGM circular models, (ii) the radial direction is more susceptible to the variation of the magnitude of contact force and homogeneous thickness, and (iii) the variation of homogeneous thickness is highly influential to thermoelastic characteristics over the area of $0.2 < (r - a)/(b - a) < 0.8$ in FGM circular domain.

The process for the mathematical approach is presented in Section 2. A pair of partial differential equations is derived based on Hooke's law in Section 2.1. Due to the complexity of the governing equation, a finite volume method is introduced in Section 2.2 to obtain numerical solutions. In Section 3, numerical solutions are displayed and the elastic characteristics are discussed according to the results obtained. The significances of the results are addressed in the conclusions in Section 4.

2. Mathematical Modeling

A rotating FGM circular disk with a concentric circular hole is considered (see Figure 1). The origin of the polar coordinate system $r - \theta$ is assumed to be located at the center of the disk and hole. A and B, denoted by the dark and the white colors, represent constituent materials of FGM circular disk, as shown in the figure. The distribution of each material varies continuously along the radial direction only. The radii of the hole and outer surface of the disk are designated by a and b. The angular velocity ω can be determined from the relation $\omega = (2\pi N/60)$, N represents the revolutions per minute (rpm). Since the material distributions vary along the radial direction only, the FGM disk can be reduced to an axisymmetric problem. Thus, all properties of the disk can be treated as a function of r only. Young's modulus, coefficient of thermal expansion, and the density of the disk are denoted by E, α, and ρ, respectively, and each property is assumed to vary exponentially as follows (for various and detailed distribution profiles, see [15]):

$$E = E_0 e^{\beta r}, \tag{1a}$$

$$\alpha = \alpha_0 e^{\xi r}, \tag{1b}$$

$$\rho = \rho_0 e^{\mu r}. \tag{1c}$$

By the assumption that the disk is composed of 100% material A at the surface of the hole $(r = a)$ and 100% material B at the outer surface $(r = b)$, the constants in equations (1a)–(1c) can be determined as follows:

$$E_0 = E_A e^{-\beta a}, \tag{2a}$$

$$\alpha_0 = \alpha_A e^{-\xi a}, \tag{2b}$$
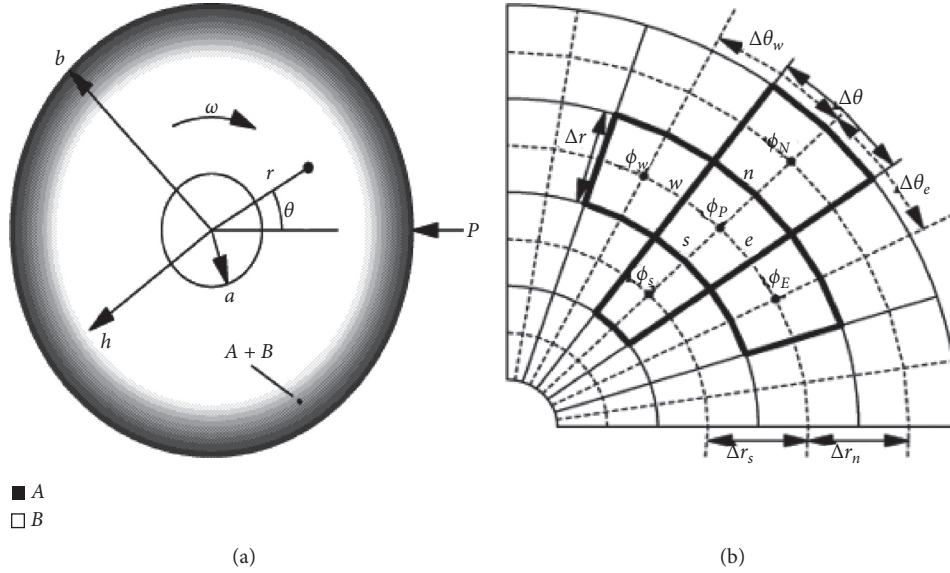
FIGURE 1: (a) Schematic diagram of functionally graded circular disk models. (b) Notations of finite control volumes.

$$\rho_0 = \rho_A e^{-\mu a}, \tag{2c}$$

$$\beta = \frac{1}{a-b} \ln\left(\frac{E_A}{E_B}\right), \tag{3a}$$

$$\xi = \frac{1}{a-b} \ln\left(\frac{\alpha_A}{\alpha_B}\right), \tag{3b}$$

$$\mu = \frac{1}{a-b} \ln\left(\frac{\rho_A}{\rho_B}\right). \tag{3c}$$

The subscripts A and B represent the properties of the constituent materials A and B, respectively, but the non-subscripted variables are used to denote the properties of FGM composed of materials A and B.

2.1. Thermoelastic Formulation.

In the polar coordinate, the relations between the strain components and deformation components are as follows:

$$\varepsilon_r = \frac{\partial u}{\partial r},$$

$$\varepsilon_\theta = \frac{1}{r}\frac{\partial v}{\partial \theta} + \frac{u}{r},$$

$$\varepsilon_z = 0,$$

$$\gamma_{r\theta} = \frac{1}{r}\frac{\partial u}{\partial \theta} + \frac{\partial v}{\partial r} - \frac{v}{r}, \tag{4}$$

$$\gamma_{z\theta} = 0,$$

$$\gamma_{rz} = 0.$$

The plane stress exposed with thermal expansion, by Hooke's law, produces the strain-stress relations undergoing thermal expansion ([16], p8):

$$\varepsilon_r = \frac{1}{E}[\sigma_r - v\sigma_\theta] + \alpha T,$$

$$\varepsilon_\theta = \frac{1}{E}[\sigma_\theta - v\sigma_r] + \alpha T,$$

$$\tau_{r\theta} = \frac{E}{2(1+v)}\gamma_{r\theta}, \tag{5}$$

$$\tau_{\theta z} = 0,$$

$$\tau_{rz} = 0.$$

$T(r)$ is the function of temperature variation with radius variable r. The temperature function can be expressed as

$$T(r) = c_1 \ln r + c_2, \tag{6}$$

under the assumption that the circular disk is subjected by a loading of symmetric temperature to the radial direction only [17]. c_1 and c_2 will be determined based on the boundary conditions. The equilibrium equations in polar coordinates are

$$\frac{\partial \sigma_r}{\partial r} + \frac{1}{r}\frac{\partial \tau_{r\theta}}{\partial \theta} + \frac{\sigma_r - \sigma_\theta}{r} + \rho\omega^2 r = 0, \tag{7a}$$

$$\frac{\partial \sigma_\theta}{\partial \theta} + r\frac{\partial \tau_{r\theta}}{\partial r} + 2\tau_{r\theta} = 0, \tag{7b}$$

and the algebra among equations (4), (5), (7a), and (7b) yields the following governing equations:

TABLE 1: Mechanical and thermal properties used for analyzing thermoelastic characteristics of rotating CM circular disks.

Material/property	Elastic modulus (MPa)	Thermal expansion coefficient (10^{-6}/°C)	Density (g/cm^3)
Substrate (Al)	71	23.1	2.70
Bond coating (Al/Al$_2$O$_3$)	164.3	13.6	1.61
Top (Al$_2$O$_3$)	380	8.0	0.96

(a)

(b)
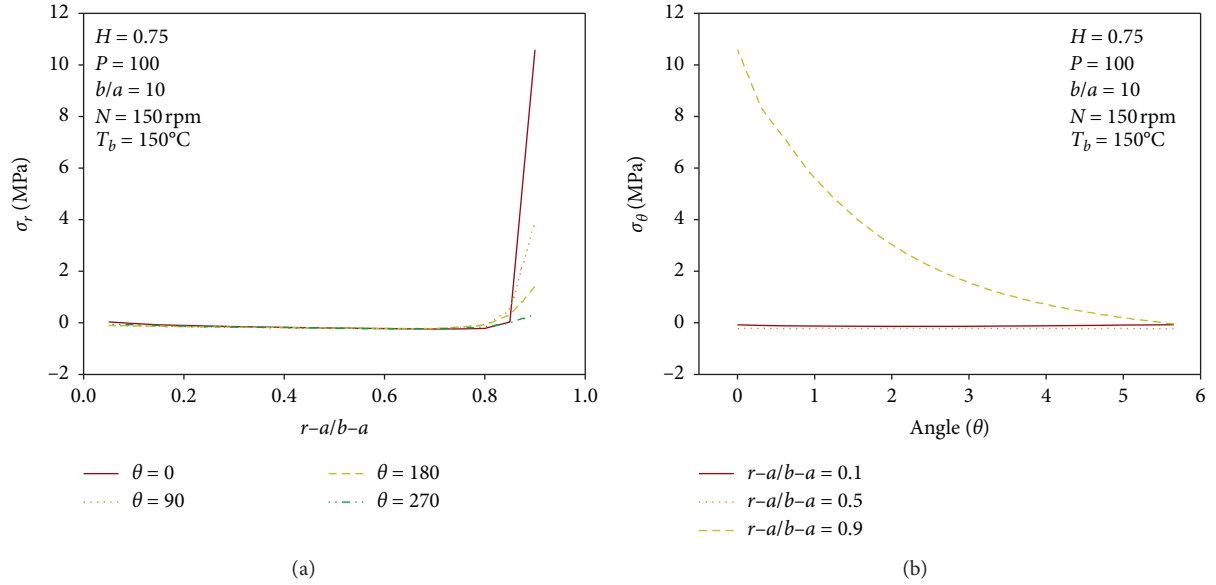
FIGURE 2: Stress distribution profiles in the (a) radial direction and (b) circumferential direction.

$$\frac{\partial}{\partial r}\left(r\frac{\partial u}{\partial r}\right) + \frac{1-v}{2r}\frac{\partial^2 u}{\partial \theta^2} - \frac{3-v}{2r}\frac{\partial v}{\partial \theta} + \frac{1+v}{2}\frac{\partial^2 v}{\partial r \partial \theta} - \frac{u}{r}$$

$$+ \frac{1-v^2}{E}\rho\omega^2 r^2 = (v+1)\alpha r\frac{dT(r)}{dr},$$

(8a)

$$\frac{1-v}{2}\frac{\partial}{\partial r}\left(r\frac{\partial v}{\partial r}\right) + \frac{1}{r}\frac{\partial^2 v}{\partial \theta^2} + \frac{3-v}{2r}\frac{\partial u}{\partial \theta} + \frac{1+v}{2}\frac{\partial^2 u}{\partial r \partial \theta} - \frac{1-v}{2}\frac{v}{r} = 0.$$

(8b)

The governing equations (8a) and (8b) are a pair of partial differential equations in the polar coordinate system expressed with the radial and circumferential displacement distribution profiles under the loading of temperature. The thermoelastic characteristics of a functionally graded rotating circular disk subjected to a contact force are investigated according to the boundary conditions:

$$\sigma_r(a, \theta) = 0,$$
$$\sigma_r(b, \theta - \{0\}) = 0,$$
$$\sigma_r(b, 0) = P,$$

(9)

at a contact point.

The boundary condition implies that the circular model is under the loading of thermal expansion over the entire domain and of radial pressure P at the outer boundary contact point $(b, 0)$.

2.2. Finite Volume Formulation. Due to the complexity of the governing equations, a numerical technique is required, and a finite volume method is applied for approximation. The domain is divided up into control volume and integrates the field equations over each control volume (see Figure 1(b)). Equations (8a) and (8b) thus are discretized as follows [18]:

$$A_{11}u_{i+1,j} + A_{12}u_{i,j+1} + A_{13}u_{i,j} + A_{14}u_{i,j-1} + A_{15}u_{i-1,j}$$

$$+ B_{11}v_{i,j+1} + B_{12}v_{i,j} + B_{13}v_{i,j-1} + B_{14}v_{i-1,j+1} + B_{15}v_{i-1,j} + B_{16}v_{i-1,j-1} + B_{17}v_{i-2,j+1} + B_{18}v_{i-2,j} + B_{19}v_{i-2,j-1} = f_{i,j},$$

$$A_{21}u_{i,j+1} + A_{22}u_{i,j} + A_{23}u_{i,j-1} + A_{24}u_{i-1,j+1} + A_{25}u_{i-1,j} + A_{26}u_{i-1,j-1} + A_{27}u_{i-2,j+1} + A_{28}u_{i-2,j} + A_{29}u_{i-2,j-1}$$

$$+ B_{21}v_{i+1,j} + B_{22}v_{i,j+1} + B_{23}v_{i,j} + B_{24}v_{i,j-1} + B_{25}v_{i-1,j} = 0,$$

(10)

$$A_{11} = \frac{1-v}{2}\frac{\Delta r}{\Delta\theta}\frac{1}{r_{i,j}},$$

$$A_{12} = \frac{\Delta\theta}{\Delta r}r_{i,j+(1/2)},$$

$$A_{13} = -\frac{\Delta\theta}{\Delta r}\left(r_{i,j+(1/2)} + r_{i,j-(1/2)}\right) - (1-v)\frac{\Delta r}{\Delta\theta}\frac{1}{r_{i,j}} - \Delta r\Delta\theta\frac{1}{r_{i,j}},$$

$$A_{14} = \frac{\Delta\theta}{\Delta r}r_{i,j-(1/2)},$$

$$A_{15} = \frac{1-v}{2}\frac{\Delta r}{\Delta\theta}\frac{1}{r_{i,j}},$$

$$B_{11} = \frac{3}{8}(1+v),$$

$$B_{12} = -\frac{3}{4}(3-v)\Delta r\frac{1}{r_{i,j}},$$

$$B_{13} = -\frac{7}{16}(1+v),$$

$$B_{14} = -\frac{1}{2}(1+v),$$

$$B_{15} = \frac{5}{2}(3-v)\frac{1}{r_{i,j}},$$

$$B_{16} = \frac{9}{16}(1+v),$$

$$B_{17} = \frac{1}{8}(1+v),$$

$$B_{18} = -\frac{3}{4}(3-v)\Delta r\frac{1}{r_{i,j}},$$

$$B_{19} = -\frac{1}{8}(1+v),$$

$$f_{i,j} = (1+v)\alpha r_{i,j}\Delta\theta\left(T_{i,j+(1/2)} - T_{i,j-(1/2)}\right) - \Delta r\Delta\theta\rho\omega^2\frac{1-v^2}{E}r_{i,j}^2,$$

$$A_{21} = \frac{3}{8}(1+v),$$

$$A_{22} = \frac{3}{4}(3-v)\Delta r\frac{1}{r_{i,j}},$$

$$A_{23} = -\frac{7}{16}(1+v),$$

$$A_{24} = -\frac{1}{2}(1+v),$$

$$A_{25} = -(3-v)\Delta r\frac{1}{r_{i,j}},$$

$$A_{26} = \frac{9}{16}(1+v),$$

$$A_{27} = \frac{1}{8}(1+v),$$

$$A_{28} = (3-v)\Delta r\frac{1}{r_{i,j}},$$

$$A_{29} = -\frac{1}{8}(1+v),$$

$$B_{21} = \frac{\Delta r}{\Delta\theta}\frac{1}{r_{i,j}},$$

$$B_{22} = \frac{\Delta\theta}{\Delta r}r_{i,j+(1/2)},$$

$$B_{23} = -\frac{\Delta\theta}{\Delta r}\left(r_{i,j+(1/2)} + r_{i,j-(1/2)}\right) - \frac{1-v}{2}\Delta r\Delta\theta\frac{1}{r_{i,j}} - 2\frac{\Delta r}{\Delta\theta}\frac{1}{r_{i,j}},$$

$$B_{24} = \frac{\Delta\theta}{\Delta r}r_{i,j-(1/2)}, \tag{11}$$

$$B_{25} = \frac{\Delta r}{\Delta\theta}\frac{1}{r_{i,j}}.$$

The validation and convergence of the above finite volume method (FVM) were presented in [17], and Mathematica (version 5.0) is used to obtain numerical solutions.

3. Numerical Results and Discussion

In this section, the differential equation induced in Section 2.1 and the finite volume formula developed in Section 2.2 are used to evaluate the approximated results of different components of displacement, stress, and strain for an (Al_2O_3/Al) FGM circular disk. The mechanical and thermal properties of these ingredient materials are shown in Table 1.

Stress distribution profiles are presented in Figure 2. As shown in Figure 2(a), the circular disk is undergoing tensile radial stress. All areas of the disk except near outer boundary experience trivial influence in radial stress distribution, whereas the contact point suffers from the largest radial stress. But different phase develops in circumferential stress. At normalized values $(r-a)/(b-a) = 0.1$ and 0.5, the magnitude of circumferential stresses is ignorable in comparison with circumferential stress at $(r-a)/(b-a) = 0.9$ (see Figure 2(b)). In addition, the entire area of the disk is under the loading of tensile circumferential stress at $(r-a)/(b-a) = 0.9$ and the circumferential stress distribution exhibits exponential decay with the increase of angle. The strain distribution profiles are described in Figure 3. Near area of outer boundary in circular domain presents that the magnitude increases with the increase of angle value in the radial strain distribution (see Figure 3(a)). Positive radial strain distribution appears over the disk, and the largest radial strain value occurring at the contact point generates. However, the circumferential strain distribution shows different pattern (see Figure 3(b)). At $(r-a)/(b-a) = 0.9$, the circumferential strain deploys to the positive direction, while negative circumferential strain distributions are obtained at $(r-a)/(b-a) = 0.1$ and 0.5. The changing shape of the circumferential strain is a parabola as the angle increases at $(r-a)/(b-a) = 0.1$ and 0.5, whereas the circumferential strain distribution profile fluctuates at the beginning and logarithmic decay appears after $\theta = 2$ at $(r-a)/(b-a) = 0.9$. The results inform that (i) contact force is highly influential to near area of contact point in radial direction, (ii) the circumference stress is more sensitive to contact force than the radial stress distribution, and (iii) various phenomena appear in circumferential strain distribution depending on the value of $(r-a)/(b-a)$.

Figure 4 presents the influences of contact force on the stress distribution by choosing the representative angles $\theta = 0$ and 180 and the normalized radius $(r-a)/(b-a) = 0.1$

and 0.9. The radial stress distribution is susceptible to the change of contact force, especially near the area of contact point (see Figures 4(a) and 4(b)). Entire domain of the circular disk suffers from a tensile stress and the magnitude of the radial stress is getting larger as the contact force increases. As shown in Figure 4(c), the area near the inner boundary of the disk sits loose to the variation of contact force, but the area near the outer boundary reacts sensitively to the change of contact force, and noticeable impact appears when $\theta = 0$ (see Figure 4(d)). By the increase of contact force, the radial and circumferential stresses exhibit exponential growth near area of contact point, even though minor effects appear over entire circular domain.

The effects of contact force on the strain distributions are described in Figure 5. The reactions of the radial strain distribution to the change of contact force are similar to those of radial stress distribution (see Figures 5(a) and 5(b)). Nearby area of the outer boundary is particularly susceptible to the increase of contact force and the magnitude of the radial strain grows with the increment of contact force. Trivial reaction appears in the circumferential strain distribution to the variation of contact force for $(r-a)/(b-a) = 0.1$ (see Figure 5(c)), whereas nearby part of the outer boundary is sensitive to the change of contact force (see Figure 5(d)). Pronounced alterations in the circumferential strain distribution appear on area around $\theta = 0$. The numerical solutions imply that (i) the magnitude of contact force is a critical factor to determine the thermoelastic characteristics of circular FGM models and (ii) the radial direction is more susceptible to the variation of the magnitude of contact force.

The influences of homogeneous thickness on thermoelastic characteristics, denoted by H, are explained through Figures 6–8. H = 1 implies that the circular disk is composed of homogeneous material. The representative values H = 0.25, 0.5, and 0.75 are applied. Figure 6 expresses the effects of H on the displacement distributions.

The area between normalized values $(r-a)/(b-a) = 0.2$ and $(r-a)/(b-a) = 0.85$ reveals noticeable reactions to homogeneous thickness variation. The magnitude of the radial displacement increases with the growth of homogeneous part (see Figures 6(a) and 6(b)), but nearby area of the outer boundary displays that the magnitude to the positive direction decreases as the value of H increases. The results imply that the growth of functionally graded area in the circular disk yields more stability in the radial displacement distribution profiles.

As shown in Figures 6(c) and 6(d)), minor influence appears in the circumferential displacement except nearby area of contact force. The circumferential displacement

(a)

(b)
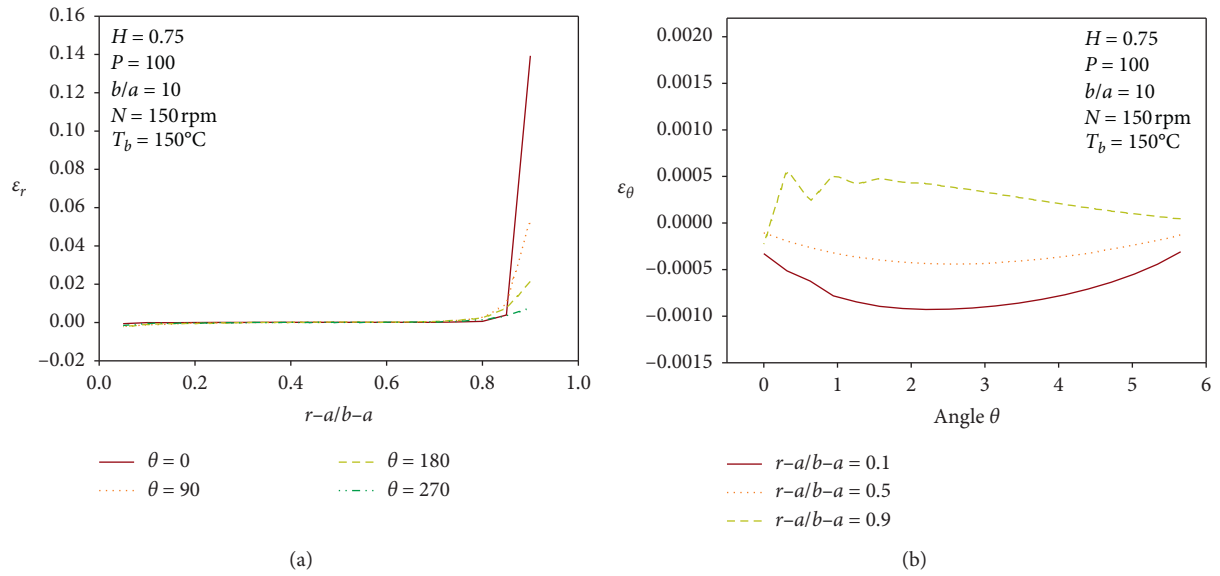
Figure 3: Strain distribution profiles in the (a) radial direction and (b) circumferential direction.

(a)

(b)

(c)

(d)
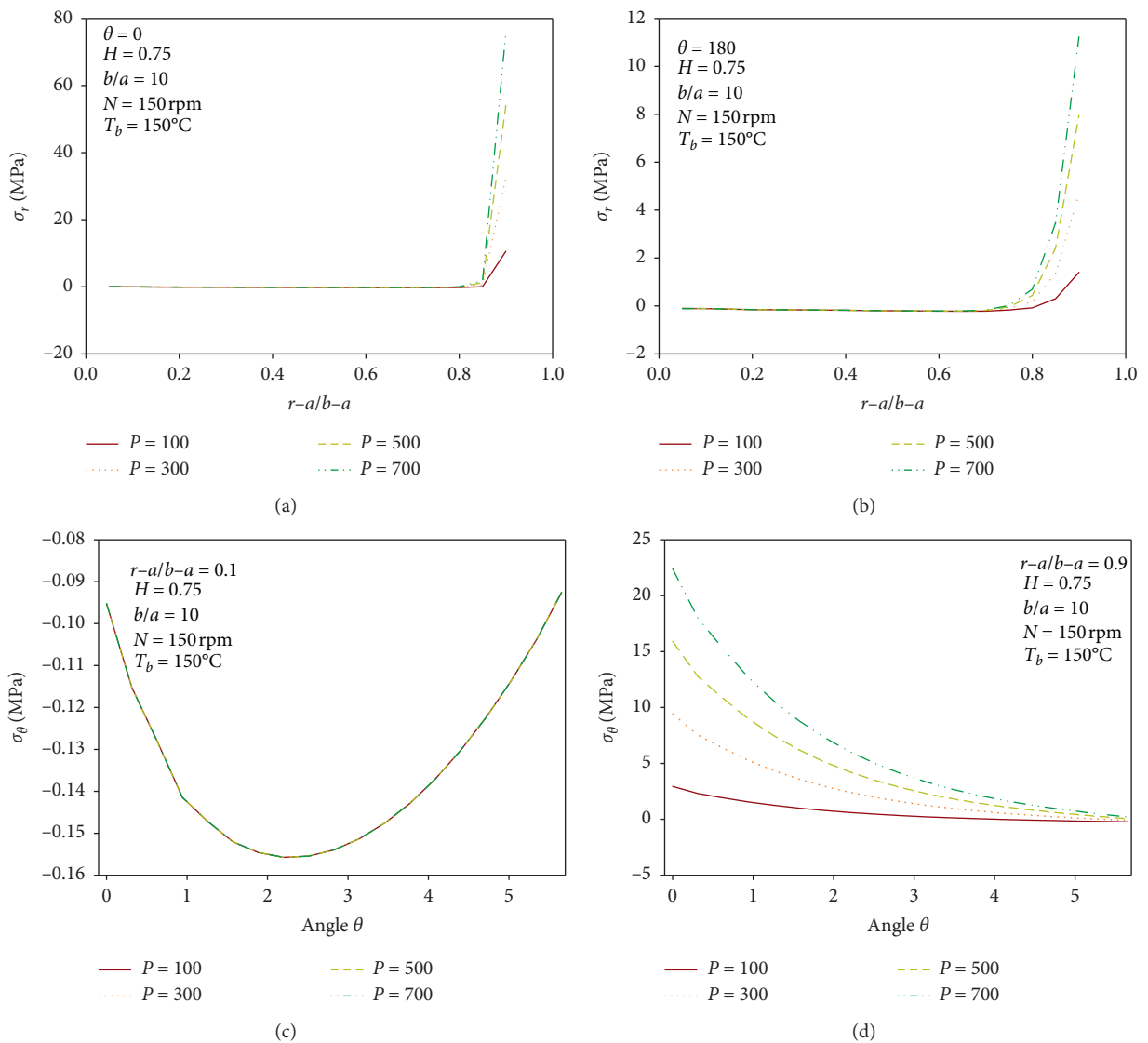
Figure 4: Effects of contact force on the stress in the radial direction (a) at $\theta = 0$ and (b) at $\theta = 180$ and in the circumferential direction (c) at $(r - a)/(b - a) = 0.1$ and (d) at $(r - a)/(b - a) = 0.9$.

$\theta = 0$
$H = 0.75$
$b/a = 10$
$N = 150\,\text{rpm}$
$T_b = 150°\text{C}$

— $P = 100$ — — $P = 500$
······ $P = 300$ —·— $P = 700$

(a)

$\theta = 180$
$H = 0.75$
$b/a = 10$
$N = 150\,\text{rpm}$
$T_b = 150°\text{C}$

— $P = 100$ — — $P = 500$
······ $P = 300$ —·— $P = 700$

(b)

$r-a/b-a = 0.1$
$H = 0.75$
$b/a = 10$
$N = 150\,\text{rpm}$
$T_b = 150°\text{C}$

— $P = 100$ — — $P = 500$
······ $P = 300$ —·— $P = 700$

(c)

$r-a/b-a = 0.9$
$H = 0.75$
$b/a = 10$
$N = 150\,\text{rpm}$
$T_b = 150°\text{C}$

— $P = 100$ — — $P = 500$
······ $P = 300$ —·— $P = 700$

(d)
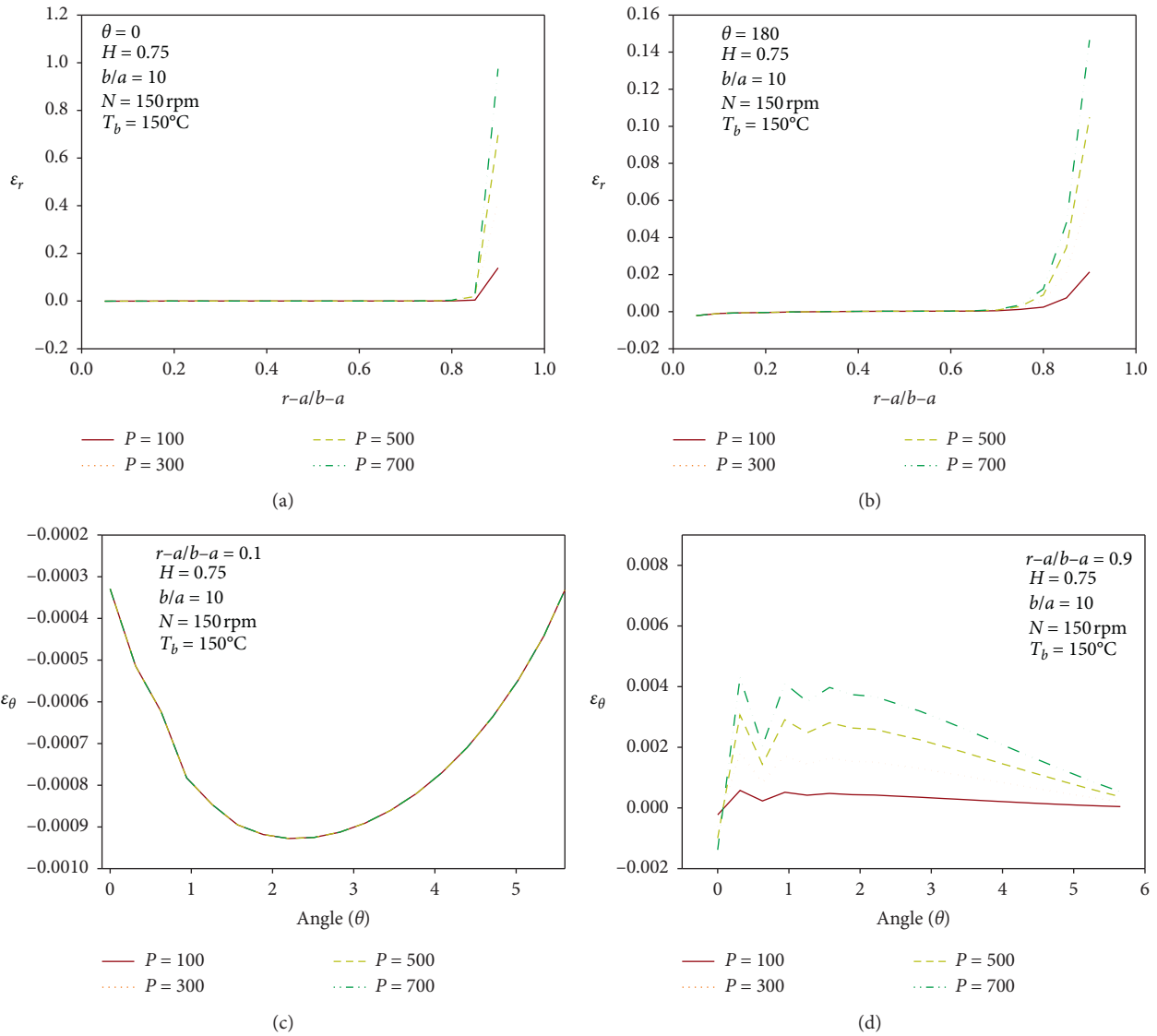
FIGURE 5: Effects of contact force on the strain in the radial direction (a) at $\theta = 0$ and (b) at $\theta = 180$ and in the circumferential direction (c) at $(r - a)/(b - a) = 0.1$ and (d) at $(r - a)/(b - a) = 0.9$.

$\theta = 180$
$P = 100$
$b/a = 10$
$N = 150\,\text{rpm}$
$T_b = 150°\text{C}$

— $H = 0.25$
······ $H = 0.5$
— — $H = 0.75$

(a)

$\theta = 180$
$P = 100$
$b/a = 10$
$N = 150\,\text{rpm}$
$T_b = 150°\text{C}$

— $H = 0.25$
······ $H = 0.5$
— — $H = 0.75$

(b)

FIGURE 6: Continued.

(c)
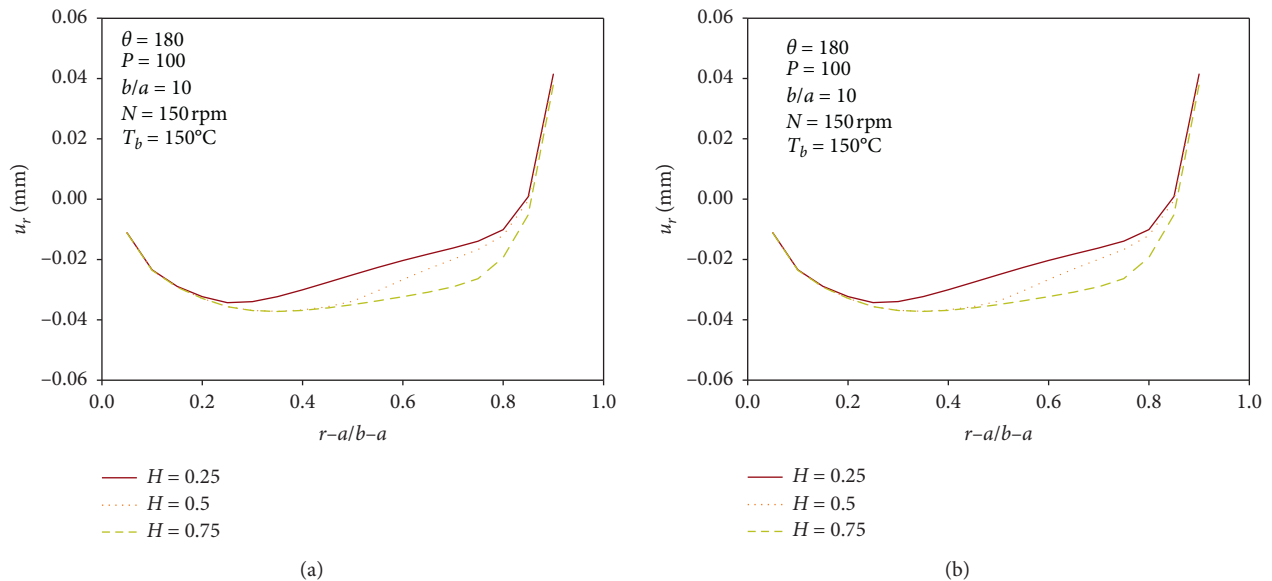
(d)
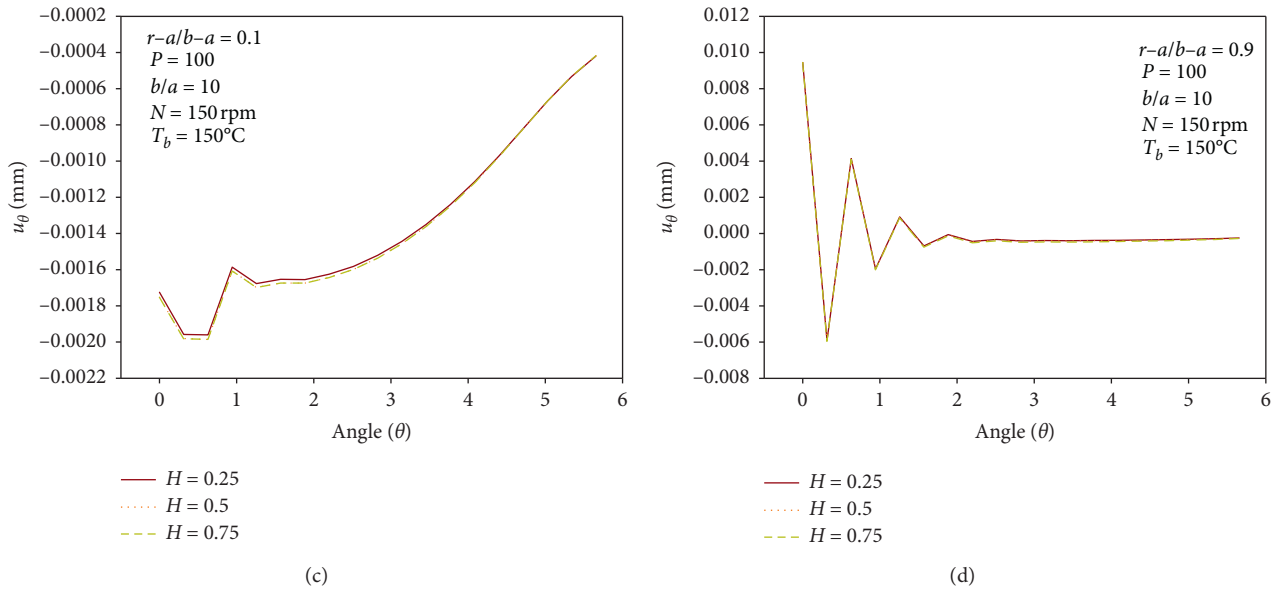
FIGURE 6: Effects of homogeneous thickness on the displacement in the radial direction (a) at $\theta = 0$ and (b) at $\theta = 180$ and in the circumferential direction (c) at $(r - a)/(b - a) = 0.1$ and (d) at $(r - a)/(b - a) = 0.9$.

(a)

(b)

FIGURE 7: Continued.

(c)
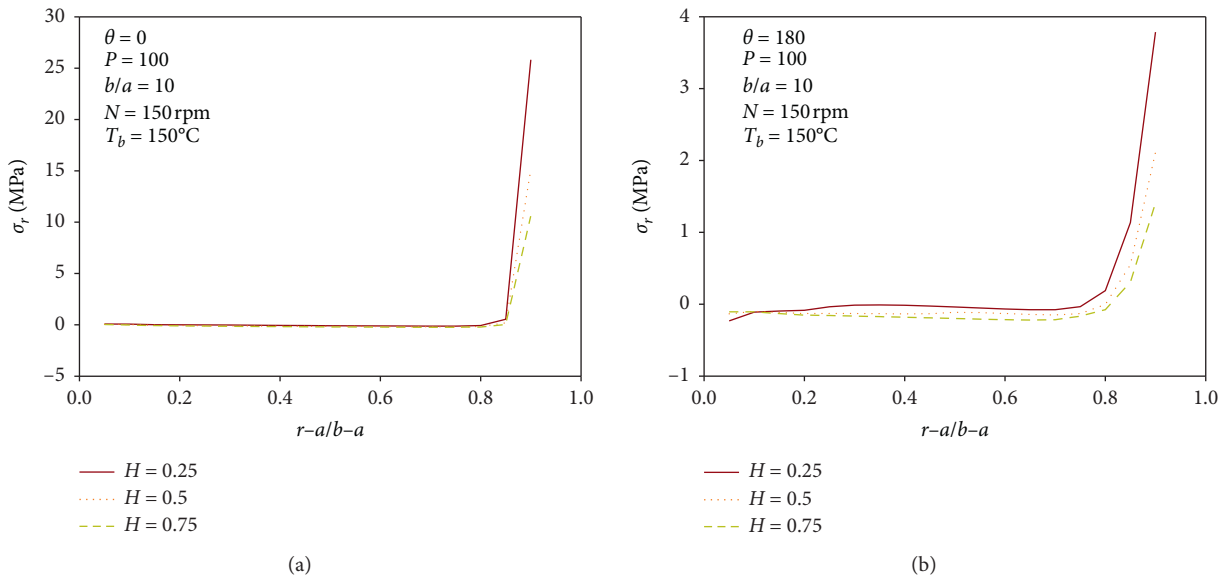
(d)
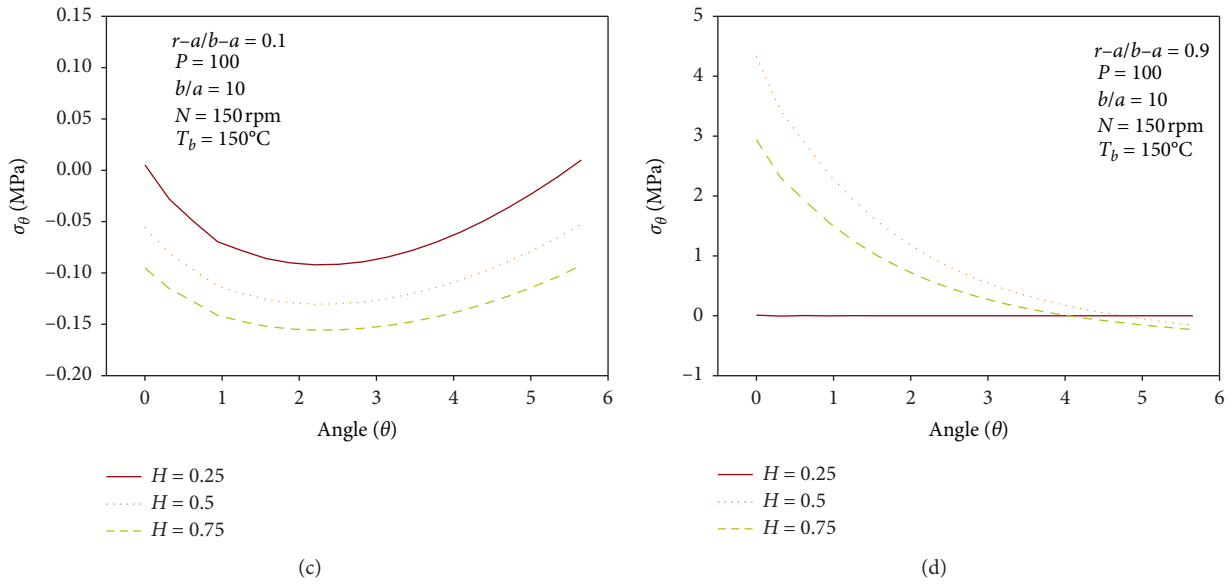
FIGURE 7: Effects of homogeneous thickness on the stress in the radial direction (a) at $\theta = 0$ and (b) at $\theta = 180$ and in the circumferential direction (c) at $(r - a)/(b - a) = 0.1$ and (d) at $(r - a)/(b - a) = 0.9$.

(a)

(b)
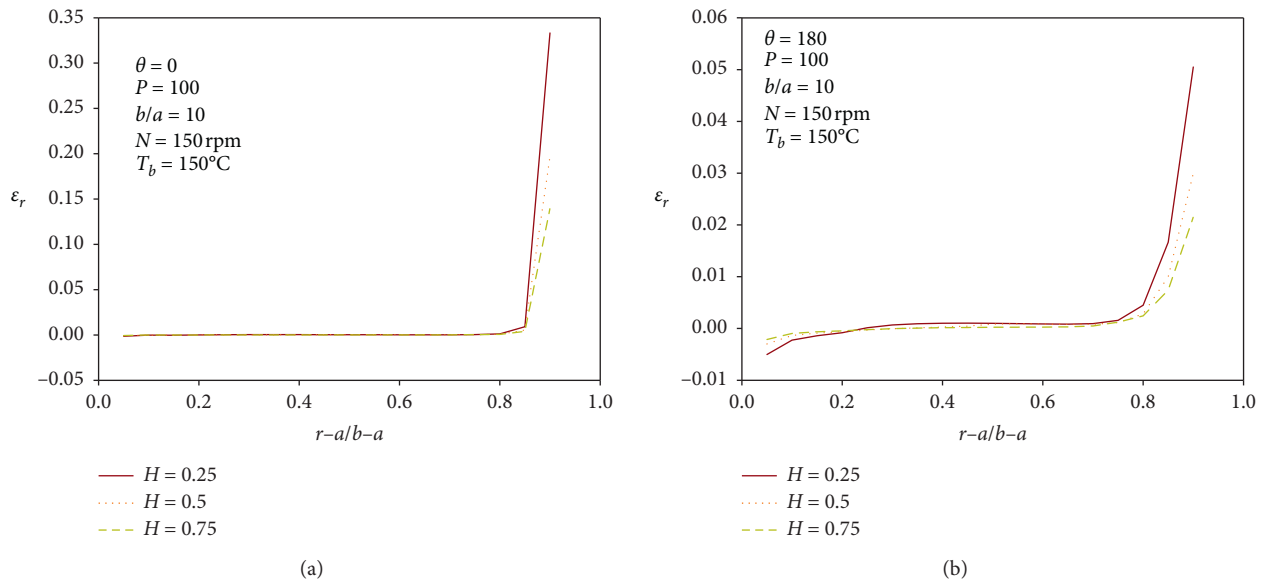
FIGURE 8: Continued.
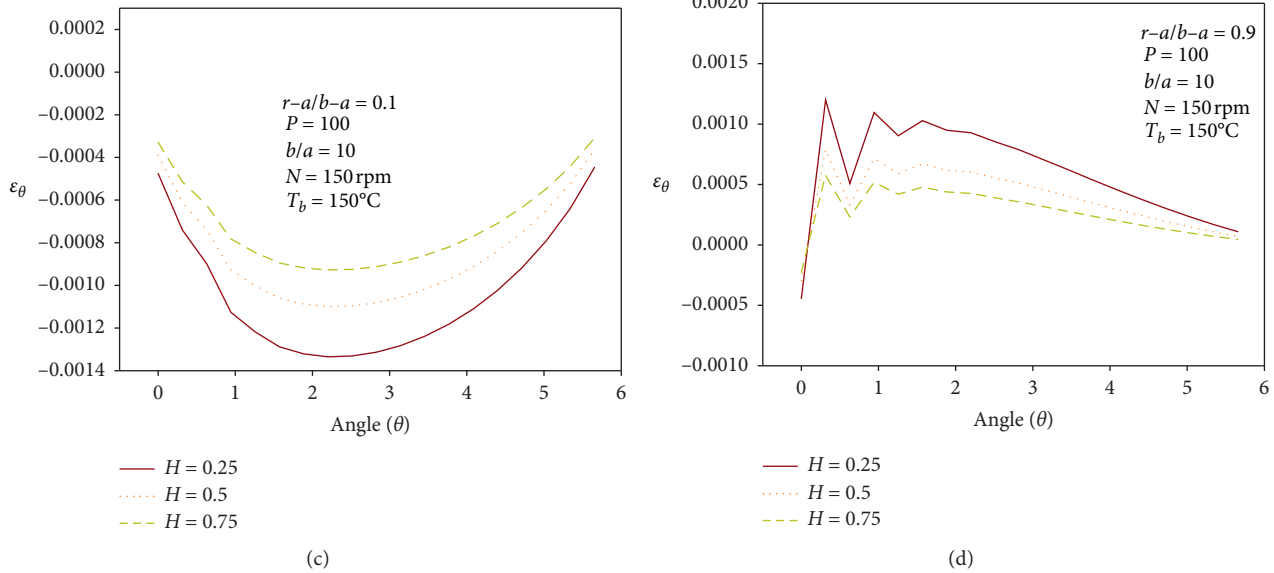
FIGURE 8: Effects of homogeneous thickness on the strain in the radial direction (a) at $\theta = 0$ and (b) at $\theta = 180$ and in the circumferential direction (c) at $(r - a)/(b - a) = 0.1$ and (d) at $(r - a)/(b - a) = 0.9$.

increases with growth of the value of H over the area around contact force.

Figure 7 presents the effects of H on the stress distributions. The radial distribution exhibits smaller tensile stress over the nearby area of outer boundary with increase of the value of H when $\theta = 0$ (see Figure 7(a)). But the circular disk undergoes larger compressive radial stress over area between normalized values $(r - a)/(b - a) = 0.1$ and $(r - a)/(b - a) = 0.8$ when $\theta = 180$ (see Figure 7(b)). According to the radial stress distributions, the circular disk with larger functionally graded area may not guarantee higher stability over nearby area of outer boundary. Different phase develops in circumferential stress distributions. Over nearby area of the inner boundary, entire domain of the disk experiences compressive circumferential stress for the values of H = 0.5 and 0.75, whereas some part of the disk with H = 0.25 undergoes tensile circumferential stress (see Figure 7(c)). Over nearby area of the outer boundary of the disk, the circumferential stress with H = 0.75 is trivial in comparison with the value of H = 0.25 and 0.5 (see Figure 7(d)). The magnitude of the circumferential stress is higher near contact point as the homogeneous thickness decreases. Based on the circumferential stress distributions, greater functionally graded area affords higher stability in the circular disk. The influences of homogeneous thickness H on the strain distributions are described in Figure 8. Nearby area of the outer boundary of the disk is sensitive to the change of homogeneous thickness in the radial strain distributions. The magnitude of strain decreases with the growth of the value of H (see Figures 8(a) and 8(b)), which signifies that the circular disk with larger homogeneous area is more stable over nearby area of the outer boundary. Similar movements occur in the circumferential strain. As shown in Figures 8(c) and 8(d), the magnitude of the circumferential strain is getting larger according to the decline

of the value of H. The outcomes describe that the circular disk stability with greater functionally graded area is greater in the circumferential strain distribution. The numerical approaches make point of the following: (i) the variation of homogeneous thickness is highly influential to thermoelastic characteristics over the area of $0.2 < (r - a)/(b - a) < 0.8$ and (ii) the radial direction is more susceptible to the change of homogeneous thickness.

4. Conclusions

A rotating FGM circular disk with a concentric circular hole is taken into account to investigate the thermoelastic characteristics. The circular disk is under the loading of a contact force. The effects of the variation of contact force and homogeneous thickness on the components of displacement, stress, and strain have been described. Over nearby area of the contact point, the thermoelastic behavior reacts sensitively to the change of contact force and exhibits exponential growth in the magnitude, whereas the influence of contact force over the other area is greater in the circumferential stress distributions. The outcomes explain that the outer boundary area is exposed to become brittle with the growth of a contact force. In the radial displacement distribution, the growth of functionally graded area grants more stability in the circular disk, while, according to the radial stress distributions, the circular disk with larger functionally graded area may not guarantee higher stability over nearby area of outer boundary. Based on the circumferential distribution profiles, the circular disk with greater functionally area evinces higher stability. Overall, the results demonstrate that contact force and homogeneous thickness are crucial parameters to determine the thermoelastic characteristics of FGM circular disks, and the movements of an FGM circular disk can be controlled by

controlling of these parameters. Therefore, a FGM circular cutter or grinding disk suffering from the loading of a contact force can be designed applying the finite volume analysis used in this investigation to promote proper and reliable thermoelastic characteristics in service.

Nomenclature

u: Radial displacement component (mm)
v: Circumferential displacement component (mm)
ε_r: Radial strain
ε_θ: Circumferential strain
γ: Shearing strain
σ_r: Radial stress (MPa)
σ_θ: Circumferential stress (MPa)
τ: Shearing stress
ν: Poisson's ratio
ω: Angular velocity
N: Revolutions per minute (rpm)
E: Young's modulus (MPa)
α: Coefficient of thermal expansion (10^{-6}/°C)
ρ: Density of the disk (g/cm^3).

Data Availability

The data used to support the findings of this study are available from the corresponding author upon request.

Conflicts of Interest

The author declares that there are no conflicts of interest.

Acknowledgments

References

[1] J. B. Holt, M. Koizumi, T. Hirai, and Z. A. Munir, *Ceramic Transactions, Functionally Gradient Materials*, The American Ceramic Society, p. 34, Westerville, Ohio, USA, 1993.

[2] K. BnvsGaneshGupta, M. M. Hiremath, A. Fulmali, R. K. Prusty, and B. C. Ray, "Multimaterial laminated composites: an assessment of effect of stacking sequence on flexural response," *Material Today: Proceedings*, 2020.

[3] N. Zimmermann and P. H. Wang, "A review of failure modes and fracture analysis of aircraft composite materials," *Engineering Failure Analysis*, vol. 115, Article ID 104692, 2020.

[4] Y. Obata and N. Noda, "Steady thermal stresses in a hollow circular cylinder and a hollow sphere of a functionally gradient material," *Journal of Thermal Stresses*, vol. 17, no. 3, pp. 471–487, 1994.

[5] K. M. Liew, S. Kitipornchai, X. Z. Zhang, and C. W. Lim, "Analysis of the thermal stress behaviour of functionally graded hollow circular cylinders," *International Journal of Solids and Structures*, vol. 40, no. 10, pp. 2355–2380, 2003.

[6] A. M. Afsar, M. Anisuzzaman, and J. I. Song, "Inverse problem of material distribution for desired fracture characteristics in a thick-walled functionally graded material cylinder with two diametrically-opposed edge cracks," *Engineering Fracture Mechanics*, vol. 76, no. 7, pp. 845–855, 2009.

[7] Y. Kovalyshen, "Analytical model of oscillatory disc cutting," *International Journal of Rock Mechanics and Mining Sciences*, vol. 77, pp. 378–383, 2015.

[8] Y. Huang and X.-F. Li, "Effect of radial reaction force on the bending of circular plates resting on a ring support," *International Journal of Mechanical Sciences*, vol. 119, pp. 197–207, 2016.

[9] H.-L. Dai, T. Dai, and X. Yan, "Thermoelastic analysis for rotating circular HSLA steel plates with variable thickness," *Applied Mathematics and Computation*, vol. 268, pp. 1095–1109, 2015.

[10] A. B. Rad, "Static analysis of non-uniform 2D functionally graded auxetic-porous circular plates interacting with the gradient elastic foundations involving friction force," *Aerospace Science and Technology*, vol. 76, pp. 315–339, 2018.

[11] C. Tadokoro, T. Nagamine, and K. Nakano, "Stabilizing effect arising from parallel misalignment in circular sliding contact," *Tribology International*, vol. 120, pp. 16–22, 2018.

[12] S. Yildirim, "Hydrogen elasticity solution of functionally-graded spheres, cylinders and disks," *International Journal of Hydrogen Energy*, vol. 45, no. 41, pp. 22094–22101, 2020.

[13] L. Sondhi, A. Kumar Thawait, S. Sanyal, and S. Bhowmick, "Stress and deformation analysis of variable thickness clamped rotating disk of functionally graded orthotropic material," *Materials Today: Proceedings*, vol. 18, pp. 4431–4440, 2019.

[14] J. Go, A. M. Afsar, and J. I. Song, "Analysis of thermoelastic characteristics of a rotating FGM circular disk by finite element method," *Advanced Composite Materials*, vol. 19, no. 2, pp. 197–213, 2010.

[15] A. M. Afsar and J. Go, "Finite element analysis of thermoelastic field in a rotating FGM circular disk," *Applied Mathematical Modelling*, vol. 34, no. 11, pp. 3309–3320, 2010.

[16] S. P. Timoshenko and J. N. Goodier, *Theory of Elasticity*, McGraw-Hill Book Company, New York, NY, USA, 3rd edition, 2010.

[17] M. Tadi, "Finite volume method for 2D elastic wave propagation," *Bulletin of the Seismological Society of America*, vol. 94, no. 4, pp. 1500–1509, 2004.

[18] J. Go, "Thermo-elastic characteristics of homogeneous circular disk models subjecting to a contact force," *Contemporary Engineering Sciences*, vol. 12, no. 1, pp. 51–64, 2019.

Research Article

New Vertically Planed Pendulum Motion

A. I. Ismail [ID][1,2]

[1]*Mechanical Engineering Department, Faculty of Engineering and Islamic Architecture, Umm Al-Qura University,
 P.O. Box 5555, Makkah, Saudi Arabia*
[2]*Department of Mathematics, Faculty of Science, Tanta University, Tanta, P.O. Box 31527, Egypt*

Correspondence should be addressed to A. I. Ismail; aiismail@uqu.edu.sa

This article is concerned about the planed rigid body pendulum motion suspended with a spring which is suspended to move on a vertical plane moving uniformly about a horizontal X-axis. This model depends on a system containing three generalized coordinates. The three nonlinear differential equations of motion of the second order are obtained to the elastic string length and the oscillation angles φ_1 and φ_2 which represent the freedom degrees for the pendulum motions. It is assumed that the body moves in a rotating vertical plane uniformly with an arbitrary angular velocity ω. The relative periodic motions of this model are considered. The governing equations of motion are obtained using Lagrange's equations and represent a nonlinear system of second-order differential equations that can be solved in terms of generalized coordinates. The numerical solutions are investigated using the approximated fourth-order Runge–Kutta method through programming packages. These solutions are represented graphically to describe and discuss the behavior of the body at any instant for different values of the different physical parameters of the body. The obtained results have been discussed and compared with some previously published works. Some concluding remarks have been presented at the end of this work. The value of this study comes from its wide applications in both civil and military life. The main findings and objectives of the current study are obtaining periodic solutions for the problem and satisfying their accuracy and stabilities through the numerical procedure.

1. Introduction

The pendulum motion is studied by many outstanding scientists in the last century due to the wide application of this problem in applied mathematics, physics, and engineering. In [1], El-Barki and others studied the rotary motion of a pendulum model about an elliptic path. They described the problem dynamically and then deduced the equations of motion for this model using Lagrange's equation. The authors defined a small parameter that depends on the different parameters of the moving model. They solved the problem analytically using the small parameter technique and numerically using the Runge–Kutta method to make a comparison between the two sets of solutions. This comparison proved the validity of both obtained solutions.

Ismail in [2] presented a case of relative periodicity motion of a rigidity pendulum model in presence of multidegrees of freedom. He described the motion dynamically and used the Lagrangian function to describe the motion. The system of equations of motion is obtained. He defined a small parameter and used the small parameter technique to find the approximated periodic solutions of the obtained motion. He achieved computer programs through numerical consideration for proving the validity of the obtained solutions. In [3], the author studied the periodic solutions of a pendulum in a relative case. This case is considered as an especial one from the problem in [2]. The author used Poincare's method to find the approximated solutions. In [4], the author studied the oscillated motion of a simple pendulum model. He used the Lagrangian function for deriving the equations of motion. The processing method of analysis is used to find approximated solutions of the second order. In [5], the elastic pendulum oscillations are given by Vitt and Gorelik in 1933. They give an example of oscillated linear systems with two parametrical couples.

In [6], Lynch presented the three dimensions of elastic pendulum motions in the resonant case. He used the Lagrangian function for describing the motion. In [7], Holm and others studied a resonant elastic pendulum in the case of stepwise precession. In [8], the authors studied the motion of a harmonically excited elastic pendulum in the chaos response case. They derived the equations of motion of the pendulum model using Lagrange's equations. In [9], Amer described the dynamical oscillations of an elastic rigid pendulum in a plane to the equilibrium position. The author considered the plane rotates about the downward vertical fixed axis with uniform velocity. He used the Lagrangian function to deduce the equations of motion of the model. The numerical considerations [10] are considered using one of the numerical methods for searching the accuracy of the solutions.

The phrase diagram procedure is used for studying the stability of the solutions [11]. In [12], Brearley studied a simple pendulum model when its string length is changing uniformly. In [13], Pinsky and others studied the oscillated pendulum model for swing with a length which varies periodically.

Nayfeh in [14] presented many perturbation techniques for solving a lot of problems in mathematics, physics, and engineering. Such techniques are named the multiple scales, small parameter, KBM, processing analysis, and finite element method which are used in solving most of the previous problems. None of the authors thought about the use of the large parameter technique which gives accuring results for the required solutions. In [15], the two freedom degrees motion of a dynamic nonlinear model for an elastic damped pendulum in the inviscid flow of fluid was considered. The system for equations of motion was considered applying the Lagrangian function. The multiple scales technique is used for solving such equations to obtain the approximated solutions. The cases of resonance and steady state were investigated. The graphical representations of the motion were considered to show the behavior of the motion. The stabilities of the motion were studied. In [16, 17], the restricted motion for the harmonically damped elastic pendulum motion of a rigid body in the elliptic path was investigated when the damped coefficients are linear. In [18], the near resonance pendulum motions in the presence of a tunned absorber dynamical model system were considered. The authors in [19] studied the pendulum motion of a rigid body which moves in a plane with a constant angular velocity ω attached to a damped spring. The obtained solutions are analyzed numerically through computerized programs for showing motion behavior.

In this paper, a new problem is given for the elastic rigid pendulum motion in a vertical plane which rotates about a horizontal fixed axis in space by a uniform angular velocity ω. The importance of this motion comes from its wide applications in physics, engineering, and other fields.

2. Formulation of the Problem

In this section, the motion of an elastic pendulum model is considered which consists of a rigid body suspended with a massless spring at point O_2 which is suspended from the other hand by point O_1, see Figure 1. Let the coordinate system OXY rotate about its horizontal axis OX with a uniform angular velocity ω relative to the pendulum motion. Consider $OO_1 = h \cos \omega t$ at any instant of the time t such that at $t = 0$, $OO_1 = h$. Let the point C represent a mass center of the body, φ_1 represent the angle between $O_1 Y_1$ and $O_1 C$, and φ_2 denote the angle between $O_2 C$ and the vertical. Assuming $C\xi$, $C\eta$, and $C\zeta$ are the principal axes of inertia of the body such that $C\zeta$ is perpendicular to the plane OXY.

Thus, the mass center (x_C, y_C) of the body to the system OXY becomes

$$
\begin{aligned}
x_C &= h \cos \omega t + \rho \sin \varphi_1 + a \sin \varphi_2, \\
y_C &= \rho \cos \varphi_1 + a \cos \varphi_2, a = O_2 C,
\end{aligned}
\tag{1}
$$

where ρ is the elastic string length.

The potential and kinetic energies V and T are given as

$$
\begin{aligned}
V &= 0.5k^2 (\rho - \ell)^2 - mg(\rho \cos \varphi_1 + a \cos \varphi_2), \\
T &= 0.5m \Big\{ (-h\omega \sin \omega t)^2 + \dot{\rho}^2 + (\rho \dot{\varphi}_1)^2 + (a\dot{\varphi}_2)^2 \\
&\quad - 2h\omega \left[\dot{\rho} \sin \varphi_1 \sin \omega t + \rho \dot{\varphi}_1 \sin \omega t \cos \varphi_1 + a\dot{\varphi}_2 \sin \omega t \cos \varphi_2 \right] \\
&\quad + 2a \left[\dot{\rho} \dot{\varphi}_2 \sin(\varphi_1 - \varphi_2) + \dot{\varphi}_1 \dot{\varphi}_2 \cos(\varphi_1 - \varphi_2) \right] \\
&\quad + \omega^2 \left(h \cos \omega t + \rho \sin \varphi_1 + a \sin \varphi_2 \right)^2 + m^{-1} I_3 \dot{\varphi}_2^2 \\
&\quad + m^{-1} \omega^2 \left(I_1 \sin^2 \varphi_2 + I_2 \cos^2 \varphi_2 \right) \Big\},
\end{aligned}
\tag{2}
$$

where I_1, I_2, and I_3 are the principal inertia moments to the axes $C\xi\eta\zeta$, k^2 is the constant of the spring, ℓ denotes the unstretched spring length, and g is the acceleration of gravity.

The Lagrangian function L for this model is of the form [15]

$$
L = T - V,
\tag{3}
$$

where L is a function of ρ, φ_1, and φ_2 and their derivatives. Applying Lagrange's equations

$$
\frac{d}{dt} \left(\frac{\partial L}{\partial \dot{\rho}} \right) = \frac{\partial L}{\partial \rho}, \rho, \varphi_1, \varphi_2.
\tag{4}
$$

Making use of equations (1) to (4), the second-order differential equations of the motion are obtained as follows:
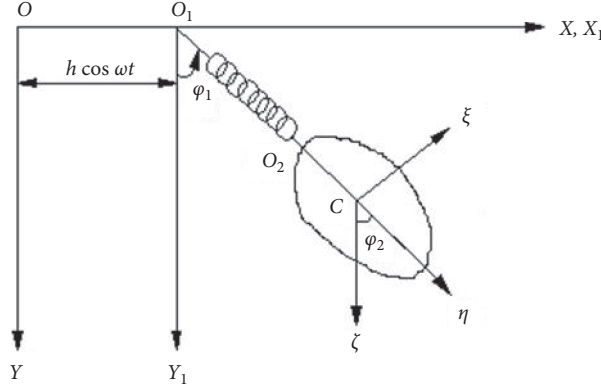
FIGURE 1: The elastic rigid pendulum model.

$$\ddot{\rho} + a\ddot{\varphi}_2 \sin(\varphi_1 - \varphi_2) - a\dot{\varphi}_2^2 \cos(\varphi_1 - \varphi_2) - \rho\dot{\varphi}_1^2$$
$$- \omega^2 (2h \cos\omega t + \rho \sin\varphi_1 + a \sin\varphi_2)\sin\varphi_1 - g\cos\varphi_1$$
$$+ k^2 m^{-1}(\rho - \ell) = 0,$$
$$\rho\ddot{\varphi}_1 + 2\dot{\rho}\dot{\varphi}_1 + a\ddot{\varphi}_2 \cos(\varphi_1 - \varphi_2) + a\dot{\varphi}_2^2 \sin(\varphi_1 - \varphi_2)$$
$$- \omega^2(2h\cos\omega t + \rho\sin\varphi_1 + a\sin\varphi_2)\cos\varphi_1 + g\sin\varphi_1 = 0,$$
$$\ell_1\ddot{\varphi}_2 + (2\dot{\rho}\dot{\varphi}_1 + \rho\ddot{\varphi}_1)\cos(\varphi_1 - \varphi_2) + (\ddot{\rho} - \rho\dot{\varphi}_1^2)\sin(\varphi_1 - \varphi_2)$$
$$- \omega^2(2h\cos\omega t + \rho\sin\varphi_1 + a\sin\varphi_2)\cos(\varphi_1 - \varphi_2) + g\sin\varphi_2$$
$$+ 2m^{-1}\omega^2(I_2 - I_1)\sin 2\varphi_2 = 0,$$
$$\ell_1 = a - I_3 m^{-1} a^{-1}.$$

$$(5)$$

Equations (5) are the differential equations of motion of second order in the three generalized coordinates.

Let the system oscillate in the closing relative equilibrium position, and the following is obtained:

$$I_1 = I_2. \tag{6}$$

The relative equilibrium admits the equality of the initial values for the angles φ_1 and φ_2, and thus

$$\rho = b + \xi(t),$$
$$\varphi_1 = \varphi_0 + \varphi(t), \tag{7}$$
$$\varphi_2 = \varphi_0 + \psi(t),$$

where b is the relative equilibrium for the length of the pendulum string. The quantities b and φ_0 are determined as follows:

$$m^{-1}k^2(b - \ell) = \omega^2(a + b)\sin^2\varphi_0 + g\cos\varphi_0,$$
$$g = \omega^2(a + b)\cos\varphi_0. \tag{8}$$

Making use of (7) into (5) and then (6) and (8), one obtains

$$\ddot{\xi} + a_{11}\xi + a_{12}\varphi + a_{13}\psi = f_1,$$
$$b\ddot{\varphi} + a\ddot{\psi} + b_{11}\xi + b_{12}\varphi + b_{13}\psi = f_2, \tag{9}$$
$$b\ddot{\psi} + \ell_1\ddot{\psi} + c_{11}\xi + c_{12}\varphi + c_{13}\psi = f_3,$$

where

$$a_{11} = m^{-1}k^2 - \omega^2(\sin^2\varphi_0 + 2h\cos\varphi_0 \cos\omega t),$$

$$a_{12} = bc_{11},$$

$$a_{13} = ac_{11},$$

$$b_{11} = c_{11},$$

$$b_{12} = \frac{k^2(b - \ell)}{m - \omega^2 b\cos^2\varphi_0}, \tag{10}$$

$$b_{13} = -\omega^2 a\cos^2\varphi_0,$$

$$c_{11} = -\omega^2 \sin\varphi_0 \cos\varphi_0,$$

$$c_{12} = -\omega^2 b\cos^2\varphi_0,$$

$$c_{13} = k^2 m^{-1}(b - \ell) + \omega^2(2h\sin\varphi_0 \cos\omega t - a\cos^2\varphi_0),$$

$$f_1 = (\xi + b)\dot{\varphi}^2 + A\xi\varphi + a\ddot{\psi}(\psi - \varphi) + a\dot{\psi}^2 + B\psi\varphi + C_1,$$
$$f_2 = -\xi\ddot{\varphi} - 2\dot{\xi}\dot{\varphi} + (\psi - \varphi)a\dot{\psi} + c_{11}(\xi + b)\dot{\varphi}^2$$
$$+ (D\xi + 2a_{13}\psi)\varphi + C_2,$$
$$f_3 = \ddot{\xi}(\psi - \varphi) - \dot{\varphi}^2(b + \xi)(\psi - \varphi) - \xi\ddot{\varphi} - 2\dot{\xi}\dot{\varphi}$$
$$+ 2\omega^2 h \cos\omega t \cos\varphi_0$$
$$- [b + (1 - \psi^2) - (b + \xi)\varphi\psi]c_{11} - g\sin\varphi_0$$
$$+ \omega^2\xi(\varphi\cos^2\varphi_0 - \psi\sin^2\varphi_0),$$

$$(11)$$

$$A = -2c_{11},$$
$$B = a\omega^2\cos^2\varphi_0,$$
$$D = \frac{B}{a},$$
$$C_1 = -(k^2 - \omega^2\sin^2\varphi_0) + \omega^2[2h\sin\varphi_0 \cos\omega t \tag{12}$$
$$+ a(\cos^2\omega t + \sin^2\varphi_0)] + g\cos\varphi_0 + k^2\ell,$$
$$C_2 = 2h\omega^2 \cos\omega t$$
$$- (b + a)c_{11} - g\sin\varphi_0.$$
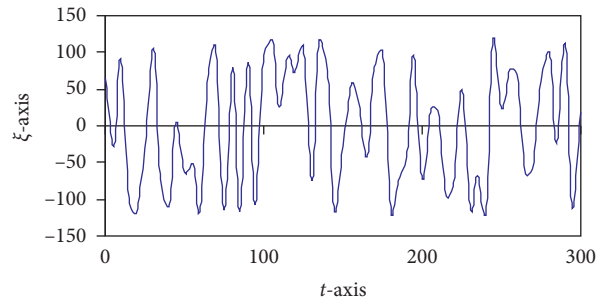
FIGURE 2: The solution ξ against the time t.
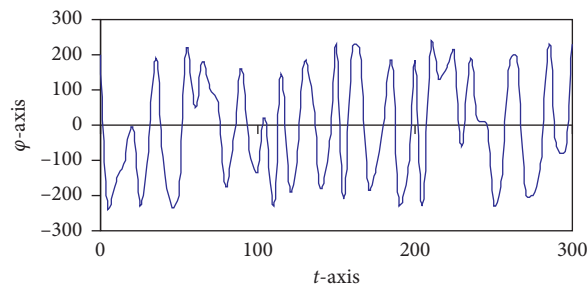
FIGURE 3: The solution φ against the time t.
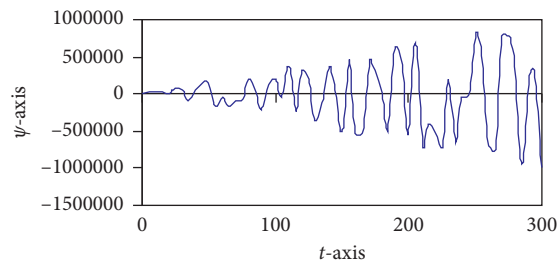
FIGURE 4: The solution ψ against the time t.
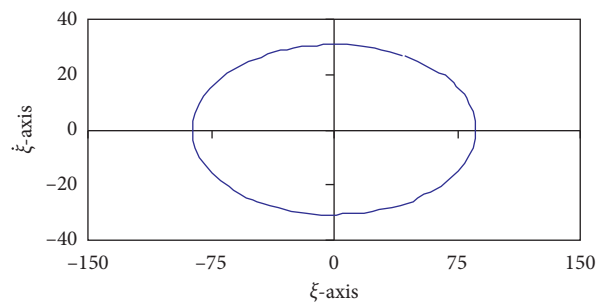
FIGURE 5: The stability $\dot{\xi}$ diagram against ξ.
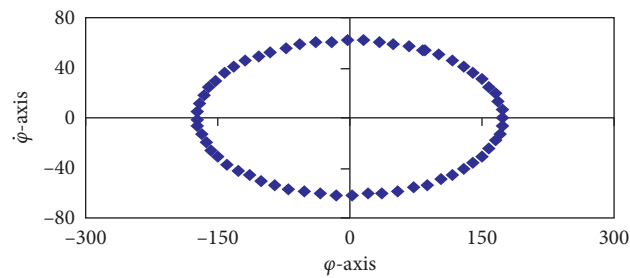
FIGURE 6: The stability $\dot{\varphi}$ diagram against φ.
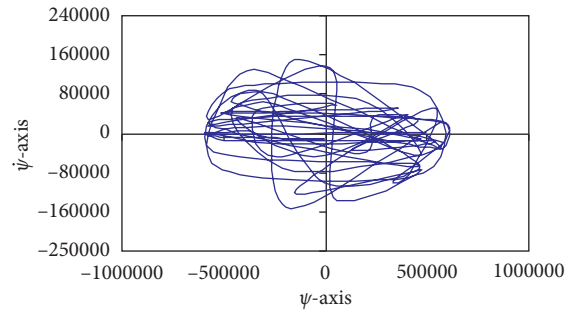
Figure 7: The instability $\dot{\psi}$ diagram against ψ.

Next, numerical considerations for solving system (9) in three degrees of freedom ξ, φ, and ψ are presented. The fourth-order Runge–Kutta method [10] is used for satisfying the numerical solutions for this system.

3. Numerical Investigations

In this section, the fourth-order Runge–Kutta method is used for solving the problem in the previous sections through computerized data. These solutions are investigated to illustrate and describe the oscillations of this system at different values of the time.

Making use of (10), (11), and (12), system (9) is reformulated in the form:

$$\ddot{\xi} = \ddot{\xi}(\xi, \varphi, \psi, \dot{\xi}, \dot{\varphi}, \dot{\psi}), (\xi\varphi\psi), \tag{13}$$

where the symbol $(\xi\varphi\psi)$ refers to the equations which are neglected. These functions are determined accordingly to equations (9)–(12). Introducing the following data:

$$\begin{aligned}
m &= 10\text{kg}, \\
g &= 9.8\text{m} \cdot \text{s}^{-2}, \\
I_1 &= 3\text{kg} \cdot \text{m}^2, \\
\ell &= 0.9\text{m}, \\
\omega &= 2\text{rad} \cdot \text{s}^{-1}, \\
a &= 0.7\text{m}, \\
b &= 0.5\text{m}, \\
\varphi_0 &= 0.2\text{rad}, \\
h &= 4, \\
t &= 0 \longrightarrow 300\text{s}.
\end{aligned} \tag{14}$$

The graphical representations for the solutions $\xi, \varphi, \psi, \dot{\xi}, \dot{\varphi}$, and $\dot{\psi}$ are given in Figures 2–7.

4. Conclusion

It is concluded that the model of relativistic elastic rigid pendulum motions is considered a wide application problem in many scientific fields. The Lagrangian function was used, and Lagrange's equations were applied for deriving the system of equations of motion for this problem. Computer programs were achieved applying the fourth-order Runge–Kutta method for obtaining the numerical solutions for the considered system. The obtained solutions are sketched at different values of rigid body parameters. From the figures, it is deduced that the approximated solutions are seemed to be periodic in a big interval of the motion. ξ and φ solutions represented in Figures 2, 3, 5, and 6 have uniform motion and stable solutions, but ψ is a chaotic and excited solution, see Figures 4 and 7. In all figures, the positive vibration waves come from the motion of the vertical plane above the horizontal axis and vice versa. The solution ψ is not stable since it moves with fast oscillations with small amplitudes in the beginning time and then goes slowly with larger amplitudes. The changing of the values of h, b, and φ_0 affects the behavior of the motion and vice versa.

Data Availability

Data sharing is not applicable to this article as no datasets were generated or analyzed during the current study.

Conflicts of Interest

The author declares that there are no conflicts of interest.

References

[1] F. A. El-Barki, A. I. Ismail, M. O. Shaker, and T. S. Amer, "On the motion of the pendulum on an ellipse," *Zeitschrift für Angewandte Mathematik und Mechanik*, vol. 79, no. 1, pp. 65–72, 1999.

[2] A. I. Ismail, "Relative periodic motion of a rigid body pendulum on an ellipse," *Journal of Aerospace Engineering*, vol. 22, no. 1, pp. 67–77, 2009.

[3] N. V. Stoianov, "On the relative periodic motions of a pendulum," *Journal of Applied Mathematics and Mechanics*, vol. 28, no. 1, pp. 188–193, 1964.

[4] S. J. Liao, "A second-order approximate analytical solution of a simple pendulum by the process analysis method," *Journal of Applied Mechanics*, vol. 59, no. 4, pp. 970–975, 1992.

[5] A. Vitt and G. Gorelik, "Oscillations of an elastic pendulum as an example of the oscillations of two parametrically coupled linear systems," in *Historical Note No. 3*Met Éireann, Dublin, Ireland, Translated by Lisa Shields, with an Introduction by Peter Lynch, 1999.

[6] P. Lynch, "Resonant motions of the three-dimensional elastic pendulum," *International Journal of Non-linear Mechanics*, vol. 37, no. 2, pp. 345–367, 2002.

[7] D. D. Holm and P. Lynch, "Stepwise precession of the resonant swinging spring," *SIAM Journal on Applied Dynamical Systems*, vol. 1, no. 1, pp. 44–64, 2002.

[8] T. S. Amer and M. A. Bek, "Chaotic responses of a harmonically excited spring pendulum moving in circular path," *Nonlinear Analysis: Real World Applications*, vol. 10, no. 5, pp. 3196–3202, 2009.

[9] T. S. Amer, "The dynamical behavior of a rigid body relative equilibrium position," *Advances in Mathematical Physics*, vol. 2017, Article ID 8070525, 13 pages, 2017.

[10] A. Gilat, *Numerical Methods for Engineers and Scientists*, Wiley, New York, NY, USA, 2013.

[11] R. Starosta, G. Sypniewska-Kamińska, and J. Awrejcewicz, "Asymptotic analysis of kinematically excited dynamical systems near resonances," *Nonlinear Dynamics*, vol. 68, no. 4, pp. 459–469, 2012.

[12] M. N. Brearley, "The simple pendulum with uniformly changing string length," *Proceedings of the Edinburgh Mathematical Society*, vol. 15, no. 1, pp. 61–66, 1966.

[13] M. A. Pinsky and A. A. Zevin, "Oscillations of a pendulum with a periodically varying length and a model of swing," *International Journal of Non-Linear Mechanics*, vol. 34, no. 1, pp. 105–109, 1999.

[14] A. H. Nayfeh, "A perturbation method for treating nonlinear oscillation problems," *Journal of Mathematics and Physics*, vol. 44, no. 1–4, p. 368, 1965.

[15] M. A. Bek, T. S. Amer, M. A. Sirwah, J. Awrejcewicz, and A. A. Araba, "The vibrational motion of a spring pendulum in a fluid flow," *Results in Physics*, vol. 19, Article ID 103465, 2020.

[16] T. S. Amer, M. A. Bek, and M. K. Abouhmr, "On the vibrational analysis for the motion of a harmonically damped rigid body pendulum," *Nonlinear Dynamics*, vol. 91, no. 4, pp. 2485–2502, 2018.

[17] T. S. Amer, M. A. Bek, and M. K. Abohamer, "On the motion of a harmonically excited damped spring pendulum in an elliptic path," *Mechanics Research Communications*, vol. 95, pp. 23–34, 2019.

[18] W. S. Amer, M. A. Bek, and M. K. Abohamer, "On the motion of a pendulum attached with tuned absorber near resonances," *Results in Physics*, vol. 11, pp. 291–301, 2018.

[19] F. M. El-Sabaa, T. S. Amer, H. M. Gad, and M. A. Bek, "On the motion of a damped rigid body near resonances under the influence of harmonically external force and moments," *Results in Physics*, vol. 19, Article ID 103352, 2020.

Research Article

Nonlinear Dynamics and Suppressing Chaos in Magnetic Bearing System

Shun-Chang Chang ⓘD

Department of Mechanical and Automation Engineering, Da-Yeh University, Changhua 51591, Taiwan

Correspondence should be addressed to Shun-Chang Chang; changsc@mail.dyu.edu.tw

A nonlinear mathematical model of a magnetic bearing system has been obtained by applying a modified conventional identification technique based on the principle of harmonic balance. In this study, we examined the rich nonlinear dynamics of a magnetic bearing system with closed-loop control using phase portraits, Poincaré maps, and frequency spectra. The resulting bifurcation diagram can be used to evaluate the operational range of systems employing nonlinear actuators. Estimates of the largest Lyapunov exponent based on the properties of synchronization revealed the occurrence of chatter vibration indicative of chaotic motion. Various control methods, such as the state feedback control and the injection of dither signals, were then used to quench the chaotic behavior.

1. Introduction and System Description

The rotor in magnetic bearing systems is suspended by magnetic bearings to ensure stable rotation at high speeds; however, a closed-loop control system is required to stabilize the system by eliminating vibrations caused by disturbing forces. The characteristics of magnetic bearings are inherently nonlinear due to nonlinearities in electromagnetic forces. The occurrence of large unbalanced forces in rotor bearings can cause nonlinear motion of high amplitude in magnetic bearing systems. Accurate control of the system is required which designers account for the effects of nonlinearities. In a previous work [1], we conducted experiments on an unloaded symmetric rotor with flexible coupler at one end and a bearing comprising two pairs of electromagnets at the other end (Figure 1). It was carried out by applying a series of nonlinear electromagnetic forces to identify a nonlinear model for this system. These rich nonlinear dynamics must be taken into account in the design of magnetic bearing systems. In this study, we sought to predict these nonlinear dynamics by modifying the conventional identification technique based on the principle of harmonic balance in order to characterize the system with a higher degree of precision. The resulting nonlinear model [1] is obtained as follows:

$$\dot{x}_1 = x_2, \tag{1a}$$

$$\dot{x}_2 = -d_1 x_2 - d_2 x_1 + d_3 x_3 + d_4 x_4 + d_5 x_1^2 + d_6 x_1 x_3 \\ + d_7 x_1 x_4 + d_8 x_3^2 + d_9 x_4^2 + d_{10} x_1^3, \tag{1b}$$

$$L\dot{x}_3 + R x_3 = K_A \left(e_{c1} + A_0 \sin \Omega t \right), \tag{1c}$$

$$L\dot{x}_4 + R x_4 = K_A \left(e_{c2} + A_0 \sin \Omega t \right), \tag{1d}$$

where

$$e_{c1} = K_H \left(K_P x_1 + K_D x_2 + K_I \int x_1 \mathrm{d}t \right),$$

$$e_{c2} = K_H \left(-K_P x_1 - K_D x_2 - K_I \int x_1 \mathrm{d}t \right), \tag{2}$$
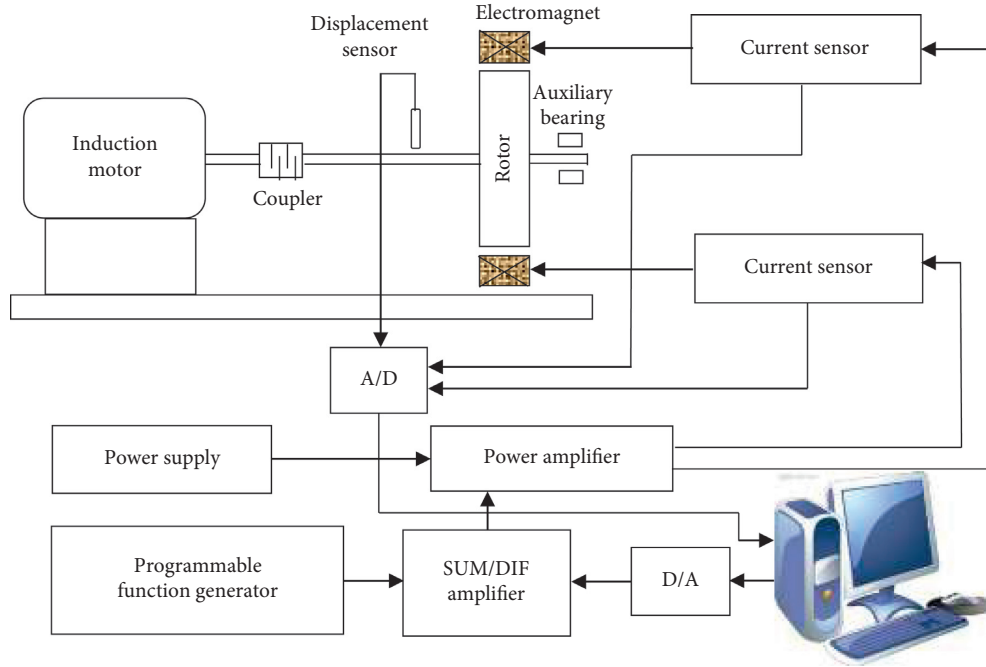
FIGURE 1: Schematic diagram of a magnetic bearing system.

with the limitations

$$-3.5\,\text{volts} < e_{c1} < 6.5\,\text{volts},$$
$$-3.5\,\text{volts} < e_{c2} < 6.5\,\text{volts}, \quad (3)$$
$$0.0\,\text{amp} < x_3 \text{ and } x_4 < 2.0\,\text{amp},$$

where x_1 is the displacement of the rotor around the equilibrium point; x_2 is the velocity of the rotor; x_3 and x_4 are coil currents oscillating around the bias current; e_{c1} and e_{c2} are the outputs of the PID controller to the two coils; $K_P = -55$, $K_D = -0.3$, and $K_I = -50$ are the control gains; K_A (=2.4) and K_H (=10000) represent the gains of the power amplifier and displacement sensor; and $A_0\sin\Omega t$ is the forcing voltage generated by a programmable function generator. The procedures used to derive the other coefficients necessary for (1a)–(1d) are listed in Table 1 [1].

This model captures the primary characteristics of the system by comparing the frequency responses from simulations with those from experiments [1]. However, this model has not been subjected to dynamic analysis to determine whether the nonlinear mathematical model derived from experiments can be used to characterize and/or predict the dynamics in a physical system. Furthermore, the chaotic motion that occurs at the moment the rotor strikes the electromagnet has not been characterized.

In this study, we employed bifurcation diagrams, phase portraits, Poincaré maps, frequency spectra, and Lyapunov exponents to observe periodic and chaotic motions. Across a broad range of parameters, the Lyapunov exponent provides the most powerful means by which to measure the sensitivity of a dynamic system as it pertains to its initial conditions. This approach can be used to determine whether a system is susceptible to chaotic motion. The algorithms used to

TABLE 1: Identified results [1].

System parameter	Identified value
d_1	3.066133
d_2	4.3315×10^3
d_3	-5.5786683
d_4	6.5562
d_5	1.43371×10^7
d_6	-2.531×10^4
d_7	-4.53203×10^4
d_8	0.34514
d_9	-0.40171
d_{10}	-2.399816×10^{10}
L	0.0161203
R	14.3128231

compute Lyapunov exponents associated with smooth dynamic systems are well-established [2–5]. However, a number of nonsmooth dynamic systems possess discontinuities to which this algorithm cannot be applied directly, such as those associated with dry friction, backlash, and saturation. Many studies have proposed methods for the calculation of Lyapunov exponents associated with nonsmooth dynamic systems [6–8]. In this study, we adopted the method developed by Stefanski [8] for estimating the largest Lyapunov exponent in a magnetic bearing system with closed-loop control.

Many practical engineering problems involving chaos require control techniques to convert chaotic attractors into stable periodic orbits. Since the pioneering work of Ott et al. [9], numerous methods for the control of chaos have been devised [10–19]. Improving the performance of a controlled magnetic bearing system and/or eliminating chatter behavior require the conversion of chaotic behavior into periodic motion. Two control methods have been developed

for chaos suppression: state feedback control [11–15] and dither control [16–19].

2. System Characteristics: Simulations and Discussion

We conducted a series of numerical simulations based on (1a)–(1d) to clearly elucidate the dynamic characteristics of the system in this study. In (1a)–(1d), the amplitude of the input excitation, A_0, equals 3.5 V. We employed FORTRAN subroutines in the commercial software package DIVPRK (IMSL) to solve ordinary differential equations [20]. The resulting bifurcation diagram is presented in Figure 2. This figure clearly shows that the first period-doubling bifurcation occurred at approximately $\Omega = 19.5$ Hz and chaotic motion appeared at approximately $\Omega = 18.5$ Hz. Further details of the responses exhibited by the system are presented in Figures 3–5, in which each type of response is characterized by a phase portrait, Poincaré map, and frequency spectrum. Figures 3(a)–3(c) show that the T_f-period includes the constant term and fundamental components. From Figure 4, we determined that a cascade of period-doubling bifurcations produced a series of subharmonic components, revealing the bifurcations with new frequency components at $\Omega/2$, $3\Omega/2$, $5\Omega/2$, ... The essence of chaotic behavior can be described using Poincaré maps, which present an infinite set of points referred to as a strange attractor. Chaotic motion also presents a broad continuous frequency spectrum. Thus, strange attractors and continuous-type Fourier spectra are generally regarded as strong indictors of chaos, as illustrated in Figures 5(a)–5(c).

3. Synchronization and the Lyapunov Exponent

The largest Lyapunov exponent is a useful diagnostic element for the analysis of chaotic systems. Every dynamic system possesses a spectrum of Lyapunov exponents (λ), which determine length, area, and volume changes in the phase space. In other words, Lyapunov exponents measure the rate of divergence (or convergence) between two adjacent orbits. Chaos can be identified simply by calculating the largest Lyapunov exponent, thereby determining whether nearby trajectories generally diverge ($\lambda > 0$) or converge ($\lambda < 0$). Any bounded motion in a system containing at least one positive Lyapunov exponent is defined as chaotic, whereas nonpositive Lyapunov exponents indicate periodic motion. There are a number of well-established algorithms that compute the Lyapunov spectrum of smooth dynamic systems [2–5]. However, nonsmooth dynamic systems with discontinuities, such as dry friction, backlash, and saturation, do not allow for the direct application of such algorithms. In this study, we estimated the largest Lyapunov exponent in order to identify the onset of chaotic motion in a controlled magnetic bearing system. Stefanski [8] proposed a simple method for estimating the largest Lyapunov exponent based on properties associated with synchronization. Synchronization controls the response system by accessing the output of the drive system such that the output of the
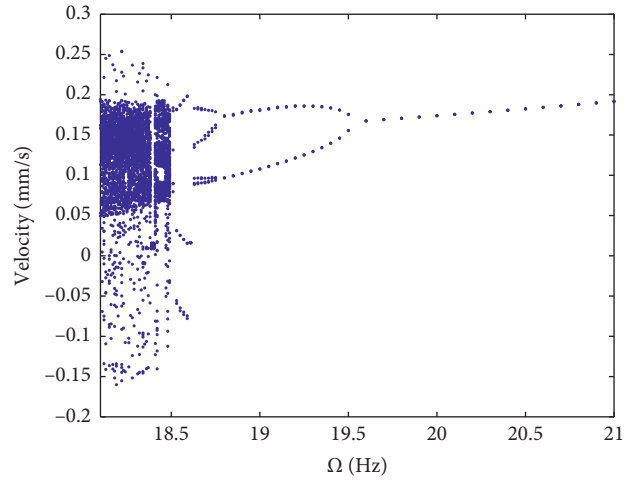
FIGURE 2: Bifurcation diagram of the system for $A_0 = 3.5$ V.

response system asymptotically follows the output of the drive system. This method is described briefly as follows.

The dynamic system is decomposed into the following two subsystems:

A drive system

$$\dot{x} = f(x). \tag{4}$$

A response system

$$\dot{y} = f(y). \tag{5}$$

Consider a dynamic system comprising two identical n-dimensional subsystems, where the response system (5) is combined with coupling coefficient d, and the drive system (4) remains the same. The first-order differential equations used to describe such a system are written as follows:

$$\dot{x} = f(x), \\ \dot{y} = f(y) + d(x - y). \tag{6}$$

The condition of synchronization is given by the following inequality:

$$d > \lambda_{\max}. \tag{7}$$

The smallest value of coupling coefficient d in synchronization d_s is assumed to be equal to the largest Lyapunov exponent, as follows:

$$d_s = \lambda_{\max}. \tag{8}$$

(6) provides an augmented system based on (1a)–(1d), as follows:

$$\dot{x}_1 = x_2, \tag{9a}$$

$$\dot{x}_2 = -d_1 x_2 - d_2 x_1 + d_3 x_3 + d_4 x_4 + d_5 x_1^2 + d_6 x_1 x_3 \\ + d_7 x_1 x_4 + d_8 x_3^2 + d_9 x_4^2 + d_{10} x_1^3, \tag{9b}$$

(a)

(b)

(c)
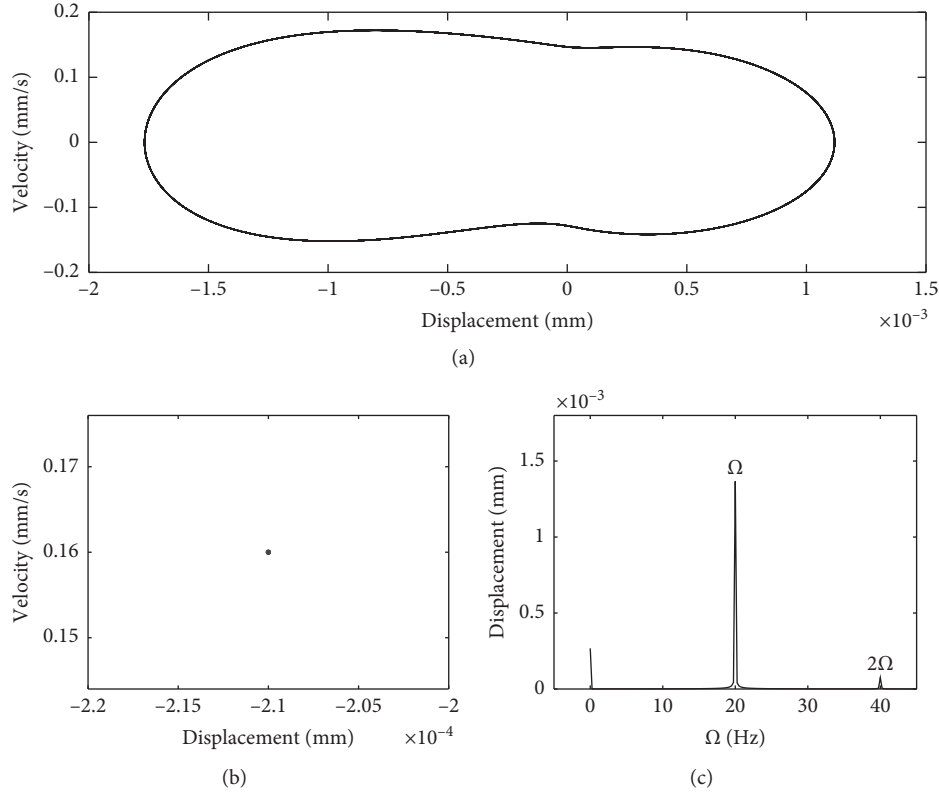
FIGURE 3: Period-one orbit for $\Omega = 20.0$ Hz: (a) phase portrait; (b) Poincaré map; (c) frequency spectrum.

$$L\dot{x}_3 + Rx_3 = K_A\left(e_{c1x} + A_0 \sin \Omega t\right), \qquad (9c)$$

$$L\dot{x}_4 + Rx_4 = K_A\left(e_{c2x} + A_0 \sin \Omega t\right), \qquad (9d)$$

$$\dot{y}_1 = y_2 + d\left(x_1 - y_1\right), \qquad (10a)$$

$$\dot{y}_2 = -d_1 y_2 - d_2 y_1 + d_3 y_3 + d_4 y_4 + d_5 y_1^2 + d_6 y_1 y_3$$
$$+ d_7 y_1 y_4 + d_8 y_3^2 + d_9 y_4^2 + d_{10} y_1^3 + d\left(x_2 - y_2\right), \qquad (10b)$$

$$L\dot{y}_3 + Ry_3 = K_A\left(e_{c1y} + A_0 \sin \Omega t\right) + d\left(x_3 - y_3\right), \qquad (10c)$$

$$L\dot{y}_4 + Ry_4 = K_A\left(e_{c2y} + A_0 \sin \Omega t\right) + d\left(x_4 - y_4\right), \qquad (10d)$$

where

$$e_{c1x} = K_H\left(K_P x_1 + K_D x_2 + K_I \int x_1 dt\right),$$

$$e_{c2x} = K_H\left(-K_P x_1 - K_D x_2 - K_I \int x_1 dt\right),$$

$$e_{c1y} = K_H\left(K_P y_1 + K_D y_2 + K_I \int y_1 dt\right),$$

$$e_{c2y} = K_H\left(-K_P y_1 - K_D y_2 - K_I \int y_1 dt\right), \qquad (11)$$

with the following limitations:

$$-3.5 \text{ volts} < e_{c1x} < 6.5 \text{ volts},$$

$$-3.5 \text{ volts} < e_{c2x} < 6.5 \text{ volts},$$

$$0.0 \text{ amp} < x_3 \text{ and } x_4 < 2.0 \text{ amp},$$

$$-3.5 \text{ volts} < e_{c1y} < 6.5 \text{ volts}, \qquad (12)$$

$$-3.5 \text{ volts} < e_{c2y} < 6.5 \text{ volts},$$

$$0.0 \text{ amp} < y_3 \text{ and } y_4 < 2.0 \text{ amp}.$$

In the next step, we estimate the largest Lyapunov exponent for the selected parametric values in accordance with the method described above. Figure 6 presents the results of numerical calculations showing the estimated largest Lyapunov exponents obtained using the above synchronization method. All of the largest Lyapunov exponents are positive with regard to the forcing frequency ($\Omega < 18.5$ Hz), indicating that the system exhibits chaotic motion. These results help to enhance our understanding of chatter vibration in a controlled magnetic bearing system.

4. Quenching Chatter

Chaotic motion can induce chatter vibrations capable of destroying a magnetic bearing system. Accurate prediction of the behavior of a chaotic system can be beneficial;
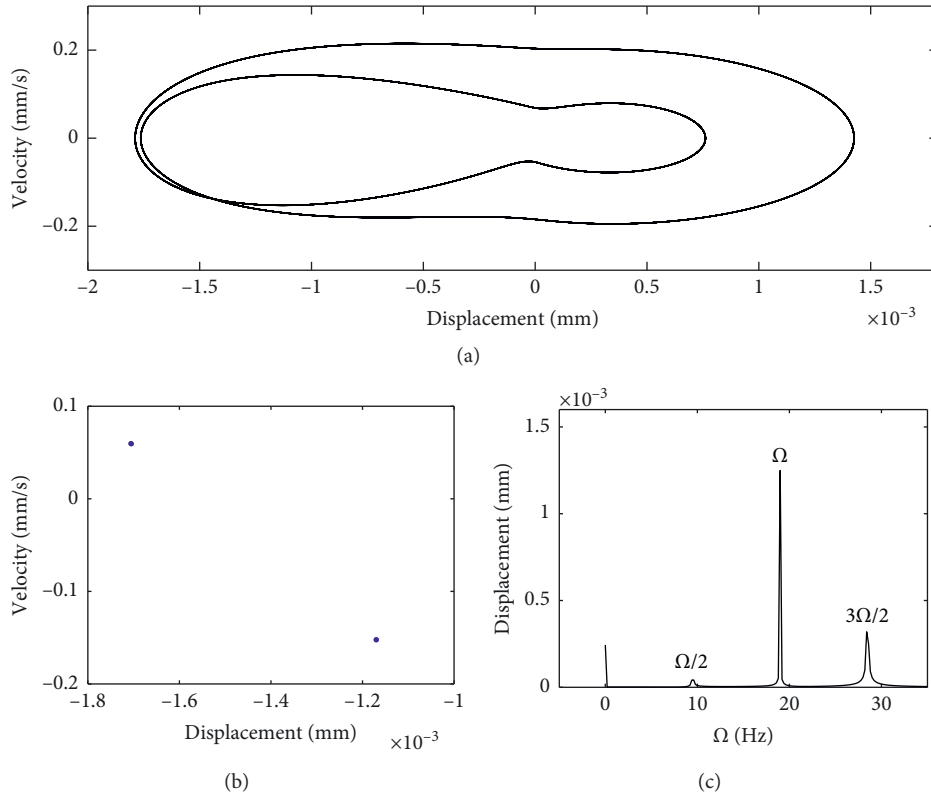
FIGURE 4: Period-two orbit for $\Omega = 19.0$ Hz: (a) phase portrait; (b) Poincaré map; (c) frequency spectrum.

however, maximizing the benefits requires the ability to control this behavior. A chaotic system must be transformed into periodic motion in order to work under specific conditions and thereby improve the performance of a dynamic system and/or avoid chatter. In this section, we discuss the means by which chaos can be converted into periodic motion using minimal efforts. We present two methods of controlling chaos: the addition of state feedback control [12, 13] and the application of dither signals [16, 17].

4.1. State Feedback Control.
Cai et al. [12, 13] proposed a simple, yet effective, state feedback control algorithm. This method for the n-dimensional dynamical system is explained briefly as follows:

$$\dot{\mathbf{x}} = \mathbf{f}(\mathbf{x}, t), \tag{13}$$

where $\mathbf{x}(t) \in R^n$ is the state vector and $\mathbf{f} = (f_1, \ldots, f_i, \ldots, f_n)$, where f_i is a linear or a nonlinear function and $\mathbf{f}$ includes at least one nonlinear function. Suppose that $f_k(x, t)$ is the key nonlinear function leading to chaotic motion in system (13). We add to the equation only one term of state feedback of an available system variable x_m that includes $f_k(x, t)$, as follows:

$$\dot{x}_k = f_k(\mathbf{x}, t) + G x_m, \quad k, m \in \{1, 2, \ldots, n\}, \tag{14}$$

where G is feedback gain. Other functions retain their original forms. We applied this method to (1a)–(1d) to more clearly elucidate the simple control scheme.

In the absence of state feedback control, (1a)–(1d) exhibits chaotic behavior under the following parameters: $A_0 = 3.5$ V and $\Omega = 18.2$ Hz. Consider how the addition of state feedback control to the right-hand side of the (1a)–(1d) would affect the results. Figure 7 presents the resulting bifurcation diagram for $\Omega = 18.2$ Hz with state feedback control. When $G = 0$, (1a)–(1d) displays chaotic motion (see Figure 5). This figure shows that chaotic motion occurs at approximately $G > -7.0$ and disappears at approximately $G \leq -7.0$. When the feedback gain G falls below -7.0, the system described by (1a)–(1d) exhibits stable periodic motion. After 10 seconds, the control signal is applied to the system to control chaotic oscillation (Figure 8). In so doing, the state feedback control can be used to suppress chaotic motion and improve the performance of a magnetic bearing system with closed-loop control.

4.2. Dither Control.
In this section, we describe how chaotic motion can be controlled by injecting an external dither signal to adjust nonlinear terms. A dither is a high-frequency signal introduced to modify the behaviors of nonlinear systems through the elimination of nonlinearities. The ability of a dither signal to average out nonlinearities can be attributed to its high frequency and periodic nature. Dither smoothing techniques were proposed in references [16, 17] to stabilize chaotic systems. Some of the most common dither signals were proposed by Cook [21].

(i) Square-wave dither: the simplest type of dither signal is the square-wave signal as shown in Figure 9, where

(a)

(b)

(c)
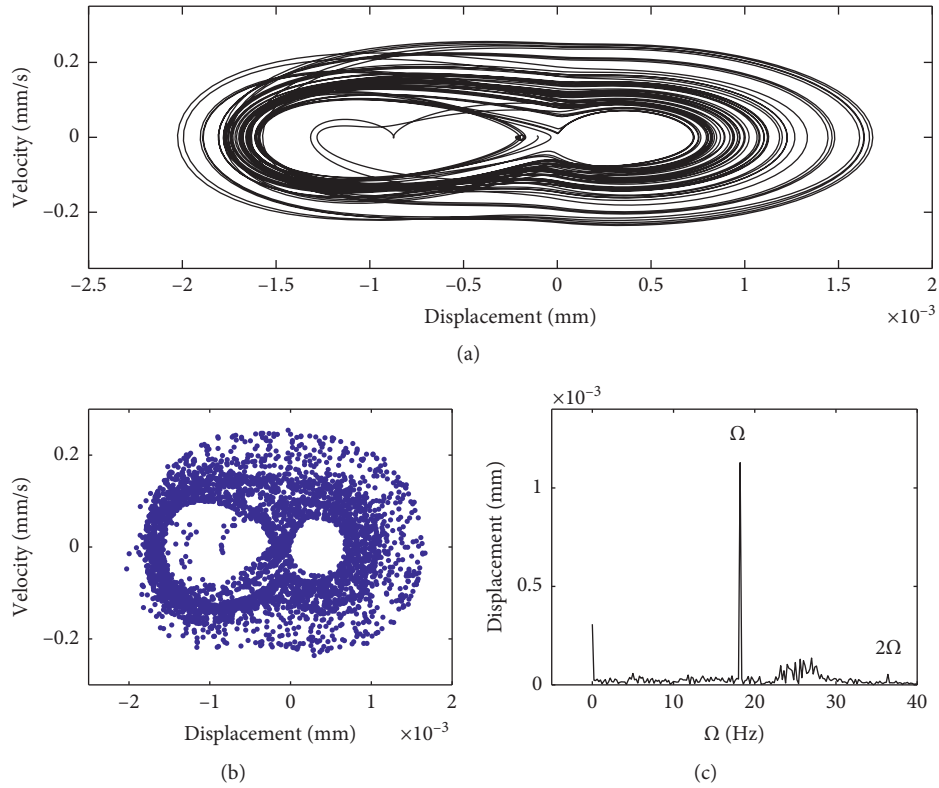
FIGURE 5: Chaotic motion for $\Omega = 18.2$ Hz: (a) phase portrait; (b) Poincaré map; (c) frequency spectrum.
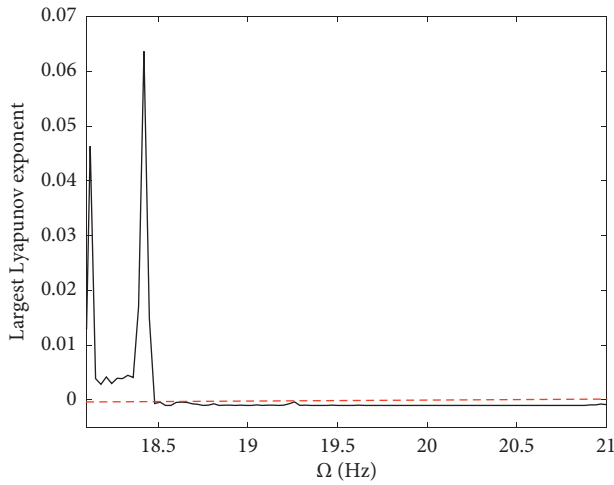
FIGURE 6: Evolutions of the largest Lyapunov exponent.

FIGURE 7: Bifurcation diagram of system with state feedback control, where G denotes the feedback gain.

dither signal takes the constant values W and $-W$ alternately, each holding for a half-period $T/2$, with T being much smaller than the time constant of the system. The amplitude W is applied in front of the nonlinearity $f(\cdot)$. Thus, the effective value of $\bar{n}$ (the output of the nonlinear element) can be written as [16]

$$\bar{n} = \frac{1}{2}\left[f(y + W) + f(y - W)\right]. \tag{15}$$

Thus, the system equations can be written as follows:

$$\dot{y} = \bar{n}. \tag{16}$$

Consider the effect of adding square-wave dither control to the system described in (1a)–(1d), where $\Omega = 18.2$ Hz. Increasing the amplitude of the square-wave dither signal from $W = 0$ to 0.0005 V would
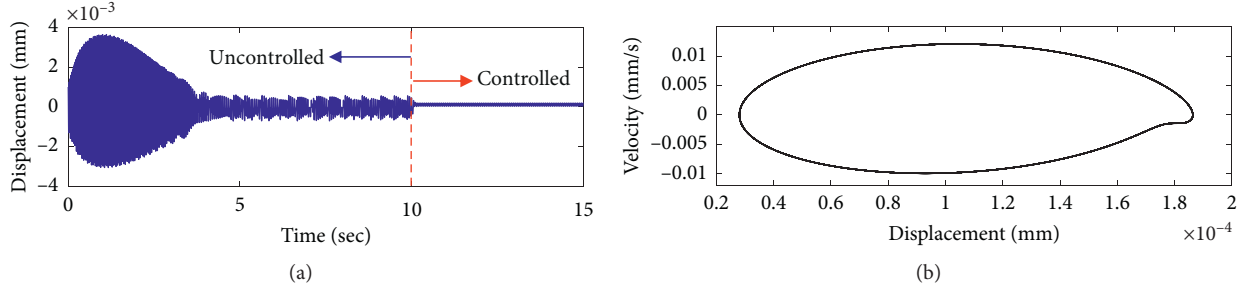
FIGURE 8: Transforming chaotic motion to a desired period-one orbit at $G = -50$ and $\Omega = 18.2$ Hz where the state feedback control signal is introduced after 10 s: (a) time responses; (b) phase portrait of the controlled system.
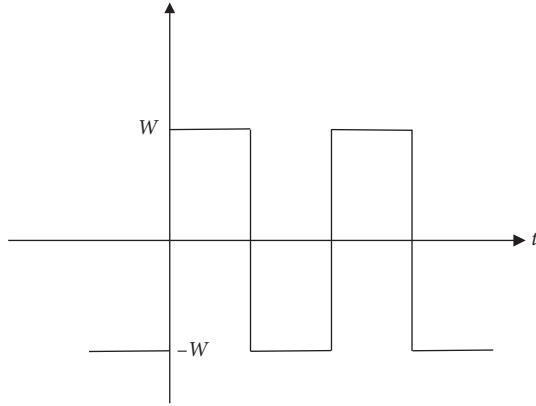
FIGURE 9: A square-wave dither signal.

change the chaotic behavior to period-one motion. The resulting bifurcation diagram under $\Omega = 18.2$ Hz with a square-wave dither signal is shown in Figure 10. Figure 11 shows the effects 10 seconds after applying a control signal to the system in order to illustrate the effectiveness of this controller in controlling chaotic oscillations.

(ii) Sinusoidal dither: one simple dither signal is a high-frequency sinusoid. Here, the effective value of n is its average over a complete period of the sinusoidal dither signal oscillation:

$$n = \frac{1}{2\pi} \int_0^{2\pi} f(x + W \sin \theta) d\theta. \tag{17}$$

Adding a sinusoidal dither signal to (1a)–(1d) yields the following coupled system:

$$\dot{\tilde{x}}_1 = \tilde{x}_2, \tag{18a}$$

$$\dot{\tilde{x}}_2 = -d_1 \tilde{x}_2 - d_2 \tilde{x}_1 + d_3 \tilde{x}_3 + d_4 \tilde{x}_4 + n, \tag{18b}$$

$$L\dot{\tilde{x}}_3 + R\tilde{x}_3 = K_A \left(\tilde{e}_{c1} + A_0 \sin \Omega t \right), \tag{18c}$$

$$L\dot{\tilde{x}}_4 + R\tilde{x}_4 = K_A \left(\tilde{e}_{c2} + A_0 \sin \Omega t \right), \tag{18d}$$

where
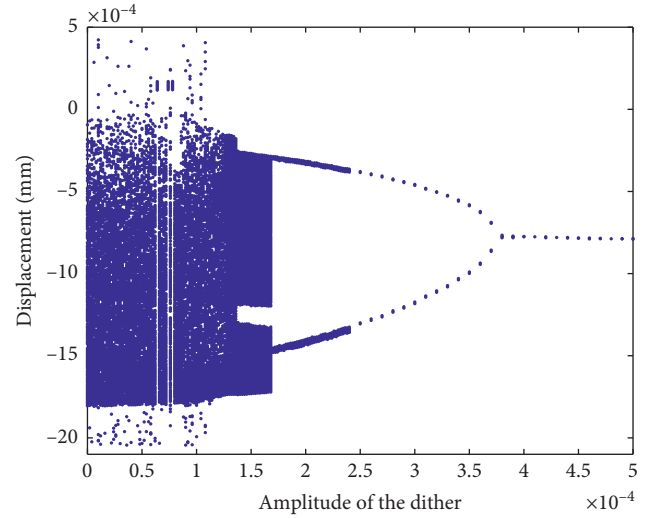
FIGURE 10: Bifurcation diagram of the system with a square-wave dither, where W denotes the amplitude of the dither signal.

$$\tilde{e}_{c1} = K_H \left(K_P \tilde{x}_1 + K_D \tilde{x}_2 + K_I \int \tilde{x}_1 dt \right),$$

$$\tilde{e}_{c2} = K_H \left(-K_P \tilde{x}_1 - K_D \tilde{x}_2 - K_I \int \tilde{x}_1 dt \right),$$

$$n = \frac{1}{2\pi} \int_0^{2\pi} \left[d_5 \left(\tilde{x}_1 + W \sin \theta \right)^2 + d_6 \left(\tilde{x}_1 + W \sin \theta \right) \right.$$

$$\cdot \left(\tilde{x}_3 + W \sin \theta \right) + d_7 \left(\tilde{x}_1 + W \sin \theta \right) \left(\tilde{x}_4 + W \sin \theta \right)$$

$$\left. + d_8 \left(\tilde{x}_3 + W \sin \theta \right)^2 + d_9 \left(\tilde{x}_4 + W \sin \theta \right)^2 + d_{10} \left(\tilde{x}_1 + W \sin \theta \right)^3 \right],$$

$$\tag{19}$$

with the following limitations:

$$-3.5 \text{ volts} < \tilde{e}_{c1} < 6.5 \text{ volts},$$

$$-3.5 \text{ volts} < \tilde{e}_{c2} < 6.5 \text{ volts}, \tag{20}$$

$$0.0 \text{ amp} < \tilde{x}_3 \text{ and } \tilde{x}_4 < 2.0 \text{ amp}.$$

The dither frequency must substantially exceed that of any other frequency used to operate the system in order to ensure that the dither signal does not introduce other undesirable oscillations at the same frequency as the dither signal. For example, Figure 12 presents the resulting

(a)

(b)
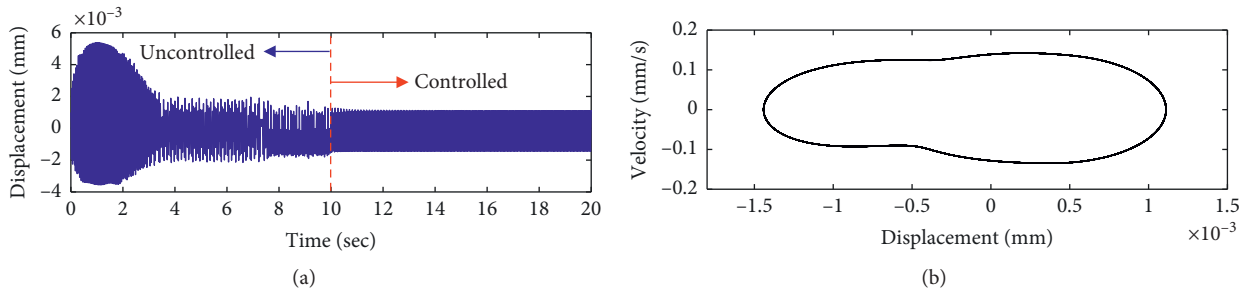
FIGURE 11: Injecting a square-wave dither signal control which is used to control chaotic motion of the system for $A_0 = 3.5$ V at $\Omega = 18.2$ Hz. The dither signal ($W = 0.0004$) is added after 10 seconds: (a) displacement time series; (b) controlled orbit.
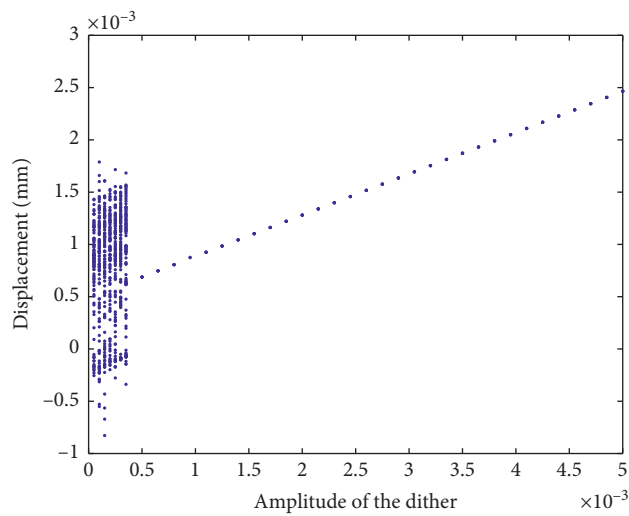
FIGURE 12: Bifurcation diagram of system with a sinusoidal dither, where W is the amplitude of the dither.

--- Original nonlinearity
— Equivalent nonlinearity
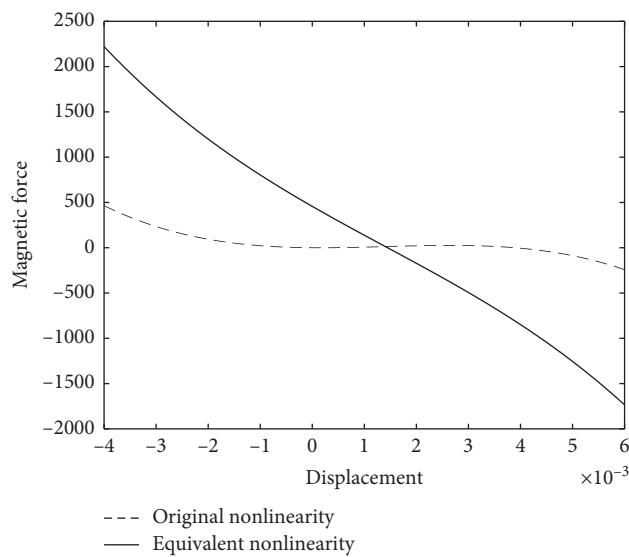
FIGURE 13: Equivalent nonlinearity n (solid line) described by equation (17). Original nonlinearity f (dashed line) is given in equation (1b).

(a)

(b)
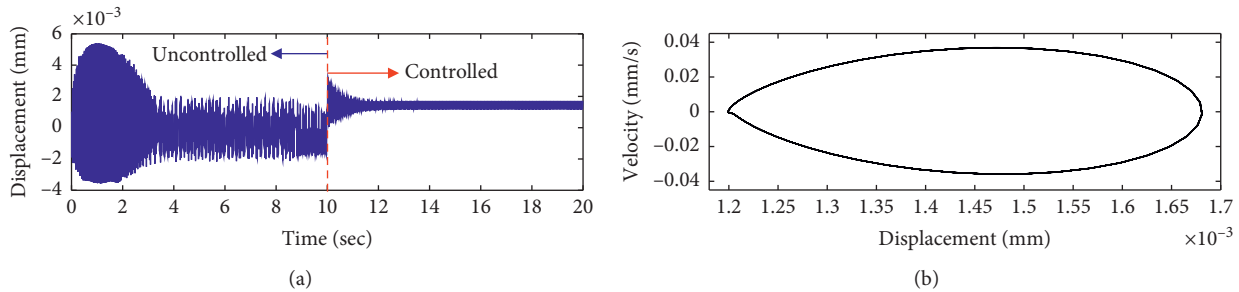
FIGURE 14: Controlling chaotic motion to desired period-one orbit for $W = 0.003$ V and $\Omega = 18.2$ Hz: (a) time responses of displacement. The sinusoidal dither signal is injected after 1 s. (b) phase portrait of controlled system.

bifurcation diagram for a system with a sinusoidal dither in which parameter Ω is 18.2 Hz and the frequency of the sinusoidal dither is 6000 rad/s. This reveals that a sinusoidal dither with amplitude exceeding 0.0005 V can convert chaotic behavior into stable periodic motion in a magnetic bearing system. The next steps are setting $W = 0.008$ V and plotting the effective nonlinearity n and original nonlinearity f, as shown in Figure 13. The time response of displacement 10 seconds after the injection of a sinusoidal dither signal is shown in Figure 14(a). The chaotic behavior is converted into period-one motion. Figure 14(b) presents a phase portrait of the controlled system. Note that the behavior of the system is initially chaotic, but gradually becomes periodic following dither injection.

5. Conclusions

This work uses the identified nonlinear model examine global bifurcation and chaos control in the magnetic bearing system. Dynamic behavior over the entire range of parameter values is observable in the resulting bifurcation diagram, which reveals that the magnetic bearing system exhibits period-doubling bifurcations and chaotic motions. The largest Lyapunov exponent derived using the properties of synchronization provided the most powerful tool to measure and analyze chaotic motion in such a system. Controlling chaotic motion is an effective way to prevent chatter vibration in magnetic bearing systems. State feedback control is a simple, yet effective, approach to suppressing chaos. It can be implemented by adding feedback associated with a suitable variable into the original system with control gain sufficient to overcome the development of chaos in dynamic systems prone to chaotic behavior. It is also possible to convert chaotic behavior into a periodic orbit through the injection of a dither signal in front of nonlinearities in a chaotic magnetic bearing system.

Our analysis revealed that the proposed nonlinear model is able to predict the occurrence of bifurcation and chaos in an active magnetic bearing system, which means that it is potentially applicable to a wide range of functions in the design of active magnetic bearing systems. Chaotic behavior must be accepted in some situations; however, it is normally deemed undesirable, as it degrades performance and restricts the operating range of electric and mechanical devices. Accordingly, we applied state feedback and dither control methods to quench chaos, improve the performance of the magnetic bearing system, and prevent the occurrence of chaos behaviors. Furthering the development of magnetically levitated vehicles requires an understanding of their nonlinear dynamic characteristics from the viewpoint of stability, safety, and ride quality at high speeds. Our contribution of this study is that studying nonlinear dynamics and controlling chaotic vibrations in the active magnetic bearing systems will help to advance the development of magnetic transportation systems.

Data Availability

No data were used to support this study. We only used computer for simulation. Therefore, we can only provide simulation programming, which can be obtained from the corresponding author upon request.

Conflicts of Interest

The author declares that there are no conflicts of interest regarding the publication of this paper.

Acknowledgments

References

[1] S. C. Chang and P. C. Tung, "Nonlinear identification of a magnetic bearing system with closed loop control," *JSME International Journal Series C Mechanical Systems, Machine Elements and Manufacturing*, vol. 42, no. 4, pp. 982–990, 1999.

[2] I. Shimada and T. Nagashima, "A numerical approach to ergodic problem of dissipative dynamical systems," *Progress of Theoretical Physics*, vol. 61, no. 6, pp. 1605–1616, 1979.

[3] A. Wolf, J. B. Swift, H. L. Swinney, and J. A. Vastano, "Determining Lyapunov exponents from a time series," *Physica D: Nonlinear Phenomena*, vol. 16, no. 3, pp. 285–317, 1985.

[4] G. Benettin, L. Galgani, A. Giorgilli, and J. M. Strelcyn, "Lyapunov characteristic exponents for smooth dynamical systems and for Hamiltonian systems; a method for computing all of them. Part 1: theory," *Meccanica*, vol. 15, no. 1, pp. 9–20, 1980.

[5] G. Benettin, L. Galgani, A. Giorgilli, and J. M. Strelcyn, "Lyapunov characteristic exponents for smooth dynamical systems and for Hamiltonian systems; a method for computing all of them. Part 2: numerical application," *Meccanica*, vol. 15, no. 1, pp. 21–30, 1980.

[6] P. C. Müller, "Calculation of Lyapunov exponents for dynamical systems with discontinuities," *Chaos, Solitons & Fractals*, vol. 5, no. 9, pp. 1671–1681, 1995.

[7] N. Hinrichs, M. Oestreich, and K. Popp, "Dynamics of oscillators with impact and friction," *Chaos, Solitons & Fractals*, vol. 8, no. 4, pp. 535–558, 1997.

[8] A. Stefanski, "Estimation of the largest Lyapunov exponent in systems with impacts," *Chaos, Solitons & Fractals*, vol. 11, no. 15, pp. 2443–2451, 2000.

[9] E. Ott, C. Grebogi, and J. A. Yorke, "Controlling chaos," *Physical Review Letters*, vol. 64, no. 11, pp. 1196–1199, 1990.

[10] Z. Shen and J. Li, "Chaos control for a unified chaotic system using output feedback controllers," *Mathematics and Computers in Simulation*, vol. 132, pp. 208–219, 2017.

[11] S. M. A. Pahnehkolaei, A. Alfi, and J. A. Tenreiro Machado, "Chaos suppression in fractional systems using adaptive fractional state feedback control," *Chaos, Solitons & Fractals*, vol. 103, pp. 488–503, 2017.

[12] C. Cai, Z. Xu, W. Xu, and B. Feng, "Notch filter feedback control in a class of chaotic systems," *Automatica*, vol. 38, no. 4, pp. 695–701, 2002.

[13] C. Cai, Z. Xu, and W. Xu, "Converting chaos into periodic motion by state feedback control," *Automatica*, vol. 38, no. 11, pp. 1927–1933, 2002.

[14] W. S. Wu, Z. S. Zhao, J. Zhang, and L. K. Sun, "State feedback synchronization control of coronary artery chaos system with interval time-varying delay," *Nonlinear Dynamics*, vol. 87, no. 3, pp. 1773–1783, 2017.

[15] M. Z. Ullah, F. Mallawi, D. Baleanu, and A. S. Alshomrani, "A new fractional study on the chaotic vibration and state-feedback control of a nonlinear suspension system," *Chaos, Solitons & Fractals*, vol. 132, Article ID 109530, 2020.

[16] C. C. Fun and P. C. Tung, "Experimental and analytical study of dither signals in a class of chaotic system," *Physics Letters A*, vol. 229, no. 4, pp. 228–234, 1997.

[17] Y. M. Liaw and P. C. Tung, "Application of the differential geometric method to control a noisy chaotic system via dither smoothing," *Physics Letters A*, vol. 239, no. 1-2, pp. 51–58, 1998.

[18] Q. Wei and X. Y. Wang, "Chaos controlling of permanent magnet synchronous motor base on dither signal," *Journal of Vibration and Control*, vol. 19, no. 16, pp. 2541–2550, 2013.

[19] S. C. Chen and E. T. Mbitu, "Quench limit cycle using different dither signal in a servo motor system," in *Proceedings of the International Conference on Advanced Materials for Science and Engineering (ICAMSE)*, pp. 501–504, Tainan, Taiwan, November 2016.

[20] IMSL, Inc, *User's Manual–IMSL MATH/LIBRARY*, IMSL, Inc., Louisville, CO, USA, 1989.

[21] P. A. Cook, *Nonlinear Dynamical Systems*, Prentice-Hall, London, UK, 1994.

Research Article

On a System of *k*-Difference Equations of Order Three

Ibrahim Yalçınkaya,[1] Hijaz Ahmad [ID],[2] Durhasan Turgut Tollu [ID],[1] and Yong-Min Li [ID][3]

[1]*Necmettin Erbakan University, Faculty of Science, Department of Mathematics and Computer Sciences, Konya, Turkey*
[2]*Department of Basic Sciences, University of Engineering and Technology, Peshawar, Pakistan*
[3]*Department of Mathematics, Huzhou University, Huzhou 313000, China*

Correspondence should be addressed to Yong-Min Li; ymlwww@163.com

In this paper, we deal with the global behavior of the positive solutions of the system of k-difference equations $u_{n+1}^{(1)} = (\alpha_1 u_{n-1}^{(1)}/\beta_1 + \alpha_1 (u_{n-2}^{(2)})^{r_1})$, $u_{n+1}^{(2)} = \alpha_2 u_{n-1}^{(2)}/\beta_2 + \alpha_2 (u_{n-2}^{(3)})^{r_2}, \ldots, u_{n+1}^{(k)} = \alpha_k u_{n-1}^{(k)}/\beta_k + \alpha_k (u_{n-2}^{(1)})^{r_k}, n \in \mathbb{N}_0$, where the initial conditions $u_{-l}^{(i)}$ $(l = 0, 1, 2)$ are nonnegative real numbers and the parameters $\alpha_i, \beta_i, \gamma_i$, and r_i are positive real numbers for $i = 1, 2, \ldots, k$, by extending some results in the literature. By the end of the paper, we give three numerical examples to support our theoretical results related to the system with some restrictions on the parameters.

1. Introduction

Recently, many works have been published on rational difference equations, which have an important position in applied sciences. In this process, many rational difference equations have been studied by mathematicians. And so, some equations have frequently been the subject of many articles using generalizations. Many typical examples of these can be found in the literature. For example, in [1], El-Owaidy et al. dealt with global behavior of the difference equation

$$ x_{n+1} = \frac{\alpha x_{n-1}}{\beta + \gamma x_{n-2}^p}, \quad n \in \mathbb{N}_0, \tag{1} $$

with nonnegative parameters and initial conditions. Gumus and Soykan [2] dealt with the dynamical behavior of the positive solutions for a system of rational difference equations of the following form:

$$ u_{n+1} = \frac{\alpha u_{n-1}}{\beta + \gamma v_{n-2}^p}, $$
$$ -4pt $$
$$ v_{n+1} = \frac{\alpha_1 v_{n-1}}{\beta_1 + \gamma_1 u_{n-2}^p}, \quad n \in \mathbb{N}_0, \tag{2} $$

where the parameters and initial conditions are positive real numbers. Tollu and Yalcinkaya [3] dealt with the dynamical behavior of the positive solutions for the following three-dimensional system of rational difference equations:

$$ u_{n+1} = \frac{\alpha_1 u_{n-1}}{\beta_1 + \gamma_1 v_{n-2}^p}, $$

$$ v_{n+1} = \frac{\alpha_2 v_{n-1}}{\beta_2 + \gamma_2 w_{n-2}^q}, \tag{3} $$

$$ w_{n+1} = \frac{\alpha_3 w_{n-1}}{\beta_3 + \gamma_3 u_{n-2}^r}, \quad n \in \mathbb{N}_0, $$

where the parameters and initial conditions are positive real numbers. For more papers on this topic, see, for example, [4–29].

In the present paper, we investigate the global behavior of the positive solutions of the k-dimensional system of difference equations:

$$u_{n+1}^{(1)} = \frac{\alpha_1 u_{n-1}^{(1)}}{\beta_1 + \gamma_1\left(u_{n-2}^{(2)}\right)^{r_1}}, u_{n+1}^{(2)} = \frac{\alpha_2 u_{n-1}^{(2)}}{\beta_2 + \gamma_2\left(u_{n-2}^{(3)}\right)^{r_2}}, \ldots, u_{n+1}^{(k)}$$

$$= \frac{\alpha_k u_{n-1}^{(k)}}{\beta_k + \gamma_k\left(u_{n-2}^{(1)}\right)^{r_k}}, \quad n \in \mathbb{N}_0,$$

$$(4)$$

where the initial conditions $u_{-l}^{(i)}$ ($l = 0, 1, 2$) are nonnegative real numbers and the parameters $\alpha_i, \beta_i, \gamma_i$, and r_i are positive real numbers for $i = 1, 2, \ldots, k$, by extending some recent results in the literature.

Remark 1. This paper extends the results of studies in the references [1–3]. That is to say, if we take $k = 1$, then system (4) reduces equation (1). If we take $k = 2$, then system (4) reduces system (2). Finally, if we take $k = 3$, then system (4) reduces system (3). So, system (4) is a natural generalization of equation (1), system (2), and system (3).

Note that system (4) can be written as

$$\begin{cases} u_{n+1}^{(1)} = f_1\left(u_n^{(1)}, u_{n-1}^{(1)}, u_{n-2}^{(1)}, u_n^{(2)}, u_{n-1}^{(2)}, u_{n-2}^{(2)}, \ldots, u_n^{(k)}, u_{n-1}^{(k)}, u_{n-2}^{(k)}\right), \\ u_{n+1}^{(2)} = f_2\left(u_n^{(1)}, u_{n-1}^{(1)}, u_{n-2}^{(1)}, u_n^{(2)}, u_{n-1}^{(2)}, u_{n-2}^{(2)}, \ldots, u_n^{(k)}, u_{n-1}^{(k)}, u_{n-2}^{(k)}\right), \\ \vdots \\ u_{n+1}^{(k)} = f_k\left(u_n^{(1)}, u_{n-1}^{(1)}, u_{n-2}^{(1)}, u_n^{(2)}, u_{n-1}^{(2)}, u_{n-2}^{(2)}, \ldots, u_n^{(k)}, u_{n-1}^{(k)}, u_{n-2}^{(k)}\right), \end{cases} \quad n \in \mathbb{N}_0, \qquad (6)$$

has the unique solution $\{(u_n^{(1)}, u_n^{(2)}, \ldots, u_n^{(k)})\}_{n=-2}^{\infty}$. Also, an equilibrium point of system (6) is a point $(\overline{u}^{(1)}, \overline{u}^{(2)}, \ldots, \overline{u}^{(k)})$ that satisfies the following system:

$$\overline{u}^{(1)} = f_1\left(\overline{u}^{(1)}, \overline{u}^{(1)}, \overline{u}^{(1)}, \overline{u}^{(2)}, \overline{u}^{(2)}, \overline{u}^{(2)}, \ldots, \overline{u}^{(k)}, \overline{u}^{(k)}, \overline{u}^{(k)}\right),$$

$$\overline{u}^{(2)} = f_2\left(\overline{u}^{(1)}, \overline{u}^{(1)}, \overline{u}^{(1)}, \overline{u}^{(2)}, \overline{u}^{(2)}, \overline{u}^{(2)}, \ldots, \overline{u}^{(k)}, \overline{u}^{(k)}, \overline{u}^{(k)}\right),$$

$$\vdots$$

$$\overline{u}^{(k)} = f_k\left(\overline{u}^{(1)}, \overline{u}^{(1)}, \overline{u}^{(1)}, \overline{u}^{(2)}, \overline{u}^{(2)}, \overline{u}^{(2)}, \ldots, \overline{u}^{(k)}, \overline{u}^{(k)}, \overline{u}^{(k)}\right).$$

$$(7)$$

$$x_{n+1}^{(1)} = \frac{a_1 x_{n-1}^{(1)}}{1 + \left(x_{n-2}^{(2)}\right)^{r_1}}, x_{n+1}^{(2)} = \frac{a_2 x_{n-1}^{(2)}}{1 + \left(x_{n-2}^{(3)}\right)^{r_2}}, \ldots, x_{n+1}^{(k)}$$

$$(5)$$

$$= \frac{a_k x_{n-1}^{(k)}}{1 + \left(x_{n-2}^{(1)}\right)^{r_k}}, \quad n \in \mathbb{N}_0,$$

by the change of variables $u_n^{(1)} = (\beta_k/\gamma_k)^{1/r_k} x_n^{(1)}$, $u_n^{(2)} = (\beta_1/\gamma_1)^{(1/r_1)} x_n^{(2)}, \ldots, u_n^{(k)} = (\beta_{k-1}/\gamma_{k-1})^{(1/r_{k-1})} x_n^{(k)}$ with $a_i = (\alpha_i/\beta_i)$ for $i = 1, 2, \ldots k$. So, we will consider system (5) instead of system (4) from now.

2. Preliminaries

Let $I_1, I_2, \ldots, I_k$ be some intervals of real numbers and $f_1: I_1^3 \times I_2^3 \times \cdots \times I_k^3 \longrightarrow I_1$, $f_2: I_1^3 \times I_2^3 \times \cdots \times I_k^3 \longrightarrow I_2$, $\ldots, f_k: I_1^3 \times I_2^3 \times \cdots \times I_k^3 \longrightarrow I_k$ be continuously differentiable functions. Then, for initial conditions $(u_0^{(1)}, u_{-1}^{(1)}, u_{-2}^{(1)}, u_0^{(2)}, u_{-1}^{(2)}, u_{-2}^{(2)}, \ldots, u_0^{(k)}, u_{-1}^{(k)}, u_{-2}^{(k)}) \in I_1^3 \times I_2^3 \times \cdots \times I_k^3$, the system of difference equations,

We rewrite system (6) in the vector form

$$U_{n+1} = F(U_n), \quad n \in \mathbb{N}_0, \qquad (8)$$

where $U_n = (u_n^{(1)}, u_{n-1}^{(1)}, u_{n-2}^{(1)}, u_n^{(2)}, u_{n-1}^{(2)}, u_{n-2}^{(2)}, \ldots, u_n^{(k)}, u_{n-1}^{(k)}, u_{n-2}^{(k)})^T$, F is a vector map such that $F: I_1^3 \times I_2^3 \times \cdots \times I_k^3 \longrightarrow I_1^3 \times I_2^3 \times \cdots \times I_k^3$, and

$$F\left(\begin{pmatrix} v_0^{(1)} \\ v_1^{(1)} \\ v_2^{(1)} \\ v_0^{(2)} \\ v_1^{(2)} \\ v_2^{(2)} \\ \vdots \\ v_0^{(k)} \\ v_1^{(k)} \\ v_2^{(k)} \end{pmatrix}\right) = \begin{pmatrix} f_1\left(v_0^{(1)}, v_1^{(1)}, v_2^{(1)}, v_0^{(2)}, v_1^{(2)}, v_2^{(2)}, \ldots, v_0^{(k)}, v_1^{(k)}, v_2^{(k)}\right) \\ v_0^{(1)} \\ v_1^{(1)} \\ f_2\left(v_0^{(1)}, v_1^{(1)}, v_2^{(1)}, v_0^{(2)}, v_1^{(2)}, v_2^{(2)}, \ldots, v_0^{(k)}, v_1^{(k)}, v_2^{(k)}\right) \\ v_0^{(2)} \\ v_1^{(2)} \\ \vdots \\ f_k\left(v_0^{(1)}, v_1^{(1)}, v_2^{(1)}, v_0^{(2)}, v_1^{(2)}, v_2^{(2)}, \ldots, v_0^{(k)}, v_1^{(k)}, v_2^{(k)}\right) \\ v_0^{(k)} \\ v_1^{(k)} \end{pmatrix}. \qquad (9)$$

It is clear that if an equilibrium point of system (6) is $(\overline{u}^{(1)}, \overline{u}^{(2)}, \ldots, \overline{u}^{(k)})$, then the corresponding equilibrium point of system (8) is the point $\overline{U} = (\overline{u}^{(1)}, \overline{u}^{(1)}, \overline{u}^{(1)}, \overline{u}^{(2)}, \overline{u}^{(2)}, \overline{u}^{(2)}, \ldots, \overline{u}^{(k)}, \overline{u}^{(k)}, \overline{u}^{(k)})^T$.

In this study, we denote by $\| \cdot \|$ any convenient vector norm and the corresponding matrix norm. Also, we denote by $U_0 \in I_1^3 \times I_2^3 \times \cdots \times I_k^3$ a initial condition of system (8).

Definition 1. Let $\overline{U}$ be an equilibrium point of system (8). Then,

  (i) The equilibrium point $\overline{U}$ is called stable if for every $\epsilon > 0$ there exists $\delta > 0$ such that $\|U_0 - \overline{U}\| < \delta$ implies $\|U_n - \overline{U}\| < \epsilon$, for all $n \geq 0$. Otherwise, the equilibrium point $\overline{U}$ is called unstable.

  (ii) The equilibrium point $\overline{U}$ is called locally asymptotically stable if it is stable and there exists $\gamma > 0$ such that $\|U_0 - \overline{U}\| < \gamma$ and $U_n \longrightarrow \overline{U}$ as $n \longrightarrow \infty$.

  (iii) The equilibrium point $\overline{U}$ is called a global attractor if $U_n \longrightarrow \overline{U}$ as $n \longrightarrow \infty$.

  (iv) The equilibrium point $\overline{U}$ is called globally asymptotically stable if it is both locally asymptotically stable and global attractor.

The linearized system of (8) evaluated at the equilibrium $\overline{U}$ is

$$Z_{n+1} = J_F Z_n, \quad n \in \mathbb{N}_0, \tag{10}$$

where J_F is the Jacobian matrix of F at the equilibrium $\overline{U}$. The characteristic equation of system (10) about the equilibrium $\overline{U}$ is

$$P(\lambda) = a_0 \lambda^{3k} + a_1 \lambda^{3k-2} + \cdots + a_{3k-1}\lambda + a_{3k} = 0, \tag{11}$$

with real coefficients and $a_0 > 0$.

Theorem 1 (see [30]). *Assume that $\overline{U}$ is a equilibrium point of system (8). If all eigenvalues of the Jacobian matrix J_F evaluated at $\overline{U}$ lie in the open unit disk $|\lambda| < 1$, then $\overline{U}$ is locally asymptotically stable. If one of them has a modulus greater than one, then $\overline{U}$ is unstable.*

3. Global Stability

In this section, we investigate the stability of the two equilibrium points of system (5). When $a_i \in (0, 1)$ for $i = 1, 2, \ldots, k$, the point $\overline{X}_0 = (\overline{x}_1^{(1)}, \overline{x}_1^{(2)}, \ldots, \overline{x}_1^{(k)}) = (0, 0, \ldots, 0)$ is the unique nonnegative equilibrium point of system (5). When $a_i \in (1, \infty)$ for $i = 1, 2, \ldots, k$, the unique positive equilibrium point of system (5) is

$$\overline{X}_{a_i} = \left(\overline{x}_2^{(1)}, \overline{x}_2^{(2)}, \ldots, \overline{x}_2^{(k)} \right) = \left((a_k - 1)^{(1/r_k)}, (a_1 - 1)^{(1/r_1)}, \ldots, (a_{k-1} - 1)^{(1/r_{k-1})} \right). \tag{12}$$

Theorem 2. *The following statements hold:*

  (i) If $a_i \in (0, 1)$ for $i = 1, 2, \ldots, k$, then the equilibrium point $(\overline{x}_1^{(1)}, \overline{x}_1^{(2)}, \ldots, \overline{x}_1^{(k)})$ of system (5) is locally asymptotically stable

  (ii) If $a_i \in (1, \infty)$ for $i = 1, 2, \ldots, k$, then the equilibrium point $(\overline{x}_1^{(1)}, \overline{x}_1^{(2)}, \ldots, \overline{x}_1^{(k)})$ of system (5) is unstable

  (iii) If $a_i \in (1, \infty)$ for $i = 1, 2, \ldots, k$, then the positive equilibrium point $(\overline{x}_2^{(1)}, \overline{x}_2^{(2)}, \ldots, \overline{x}_2^{(k)})$ of system (5) is unstable

Proof

  (i) The characteristic equation of $J_F(\overline{X}_0)$ is given by

$$P(\lambda) = \lambda^k (\lambda^2 - a_1)(\lambda^2 - a_2), \ldots, (\lambda^2 - a_k) = 0. \tag{13}$$

It is easy to see that if $a_i \in (0, 1)$ for $i = 1, 2, \ldots, k$, then all the roots of the characteristic equation (13) lie in the open unit disk $|\lambda| < 1$. So, the equilibrium point $(\overline{x}_1^{(1)}, \overline{x}_1^{(2)}, \ldots, \overline{x}_1^{(k)})$ of (5) is locally asymptotically stable.

  (ii) It is clearly seen that if $a_i \in (1, \infty)$ for $i = 1, 2, \ldots, k$, then some roots of characteristic equation (13) have absolute value greater than one. In this case, the equilibrium point $(\overline{x}_1^{(1)}, \overline{x}_1^{(2)}, \ldots, \overline{x}_1^{(k)})$ of (5) is unstable.

  (iii) The characteristic polynomial of $J_F(\overline{X}_{a_i})$ is given by

$$P(\lambda) = \sum_{j=0}^{k} (-1)^j \binom{k}{j} \lambda^{3k-2j} + (-1)^{k+1} \prod_{i=1}^{k} \frac{r_i(a_i - 1)}{a_i}, \tag{14}$$

where $\binom{k}{j}$ is the binomial coefficient. It is clear that if k is an odd number, then $P(\lambda)$ has a root in interval $(-\infty, -1)$ since

$$P(-1) = \prod_{i=1}^{k} \frac{r_i(a_i - 1)}{a_i} > 0, \tag{15}$$

$$\lim_{\lambda \longrightarrow -\infty} P(\lambda) = -\infty.$$

Also, if k is an even number, then $P(\lambda)$ has a root in interval $(1, \infty)$ since

$$P(1) = -\prod_{i=1}^{k} \frac{r_i(a_i - 1)}{a_i} < 0, \tag{16}$$

$$\lim_{\lambda \longrightarrow \infty} P(\lambda) = \infty.$$

So, from Theorem 1, we can say that if $a_i \in (1, \infty)$ for $i = 1, 2, \ldots, k$, then the positive equilibrium point $(\overline{x}_2^{(1)}, \overline{x}_2^{(2)}, \ldots, \overline{x}_2^{(k)})$ of system (5) is unstable. $\quad \square$

Theorem 3. *If $a_i \in (0,1)$ for $i = 1, 2, \ldots, k$, then the equilibrium point $(\overline{x}_1^{(1)}, \overline{x}_1^{(2)}, \ldots, \overline{x}_1^{(k)})$ of system (5) is globally asymptotically stable.*

Proof. From Theorem 2, we know that if $a_i \in (0,1)$ for $i = 1, 2, \ldots, k$, then the equilibrium point $(\overline{x}_1^{(1)}, \overline{x}_1^{(2)}, \ldots, \overline{x}_1^{(k)})$ of system (5) is locally asymptotically stable. Hence, it suffices to show that

$$\lim_{n \to \infty} \left(x_n^{(1)}, x_n^{(2)}, \ldots, x_n^{(k)} \right) = (0, 0, \ldots, 0). \tag{17}$$

From system (5), we have that

$$0 \le x_{n+1}^{(1)} = \frac{a_1 x_{n-1}^{(1)}}{1 + \left(x_{n-2}^{(2)}\right)^{r_1}} \le a_1 x_{n-1}^{(1)},$$

$$0 \le x_{n+1}^{(2)} = \frac{a_2 x_{n-1}^{(2)}}{1 + \left(x_{n-2}^{(3)}\right)^{r_2}} \le a_2 x_{n-1}^{(2)},$$

$$\vdots \tag{18}$$

$$0 \le x_{n+1}^{(k)} = \frac{a_k x_{n-1}^{(k)}}{1 + \left(x_{n-2}^{(1)}\right)^{r_k}} \le a_k x_{n-1}^{(k)},$$

for $n \in \mathbb{N}_0$. From (18), we have by induction

$$0 \le x_{2n-l}^{(i)} \le a_i^n x_{-l}^{(i)}, \tag{19}$$

where $x_{-l}^{(i)}$ ($l = 0, 1$) for $i = 1, 2, \ldots, k$ are the initial conditions. Consequently, by taking limits of inequalities in (19) when $a_i \in (0,1)$ for $i = 1, 2, \ldots, k$, we have the limit in (17) which completes the proof. □

4. Oscillation Behavior and Existence of Unbounded Solutions

In the following result, we are concerned with the oscillation of positive solutions of system (5) about the equilibrium point $(\overline{x}_2^{(1)}, \overline{x}_2^{(2)}, \ldots, \overline{x}_2^{(k)})$.

Theorem 4. *Assume that $a_i \in (1, \infty)$, and let $\{(x_n^{(1)}, x_n^{(2)}, \ldots, x_n^{(k)})\}_{n=-2}^{\infty}$ be a positive solution of system (5) such that*

$$x_{-2}^{(i)}, x_0^{(i)} \ge \overline{x}_2^{(i)}, \tag{20}$$
$$x_{-1}^{(i)} < \overline{x}_2^{(i)},$$

or

$$x_{-2}^{(i)}, x_0^{(i)} < \overline{x}_2^{(i)}, \tag{21}$$
$$x_{-1}^{(i)} \ge \overline{x}_2^{(i)},$$

for $i = 1, 2, \ldots, k$. Then, $\{(x_n^{(1)}, x_n^{(2)}, \ldots, x_n^{(k)})\}_{n=-2}^{\infty}$ oscillates about the equilibrium point $(\overline{x}_2^{(1)}, \overline{x}_2^{(2)}, \ldots, \overline{x}_2^{(k)})$ with semicycles of length one.

Proof. Assume that (20) holds. (The case where (21) holds is similar and will be omitted.) From (5), we have

$$x_1^{(1)} = \frac{a_1 x_{-1}^{(1)}}{1 + \left(x_{-2}^{(2)}\right)^{r_1}} < \frac{a_1 \overline{x}_2^{(1)}}{1 + \left(\overline{x}_2^{(2)}\right)^{r_1}} = \overline{x}_2^{(1)}, \quad x_1^{(2)} = \frac{a_2 x_{-1}^{(2)}}{1 + \left(x_{-2}^{(3)}\right)^{r_2}} < \frac{a_2 \overline{x}_2^{(2)}}{1 + \left(\overline{x}_2^{(3)}\right)^{r_2}} = \overline{x}_2^{(2)}, \quad \vdots \quad x_1^{(k)} = \frac{a_k x_{-1}^{(k)}}{1 + \left(x_{-2}^{(1)}\right)^{r_k}} < \frac{a_k \overline{x}_2^{(k)}}{1 + \left(\overline{x}_2^{(1)}\right)^{r_k}} = \overline{x}_2^{(k)}, \quad x_2^{(1)}$$

$$= \frac{a_1 x_0^{(1)}}{1 + \left(x_{-1}^{(2)}\right)^{r_1}} \ge \frac{a_1 \overline{x}_2^{(1)}}{1 + \left(\overline{x}_2^{(2)}\right)^{r_1}} = \overline{x}_2^{(1)}, \quad x_2^{(2)} = \frac{a_2 x_0^{(2)}}{1 + \left(x_{-1}^{(3)}\right)^{r_2}} \ge \frac{a_2 \overline{x}_2^{(2)}}{1 + \left(\overline{x}_2^{(3)}\right)^{r_2}} = \overline{x}_2^{(2)}, \quad \vdots \quad x_2^{(k)} = \frac{a_k x_0^{(k)}}{1 + \left(x_{-1}^{(1)}\right)^{r_k}} \ge \frac{a_k \overline{x}_2^{(k)}}{1 + \left(\overline{x}_2^{(1)}\right)^{r_k}} = \overline{x}_2^{(k)}.$$

$$\tag{22}$$

Then, the proof follows by induction.

In the following theorem, we show the existence of unbounded solutions for system (5). □

Theorem 5. *Assume that $a_i \in (1, \infty)$ for $i = 1, 2, \ldots, k$, then system (5) possesses an unbounded solution.*

Proof. From Theorem 4, we can assume that, without loss of generality, the solution $\{(x_n^{(1)}, x_n^{(2)}, \ldots, x_n^{(k)})\}_{n=-2}^{\infty}$ of system (5) is such that $x_{2n-1}^{(i)} < \overline{x}_2^{(i)}$ and $x_{2n}^{(i)} > \overline{x}_2^{(i)}$ for $i = 1, 2, \ldots, k$ and $n \in \mathbb{N}_0$. Then, we have

$$x_{2n+2}^{(1)} = \frac{a_1 x_{2n}^{(1)}}{1 + \left(x_{2n-1}^{(2)}\right)^{r_1}} > \frac{a_1 x_{2n}^{(1)}}{1 + \left(\overline{x}_2^{(2)}\right)^{r_1}} = \frac{a_1 x_{2n}^{(1)}}{1 + (a_1 - 1)} = x_{2n}^{(1)},$$

$$x_{2n+2}^{(2)} = \frac{a_2 x_{2n}^{(2)}}{1 + \left(x_{2n-1}^{(3)}\right)^{r_2}} > \frac{a_2 x_{2n}^{(2)}}{1 + \left(\overline{x}_2^{(3)}\right)^{r_2}} = \frac{a_2 x_{2n}^{(2)}}{1 + (a_2 - 1)} = x_{2n}^{(2)},$$

$$\vdots$$

$$x_{2n+2}^{(k)} = \frac{a_k x_{2n}^{(k)}}{1 + \left(x_{2n-1}^{(1)}\right)^{r_k}} > \frac{a_k x_{2n}^{(k)}}{1 + \left(\overline{x}_2^{(1)}\right)^{r_k}} = \frac{a_k x_{2n}^{(k)}}{1 + (a_k - 1)} = x_{2n}^{(k)},$$

$$x_{2n+3}^{(1)} = \frac{a_1 x_{2n+1}^{(1)}}{1 + \left(x_{2n}^{(2)}\right)^{r_1}} < \frac{a_1 x_{2n+1}^{(1)}}{1 + \left(\overline{x}_2^{(2)}\right)^{r_1}} = \frac{a_1 x_{2n+1}^{(1)}}{1 + (a_1 - 1)} = x_{2n+1}^{(1)},$$

$$x_{2n+3}^{(2)} = \frac{a_2 x_{2n+1}^{(2)}}{1 + \left(x_{2n}^{(3)}\right)^{r_2}} < \frac{a_2 x_{2n+1}^{(2)}}{1 + \left(\overline{x}_2^{(3)}\right)^{r_2}} = \frac{a_2 x_{2n+1}^{(2)}}{1 + (a_2 - 1)} = x_{2n+1}^{(2)},$$

$$\vdots$$

$$x_{2n+3}^{(k)} = \frac{a_k x_{2n+1}^{(k)}}{1 + \left(x_{2n}^{(1)}\right)^{r_k}} < \frac{a_k x_{2n+1}^{(k)}}{1 + \left(\overline{x}_2^{(1)}\right)^{r_k}} = \frac{a_k x_{2n+1}^{(k)}}{1 + (a_k - 1)} = x_{2n+1}^{(k)},$$

$$(23)$$

from which it follows that

$$\lim_{n \to \infty} \left(x_{2n}^{(1)}, x_{2n}^{(2)}, \ldots, x_{2n}^{(k)}\right) = (\infty, \infty, \ldots, \infty),$$

$$\lim_{n \to \infty} \left(x_{2n+1}^{(1)}, x_{2n+1}^{(2)}, \ldots, x_{2n+1}^{(k)}\right) = (0, 0, \ldots, 0),$$

$$(24)$$

which completes the proof. □

5. Periodicity

In this section, we investigate the existence of period-two solution of system (5).

Theorem 6. *If $a_i = 1$ for $i = 1, 2, \ldots, k$, then system (5) possesses the prime period-two solution*

$$\ldots, (0, 0, \ldots, 0, \varphi), (0, 0, \ldots, 0, \psi), (0, 0, \ldots, 0, \varphi), (0, 0, \ldots, 0, \psi), \ldots,$$

$$(25)$$

with $\varphi, \psi > 0$. Furthermore, every solution of system (5) converges to a period-two solution.

Proof. Assume that $a_i = 1$ for $i = 1, 2, \ldots, k$, and let $\{(x_n^{(1)}, x_n^{(2)}, \ldots, x_n^{(k)})\}_{n=-2}^{\infty}$ be a solution of system (5). Then, from system (5), we have

$$x_{2n+1}^{(1)} = \frac{x_{2n-1}^{(1)}}{1 + \left(x_{2n-2}^{(2)}\right)^{r_1}},$$

$$x_{2n+2}^{(1)} = \frac{x_{2n}^{(1)}}{1 + \left(x_{2n-1}^{(2)}\right)^{r_1}},$$

$$x_{2n+1}^{(2)} = \frac{x_{2n-1}^{(2)}}{1 + \left(x_{2n-2}^{(3)}\right)^{r_2}},$$

$$x_{2n+2}^{(2)} = \frac{x_{2n}^{(2)}}{1 + \left(x_{2n-1}^{(3)}\right)^{r_2}},$$

$$(26)$$

$$\vdots$$

$$x_{2n+1}^{(k)} = \frac{x_{2n-1}^{(k)}}{1 + \left(x_{2n-2}^{(1)}\right)^{r_k}},$$

$$x_{2n+2}^{(k)} = \frac{x_{2n}^{(k)}}{1 + \left(x_{2n-1}^{(1)}\right)^{r_k}},$$

for $n \in \mathbb{N}_0$. From (26), we obtain

$$x_{2n-1}^{(1)} = x_{-1}^{(1)} \prod_{i=0}^{n-1} \left(\frac{1}{1 + \left(x_{2i-2}^{(2)}\right)^{r_1}}\right),$$

$$x_{2n}^{(1)} = x_0^{(1)} \prod_{i=0}^{n-1} \left(\frac{1}{1 + \left(x_{2i-1}^{(2)}\right)^{r_1}}\right),$$

$$x_{2n-1}^{(2)} = x_{-1}^{(2)} \prod_{i=0}^{n-1} \left(\frac{1}{1 + \left(x_{2i-2}^{(3)}\right)^{r_2}}\right),$$

$$x_{2n}^{(2)} = x_0^{(2)} \prod_{i=0}^{n-1} \left(\frac{1}{1 + \left(x_{2i-1}^{(3)}\right)^{r_2}}\right),$$

$$(27)$$

$$\vdots$$

$$x_{2n-1}^{(k)} = x_{-1}^{(k)} \prod_{i=0}^{n-1} \left(\frac{1}{1 + \left(x_{2i-2}^{(1)}\right)^{r_k}}\right),$$

$$x_{2n}^{(k)} = x_0^{(k)} \prod_{i=0}^{n-1} \left(\frac{1}{1 + \left(x_{2i-1}^{(1)}\right)^{r_k}}\right),$$

for $n \in \mathbb{N}_0$. If $x_{-l}^{(i)} = 0$ for $l = 0, 1$ and $i = 1, 2, \ldots, k - 1$, then $x_n^{(i)} = 0$ for $i = 1, 2, \ldots, k - 1$ and $(x_{2n-1}^{(k)}, x_{2n}^{(k)}) = (x_{-1}^{(k)}, x_0^{(k)})$ for $n \in \mathbb{N}_0$. Therefore,

$$\ldots, (0, 0, \ldots, 0, \varphi), (0, 0, \ldots, 0, \psi), (0, 0, \ldots, 0, \varphi), (0, 0, \ldots, 0, \psi), \ldots$$

$$(28)$$

is a period-two solution of system (5) with $x_{-2}^{(k)} = x_0^{(k)} = \varphi > 0$ and $x_{-1}^{(k)} = \psi > 0$. Furthermore, from (26), we have

$$x_{2n+1}^{(1)} - x_{2n-1}^{(1)} = -\frac{x_{2n-1}^{(1)}\left(x_{2n-2}^{(2)}\right)^{r_1}}{1 + \left(x_{2n-2}^{(2)}\right)^{r_1}} \leq 0,$$

$$x_{2n+1}^{(2)} - x_{2n-1}^{(2)} = -\frac{x_{2n-1}^{(2)}\left(x_{2n-2}^{(3)}\right)^{r_2}}{1 + \left(x_{2n-2}^{(3)}\right)^{r_2}} \leq 0,$$

$$\vdots \qquad\qquad\qquad (29)$$

$$x_{2n+1}^{(k)} - x_{2n-1}^{(k)} = -\frac{x_{2n-1}^{(k)}\left(x_{2n-2}^{(1)}\right)^{r_k}}{1 + \left(x_{2n-2}^{(1)}\right)^{r_k}} \leq 0,$$

$$x_{2n+2}^{(1)} - x_{2n}^{(1)} = -\frac{x_{2n}^{(1)}\left(x_{2n-1}^{(2)}\right)^{r_1}}{1 + \left(x_{2n-1}^{(2)}\right)^{r_1}} \leq 0,$$

$$x_{2n+2}^{(2)} - x_{2n}^{(2)} = -\frac{x_{2n}^{(2)}\left(x_{2n-1}^{(3)}\right)^{r_2}}{1 + \left(x_{2n-1}^{(3)}\right)^{r_2}} \leq 0,$$

$$\vdots \qquad\qquad\qquad (30)$$

$$x_{2n+2}^{(k)} - x_{2n}^{(k)} = -\frac{x_{2n}^{(k)}\left(x_{2n-1}^{(1)}\right)^{r_k}}{1 + \left(x_{2n-1}^{(1)}\right)^{r_k}} \leq 0.$$

From (29) and (30), we obtain $x_{2n+1}^{(i)} \leq x_{2n-1}^{(i)}$ and $x_{2n+2}^{(i)} \leq x_{2n}^{(i)}$ for $i = 1, 2, \ldots, k$. That is, the sequences $(x_{2n-1}^{(i)})$ and $(x_{2n}^{(i)})$ for $i = 1, 2, \ldots, k$ are nonincreasing. On the other hand, from (26), we have the inequalities

$$x_{2n-1}^{(1)} = x_{-1}^{(1)} \prod_{i=0}^{n-1}\left(\frac{1}{1 + \left(x_{2i-2}^{(2)}\right)^{r_1}}\right) \leq x_{-1}^{(1)},$$

$$x_{2n}^{(1)} = x_0^{(1)} \prod_{i=0}^{n-1}\left(\frac{1}{1 + \left(x_{2i-1}^{(2)}\right)^{r_1}}\right) \leq x_0^{(1)},$$

$$x_{2n-1}^{(2)} = x_{-1}^{(2)} \prod_{i=0}^{n-1}\left(\frac{1}{1 + \left(x_{2i-2}^{(3)}\right)^{r_2}}\right) \leq x_{-1}^{(2)},$$

$$x_{2n}^{(2)} = x_0^{(2)} \prod_{i=0}^{n-1}\left(\frac{1}{1 + \left(x_{2i-1}^{(3)}\right)^{r_2}}\right) \leq x_0^{(2)}, \qquad (31)$$

$$\vdots$$

$$x_{2n-1}^{(k)} = x_{-1}^{(k)} \prod_{i=0}^{n-1}\left(\frac{1}{1 + \left(x_{2i-2}^{(1)}\right)^{r_k}}\right) \leq x_{-1}^{(k)},$$

$$x_{2n}^{(k)} = x_0^{(k)} \prod_{i=0}^{n-1}\left(\frac{1}{1 + \left(x_{2i-1}^{(1)}\right)^{r_k}}\right) \leq x_0^{(k)},$$

which show the boundedness of the solutions. Hence, the odd-index terms tend to one periodic point and the even-index terms tend to another periodic point. This completes the proof. □

6. Numerical Examples

In this section, we give some numerical examples to support our theoretical results related to system (5) with some restrictions on the parameters a_i and r_i for $i = 1, 2, \ldots k$.

Example 1. If $k = 3$, $x_n^{(1)} = x_n$, $x_n^{(2)} = y_n$, $x_n^{(3)} = z_n$, $r_1 = 2$, $r_2 = 3$, and $r_3 = 4$ in system (5), we obtain the following system:

$$x_{n+1} = \frac{a_1 x_{n-1}}{1 + \left(y_{n-2}\right)^2},$$

$$y_{n+1} = \frac{a_2 y_{n-1}}{1 + \left(z_{n-2}\right)^3}, \qquad (32)$$

$$z_{n+1} = \frac{a_3 z_{n-1}}{1 + \left(x_{n-2}\right)^4}.$$

We visualize the solutions of system (32) in Figures 1–3 for the initial conditions $x_{-2} = 1.34$, $x_{-1} = 2.13$, $x_0 = 3.1$, $y_{-2} = 0.17$, $y_{-1} = 4.03$, $y_0 = 2.21$, $z_{-2} = 0.32$, $z_{-1} = 2.76$, and $z_0 = 3.12$.

Example 2. If $k = 4$, $x_n^{(1)} = x_n$, $x_n^{(2)} = y_n$, $x_n^{(3)} = z_n$, $x_n^{(4)} = p_n$, $r_1 = 2$, $r_2 = 3$, $r_3 = 4$, and $r_4 = 5$ in system (5), we obtain the following system:

$$x_{n+1} = \frac{a_1 x_{n-1}}{1 + \left(y_{n-2}\right)^2},$$

$$y_{n+1} = \frac{a_2 y_{n-1}}{1 + \left(z_{n-2}\right)^3},$$

$$z_{n+1} = \frac{a_3 z_{n-1}}{1 + \left(p_{n-2}\right)^4}, \qquad (33)$$

$$p_{n+1} = \frac{a_4 p_{n-1}}{1 + \left(x_{n-2}\right)^5}.$$

We visualize the solutions of system (33) in Figures 4–6 for the initial conditions $x_{-2} = 1.34$, $x_{-1} = 2.13$, $x_0 = 3.1$, $y_{-2} = 0.17$, $y_{-1} = 4.03$, $y_0 = 2.21$, $z_{-2} = 0.32$, $z_{-1} = 2.76$, $z_0 = 3.12$, $p_{-2} = 3.27$, $p_{-1} = 1.33$, and $p_0 = 2.78$.

Example 3. If $k = 5$, $x_n^{(1)} = x_n$, $x_n^{(2)} = y_n$, $x_n^{(3)} = z_n$, $x_n^{(4)} = p_n$, and $x_n^{(5)} = q_n$ in system (5), we obtain the following system:
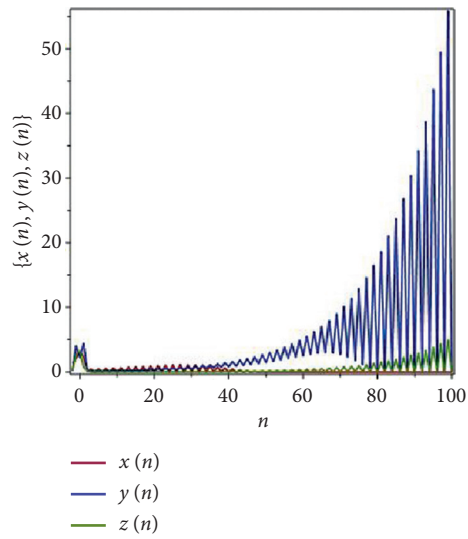
FIGURE 1: The solutions of system (32) when $a_1 = 1.12$, $a_2 = 1.13$, and $a_3 = 1.14$.
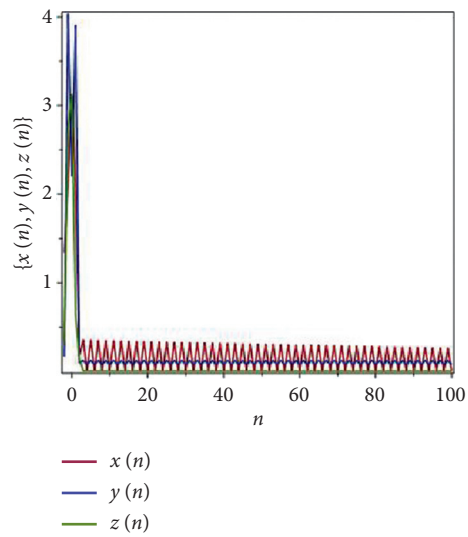
FIGURE 2: The solutions of system (32) when $a_1 = 1$, $a_2 = 1$, and $a_3 = 1$.
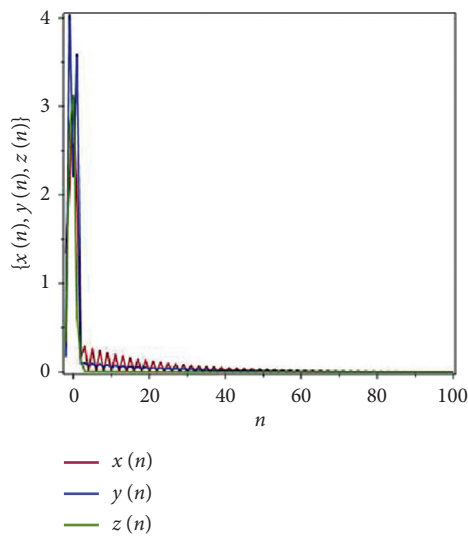
FIGURE 3: The solutions of system (32) when $a_1 = 0.91$, $a_2 = 0.92$, and $a_3 = 0.93$.

FIGURE 4: The solutions of system (33) when $a_1 = 1.12$, $a_2 = 1.13$, $a_3 = 1.14$, and $a_4 = 1.15$.

FIGURE 5: The solutions of system (33) when $a_1 = 1$, $a_2 = 1$, $a_3 = 14$, and $a_4 = 1$.

FIGURE 6: The solutions of system (33) when $a_1 = 0.91$, $a_2 = 0.92$, $a_3 = 0.93$, and $a_4 = 0.94$.

Figure 7: The solutions of system (34) when $a_1 = 1.12$, $a_2 = 1.13$, $a_3 = 1.14$, $a_4 = 1.15$, and $a_5 = 1.16$.

Figure 8: The solutions of system (34) when $a_1 = 1$, $a_2 = 1$, $a_3 = 14$, $a_4 = 1$, and $a_5 = 1$.
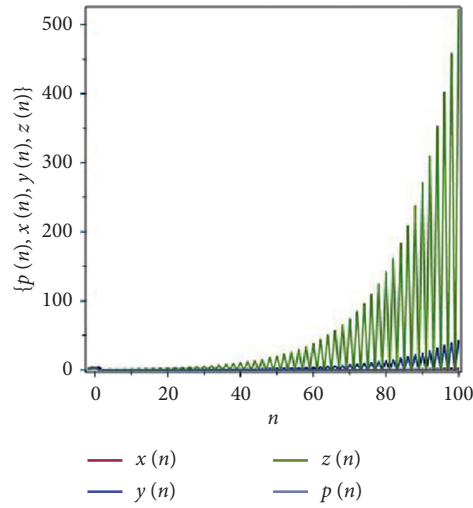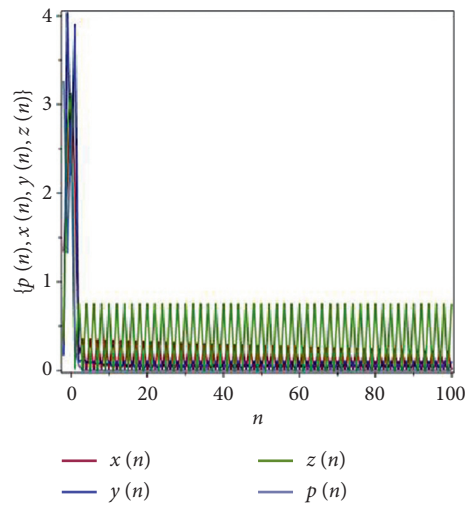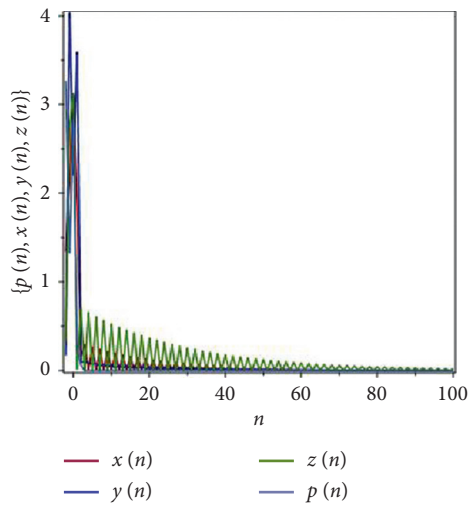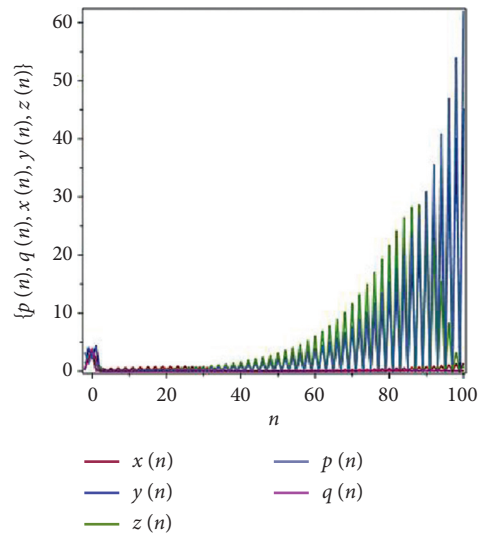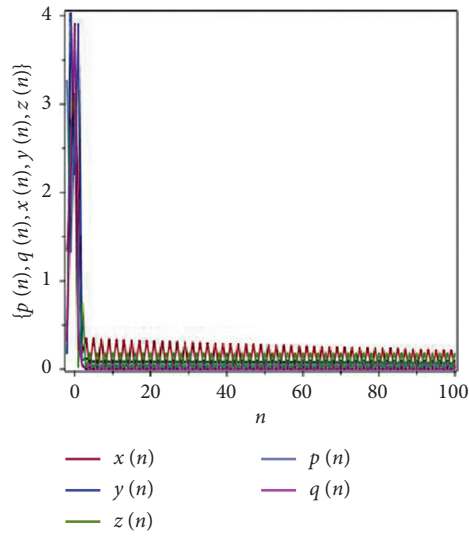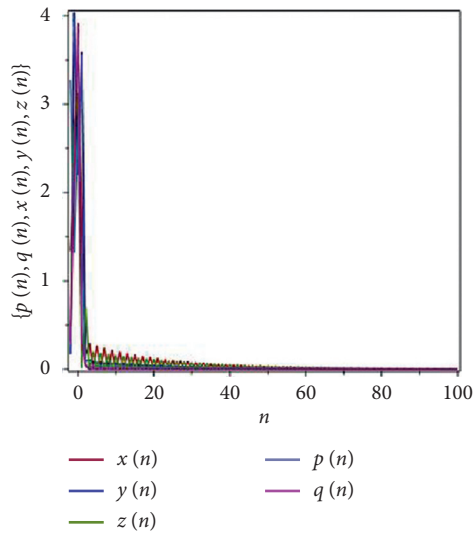

Figure 9: The solutions of system (34) when $a_1 = 0.91$, $a_2 = 0.92$, $a_3 = 0.93$, $a_4 = 0.94$, and $a_1 = 0.95$.

$$
\begin{cases}
x_{n+1} = \dfrac{a_1 x_{n-1}}{1 + \left(y_{n-2}\right)^2}, \\[2mm]
y_{n+1} = \dfrac{a_2 y_{n-1}}{1 + \left(z_{n-2}\right)^3}, \\[2mm]
z_{n+1} = \dfrac{a_3 z_{n-1}}{1 + \left(p_{n-2}\right)^4}, \qquad (34) \\[2mm]
p_{n+1} = \dfrac{a_4 p_{n-1}}{1 + \left(q_{n-2}\right)^5}, \\[2mm]
q_{n+1} = \dfrac{a_5 q_{n-1}}{1 + \left(x_{n-2}\right)^6},
\end{cases}
$$

with $r_1 = 2$, $r_2 = 3$, $r_3 = 4$, $r_4 = 5$, and $r_5 = 6$. We visualize the solutions of system (34) in Figures 7–9 for the initial conditions $x_{-2} = 1.34$, $x_{-1} = 2.13$, $x_0 = 3.1$, $y_{-2} = 0.17$, $y_{-1} = 4.03$, $y_0 = 2.21$, $z_{-2} = 0.32$, $z_{-1} = 2.76$, $z_0 = 3.12$, $p_{-2} = 3.27$, $p_{-1} = 1.33$, $p_0 = 2.78$, $q_{-2} = 0.32$, $q_{-1} = 2.16$, and $q_0 = 3.91$.

7. Conclusion

In this study, we have generalized some of the results in the literature. As shown in Section 1, equation (1) was developed systematically. By this study, we ended this development. More concretely, we investigated the local asymptotic stability, global asymptotic stability, periodicity, and oscillation behavior of system (5) which is the k-dimensional generalization of equation (1). According to our findings, our results are consistent with the results of the paper [1] in the case of $k = 1$. Similarly, our results are in line with the results of the papers [2, 3] in the case of $k = 2$ and $k = 3$, respectively.

Data Availability

The data used to support the findings of this study are available from the first author upon request.

Conflicts of Interest

The authors declare that there are no conflicts of interest associated with this publication.

Acknowledgments

References

[1] H. M. El-Owaidy, A. M. Ahmed, and A. M. Youssef, "The dynamics of the recursive sequence $x_{n+1} = (\alpha x_{n-1}/\beta + \gamma x_{n-2}^p)$," *Applied Mathematics Letters*, vol. 18, no. 9, pp. 1013–1018, 2005.

[2] M. Gumus and Y. Soykan, "Global character of a six dimensional nonlinear system of difference equations," *Discrete Dynamics in Nature and Society*, vol. 2016, Article ID 6842521, 7 pages, 2016.

[3] D. T. Tollu and I. Yalcinkaya, "Global behavior of a three-dimensional system of difference equations of order three," *Communications, Series A1: Mathematics and Statistics*, vol. 68, no. 1, pp. 1–16, 2019.

[4] Q. Din and E. M. Elsayed, "Stability analysis of a discrete ecological model," *Computational Ecology and Software*, vol. 4, no. 2, pp. 89–103, 2014.

[5] E. M. Elabbasy, H. El-Metwally, and E. M. Elsayed, "Some properties and expressions of solutions for a class of nonlinear difference equation," *Utilitas Mathematica*, vol. 87, pp. 93–110, 2012.

[6] H. El-Metwally and E. M. Elsayed, "Solution and behavior of a third rational difference equation," *Utilitas Mathematica*, vol. 88, pp. 27–42, 2012.

[7] H. El-Metwally, I. Yalcinkaya, and C. Cinar, "Global stability of an economic model," *Utilitas Mathematica*, vol. 95, pp. 235–244, 2014.

[8] E. M. Elsayed, M. M. El-Dessoky, and A. Alotaibi, "On the solutions of a general system of difference equations," *Discrete Dynamics in Nature and Society*, vol. 2012, Article ID 892571, , 2012.

[9] N. Haddad and J. F. T. Rabago, "Dynamics of a system of k-difference equations," *Electronic Journal of Mathematical Analysis and Applications*, vol. 5, no. 2, pp. 242–249, 2017.

[10] A. S. Kurbanli, C. Cinar, and I. Yalcinkaya, "On the behavior of positive solutions of the system of rational difference equations $x_{n+1} = (x_{n-1}/(y_n x_{n-1} + 1))$, $y_{n+1} = (y_{n-1}/(x_n y_{n-1} + 1))$," *Mathematical and Computer Modelling*, vol. 53, no. 5-6, pp. 1261–1267, 2011.

[11] A. S. Kurbanli, "On the behavior of solutions of the system of rational difference equations $x_{n+1} = (x_{n-1}/(y_n x_{n-1} - 1))$, $y_{n+1} = (y_{n-1}/(x_n y_{n-1} - 1))$, $z_{n+1} = (1/(y_n z_n))$," *Advances in Difference Equations*, vol. 2011, no. 1, p. 40, 2011.

[12] A. S. Kurbanli, "On the behavior of solutions of the system of rational difference equations $x_{n+1} = (x_{n-1}/(y_n x_{n-1} - 1))$, $y_{n+1} = (y_{n-1}/(x_n y_{n-1} - 1))$, $z_{n+1} = (z_{n-1}/(y_n z_{n-1} - 1))$," *Discrete Dynamics in Nature and Society*, vol. 2011, Article ID 932362, 12 pages, 2011.

[13] O. Ozkan and A. S. Kurbanli, "On a system of difference equations," *Discrete Dynamics in Nature and Society*, vol. 2013, Article ID 970316, 7 pages, 2013.

[14] G. Papaschinopoulos, G. Ellina, and K. B. Papadopoulos, "Asymptotic behavior of the positive solutions of an exponential type system of difference equations," *Applied Mathematics and Computation*, vol. 245, pp. 181–190, 2014.

[15] G. Papaschinopoluos, N. Psarros, and K. B. Papadopoulos, "On a cyclic system of m difference equations having exponential terms," *Electronic Journal of Qualitative Theory of Differential Equations*, vol. 5, pp. 1–13, 2015.

[16] J. F. T. Rabago and J. B. Bacani, "On two nonlinear difference equations," *Dynamics of Continuous, Discrete and Impulsive Systems Series A: Mathematical Analysis*, vol. 24, pp. 375–394, 2017.

[17] J. F. T. Rabago, "Effective methods on determining the periodicity and form of solutions of some systems of non-linear difference equations," *International Journal of Dynamical Systems and Differential Equations*, vol. 7, no. 2, pp. 112–135, 2017.

[18] J. F. T. Rabago, "Forbidden set of the rational difference equation," *Buletinul Academiei De Stiinte a Republicii Moldova. Matematica*, vol. 1, no. 83, pp. 29–38, 2017.

[19] N. Taskara, D. T. Tollu, and Y. Yazlik, "Solutions of rational difference system of order three in terms of Padovan numbers," *Journal of Advanced Research in Applied Mathematics*, vol. 7, no. 3, pp. 18–29, 2015.

[20] D. T. Tollu, Y. Yazlik, and N. Taskara, "On fourteen solvable systems of difference equations," *Applied Mathematics and Computation*, vol. 233, pp. 310–319, 2014.

[21] N. Touafek and E. M. Elsayed, "On the periodicity of some systems of nonlinear difference equations," *Bulletin Mathématique De La Société Des Sciences Mathématiques De Roumanie*, vol. 55 (103), no. 2, pp. 217–224, 2012.

[22] V. Van Khuong and M. Nam Phong, "On a system of two difference equations of exponential form," *International Journal of Difference Equations*, vol. 8, no. 2, pp. 215–223, 2013.

[23] I. Yalcinkaya, C. Cinar, and D. Simsek, "Global asymptotic stability of a system of difference equations," *Applicable Analysis*, vol. 87, no. 6, pp. 689–699, 2008.

[24] I. Yalcinkaya, "On the global asymptotic stability of a second-order system of difference equations," *Discrete Dynamics in Nature and Society*, vol. 2008, Article ID 860152, 12 pages, 2008.

[25] I. Yalcinkaya, C. Cinar, and M. Atalay, "On the solutions of systems of difference equations," *Advances in Difference Equations*, vol. 2008, Article ID 143943, 2008.

[26] Y. Yazlik, D. T. Tollu, and N. Taskara, "On the solutions of difference equation systems with Padovan numbers," *Applied Mathematics*, vol. 4, no. 12, pp. 15–20, 2013.

[27] Y. Yazlik, E. M. Elsayed, and N. Taskara, "On the behaviour of the solutions of difference equation systems," *Journal of Computational Analysis and Applications*, vol. 16, no. 5, pp. 932–941, 2014.

[28] Y. Yazlik, D. T. Tollu, and N. Taskara, "On the behaviour of solutions for some systems of difference equations," *Journal of Computational Analysis & Applications*, vol. 18, no. 1, pp. 166–178, 2015.

[29] Y. Yazlik, D. T. Tollu, and N. Taskara, "On the solutions of a three-dimensional system of difference equations," *Kuwait Journal of Science*, vol. 43, no. 1, pp. 95–111, 2016.

[30] V. L. Kocic and G. Ladas, *Global Behavior of Nonlinear Difference Equations of Higher Order with Applications*, Kluwer Academic, Dordrecht, Netherlands, 1993.

Research Article

Second-Order Differential Equation: Oscillation Theorems and Applications

Shyam S. Santra,[1] Omar Bazighifan [ID],[2,3] Hijaz Ahmad [ID],[4,5] and Yu-Ming Chu [ID][6,7]

[1]*Department of Mathematics, JIS College of Engineering, Kalyani 741235, India*
[2]*Department of Mathematics, Faculty of Science, Hadhramout University, Hadhramout, Yemen*
[3]*Department of Mathematics, Faculty of Education, Seiyun University, Hadhramout, Yemen*
[4]*Department of Basic Sciences, University of Engineering and Technology, Peshawar, Pakistan*
[5]*Section of Mathematics, International Telematic University Uninettuno, Corso Vittorio Emanuele II, 39, Roma 00186, Italy*
[6]*Department of Mathematics, Huzhou University, Huzhou 313000, China*
[7]*Hunan Provincial Key Laboratory of Mathematical Modeling and Analysis in Engineering, Changasha, University of Science & Technology, Changsha 410114, China*

Correspondence should be addressed to Yu-Ming Chu; chuyuming@zjhu.edu.cn

Differential equations of second order appear in a wide variety of applications in physics, mathematics, and engineering. In this paper, necessary and sufficient conditions are established for oscillations of solutions to second-order half-linear delay differential equations of the form $(\varsigma(y)(u'(y))^a)' + p(y)u^c(\vartheta(y)) = 0$, for $y \geq y_0$, under the assumption $\int^{\infty}(\varsigma(\eta))^{-(1/a)} = \infty$. Two cases are considered for $a < c$ and $a > c$, where a and c are the quotients of two positive odd integers. Two examples are given to show the effectiveness and applicability of the result.

1. Introduction

Differential equations (DEs) have received a lot of attention, and it is an active research area among scientists and engineers [1–8]. The DEs have ability to formulate many complex phenomena in various fields such as biology, fluid mechanics, plasma physics, fluid mechanics, and optics; many exact and numerical schemes have been being derived such as [9–15]. Differential equation of second order appears in models as well as in physical applications such as fluid dynamics, electromagnetism, acoustic vibrations and quantum mechanics, biological, physical and chemical phenomena, optimization, mathematics of networks, and dynamical systems (see [16–24]).

In this article, we consider the differential equation

$$\left(\varsigma(y)\left(u'(y)\right)^a\right)' + p(y)u^c(\vartheta(y)) = 0, \quad \text{for } y \geq y_0, \quad (1)$$

where a and c are the quotient of two positive odd integers, and the functions p, ς, and ϑ are continuous that satisfy the conditions stated below:

(A1) $\vartheta \in C([0, \infty), \mathbb{R})$, $\vartheta(y) < y$, $\lim_{y \to \infty} \vartheta(y) = \infty$.

(A2) $\varsigma \in C^1([0, \infty), \mathbb{R})$, $p \in C([0, \infty), \mathbb{R})$; $0 < \varsigma(y)$, $0 \leq p(y)$ for all $y \geq 0$; $p(y)$ is not identically zero in any interval $[b, \infty)$.

(A3) $\Upsilon(y) = \int_{y_1}^{y} \varsigma^{-1/a}(\eta) \mathrm{d}\eta$ with $\lim_{y \to \infty} \Upsilon(y) = \infty$.

(A4) the existence of a differentiable function ϑ_0 such that $0 < \vartheta_0(y) \leq \vartheta(y)$, for $\vartheta_0'(y) \geq \vartheta_0 > 0$, for $y \geq y_0$.

In [25, 26], Baculíková and Džurina have considered

$$\left(\varsigma(y)\left(z'(y)\right)^a\right)' + p(y)u^c(\vartheta(y)) = 0,$$
$$z(y) = u(y) + q(y)u(\tau(y)), \quad y \geq y_0, \quad (2)$$

and obtained oscillation criteria for the solutions of (2) using comparison techniques when $a = c = 1$, $0 \le q(y) < \infty$, and $\lim_{y \to \infty} \Upsilon(y) = \infty$. In the same technique, Džurina and Dzurina [27] have studied the oscillatory behavior of the solutions of (2) under the assumptions $0 \le q(y) < \infty$ and $\lim_{y \to \infty} \Upsilon(y) = \infty$. In [28], Bohner et al. have studied the oscillatory behavior of solutions of (2) under $a = c$, $\lim_{y \to \infty} \Upsilon(y) < \infty$, and $0 \le q(y) < 1$. Grace et al. [29] have studied the oscillatory behavior of (2) when $a = c$ and $\lim_{y \to \infty} \Upsilon(y) < \infty$ and $\lim_{y \to \infty} \Upsilon(y) = \infty$ and $0 \le q(y) < 1$. In [30], Ali has studied the oscillatory behavior of the solutions of (2), under the assumptions $\lim_{y \to \infty} \Upsilon(y) < \infty$ and $q(y) \ge 0$. Karpuz and Santra [31] have studied the oscillatory behavior of

$$\left(\varsigma(y)(u(y) + q(y)u(\tau(y)))' \right)' + p(y)f(u(\vartheta(y))) = 0, \tag{3}$$

by considering the assumptions $\lim_{y \to \infty} \Upsilon(y) < \infty$ and $\lim_{y \to \infty} \Upsilon(y) = \infty$ for different ranges of the neutral coefficient q.

For further work on the oscillation of this type of equations, we refer the readers to the references. Note that the majority of works consider only sufficient conditions, and merely a few consider both necessary and sufficient conditions. Hence, the objective of this work is to establish both necessary and sufficient conditions for the oscillation of solutions of (1) without using the comparison and the Riccati techniques. In this paper, we restrict our attention to the study (1), which includes the class of functional differential equations of neutral type.

Remark 1. When the domain is not specified explicitly, all functional inequalities considered in this paper are assumed to hold eventually, i.e., they are satisfied for all y large enough.

2. Necessary and Sufficient Conditions

Lemma 1. *Let (A1)–(A3) hold and that u is an eventually positive solution of (1). Then, there exist $y_1 \ge y_0$ and $d > 0$ such that*

$$0 < u(y) \le d\Upsilon(y), \tag{4}$$

$$\Upsilon(y) \left[\int_y^\infty p(\zeta)u^c(\vartheta(\zeta))d\zeta \right]^{1/a} \le u(y), \tag{5}$$

for $y \ge y_1$.

Proof. Let u be an eventually positive solution of (1). Then, by (A1), there exists a y^* such that $u(y) > 0$ and $u(\vartheta(y)) > 0$ for all $y \ge y^*$. From (1) it follows that

$$\left(\varsigma(y)(u'(y))^a \right)' = -p(y)u^c(\vartheta(y)) \le 0. \tag{6}$$

Therefore, $\varsigma(y)(u'(y))^a$ is nonincreasing for $y \ge y^*$. Next, we show that $\varsigma(y)(u'(y))^a$ is positive. By contradiction, assume that $\varsigma(y)(u'(y))^a \le 0$ at a certain time

$y \ge y^*$. Using that p is not identically zero on any interval $[b, \infty)$ and by (6), there exists $y_1 \ge y^*$ such that

$$\varsigma(y)(u'(y))^a \le \varsigma(y_1)(u'(y_1))^a < 0, \quad \text{for all } y \ge y_1. \tag{7}$$

Recall that a is the quotient of two positive odd integers. Then,

$$u'(y) \le \left(\frac{\varsigma(y_1)}{\varsigma(y)} \right)^{1/a} u'(y_1), \quad \text{for } y \ge y_1. \tag{8}$$

Integrating from y_2 to y, we have

$$u(y) \le u(y_1) + (\varsigma(y_1))^{1/a} u'(y_1) \Upsilon(y). \tag{9}$$

By (A3), the right-hand side approaches $-\infty$; then, $\lim_{y \to \infty} u(y) = -\infty$. This is a contradiction to the fact that $u(y) > 0$. Therefore, $\varsigma(y)(u'(y))^a > 0$ for all $y \ge y^*$. From $\varsigma(y)(u'(y))^a$ being nonincreasing, we have

$$u'(y) \le \left(\frac{\varsigma(y_1)}{\varsigma(y)} \right)^{1/a} u'(y_1), \quad \text{for } y \ge y_1. \tag{10}$$

Integrating this inequality from y_1 to y and using that u is continuous,

$$u(y) \le u(y_1) + (\varsigma(y_1))^{1/a} u'(y_1) \Upsilon(y). \tag{11}$$

Since $\lim_{y \to \infty} \Upsilon(y) = \infty$, there exists a positive constant d such that (4) holds.

Since $\varsigma(y)(u'(y))^a$ is positive and nonincreasing, $\lim_{y \to \infty} \varsigma(y)(u'(y))^a$ exists and is nonnegative. Integrating (1) from y to b, we have

$$\varsigma(b)(u'(b))^a - \varsigma(y)(u'(y))^a + \int_y^\infty p(\eta)u^c(\vartheta(\eta))d\eta = 0. \tag{12}$$

Letting limit as $b \to \infty$, we get

$$\varsigma(y)(u'(y))^a \ge \int_y^\infty p(\eta)u^c(\vartheta(\eta))d\eta. \tag{13}$$

Then,

$$u'(y) \ge \left[\frac{1}{\varsigma(y)} \int_y^\infty p(\eta)u^c(\vartheta(\eta))d\eta \right]^{1/a}. \tag{14}$$

Since $u(y_1) > 0$, integrating the above inequality yields

$$u(y) \ge \int_{y_1}^y \left[\frac{1}{\varsigma(\eta)} \int_\eta^\infty p(\zeta)u^c(\vartheta(\zeta))d\zeta \right]^{1/a} d\eta. \tag{15}$$

Since the integrand is positive, we can increase the lower limit of integration from η to y and then use the definition of $\Upsilon(y)$ to obtain

$$u(y) \ge \Upsilon(y) \left[\int_y^\infty p(\zeta)u^c(\vartheta(\zeta))d\zeta \right]^{1/a}, \tag{16}$$

which yields (5). □

Theorem 1. *Assume that there exists a constant b_1, the quotient of two positive odd integers, such that $0 < c < b_1 < a$.*

If (A1)–(A3) hold, then each solution of (1) is oscillatory if and only if

$$\int_0^\infty p(\zeta)\Upsilon^c(\vartheta(\zeta))d\zeta = \infty. \tag{17}$$

Proof. On the contrary, we assume that u is eventually positive solution. So, Lemma 1 holds, and then there exists $y_1 \ge y_0$ such that

$$u(y) \ge \Upsilon(y)w^{1/a}(y) \ge 0, \quad \text{for } y \ge y_1, \tag{18}$$

where

$$w(y) = \int_y^\infty p(\zeta)u^c(\vartheta(\zeta))d\zeta. \tag{19}$$

Computing the derivative of w, we have

$$w'(y) = -p(y)u^c(\vartheta(y)). \tag{20}$$

Thus, w is nonnegative and nonincreasing. Since $u > 0$, by (A2), it follows that $p(y)u^c(\vartheta(y))$ cannot be identically zero in any interval $[b,\infty)$; thus, w' cannot be identically zero, and w cannot be constant on any interval $[b,\infty)$. Therefore, $w(y) > 0$ for $y \ge y_1$. Computing the derivative, we have

$$\left(w^{1-b_1/a}(y)\right)' = \left(1 - \frac{b_1}{a}\right)w^{-b_1/a}(y)w'(y). \tag{21}$$

Integrating (21) from y_2 to y and using that $w > 0$, we have

$$w^{1-b_1/a}(y_2) \ge \left(1 - \frac{b_1}{a}\right)\left[-\int_{y_2}^y w^{-b_1/a}(\zeta)w'(\zeta)d\zeta\right]$$
$$= \left(1 - \frac{b_1}{a}\right)\left[\int_{y_2}^y w^{-b_1/a}(\zeta)\left(p(\zeta)u^c(\vartheta(\zeta))\right)d\zeta\right]. \tag{22}$$

Note that when u is continuous, Ωu is also continuous on $[0,\infty)$. If u is a fixed point of Ω, i.e., $\Omega u = u$, then u is a solution of (1).

First, we estimate $(\Omega u)(y)$ from below. By (A3), we have

$$(\Omega u)(y) \ge \int_{y_1}^y \left[\frac{1}{\varsigma(\eta)}\left[\frac{\kappa}{2} + 0\right]\right]^{1/a}d\eta = \left(\frac{\kappa}{2}\right)^{1/a}\Upsilon(y). \tag{29}$$

Now, we estimate $(\Omega u)(y)$ from above. For u in S, we have $u^c(\vartheta(\zeta)) \le (\kappa^{1/a}\Upsilon(\vartheta(\zeta)))^c$. Then, by (26),

Next, we find a lower bound for the right-hand side of (25), independent of the solution u. By (4) and (19), we have

$$u^c(y) = u^{c-b_1}(y)u^{b_1}(y) \ge (d\Upsilon(y))^{c-b_1}u^{b_1}(y)$$
$$\ge (d\Upsilon(y))^{c-b_1}\left(\Upsilon(y)w^{1/a}(y)\right)^{b_1} \tag{23}$$
$$= d^{c-b_1}\Upsilon^c(y)w^{b_1/a}(y), \quad \text{for } y \ge y_2.$$

Since w is nonincreasing, $b_1/a > 0$, and $\vartheta(\eta) < \eta$, it follows that

$$u^c(\vartheta(\eta)) \ge d^{c-b_1}\Upsilon^c(\vartheta(\eta))w^{b_1/a}(\vartheta(\eta))$$
$$\ge d^{c-b_1}\Upsilon^c(\vartheta(\eta))w^{b_1/a}(\eta). \tag{24}$$

Going back to (22), we have

$$w^{1-b_1/a}(y_2) \ge \left(1 - \frac{b_1}{a}\right)d^{c-b_1}\left[\int_{y_2}^y p(\eta)\Upsilon^c(\vartheta(\eta))d\eta\right]. \tag{25}$$

Since $(1 - b_1/a) > 0$, by (17) the right-hand side approaches $+\infty$ as $y \longrightarrow \infty$. This contradicts (25) and completes the proof of sufficiency for eventually positive solutions.

The eventually negative solution can be dealt similarly by introducing the variables $v = -u$.

Next, we show the necessity part by a contrapositive argument. If (17) does not hold, then for each $\kappa > 0$ there exists $y_1 \ge y_0$ such that

$$\int_\eta^\infty p(\zeta)\Upsilon^c(\vartheta(\zeta))d\zeta \le \frac{\kappa^{(1-c/a)}}{2}, \tag{26}$$

for all $\eta \ge y_1$. We define the set of continuous functions

$$S = \left\{u \in C([0,\infty)): \left(\frac{\kappa}{2}\right)^{1/a}\Upsilon(y) \le u(y) \le \kappa^{1/a}\Upsilon(y), \quad y \ge y_1\right\}. \tag{27}$$

We define an operator Ω on S by

$$(\Omega u)(y) = \begin{cases} 0, & \text{if } y \le y_1, \\ \int_{y_1}^y\left[\frac{1}{\varsigma(\eta)}\left[\frac{\kappa}{2} + \int_\eta^\infty p(\zeta)u^c(\vartheta(\zeta))d\zeta\right]\right]^{1/a}d\eta, & \text{if } y > y_1. \end{cases} \tag{28}$$

$$(\Omega u)(y) \le \int_{y_1}^y\left[\frac{1}{\varsigma(\eta)}\left[\frac{\kappa}{2} + \int_\eta^\infty p(\zeta)u^c(\vartheta(\zeta))d\zeta\right]\right]^{1/a}d\eta$$
$$\le \kappa^{1/a}\Upsilon(y). \tag{30}$$

Therefore, Ω maps S to S.

Next, we find a fixed point for Ω in S. Let us define a sequence of functions in S by the recurrence relation

$$v_0(y) = 0, \quad \text{for } y \geq y_0,$$

$$v_1(y) = (\Omega v_0)(y) = \begin{cases} 0, & \text{if } y < y_1, \\ \kappa^{1/a} \Upsilon(y), & \text{if } y \geq y_1, \end{cases} \tag{31}$$

$$v_{n+1}(y) = (\Omega v_n)(y), \quad \text{for } n \geq 1, \ y \geq y_1.$$

Note that for each fixed y, we have $v_1(y) \geq v_0(y)$. Using mathematical induction, we can show that $v_{n+1}(y) \geq v_n(y)$. Therefore, the sequence $\{v_n\}$ converges pointwise to a function v. Using the Lebesgue dominated convergence theorem, we can show that v is a fixed point of Ω in S. This shows under assumption (26), there is a nonoscillatory solution that does not converge to zero. This completes the proof. □

Theorem 2. *Assume that there exists a constant b_2, the quotient of two positive odd integers such that $0 < a < b_2 < c$. If (A1)–(A4) hold and $\varsigma(y)$ is nondecreasing, then each solution of (1) is oscillatory if and only if*

$$\int_{y_1}^{\infty} \left[\frac{1}{\varsigma(s)} \int_s^{\infty} p(\zeta) d\zeta \right]^{1/a} d\eta = \infty. \tag{32}$$

Proof. On the contrary, we assume that u is an eventually positive solution that does not converge to zero. Using the same argument as in Lemma 1, there exists $y_1 \geq y_0$ such that $u(\vartheta(y)) > 0$ and $\varsigma(y)(u'(y))^a$ is positive and nonincreasing. Since $\varsigma(y) > 0$, $u(y)$ is increasing for $y \geq y_1$. Using $u(y) \geq u(y_1)$, we have

$$u^c(y) \geq u^{c-b_2}(y) u^{b_2}(y) \geq u^{c-b_2}(y_1) u^{b_2}(y), \tag{33}$$

and hence

$$u^c(\vartheta(y)) \geq u^{c-b_2}(y_1) u^{b_2}(\vartheta(y)), \quad \text{for } y \geq y_2. \tag{34}$$

Using (34) and $\vartheta(y) \geq \vartheta_0(y)$, from (13), we have

$$\varsigma(y)(u'(y))^a \geq u^{c-b_2}(y_1) u^{b_2}(\vartheta_0(y)) \int_y^{\infty} p(\eta) d\eta, \tag{35}$$

for $y \geq y_2$. From $\varsigma(y)(u'(y))^a$ being nonincreasing and $\vartheta_0(y) \leq y$, we have

$$\varsigma(\vartheta_0(y))(u'(\vartheta_0(y)))^a \geq \varsigma(y)(u'(y))^a. \tag{36}$$

We use this in the left-hand side of (35). Then, dividing by $\varsigma(\vartheta_0(y)) u^{b_2}(\vartheta_0(y)) > 0$ and raising both sides to the $1/a$ power, we have

$$\frac{u'(\vartheta_0((y)))}{u^{b_2/a}(\vartheta_0(y))} \geq \left[\frac{u^{c-b_2}(y_1)}{\varsigma(\vartheta_0(y))} \int_y^{\infty} p(\eta) d\eta \right]^{1/a}, \tag{37}$$

for $y \geq y_2$. Multiplying the left-hand side by $\vartheta_0'(y)/\vartheta_0 \geq 1$ and integrating from y_2 to y, we have

$$\frac{1}{\vartheta_0} \int_{y_2}^{y} \frac{u'(\vartheta_0(\eta)) \vartheta_0'(\eta)}{u^{b_2/a}(\vartheta_0(\eta))} d\eta$$

$$\geq u^{c-b_2}(y_1) \int_{y_2}^{y} \left[\frac{1}{\varsigma(\vartheta_0(\eta))} \int_{\eta}^{\infty} p(\zeta) d\zeta \right]^{1/a} d\eta. \tag{38}$$

On the left-hand side, since $a < b_2$, integrating, we have

$$\frac{1}{\alpha(1 - b_2/a)} \left[z^{1-b_2/a}(\vartheta_0(\eta)) \right]_{s=y_2}^{y}$$

$$\leq \frac{1}{\alpha(b_2/a - 1)} z^{1-b_2/a}(\vartheta_0(y_2)) < \infty. \tag{39}$$

On the right-hand side of (38), we use that $\varsigma(\vartheta_0(\eta)) \leq \varsigma(\eta)$ to conclude that (32) implies the right-hand side approaching $+\infty$, as $y \longrightarrow \infty$, which is a contradiction. Hence, the solution u cannot be eventually positive.

For eventually negative solutions, we use the same change of variables as in Theorem 1 and proceed as above.

To prove the necessity part, we assume that (32) does not hold and obtain an eventually positive solution that does not converge to zero. If (32) does not hold, then for each $\kappa > 0$ there exists $y_1 \geq y_0$ such that

$$\int_{y_1}^{\infty} \left[\frac{1}{\varsigma(\eta)} \int_{\eta}^{\infty} p(\zeta) d\zeta \right]^{1/a} d\eta \frac{\kappa^{(1-c/a)}}{2}, \quad \forall y \geq y_1. \tag{40}$$

We define the set of continuous function

$$S = \left\{ u \in C([0, \infty)): \frac{\kappa}{2} \leq u(y) \leq \kappa \text{ for } y \geq y_1 \right\}. \tag{41}$$

Then, we define the operator

$$(\Omega u)(y) = \begin{cases} 0, & \text{if } y \leq y_1, \\ \frac{\kappa}{2} + \int_{y_1}^{y} \frac{1}{\varsigma(\eta)} \left[\int_{\eta}^{\infty} p(\zeta) u^c(\vartheta(\zeta)) d\zeta \right]^{1/a} d\eta, & \text{if } y > y_1. \end{cases} \tag{42}$$

Note that if u is continuous, Ωu is also continuous at $y = y_1$. Also, note that if $\Omega u = u$, then u is solution of (1).

First, we estimate $(\Omega u)(y)$ from below. Let $u \in M$, we have $(\Omega u)(y) \geq \kappa/2 + 0$, on $[y_1, \infty)$.

Now, we estimate $(\Omega u)(y)$ from above. Let $u \in M$. Then, $u \leq \kappa$ and by (40), we have

$$(\Omega u)(y) \leq \frac{\kappa}{2} + \kappa^{c/a} \int_{y_1}^{y} \left[\frac{1}{\varsigma(\eta)} \int_{\eta}^{\infty} p(\zeta) d\zeta \right]^{1/a} d\eta$$

$$\leq \frac{\kappa}{2} + \frac{\kappa}{2} = \kappa. \tag{43}$$

Therefore, Ω maps S to S. To find a fixed point for Ω in S, we define a sequence of functions by the recurrence relation

$$
\begin{aligned}
v_0(y) &= 0, \quad \text{for } y \geq y_0, \\
v_1(y) &= (\Omega v_0)(y) = 1, \quad \text{for } y \geq y_1, \\
v_{n+1}(y) &= (\Omega v_n)(y), \quad \text{for } n \geq 1,\ y \geq y_1.
\end{aligned} \tag{44}
$$

Note that for each fixed y, we have $v_1(y) \geq v_0(y)$. Using mathematical induction, we can prove that $v_{n+1}(y) \geq v_n(y)$. Therefore, $\{v_n\}$ converges pointwise to a function v in S. Then, v is a fixed point of Ω and a positive solution of (1). The proof is completed. □

Example 1. Consider the differential equations

$$
\left(e^{-y}(u'(y))^{11/3}\right)' + \frac{1}{y+1}(u(y-2))^{1/3} = 0. \tag{45}
$$

Here, $a = 11/3$, $\varsigma(y) = e^{-y}$, $\vartheta_1(y) = y - 2$, $\Upsilon(y) = \int_{y_1}^{y} e^{11\eta/3}\mathrm{d}\eta = (3/11)(e^{11y/3} - e^{11y_1/3})$, and $c_1 = 1/3$. For $b = 7/3$, we have $0 < c < b < a$. To check (17), we have

$$
\begin{aligned}
&\int_0^\infty p(s)\Upsilon^c(\vartheta(s))\mathrm{d}s \\
&= \int_0^\infty \frac{1}{\eta+1}\left(\frac{3}{11}\left(e^{11(s-2)/3} - e^{11y_1/3}\right)\right)^{1/3}\mathrm{d}s = \infty.
\end{aligned} \tag{46}
$$

So, every conditions of Theorem 1 hold true, and therefore, all solutions of (45) are oscillatory or converge to zero.

Example 2. Consider the differential equations

$$
\left((u'(y))^{1/3}\right)' + y(u(y-2))^{7/3} = 0. \tag{47}
$$

Here, $a = 1/3$, $\varsigma(y) = 1$, $\vartheta_1(y) = y - 2$, and $c_1 = 7/3$. For $b = 5/3$, we have $c > b > a$. To check (32), we have

$$
\int_{y_0}^\infty \left[\frac{1}{\varsigma(s)}\int_s^\infty p(\zeta)\mathrm{d}\zeta\right]^{1/a}\mathrm{d}s = \int_2^\infty \left[\int_s^\infty \zeta\mathrm{d}\zeta\right]^3 \mathrm{d}s = \infty. \tag{48}
$$

So, every conditions of Theorem 2 hold true. Thus, all solutions of (47) are oscillatory or converge to zero.

3. Conclusion

The aim of this work is to establish necessary and sufficient conditions for the oscillation of solution to second-order half-linear differential equation. The obtained oscillation theorems complement the well-known oscillation results present in the literature. This work, as well as [31–41], leads us to pose an open problem: Can we find necessary and sufficient conditions for the oscillation of solutions to second-order differential equation

$$
\left[r(t)\left(\left(y(t) + p(t)y(\tau(t))\right)'\right)^\gamma\right]' + \sum_{i=1}^m q_i(t)y^{\alpha_i}(\tau_i(t)) = 0,
$$

$$
\text{for } p \in C(\mathbb{R}_+, \mathbb{R})?. \tag{49}
$$

Data Availability

No data were used to support the findings of this study.

Conflicts of Interest

The authors declare that they have no conflicts of interest.

Acknowledgments

References

[1] H. Ahmad, T. A. Khan, P. S. Stanimirovic et al., "Modified variational iteration technique for the numerical solution of fifth order KdV type equations," *Journal of Applied and Computational Mechanics*, vol. 6, pp. 1220–1227, 2020.

[2] F. Mebarek-Oudina, "Convective heat transfer of titania nanofluids of different base fluids in cylindrical annulus with discrete heat source," *Heat Transfer-Asian Research*, vol. 48, no. 1, pp. 135–147, 2019.

[3] H. Ahmad, A. Akgül, T. A. Khan, P. S. Stanimirović, and Y.-M. Chu, "New perspective on the conventional solutions of the nonlinear time-fractional partial differential equations," *Complexity*, vol. 2020, p. 1, Article ID 8829017, 2020.

[4] M. Farhan, Z. Omar, F. Mebarek-Oudina et al., "Implementation of the one-step one-hybrid block method on the nonlinear equation of a circular sector oscillator," *Computational Mathematics and Modeling*, vol. 31, no. 1, pp. 116–132, 2020.

[5] M. Srivastava, H. Ahmad, I. Ahmad, P. Thounthong, and N. Khan, "Numerical simulation of three-dimensional fractional-order convection-diffusion PDEs by a local meshless method," *Thermal Science*, p. 210, 2020.

[6] I. Ahmad, H. Ahmad, A. E. Abouelregal et al., "Numerical study of integer-order hyperbolic telegraph model arising in physical and related sciences," *The European Physical Journal Plus*, vol. 135, pp. 1–14, 2020.

[7] P. Thounthong, M. Khan, I. Hussain, I. Ahmad, and P. Kumam, "Symmetric radial basis function method for simulation of elliptic partial differential equations," *Mathematics*, vol. 6, no. 12, p. 327, 2018.

[8] H. Ahmad, T. A. Khan, P. S. Stanimirović, Y.-M. Chu, and I. Ahmad, "Modified variational iteration algorithm-II: convergence and applications to diffusion models," *Complexity*, vol. 2020, Article ID 8841718, 14 pages, 2020.

[9] S. Hamrelaine, F. Mebarek-Oudina, and M. R. Sari, "Analysis of MHD Jeffery Hamel flow with suction/injection by homotopy analysis method," *Journal of Advanced Research in Fluid Mechanics and Thermal Sciences*, vol. 58, pp. 173–186, 2019.

[10] F. Mebarek-Oudina, N. Keerthi Reddy, and M. Sankar, "Heat source location effects on buoyant convection of nanofluids in an annulus," *Advances in Fluid Dynamics*, pp. 923–937, 2021.

[11] I. Ahmad, M. N. Khan, M. Inc, H. Ahmad, and K. S. Nisar, "Numerical simulation of simulate an anomalous solute transport model via local meshless method," *Alexandria Engineering Journal*, vol. 59, no. 4, pp. 2827–2838, 2020.

[12] M. Inc, M. N. Khan, I. Ahmad, S.-W. Yao, H. Ahmad, and P. Thounthong, "Analysing time-fractional exotic options via

efficient local meshless method," *Results in Physics*, vol. 19, p. 103385, 2020.

[13] A. Yokus, H. Durur, H. Ahmad, P. Thounthong, and Y.-F. Zhang, "Construction of exact traveling wave solutions of the Bogoyavlenskii equation by $(G'/G, 1/G)$-expansion and $(1/G')$-expansion techniques," *Results in Physics*, vol. 19, p. 103409, 2020.

[14] S. Abdel-khalek, A. Alhag, S. M. Abo-Dahab et al., "Atomic Fisher information and entanglement forecasting for quantum system based on artificial neural network and time series model," *International Journal of Quantum Chemistry*, p. e26446, 2020.

[15] I. Ahmad, H. Ahmad, P. Thounthong, Y.-M. Chu, and C. Cesarano, "Solution of multi-term time-fractional PDE models arising in mathematical biology and physics by local meshless method," *Symmetry*, vol. 12, no. 7, p. 1195, 2020.

[16] J. Hale, *Theory of Functional Differential Equations*p. 1, 2nd edition, Springer-Verlag, Berlin, Germany, 1977.

[17] S. B. Chen, S. Rashid, M. A. Noor, R. Ashraf, and Y. M. Chu, "A new approach on fractional calculus and probability density function," *AIMS Mathematics*, vol. 5, no. 6, 2020.

[18] F. Mebarek-Oudina, A. Aissa, B. Mahanthesh, and H. F. Öztop, "Heat transport of magnetized Newtonian nanoliquids in an annular space between porous vertical cylinders with discrete heat source," *International Communications in Heat and Mass Transfer*, vol. 117, p. 104737, 2020.

[19] S. Rashid, D. Baleanu, and Y. M. Chu, "Some new extensions for fractional integral operator having exponential in the kernel and their applications in physical systems," *Open Physics*, vol. 18, pp. 478–549, 2020.

[20] S. Rashid, H. Ahmad, A. Khalid, and Y.-M. Chu, "On discrete fractional integral inequalities for a class of functions," *Complexity*, vol. 2020, Article ID 8845867, 13 pages, 2020.

[21] H. Ahmad, T. A. Khan, I. Ahmad, P. S. Stanimirović, and Y.-M. Chu, "A new analyzing technique for nonlinear time fractional Cauchy reaction-diffusion model equations," *Results in Physics*, vol. 19, p. 103462, 2020.

[22] S.-S. Zhou, S. Rashid, S. Rashid et al., "New Hermite-Hadamard type inequalities for exponentially convex functions and applications," *AIMS Mathematics*, vol. 5, no. 6, pp. 6874–6901, 2020.

[23] O. Bazighifan, H. Ahmad, and S.-W. Yao, "New oscillation criteria for advanced differential equations of fourth order," *Mathematics*, vol. 8, no. 5, p. 728, 2020.

[24] H. G. Jile, S. Rashid, M. A. Noor, A. Suhail, and Y. M. Chu, "Some unified bounds for exponentially tgs-convex functions governed by conformable fractional operators," *AIMS Mathematics*, vol. 5, no. 6, pp. 6108–6123, 2020.

[25] B. Džurina and J. Dzurina, "Oscillation theorems for second order neutral differential equations," *Computers & Mathematics with Applications*, vol. 61, no. 1, pp. 94–99, 2011.

[26] J. Džurina, "Oscillation theorems for second-order advanced neutral differential equations," *Tatra Mountains Mathematical Publications*, vol. 48, pp. 61–71, 2011.

[27] B. Džurina and J. Dzurina, "Oscillation theorems for second-order nonlinear neutral differential equations," *Computers & Mathematics with Applications*, vol. 62, no. 12, pp. 4472–4478, 2011.

[28] M. Bohner, S. Grace, I. Jadlovská et al., "Oscillation criteria for second-order neutral delay differential equations," *Electronic Journal of Qualitative Theory of Differential Equations*, vol. 60, pp. 1–12, 2017.

[29] S. R. Grace, J. Džurina, I. Jadlovska, T. Li et al., "An improved approach for studying oscillation of second-order neutral delay differential equations," *Journal of Inequalities and Applications*, vol. 2018, p. 11, 2018.

[30] A. Ali, "Reproducing kernel Hilbert space method based on reproducing kernel functions for investigating boundary layer flow of a Powell–Eyring non-Newtonian fluid," *Journal of Taibah University for Science*, vol. 13, no. 1, pp. 858–863, 2019.

[31] B. Karpuz and S. S. Santra, "Oscillation theorems for second-order nonlinear delay differential equations of neutral type," *Hacettepe Journal of Mathematics and Statistics*, vol. 48, no. 3, pp. 633–643, 2019.

[32] G. E. Chatzarakis, J. Džurina, I. Jadlovská et al., "New oscillation criteria for second-order half-linear advanced differential equations," *Applied Mathematics and Computation*, vol. 347, pp. 404–416, 2019.

[33] J. Džurina, S. R. Grace, I. Jadlovska, T. Li et al., "Oscillation criteria for second-order Emden-Fowler delay differential equations with a sublinear neutral term," *Mathematische Nachrichten*, vol. 293, 2019.

[34] S. Pinelas and S. S. Santra, "Necessary and sufficient condition for oscillation of nonlinear neutral first-order differential equations with several delays," *Journal of Fixed Point Theory and Applications*, vol. 20, no. 27, pp. 1–13, 2018.

[35] S. Pinelas and S. S. Santra, "Necessary and sufficient conditions for oscillation of nonlinear first-order forced differential equations with several delays of neutral type," *Analysis*, vol. 39, no. 3, pp. 97–105, 2019.

[36] S. S. Santra, "Existence of positive solution and new oscillation criteria for nonlinear first-order neutral delay differential equations," *Differential Equations & Applications*, vol. 8, no. 1, pp. 33–51, 2016.

[37] S. S. Santra, "Oscillation analysis for nonlinear neutral differential equations of second-order with several delays," *Mathematica*, vol. 59, no. 1-2, pp. 111–123, 2017.

[38] S. S. Santra, "Oscillation analysis for nonlinear neutral differential equations of second-order with several delays and forcing term," *Mathematica*, vol. 61, no. 84, pp. 63–78, 2019.

[39] S. S. Santra, "Necessary and sufficient condition for the solutions of first-order neutral differential equations to be oscillatory or tend to zero," *Kyungpook Mathematical Journal*, vol. 59, pp. 73–82, 2019.

[40] S. S. Santra, "Necessary and sufficient condition for oscillatory and asymptotic behaviour of second-order functional differential equations," *Kragujevac Journal of Mathematics*, vol. 44, no. 3, pp. 459–473, 2020.

[41] S. S. Santra, "Necessary and sufficient conditions for oscillatory and asymptotic behaviour of solutions to second-order nonlinear neutral differential equations with several delays," *Tatra Mountains Mathematical Publications*, vol. 75, no. 1, pp. 121–134, 2020.

Research Article
The Stability Conditions for a Heavy Solid Motion

A. I. Ismail [1,2]

[1]*Mechanics Department, Faculty of Engineering and Islamic Architecture, Umm Al-Qura University, P. O. Box 5555, Makkah, Saudi Arabia*
[2]*Department of Mathematics, Faculty of Science, Tanta University, Tanta, P. O. Box 31527, Egypt*

Correspondence should be addressed to A. I. Ismail; aiismail@uqu.edu.sa

In this paper, the stability conditions for the rotary motion of a heavy solid about its fixed point are considered. The center of mass of the body is assumed to lie on the moving z-axis which is assumed to be the minor axis of the ellipsoid of inertia. The nonlinear equations of motion and their three first integrals are obtained when the principal moments of inertia are distributed as $I_1 < I_2 < I_3$. We construct a Lyapunov function L to investigate the stability conditions for this motion. We give a numerical example to illustrate the necessary and sufficient conditions for the stability of the body at certain moments of inertia. This problem has many important applications in different sciences.

1. Introduction

The problem of stability of a rotary motion of a heavy solid moving in a uniform gravity field or a rigid body moving in a Newtonian one is considered as one of the vital problems in the nonlinear dynamics. These problems were searched in the last half century. These problems are classified according to the bodies containing partially fluid or fully fluid or lie in attracting centers. In [1], the rotational motion about the center of mass for an asymmetric dynamic body with an aspheric cavity filled with liquid is studied. Numerical analysis for changing the kinetic momentum vector of the body was given. The extreme position for the stability of the axis of rotation of a body was obtained. A mass geometry solid of the Earth was attained. In [2], the authors studied the stability conditions of rotary motion for a heavy solid containing cavity filled fully or partially with a viscous fluid. The author in [3] considered the stability problem for a steady rotary motion of a gyro filled with liquid in a cavity. The author achieved the conditions of stability for this case of studied motion. The authors in [4] studied a branching for the stability of permanent rotatory motions of a rigid body filled with a viscous fluid. In [5], the stability problem of a permanent rotary motion of an asymmetric top about a fixed point under the influence of a central Newtonian force field

is considered for different cases. In [6], the evolution of the stability for the rotary motion of a planet containing a liquid core is considered. For some special cases of the orbiting motions for a planet, the stability conditions are obtained in [7]. The work of [8] gave the conditions for stability of a rotating unperturbed rigid body about a fixed point in different problems using the well-known energy first integral.

Moreover, the first integral related to energy was used in [8] for the aim of obtaining sufficient conditions of stability when the governing system of the body has not any perturbation. In [9], the authors evaluated the orbiting for a satellite containing a cavity filled with a viscous fluid. For both the uniform and the Newtonian force fields, the problems of stabilities of the orbiting bodies about fixed points are considered in some steady motion cases in [10]. In [11], the stability spin for a Lagrange top with linear oscillators is considered. In [12], the authors evaluated the plane periodic rotary motion stabilities of a symmetric rigid body moving about a fixed point when the principal moments of inertia $I_1 = I_2 = 2I_3$. The permanent orbiting stability problem of an asymmetric gyro is considered in [13] when the gyro moved under a Newtonian force field. In [14], the author considered the conditions of stability motion of a

rigid body rotating about the x-axis when $I_1 > I_2 > I_3$. He assumed a moment λ_1 about the x-axis and deduced the equations of motion. There are some new applications of nano-/microcomponents related to stability conditions in different application subjects that should be mentioned here. The applications such as the Chebyshev–Ritz technique for static stability and vibration analysis of nonlocal microstructure-dependent nanostructures are given by Ebrahimi et al. [15].

Our article is searching the conditions of stability of a nonperturbed coupled heavy solid rotating about a fixed point in a uniform field of gravity. The body is assumed to rotate about the minor z-axis of the ellipsoid of inertia with couple λ_3. We consider the body rotates with principal moments of inertia to satisfy the condition $I_1 < I_2 < I_3$. We use the three well-known first integral of the problem for finding the stability conditions using a modified definition of Lyapunov function L. A numerical example is considered to show the stability conditions for a certain case.

2. Definition of the Problem

In this section, we define the problem of the motion of a heavy solid rotating about the minor z-axis of the ellipsoid of inertia. Consider the coordinate frame $OXYZ$ is the fixed coordinate system in space and $Oxyz$ is the fixed system in the body. Let the body rotates with an angular velocity vector $\underline{\omega} = (\omega_1, \omega_2, \omega_3)$ to the system $Oxyz$. Assume the couple $\underline{\lambda} = (0, 0, \lambda_3)$ to the moving coordinate system $Oxyz$. Let the mass center of the body lies on the z-axis (see Figure 1), and the moments of inertia of the body satisfy the conditions:

$$I_1 < I_2 < I_3, \quad z_0 \neq 0, \tag{1}$$

where $(0, 0, z_0)$ is the position of the mass center for the origin.

Thus, the nonlinear system of equations of motion for this case and its first integrals are obtained as follows:

$$I_1\dot{\omega}_1 + (I_3 - I_2)\omega_2\omega_3 + \lambda_3\omega_2 = -mgz_0\gamma_2,$$
$$I_2\dot{\omega}_2 + (I_1 - I_3)\omega_3\omega_1 - \lambda_3\omega_1 = mgz_0\gamma_1, \tag{2}$$
$$I_3\dot{\omega}_3 + (I_2 - I_1)\omega_1\omega_2 = 0,$$

$$\dot{\gamma}_1 = \omega_3\gamma_2 - \omega_2\gamma_3,$$
$$\dot{\gamma}_2 = \omega_1\gamma_3 - \omega_3\gamma_1, \tag{3}$$
$$\dot{\gamma}_3 = \omega_2\gamma_1 - \omega_1\gamma_2,$$

$$I_1\omega_1^2 + I_2\omega_2^2 + I_3\omega_3^2 - 2mgz_o\gamma_3 = E_1,$$
$$I_1\omega_1\gamma_1 + I_2\omega_2\gamma_2 + (I_3\omega_3 + \lambda_3)\gamma_3 = H_1, \tag{4}$$
$$\gamma_1^2 + \gamma_2^2 + \gamma_3^2 = 1,$$

where the unit vector in the direction of the Z-axis is $\underline{\widehat{Z}} = (\gamma_1, \gamma_2, \gamma_3)$, m is the solid mass, g is the gravity acceleration, $\cdot \equiv d/dt$ is the differentiation to time, and E_1 and H_1 are the initial energy and momentum constants. Assuming that $mgz_0 = a$, equation (2) can be rewritten as follows:

$$I_1\dot{\omega}_1 = (I_2 - I_3)\omega_2\omega_3 - \lambda_3\omega_2 - a\gamma_2,$$
$$I_2\dot{\omega}_2 = (I_3 - I_1)\omega_3\omega_1 + \lambda_3\omega_1 + a\gamma_1, \tag{5}$$
$$I_3\dot{\omega}_3 = (I_1 - I_2)\omega_1\omega_2.$$

Assuming that the following special solutions satisfy the six nonlinear differential equations of motion (5) and (3),

$$\omega_1 = \omega_2 = \gamma_1 = \gamma_2 = \lambda_3 = 0,$$
$$\omega_3 = r = \text{const}, \tag{6}$$
$$\gamma_3 = 1.$$

This is a case of uniform rotation of the solid about the minor axis of the ellipsoid of inertia (z-axis).

3. Stability Investigation

In this section, the stability procedure of the unperturbed solid is investigated. Consider that the variables in (6) change according to

$$\omega_1 = \Gamma_1,$$
$$\omega_2 = \Gamma_2,$$
$$\omega_3 = r + \Gamma_3,$$
$$\gamma_1 = \xi_1, \tag{7}$$
$$\gamma_2 = \xi_2,$$
$$\gamma_3 = 1 + \xi_3.$$

Substituting the variables in (7) into the equations of motion (5) and (3), it gives

$$I_1\dot{\Gamma}_1 = (I_2 - I_3)\Gamma_2(r + \Gamma_3) - a\xi_2,$$
$$I_2\dot{\Gamma}_2 = (I_3 - I_1)(r + \Gamma_3)\Gamma_1 + a\xi_1,$$
$$I_3\dot{\Gamma}_3 = (I_1 - I_2)\Gamma_1\Gamma_2,$$
$$\dot{\xi}_1 = (r + \Gamma_3)\xi_2 - \Gamma_2(1 + \xi_3), \tag{8}$$
$$\dot{\xi}_2 = \Gamma_1(1 + \xi_3) - (r + \Gamma_3)\xi_1,$$
$$\dot{\xi}_3 = \Gamma_2\xi_1 - \Gamma_1\xi_2.$$

Substituting the variables in (7) into the first integrals (4), it gives

$$V_1 = I_1\Gamma_1^2 + I_2\Gamma_2^2 + I_3\Gamma_3^2 + 2I_3r\Gamma_3 - 2a\xi_3,$$
$$V_2 = I_1\Gamma_1\xi_1 + I_2\Gamma_2\xi_2 + I_3\Gamma_3\xi_3 + I_3r\xi_3, \tag{9}$$
$$V_3 = \xi_1^2 + \xi_2^2 + \xi_3^2 + 2\xi_3,$$

where V_1, V_2, and V_3 are constants.

We make a linear combination of the relations in (9) to satisfy the Lyapunov and Chetayev stability procedures. the Lyapunov function L is modified to be in the form:

$$L = V_1 - 2rV_2 + (I_3r^2 + a)V_3. \tag{10}$$

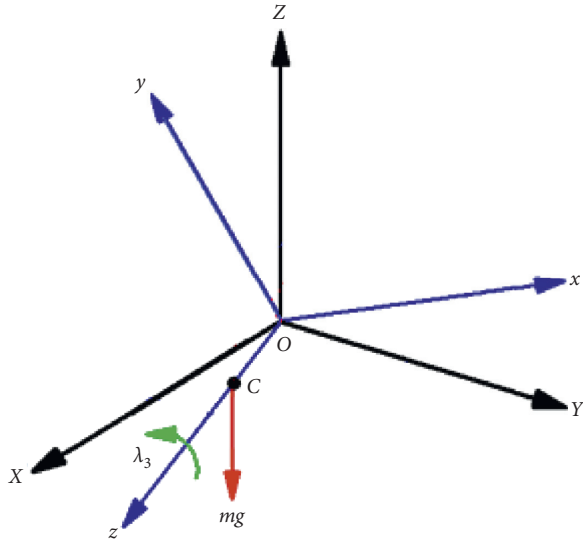Thus, using the relations in (9), we obtain

$$L = L_1 + L_2 + L_3, \tag{11}$$

FIGURE 1: Description of forces.

where

$$L_1 = I_1\Gamma_1^2 - 2I_1 r \Gamma_1 \xi_1 + (I_3 r^2 + a)\xi_1^2,$$
$$L_2 = I_2\Gamma_2^2 - 2I_2 r \Gamma_2 \xi_2 + (I_3 r^2 + a)\xi_2^2, \quad (12)$$
$$L_3 = I_3\Gamma_3^2 - 2I_3 r \Gamma_3 \xi_3 + (I_3 r^2 + a)\xi_3^2.$$

We deduce from the relations in (12) that $L_i > 0, i = 1, 2, 3$, if and only if the following inequalities are satisfied [14], respectively:

$$\begin{vmatrix} I_1 & -I_1 r \\ -I_1 r & (I_3 r^2 + a) \end{vmatrix} = I_1(I_3 r^2 + a) - I_1^2 r^2 > 0,$$

$$\begin{vmatrix} I_2 & -I_2 r \\ -I_2 r & (I_3 r^2 + a) \end{vmatrix} = I_2(I_3 r^2 + a) - I_2^2 r^2 > 0, \quad (13)$$

$$\begin{vmatrix} I_3 & -I_3 r \\ -I_3 r & (I_3 r^2 + a) \end{vmatrix} = I_3(I_3 r^2 + a) - I_3^2 r^2 = I_3 a > 0.$$

Thus, we obtain from the back substitution

$$a > 0,$$
$$I_3 > I_2, \quad (14)$$
$$I_3 > I_1.$$

We note that when condition (1) is satisfied, inequalities (13) and (14) are investigated automatically.

Thus, the conditions in (13) considered the sufficient and necessary conditions for the unperturbed stability motion of the solid concerning the variables $\omega_1, \omega_2, \omega_3, \gamma_1, \gamma_2,$ and γ_3.

4. A Simple Application Example

A simple application example can be given in this section. Just formulation the sufficient and necessary conditions for the unperturbed stability motion are studied.

Consider a rigid body of mass M with moments of inertia as follows:

$$\begin{aligned} I_1 &= 10 \,\text{kg.m}^2, \\ I_2 &= 15 \,\text{kg.m}^2, \\ I_3 &= 20 \,\text{kg.m}^2, \\ M &= 100 \,\text{kg}, \quad (15) \\ g &= 9.81 \,\text{m.s}^{-2}, \\ z_o &= 50 \,\text{m}, \\ r &= 10 \,\text{rad.s}^{-1}. \end{aligned}$$

From (15), we deduce that

$$\begin{aligned} a &= 49050 \,\text{kgm}^2.\text{s}^{-2}, \\ (I_3 r^2 + a) &= 51050. \end{aligned} \quad (16)$$

From (13), (14), and (15), we deduce that

$$\begin{aligned} I_1(I_3 r^2 + a) - I_1^2 r^2 &= 500500 > 0, \\ I_2(I_3 r^2 + a) - I_2^2 r^2 &= 743250 > 0, \quad (17) \\ I_3 a &= 981000 > 0. \end{aligned}$$

From this example, we deduce that if condition (1) is satisfied by (15), $L_i > 0, i = 1, 2, 3$, is satisfied if and only if relation (17) is satisfied.

5. Conclusion

The necessary and sufficient conditions for the stability of the rotary motion of a solid about a fixed point are considered when the center of mass of the body lies on the minor z-axis of the ellipsoid of inertia. The system of equations of motion and their first integrals are obtained. The modified Lyapunov function L is constructed depending on the three first integrals. The necessary and sufficient conditions are constructed in the case $I_3 > I_2 > I_1$ that the x-axis is the major axis of the ellipsoid of inertia and the y-axis is the intermediate axis while the z-axis is the minor one. The moments of inertia I_i, $i = 1, 2, 3$ are assumed as arbitrary constants that satisfy the above condition, and λ_3 is estimated by substituting (7) into the second equation from (4). This problem has wide applications in satellite motions which assumed moments of inertia according to the above relations [16–18]. A numerical example is given to show the stability conditions for a special case.

Data Availability

Data sharing not applicable to this article as no datasets were generated or analyzed during the current study.

Conflicts of Interest

The author declares he has no conflicts of interest.

References

[1] A. L. Rachinskaya, "Motion of a solid body with cavity filled with viscous liquid," *Cosmic Research*, vol. 53, no. 6, pp. 476–480, 2015.

[2] V. Z. Osipov and R. S. Sulikashvili, "Oscillation of a solid body with a spherical cavity filled fully with a viscous fluid on an elliptic orbit," *Trudy Tbilis*, vol. 58, pp. 175–186, 1978.

[3] F. L. Chernous'ko, Motion of a Solid Body with Cavities Filled with a Viscous Fluid, VTs ANSSSR, Moscow, Russia, 1968.

[4] F. L. Chernous'ko, "Motion of a solid with cavities filled with a viscous fluid at small Reynolds numbers," *Zh Vychisl Mat Fiz*, vol. 5, no. 6, pp. 1049–1070, 1965.

[5] E. P. Smirnova, "Stabilization of the free rotation of an asymmetric top with a cavity filled fully with a viscous fluid," *Prikl Mat Mekh*, vol. 33, no. 6, pp. 980–985, 1974.

[6] V. V. Sidorenko, "Evolution of rotational motion of a planet with a liquid core," *Astron Vestn*, vol. 27, no. 2, pp. 119–127, 1993.

[7] V. G. Vil'ke and A. V. Shatina, "Evolution of a rotating satellite with a cavity filled with a viscous fluid," *Kosm Issled*, vol. 31, no. 6, pp. 22–30, 1993.

[8] N. S. Sidorenkov, *Physics of the Earth's Rotation Instabilities*, Nauka/Fizmatlit, Moscow, Russia, 2002.

[9] L. D. Akulenko, D. D. Leshchenko, and A. L. Rachinskaya, "Evolution of rotations of a satellite with a cavity filled with a viscous fluid," *Mekh. Tverd. Tela*, vol. 37, pp. 126–139, 2007.

[10] Y. V. Abrarova, "The stability of the steady motions of a rigid body in a central field," *Journal of Applied Mathematics and Mechanics*, vol. 59, no. 6, pp. 903–910, 1995.

[11] Y. N. Kononov, "Spin stability of a Lagrange top containing linear oscillators," *Journal of Mathematical Sciences*, vol. 103, no. 1, pp. 38–42, 2001.

[12] B. S. Bardin and A. A. Savin, "The stability of the plane periodic motions of a symmetrical rigid body with a fixed point," *Journal of Applied Mathematics and Mechanics*, vol. 77, no. 6, pp. 578–587, 2013.

[13] M. Iñarrea, V. Lanchares, A. I. Pascual, and A. Elipe, "Stability of the permanent rotations of an asymmetric gyrostat in a uniform Newtonian field," *Applied Mathematics and Computation*, vol. 293, pp. 404–415, 2017.

[14] W. S. Amer, "The necessary and sufficient condition for the stability of a rigid body," *Journal of Advances in Physics*, vol. 13, no. 6, pp. 4999–5003, 2017.

[15] F. Ebrahimi, M. R. Barati, and O. Civalek, "Application of Chebyshev–Ritz method for static stability and vibration analysis of nonlocal microstructure-dependent nanostructures," *Engineering with Computers*, vol. 36, no. 3, pp. 953–964, 2020.

[16] L. D. Akulenko, D. D. Leshchenko, and A. L. Rachinskaya, "Evolution of the satellite fast rotation due to the gravitational torque in a dragging medium," *Mechanics of Solids*, vol. 43, no. 2, pp. 173–184, 2008.

[17] L. D. Akulenko, Y. S. Zinkevich, D. D. Leshchenko, and A. L. Rachinskaya, "Rapid rotations of a satellite with a cavity filled with viscous fluid under the action of moments of gravity and light pressure forces," *Cosmic Research*, vol. 49, no. 5, pp. 440–451, 2011.

[18] A. L. Rachinskaya and A. N. Dutsa, "Evolution of fast rotations of a satellite due to perturbation torques," *Visnik Odes'k. NATS*, vol. 17, pp. 175–184, 2012.

Research Article

Existence and Uniqueness of Uncertain Fractional Backward Difference Equations of Riemann–Liouville Type

Pshtiwan Othman Mohammed [ID],[1] **Thabet Abdeljawad** [ID],[2,3,4] **Fahd Jarad** [ID],[5] **and Yu-Ming Chu** [ID][6,7]

[1]*Department of Mathematics, College of Education, University of Sulaimani, Kurdistan Region, Sulaimani, Iraq*
[2]*Department of Mathematics and General Sciences, Prince Sultan University, P.O. Box 66833, Riyadh 11586, Saudi Arabia*
[3]*Department of Medical Research, China Medical University, Taichung 40402, Taiwan*
[4]*Department of Computer Science and Information Engineering, Asia University, Taichung, Taiwan*
[5]*Department of Mathematics, Cankaya University, Etimesgut, Ankara 06790, Turkey*
[6]*Department of Mathematics, Huzhou University, Huzhou 313000, China*
[7]*Hunan Provincial Key Laboratory of Mathematical Modeling and Analysis in Engineering,*
 Changsha University of Science & Technology, Changsha 410114, China

Correspondence should be addressed to Thabet Abdeljawad; tabdeljawad@psu.edu.sa and Yu-Ming Chu; chuyuming@zjhu.edu.cn

In this article, we consider the analytic solutions of the uncertain fractional backward difference equations in the sense of Riemann–Liouville fractional operators which are solved by using the Picard successive iteration method. Also, we consider the existence and uniqueness theorem of the solution to an uncertain fractional backward difference equation via the Banach contraction fixed-point theorem under the conditions of Lipschitz constant and linear combination growth. Finally, we point out some examples to confirm the validity of the existence and uniqueness of the solution.

1. Introduction

Fractional calculus is based on an old idea that has become important and popular in applications only recently. The idea is to generalize integration and differentiation to noninteger orders in order to develop and extend the theory of calculus and to describe a more extensive range of possible doings in reality. During the past decades, fractional differential equations have been widely employed in many fields: mathematical analysis, optics and thermal systems, control engineering, and robotics, see, for example, [1–9].

In recent years, uncertain fractional differential and difference equations and discrete difference equations have become popular in both theory and applications. These represent a new area for researchers which was developed slowly in their early stages. By using modeling techniques with discrete fractional calculus, some researchers established the existence, uniqueness, monotonicity, multiplicity, and qualitative properties of solutions to uncertain fractional difference equations (UFDEs) in the sense of Riemann–Liouville, Caputo, and AB operators; for further details, see [10–22] and the references cited therein.

The aim of this attempt is to investigate the existence and uniqueness of fractional difference equations in the sense of Riemann–Liouville-like difference operator with assuming Lipschitz condition on its nonlinear term. Our findings are partial continuation of some results obtained in [23–25]. It is worth mentioning that the uncertainty theory of fractional difference equations is used to make the problems have a unique solution almost surely.

2. Preliminaries

This section presents some preliminaries, definitions, and facts in the field of uncertainty theory and discrete fractional calculus, see, e.g., [12, 26–28]. Throughout the article, we consider $\mathbb{N}_a = \{a, a+1, a+2, \ldots\}$ for $a \in \mathbb{R}$ and the backward jump operator $\rho(r) := r - 1$ for $r \in \mathbb{N}_a$.

Definition 1 (see [26]). For any function $f: \mathbb{N}_a \longrightarrow \mathbb{R}$, the backward difference operator is defined by

$$\nabla f(t) = f(t) - f(\rho(t)), \quad t \in \mathbb{N}_a, \tag{1}$$

while the backward sum is given by

$$\nabla_a^{-1} f(t) = \sum_{r=a+1}^{t} f(r), \quad t \in \mathbb{N}_{a+1}. \tag{2}$$

Definition 2 (see [26–29]). For any natural number j, the ∇-rising factorial function of t is defined by

$$t^{\overline{j}} = \prod_{\ell=0}^{j-1} (t + \ell), \quad t^{\overline{0}} = 1. \tag{3}$$

Moreover, for any $\nu \in \mathbb{R}$, the ∇-rising factorial function is defined by

$$t^{\overline{\nu}} = \frac{\Gamma(t + \nu)}{\Gamma(t)}, \quad 0^{\overline{\nu}} = 0, \tag{4}$$

for $t \in \mathbb{R} \setminus \{\ldots, -2, -1, 0\}$. Also, note that the division by negative integer poles of the gamma function gives zero.

A major property of the rising factorial function is as follows:

$$\nabla\left(t^{\overline{\nu}}\right) = \nu t^{\overline{\nu-1}}. \tag{5}$$

This implies that $t^{\overline{\nu}}$ is increasing on $\mathbb{N}_0$ such that $\nu > 0$.

Definition 3 (see [13, 14, 26–29]). For any function $f: \mathbb{N}_a \longrightarrow \mathbb{R}$, the nabla fractional sum of order $\nu > 0$ in the sense of Riemann–Liouville is defined by

$$\left(\nabla_a^{-\nu} f\right)(t) = \frac{1}{\Gamma(\nu)} \sum_{r=a+1}^{t} (t - \rho(r))^{\overline{\nu-1}} f(r),$$

$$\left(\nabla_a^{0} f\right)(t) = f(t). \tag{6}$$

Lemma 1 (see [13, 14, 26–28]). *For any function f defined on $\mathbb{N}_a$ and any $\nu, \alpha > 0$, we have*

$$\left(\nabla_a^{-\nu} \nabla_a^{-\alpha} f\right)(t) = \left(\nabla_a^{-(\alpha+\nu)} f\right)(t) = \left(\nabla_a^{-\alpha} \nabla_a^{-\nu} f\right)(t). \tag{7}$$

Lemma 2 (see [13, 14, 26–28]). *For any function f defined on $\mathbb{N}_a$ and any $\nu > 0$, we have*

$$\left(\nabla_a^{\nu} f\right)(t) = \left(\nabla \nabla_a^{-(1-\nu)} f\right)(t). \tag{8}$$

Lemma 3 (see [13, 14, 26–28]). *For any function f defined on $\mathbb{N}_a$ and any $\nu > 0$, we have*

$$\left(\nabla_a^{-\nu} \nabla f\right)(t) = \left(\nabla \nabla_a^{-\nu} f\right)(t) - \frac{(t-a)^{\overline{\nu-1}}}{\Gamma(\nu)} f(a). \tag{9}$$

Lemma 4 (see [13, 14, 26–28]). *For any function f defined on $\mathbb{N}_a$ and any $\nu > 0$, we have*

$$\left(\nabla_a^{-\nu} \nabla^{\nu} f\right)(t) = \left(\nabla_a^{\nu} \nabla^{-\nu} f\right)(t) = f(t), \quad \nu \notin \mathbb{N},$$

$$\left(\nabla_a^{-\nu} \nabla^{\nu} f\right)(t) = f(t) - \sum_{k=0}^{\nu-1} \frac{(t-a)^{\overline{k}}}{k!} \nabla^k f(a), \quad \nu \in \mathbb{N}. \tag{10}$$

Lemma 5 (see [13, 14, 26–28]). *For any $a \in \mathbb{R}$ and $\nu, \alpha > 0$, we have*

$$\nabla_a^{-\nu} (t-a)^{\overline{\alpha}} = \frac{\Gamma(\alpha+1)}{\Gamma(\alpha+\nu+1)} (t-a)^{\overline{\alpha+\nu}}. \tag{11}$$

Motivated by the definition of the nth-order backward sum for uncertain sequence ξ_t, we define the νth-order backward sum for uncertain sequence ξ_t as follows:

Definition 4 (see [13, 14, 28]). Let $\nu > 0$, $a \in \mathbb{R}$, and ξ_t be an uncertain sequence indexed by $t \in \mathbb{N}_a$. Then, we have

$$\nabla_a^{-\nu} \xi_t = \frac{1}{\Gamma(\nu)} \sum_{r=a+1}^{t} (t - \rho(r))^{\overline{\nu-1}} \xi_r, \tag{12}$$

which is called the νth-order backward fractional sum of uncertain sequence ξ_t.

Definition 5 (see [13, 14, 28]). For any $\nu > 0$, the fractional Riemann–Liouville-like backward difference for uncertain sequence ξ_t is defined by

$$\nabla_a^{\nu} \xi_t = \nabla_a\left(\nabla_a^{-(1-\nu)} \xi_t\right). \tag{13}$$

Next, we recall the definition of nabla discrete Mittag-Leffler (ML).

Definition 6 (see [28]). For any $\lambda \in \mathbb{R}$ and $\nu, \mu, \eta \in \mathbb{C}$ with $\operatorname{Re}(\nu) > 0$, the two-parameter discrete ML function is defined by

$$E_{\overline{\nu, \mu}}(\lambda, \eta) := \sum_{\ell=0}^{\infty} \lambda^{\ell} \frac{\eta^{\overline{\ell\nu+\mu-1}}}{\Gamma(\ell\nu+\mu)}, \quad |\lambda| < 1. \tag{14}$$

Particularly, if $\mu = 1$, we get the one-parameter discrete ML function:

$$E_{\overline{\nu}}(\lambda, \eta) := \sum_{\ell=0}^{\infty} \lambda^{\ell} \frac{\eta^{\overline{\ell\nu}}}{\Gamma(\ell\nu+1)}, \quad |\lambda| < 1. \tag{15}$$

3. UFBDE and Existence and Uniqueness Theorem

First, we recall the inverse uncertainty distribution theory.

Definition 7. (see [11]). An uncertainty distribution Ψ is called regular if it is a continuous and strictly increasing function and satisfies

$$\lim_{x \longrightarrow -\infty} \Psi(x) = 0,$$
$$\lim_{x \longrightarrow +\infty} \Psi(x) = 1. \tag{16}$$

Definition 8. (see [11]). Let ξ be an uncertain variable with a regular uncertainty distribution Ψ. Then, the inverse function Ψ^{-1} is called the inverse uncertainty distribution of ξ.

Example 1. From Definition 8, we deduce that the following:

(i) The inverse uncertainty distribution of a linear uncertain variable $\mathscr{L}(a, b)$ is given by

$$\Psi^{-1}(\alpha) = (1 - \alpha)a + \alpha b. \tag{17}$$

(ii) The inverse uncertainty distribution of a normal uncertain variable $\mathscr{L}(e, \sigma)$ is given by

$$\Psi^{-1}(\alpha) = e + \frac{\sqrt{3}\sigma}{\pi} \ln\left(\frac{\alpha}{1 - \alpha}\right). \tag{18}$$

(iii) The inverse uncertainty distribution of a normal uncertain variable $\mathscr{LOGN}(e, \sigma)$ is given by

$$\Psi^{-1}(\alpha) = \exp(e) + \left(\frac{\alpha}{1 - \alpha}\right)^{(\sqrt{3} \, \sigma/\pi)}. \tag{19}$$

Definition 9. (see [11]). We say that an uncertain variable ξ is symmetrical if

$$\Psi(x) + \Psi(-x) = 1, \tag{20}$$

where $\Psi(x)$ is a regular uncertainty distribution of ξ.

Remark 1. From Definition 9, we can deduce that the symmetrical uncertain variable has the inverse uncertainty distribution $\Psi^{-1}(\alpha)$ that satiates

$$\Psi^{-1}(\alpha) + \Psi^{-1}(1 - \alpha) = 0. \tag{21}$$

Example 2. From Definition 9, we deduce that the following:

(1) The linear uncertain variable $\mathscr{L}(-a, a)$ is symmetrical for any positive real number a

(2) The normal uncertain variable $\mathscr{L}(0, 1)$ is symmetrical

Definition 10. (see [11]; i.i.d. definition). In statistics and probability theory, a collection of random variables $\xi_i s$ is independent and identically distributed (or briefly, i.i.d.) if each random variable ξ_i has the same probability distribution as the others and all are mutually independent.

Then, we state the definition of the UFBDE.

Definition 11. An uncertain fractional difference equation is a fractional difference equation which is driven by an uncertain sequence. Moreover, an uncertain fractional backward difference equation for the Riemann–Liouville type is the uncertain fractional difference equation with Riemann–Liouville-like backward difference.

Consider the following generalized Riemann–Liouville fractional difference equation:

$$\left(\nabla_{\alpha-1}^{\alpha} y\right)(t) = G(t, y(t)) + H(t, y(t))\xi_t, \tag{22}$$

subject to the initial condition (i.c.)

$$\left(\nabla_{\alpha-1}^{-(1-\alpha)} y\right)(t)\big|_{t=\alpha} = y(\alpha), \tag{23}$$

where $\nabla_{\alpha-1}^{\alpha}$ denotes fractional Riemann–Liouville-like backward difference with $0 < \alpha < 1$, G, H are two real-valued functions defined on $[1, \infty] \times \mathbb{R}$, $t \in \mathbb{N}_1 \cap [1, T+1]$, $y(\alpha) \in \mathbb{R}$ is a crisp number, and $\xi_1, \xi_2, \ldots, \xi_{T+1}$ are $(T+1)$-i.i.d. uncertain variables with symmetrical uncertainty distribution $\mathscr{L}(a, b)$.

Remark 2. Observe that the i.i.d. uncertain variables are those uncertain variables that are independent and have the same uncertainty distribution. See [11] for more detail.

Lemma 6. *Initial value problem (22) with i.c. (23) is equivalent to the following uncertain fractional sum equation:*

$$y(t) = \frac{(t - \alpha + 1)^{\overline{\alpha-1}}}{\Gamma(\alpha)} y(\alpha)$$
$$+ \frac{1}{\Gamma(\alpha)} \sum_{r=\alpha+1}^{t} (t - \rho(r))^{\overline{\alpha-1}} [G(r, y(r)) + H(r, y(r))\xi_r], \tag{24}$$

for $t \in \mathbb{N}_{\alpha+1} \cap [1, T+1]$.

Proof. The proof is very similar to [29], Lemma 5.1, and [30], Theorem 2, hereby applying the operator $\nabla_{\alpha}^{-\alpha}$ to IVP (22) with Definition 3, Lemma 2, and Lemma 3, so we omit this.

In this paper, the following special linear UFBDE will be considered:

$$\nabla_{\alpha-1}^{\alpha} y(t) = \lambda y(t) + \lambda \xi_t, \tag{25}$$

$$\nabla_{\alpha-1}^{-(1-\alpha)} y(t)\big|_{t=\alpha} = y(\alpha), \tag{26}$$

for $t \in \mathbb{N}_1 \cap [1, T+1]$, $n \in \mathbb{N}_1$, and $\lambda \in (0, 1)$. $\qquad\square$

Remark 3. The following identity is useful in proving the upcoming theorem. From Definition 3 and Lemma 5, we can deduce for any real number a

$$\nabla_a^{-\alpha}(t - a + 1)^{\overline{\beta}} = \frac{\Gamma(\beta + 1)}{\Gamma(\alpha + \beta + 1)}(t - a + 1)^{\overline{\alpha + \beta}}$$

$$- \frac{\Gamma(\beta + 1)}{\Gamma(\alpha)}(t - a + 1)^{\overline{\alpha - 1}}, \tag{27}$$

where $\alpha > 0$ and $\beta > -1$.

Theorem 1. *For any $t \in \mathbb{N}_{\alpha+1} \cap [1, T + 1]$ and $|\lambda| < 1$, linear UFBDE (25) with the initial condition (26) has a solution*

$$y(t) = (1 - \lambda)E_{\overline{\alpha,\alpha}}(\lambda, t - \alpha + 1)y(\alpha) + \xi_t, \tag{28}$$

where ξ_t is an uncertain sequence with the uncertainty distribution $\mathcal{L}(a \cdot \lambda E_{\overline{\alpha,\alpha+1}}(\lambda, t - \alpha), b \cdot \lambda E_{\overline{\alpha,\alpha+1}}(\lambda, t - \alpha))$.

Proof. Applying the operator $\nabla_\alpha^{-\alpha}$ to equation (25), we get

$$\nabla_\alpha^{-\alpha}\left(\nabla_{\alpha-1}^\alpha y(t)\right) = \lambda \nabla_\alpha^{-\alpha}y(t)) + \lambda \nabla_\alpha^{-\alpha}\xi_t,$$
$$t \in \mathbb{N}_{\alpha+1} \cap [1, T + 1]. \tag{29}$$

Making use of Lemma 2 and Lemma 3 to the left-hand side of (29), we get

$$\nabla_\alpha^{-\alpha}\left(\nabla_{\alpha-1}^\alpha y(t)\right) = \nabla_\alpha^{-\alpha}\left(\nabla_\alpha \nabla_{\alpha-1}^{-(1-\alpha)} y(t)\right),$$

$$= \nabla_\alpha\left(\nabla_\alpha^{-\alpha}\nabla_{\alpha-1}^{-(1-\alpha)} y(t)\right) - \frac{(t - \alpha + 1)^{\overline{\alpha - 1}}}{\Gamma(\alpha)}y(\alpha),$$

$$= y(t) - \frac{(t - \alpha + 1)^{\overline{\alpha - 1}}}{\Gamma(\alpha)}y(\alpha),$$

$$t \in \mathbb{N}_{\alpha+1} \cap [1, T + 1]. \tag{30}$$

It follows from this and equation (29) that

$$y(t) = \frac{(t - \alpha + 1)^{\overline{\alpha - 1}}}{\Gamma(\alpha)}y(\alpha) + \lambda \nabla_\alpha^{-\alpha}y(t) + \lambda \nabla_\alpha^{-\alpha}\xi_t,$$

$$t \in \mathbb{N}_{\alpha+1} \cap [1, T + 1], \tag{31}$$

which is the solution of UFBDE (28).

To derive the solution, we use the Picard approximation recurrence formula with a starting point $y_0(t) = ((t - \alpha + 1)^{\overline{\alpha - 1}}/\Gamma(\alpha))y(\alpha)$ for each $t \in \mathbb{N}_{\alpha-1} \cap [1, T + 1]$. The other components can be determined by using the following recurrence relation:

$$y_j(t) = \frac{(t - \alpha + 1)^{\overline{\alpha - 1}}}{\Gamma(\alpha)}y(\alpha) + \lambda \nabla_\alpha^{-\alpha}y_{j-1}(t) + \lambda \nabla_\alpha^{-\alpha}\xi_t, \tag{32}$$

for $t \in \mathbb{N}_{\alpha+1} \cap [1, T + 1]$ and $j \in \mathbb{N}_1$. Since $\xi_1, \xi_2, \ldots, \xi_{T+1}$ are i.i.d. uncertain variables, we write $\xi_t = \xi$ in distribution. By using Lemma 5, Remark 3, and the fact that the linear combination of finite independent uncertain variables is an uncertain variable with a positive linear combination coefficient (see Theorems 1.21–1.24 of [11]), we can deduce

$$y_1(t) = \frac{(t - \alpha + 1)^{\overline{\alpha - 1}}}{\Gamma(\alpha)}y(\alpha) + \lambda \nabla_\alpha^{-\alpha}y_0(t) + \lambda \nabla_\alpha^{-\alpha}\xi$$

$$= \frac{(t - \alpha + 1)^{\overline{\alpha - 1}}}{\Gamma(\alpha)}y(\alpha)$$

$$+ \lambda\left[\frac{(t - \alpha + 1)^{\overline{2\alpha - 1}}}{\Gamma(2\alpha)} - \frac{(t - \alpha + 1)^{\overline{\alpha - 1}}}{\Gamma(\alpha)}\right]y(\alpha)$$

$$+ \lambda\frac{(t - \alpha)^{\overline{\alpha}}}{\Gamma(\alpha + 1)}\xi,$$

$$y_2(t) = \frac{(t - \alpha + 1)^{\overline{\alpha - 1}}}{\Gamma(\alpha)}y(\alpha) + \lambda \nabla_\alpha^{-\alpha}y_1(t) + \lambda \nabla_\alpha^{-\alpha}\xi$$

$$= \frac{(t - \alpha + 1)^{\overline{\alpha - 1}}}{\Gamma(\alpha)}y(\alpha)$$

$$+ \lambda\left[\frac{(t - \alpha + 1)^{\overline{2\alpha - 1}}}{\Gamma(2\alpha)} - \frac{(t - \alpha + 1)^{\overline{\alpha - 1}}}{\Gamma(\alpha)}\right]y(\alpha)$$

$$+ \lambda^2\left[\frac{(t - \alpha + 1)^{\overline{3\alpha - 1}}}{\Gamma(3\alpha)} - \frac{(t - \alpha + 1)^{\overline{2\alpha - 1}}}{\Gamma(2\alpha)}\right]y(\alpha)$$

$$+ \left[\frac{\lambda(t - \alpha)^{\overline{\alpha}}}{\Gamma(\alpha + 1)} + \frac{\lambda^2(t - \alpha)^{\overline{2\alpha}}}{\Gamma(2\alpha + 1)}\right]\xi,$$

$$\vdots \tag{33}$$

and so on, continuing the process up to the jth term to get

$$y_j(t) = \sum_{k=0}^{j} \lambda^k\left[\frac{(t - \alpha + 1)^{\overline{k\alpha + \alpha - 1}}}{\Gamma((k + 1)\alpha)} - \frac{(t - \alpha + 1)^{\overline{k\alpha - 1}}}{\Gamma(k\alpha)}\right]y(\alpha)$$

$$+ \sum_{k=1}^{j} \lambda^k\frac{(t - \alpha)^{\overline{k\alpha}}}{\Gamma(k\alpha + 1)}\xi, \tag{34}$$

for each $t \in \mathbb{N}_{\alpha+1} \cap [1, T + 1]$. Observe that the two series

$$\sum_{k=0}^{\infty} \lambda^k \left[\frac{(t-\alpha+1)^{\overline{k\alpha+\alpha-1}}}{\Gamma((k+1)\alpha)} - \frac{(t-\alpha+1)^{\overline{k\alpha-1}}}{\Gamma(k\alpha)} \right] = E_{\overline{\alpha,\alpha}}(\lambda, t-\alpha+1) - \lambda E_{\overline{\alpha,\alpha}}(\lambda, t-\alpha+1)$$

$$= (1-\lambda) E_{\overline{\alpha,\alpha}}(\lambda, t-\alpha+1), \tag{35}$$

$$\sum_{k=1}^{\infty} \lambda^k \frac{(t-\alpha)^{\overline{k\alpha}}}{\Gamma(k\alpha+1)} = \lambda E_{\overline{\alpha,\alpha+1}}(\lambda, t-\alpha), \tag{}$$

are absolutely convergent for $|\lambda| < 1$ by the d'Alembert ratio comparison test, and the limitation $\overline{Y}(t) := \lim_{j \to \infty} y_j$ exists. Thus, we have

$$\overline{Y}(t) = \lambda E_{\overline{\alpha,\alpha+1}}(\lambda, t-\alpha)\xi + (1-\lambda) E_{\overline{\alpha,\alpha}}(\lambda, t-\alpha+1) y(\alpha),$$

$$t \in \mathbb{N}_{\alpha+1} \cap [1, T+1]. \tag{36}$$

On the contrary, taking the limit on both sides of (32) yields

$$\overline{Y}(t) = \frac{(t-\alpha+1)^{\overline{\alpha-1}}}{\Gamma(\alpha)} y(\alpha) + \lambda \nabla_{\alpha}^{-\alpha} \overline{Y}(t) + \lambda \nabla_{\alpha}^{-\alpha} \xi_t,$$

$$\tag{37}$$

$$t \in \mathbb{N}_{\alpha+1} \cap [1, T+1].$$

That is, $\overline{Y}(t)$ satisfies equation (31), and hence, $\overline{Y}(t)$ is a solution of equation (25) subject to the initial condition (26). Thus, our proof is completed.

The following theorem provides and confirms the existence and uniqueness of the solution of UFBDEs. □

Theorem 2. *Assume that $G(t,x)$ and $H(t,x)$ satisfy the Lipschitz condition*

$$|G(t,x) - G(t,y)| + |H(t,x) - H(t,y)| \le L|x-y|, \tag{38}$$

and there is a positive number L that satisfies the following inequality:

$$L < \frac{\Gamma(\alpha+1)\Gamma(T+1-\alpha)}{\Gamma(T+1)(Q+1)}, \tag{39}$$

where $Q = |a| \vee |b|$. Then, UFBDE (25) subject to the initial condition (26) has a unique solution $y(t)$ for $t \in \mathbb{N}_{\alpha+1} \cap [1, T+1]$ almost surely.

Proof. Define

$$l_{\alpha}^k := \left\{ x; x = \{x(t)\}_{\alpha+1}^k, k \in \mathbb{N}_1 \right\}, \|x\|,$$

$$:= \max_{t \in \mathbb{N}_{\alpha+1} \cap [1, T+1]} |x(t)|, \tag{40}$$

where $\{x(t)\}_{\alpha+1}^k$ are finite real sequences which have k terms. It is clear that $(l_{\alpha}^k, \|\cdot\|)$ is a Banach space (see [31], Chapter 4). Now, for any $y_t \in l_{\alpha}^k$, we define the operator P as follows:

$$P y_t = \frac{(t-\alpha)^{\overline{\alpha-1}}}{\Gamma(\alpha)} y(\alpha) + \frac{1}{\Gamma(\alpha)} \sum_{r=\alpha+1}^{t} (t-\rho(r))^{\overline{\alpha-1}} \left[G(r, y_r) \right.$$

$$\left. + H(r, y_r)\xi_r \right]. \tag{41}$$

Since ξ_t ($t \in \mathbb{N}_{\alpha+1} \cap [1, T+1]$) is an uncertain variable at each time t with the linear uncertainty distribution $\mathscr{L}(a,b)$, we have $\mathscr{M}\{(\xi_t < a) \cup (\xi_t > b)\} = 0$. The inequality $\xi_t(\gamma) \le Q$ (where $Q = |a| \vee |b|$) holds almost surely for any $\gamma \in \chi\{(\xi_t < a) \cup (\xi_t > b); t \in \mathbb{N}_{\alpha+1} \cap [1, T+1]\}$, where χ represents the universal set on the uncertainty space. Then, by making use of the assumptions and Lemma 5, we have, for any $x_t, y_t \in l_{\alpha}^k$,

$$
\begin{aligned}
\left\| Px_t(\gamma) - Py_t(\gamma) \right\| &= \max_{t \in \mathbb{N}_{\alpha+1} \cap [1,T+1]} \left| Px_t(\gamma) - Py_t(\gamma) \right|, \\[6pt]
&\leq \frac{1}{\Gamma(\alpha)} \max_{t \in \mathbb{N}_{\alpha+1} \cap [1,T+1]} \sum_{r=\alpha+1}^{t} (t - \rho(r))^{\overline{\alpha-1}}, \\[6pt]
&\quad \times \left(\left| G(r, x_r(\gamma) - G(r, y_r(\gamma)) \right| + \left| [H(r, x_r(\gamma) - H(r, y_r(\gamma)] \xi_r \right| \right), \\[6pt]
&\leq \frac{1}{\Gamma(\alpha)} \max_{t \in \mathbb{N}_{\alpha+1} \cap [1,T+1]} \sum_{r=\alpha+1}^{t} (t - \rho(r))^{\overline{\alpha-1}}, \\[6pt]
&\quad \times \left(\left| G(r, x_r(\gamma) - G(r, y_r(\gamma)) \right| + Q \left| H(r, x_r(\gamma) - H(r, y_r(\gamma)) \right| \right), \\[6pt]
&\leq L(1+Q) \frac{1}{\Gamma(\alpha)} \max_{t \in \mathbb{N}_{\alpha+1} \cap [1,T+1]} \sum_{r=\alpha+1}^{t} (t - \rho(r))^{\overline{\alpha-1}} \left| x_r(\gamma) - y_r(\gamma) \right|, \\[6pt]
&\leq L(1+Q) \left\| x_t(\gamma) - y_t(\gamma) \right\| \max_{t \in \mathbb{N}_{\alpha+1} \cap [1,T+1]} \left(\nabla_\alpha^{-\alpha} (t - \alpha)^{\overline{0}} \right), \\[6pt]
&= L(1+Q) \left\| x_t(\gamma) - y_t(\gamma) \right\| \max_{t \in \mathbb{N}_{\alpha+1} \cap [1,T+1]} \left(\frac{1}{\Gamma(\alpha+1)} (t - \alpha)^{\overline{\alpha}} \right), \\[6pt]
&\leq \frac{L(1+Q)(T+1-\alpha)^{\overline{\alpha}}}{\Gamma(\alpha+1)} \left\| x_t(\gamma) - y_t(\gamma) \right\|, \\[6pt]
&= \frac{L(1+Q)\Gamma(T+1)}{\Gamma(\alpha+1)\Gamma(T-\alpha+1)} \left\| x_t(\gamma) - y_t(\gamma) \right\|.
\end{aligned}
\tag{42}
$$

Now, we can observe that the mapping P is a contraction in l_α^k almost surely with $0 < L < (\Gamma(\alpha+1)\Gamma(T-\alpha+1)/(1+Q)\Gamma(T+1))$ (see [31], Chapter 4). Then, by using the Banach contraction mapping theorem (see [31], Chapter 4), we get a unique fixed point $y_t(\gamma)$ of P in l_α^k almost surely. Moreover, $y_t(\gamma) = \lim_{j \to \infty} y_t^j(\gamma)$, where $y_t^j(\gamma) = P(y_t^{j-1}(\gamma))$, with $y_t^0(\gamma) = ((t-\alpha)^{\overline{\alpha-1}}/\Gamma(\alpha)) y(\alpha)$.

For any given $t \in \mathbb{N}_{\alpha+1} \cap [1, T+1]$, as G and H are Lipschitz continuous functions, the operator P is measurable. Since $y_t^1(\gamma), y_t^2(\gamma), \ldots, y_t^j(\gamma), \ldots$ are uncertain variables and $y_t^0(\gamma)$ is a real-valued measurable function of uncertain variables, $y_t^0(\gamma)$ is an uncertain variable by [11], Theorem 1.10. Hence, $y_t = \lim_{j \to \infty} y_t^j$ is an uncertain variable (see [21], Theorem 3).

Consequently, UFBDE (25) with i.c. (26) has a unique solution y_t for $t \in \mathbb{N}_{\alpha+1} \cap [1, T+1]$ almost surely. □

4. Example Illustrations

This section deals with some examples to confirm the validity of Theorem 2.

Example 3. Consider the following UFBDE:

$$
\nabla_{(-1/2)}^{(1/2)} y(t) = \begin{cases} \dfrac{\ln(|y(t)| + 1)}{2t^3} + 0.5\xi_t, & t \in \mathbb{N}_1 \cap [1,4], \\[10pt] y\left(\dfrac{1}{2}\right) = 1, \end{cases}
\tag{43}
$$

where $\xi_1, \ldots, \xi_4$ are four i.i.d. uncertain variables with uncertainty distribution $\mathscr{L}(-1, 2)$.

According to Lemma 6 with $\alpha = (1/2)$, the inverse uncertainty distribution of the solution for UFBDE (43) is the solution of the following sum equation:

$$
y(t) = \frac{(t + (1/2))^{\overline{-0.5}}}{\Gamma(0.5)} y(\alpha) + \frac{1}{\Gamma(0.5)} \sum_{r=(3/2)}^{t} (t - \rho(r))^{\overline{-0.5}}
$$

$$
\cdot \left(\frac{\ln(|y(r)| + 1)}{4r^3} + 0.25\xi_r \right), \quad t \in \mathbb{N}_{0.5} \cap [1,4].
\tag{44}
$$

Then, for $t \in \mathbb{N}_{0.5} \cap [1, 4]$, we have

$$
\begin{aligned}
|G(t, x) - G(t, y)| + |H(t, x) - H(t, y)| &= \left| \frac{\ln(|x| + 1)}{2t^3} - \frac{\ln(|y| + 1)}{2t^3} \right|, \\
&= \frac{1}{2t^3} |\ln(|x| + 1) - \ln(|y| + 1)|, \\
&\leq \frac{1}{2(3/2)^3} \|x| - |y\| \leq \frac{4|x - y|}{27},
\end{aligned}
\tag{45}
$$

$$
\frac{\Gamma(0.5 + 1)\Gamma(4 + 1 - 0.5)}{3\Gamma(4 + 1)} \approx 0.1636 > \frac{4}{27} = 0.1481.
$$

Thus, UFBDE (43) has a unique solution almost surely by Theorem 2.

Example 4. We consider the following UFBDE:

$$
\nabla^{0.25}_{-0.25} y(t) = \frac{y^2 t}{40} + \xi_t, \quad t \in \mathbb{N}_1 \cap [1, 4],
\tag{46}
$$

where $\xi_1, \xi_2, \xi_3, \xi_4$ are four i.i.d. linear uncertain variables with linear uncertainty distribution $\mathscr{L}(-3, 3)$.

According to Lemma 6 with $\alpha = (1/4)$, the inverse uncertainty distribution of the solution for UFBDE (46) is the solution of the following sum equation:

$$
\begin{aligned}
y(t) = {} & \frac{(t + (1/2))^{\overline{-(3/4)}}}{\Gamma(0.25)} y(\alpha) \\
& + \frac{1}{\Gamma(0.25)} \sum_{r=1.25}^{t} (t - \rho(r))^{\overline{-(3/4)}} \left(\frac{y^2 r}{40} + \xi_r \right).
\end{aligned}
\tag{47}
$$

Observe that $|G(t, x) - G(t, y)| + |H(t, x) - H(t, y)|$ is Lipschitz-continuous in $[-20, 20]$ with Lipschitz constant 0.1 as follows:

$$
\begin{aligned}
|G(t, x) - G(t, y)| + |H(t, x) - H(t, y)| &\leq \frac{1}{40} |x + y| |x - y| \\
&= 0.1 |x - y|.
\end{aligned}
\tag{48}
$$

Also, we have

$$
\frac{\Gamma(0.25 + 1)\Gamma(3 + 1 - 0.25)}{4\Gamma(3 + 1)} \approx 0.167 > 0.1.
\tag{49}
$$

Consequently, UFBDE (50) has a unique solution almost surely by Theorem 2.

Example 5. Consider the following UFBDE:

$$
\nabla^{0.5}_{-0.5} y(t) = \frac{\sin(ty)}{10 + t^2} + 0.1\xi_t, \quad t \in \mathbb{N}_1 \cap [1, 4],
\tag{50}
$$

where $\xi_1, \xi_2, \xi_3, \xi_4$ are 4 i.i.d. linear uncertain variables with linear uncertainty distribution $\mathscr{L}(-1, 1)$.

According to Lemma 6 with $\alpha = (1/2)$, the inverse uncertainty distribution of the solution for UFBDE (50) is the solution of the following sum equation:

$$
\begin{aligned}
y(t) = {} & \frac{(t + (1/2))^{\overline{-0.5}}}{\sqrt{\pi}} y(\alpha) \\
& + \frac{1}{\sqrt{\pi}} \sum_{r=1.5}^{t} (t - \rho(r))^{\overline{-0.5}} \left(\frac{\sin(ry)}{10 + r^2} + 0.1\xi_r \right).
\end{aligned}
\tag{51}
$$

Then, we can directly verify that

$$
|G(t, x) - G(t, y)| + |H(t, x) - H(t, y)| \leq \frac{1}{10} |x - y|,
$$

$$
\frac{\Gamma(0.5 + 1)\Gamma(3 + 1 - 0.5)}{2\Gamma(3 + 1)} \approx 0.2454 > \frac{1}{10} = 0.1.
\tag{52}
$$

Consequently, UFBDE (50) has a unique solution almost surely by Theorem 2.

5. Conclusion

We have presented analytical solutions to a special type of linear UFBDEs. Moreover, a Lipschitz condition with its constant is given to provide a unique solution almost surely to an UFBDE. It can be seen that our obtained results pave the way for the future works, that is, to investigate the stability analysis and applications of UFBDEs.

Data Availability

No data were used to support this study.

Conflicts of Interest

The authors declare that they have no conflicts of interest.

Authors' Contributions

All authors contributed equally and significantly to writing this article. All authors read and approved the final manuscript.

Acknowledgments

References

[1] K. S. Miller and B. Ross, *An Introduction to the Fractional Calculus and Fractional Differential Equations*, John Wiley & Sons, New York, NY, USA, 1993.

[2] I. Podlubny, *Fractional Differential Equations*, Academic Press, San Diego, CA, USA, 1999.

[3] A. A. Kilbas, H. M. Srivastava, and J. J. Trujillo, *Theory and Applications of Fractional Differential Equations*, Elsevier B.V., Amsterdam, Netherlands, 2006.

[4] K. Diethelm, *The Analysis of Fractional Differential Equations*, Springer, Berlin, Germany, 2010.

[5] F. K. Hamasalh and P. O. Muhammad, "Generalized quartic fractional spline interpolation with applications," *International Journal of Open Problems in Computer Science and Mathematics*, vol. 8, no. 1, pp. 67–80, 2015.

[6] F. K. Hamasalh and P. O. Muhammed, "Computational method for fractional differential equations using non-polynomial fractional spline," *Mathematical Sciences Letters*, vol. 5, no. 2, pp. 131–136, 2016.

[7] R. Almeida, N. R. O. Bastos, and M. T. T. Monteiro, "Modeling some real phenomena by fractional differential equations," *Mathematical Methods in the Applied Sciences*, vol. 39, no. 16, pp. 4846–4855, 2016.

[8] M. Martinez, P. O. Mohammed, and J. E. N. Valdes, "Non-conformable fractional Laplace transform," *Kragujevac Journal of Mathematics*, vol. 46, no. 3, pp. 341–354, 2022.

[9] P. O. Mohammed and M. Z. Sarikaya, "On generalized fractional integral inequalities for twice differentiable convex functions," *Journal of Computational and Applied Mathematics*, vol. 372, Article ID 112740, 2020.

[10] M. Bohner and A. C. Peterson, *Advances in Dynamic Equations on Time Scales*, Birkhauser, Boston, MA, USA, 2003.

[11] B. Liu, *Uncertainty Theory: A Branch of Mathematics for Modeling Human Uncertainty*, Springer, Berlin, Germany, 2010.

[12] C. Goodrich and A. Peterson, *Discrete Fractional Calculus*, Springer, Berlin, Germany, 2015.

[13] F. Atici and P. Eloe, "A transform method in discrete fractional calculus," *IJDE*, vol. 2, no. 2, pp. 165–176, 2007.

[14] F. Atici and P. Eloe, "Initial value problems in discrete fractional calculus," *Proceedings of the American Mathematical Society*, vol. 137, no. 3, pp. 981–989, 2009.

[15] C. S. Goodrich, "Existence of a positive solution to a system of discrete fractional boundary value problems," *Applied Mathematics and Computation*, vol. 217, no. 9, pp. 4740–4753, 2011.

[16] G.-C. Wu and D. Baleanu, "Discrete chaos in fractional delayed logistic maps," *Nonlinear Dynamics*, vol. 80, no. 4, pp. 1697–1703, 2015.

[17] G.-C. Wu, D. Baleanu, and W.-H. Luo, "Lyapunov functions for Riemann-Liouville-like fractional difference equations," *Applied Mathematics and Computation*, vol. 314, pp. 228–236, 2017.

[18] I. Suwan, T. Abdeljawad, and F. Jarad, "Monotonicity analysis for nabla *h*-discrete fractional Atangana-Baleanu differences," *Chaos, Solitons & Fractals*, vol. 117, pp. 50–59, 2018.

[19] T. Abdeljawad and D. Baleanu, "Monotonicity analysis of a nabla discrete fractional operator with discrete Mittag-Leffler kernel," *Chaos Solitons & Fractals*, vol. 116, pp. 1–5, 2017.

[20] Y. Zhu, "Uncertain fractional differential equations and an interest rate model," *Mathematical Methods in the Applied Sciences*, vol. 38, no. 15, pp. 3359–3368, 2015.

[21] Y. Zhu, "Existence and uniqueness of the solution to uncertain fractional differential equation," *Journal of Uncertainty Analysis and Applications*, vol. 3, pp. 1–11, 2015.

[22] Z. Lu and Y. Zhu, "Numerical approach for solution to an uncertain fractional differential equation," *Applied Mathematics and Computation*, vol. 343, pp. 137–148, 2019.

[23] J. W. He, L. Zhang, Y. Zhou, and B. Ahmad, "Existence of solutions for fractional difference equations via topological degree methods," *Advances in Difference Equations*, vol. 2018, p. 153, 2018.

[24] P. O. Mohammed, "A generalized uncertain fractional forward difference equations of Riemann-Liouville type," *Journal of Mathematics Research*, vol. 11, no. 4, pp. 43–50, 2019.

[25] Q. Lu, Y. Zhu, and Z. Lu, "Uncertain fractional forward difference equations for Riemann–Liouville type," *Advances in Difference Equations*, vol. 2019, p. 147, 2019.

[26] T. Abdeljawad, "On delta and nabla caputo fractional differences and dual identities," *Discrete Dynamics in Nature and Society*, vol. 2013, Article ID 406910, 12 pages, 2013.

[27] T. Abdeljawad, F. Jarad, and J. Alzabut, "Fractional proportional differences with memory," *The European Physical Journal Special Topics*, vol. 226, no. 16–18, pp. 3333–3354, 2017.

[28] T. Abdeljawad, "Different type kernel *h*−fractional differences and their fractional *h*−sums," *Chaos, Solitons & Fractals*, vol. 116, pp. 146–156, 2018.

[29] T. Abdeljawad and F. M. Atici, "On the definitions of nabla fractional operators," *Abstract and Applied Analysis*, vol. 2012, Article ID 406757, 13 pages, 2012.

[30] F. Atici and P. Eloe, "Gronwall's inequality on discrete fractional calculus," *Computers & Mathematics with Applications*, vol. 64, pp. 3193–3200, 2012.

[31] P. Sacks, *Techniques of Functional Analysis for Differential and Integral Equations*, Academic Press, London, UK, 2017.